

Michael Mains · Brandon J. Dilworth *Editors*

Topics in Modal Analysis & Testing, Volume 9

Proceedings of the 36th IMAC, A Conference and
Exposition on Structural Dynamics 2018



Conference Proceedings of the Society for Experimental Mechanics Series

Series Editor

Kristin B. Zimmerman, Ph.D.
Society for Experimental Mechanics, Inc.,
Bethel, CT, USA

More information about this series at <http://www.springer.com/series/8922>

Michael Mains • Brandon J. Dilworth
Editors

Topics in Modal Analysis & Testing, Volume 9

Proceedings of the 36th IMAC, A Conference and Exposition
on Structural Dynamics 2018

Editors

Michael Mains
Suite 310
Brüel & Kjær North America
Duluth, GA, USA

Brandon J. Dilworth
Massachusetts Institute of Technology
Lincoln Laboratory
Lexington, MA, USA

ISSN 2191-5644 ISSN 2191-5652 (electronic)
Conference Proceedings of the Society for Experimental Mechanics Series
ISBN 978-3-319-74699-9 ISBN 978-3-319-74700-2 (eBook)
<https://doi.org/10.1007/978-3-319-74700-2>

Library of Congress Control Number: 2018942655

© The Society for Experimental Mechanics, Inc. 2019

This work is subject to copyright. All rights are reserved by the Publisher, whether the whole or part of the material is concerned, specifically the rights of translation, reprinting, reuse of illustrations, recitation, broadcasting, reproduction on microfilms or in any other physical way, and transmission or information storage and retrieval, electronic adaptation, computer software, or by similar or dissimilar methodology now known or hereafter developed.

The use of general descriptive names, registered names, trademarks, service marks, etc. in this publication does not imply, even in the absence of a specific statement, that such names are exempt from the relevant protective laws and regulations and therefore free for general use.

The publisher, the authors and the editors are safe to assume that the advice and information in this book are believed to be true and accurate at the date of publication. Neither the publisher nor the authors or the editors give a warranty, express or implied, with respect to the material contained herein or for any errors or omissions that may have been made. The publisher remains neutral with regard to jurisdictional claims in published maps and institutional affiliations.

Printed on acid-free paper

This Springer imprint is published by the registered company Springer International Publishing AG part of Springer Nature.
The registered company address is: Gewerbestrasse 11, 6330 Cham, Switzerland

Preface

Topics in Modal Analysis & Testing represents one of nine volumes of technical papers presented at the 36th IMAC, A Conference and Exposition on Structural Dynamics, organized by the Society for Experimental Mechanics, and held in Orlando, Florida, February 12–15, 2018. The full proceedings also include volumes on Nonlinear Dynamics; Dynamics of Civil Structures; Model Validation and Uncertainty Quantification; Dynamics of Coupled Structures; Special Topics in Structural Dynamics; Structural Health Monitoring, Photogrammetry & DIC; Rotating Machinery, Vibro-Acoustics and Laser Vibrometry; and Sensors and Instrumentation, Aircraft/Aerospace and Energy Harvesting.

Each collection presents early findings from experimental and computational investigations on an important area within Structural Dynamics. *Topics in Modal Analysis & Testing* represents papers on enabling technologies for Modal Analysis measurements and applications of Modal Analysis in specific application areas.

The organizers would like to thank the authors, presenters, session organizers, and session chairs for their participation in this track.

Brüel & Kjær North America, Duluth, GA, USA
MIT Lincoln Laboratory, Lexington, MA, USA

Michael Mains
Brandon J. Dilworth

Contents

1	Stochastic Modal Appropriation (SMA)	1
	M. Abdelghani and M. I. Friswell	
2	Derivation of Six Degree of Freedom Shaker Inputs Using Sub-structuring Techniques	5
	T. F. Schoenherr	
3	Forced Response of 2-Dof Gyroscopic Systems with Stable Eigenvalues	15
	O. Giannini	
4	Modal Testing of a Composite Bladed Disc Using Travelling Wave Excitation Method	25
	D. Di Maio, M. Vater, R. Seidel, and S. Foglia	
5	Simulation of the Dynamic Behavior of a Bi-Cable Ropeway with Modal Bases	43
	Gabriel Hurel, Jerome Laborde, and Louis Jézéquel	
6	Influence of Noise in Correlation Function Estimates for Operational Modal Analysis	55
	Esben Orlowitz and Anders Brandt	
7	Comparison of Two (Geometric) Algorithms for Auto OMA	65
	Martin Juul, Peter Olsen, Ole Balling, Sandro Amador, and Rune Brincker	
8	Operational Modal Analysis on Wind Turbine Hub	69
	Martin Juul, Ole Balling, and Rune Brincker	
9	The Influence of Edge Boundary Conditions and Cracks on Vibrational Modes of Multilayer Ceramic Capacitors	79
	Jonel Ortiz, Giuliana Davis, Kevin Troyer, and Paul Heyliger	
10	The Cross Spectrum in Multiple Input Multiple Response Vibration Testing	91
	Norman F. Hunter, Kevin R. Cross, and Garrett Nelson	
11	A Systematic Evaluation of Test Specification Derivation Methods for Multi-axis Vibration Testing	103
	Garrett Nelson	
12	Designing Hardware for the Boundary Condition Round Robin Challenge	119
	David E. Soine, Richard J. Jones, Julie M. Harvie, Troy J. Skousen, and Tyler F. Schoenherr	
13	Modal Comparison of Stock and Performance Brake Rotors	127
	Kaitlin Spak	
14	On the Veering Phenomenon Potential in High Speed Gears Design	135
	Carlo Rosso, Elvio Bonisoli, and Fabio Bruzzone	
15	Modal Truncation in Experimental Modal Analysis	143
	Marius Tarpø, Michael Vigsø, and Rune Brincker	
16	Combined Mechanical Environments for Design and Qualification	153
	Brian C. Owens and Julie M. Harvie	

17	Comparing Free-Free and Shaker Table Model Correlation Methods Using Jim Beam	165
	James Ristow, Kenneth Wayne Smith, Jr., Nathaniel Johnson, and Jackson Kinney	
18	Real-Time Hybrid Testing: Challenges and Experiences from a Teaching Point of View	175
	Markus J. Hochrainer	
19	Comparison of Computational Generalized and Standard Eigenvalue Solutions of Rotating Systems	187
	Ali Tatar, Loic Salles, Alexander H. Haslam, and Christoph W. Schwingshackl	
20	Residual States for Modal Models Identified from Accelerance Data	195
	Mladen Gibanica, Thomas J. S. Abrahamsson, and Randall J. Allemang	
21	Comparison of Time-Domain Objective Functions in Dynamic Fixture Optimization	207
	Michael J. Starr and Timothy Walsh	
22	Advanced Hammer Excitation Technique for Impact Modal Testing on Lightweight Materials Using Scalable Automatic Modal Hammer	211
	Tarun Teja Mallareddy, Sarah Schneider, and Peter G. Blaschke	
23	Evaluation of MIMO Input Derivations and Their Physical Context	217
	Arup Maji	
24	Using Modal Substructuring to Improve Shock & Vibration Qualification	227
	Julie M. Harvie	
25	Off-Axis Input Characterization of Random Vibration Laboratory Data for Model Credibility	241
	Jill Blecke, James Freymiller, and Michael Ross	
26	Modal Analysis of a Brake-Ruess Beam and Computational Modeling at the Undergraduate Level	249
	Aaron J. Misla, Curtis J. O'Malley, and Siavash Norouzi	
27	A Primer on Multiple Degree of Freedom Vibration Test for Aerospace and Military Applications	253
	Luke A. Martin	
28	A Study on the Generation and Propagation of Traveling Waves in Strings	257
	Isil Anakok, V. V. N. Sriram Malladi, and Pablo A. Tarazaga	
29	A Color-Coded Complex Mode Indicator Function for Selecting a Final Mode Set	263
	Randy L. Mayes and Daniel P. Rohe	
30	Using Manual Excitation for Large Displacement on a Highly Damped System	271
	Douglas J. Osterholt and David E. Cloutier	
31	Traveling Wave Generation on a Clamped, Thin Plate with Flush-Mounted Piezoelectric Actuators	283
	Patrick F. Musgrave, Mohammad I. Albakri, and Pablo A. Tarazaga	
32	Experimental Modal Analysis of an Aircraft Fuselage Panel: Part II	289
	Travis A. Wyen, Ricardo A. Perez, Jonathan Knox, Joshua J. Schoettelkotte, and Thomas G. Eason	
33	Combining Virtual Simulation with Hands-on Experiments for Teaching Mechanical Vibrations	299
	Changrui Bai and Surendra (Suri) Ganeriwala	
34	Finite Element Model Updating Using the Local Correspondence Principle	309
	Sandro Amador, Martin Juul, Tobias Friis, and Rune Brincker	
35	Approximate General Responses of Tuned and Mistuned 4-Degree-of-Freedom Systems with Parametric Stiffness	315
	Ayse Sapmaz, Gizem D. Acar, and Brian F. Feeny	
36	Modal Analysis of a Vertical-Axis Darrieus Wind Turbine Blade with a Troposkein Shape	325
	Amr Saleh and Brian F. Feeny	
37	Floquet-Type Analysis of Transient Vibrations of a Horizontal Axis Wind Turbine	329
	Gizem D. Acar and Brian F. Feeny	

38	Evaluation of Traveling Wave Models for Carangiform Swimming Based on Complex Modes	335
	Mahdiah Tanha and Brian F. Feeny	
39	Application of Frequency Domain Decomposition Identification Technique to Half Spectral Densities	343
	Sandro Amador, Martin Ørum, Tobias Friis, and Rune Brincker	
40	Modal Survey of the MPCV Orion European Service Module Structural Test Article Using a Multi-axis Shake Table	347
	James P. Winkel, James C. Akers, Vicente J. Suarez, Lucas D. Staab, and Kevin L. Napolitano	
41	Modal Analysis of Healthy and Cracked Isotropic Plates in Peridynamics	359
	Andris Freimanis and Ainārs Paeglītis	
42	Initial Modal Results and Operating Data Acquisition of Shock/Vibration Fixture	363
	William Larsen, Jason R. Blough, James P. DeClerck, Charles D. VanKarsen, David E. Soine, and Richard Jones	
43	Effects of Variable Thickness Circular Plates on Frequency Response Functions and Shock Response Spectrum	371
	William Larsen, Jason R. Blough, James DeClerck, Charles VanKarsen, David Soine, and Richard Jones	
44	Inverse Force Estimation for Resonant Shock Plate Application	381
	William Larsen, Jason R. Blough, James DeClerck, Charles VanKarsen, David Soine, and Richard Jones	

Chapter 1

Stochastic Modal Appropriation (SMA)

M. Abdelghani and M. I. Friswell

Abstract All available modal identification algorithms (for example SSI, FDD, ARMA) are based on the principle of subspaces in the sense that the pole is identified which characterizes the signal subspace and the noise subspace is taken automatically as its orthogonal complement. This is a response type characterization. For structural dynamics applications however, one is interested in different subspaces, namely the non-conservative subspace and the conservative subspace. The only currently available method that does this is the force appropriation method for in-laboratory testing. In this work, we propose an In-Operation structural identification algorithm based on a different principle, namely the anti-symmetry principle. The idea is as follows: Consider the response of a structure. Construct the anti-symmetric response depending on a certain unknown parameter and consider the resultant of both. This introduces a rotation to the original signal. By varying the parameter, one spans a lot of different subspaces and by proper (mathematically derived) operations on these subspaces and the original one it is possible to cancel out one subspace leaving the data in a single subspace from which the proper parameters can be estimated. This idea is formulated mathematically for a SDOF system subject to unmeasured white noise excitation and it is shown that it provides highly accurate modal parameter estimates.

1.1 Introduction

In-Operation Modal Analysis (OMA) is a good complement to the classical modal testing methods where the structure is installed in a laboratory and tested under well controlled conditions. For in-operation structures the excitation is unknown, of complex nature, diffuse and cannot be measured. Examples are offshore structures under swell, airplanes under turbulence, and bridges under traffic.

Several algorithms have been proposed to solve this problem. Examples are the Stochastic Subspace Algorithms (SSI), the frequency domain algorithm (FDD), and ARMA. These algorithms rely mostly on the identification of the pole part of the system. This is a response type characterization and the identification of the modal parameters is done in a second step. In structural dynamics however, one is interested in different subspaces, namely the conservative subspace and the con-conservative one. This is done with Modal Appropriation algorithms for in-laboratory testing. The INOPMA algorithm [1] proposed recently by the author is an attempt to do that for In-operation structures. The mode is however isolated not at its natural frequency but at a different frequency that depends on damping. This may be considered as a limitation of this algorithm.

In this paper we overcome this difficulty and propose a new algorithm (SMA) that isolates the mode at exactly its natural frequency using output correlations only. The algorithm is developed on a SDOF system and it is validated on a simulated SDOF system excited with white noise.

1.2 The SMA Algorithm

We elaborate in this section the theory behind the SMA algorithm on a Single Degree Of Freedom (SDOF) system. The extension to the Multi Degree of Freedom (MDOF) Systems will be treated elsewhere.

M. Abdelghani (✉)
University of Sousse, Sousse, Tunisia

M. I. Friswell
College of Engineering, University of Swansea, Bay Campus, Swansea, UK
e-mail: M.I.Friswell@swansea.ac.uk

Consider a SDOF system excited with unmeasured white noise. The impulse response of the system may be written as [3]:

$$h(t) = C_h e^{-\xi \omega_n t} \sin(\omega_d t) \quad (1.1)$$

where ξ is the system damping ratio, ω_n is the system natural frequency and ω_d is the damped natural frequency.

The correlation sequence of the system output may be written as [3]:

$$R(t) = C_r e^{-\xi \omega_n t} \sin(\omega_d t - \phi(\xi)) \quad (1.2)$$

where $\phi(\xi)$ is a phase shift that depends on the damping ratio. Both the impulse response and the correlation sequence can be considered as rotating vectors in the complex plane but with decaying amplitudes (spirals).

In the INOPMA algorithm [1], the correlation sequence was assumed to be an impulse response. This has led to the fact that the mode is isolated at a frequency $\omega^* = \omega_n \sqrt{1 - 4\xi^2}$ and not the natural frequency ω_n . This may be considered as a limitation of INOPMA. In this work we overcome this limitation and we show that it is still possible to isolate the mode at its natural frequency.

Let $\bar{R}(t, \alpha)$ be the image of $R(t)$ by a linear anti-symmetric function that depends on a certain design parameter α and consider the following sequence:

$$H(t, \alpha) = R(t) + \bar{R}(t, \alpha) \quad (1.3)$$

$H(t, \alpha)$ is then a rotation and stretching of the sequence $R(t)$. By varying α , it is possible to modify the phase shift as well as the amplitude of the correlation sequence and hence modify the damping ratio leading to a pure sinusoid. At this stage the mode is isolated.

In this work, we consider the following anti-symmetric function:

$$F(R(t), \alpha) = j\alpha R(t) \quad (1.4)$$

The SMA algorithm is similar to the INOPMA algorithm in the sense that one takes the convolution of the modified correlation sequence with a harmonic force with varying frequency.

In the frequency domain this means that the system transfer function (the Laplace transform of the correlation sequence) is multiplied by a complex factor $(1 + j\alpha)$. It can easily be shown that the transfer function phase angle is zero exactly at the following condition:

$$\begin{cases} \omega = \omega_n \\ \alpha = 2\xi \end{cases}$$

Geometrically this means that when the mode is isolated the vector representing the correlation sequence describes a circle meaning that the conservative part of the system is isolated. The non-conservative part follows immediately. Hence the system natural frequency as well as the damping ratio are identified at the same step.

1.3 Simulation Validation

We consider in this section the validation of the SMA algorithm on a SDOF system excited with white noise. The considered system parameters are taken as $m = 2$ kg, $k = 10,000$ N/m and $c = 8$ Ns/m. The excitation is a white noise with unit variance. This leads to the following modal parameters; $\omega_n = 11.254$ Hz and $\xi = 2.83\%$. The output is then simulated using a sampling frequency of $F_s = 64$ Hz and 2% measurement noise is added to the output.

The fundamental step in SMA is the computation of the output correlation sequence. Given the random nature of the output signal as well as its finite sample length, computing the correlation sequence using direct computation can lead to errors. Instead, the output spectrum is carefully estimated and the correlation sequence is taken as its Inverse Fourier Transform (IFFT). This leads to better estimates. A total of 512 time lags were computed (see Fig. 1.1). The number of lags can be considered as a design parameter. We consider here the following number of lags: 64, 128, 256 and 512. For a considered lag, the convolution of the modified correlation sequence (\bar{R}) with a harmonic force at varying frequency is then computed. In order to identify the modal parameters, the alpha parameter is varied from 0.1 to 0.3 with a resolution of 0.01. At each value of alpha, the frequency is varied from 10 to 12 Hz and the phase shift between the input and output is computed. This leads to a set of angle values, and when the angle crosses zero the mode is isolated (see Fig. 1.2). In order to study the effect

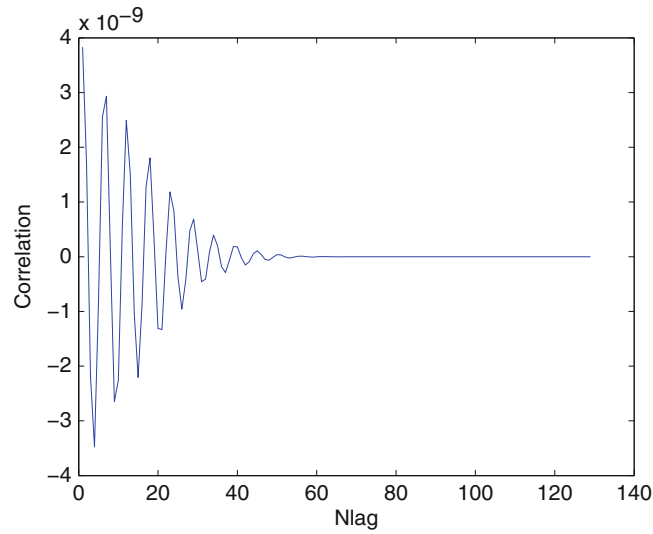


Fig. 1.1 The correlation sequence

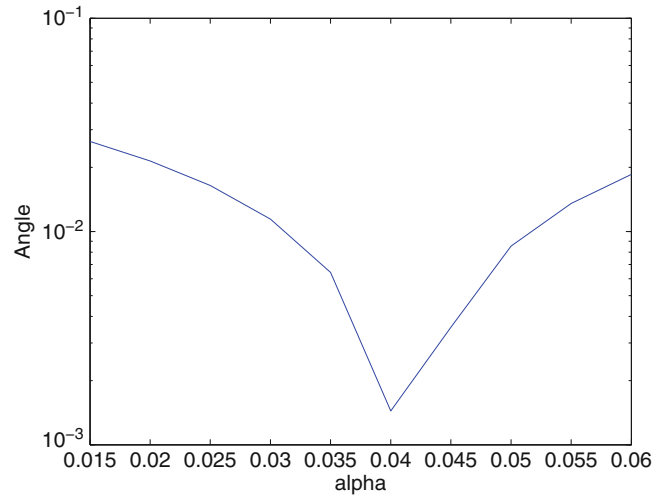


Fig. 1.2 The phase angle vs. the α value

Table 1.1 The modal model for different correlation lags

Nlag	ω_n (Hz)	ξ (%)
64	11.2	1.85
128	11.2	2.5
256	11	2.15
512	11.4	2.25

of the number of lags, the identified modal parameters for each lag are computed and the results are reported in Table 1.1. In this case the frequency resolution used is 0.1 Hz and that of α is 0.5%. Another design parameter is the resolution on the α parameter which is directly related to that of the damping ratio. The results for different resolutions are reported in Table 1.2. These results are for a single sample of the noise and the variability observed is expected. With SMA the correlation sequence is a truncated version of the true one. If the number of time lags Nlag is too small the mode has not decayed enough and if it is too big noise is included. By taking its convolution with a pure sine wave this will affect the resulting sinusoid phase shift (noisy) as well as the smoothness of its amplitude. By varying α and its resolution there will be a value for which the mode is isolated. At this stage the conservative part of the system is isolated (a circle) and hence the frequency is robustly estimated. The non-conservative part is the remaining part which also contains noise leading to less robust estimates (the damping ratio is proportional to α).

Table 1.2 The effect of the resolution of α on the modal model

α resolution (%)	ω_n (Hz)	ξ (%)
1	11.2	2.5
0.7	11.3	2.15
0.5	11.3	2
0.1	11.38	2.25

1.4 Conclusion

We proposed in this paper a new In-Operation modal identification algorithm based on modal appropriation ideas. Unlike the INOPMA algorithm [1] that isolates the mode at a frequency that depends on the damping ratio, the present algorithm (SMA) isolates the mode at exactly the system natural frequency. The damping ratio is identified at the same step. This makes modal appropriation possible using data correlations as an impulse response. The algorithm is validated on a SDOF system excited with white noise and good results were obtained. The extension of this algorithm to the MDOF case, as well as its experimental validation, is on-going.

References

1. Abdelghani, M., Inman, D.J.: Modal appropriation for use with in-operation modal analysis. *J Shock Vib.* **2015**, 537030 (2015)
2. Balmès, E., Chapelier, C., Lubrina, P., Fargette, P.: An evaluation of modal testing results based on the force appropriation method. *International Modal Analysis Conference, Orlando* (1996).
3. Meirovitch, L.: *Elements of Vibration Analysis*. McGraw-Hill, New York (1986)

Chapter 2

Derivation of Six Degree of Freedom Shaker Inputs Using Sub-structuring Techniques

Tyler F. Schoenherr

Abstract Multi-degree of freedom testing is growing in popularity and in practice. This is largely due to its inherent benefits in producing realistic stresses that the test article observes in its working environment and the efficiency of testing all axes at one time instead of individually. However, deriving and applying the “correct” inputs to a test has been a challenge. This paper explores a recently developed theory into deriving rigid body accelerations as an input to a test article through sub-structuring techniques. The theory develops a transformation matrix that separates the complete system dynamics into two sub-structures, the test article and next level assembly. The transformation does this by segregating the test article’s fixed base modal coordinates and the next level assembly’s free modal coordinates. This transformation provides insight into the damage that the test article acquires from its excited fixed base shapes and how to properly excite the test article by observing the next level assembly’s rigid body motion. This paper examines using next level assembly’s rigid body motion as a direct input in a multi-degree of freedom test to excite the test article’s fixed base shapes in the same way as the working environment.

2.1 Introduction

Performing tests in a laboratory setting provides benefits to proving a product will perform as designed. Two benefits are cost and time. They are saved by not performing field tests to prove design intent for a product. The ability to replicate failures experienced in the field quickly and accurately in a laboratory during the design phase also saves a development program time and money. Last, laboratory tests provide the opportunity to test the product’s margin to determine the product’s true factor of safety.

All of these benefits of laboratory testing is contingent on the laboratory test accurately producing the same strain and stress values that the product would experience in the field. The ability to replicate the field stress and strain values has proved over many years to be a very difficult task. Through the years, this task has been separated into two separate issues. The first is how to replicate the correct boundary conditions as to force the stress and strain fields to represent the field environment. The second issue is how to develop the forcing input to excite the structure to produce the same responses and consequentially the same stresses. Examples of complicated inputs could be multi-degree of freedom inputs at several mounting locations and acoustical loading. Some recent work has been done to address complicated forcing inputs [1, 2]. This paper will address how to form a set of six degree of freedom forcing inputs to a test article using sub-structuring techniques.

This paper demonstrates theory developed by Mayes [3] for a realistic complex system. It demonstrates how to take a modal model of the unit under test (UUT) connected to its next level assembly (NLA) and transform its coordinates to gain insight on stress that the UUT experiences and the rigid body inputs that are needed to cause those stresses.

To explore and demonstrate this theory, a finite element model of the Box Assembly with Removable Component (BARC) hardware is used. The paper demonstrates the process of how a six degree of freedom (DOF) input to the removable component is derived to replicate the environment it experiences when it was attached to the box assembly. This paper discusses the results with respect to the process’s shortcomings and successes and draws conclusions to their causes and effects.

Sandia National Laboratories is managed by NTESS.

T. F. Schoenherr (✉)

Analytical Structural Dynamics, Sandia National Laboratories, Albuquerque, NM, USA

e-mail: tfschoe@sandia.gov

2.2 Theory

The theory in this section is presented with respect to the BARC hardware referenced in the Introduction with a picture of the hardware shown in Fig. 2.1. As in any sub-structuring problem, the different members must be identified and assigned names for clarity. Figure 2.1 provides a breakout of the different parts of the sub-structure and their corresponding names that is used throughout this paper.

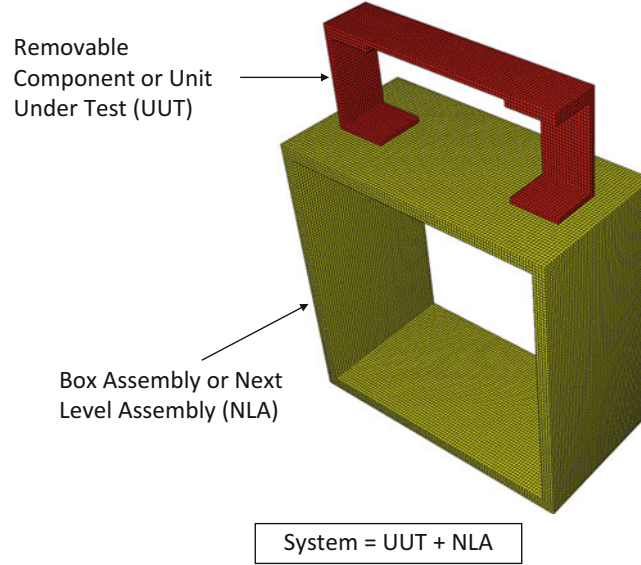


Fig. 2.1 Pictorial of the BARC system

The derivation of this theory starts with the 2nd order linear equations of motion of the NLA and the UUT assembled as a system,

$$\mathbf{M}_s \ddot{\bar{x}} + \mathbf{C}_s \dot{\bar{x}} + \mathbf{K}_s \bar{x} = \bar{F}_s, \quad (2.1)$$

where \mathbf{M}_s is the mass matrix, \mathbf{C}_s the damping matrix, and \mathbf{K}_s the stiffness matrix. The subscript s indicates the matrices are from the system. Modal substitution is used to estimate the physical response with modal degrees of freedom shown by

$$\phi \bar{q} \approx \bar{x}, \quad (2.2)$$

where ϕ is the mode shapes of the system and \bar{q} is the generalized modal coordinates. The modal approximation shown in Eq. 2.2 is substituted into Eq. 2.1 and premultiplied by ϕ^T to get

$$\phi^T \mathbf{M}_s \phi \ddot{\bar{q}} + \phi^T \mathbf{C}_s \phi \dot{\bar{q}} + \phi^T \mathbf{K}_s \phi \bar{q} = \phi^T \bar{F}. \quad (2.3)$$

Scaling the mode shapes to be mass normalized allows Eq. 2.3 to be rewritten in terms of the system's modal parameters as

$$[-\omega^2 \mathbf{I} + 2i\omega \omega_n \boldsymbol{\zeta} + \omega_n^2] \bar{q} = \phi^T \bar{F}, \quad (2.4)$$

where ω is the frequency in radians, ω_n is the diagonal matrix of natural frequencies corresponding to each mode, \mathbf{I} is the identity matrix, and $\boldsymbol{\zeta}$ is the diagonal matrix of modal damping factors corresponding to each mode. The system equations represented in Eq. 2.4 are of a free system with only external forces acting on it.

At this point, a transformation matrix, T , is proposed to transform the modal degrees of freedom of the system to the fixed base degrees of freedom of the UUT, p , and the free modal degrees of freedom of the NLA, s , written as

$$\bar{q} = \mathbf{T} \begin{bmatrix} \bar{p} \\ \bar{s} \end{bmatrix}. \quad (2.5)$$

To formulate the transformation matrix, T , expressions are formulated that relate the modal coordinates of the UUT, p , and the NLA, s , to modal coordinates of the system, q .

A relationship between the s degrees of freedom and the q degrees of freedom are noted as

$$\phi_b \bar{q} = \psi \bar{s}, \quad (2.6)$$

where ϕ_b is the mode shapes of the system at the degrees of freedom of the next level of assembly and ψ is the mode shapes of the NLA in a free condition. This relationship is a good approximation if the mode shapes of ψ span the space of ϕ_b . The relationship between q and s is completed by taking the pseudo inverse of ϕ_b , written as

$$\bar{q} = \phi_b^+ \psi \bar{s}, \quad (2.7)$$

with the $+$ symbol denoting a pseudo inverse.

Relating the fixed base degrees of freedom, p , to the free modal coordinates of the system, q , is done through component mode synthesis of analytically fixing the base [4]. This method develops constraint modes used to fix the base of the system. The expression for this relationship is given as

$$\bar{q} = \mathbf{L}\mathbf{\Gamma}\bar{p}, \quad (2.8)$$

where the expression $\mathbf{L}\mathbf{\Gamma}$ is developed as the transformation of the fixed base modal coordinates to the free modal coordinates.

The transformation matrix, T , is written as a concatenation of the relationships in Eqs. 2.7 and 2.8 as

$$\bar{q} = [\mathbf{L}\mathbf{\Gamma} \quad \phi_b^+ \psi] \begin{bmatrix} \bar{p} \\ \bar{s} \end{bmatrix}. \quad (2.9)$$

The transformation given in Eq. 2.9 is applied to the system's equations of motion in Eq. 2.4 and premultiplied by the transform of T to get

$$T^T[-\omega^2\mathbf{I} + 2i\omega\omega_n\zeta_n + \omega_n^2]T \begin{bmatrix} \bar{p} \\ \bar{s} \end{bmatrix} = T^T\phi^T\bar{F} \quad (2.10)$$

and can be rewritten as

$$\left(-\omega^2 \begin{bmatrix} \mathbf{I} & \mathbf{M}_{ps} \\ \mathbf{M}_{ps}^T & \mathbf{M}_{ss} \end{bmatrix} + 2i\omega \begin{bmatrix} \omega_{nfix} \cdot \zeta_{nfix} & \mathbf{C}_{ps} \\ \mathbf{C}_{ps}^T & \mathbf{C}_{ss} \end{bmatrix} + \begin{bmatrix} \omega_{nfix}^2 & \mathbf{K}_{ps} \\ \mathbf{K}_{ps}^T & \mathbf{K}_{ss} \end{bmatrix} \right) \begin{bmatrix} \bar{p} \\ \bar{s} \end{bmatrix} = T^T\phi^T\bar{F} \quad (2.11)$$

The upper left hand partition in the transformed system matrices in Eq. 2.11 corresponds to the fixed base modal parameters of the UUT and is diagonal. The other partitioned sections of the newly formed \mathbf{M} , \mathbf{C} , and \mathbf{K} matrices are fully populated and the off diagonals tie the two sub-structures together.

The transformation matrix is square and not a reduction matrix. Because the transformation matrix is square and not a reduction, the eigenvalues and eigenvectors after the transformation are unchanged.

There are a couple of characteristics of T that aided in interpreting its physical meaning. The transformation matrix is best thought of as a method of reorganizing the system's degrees of freedom to isolate the UUT from the NLA. The transformation matrix can be interpreted as a linear combination of the fixed base modal coordinates of the UUT and free modal coordinates of the base to make up the free modal coordinates of the system.

2.3 Development of 6 DOF Specification

The purpose of using the theory presented in this paper was to take response data from a field test acting on the system and create a laboratory test to replicate the stresses of the UUT on a 6 DOF shaker table on a rigid fixture. The strategy used in this paper was to take the measured responses on the BARC system during a mechanical environment and transform them into p and s space utilizing the transforms defined in Eqs. 2.2 and 2.5 written as

$$\ddot{\bar{x}} = \phi\mathbf{T} \begin{bmatrix} \bar{p} \\ \bar{s} \end{bmatrix} \quad (2.12)$$

and

$$[\phi \mathbf{T}]^+ \ddot{\bar{x}} = \begin{bmatrix} \bar{p} \\ \bar{s} \end{bmatrix}. \quad (2.13)$$

As defined in the theory section, the s degrees of freedom are the free modes of the NLA or the box assembly in this case study. The s degrees of freedom were partitioned to separate the rigid (s_{rb}) and elastic modal coordinates (s_{el}). The s_{rb} motion was used directly as the input to the 6 DOF analysis to control the rigid fixture to the same s_{rb} levels that were measured in the field environment. Because the inputs were derived directly from the time domain data, the phase between the rigid body modes was retained. The rigid body motion derived by this method was identical to applying a rigid body modal filter to the NLA which is a common practice used for 6 DOF shaker inputs. However, the proposed method provided more insight into the test specification's effectiveness and accuracy.

2.4 Modal Analysis

Modal analysis of the BARC system and the removable component on a fixture was computed to gain insight on the structure and also to compute the necessary terms noted in the theory of this paper. The first four elastic mode shapes of the BARC system are found in Fig. 2.2 and the first three elastic modes of the removable component on the fixture are found in Fig. 2.3. All of the finite element analyses executed were computed by the SIERRA SD code package [5].

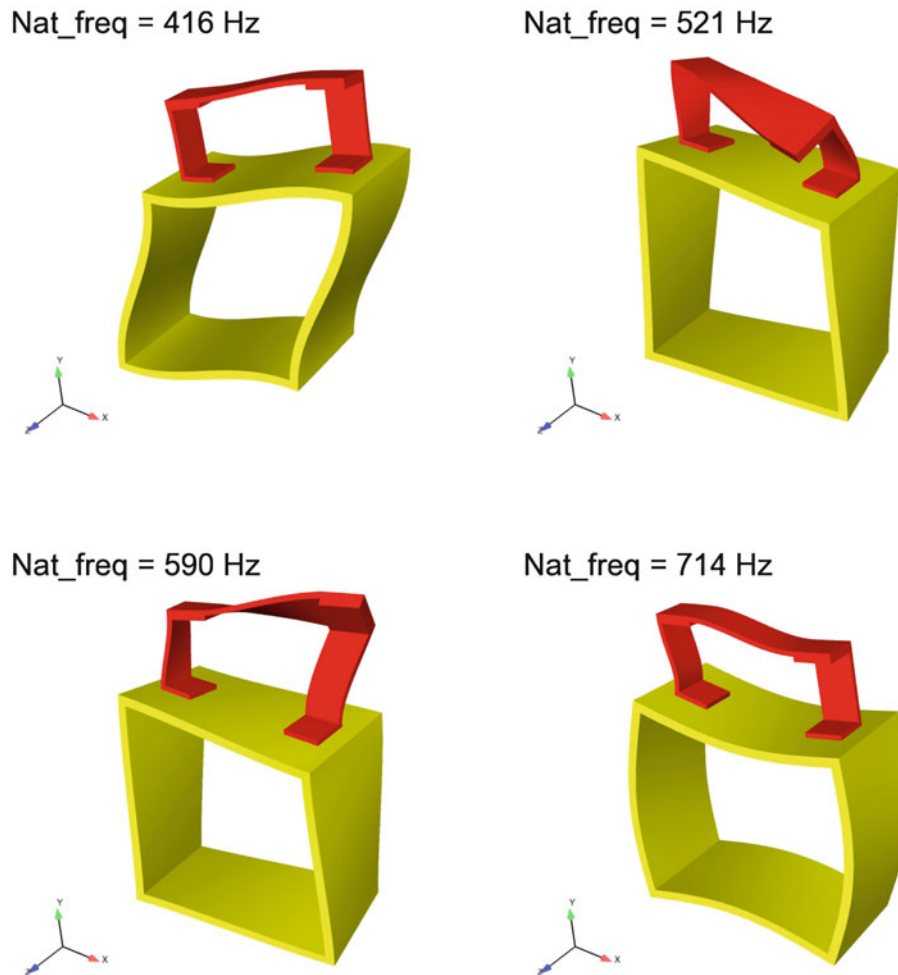


Fig. 2.2 First four elastic mode shapes of the BARC system

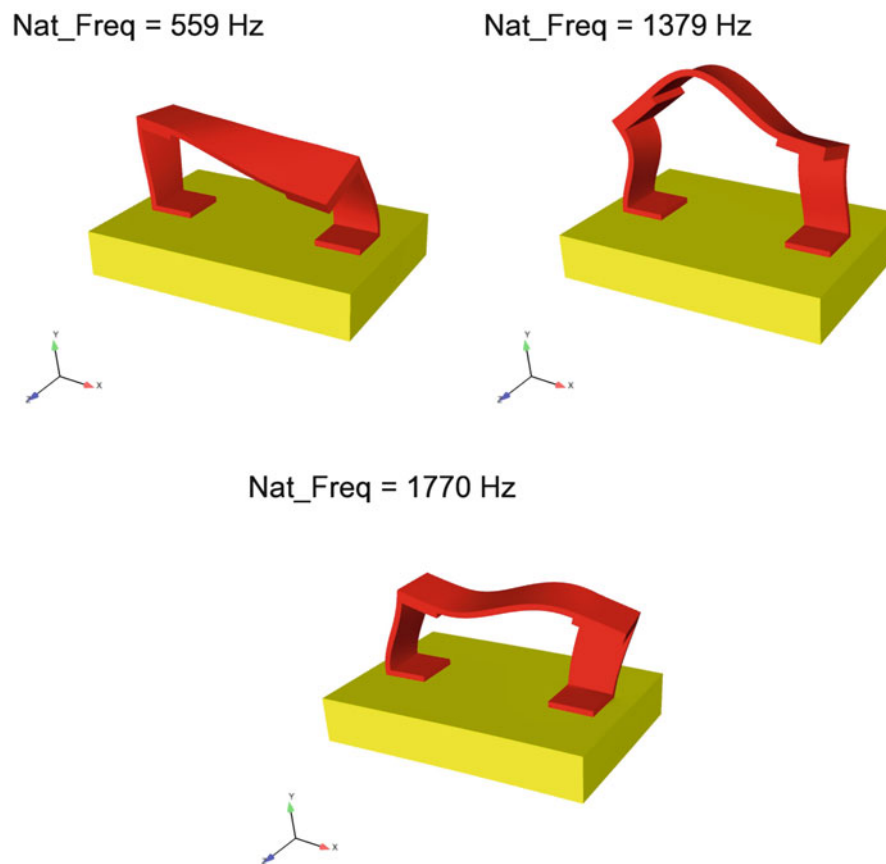


Fig. 2.3 First three elastic mode shapes of the removable component on the fixture

2.5 Environments and Results

To determine if the theory and strategy laid out above were effective in reproducing the stresses experienced by the removable component in the environment test, two verification efforts were developed. The first verification effort was to input two sine waves individually into the system. The sine waves each had a frequency of 31 Hz to only excite the rigid body modes of the system. This was done to compare the responses to hand calculations and verified for accuracy.

Figure 2.4 shows the two input locations on the box assembly and the response location on the removable component. All excitations and responses were input and measured in the y-direction per the coordinate system in Fig. 2.4. These sine waves were applied and the responses at a subset of the total nodes were calculated. The responses were transformed using Eq. 2.13 into p and s space. The first six values of s were segregated as the rigid body motion of the box assembly and that modal acceleration was enforced on the brick fixture in Fig. 2.5.

The response of Node 13 was calculated from the sine environment analysis on the BARC and the enforced acceleration analysis on the fixture. The response of Node 13 between the two analyses was compared. This comparison is plotted in Fig. 2.6. The replication of the acceleration of Node 13 in the two configurations showed that the theory properly reproduced the environment for a rigid body input, translation and rotation.

The second verification effort was to apply a flat random input that had energy content from 20 to 990 Hz at the location indicated by a blue dot in Fig. 2.7, node 127. The load was input in the Z direction so that it excited the modes of the system. From this environment, the s_{rb} motion was calculated as it had been previously and the acceleration of the fixture was forced to match the s_{rb} quantities calculated from the BARC environment.

The response of Node 13 was compared between the random environment applied to the BARC system and the enforced acceleration applied to the test fixture. The comparison of acceleration is plotted in Fig. 2.8. This comparison showed several discrepancies between the two analyses. To examine the differences between the BARC and fixture analyses, the differences

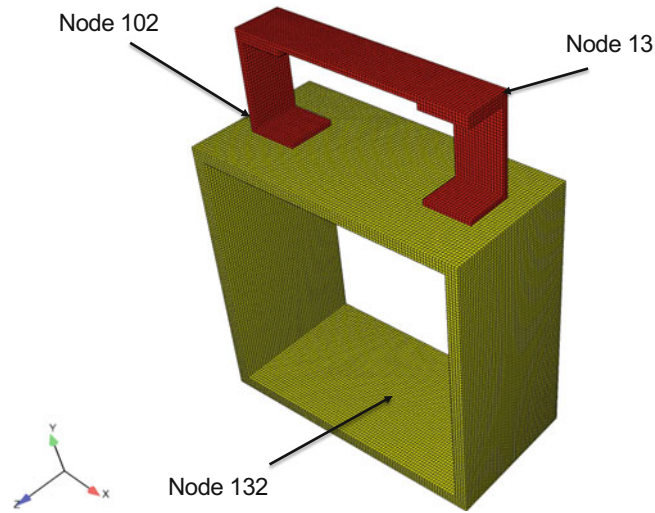


Fig. 2.4 Input (nodes 132 & 102) and response location (node 13) for the rigid body tests on the BARC system

Fig. 2.5 Pictorial of the removable component on a brick fixture

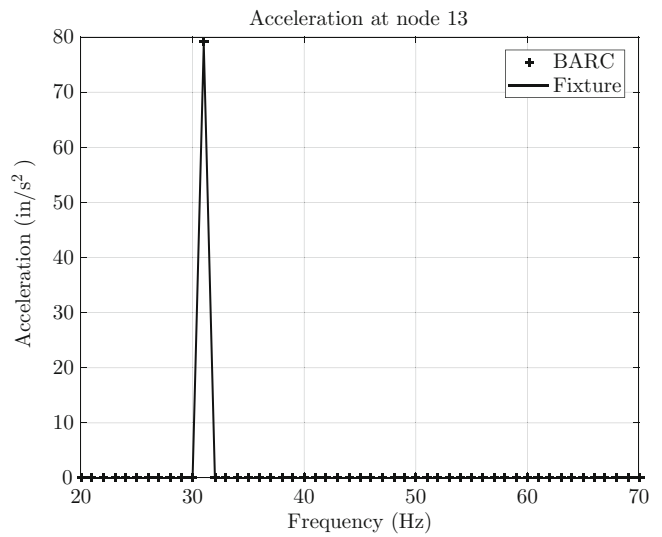
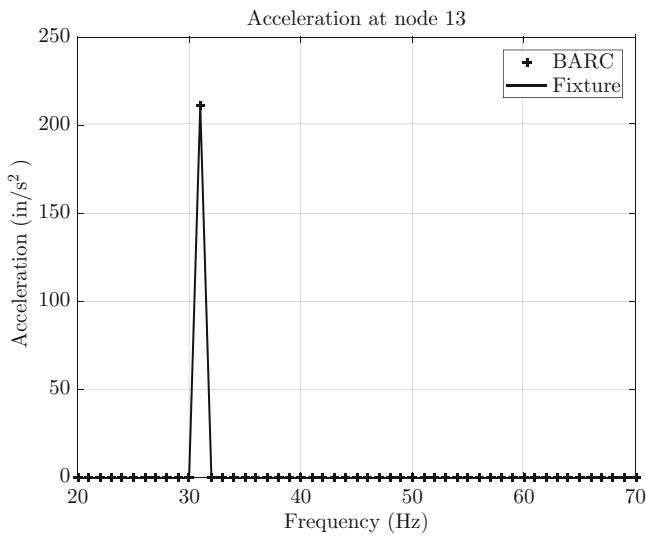
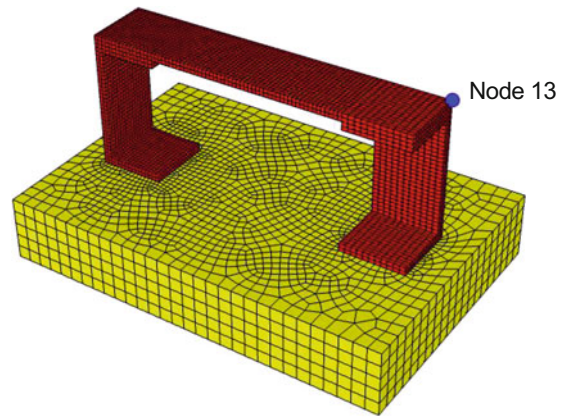


Fig. 2.6 Comparison of response with a 31 Hz sine input at node 132 (right) and node 102 (left)

Fig. 2.7 Excitation location for a random input in the Z direction at the blue dot (Node 127)

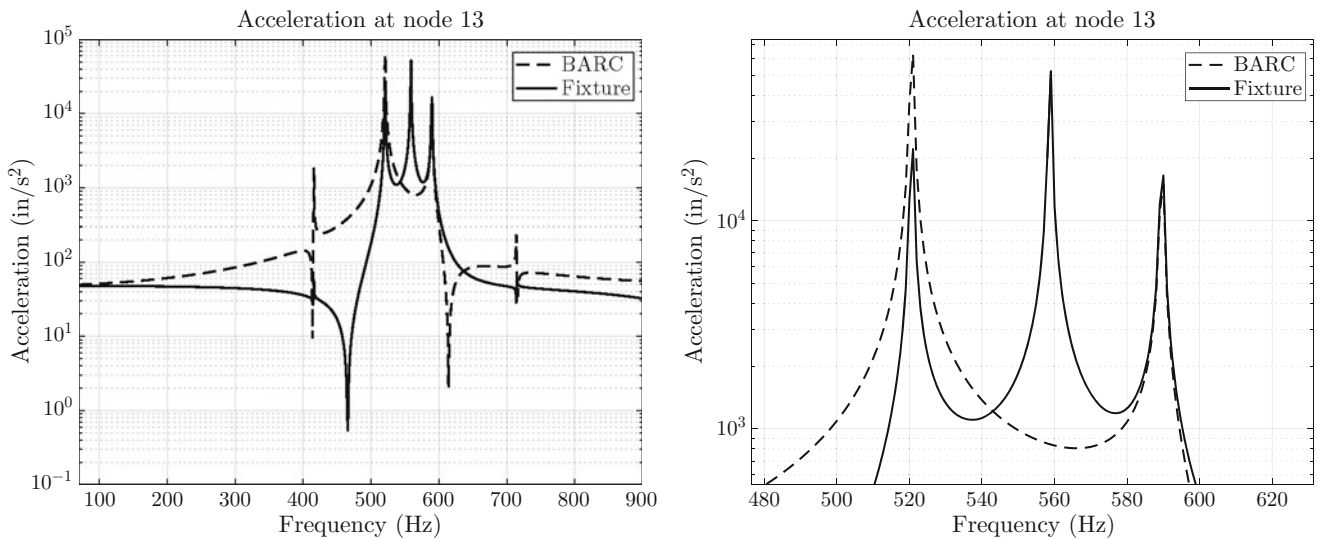
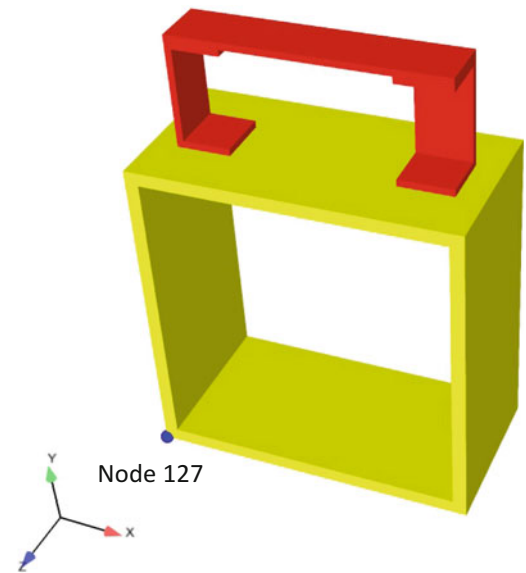


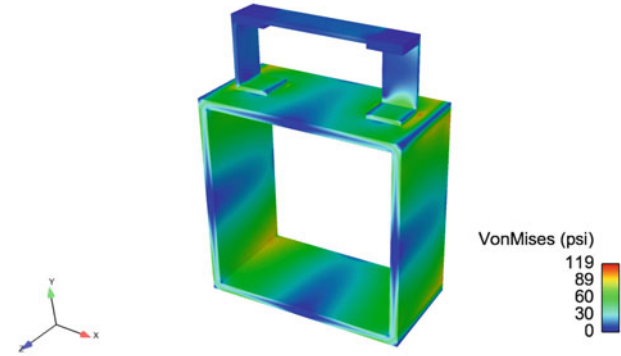
Fig. 2.8 Response comparison of Node 13 on the BARC and fixture systems

were examined at a mode by mode basis using the mode shapes in Figs. 2.2 and 2.3. Historically, comparing responses of key nodes was a common method for determining the success of a test, however, the true parameter in determining a test's success was determined to be how the stresses that the test imparts on the UUT compares to the stresses in the field environment. Therefore, stresses per frequency line were calculated and compared.

The first and fourth modes of the BARC system were very poorly replicated by the fixture analysis and had orders of magnitude of error. Figure 2.9 showed that the stress profile and the levels were both incorrect for the first mode of the BARC system. Even though this case study showed that the stresses in the removable component were insignificant in both analyses, an excitation source on the BARC that better excited its first mode would have higher and potentially damaging stresses. The reason that the first and fourth modes were so poorly replicated was because the removable component was excited by the elastic mode of the box assembly, which the fixture can not replicate with rigid body motion.

The second and third mode shapes of the BARC system and first mode of the fixture system all appeared to have similar shapes for the removable component. The shape resembled the first fixed base mode of the removable component. The analyses of the BARC system and the fixture system produced stress fields that were shown in Fig. 2.10. Observation of these stress plots showed that the stress profile of the removable component was very similar between the two modes and the two systems. However, the fixture system was an under-test of 32% for the second shape and was an over-test of 2% for

Frequency = 416 Hz



Frequency = 416 Hz

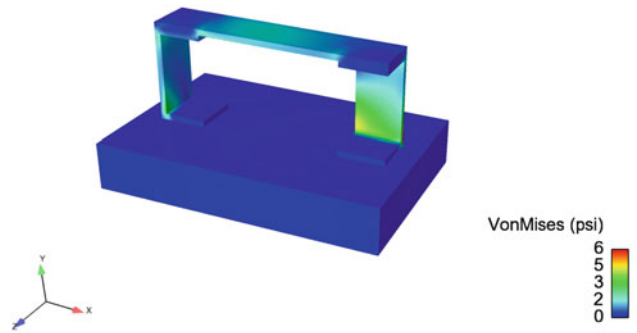
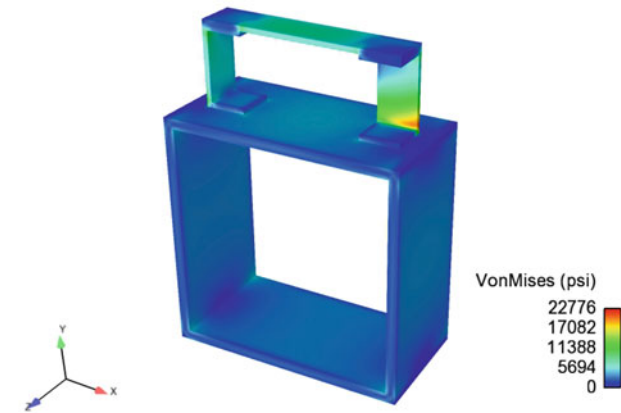


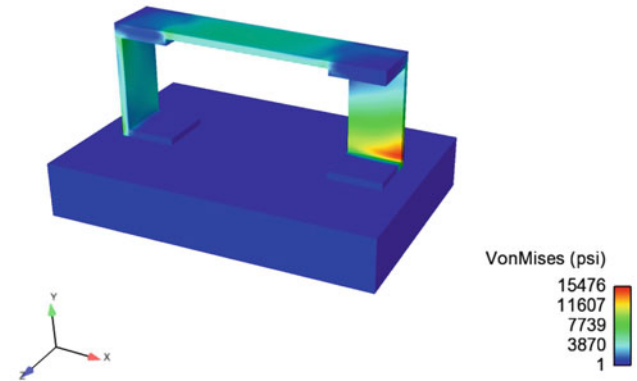
Fig. 2.9 Von Mises stress from the flat random environment input at node 127 (left) and test environment (right) at first natural frequency

the third shape. Figure 2.8 showed a resonance that was not in the BARC system that was excited in the fixture system. This was the first mode of the fixture system at 560 Hz and was a large over-test. Because the rigid body motion of the base was the control parameter, there was no feedback parameter to filter the test configuration's first natural frequency.

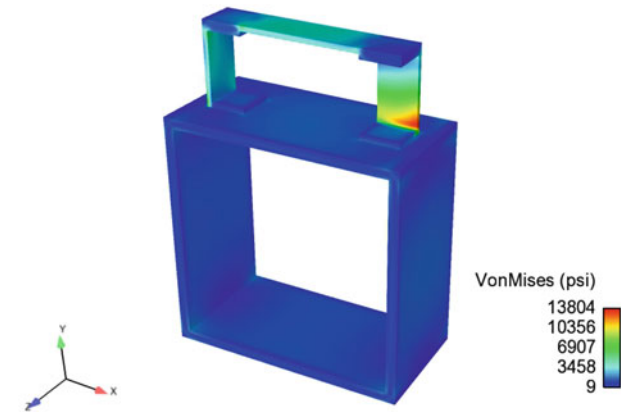
Frequency = 521 Hz



Frequency = 521 Hz



Frequency = 590 Hz



Frequency = 590 Hz

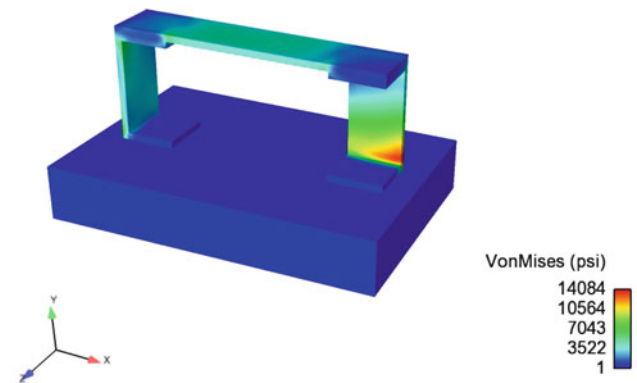


Fig. 2.10 Von Mises stress from the flat random environment input at node 127 (left) and test environment (right)

This case study showed that the elasticity of the next level of assembly interacted with the unit under test. It was proven that this interaction was a factor in how successful the fixture system can replicate the stresses of the BARC system. Through the development of this case study, it was decided to qualitatively compare the s_{rb} degrees of freedom to the s_{el} degrees of freedom of both the BARC and fixture systems. The result of this comparison was plotted in Fig. 2.11.

Upon examination of these plots, it was determined that this qualitative comparison was an indicator on how influential the elastic motion of the NLA was on the motion and stress of the unit under test. This conclusion was reached because the s_{el} degrees of freedom were the same or higher than the s_{rb} degrees of freedom for the BARC assembly and the box assembly was proven to have significant interaction with the removable component. Conversely, the fixture had little influence on the removable component as the s_{rb} degrees of freedom were about two orders of magnitude higher than the s_{el} degrees of freedom.

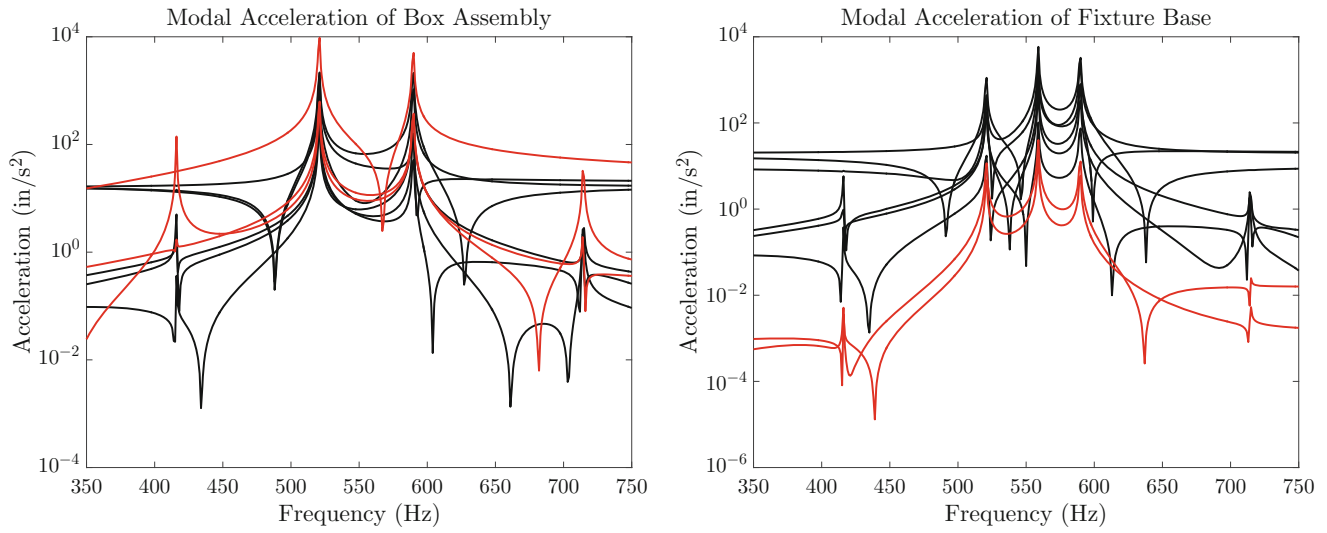


Fig. 2.11 s_{rb} rigid body degrees of freedom (black) and s_{el} elastic degrees of freedom (red) for the BARC and fixture system

2.6 Conclusion

Dynamic sub-structure theory previously developed was applied to a real life structure with the intent of creating a six DOF shaker test. This application was tested and was shown to have large similarities to calculating the input with a rigid body modal filter. Although the underlying physics were the same, more insight was produced through the sub-structuring method as the degrees of freedom of the unit under test and the NLA were separated and observable.

The effectiveness of the theory was limited as the interaction or impedance of the NLA had an effect on the stresses of the unit under test. The fixture was rigid in the frequency range where the box assembly had modes. These modes were only important if they caused any stresses on the removable component.

Comparing the s_{rb} degrees of freedom coordinates to the s_{el} degrees of freedom indicated how well a rigid fixture could replicate the motion of the NLA. This comparison could be used as a parameter or check to determine if a six DOF shaker table would be an appropriate means of replicating a mechanical environment.

References

1. Daborn, P.M., Roberts, C., Ewins, D.J., Ind, P.R.: Next-Generation Random Vibration Tests, pp. 397–410. Springer International Publishing, Cham (2014)
2. Reyes, J.M., Avitabile, P.: Adjustment of vibration response to account for fixture-test article dynamic coupling effects. In: Proceedings of the 35th IMAC, Feb 2017
3. Mayes, R.L.: A Modal Craig-Bampton Substructure for Experiments, Analysis, Control and Specifications, pp. 93–98. Springer International Publishing, Cham (2015)
4. Zwink, B.R., Mayes, R.L., Kelton, D.W., Heister, J.D., Hunter, P.S., Gomez, A.J.: Converting a Slip Table Random Vibration Test to a Fixed Base Modal Analysis, pp. 341–357. Springer, New York (2012)
5. Sierra Structural Dynamics Development Team: Sierra structural dynamics – user’s notes. Technical report SAND2017-3553, Sandia National Laboratories, Apr 2017

Chapter 3

Forced Response of 2-Dof Gyroscopic Systems with Stable Eigenvalues

O. Giannini

Abstract Gyroscopic conservative dynamical systems may exhibit flutter instability that leads to a pair of complex conjugate eigenvalues, one of which has a positive real part and thus leads to a divergent free response of the system. When dealing with non-conservative systems, the pitch fork bifurcation shifts toward the negative real part of the root locus, presenting a pair of eigenvalues with equal imaginary parts, while the real parts may or may not be negative. Several works study the stability of these systems for relevant engineering applications such as the flutter in airplane wings or suspended bridges, brake squeal, etc., and a common approach to detect the stability is the complex eigenvalue analysis that considers systems with all negative real part eigenvalues as stable systems. This paper studies the cases where the free response of these systems exhibits a transient divergent time history even if all the eigenvalues have negative real part thus usually considered as stable, and relates such a behavior to the non-orthogonality of the eigenvectors. Moreover, the forced response of these system is addressed, highlighting how and in which cases, an unexpected amplification of the forced response may occur.

3.1 Introduction

In several engineering problems, the stability of gyroscopic systems is a primary concern; in fact, these systems may be characterized by the flutter instability or mode lock-in instability that is a phenomenon that can be observed when gyroscopic terms are present. Due to the variation of one or more parameters, the natural frequencies of two or more modes approach one another and coalesce, leading to an unstable behavior.

Mode lock-in (also called modal coupling instability or flutter instability) was observed in several engineering fields such as flutter phenomena and more generally aero-elasticity in aeronautics (e.g [1, 2]), in the structural engineering field for flutter problem in cable suspended bridges [3, 4], in the automotive engineering for brake squeal or windscreen chatter (see e.g [5–13]) and in machining problems (see e.g [14, 15]). More general works tackle problems of dry contact between solid bodies [16] or gyroscopic systems with negative-definite stiffness matrices [17]. Considering specifically contact problems, mode lock-in was initially highlighted in the beam-on disk set-up, developed by Akay et al. to investigate friction driven instabilities [6]. Even if there is not an unanimous consensus in the scientific community on the causes of on brake squeal noise, several studies carried out on simplified lab set-ups have shown that squeal noise is an instability condition, that is reached when two eigen frequencies of the system, due to the gyroscopic terms induced by friction forces, coalesce and become unstable [7–9].

Several works study the effect of damping on the lock-in instability. In brake squeal literature, Hoffmann et al. [18] found that the presence of damping causes imperfect bifurcation with unstable eigenvalue (soothing effect), Sinou et al. [10, 11, 19] study the stability of a brake system taking into account the destabilizing effect of damping. Massi and Giannini [9] measured the lock-in instability and the extent of the unstable zone on the beam on disc set-up and found an experimental validation of the previous findings. Kirillov in [20] addressed the effect of damping in gyroscopic systems, while in [21] addressed a comprehensive analytical study on the interaction of eigenvalues of generic matrices relating the effect of several parameters, including damping, on the veering and the lock-in characteristics.

When dealing with gyroscopic systems, in engineering application, it is of great interest to establish design conditions that are far from the instability zone of the system: to achieve such a design, the tool usually adopted is the complex eigenvalue analysis (CEA) [7, 8, 10–13, 19, 20] that is a parametric analysis of the root locus of the eigenvalues and positive real parts are associated with the unstable behavior of the system. The CEA is used, in practice, to detect whether a given design of the system is stable or not, and through sensitivity analysis and iterative procedures, the design is optimized to obtain a dynamic

O. Giannini (✉)
Università Niccolò Cusano, Rome, Italy
e-mail: oliviero.giannini@unicusano.it

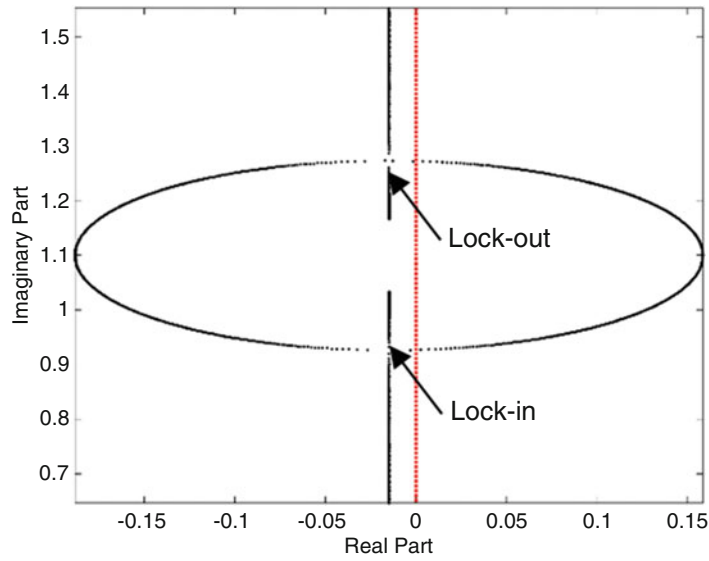


Fig. 3.1 Locus plot of the eigenvalue in the case proportional damping: numerical value: $k = 1$ N/m, $\varepsilon = 0.1$ N/m, $\alpha = 2\varepsilon$, $a = 0.015$, $b = 0$

configuration of the eigenvalues that is far from possible instabilities; in this context a robust identification of the boundary of the instabilities is of primary relevance.

Goal of this paper is to show and discuss under which conditions dynamical systems, characterized by possible mode lock-in, may exhibit divergent time responses even in the presence of only negative real part eigenvalues. The study is conducted theoretically and numerically on a two degrees of freedom system, that is able to capture the dynamics of any system with two modes interacting. The results show how, considering only the real part of the eigenvalues may cause an under-estimation of the unstable zone, and introduces a novel type of instability – called transient eigenvector instability – because is due to the non-orthogonality of the eigenvectors and can lead to very large free-response of the system especially in the vicinity of the lock-in and lock-out zones thus enlarging the area of the parameter space that exhibits unstable behavior. Finally, the forced response of these systems is analyzed and condition of unexpected resonance is highlighted.

3.2 Lock-in in Linear Non Conservative Systems with Proportional Damping

Let us consider a two degrees of freedom gyroscopic system governed by equation.

$$\begin{bmatrix} 1 & 0 \\ 0 & 1 \end{bmatrix} \begin{bmatrix} \ddot{x}_1 \\ \ddot{x}_2 \end{bmatrix} + \begin{bmatrix} c & c_2 \\ c_3 & c_1 \end{bmatrix} \begin{bmatrix} \dot{x}_1 \\ \dot{x}_2 \end{bmatrix} + \begin{bmatrix} k + \varepsilon & -\varepsilon + \alpha \\ -\varepsilon - \alpha & k_1 + \varepsilon \end{bmatrix} \begin{bmatrix} x_1 \\ x_2 \end{bmatrix} = \begin{bmatrix} 0 \\ 0 \end{bmatrix} \quad (3.1)$$

If the matrix \mathbf{C} can be expressed as $a\mathbf{M} + b\mathbf{K}$, i.e. a proportional damping model describes adequately the dissipation mechanism, the eigenvectors obtained from the undamped systems diagonalize also the damping matrix and the roots of the system shift toward the negative real part of an amount

$$s = a + b\lambda \quad (3.2)$$

where λ are the eigenvalue of the matrix \mathbf{K} . The system locks-in and, depending on the relative value of the gyroscopic term and the damping coefficients, the real parts of the eigenvalues are negative at the exceptional points [21, 22, 24] and in their vicinity, both before and slightly after. Figure 3.1 shows the locus plot of the eigenvalues for this case. In the figure the dashed vertical line marks the boundary between the stable and unstable eigenvalue regions.

In this scenario, at the exceptional points (lock-in and lock-out), the system has two coincident complex eigenvalues and one real eigenvector. If one chooses as initial condition for the dynamical system that eigenvector, the time evolution is asymptotically stable, that is an harmonic response with exponentially decreasing amplitude (see Fig. 3.2a). On the contrary, if one chooses as initial condition another vector, *e.g.* orthogonal to the eigenvector, the response of the system appears, as in

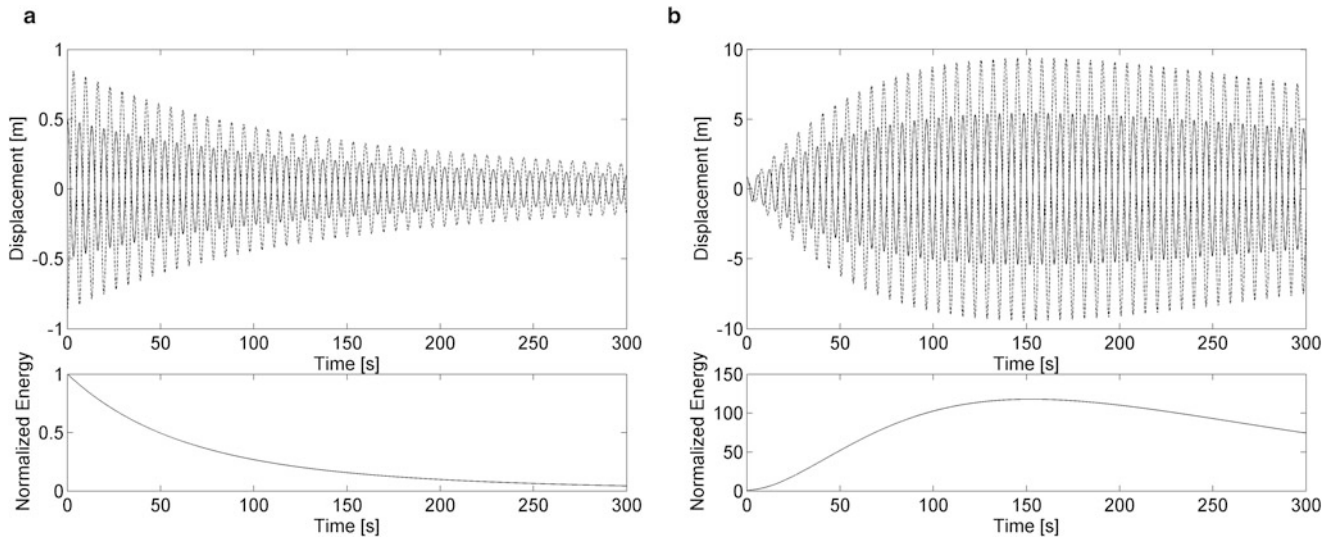


Fig. 3.2 Proportional damping: time response of free vibrations of the system and normalized energy at Exceptional Point: numerical value: $k = 1$ N/m, $k_1 = 0.65$ N/m, $\varepsilon = 0.1$ N/m, $\alpha = 2\varepsilon$; $a = 0.015$ $b = 0$; (a) initial condition parallel to one eigenvector; (b) Initial condition orthogonal to one eigenvector

Fig. 3.2b. In this case, it is possible to detect that before the damping reduces to zero the amplitude of the system vibration, there is a time period of increasing vibrations. Figure 3.2 also reports the normalized mechanical energy of the system (being 1 the initial energy), and it is possible to detect a 100 fold increase in the first part of the time history. The time length and the maximum amplitude of vibration is mainly governed by the amount of damping in the system that is the value of a and b . Experimental results that can be related to this system dynamics were found by Massi and Giannini in [23] on the *tribobrake*, that in certain configurations was stable but, once excited by an external impulse, started squealing for a certain amount of time.

If one considers points in the locus plot that are either slightly before the lock-in or after the lock-out (or after lock-in but before the real part of the eigenvalue crosses the stability region), the system is characterized by two complex eigenvalues and two “almost parallel” eigenvectors. Time integration of such systems using as initial condition one of the eigenvectors produces vibration that is qualitative analogous to that presented in Fig. 3.2a, while other initial conditions produce, with a smaller increase in energy, responses that are analogous to that of Fig. 3.2b.

To conclude this section, at the exceptional points or in their vicinity, linear non-conservative gyroscopic system with proportional damping, any initial condition that is not parallel to the eigenvectors of the system, causes the amplitude of the system response to increase over time, even if the eigenvalues of the system are stable. The increase of energy in the system is limited but can be order of magnitude larger than the initial mechanical energy in the system. These autonomous systems are indeed asymptotically stable, because after a certain amount of time, the vibrations start to decrease and the system converges toward the equilibrium position. However, given the large time span before the stabilizations, for practical applications, these systems will behave as unstable, and not taking into account this effect can be hazardous.

3.3 Transient Eigenvector Instability

Under the previous header the case of increasing response in gyroscopic autonomous systems is presented. It is important to note that, strictly speaking, these systems, since they have all negative real parts eigenvalues, are always asymptotically stable, thus the free response approaches the equilibrium configuration. However, it is highlighted the possibility of an initial growth of the system free response associated with the increase in mechanical energy of the system. So that, in practical cases, these systems may appear as unstable; we will refer to such behaviour as Transient eigenvector instability for reasons that will be explained hereafter.

Recalling the numerical case presented in Fig. 3.1 of a system with proportional damping, in Fig. 3.3 the real parts of the eigenvalues are plotted against the parameter k_1 . In this figure, five zones are highlighted. In the central part there is the unstable behaviour, induced by one eigenvalue with positive real part. Before and after the unstable zone there are the

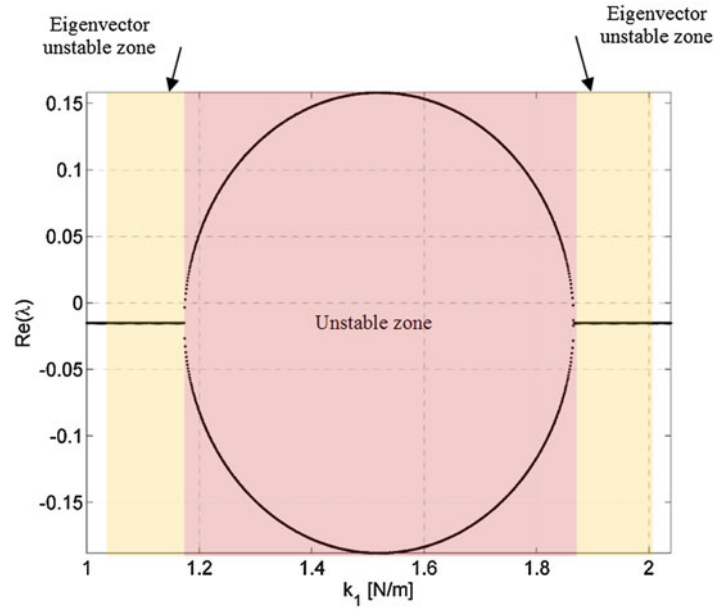
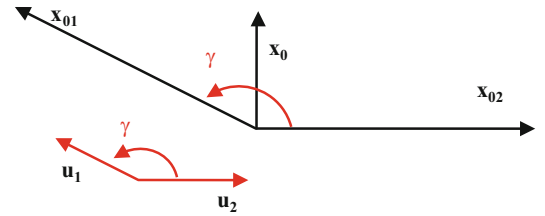


Fig. 3.3 Locus plot of the eigenvalue in the case of proportional damping and stability zones: numerical value: $k = 1 \text{ N/m}$, $\varepsilon = 0.1 \text{ N/m}$, $\alpha = 2\varepsilon$, $a = 0.015$ $b = 0$

Fig. 3.4 qualitative decomposition of the initial condition along the system eigenvectors



two transient eigenvector unstable zones, moving farther away the system behaves as stable. It is important to notice that the boundary between stability and eigenvector instability is not sharp because the maximum possible increase in amplitude gradually approaches to zero. As a convention, the boundary can be set when, in the worst case scenario, the amplitude increase is four times the initial amplitude and it is important to point out that, by following this convention, the extent of these unstable zones is comparable with the eigenvalue unstable zone.

The two transient eigenvector instabilities are called in this way because, in these zones, the angle formed by the two eigenvectors is either small or close to π . Figure 3.4 represents qualitatively the case of two eigenvectors \mathbf{u}_1 and \mathbf{u}_2 that are not orthogonal.

Given an initial condition vector \mathbf{x}_0 , this can be expressed as a linear combination of the two eigenvectors. If the angle γ between eigenvectors is close to π (or to 0), the components of \mathbf{x}_0 , x_{01} and x_{02} along \mathbf{u}_1 and \mathbf{u}_2 directions respectively, can be much larger than the norm of vector \mathbf{x}_0 .

The time evolution of the two projection vectors is an exponentially decaying sine, at slightly different frequencies and with, in general, different real exponent. Figure 3.5 shows the numerical results previously presented in Fig. 3.2b. The growth of the system response is due to the fact that the modal components $x_{01}(t)$ and $x_{02}(t)$ start almost in phase opposition and, due to the frequency difference between the two eigenvalues, end-up coherent in phase, causing the increase in the response. From Fig. 3.5b, it is possible to understand that, once projected onto the modal coordinates, the behaviour of each component is stable, while their linear combination presents a ten fold increase in time.

Based on this consideration, it is possible to identify the maximum possible increase in the response (amplification factor) $I = |x_m|/|\mathbf{x}_0|$ where:

$$x_m = \max(x_{01}(t)) + \max(x_{02}(t)) < |x_{01}| + |x_{02}| \quad (3.3)$$

By choosing the vector of the initial condition so that it bisects the angle γ , formed by the two eigenvectors, the norm of the components x_{01} and x_{02} are equal and thus:

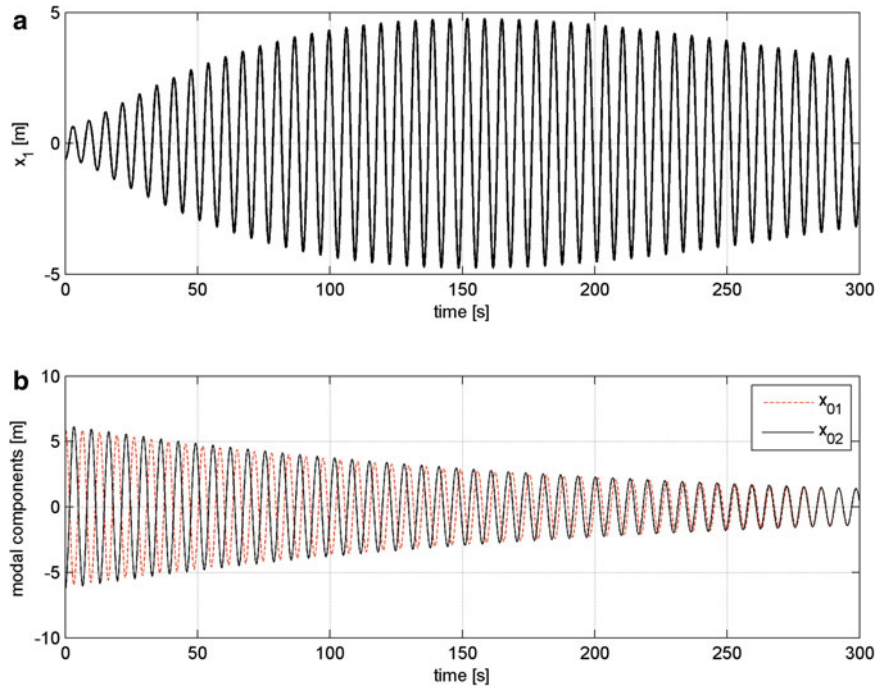


Fig. 3.5 Proportional damping: Time response of free vibrations of the system at Exceptional Point: numerical value: $k = 1$ N/m, $k_1 = 0.65$ N/m, $\varepsilon = 0.1$ N/m, $\alpha = 2\varepsilon$; $a = 0.015$; $b = 0$, Initial condition orthogonal to the eigenvector: (a) time response of the first degrees of freedom; (b) time evolution of the modal coordinates

$$|x_{01}| = |x_{02}| = \frac{|\mathbf{x}_0|}{2 \cos(\gamma/2)} \Rightarrow x_m < \frac{|\mathbf{x}_0|}{\cos(\gamma/2)} \Rightarrow I < \frac{1}{\cos(\gamma/2)} \quad (3.4)$$

Equation 3.4 links the response amplification factor I to angle γ .

If one sets the maximum value of the amplification to be $I < 4$, one obtains as a limit $29^\circ < \gamma < 151^\circ$ in order to avoid the transient eigenvector instability. During a complex eigenvalue analysis (CEA), it is simple to compute, together with the eigenvalues, also the eigenvectors and thus determine the angle between them. In this way it is possible to obtain for the parameters used in CEA, together with the limits necessary to avoid the eigenvalue instability, also the wider limit necessary to avoid the transient eigenvector instability, obtaining finally a more robust assessment of the stability of the gyroscopic system at hand.

In Fig. 3.6, the parametric analysis of the proportionally damped system presented before, is conducted calculating also the eigenvector angle, leading to an estimation of the boundary of both unstable zones, without requiring the integration of the system equations, in order to evaluate the actual maximum amplitude of the free system response.

3.4 Forced Response of Stable Gyroscopic System Close to the Exceptional Point

It is now of interest to address the forced response of stable systems that are close to the exceptional points in order to highlight if an unexpectedly large response can be obtained. It is clear that, following the definition of transient instability provided under the previous headers, if an impulse is provided, the response is expected to be up to I times that of the corresponding system that does not exhibit the eigenvector instability.

At the same, if a harmonic excitation is provided, each mode of the linear system will have, after a short period of time, an harmonic response, with frequency matching the exciting frequency and the amplitude governed mainly by the natural frequency and the damping associated with the mode. In other words, once the eigenvalues of the system are known, it is possible to characterize easily the stationary harmonic response of these systems, thus they behave in a predictable manner.

It is however interesting to address the case of the response of these systems under a periodic impulse excitation, whose pulse frequency is lower than the natural frequency of the system. If a linear non gyroscopic system (or a gyroscopic system far away from the exceptional points) is excited in such a way, the response is a sequence of harmonic decaying functions

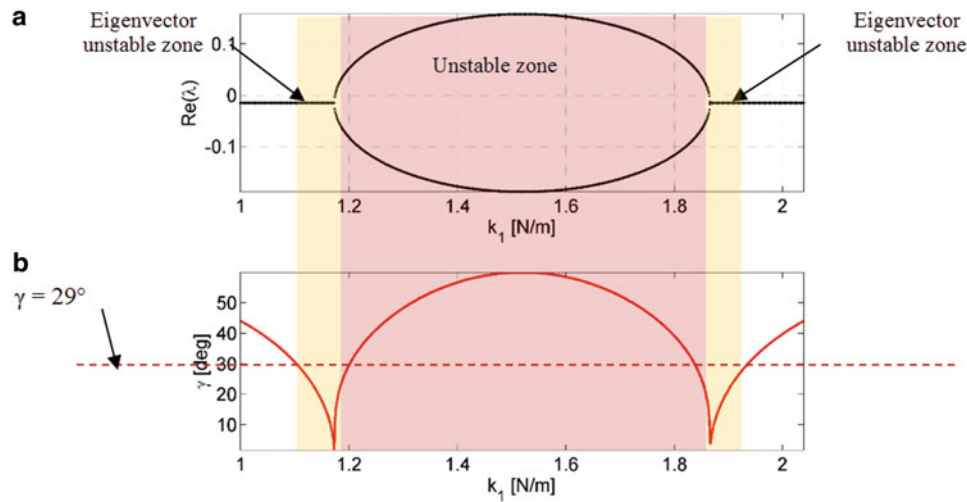


Fig. 3.6 Locus plot of the eigenvalue in the case of proportional damping and stability zones: numerical value: $k = 1$ N/m, $\varepsilon = 0.1$ N/m, $\alpha = 2\varepsilon$, $a = 0.015$; $b = 0$, (a) real part of the eigenvalues; (b) angle between eigenvectors

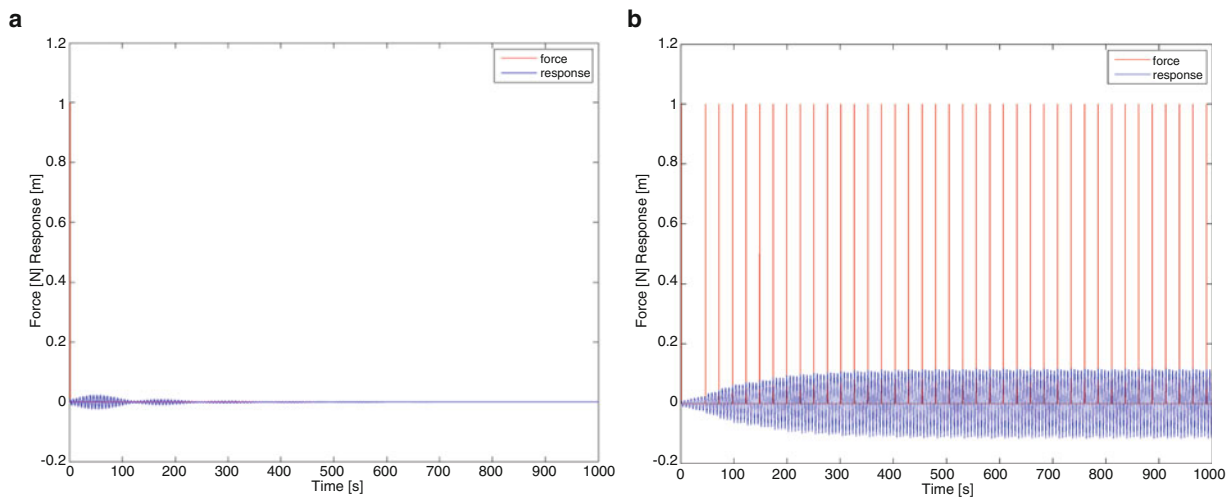


Fig. 3.7 Forced response of a mildly unstable system: numerical value: $k = 1.5$ N/m, $\varepsilon = 0.1$ N/m, $\alpha = 2\varepsilon$, $a = 0.015$, $k_I = 1.1$ N/m; $b = 0$, (a) Single impulse response; (b) periodic impulse response

occurring after each pulse. Eigenvector unstable systems, on the contrary will exhibit an increase of the response after each pulse. In order to understand such a response, the following case are analyzed: In Fig. 3.7 the case of a system before the exceptional point is considered e.g. when $k_I = 1.1$ N/m, the value of $\gamma = 22^\circ$ and $I = 5.2$ thus a mildly unstable system, the response of the system to a single excitation, shows a three-fold increase (Fig. 3.4a) in the response and, afterward, a decay.

The same system excited with periodic impulses, whose period matches a multiple of the natural period (four times in this example) shows a stationary response with a ten-fold increase in the response occurring to the system. If the case of $k_I = 1.18$, $\gamma = 8^\circ$ and $I = 9$, the results presented in Fig. 3.8 are obtained. The single impulse response presents a fivefold increased response with respect to a stable system, while considering the periodic impulse response another 15-fold increase is obtained leading to an amplification factor of about 75.

It is here important to notice that, the pulse frequency should be a sub-harmonic of the natural frequency of the system, but because the transient increase in the response of this system may include several period of the response, correspondingly, a large pulse period (10, 25 times the system one) can trigger these kind of resonances. If such excitation occurs, the response can be expected up to one order of magnitude larger that the amplification factor I presented under the previous heading (Fig. 3.9).

Finally, it is possible to compute how the system response is amplified as a function of the pulse period. Figure 3.10a, b show the results for the mild unstable and high unstable system respectively. It is interesting to note that the system

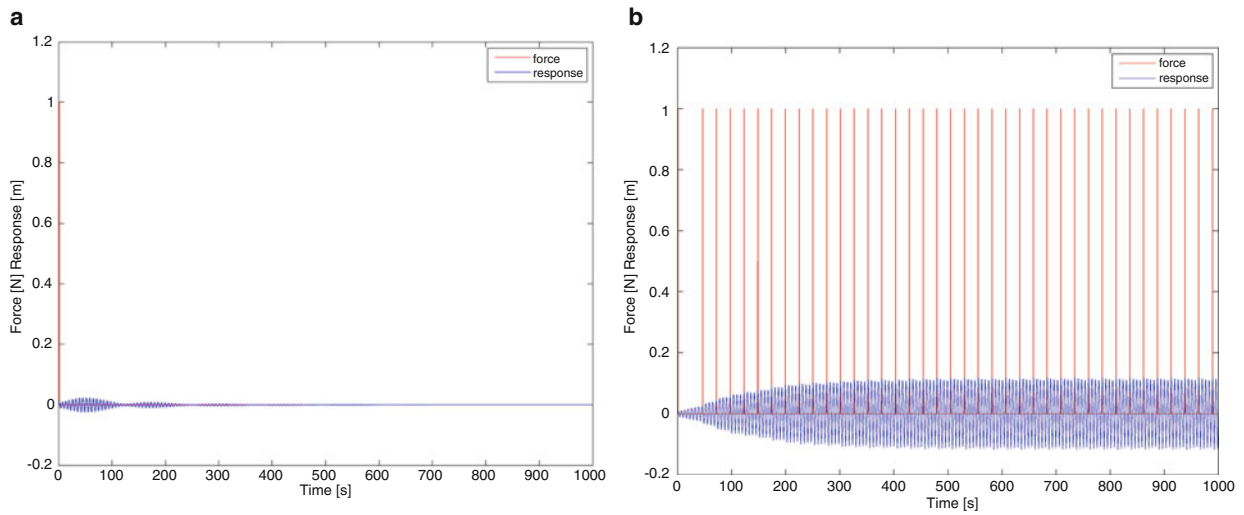


Fig. 3.8 Forced response of a mildly unstable system: numerical value: $k = 1.5 \text{ N/m}$, $\varepsilon = 0.1 \text{ N/m}$, $\alpha = 2\varepsilon$, $a = 0.015$, $k_1 = 1.1 \text{ N/m}$; $b = 0$, (a) Single impulse response; (b) periodic impulse response

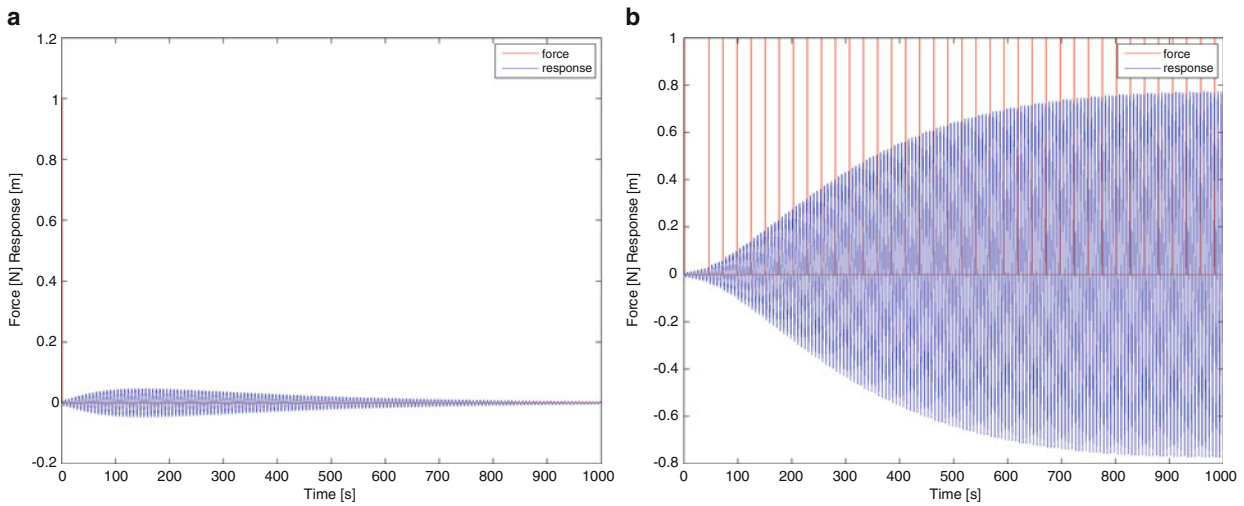


Fig. 3.9 Forced response of a highly unstable system: numerical value: $k = 1.5 \text{ N/m}$, $\varepsilon = 0.1 \text{ N/m}$, $\alpha = 2\varepsilon$, $a = 0.015$, $k_1 = 1.18 \text{ N/m}$; $b = 0$, (a) Single impulse response; (b) periodic impulse response

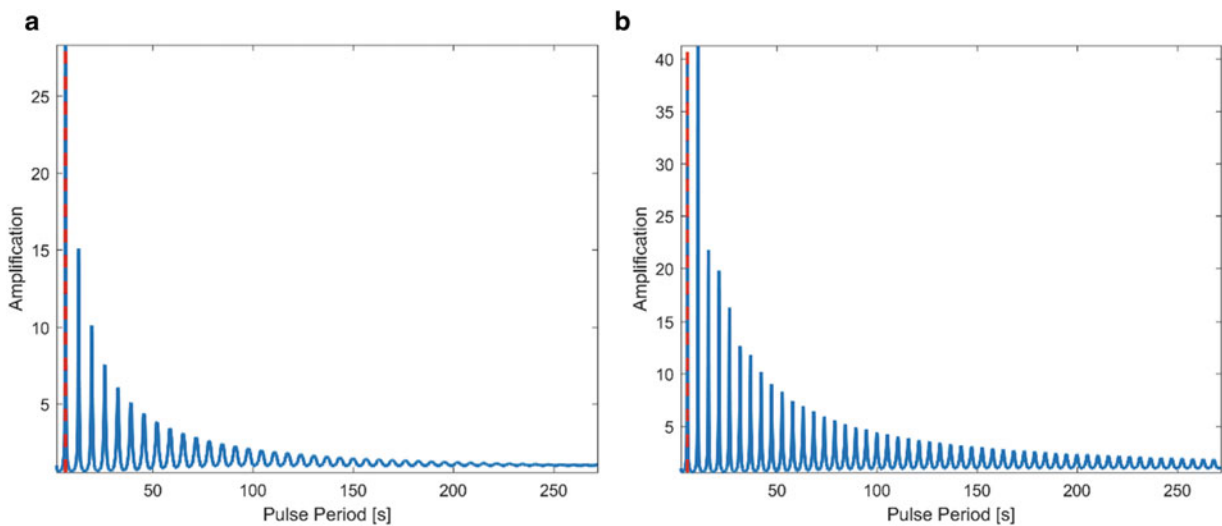


Fig. 3.10 Response amplification as function of the Pulse period. Numerical value: (a) Mildly unstable system, $k = 1.5 \text{ N/m}$, $\varepsilon = 0.1 \text{ N/m}$, $\alpha = 2\varepsilon$, $a = 0.015$, $k_1 = 1.1 \text{ N/m}$; $b = 0$; (b) highly unstable system, $k = 1.5 \text{ N/m}$, $\varepsilon = 0.1 \text{ N/m}$, $\alpha = 2\varepsilon$, $a = 0.015$, $k_1 = 1.18 \text{ N/m}$; $b = 0$

“resonates” at each subharmonic of the natural frequency of the system, in General the largest response is obtained at the first or second subharmonic but it remains large even for the following.

3.5 Conclusions

In gyroscopic systems, the flutter instability with the characteristic pitch-fork bifurcation, may occur and such instability is of concern in several engineering applications that range from aeroelasticity in aircraft wings, to flutter in bridges and brake squeal. The common way to address such problems rely on the complex eigenvalue analysis that, as a function relevant design parameters, computes complex roots of the system. In CEA, positive real part eigenvalues are related to possible instabilities, and the technique provides the boundaries for the design parameters considered in the analysis.

The results presented in this study show that, in gyroscopic systems, even negative real part eigenvalues may lead to free response of the system that increases several folds through time. This fact is generally neglected when addressing the stability of such systems.

The highlighted instability characterizes the initial time history of the free response and it is due to the non orthogonality of the eigenvectors in the vicinity of the exceptional points, thus the proposed name of “transient eigenvector instability”. The relation between the characteristics of the eigenvectors and the maximum possible amplification of the free response is analytically derived, providing a simple mathematical tool to address the boundary of this behaviour during standard CEA.

The transient eigenvector instability presented in this study occurs right before and after the pitch-fork bifurcation, *de facto* increasing its boundaries. Thus, the proposed results strongly suggest to consider this behaviour when addressing the study and the stability of gyroscopic systems. In fact, especially if the damping associated with a mode is not very large, the time necessary to damp the response may be relevant for the application and the behaviour of the system is similar to (and can be mistaken for) an unstable system.

It is also worth considering the fact that such systems, unlike the stable one, also present a resonance response when excited by a series of pulses with frequency matching any sub-harmonic of the natural frequency of the system. In these cases, the forced response can be one order of magnitude larger than the expected one as measured by the proposed amplification factor I .

References

1. Wright, J.R., Cooper, J.E.: Introduction to Aircraft Aeroelasticity and Loads, 2nd edn. Wiley, Chichester (2015.) ISBN: 978-1-118-48801-0
2. Dowell, E.H., Hall, K.C.: Modeling of fluid-structure interaction. *Annu. Rev. Fluid Mech.* **33**, 445–490 (2001)
3. Salvatori, L., Borri, C.: Frequency- and time-domain methods for the numerical modeling of full-bridge aeroelasticity. *Comput. Struct.* **85**(11–14), 675–687 (2007)
4. Jain, A., Jones, N.P., Scanlan, R.H.: Effect of modal damping on bridge aeroelasticity. *J. Wind Eng. Ind. Aerodyn.* **77-78**, 421–430 (1998)
5. Awang, I.M., AbuBakar, A.R., Ghani, B.A., Rahman, R.A., Zain, M.Z.M.: Complex eigenvalue analysis of windscreen wiper chatter noise and its suppression by structural modifications. *Int. J. Veh. Struct. Sys.* **1**(1–3), 24–29 (2009)
6. Akay, A., Wickert, J., Zu, Z.: Investigating criteria for the onset of mode lock-in, Tech. Rep. Carnegie Mellon University (1998)
7. Giannini, O., Massi, F.: Characterization of the high frequency squeal on a laboratory brake set-up. *J. Sound Vib.* **310**(1–2), 394–408 (2008)
8. Akay, A., Giannini, O., Massi, F., Sestieri, A.: Disk brake squeal characterization through simplified test rigs. *Mech. Syst. Signal Process.* **23**, 2590–2607 (2009)
9. Massi, F., Giannini, O.: Effect of damping on the propensity of squeal instability: an experimental investigation. *J. Acoust. Soc. Am.* **123**(4), 2017–2023 (2008)
10. Fritz, G., Sinoub, J.J., Duffala, J.M., Jezequel, L.: Investigation of the relationship between damping and mode-coupling patterns in case of brake squeal. *J. Sound Vib.* **307**, 591–609 (2007)
11. Fritz, G., Sinoub, J.J., Duffala, J.M., Jezequel, L.: Effects of damping on brake squeal coalescence patterns – application on a finite element model. *Mech. Res. Commun.* **34**, 181–190 (2007)
12. Cao, Q., Ouyang, H., Friswell, M.I., Mottershead, J.E.: Linear eigenvalue analysis of the disc-brake squeal problem. *Int. J. Numer. Methods Eng.* **61**(9), 1546–1563 (2004). <https://doi.org/10.1002/nme.1127>
13. Butlin, T., Woodhouse, J.: Friction-induced vibration: model development and comparison with large-scale experimental tests. *J. Sound Vib.* **332**(21), 5302–5321 (2013). <https://doi.org/10.1016/j.jsv.2013.04.045>
14. Nakano, Y., Takahara, H., Kondo, E.: Countermeasure against chatter in end milling operations using multiple dynamic absorbers. *J. Sound Vib.* **332**(6), 1626–1638 (2013)
15. Quintana, G., Ciurana, J.: Chatter in machining processes: a review. *Int. J. Mach. Tools Manuf.* **51**(5), 363–376 (2011)
16. Giannini, O., Sestieri, A.: Experimental characterization of veering crossing and lock-in in simple mechanical systems. *Mech. Syst. Signal Process.* **72**, 846–864 (2016). <https://doi.org/10.1016/j.ymssp.2015.11.012>

17. Shi, C., Parker, R.G.: Modal properties and stability of centrifugal pendulum vibration absorber systems with equally spaced, identical absorbers. *J. Sound Vib.* **331**(21), 4807–4824 (2012)
18. Hoffmann, N., Gaul, L.: Effects of damping on mode-coupling instability in friction induced oscillations. *ZAMM-J. Appl. Math. Mech.* **83**, 524–534 (2003)
19. Sinou, J., Jezequel, L.: Mode coupling instability in friction-induced vibrations and its dependency on system parameters including damping. *Eur. J. Mech.-A/Solids.* **26**(1), 106–122 (2007)
20. Kirillov, O.N.: Bifurcation of the roots of the characteristic polynomial and destabilization paradox in friction induced oscillations. *Theor. Appl. Mech.* **34**(2), 87–109 (2007)
21. Seyranian, A.P., Kirillov, O.N., Mailybaev, A.A.: Coupling of eigenvalues of complex matrices at diabolic and exceptional points. *J. Phys. A Math. Gen.* **38**(8), 1723 (2005)
22. Heiss, W.D.: Repulsion of resonance states and exceptional points. *Phys. Rev.* **61**, 929–932 (2000)
23. Massi, F., Giannini, O., Baillet, L.: Brake squeal as dynamic instability: an experimental investigation. *J. Acoust. Soc. Am.* **120**(3), 1388–1398 (2006)
24. Giannini, O.: Unstable transient response of gyroscopic systems with stable eigenvalues. *Mech. Syst. Signal Process.* **75**, 1–10 (2016). <https://doi.org/10.1016/j.ymssp.2016.01.008>

Chapter 4

Modal Testing of a Composite Bladed Disc Using Travelling Wave Excitation Method

D. Di Maio, M. Vater, R. Seidel, and S. Foglia

Abstract This research article presents a novel application of travelling wave excitation method applied to a composite bladed disc. The objective of this work is to develop a non-contact excitation method for research applications where (i) blades are non-ferromagnetic and (ii) damping is nominally high. This goal was achieved by spinning a disc, on which 14 powerful DC magnets were installed, in front the composite bladed disc. Small DC magnets were attached near each blade root to provide repellent forces. Twenty blades were manufactured with pre-pregs IM7–8552, using unidirectional stacking sequence and were installed on a rigid metallic mounting hub. The paper will present the design and make of the bladed disc, the theoretical study of normal and tangential forces in a magnet-to-magnets configuration and, finally, the experimental validation of a 14-DC magnetic exciter. The forced responses were measured in one test case by a 3D single point LDV system and in another test case by a Scanning LDV system. This work will also present an attempt to develop a DC electromagnetic exciter with its limitation and potential.

4.1 Introduction

Vibration properties of bladed discs under stationary and rotating conditions have been studied for over several decades, during which numerous experimental methods were developed both for measuring and exciting blades. Literature highlights that one of the most challenging experimental goal is to excite and measure vibrations from blades with the smallest mass loading possible, the penalty being a corrupted dynamic behaviour of the system under study. All ferromagnetic materials can be easily excited by either an AC or DC source, which will work either under stationary or rotating conditions. Alternative experimental solutions can be found in literature when bladed discs are made of aluminium, which required some metallic/magnetic tabbing to attract/repel a magnetic excitation. Experimental works are furtherly complicated when dynamics are studied under rotating and vacuum conditions, whereby solutions for exciting non-ferromagnetic structures become very limited. Research on the bladed disc is, typically, focussed on the study of vibration properties under rotations to represent as much as possible operational conditions. However, any rotating object poses challenges on both excitation and measurement methods. Researchers studied excitation methods under stationary conditions to be able to replicate force patterns as similar to the ones experienced under rotation. This type of excitation has the form of travelling wave, which reproduces a loading pattern experienced by a bladed disc passing a fixed excitation source, such as a flow of combusted gases. The development of travelling wave excitation methods are reported in some papers [1–4]. The travelling excitation can be simply obtained by setting up some AC exciters in a circumferential direction up to a maximum number equal to the number of blades to excite. Each AC magnet will be then fed by a waveform differently phased from its neighbour. The phasing angle will depend on some parameters. This method was successfully to study mistuning of nodal diameters mode of vibrating bladed discs. Application of this experimental methods is seen in both magnetic and non-magnetic components. It was clear from the literature that all experimental works were limited to lightly damped bladed discs where the required excitation force was small. The difference between this research and the past literature is about the level of excitation force able to exert by using DC magnets set in rotations.

D. Di Maio (✉)
Department of Mechanical Engineering, University of Bristol, Bristol, UK
e-mail: dario.dimaio@bristol.ac.uk

M. Vater · R. Seidel
Department of Lightweight Structures, Mechanical Engineering, TU Dresden, Dresden, Germany

S. Foglia
Department of Mechanical Engineering, Università Politecnica delle Marche, Ancona, Italy

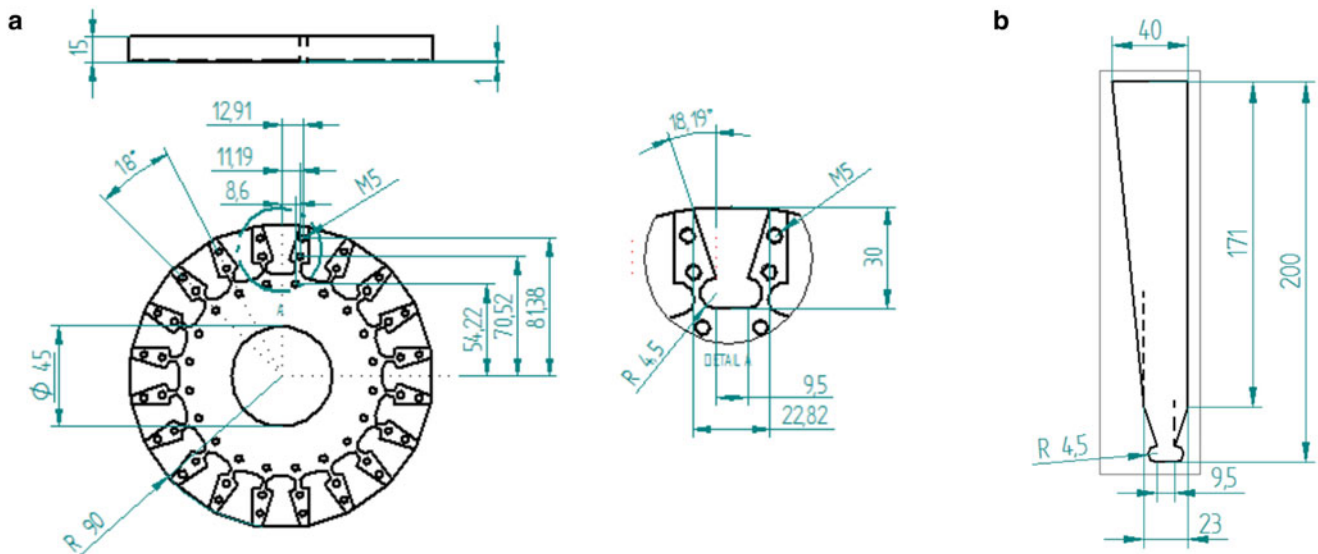


Fig. 4.1 Geometrical dimension of the mounting hub in (a) and blade in (b)

This research article is therefore focussed on the development of an excitation method for performing modal testing of a bladed disc made of non-ferromagnetic materials exhibiting considerable high damping. In fact, composite structures typically present higher damping than one made of mild steel and which can greatly affect the efficiency of the excitation method. In this research, the choice of composite materials was also due to the large expertise of the ACCIS group [5] in modelling and manufacturing thermosets composites, which are largely used in aerospace industry. One objective of this research is to develop a non-contact excitation method which is both able to (i) vibrate a bladed disc made of composites using travelling wave and (ii) to generate enough excitation force to achieve large vibration amplitudes. The paper will present various stages of this work. The first part will be focussed on the design & make of composite blades and mounting hub. Some experimental testing will be also presented. The second part will show the development of a novel DC electromagnet used to excite individual blades. Finally, the last part of the paper will focus on the theoretical study of force exchange between a magnet and a target, selected from metallic to magnetic. The study will then progress to the simulation of the magnitude and pattern of the exciting forces exchanged between a target magnet and the 14 magnets. The work will conclude by presenting the experimental validation of the 14-DC magnetic exciter used to excite the 20-bladed disc.

4.2 Design and Make of a 20-Bladed Disc

This section reports about the design and make of the composite blades and the mounting hub to hold the blades in position. The blade root was designed to have a dove tail geometry which matched the mounting hub profile. The blade root design was selected to avoid blade loss due to centrifugal load if the bladed disc were ever rotated. The mounting hub was made of two discs the inside part machined to accommodate the blade root. Figure 4.1a, b show the geometrical details of the mounting hub and the blade. The bladed disc was designed to install 20 blades made of carbon fibre composite material, IM7-8552. Each blade was made of 340 plies which were cut by a special cutter, using a segmented profile around the blade root as shown in Fig. 4.2a; this was necessary to avoid the tail to split during the cutting process. Figure 4.2b shows the prepreg plies. Figure 4.2c shows the mould and the way it was made. The angle of rotation, 20 degrees, had to be as smooth as possible along the length of the mould and therefore several attempts were made to obtain an acceptable constant curvature. Figure 4.2d shows the final manufacture of the blade after the curing process. Instead, Fig. 4.3 shows the final assembly of the bladed disc.

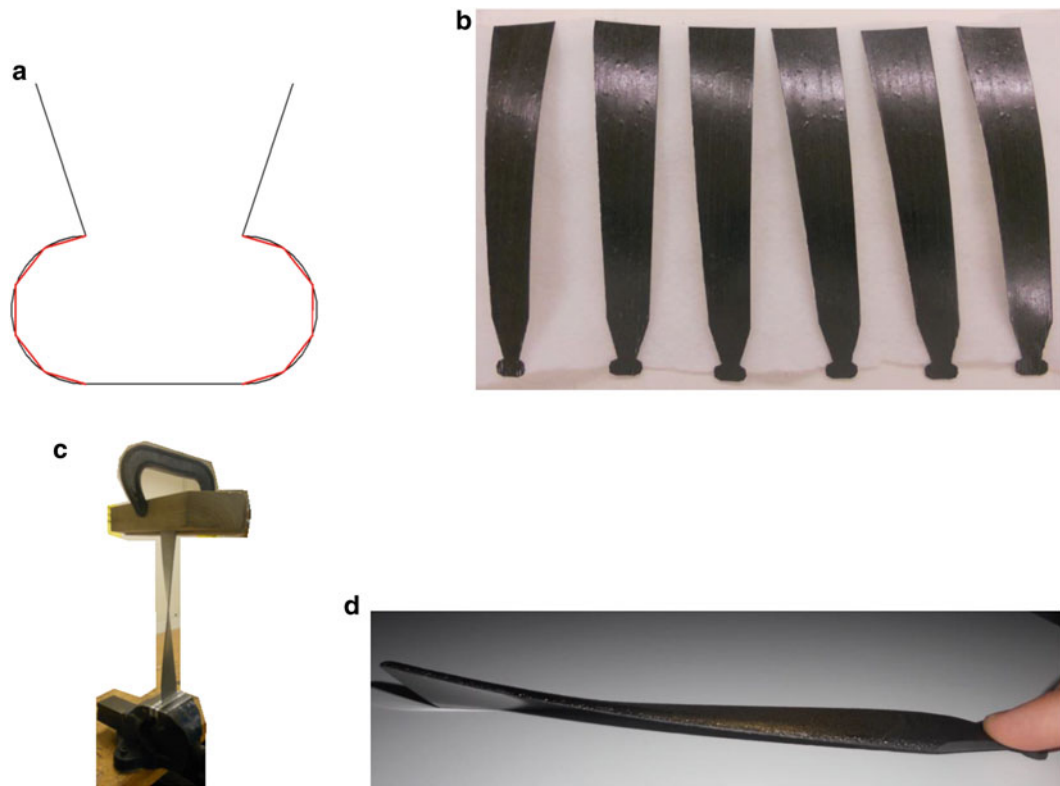


Fig. 4.2 Blade manufacturing steps. Blade root profile in (a). Unidirectional pre-pregs in (b). Tooling plate in (c). CRFP blade in (d)

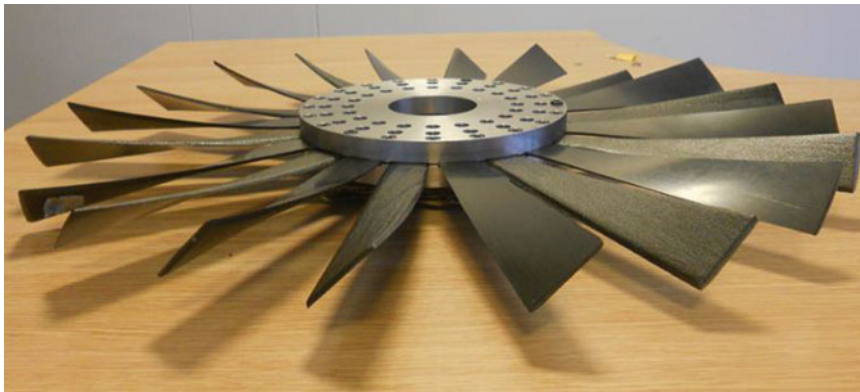


Fig. 4.3 Final bladed disc assembly

4.2.1 *Vibration Testing by Modal Hammer and a Laser Vibrometer*

After the assembly of the blades with the mounting hub, a vibration test was carried out by using a modal hammer and a 3D single point LDV. The bladed disc was installed in a rotating test rig, and reflective tape markers were stuck in each blade. Despite the silver colour sprayed on the dark blades, the laser reflectivity was not good enough. One of the major challenge was to measure all 20 blades without moving the laser head. This was achieved by fixing the laser head to a specific radial distance of the disc. All measurement points at that radial distance were rotated and positioned in front of the laser beam spot for carrying out the measurements, as showed in Fig. 4.4a, b. Then the laser head would be then moved to another radial distance, and the process would be repeated. The acquisitions were carried out by an LMS SCADAS system which measured the three outputs from the vibrometer, {X,Y,Z} vibrations, and the force of the impact hammer. Three averages per measurement point were selected. This type of measurement method proved to be very time consuming and therefore 4 points per blade were measured instead of the seven marked on each blade. Figure 4.4c-e show an example of FRFs

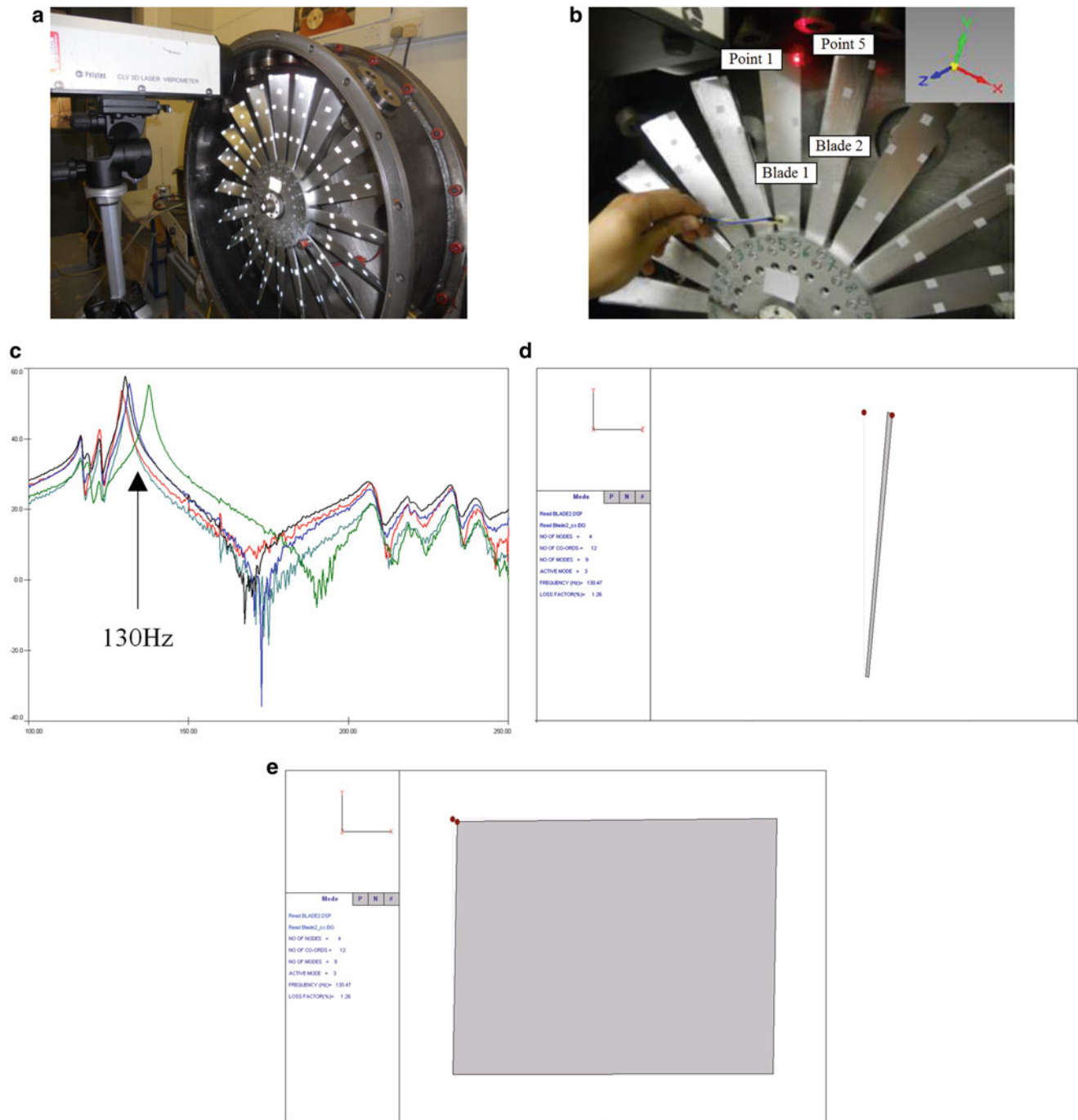


Fig. 4.4 Modal testing and analysis results. Test set-up in (a). Response and excitation location in (b). FRF in (c). Out-of-plane vibration in (d). In-plane vibration in (e)

(Z- out of plane direction), out of plane and in-plane mode of vibration, respectively. By carefully looking at Fig. 4.4c it is possible to note that the out of plane mode presents a large frequency scatter (frequency at approx. 130 Hz) indicating a large mistuning response pattern. The mounting hub is very rigid with respect to the blade stiffness, and this shows as uncoupled disc and blade modes. Surprisingly, the in-plane motion of the blades seems to be more tuned, resonances of the blades show a qualitative smaller scatter. Finally, Fig. 4.4a shows that a force gauge was installed onto one blade in an attempt to use a shaker as excitation method. It was soon realised that the poor transmissibility between the blades did not make such an exciter very useful. Hence, it was decided to excite the blades individually.

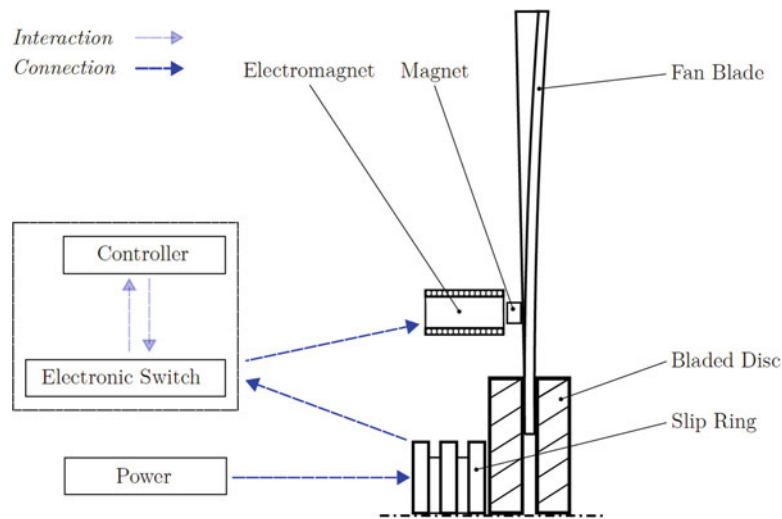


Fig. 4.5 Schematic of DC electromagnet exciter

4.3 Development of a Custom-Made DC Electromagnet Exciter

This section reports an attempt of developing a DC electromagnetic exciter. The initial idea was to develop an AC magnet rotating exciter [6] but, instead of one single magnet, there would be a magnet for each blade. Both the rotating exciter and the bladed disc would be locked on the same shaft, and the slip rings would feed the AC magnet. Unfortunately, the power requirement of 20 AC magnets would have caused issues with the slip rings power transmission. The idea was not abandoned, but a different approach was developed instead. A DC electromagnet was designed to create excitation force and, a simple schematic of the system is presented in Fig. 4.5. The basic idea is to feed an electronic circuit by a power generator. The controller and switch would create and deliver an intermittent power to the DC magnet placed right behind the blade to excite. A very small magnet is attached to the blade opposite to the DC exciter. The advantage is to feed much smaller power than the one required for AC magnets. Every blade would have its DC EM exciter with its own independent electronic circuitry. Ideally, the system could be set in rotation and the slip ring able to feed the electronic system using much smaller power than an AC system. Figure 4.6a shows the electronic system made of eight circuits able to control up to eight DC EM exciters, but only six of them were wired in. Figure 4.6b shows the electronic device installed on the rigid mounting hub, Fig. 4.6c the six DC EM exciters placed right behind the blades and Fig. 4.6d a schematic of the measurement setup controlled by a PC. An Arduino was used to control which of the exciter would be active.

The type of signal created by the electronics is an intermittent DC Voltage to the exciter, which is constantly switched on and off. A resonance frequency can be excited if pulsations is correctly built in a half period of oscillation as expressed by the following law $T_{0.5} = \frac{1}{2f} 10^6 \mu sec$. Finally, Fig. 4.7a shows the frequency steps created for exciting any resonance in a frequency range between 130 and 180 Hz and in Fig. 4.7b the time series of the LDV output signal.

The idea behind this type of design proved to be correct and, in fact, a resonance on the blade can be excited. However, the excitation system was not developed further for several reasons; it was impractical to spin such an excitation system as designed. Nonetheless, a complete rethink of the system based on this proof of concept could be set in rotation. To conclude, this design can be also suitable for excitation of travelling wave under stationary conditions if the DC EM exciters are driven with an opportune phase shift. Despite this excitation method could set in resonance a blade it was not clear if a large vibration amplitude could be obtained and so it was decided to design something simpler and more performing.

4.4 Travelling Wave Excitation Method

Having showed in the previous sections how challenging could be the excitation of a bladed disc made of composite blades, this section will show an alternative solution which is focussed on DC permanent magnets.

The introduction and section 3 presented methods based on AC/DC EM magnets which are suitable for lightly damped structures. However, these methods become less efficient when damping is high. Another drawback is small vibration

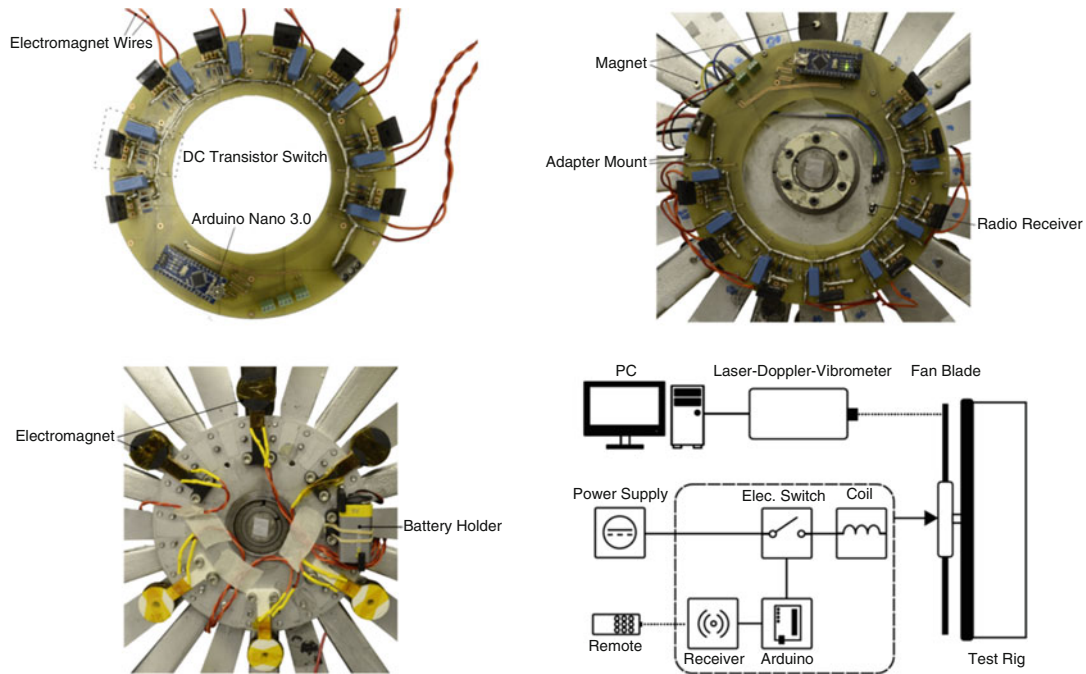


Fig. 4.6 DC EM exciters installed on the mounting hub and schematic of measurement setup

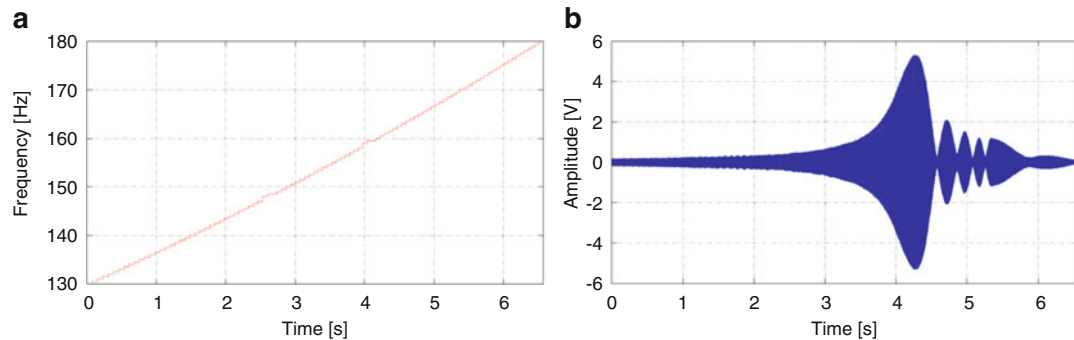


Fig. 4.7 Frequency steps in (a) and LDV output signal in (b)

amplitude achievable by these systems, which is not helpful when response amplitude dependent is studied. To overcome some limitations of the proposed exciters a different excitation method was developed. The objective was to reproduce (i) travelling excitation patterns and (ii) possible large response vibrations.

4.4.1 Modelling of Magnetic Force

Fourteen magnets (52 neodymium) were installed in an aluminium disc as shown in Fig. 4.8a. Such an excitation system would have worked with no problems with ferromagnetic materials, but composite bladed required an additional magnet to be attached to either repel or attract them. Figure 4.8b showed that the magnets were designed to repel thus avoiding any contact when the disc was spun. A Finite Element Magnetic Modelling was created to study some fundamental parameters such as the size of the magnet to install on the blade, the level of excitation force generated and the waveform pattern. For simplicity, a linearized model of the disc was created, and a target was moved incrementally alongside the set of 14 magnets, as showed in Fig. 4.9.

The density of the mesh was fine around the magnets to achieve adequate accuracy. The simulation work was divided into two parts, analysis to study the magnet-to-target and analysis to study the 14 magnets-to-target. These are presented in the next section.

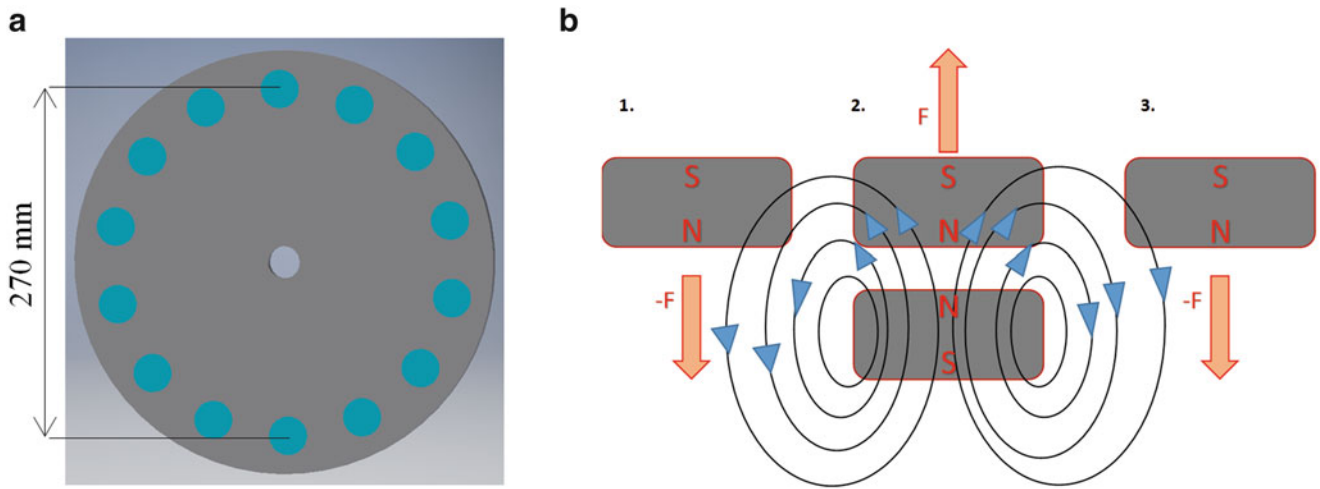


Fig. 4.8 Drawing of 14-DC magnet in disc in (a) and schematic of magnetic field in (b)

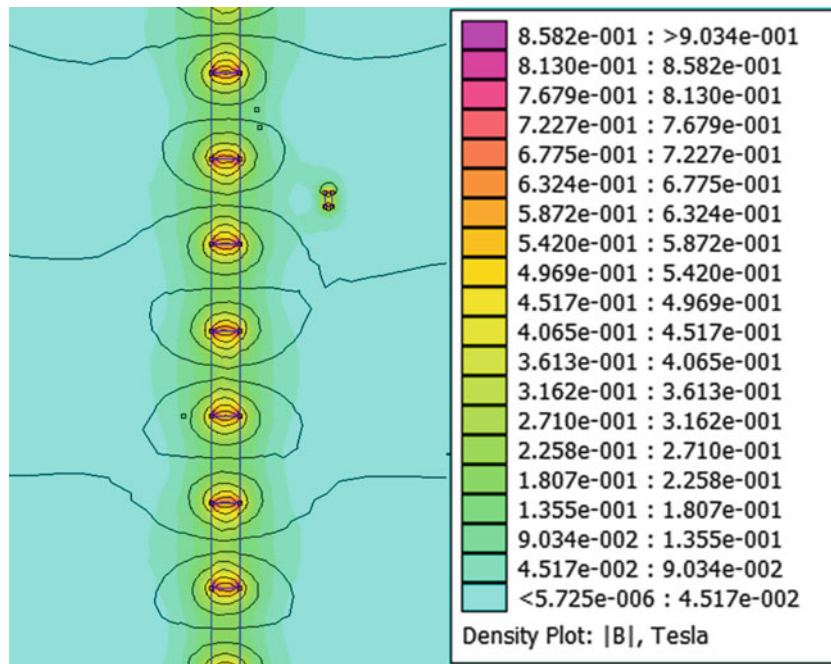






Fig. 4.9 FEMM model and magnetic force

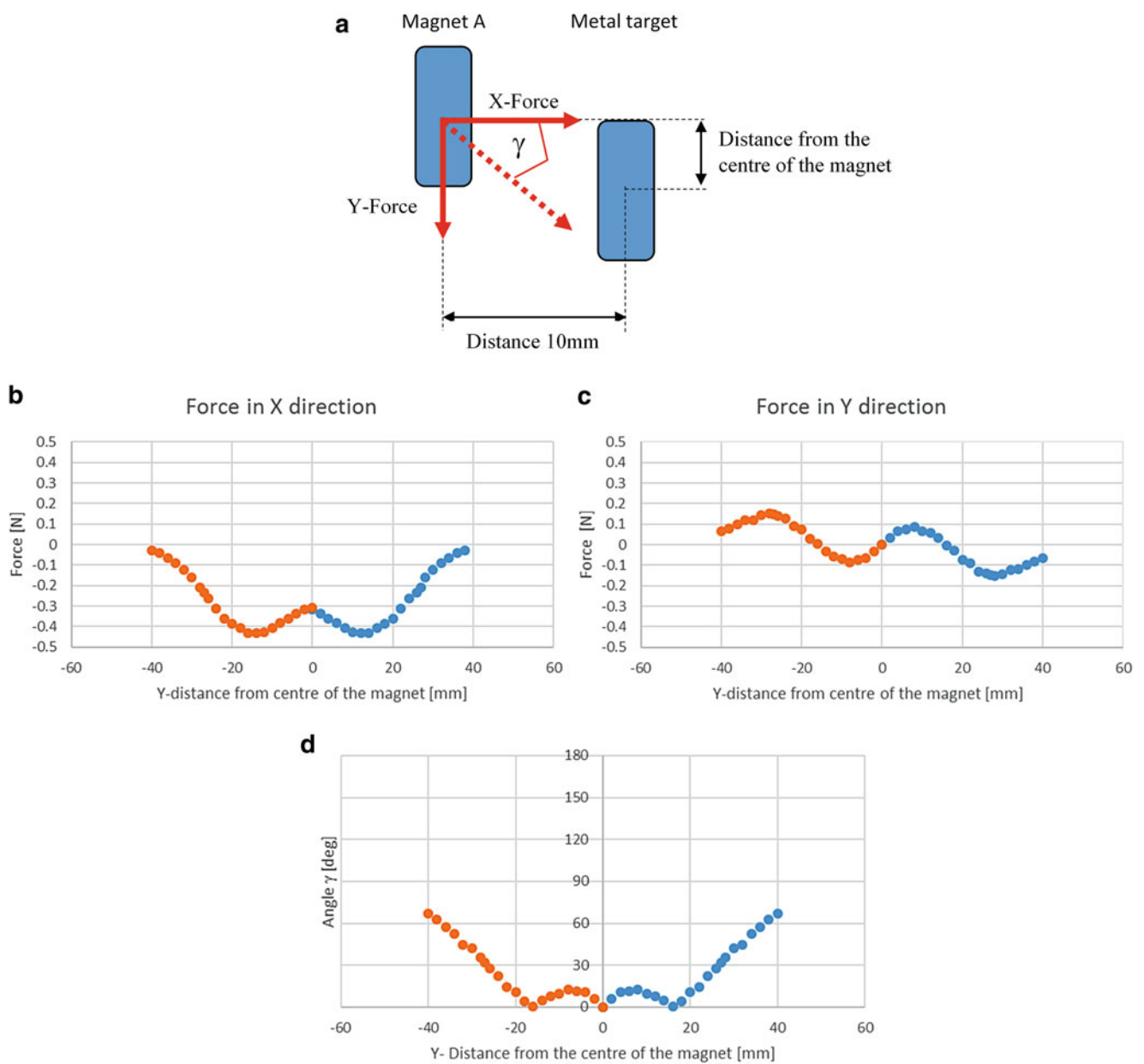
4.4.2 Single Magnet Force Characterization

The first set of simulations were aimed to understand which type of targets could be selected for a composite blade. The requirement was to achieve a good sinusoidal waveform and a suitable excitation force. Table 4.1 shows the type of targets which were all, but one, magnets of different sizes. The targets were also studied according to the distance from the excitation source. The simulations were carried out by incrementally moving the target along Y-direction, see Fig. 4.10a. Normal and tangential forces were calculated and the angle between them. Every set of data was reported in a spreadsheet and plotted to evaluate force intensity with respect to their relative position and its shape.

Figure 4.10a shows the distance from the excitation source and the metal target where Fig. 4.10a–c show the force in X and Y direction and the angle between them, which allows calculating the resultant. The metal target presents an attractive X-force, negative sign, and a shear Y-force the magnitude of which are not high. Even the shape of the X-Force is not sinusoidal.

Table 4.1 Number of targets, material type and geometrical dimensions

Target	Material type	Dimensions
Magnet A	N52 Neodymium	 \varnothing : 30mm h: 10mm
Magnet B	N52 Neodymium	 \varnothing : 5mm h: 2.5mm
Magnet C	N52 Neodymium	 \varnothing : 8mm h: 1mm
Metal	Mild steel	 \varnothing : 30mm h: 10mm

**Fig. 4.10** Metal to magnet forces at 10 mm distance. Magnet-target configuration in (a). Normal force in (b). Tangential force in (c). Angle between normal and tangential force in (d)

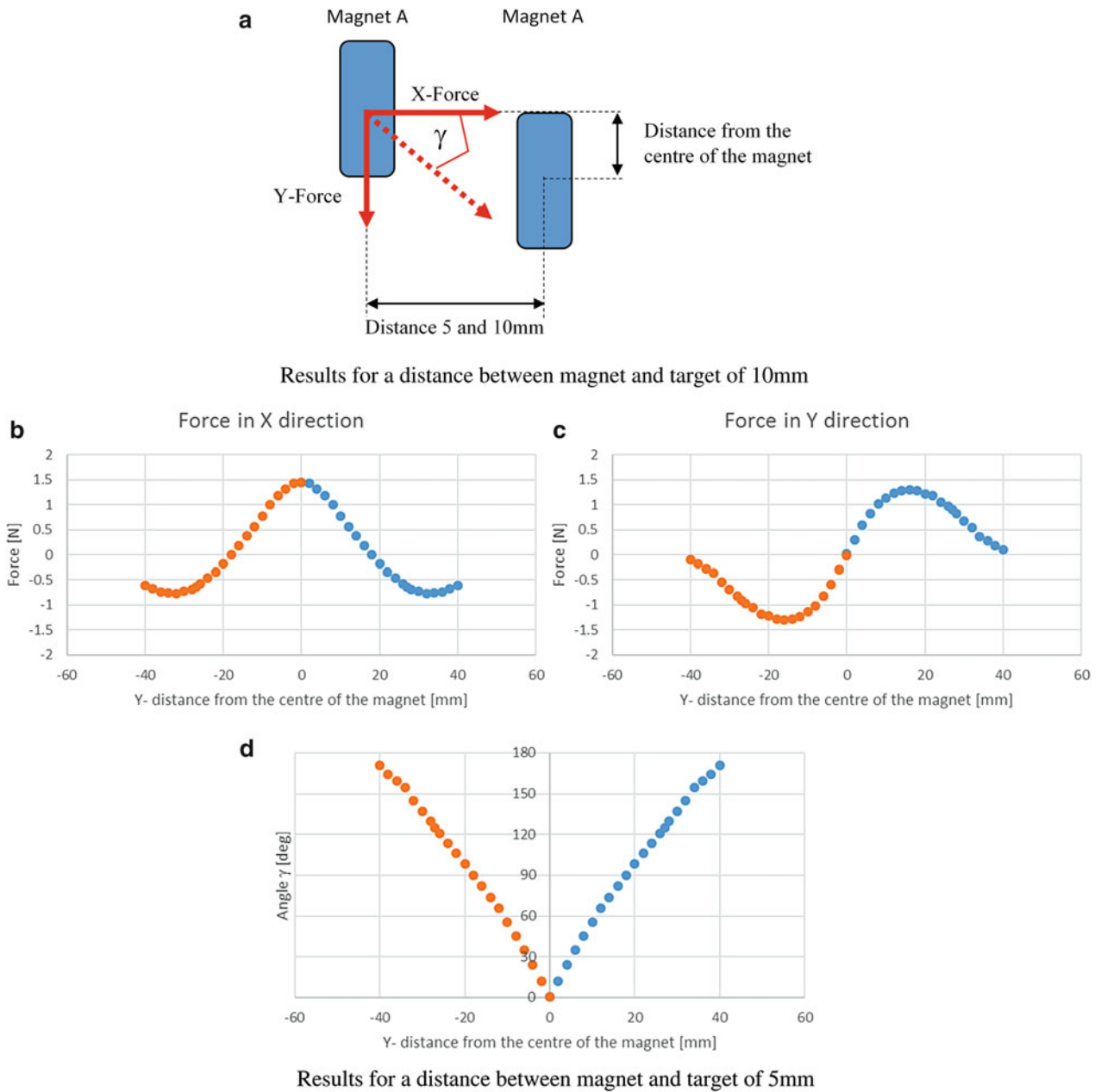


Fig. 4.11 Magnet to magnet (A-A) forces at 10 and 5 mm distance. Magnet-target configuration in (a). Normal force in (b). Tangential force in (c). Angle between normal and tangential force in (d)

Figure 4.11a shows the excitation and the target magnet of the same size, but two simulations were run for two different distances between them at 10 mm and 5 mm, respectively. Figure 4.11b–d show the forces and angle between them for a distance of 10 mm instead of the Fig. 4.11e–g show the same for a distance of 5 mm. It clear that the 10 mm distance produces a slightly better sinusoidal shape than the one for 5 mm.

Figure 4.12a–d show the results for two magnets of different dimension at a distance of 10 mm. Simulations for a distance of 30 mm were meaningless and therefore not reported. Figure 4.13a–d show results using two magnets of different size at a distance of 10 mm. Despite a similar shape of the X-forces, shown in Figs. 4.12b and 4.13b, their magnitudes seem to suggest that 5×2.5 mm size is better than the 8×1 mm.

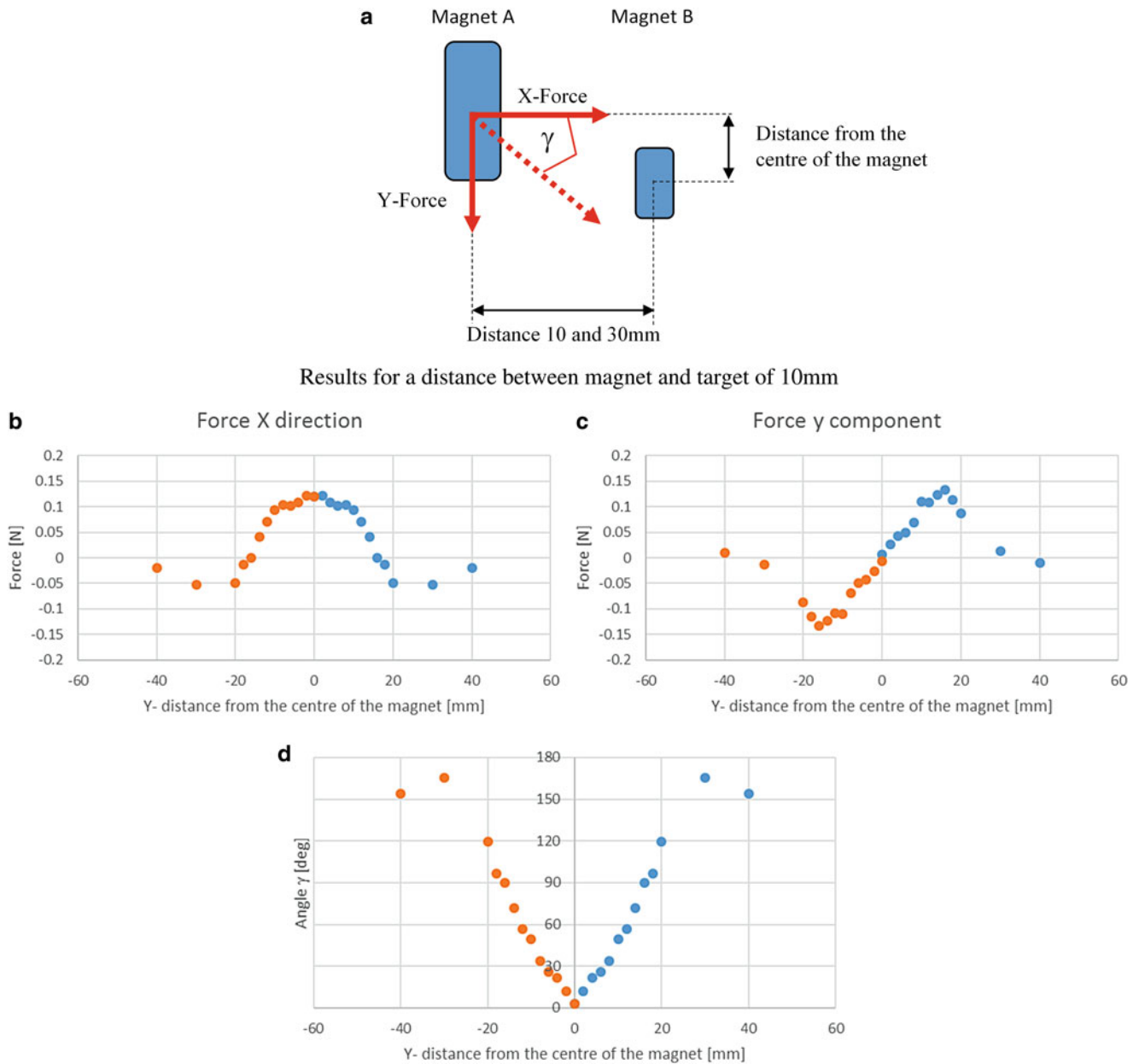


Fig. 4.12 Magnet to magnet A-B at 10 mm distance. Magnet-target configuration in (a). Normal force in (b). Tangential force in (c). Angle between normal and tangential force in (d)

4.4.3 Normal and Tangential Forces of Fourteen Magnets

The selection of the target was agreed on the 5×2.5 mm magnet since all other options were not practical for this application. Having said that, larger magnets could be used for the more specific type of tests where achievement of very large amplitudes is more important than other geometrical/dynamical parameters.

The 14 magnets, displaced in the circumferential direction, were modelled along a straight line but without altering their relative distances. Simulations were run by incrementally sliding the target magnet along the Y-direction as showed in Fig. 4.14a. Figure 4.14b–d show the X-Y forces and their relative angle. The simulations were not carried out for the full length of the original circumference ($c = \pi * 270 \text{ mm} = 848.23 \text{ mm}$) but a shorter distance such as 175 mm. The peak-peak amplitude obtained by using a 5×2.5 mm target is excellent and, also, the shape of the force which is quite sinusoidal. These results were very encouraging, but they required an experimental validation which is the focus of the next section.

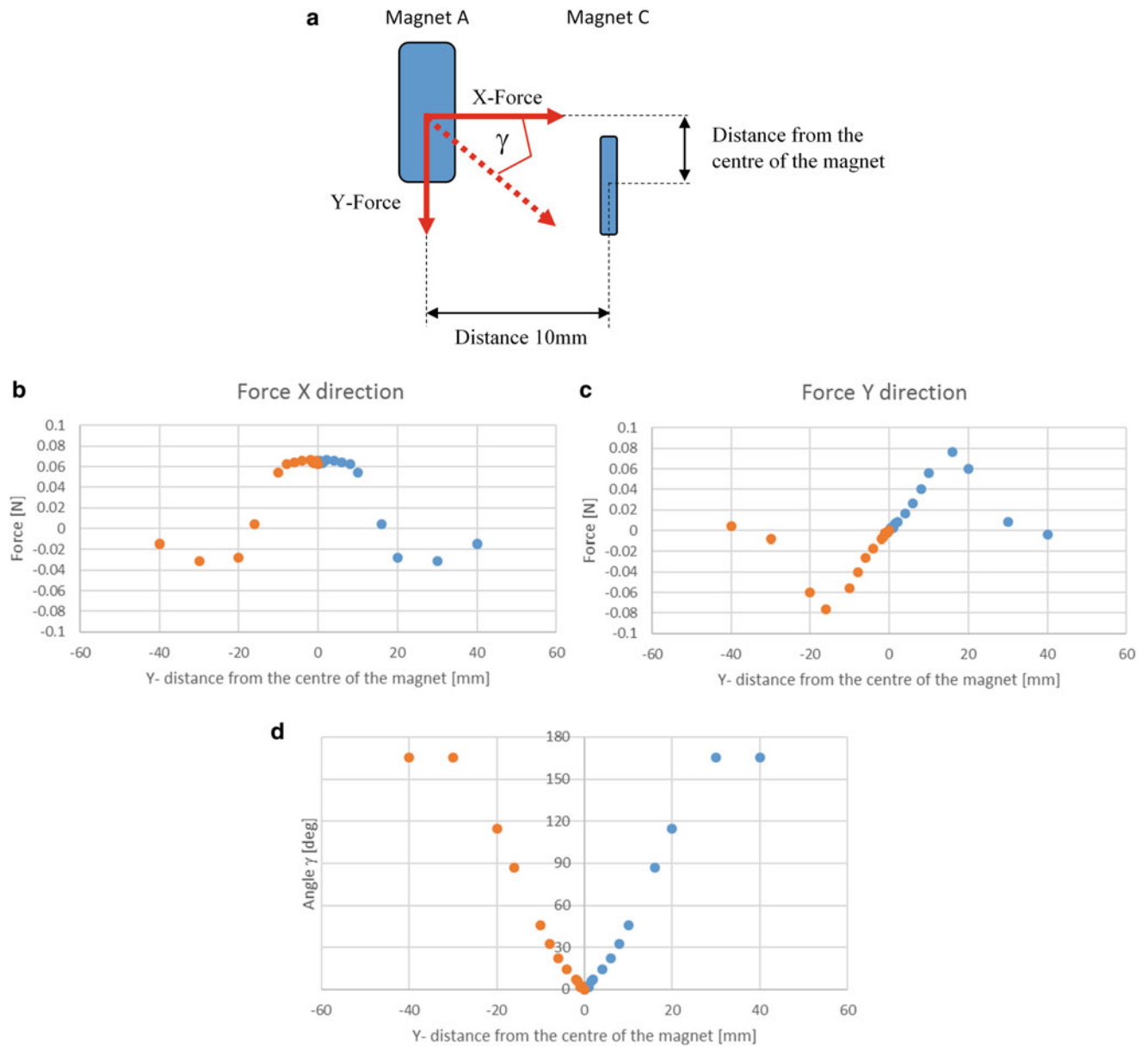


Fig. 4.13 Magnet to magnet A-C at 10 mm distance. Magnet-target configuration in (a). Normal force in (b). Tangential force in (c). Angle between normal and tangential force in (d)

4.5 Experimental Characterization

The theoretical results had to be verified against a set of experiments. These experiments were organized according to the following requirements such as (i) fixed target Vs. spinning 14-DC magnet exciter, (ii) cantilever blade with 5×2.5 mm magnet Vs. spinning 14-DC magnet exciter and, finally, fixed 20 bladed disc Vs. spinning 14-DC magnet exciter. Figure 4.15a shows the spinning test rig used for the experiments, where Fig. 4.15b shows the force gauge on which the target magnet was installed. It is also possible to observe an accelerometer which was installed to monitor any vibration caused by the shear forces of the 14 magnets. However, no significant vibrations were recorded. The 14-DC magnet exciter was installed on the shaft and spun past the fixed target using five rotational speeds such as 200, 500, 800, 1100 and 1400 rev/min. The signal from the force gauge was measured by a DAQ NI card using 10,000 Sample/sec.

Figure 4.16a shows a portion of the time series measured by the force gauge at 500 rev/min. Figure 4.16b shows the spectrum of the whole signal where it is possible to appreciate the number of harmonics present, in particular, one at approx.

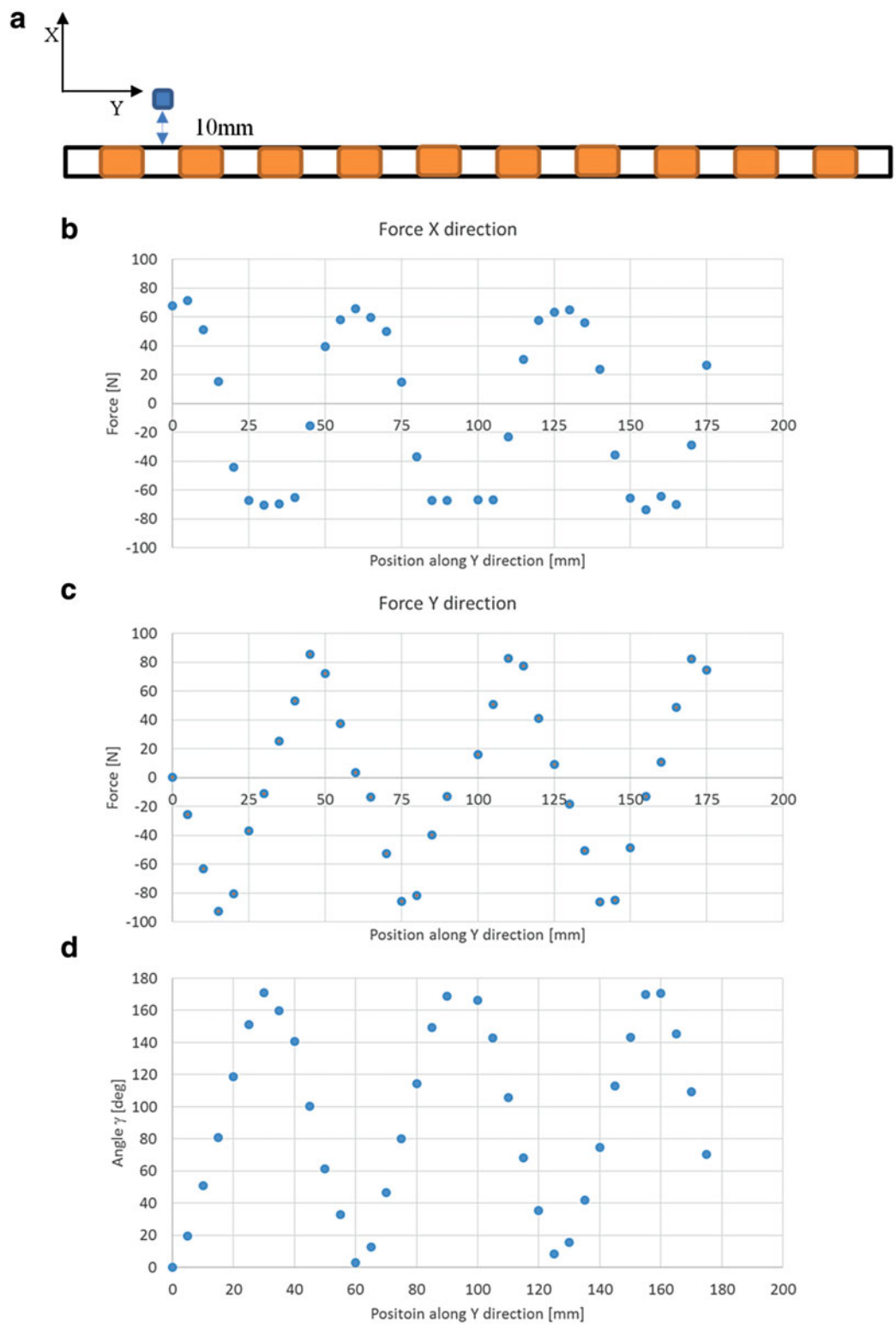


Fig. 4.14 Simulation of X-Y forces in 14-magnet configuration with 5×2.5 mm target magnet. Magnet-target configuration in (a). Normal force in (b). Tangential force in (c). Angle between normal and tangential force in (d)

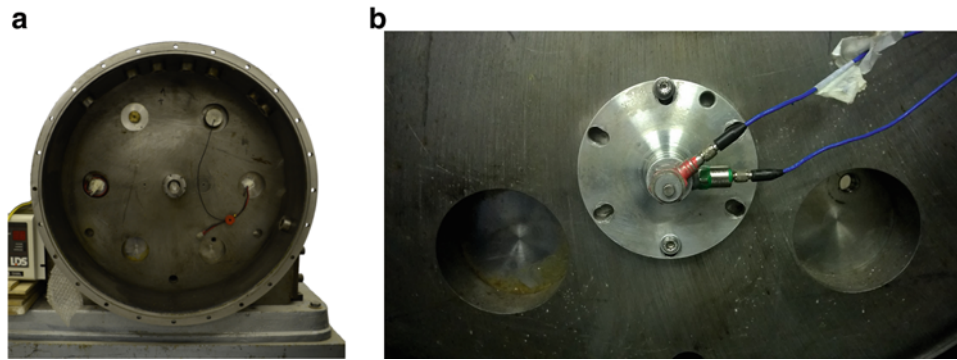


Fig. 4.15 Test chamber in (a). Target attached to force gauge in (b)

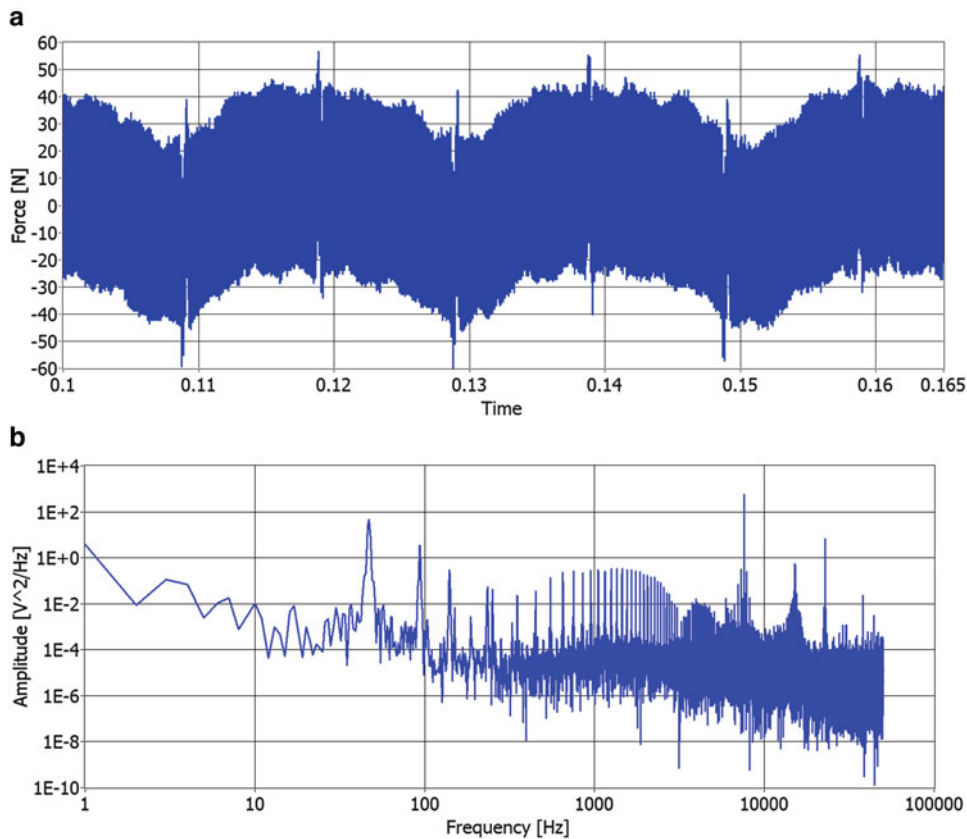


Fig. 4.16 Time series of the force measured by the gauge in (a) and its spectrum in (b)

7.586 kHz. Figure 4.17 shows a short portion of the time series in blue and the filtered signal in red. The filter was a passband Butterworth 1st order.

By filtering the 7.586 kHz oscillation it was possible to plot the underlying oscillation for different rotational speeds setup for the experiments. Figure 4.18a–d show the excitation force without all spurious harmonics and a dominant one at 7.586 kHz. The peak-peak excitation force is approx. 18 N in all the presented test cases, which show a remarkable sinusoidal waveform shape. However, the actual measured force is smaller than the simulated one. It is not clear why and what triggered the 7.586 kHz harmonic oscillation and if that frequency can be considered the peak-peak signal, which is approx. 90 N peak-peak but still lower than the one calculated (approx. 140 N).

The first set of experiments showed useful results both in terms of excitation force exerted and in terms of sinusoidal patterns at different speeds. The next phase was to use a cantilever composite blade with the same target magnet, 5×2.5 mm, and repeat the test by exciting the first bending mode of the blade. The target magnet was installed at the same location where it would be for the 20-bladed disc configuration. Figure 4.19 shows the forced response vibration of the composite

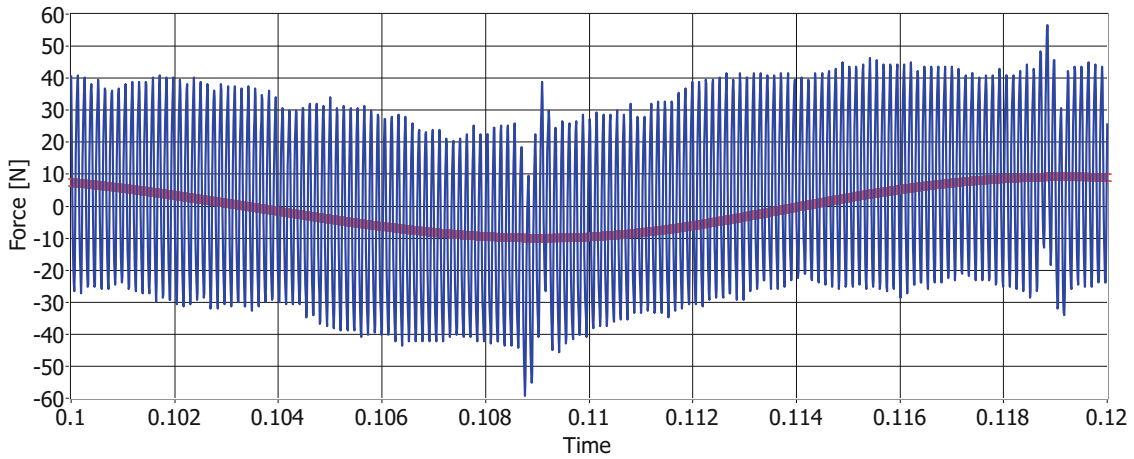


Fig. 4.17 Filtered (red) and unfiltered signals (blue) of the force gauge

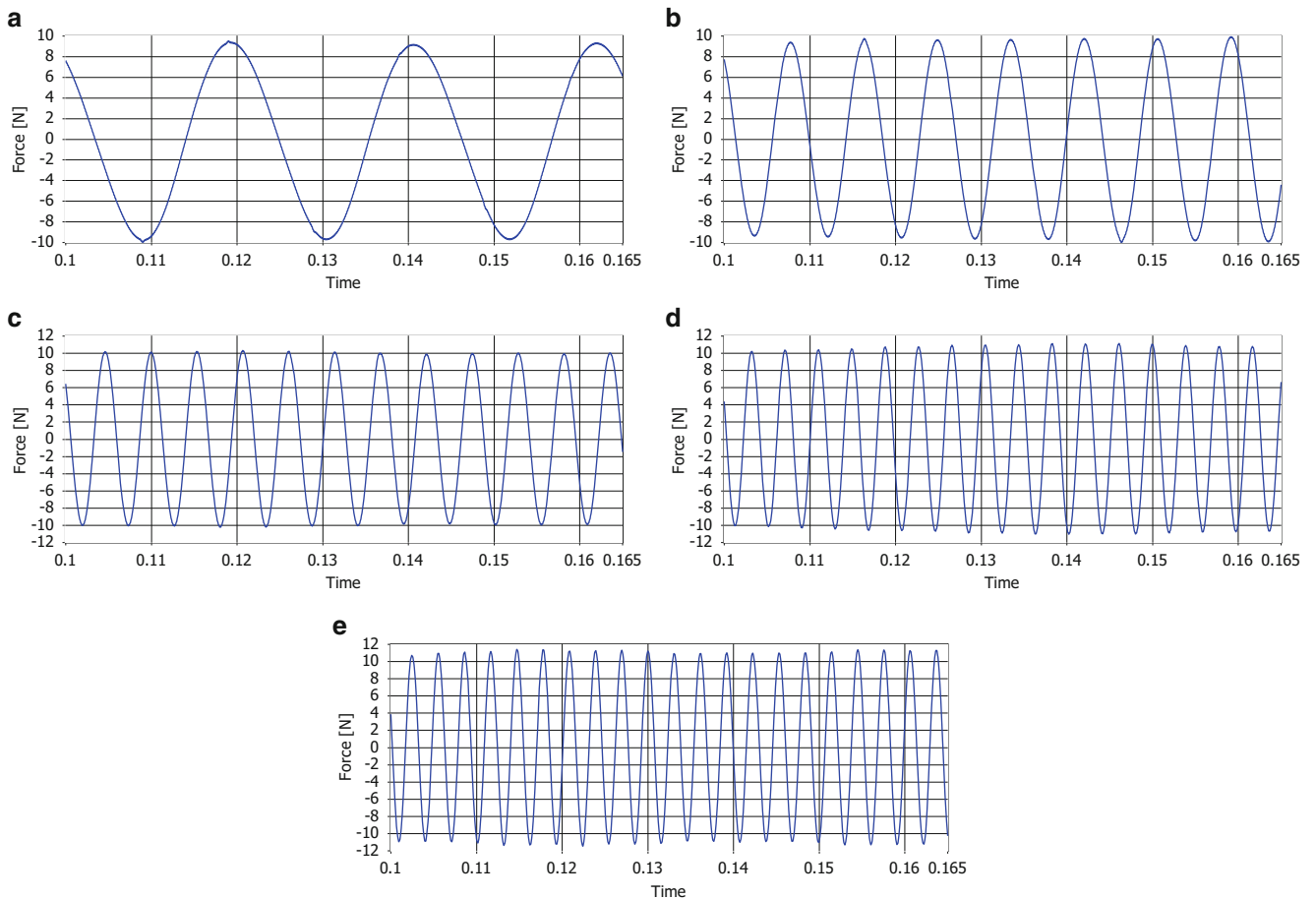


Fig. 4.18 Filtered waveforms measured at different rotational speeds, 200 rev/min in (a), 500 rev/min in (b), 800 rev/min in (c), 1100 rev/min in (d) and 1400 rev/min in (e)

blade, where it is a noticeable skewness caused by the large vibration amplitude generated by the exciter; a typical nonlinear behaviour. The final stage of the experiments was to rigidly fix the 20-bladed disc on the back plate of the test rig and have the 14-DC magnetic exciter spinning in front of it. One target magnet 5×2.5 mm was installed for each blade of the disc. Figure 4.20 shows both the bladed disc with the target magnets and the exciter installed in front of the bladed disc. A Scanning LDV system was used to measure the response from four measurement points marked by reflective tapes (mid measurement point

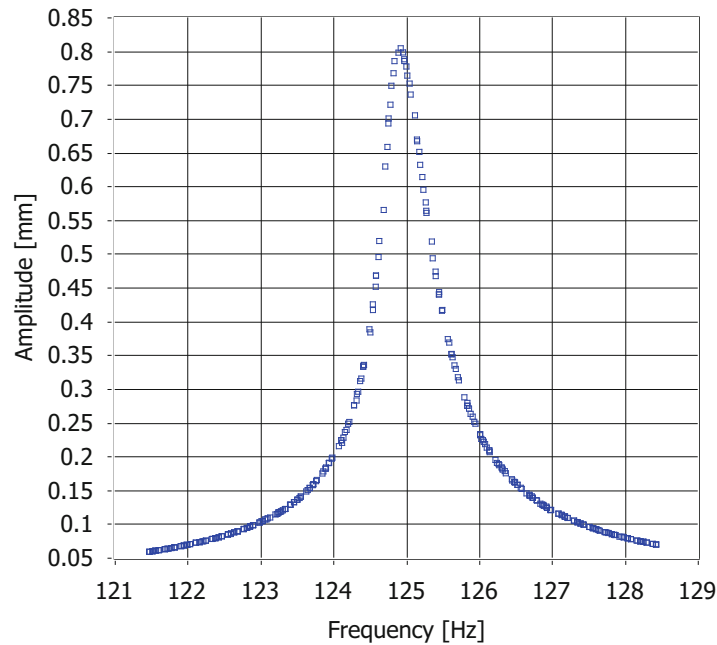


Fig. 4.19 Forced response vibration of a cantilever blade excited by the 14-DV magnet exciter

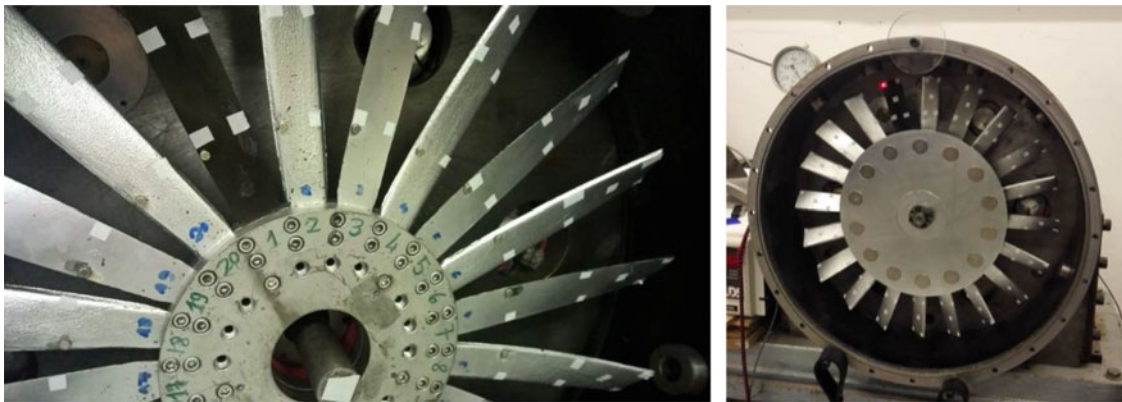


Fig. 4.20 Bladed disc on the left and exciter on the right

was not used). The 14-DC magnetic exciter was spun between 120 and 1500 rev/min with a speed increment of 0.1 rev/min. A total of 80 measurements were carried out. Figure 4.21a shows the vibration response of one measurement point, where the red arrow shows the aliased responses measured because of multiple engine orders excitations. Figure 4.21b shows a zoom around 130 Hz of the resonances of the first bending mode. This was not a surprise after the tests carried out by modal hammer and showed in Fig. 4.4c. The vibration of the aluminium disc was also monitored to check if any vibration mode would be excited as result of exchanges of forces between the magnets. Fortunately, this was not the case for the response under study.

The excitation method showed great flexibility and safe use. In fact, the mechanism is simpler than what is required by a series of amplifiers and controllers used for operating AC magnets. The level of forces generated are also higher than what can be achieved by AC systems. There could be some unknowns, but not investigate here, about the shear forces caused by spinning DC magnets. In practice, a bladed disc is immersed inside a fluid of combusted gasses, and it is not unreasonable to think a combination of normal and tangential forces acting on the spinning blades. In the presented test case, the rich magnetic environment spins around the blades causing a similar combination of tangential and normal forces. It is clear that the centrifugal load effect cannot be considered in this type of experiments but, nonetheless, these effects can be replicated by mirroring the proposed test configuration; the magnets are fixed, and the bladed disc rotates.

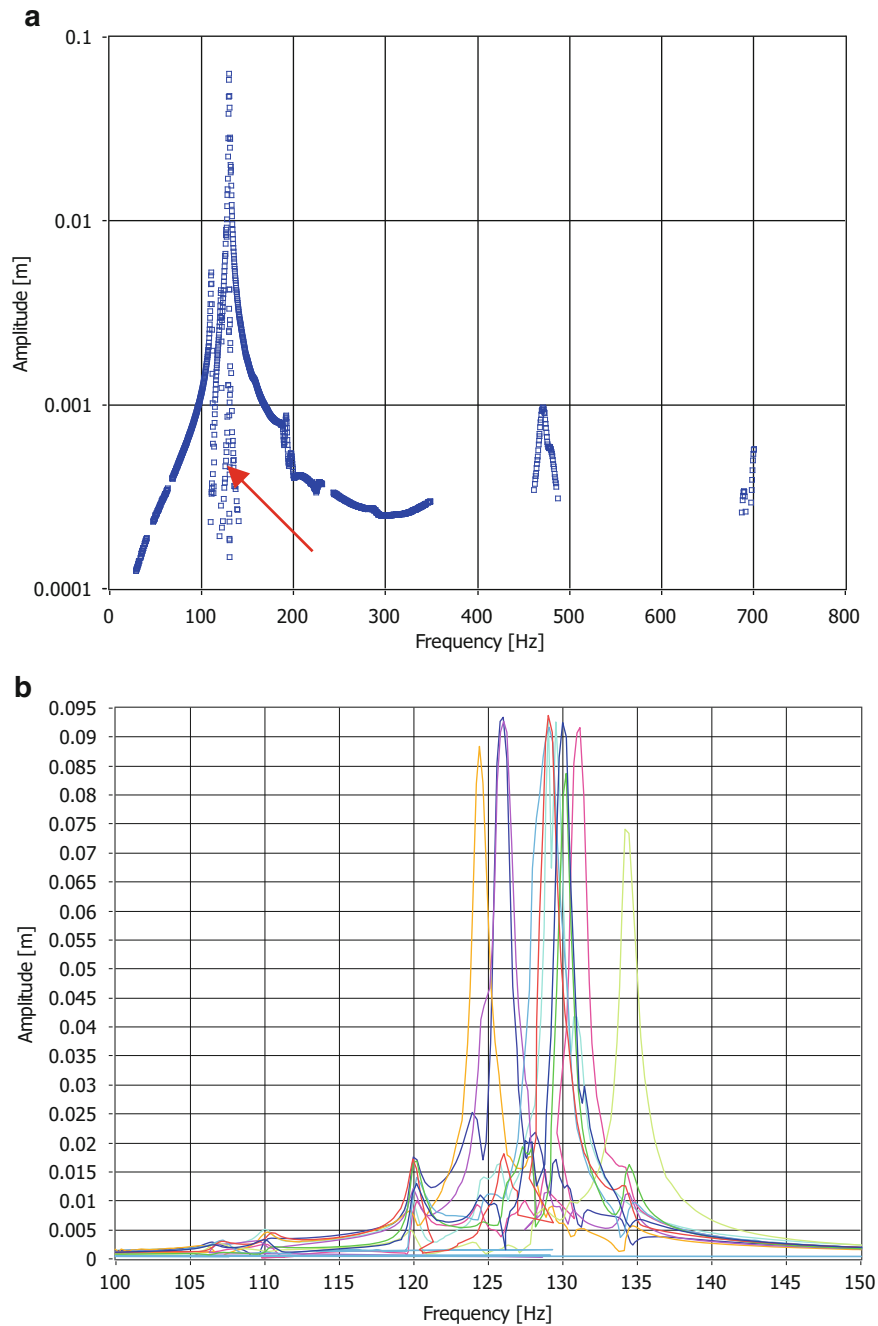


Fig. 4.21 Vibration response of one point in (a) and multiple points in (b)

4.6 Conclusions

This research paper presented the challenges of exciting a composite bladed disc. The major complication was caused by little transmissibility which required to excite the blades individually. Modal impact and the DC electromagnetic exciters testing showed a great frequency scatter for modes around 130 Hz. The use of a 3D single point LDV was very helpful to visualize the 3D motion of the measurement points but the test execution was very time consuming. The DC EM exciter showed some interesting potential but at present the excitation system also showed several drawbacks. The last excitation system was achieved by using 14 DC magnets installed on an aluminium disc. The disc could be rotated to generate a travelling wave excitation. The design of such a system was anticipated by a set of simulations to select the best target magnet to install

on the blades. Experiments on force characterisation were performed, and these yielded to encouraging results, but also to the revelation of a harmonic at 7 kHz not yet understood. The excitation forces generated were considerably high. The final phase of the tests was to perform forced response measurements on all the 20 composite blades. The results showed a clear scatter of the first bending mode resonances which, again, was expected following the modal hammer test.

In conclusion, the 14-DC magnetic exciter showed good ability to provide strong excitation forces. The measurement system is very simple. The measurements are also simple to carry out because of the stationarity of the bladed disc. The large forces exerted by this exciter can open several avenues into new studies of blade root contact conditions, which are amplitude dependents.

Acknowledgment The authors would like to thank F. Carstensen, S. Chauhan, D. Naylor, A. Tantalò Rolls-Royce graduate trainees to have supported this research study and Clive Rendall for his valuable suggestions on the design of the 14-DC magnetic exciter.

References

1. Firrone, C.M., Berruti, T.: An electromagnetic system for the non-contact excitation of bladed disks. *Exp. Mech.* **52**(5), 447–459 (2012)
2. Kühhorn, A.: GT2010- experimental and numerical investigations of HPC blisks with a focus on travelling waves. *Proc. Asme Turbo Expo* (2010)
3. Berruti, T., Firrone, C.M., Gola, M.M.: A test rig for noncontact traveling wave excitation of a bladed disk with Underplatform dampers. *J. Eng. Gas Turbines Power.* **133**(3), 32502 (2011)
4. Jones, K.W., Cross, C.J.: Traveling wave excitation system for bladed disks. *J. Propuls. Power.* **19**(1), 135–141 (2003)
5. ACCIS.: [Online]. Available: <http://www.bristol.ac.uk/composites/>
6. Di Maio, D., Ewins, D.J.: Applications of continuous tracking SLDV measurement methods to axially symmetric rotating structures using different excitation methods. *Mech. Syst. Signal Process.* **24**(8), 3013–3036 (2010)

Chapter 5

Simulation of the Dynamic Behavior of a Bi-Cable Ropeway with Modal Bases

Gabriel Hurel, Jerome Laborde, and Louis Jézéquel

Abstract This article presents the building of a dynamic model of a bi-cable ropeway. Thanks to the assumption of quasi-static advance of the vehicles, the calculation is performed step by step. At each step, a transient linearized dynamic solution is calculated around the quasi-static equilibrium using modal bases. The ropeway system is substructured considering the different elements: track rope, hauling rope and vehicles represented by pendulums. The results of time integration give the accelerations felt by the passengers according to the load case.

5.1 Introduction

5.1.1 Problematic

In order to improve mobility in cities, new types of public transport are investigated. In particular, ropeway is highlighted because it presents several benefits. First, the cost of building is relatively low compared to subway or tramway. It only needs to build stations and some pylons. The space used by the infrastructure on the floor is very low: unlike bus and tramway, the ropeway is not in the way of streets. Moreover, the speed of displacement is quite high and the throughput is similar to that of a tramway. Finally, this is one of the most secured type of transport. The rate of injuries and deaths per passengers is the lowest of all types of transportation.

On the other side, ropeways have drawbacks. The regulation can be an obstacle to the proximity between the cabins and habitation buildings. In fact, the ropeway can create some discomfort for the neighborhood. The noise and the obstruction of the view can degrade the comfort of residents. It might also have some problems for the comfort of the passengers. The comfort criteria are thermic, acoustic and vibratory.

Within the I2TC project, the objective of this article is to provide a tool able to solve dynamic and vibratory issues of an urban ropeway. In fact, the dynamic requirements for public transports are higher than touristic installations. For this, a dynamic modelling of a ropeway line is performed. Thus we aim to understand the dynamic behavior of the line and be able to predict the acceleration felt by passengers. The sensitive parameters can be found and an optimization can be performed.

5.1.2 The 3S Cable-Car

One of the technologies considered for urban transportation using ropes is the 3S cable car. As its name indicates, the number of cables is three. Two of them are track ropes which sustain the vehicles. They are fixed and the vehicles are rolling on them like a train on a railroad. The third cable is the hauling rope. Its role is to pull the vehicles along the line. This cable is moving at the same speed as the vehicles, since they are clamped on it.

The track ropes are embedded in the first and the last station. Their tension is tuned few times in the year in order to compensate the thermal expansion. In service the tension is varying mainly due to the load of vehicles. The tension of the hauling rope is kept constant at the first station by a hydraulic cylinder. The tension at the last station is imposed by the engine to haul the vehicles.

G. Hurel (✉) · J. Laborde · L. Jézéquel
Ecole Centrale de Lyon, LTDS, Ecully, France
e-mail: Gabriel.Hurel@ec-lyon.fr

The vehicles are composed of three main parts: the cabin, where the passengers are, is hanged to a carriage by a hanger. The hanger is fixed to the carriage by a damped revolute joint. The carriage is fixed to the hauling rope by a clamp and it is rolling on both track ropes.

5.1.3 Bibliography

The theory of vibration of a cable was mainly developed by Irvine [1] in the seventies. He developed analytical models able to calculate the shapes and the frequencies of the first eigenmodes of a cable with a small sag. Sack [2], Simpson [3] and Triantafyllou [4] studied the vibrations of a cable in translation.

Sergev and Iwan [5] were ones of the first to study a cable with masses. They represent a taut cable by a succession of segment. Rosenthal [6] used an iterative method to find the modes of a cable with sag and masses. Cheng and Perkins [7] calculated the eigenmodes when the position of the mass is varying from one end of the cable to the other. Al-Qassab [8] computed these eigenmodes with a Galerkin method.

The first model of a ropeway is certainly that of Portier [9]. The vehicles are represented by pendulums and the cable by springs. The results are compared with experiments. Brownjohn [10] built a model with a small sag cable to modelize the ropeway of Singapore. Sofi [11] represented the cabins with damped oscillators.

5.2 Model Building

5.2.1 Presentation

The proposed model shown in Fig. 5.1 corresponds to a span between two pylons. Since the model is planar, only the half of the system is considered: one track rope, a half of the hauling rope and half of the vehicles. Both pylons are assumed to be infinitely rigid. The cables are assumed to be elastic, with a mass. Because of low angles of bending, the bending rigidity is neglected.

Each vehicle is modelled by a pendulum as shown in Fig. 5.1. At the top, the carriage is represented by a point mass. It is in sliding contact with the track rope and clamped on the hauling rope. The hanger is attached to the carriage by a damped cylindrical joint. It has a rotational inertia and a longitudinal stiffness. Another point mass represents the cabin.

In this model, dynamic effects that could occur between cables and the atmosphere are not considered.

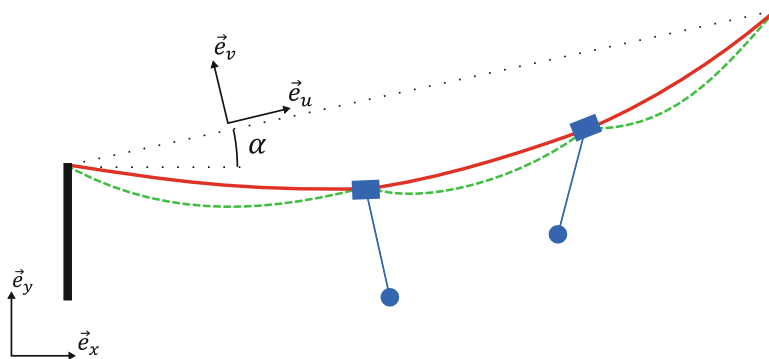


Fig. 5.1 Model of the 3S cable car (red line: track rope, green line: hauling rope, circle: carriage, square: cabin, blue line: hanger)

5.2.2 Assumptions

Considering the studied system, two strong assumptions are made. First, the speed of the vehicles C is low enough to consider the motion of the vehicles have no dynamic effect on the system. In other words, the cabins are slow enough to consider their advance as quasi-static. The system can be represented by a succession of static equilibriums.

To validate this assumption, the results of a simple model of a mass moving on a taut cable is compared with the quasi-static solution. Figure 5.2 shows the state of the cable when the mass is located at the middle of the cable for three values of speed: a low speed similar to the speed of the cable car vehicles speed, a high speed similar to the speed of high speed trains and a transitional speed. The solid line represents the quasi-static solution. In every cases, the inertial forces tend to separate the cable from its static shape but in the high speed case these forces are higher so the error on the displacement cannot be neglected.

At low speed (10 m/s), Fig. 5.3 shows that the average error E on the displacement is below 1%.

$$E = \frac{1}{T} \int_0^T \frac{1}{L} \int_0^L \left| \frac{u_R - u}{u_R} \right| dx dt \tag{5.1}$$

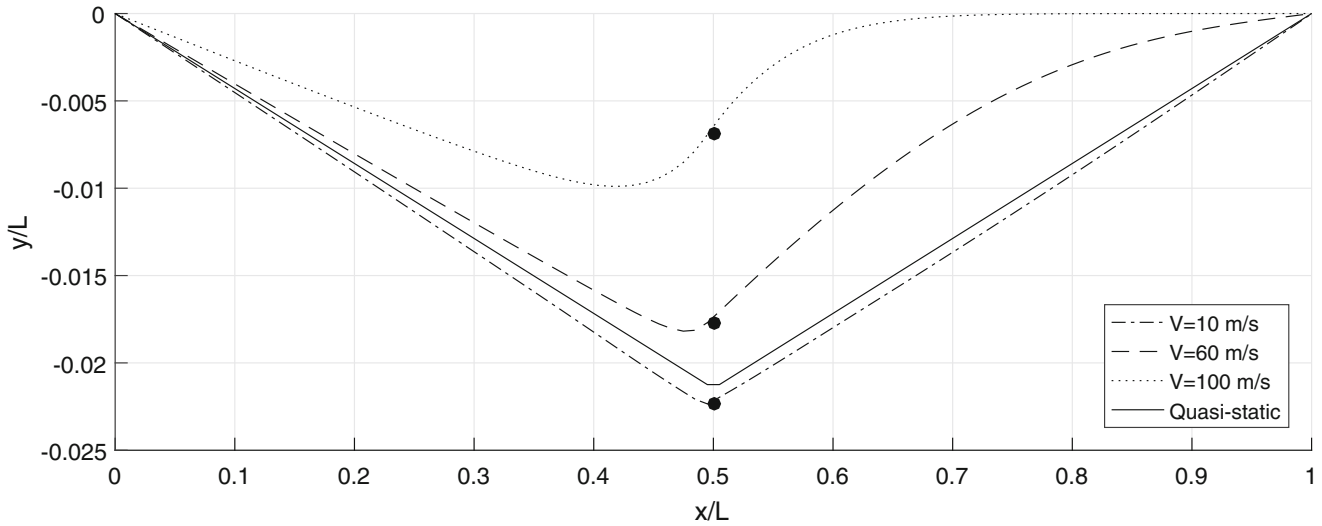


Fig. 5.2 Comparison of the shape of the cable for three different speeds of the mass and the quasi static solution

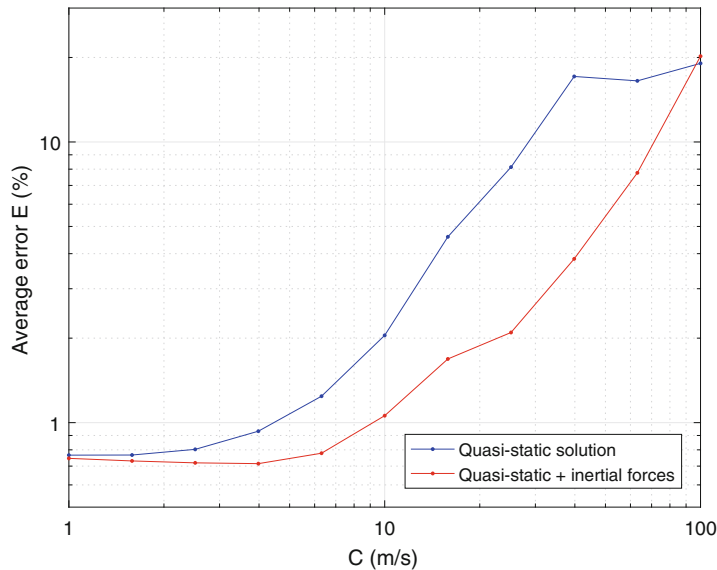


Fig. 5.3 Average error with the quasi static assumption for different speeds of the mass

Where T is the period required by the mass to travel on the cable, L is the length of the cable, u_R is the reference displacement of the cable and u is the calculated displacement.

A correction of the quasi static solution can be made by adding the inertial forces of the mass and the cable calculated with the succession of equilibrium states. The results with this correction shown in red line on Fig. 5.3 are better, in particular at speeds between 10 and 60 m/s.

Around these static equilibriums, we assume the dynamic displacement is small enough to linearize the behavior equations. This important assumption allows us to project the problem on the eigenmodes of the structure.

5.2.3 Computation Strategy

Thanks to the first assumption, the computation is performed step by step. The advance of the vehicles is discretized. Each step corresponds to a position of the whole of vehicles along the cables. At each step, a non-linear static equilibrium will be computed.

Under the assumption of small dynamic displacement, linear eigenmodes of each cable part are calculated, taking into account the position of the vehicles and parameters of the static equilibrium: shape and tension of the cables. The eigenmodes of the entire track rope constitute a modal basis on which the behavior equations are projected.

A part of the hauling rope is the portion between two vehicles or between a vehicle and a pylon. The extremities of each part of the hauling rope are not always stationary but may be linked to the vehicles. Static response modes have to be added to the natural modes. The behavior of the pendulums embodying the vehicles are considered as non-linear to keep a good coupling with cables.

After assembling all parts: reduced track rope, reduced hauling rope parts and vehicles, a time integration is performed at each step. The initial conditions of a step are provided by the final state of the previous step. The global behavior of the system is given by the sum of static and dynamic results.

5.3 Static Equilibrium

5.3.1 Static Equation of a Cable

The force on the elementary portion ds at the position (x, y) are the weight and the tension on each side:

$$\mu ds \vec{g} + \vec{T}(x) + \vec{T}(x + dx) = \vec{0} \quad (5.2)$$

Where μ is the linear mass, \vec{g} the gravitational acceleration and $\vec{T}(x)$ the tension of the cable at the global coordinate x . The vector Eq. (5.2) is projected on x and y axes:

$$\frac{dT_x(x)}{dx} = 0 \quad (5.3)$$

$$\frac{dT_y(x)}{dx} = \mu g \frac{ds}{dx} \quad (5.4)$$

The linear mass μ is not constant because of the elastic strain:

$$\mu = \frac{\mu_0}{1 + \frac{T}{ES}} \quad (5.5)$$

Where E and S are the Young modulus and the area of the section of the cable respectively. In the ropeways case, the tension T is negligible compared to the product ES . The order of magnitude of the ratio T/ES is -3 . So we consider μ as a constant. The Eqs. (5.3 and 5.4) give us the differential equation:

$$\frac{d^2y(x)}{dx^2} = \frac{1}{\tau} \sqrt{1 + \left(\frac{dy(x)}{dx}\right)^2} \quad (5.6)$$

The constant τ is homogeneous to a length and equal to $T_x/\mu g$. The solution of the Eq. (5.6) corresponds to a catenary curve:

$$y(x) = \tau \cosh\left(\frac{x}{\tau} + K_1\right) + K_2 \quad (5.7)$$

The constants K_1 and K_2 are calculated with the boundary conditions for each part of the cable. The expression of the tension of the cable is given by:

$$T(x) = T_x \cosh\left(\frac{x}{\tau} + K_1\right) \quad (5.8)$$

5.3.2 Equilibrium of a Vehicle

The forces exerted on a vehicle with a mass M at the abscissa x_M are the gravitation, the tension of the hauling rope T_H on the left side and on the right side and the reaction of the track rope \vec{N} :

$$M\vec{g} + \vec{T}_H^L(x) + \vec{T}_H^R(x) + \vec{N} = \vec{0} \quad (5.9)$$

The contact between the vehicle and the track rope is frictionless, hence the force \vec{N} is orthogonal to the track rope. However the angle of the cable on the left side φ_L is not the same as the angle on the right side φ_R . The angle φ_M of the force \vec{N} is chosen as the average of the angles of the track rope:

$$\varphi_M = \frac{\varphi_L + \varphi_R}{2} \quad (5.10)$$

The equilibrium of the point of the track rope in contact with the vehicle is given by:

$$\vec{T}_T^L(x) + \vec{T}_T^R(x) = \vec{N} \quad (5.11)$$

The projection on the direction orthogonal to \vec{N} shows that the tension of the track rope T_T is equal on the left and on the right of the vehicle.

5.3.3 Equilibrium of the Span

In the same way as the linear mass, we consider the length of the track rope L_c is not varying because of its elasticity, hence it is constant:

$$L_c = \int_A^B ds = \int_{x_A}^{x_B} \sqrt{1 + \left(\frac{dy_c(x)}{dx}\right)^2} dx = \sum_{i=1}^{n+1} \int_{x_{i-1}}^{x_i} \tau_{ci} \frac{d^2 y_c(x)}{dx^2} dx = \sum_{i=1}^{n+1} \cosh\left(\frac{x}{\tau_{ci}} + K_{1ci}\right) \quad (5.12)$$

The number n is the number of vehicles on the span. Consequently there are $n + 1$ parts on each cables in the span. The equations of the equilibrium of the vehicles (5.9 and 5.11) and the Eq. (5.12) are implemented in a nonlinear solver to determine the constants K_{1i} and K_{2i} of each cable part.

5.4 Results

Figure 5.4 shows the shape of the cables of a span with three vehicles in a certain position. Because $\tau_{ci} > \tau_{hi}$ the sag of the hauling rope is more important than the sag of the track rope.

The tension of both cables are shown in Fig. 5.5 for the same position of the vehicles. The tension of the track rope is continuous whereas the tension of the hauling rope has discontinuities at each vehicle.

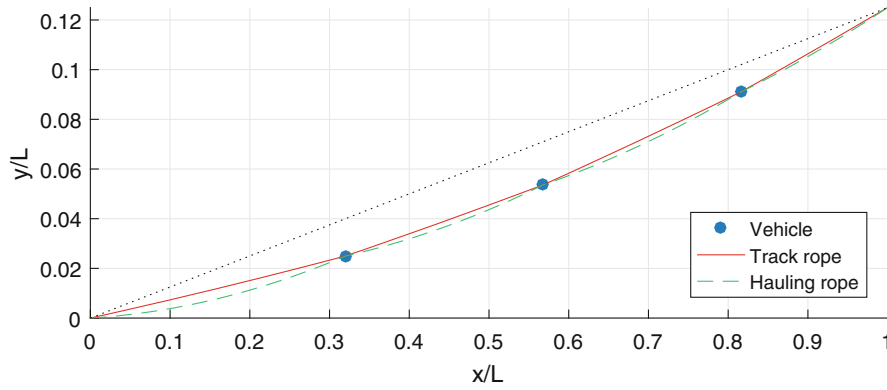


Fig. 5.4 Shape of a span with three vehicles

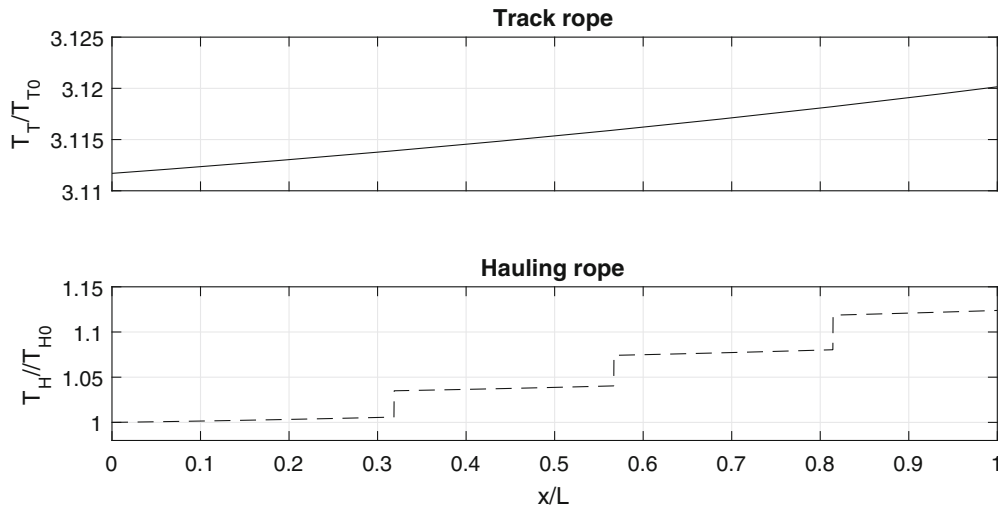


Fig. 5.5 Tension of the ropes

5.5 Dynamic Response

The objective is to predict the dynamic response of the system while the vehicles are moving forward. Hence, we need to perform transient simulations.

First, this kind of simulation is computationally expensive. The less number of degrees of freedom there is, the faster the computations are. Secondly we are interested by the low frequency dynamic phenomena of the system. Hence we choose to make a modal reduction of the cables. This method allows to take a small amount of generalized degrees of freedom while the low frequency phenomena are well described.

However, at each step, the system is changing. The modal bases have to be recalculated. The computation of modes has to be fast. The structure of a cable car is characterized by elongated parts with very small interfaces represented by points in the model. The substructuring method appears as a good solution to our problem. The computation of the eigenmodes of each part of the cable separately is not time-expensive and the representation is relatively good.

5.5.1 Track Rope

The dynamic equations of an inclined cable with a mass density are given by Irvine [1]:

$$\mu \left(\frac{\partial^2 u(s, t)}{\partial t^2} - g \sin \alpha \right) = \frac{\partial}{\partial s} \left[T(s, t) \left(\frac{\partial u(s, t)}{\partial s} + \frac{dU(s)}{ds} \right) \right] \quad (5.13)$$

$$\mu \left(\frac{\partial^2 v(s,t)}{\partial t^2} + g \cos \alpha \right) = \frac{\partial}{\partial s} \left[T(s,t) \left(\frac{\partial v(s,t)}{\partial s} + \frac{dV(s)}{ds} \right) \right] \quad (5.14)$$

At the curvilinear abscissa s , the static position of the point of the cable is described by the coordinates $U(s)$ and $V(s)$ in the frame of reference (\vec{e}_u, \vec{e}_v) . The coordinates $u(s,t)$ and $v(s,t)$ are the dynamic displacements of the point at the curvilinear abscissa s at the time t . The tension T can be split up in a static and a dynamic contribution:

$$T(s,t) = T_S(s) + T_D(s,t) \quad (5.15)$$

The equations (5.13 and 5.14) describe the dynamic and static behavior. The static terms can be subtracted:

$$\mu \frac{\partial^2 u(s,t)}{\partial t^2} = \frac{\partial}{\partial s} \left[T_S(s) \frac{\partial u(s,t)}{\partial s} + T_D(s,t) \left(\frac{\partial u(s,t)}{\partial s} + \frac{dU(s)}{ds} \right) \right] \quad (5.16)$$

$$\mu \frac{\partial^2 v(s,t)}{\partial t^2} = \frac{\partial}{\partial s} \left[T_S(s) \frac{\partial v(s,t)}{\partial s} + T_D(s,t) \left(\frac{\partial v(s,t)}{\partial s} + \frac{dV(s)}{ds} \right) \right] \quad (5.17)$$

Previously, we assumed the global length of the cable is constant because the tension was neglected compared to the stiffness. However, in order to express the dynamic tension, we consider the local strain of the cable $\varepsilon(s,t)$ with the Green-Lagrange deformation:

$$T_D(s,t) = ES\varepsilon(s,t) = ES \left[\frac{\partial u(s,t)}{\partial s} \frac{dU(s)}{ds} + \frac{\partial v(s,t)}{\partial s} \frac{dV(s)}{ds} + \frac{1}{2} \left(\left(\frac{\partial u(s,t)}{\partial s} \right)^2 + \left(\frac{\partial v(s,t)}{\partial s} \right)^2 \right) \right] \quad (5.18)$$

The expression of dynamic tension (5.15) is replaced in the Eqs. (5.13 and 5.14). The equations are linearized neglecting the terms in u and v with an order greater or equal to two:

$$\mu \frac{\partial^2 u}{\partial t^2} = \left(\frac{dT_S}{ds} + 2ES \frac{dU}{ds} \frac{d^2U}{ds^2} \right) \frac{\partial u}{\partial s} + \left(T_S + ES \left(\frac{dU}{ds} \right)^2 \right) \frac{\partial^2 u}{\partial s^2} + ES \left(\frac{dU}{ds} \frac{d^2V}{ds^2} + \frac{dV}{ds} \frac{d^2U}{ds^2} \right) \frac{\partial v}{\partial s} + ES \frac{dU}{ds} \frac{dV}{ds} \frac{\partial^2 v}{\partial s^2} \quad (5.19)$$

$$\mu \frac{\partial^2 v}{\partial t^2} = \left(\frac{dT_S}{ds} + 2ES \frac{dV}{ds} \frac{d^2V}{ds^2} \right) \frac{\partial v}{\partial s} + \left(T_S + ES \left(\frac{dV}{ds} \right)^2 \right) \frac{\partial^2 v}{\partial s^2} + ES \left(\frac{dU}{ds} \frac{d^2V}{ds^2} + \frac{dV}{ds} \frac{d^2U}{ds^2} \right) \frac{\partial u}{\partial s} + ES \frac{dU}{ds} \frac{dV}{ds} \frac{\partial^2 u}{\partial s^2} \quad (5.20)$$

Because the track rope is only in frictionless contact with the vehicles, the modes of the whole span of the cable are calculated. However, in order to better represent its behavior, masses corresponding to the vehicles are added for the computation of eigenmodes. These masses are removed before the reduction and replaced by pendulums for the assembly step.

The modes are computed with a finite difference algorithm. Figure 5.6 shows the variations of the frequencies of the first eigenmodes with respect to the positions of the vehicles. The frequency of the first mode of the cable without any vehicle is f_0 .

5.5.2 Hauling Rope

The hauling rope is moving with the vehicle with a velocity C . Convection terms appear in its dynamic Eqs. [5.2, 5.3]:

$$\mu \left(\frac{\partial^2 u(s,t)}{\partial t^2} + 2C \frac{\partial^2 u(s,t)}{\partial t \partial s} + \frac{C^2 \partial^2 u(s,t)}{\partial s^2} + \frac{dC}{dt} \frac{\partial u(s,t)}{\partial s} - g \sin \alpha \right) = \frac{\partial}{\partial s} \left[(T_S(s) + T_D(s,t)) \left(\frac{\partial u(s,t)}{\partial s} + \frac{dU(s)}{ds} \right) \right] \quad (5.21)$$

$$\mu \left(\frac{\partial^2 v(s,t)}{\partial t^2} + 2C \frac{\partial^2 v(s,t)}{\partial t \partial s} + \frac{C^2 \partial^2 v(s,t)}{\partial s^2} + \frac{dC}{dt} \frac{\partial v(s,t)}{\partial s} + g \cos \alpha \right) = \frac{\partial}{\partial s} \left[(T_S(s) + T_D(s,t)) \left(\frac{\partial v(s,t)}{\partial s} + \frac{dV(s)}{ds} \right) \right] \quad (5.22)$$

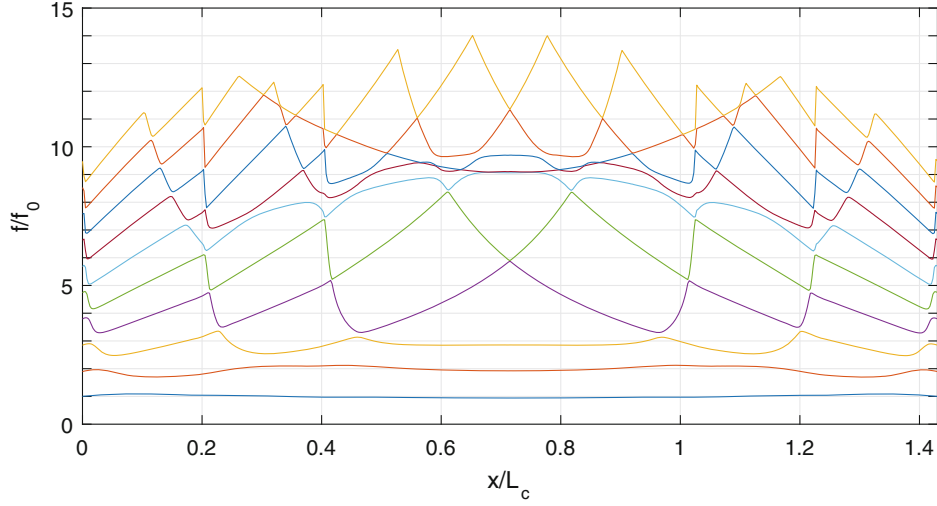


Fig. 5.6 Frequencies of the first ten modes of the track rope with the vehicles as punctual masses with respect to the progression of the track rope

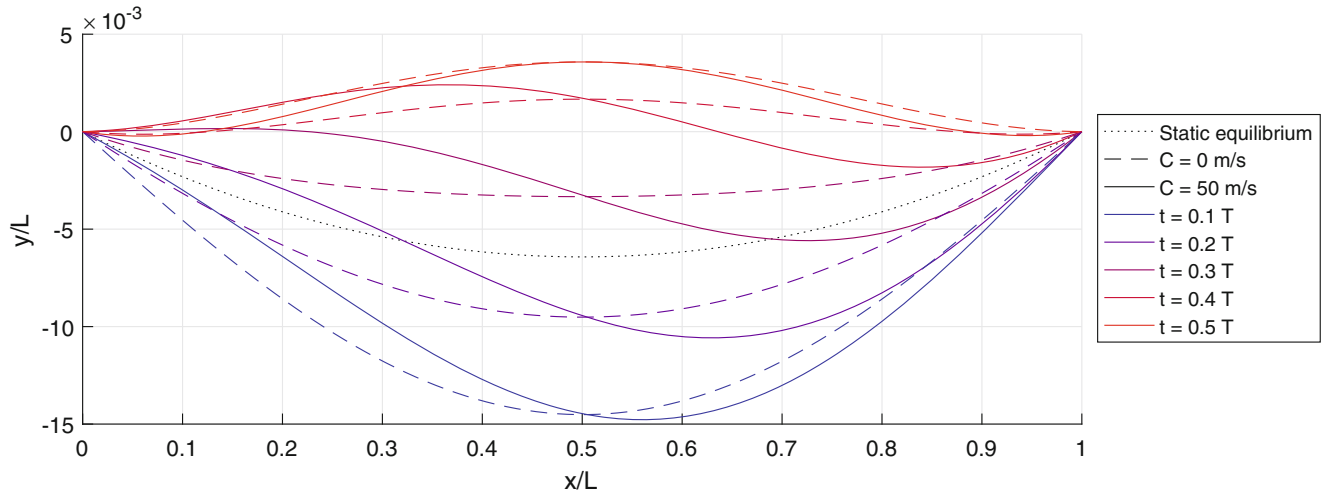


Fig. 5.7 Shapes of the first mode of a portion of a hauling rope for a speed of 0 and 50 m/s at different instants corresponding to fractions of the period T

By considering a constant speed of the cable, subtracting the static terms and replacing the dynamic tension with the Green-Lagrange strain, we obtain:

$$\begin{aligned} \mu \frac{\partial^2 u}{\partial t^2} + 2\mu C \frac{\partial^2 u}{\partial t \partial s} &= \left(\frac{dT_s}{ds} + 2ES \frac{dU}{ds} \frac{d^2 U}{ds^2} \right) \frac{\partial u}{\partial s} + \left(T_s + ES \left(\frac{dU}{ds} \right)^2 - \mu C^2 \right) \frac{\partial^2 u}{\partial s^2} \\ &+ ES \left(\frac{dU}{ds} \frac{d^2 V}{ds^2} + \frac{dV}{ds} \frac{d^2 U}{ds^2} \right) \frac{\partial v}{\partial s} + ES \frac{dU}{ds} \frac{dV}{ds} \frac{\partial^2 v}{\partial s^2} \end{aligned} \quad (5.23)$$

$$\begin{aligned} \mu \frac{\partial^2 v}{\partial t^2} + 2\mu C \frac{\partial^2 v}{\partial t \partial s} &= \left(\frac{dT_s}{ds} + 2ES \frac{dV}{ds} \frac{d^2 V}{ds^2} \right) \frac{\partial v}{\partial s} + \left(T_s + ES \left(\frac{dV}{ds} \right)^2 - \mu C^2 \right) \frac{\partial^2 v}{\partial s^2} \\ &+ ES \left(\frac{dU}{ds} \frac{d^2 V}{ds^2} + \frac{dV}{ds} \frac{d^2 U}{ds^2} \right) \frac{\partial u}{\partial s} + ES \frac{dU}{ds} \frac{dV}{ds} \frac{\partial^2 u}{\partial s^2} \end{aligned} \quad (5.24)$$

The mixed partial term creates an antisymmetric damping, resulting in complex modes. The shape of the first mode of a portion of a hauling rope of 100 m is represented on Fig. 5.7 for two values of C .

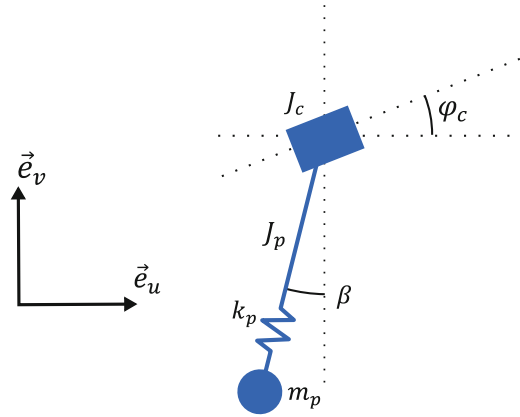


Fig. 5.8 Model of a vehicle

5.5.3 Vehicle (Fig. 5.8)

Each vehicle is modelled by a pendulum consisting of a carriage a hanger and a point mass. The kinetic and potential energies K and U are expressed by:

$$K = \frac{1}{2}m_c (\dot{u}_c^2 + \dot{v}_c^2) + \frac{1}{2}J_c\dot{\varphi}_c^2 + \frac{1}{2}J_p\dot{\beta}^2 \quad (5.25)$$

$$U = \frac{1}{2}k_p\delta^2 + g [m_c (u_c \sin \alpha + v_c \cos \alpha) + m_p (u_c \sin \alpha + v_c \cos \alpha - (l_p + \delta) \cos (\beta + \alpha))] \quad (5.26)$$

Where m_c , u_c , v_c , J_c and φ_c are the masses, the displacement in both directions, the moment of inertia and the rotation angle of the carriage respectively. The variables, l_p , J_p , β_p are the elongation, the length, the moment of inertia and the angle of the hanger respectively and m_p is the mass of the cabin.

By applying the Lagrange equations, the dynamic matrix equation is obtained:

$$\mathbf{M}_v\ddot{X} + \mathbf{C}_v\dot{X} + \mathbf{K}_vX = F_g + F_{NL}(\beta, \dot{\beta}, \dot{\delta}) \quad (5.27)$$

The vector X is the vector of the five degrees of freedom of the pendulum:

$$X = [u_c \ v_c \ \varphi_c \ \beta \ \delta]^T \quad (5.28)$$

The matrix of mass \mathbf{M} and the vector of gravitation force F_g are not constant but depend on the β angle. The non-linear terms are gathered in the nonlinear force vector:

$$F_{NL} = \begin{bmatrix} -m_p (l_p\dot{\beta}^2 \sin \beta - 2\dot{\beta}\dot{\delta} \cos \beta) \\ -m_p (l_p\dot{\beta}^2 \cos \beta + 2\dot{\beta}\dot{\delta} \sin \beta) \\ 0 \\ -2m_p l_p \dot{\beta}\dot{\delta} \\ m_p l_p \beta^2 \end{bmatrix} \quad (5.29)$$

5.5.4 Time Integration

At each step p , the track rope, the portions of the hauling rope and the pendulums are assembled to make the matrices of mass \mathbf{M}_p , damping \mathbf{C}_p and stiffness \mathbf{K}_p . The generalized degrees of freedom Q_p associated are a combination of the modes of the carrying and hauling ropes and the physical degrees of freedom of each pendulum X . Then, a transient calculation is performed on a duration of the step Δt :

$$\mathbf{M}_p \ddot{Q}_p + \mathbf{C}_p \dot{Q}_p + \mathbf{K}_p Q_p = F_{Qg} + F_{QNL}(Q) + F_I \quad (5.30)$$

The external forces F_{Qg} , $F_{QNL}(Q)$ and F_I are respectively the gravitational forces, the non-linear terms of the pendulums and the inertial forces due to the quasi-static assumption calculated with the succession of static equilibriums. The initial conditions of the transient calculation at the step p are given by the previous step projected from the previous modal basis Φ_{p-1} to the current basis Φ_p :

$$Q_p(0) = \Phi_p^{-1} \Phi_{p-1} Q_{p-1}(\Delta t) \quad (5.31)$$

5.6 Results

5.6.1 Start with an Angle

In this case, a train of three vehicles cross the span from left to right. Each vehicle arrives on the track rope with different angles: 10° , 20° and 30° . Figure 5.9 (a) shows the variations of the angles of the cabins. The acceleration felt by the passengers increases with the growth of the start angle.

5.6.2 Emergency Braking

The objective now is to simulate an emergency braking of the ropeway. With the quasi-static assumption, it is not possible to make a deceleration on the hauling rope because at each step, the vehicles are not moving in the model. To represent the deceleration, a braking force is applied on both extremity of the hauling rope. Figure 5.10 shows the accelerations felt by the passengers after the emergency braking.

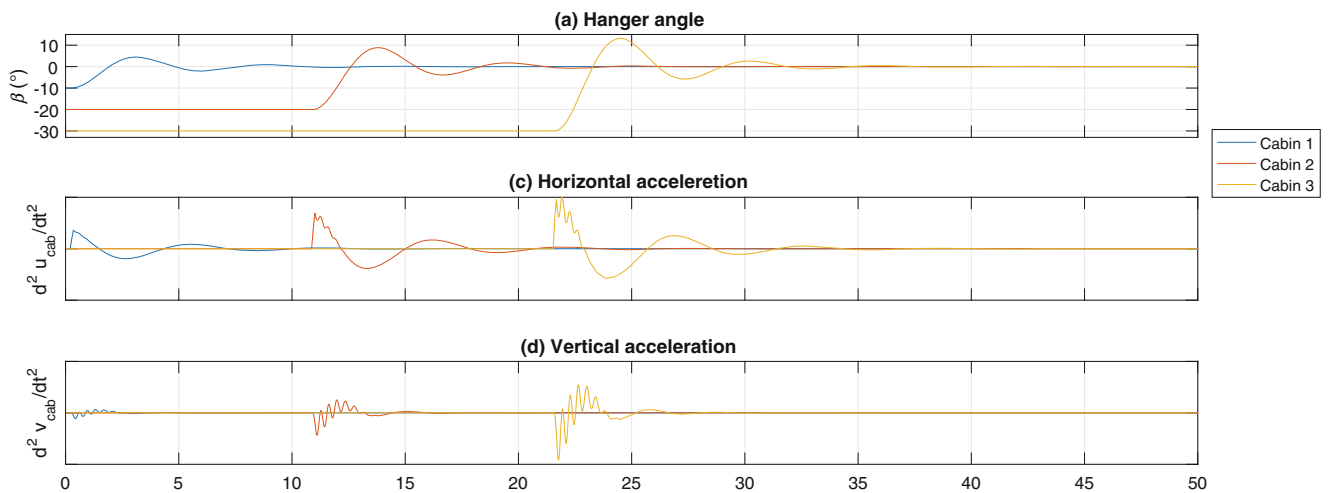


Fig. 5.9 (a) Angles of the hangers of the vehicles (b) Longitudinal acceleration of the cabins (c) Vertical acceleration of the cabins

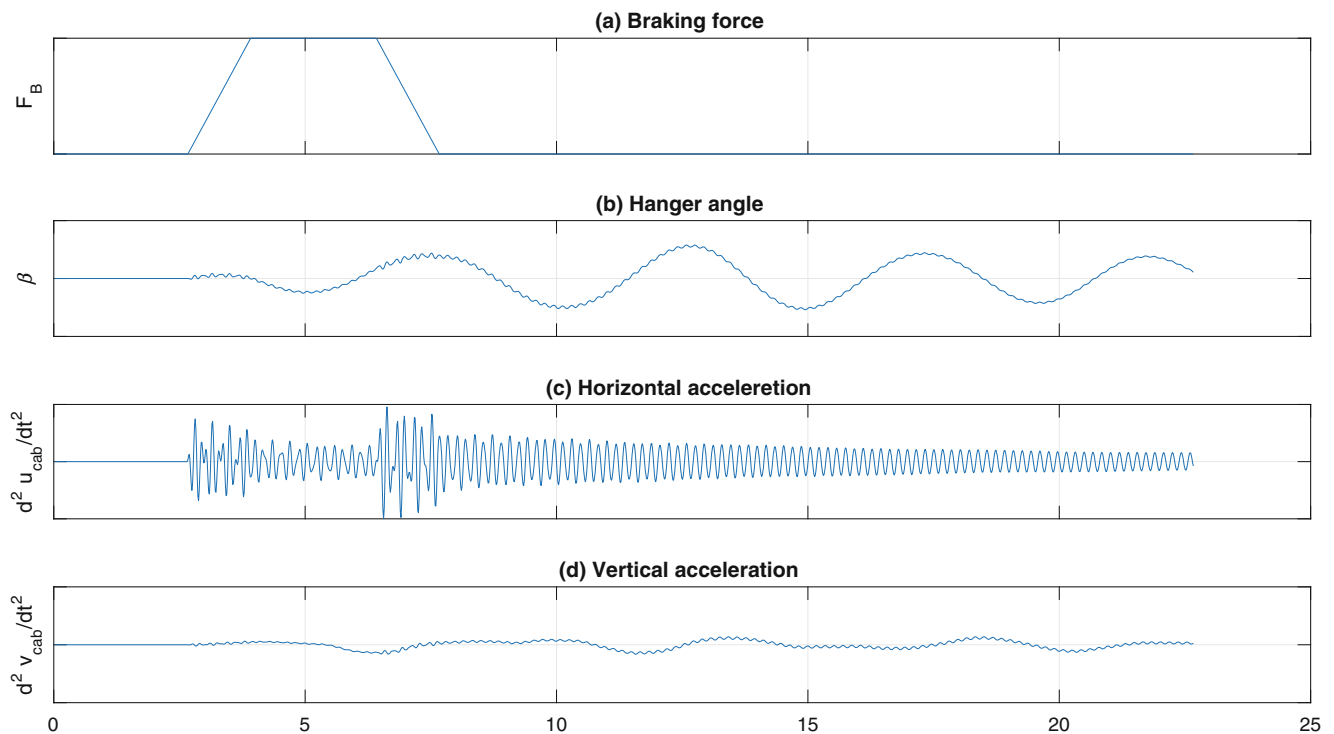


Fig. 5.10 (a) Braking force (b) Angles of the hangers of the vehicle (c) Longitudinal acceleration of the cabin (d) Vertical acceleration of the cabin



Fig. 5.11 Contributors and funders

5.7 Conclusion and Perspectives

In this article, a dynamic model of a ropeway is made. The assumptions of quasi-static advance of the cabins and small displacement allow to use a strategy of step by step computation. At each step, the quasi-static equilibrium is determined with a non-linear calculation. Then a modal basis of the track rope with masses is computed. The eigenmodes of each part of the hauling rope are calculated in considering its velocity. The vehicles are represented by non-linear pendulums.

After assembling all the parts, a transient calculation is performed to know the dynamic behavior of the ropeway according to the load case. Two examples of load cases are given: a vehicle with a start angle and an emergency braking.

The model could be improved by considering several spans, pylons as flexible structures and introducing the third dimension.

The I2TC project has been funded by the FUI I2TC, the Rhone-Alpes Region, the Ile-de-France Region and the Paris Department in collaboration with the Ecole Centrale de Lyon, EIFFAGE, POMA, RATP, CD VIA, The Vibrant Project, the University of Paris 1 Pantheon-Sorbonne and the ENSTA (Fig. 5.11).

References

1. Irvine, Caughey: The linear theory of free vibrations of a suspended cable. *Proc. R. Soc. Lond. A Math. Phys. Sci.* **341**(1626), 299–315 (1974)
2. Sack: Transverse oscillations in travelling strings. *Br. J. Appl. Phys.* **5**(6), 224 (1954)
3. Simpson: On the oscillatory motions of translating elastic cables. *J. Sound Vib.* **20**, 177–189 (1972)
4. Triantafyllou: The dynamics of translating cables. *J. Sound Vib.* **103**, 171–182 (1985)
5. Iwan: The natural frequencies and mode shapes of cables with attached masses. *J. Energy Resour. Technol.* **103**, 237 (1981)
6. Rosenthal: Vibrations of slack cables with discrete masses. *J. Sound Vib.* **78**, 573–583 (1981)
7. Cheng, Perkins: Free vibration of a sagged cable supporting a discrete mass. *J. Acoust. Soc. Am.* **91**, 2654–2662 (1992)
8. Al-Qassab, Nair: Wavelet-Galerkin method for the free vibrations of an elastic cable carrying an attached mass. *J. Sound Vib.* **270**, 191–206 (2004)
9. Portier: Dynamic phenomena in ropeways after a haul rope rupture. *Earthquake Eng. Struct. Dynam.* **12**(4), 433–449 (1984)
10. Brownjohn: Dynamics of an aerial cableway system. *Eng. Struct.* **20**, 826–836 (1998)
11. Sofi, Muscolino: Dynamic analysis of suspended cables carrying moving oscillators. *Int. J. Solids Struct.* **44**, 6725–6743 (2007)

Chapter 6

Influence of Noise in Correlation Function Estimates for Operational Modal Analysis

Esben Orlowitz and Anders Brandt

Abstract The modal parameters in Operational Modal Analysis (OMA) are often estimated based on non-parametric signatures of the structure's dynamic response. For time domain OMA methods the non-parametric signatures are often correlation functions (CFs) and the pre-processing step for these methods is thus the estimation of CFs. The present paper demonstrates how measurement noise from sensors and measurement equipment affects the estimated CFs. Furthermore, the influence of the measurement noise on the modal parameter estimates is discussed. It is shown how effects of this noise can easily be avoided by ignoring the first part of the CFs when estimating the modal parameters. This is demonstrated by a theoretical review and on simulated and experimental data. The paper also addresses how to add noise to simulated data, so that it resembles a real-life scenario.

6.1 Introduction

Characterization of the dynamic properties of civil- and mechanical engineering structures using operational modal analysis (OMA) has been given much attention in the research and the potential of using the experimental results of OMA for model validation, model updating and structural health monitoring is currently getting large attention.

Time domain modal parameter estimation (MPE) algorithms used for Operational Modal Analysis (OMA) are often based on correlation functions, sometimes referred to as covariance functions. Studies of such algorithms and their applications have been widely reported in the literature. However, a desirable feature of the correlation functions have been given little attention; the way broadband measurement noise can be handled with respect to MPE algorithms.

The present paper shows how well-known knowledge about correlation function estimation can be taken advantage of for MPE in OMA applications. The focus is on the usage of the correlation functions; for details on MPE algorithms the reader is referred to e.g. [1–4]. The focus is mainly on the estimation of damping ratios as these have been reported to be more prone to errors. Several studies have also indicated that damping is typically overestimated in OMA [5, 6] and more generally damping estimates are believed to be associated with high uncertainties.

The study is demonstrated using a MPE algorithm taking advantage of singular value decomposition, the Multi-reference Ibrahim Time Domain method [3], but similar results are found using, for example, the more well-known Stochastic Subspace Identification (SSI) method [7].

The present paper is organized as follows. First, a review of the definition of the correlation function and an estimator are given. Next, an overview of how broadband measurement noise theoretically affects the correlation function estimates is presented and it suggested that neglecting the first part of the correlation functions will remove the influence on the estimates of modal parameters. Following the suggestion is demonstrated first on a simulated SDOF system and then on experimental data.

E. Orlowitz (✉)
Siemens Gamesa Renewable Energy, Grindsted, Denmark
e-mail: esben.orlowitz@siemensgamesa.com

A. Brandt
University of Southern Denmark, Odense, Denmark

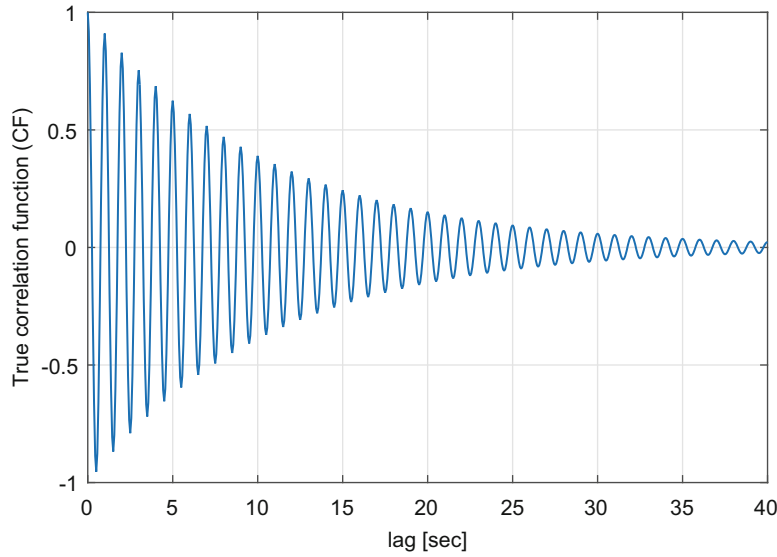


Fig. 6.1 Theoretical (auto) correlation function. Here illustrated for the response of a SDOF system with natural frequency 1 Hz and damping ratio 1.5%

6.2 Correlation Function Estimation

Let a response, $y(t)$, be a realization of the stochastic, wide-sense stationary, process $Y(t)$ with zero mean and its autocorrelation function (ACF), $R_{YY}(\tau)$, defined as

$$R_{YY}(\tau) = \mathbf{E} [Y(t)Y(t - \tau)] \quad (6.1)$$

where \mathbf{E} is the expected value operator (ensemble averaging) and τ a time shift that is also referred to as a *lag*.

An example of an ACF is shown in Fig. 6.1 for a process describing the response of a SDOF system with natural frequency $f_0 = 1$ Hz and damping ratio $\zeta_0 = 1.5\%$. As shown in [8] the ACF $R_{YY}(\tau)$ of the process $Y(t)$ of a SDOF system due to random excitation is of the form

$$R_{YY}(\tau) = Ae^{(-\zeta_0\omega_0\tau)} \sin\left(\omega_0\tau\sqrt{1-\zeta_0^2}\right) \quad (6.2)$$

where $\omega_0 = 2\pi f_0$ (the angular frequency in rad/sec) and A is a constant, that for this study is set to unity without influencing the following conclusions.

The definition of the ACF, Eq. (6.1), can be interpreted as a measure of the correlation between a process and itself at a time-shift τ . A cross-correlation function (CCF) can be similarly defined between two processes [9].

The above definition, Eq. (6.1), of the ACF is of little interest in real applications where there is no access to the ensemble, but only a single realization. Instead the assumption of ergodicity is applied, stating that the time average over an infinite realization is equivalent to the ensemble average [9, 10]. However, as a realization (response) in practice will be of finite duration T the following estimator $\hat{R}_{YY}(\tau)$ is defined

$$\hat{R}_{YY}(\tau) = \frac{1}{(T-\tau)} \int_0^{T-\tau} y(t)y(t-\tau)dt \quad , \quad 0 < \tau \leq T. \quad (6.3)$$

The estimator in Eq. (6.3) can be shown to be unbiased and it is the estimator most commonly used in OMA. The factor $\frac{1}{(T-\tau)}$ can be replaced by $\frac{1}{T}$ which gives a biased (however asymptotically unbiased) estimator, that theoretically has a smaller random error [9]. However, for OMA applications where $\tau \ll T$ and $\hat{R}_{YY}(\tau)$ decays rapidly as $\tau \rightarrow \infty$, it can be shown that the difference of the unbiased and the biased estimators of the CF is of little practical concern.

The integral in Eq. (6.3) should be recognized as a convolution integral and thus it can be computed ‘indirectly’ in the Fourier domain using the convolution theorem, where it is important to use zero padding in the FFT computations, to produce

true (not cyclic) convolution. This can in many cases increase the computation speed. Two methods for indirect estimation were compared in [11] and it was shown that they are both statistically equivalent to the ‘direct’ estimator of Eq. (6.3). It should be emphasized that no matter which method is applied, no further enhancement of the estimate can be achieved compared to the definition in Eq. (6.3) with a fixed amount of data. Formulas for indirect and direct estimation of correlation functions can be found in for example [10, 11].

6.3 The Correlation Function and Measurement Noise

In this section a short theoretical overview of the influence of measurement noise on the estimated CFs is given. Let the measured responses be represented as realizations of the random processes $Y_n(t)$ which are summations of the true processes $X_n(t)$ and noise processes $Z_n(t)$,

$$\begin{aligned} Y_1(t) &= X_1(t) + Z_1(t) \\ Y_2(t) &= X_2(t) + Z_2(t) \\ &\vdots \\ Y_{N_d}(t) &= X_{N_d}(t) + Z_{N_d}(t) \end{aligned} \quad (6.4)$$

where N_d is the total number of measured responses. The noise $Z_n(t)$ represents, for example, noise in sensors and the measurement system.

Here all noise processes, $Z_n(t)$, are considered uncorrelated with each other and with all the structural responses. As the processes $X_n(t)$ and $Z_n(t)$ are unobserved the option is limited to calculate CFs between the measured processes $Y_n(t)$.

For the ACF of a single process $Y_n(t)$, as defined in Eq. (6.4), the following result is obtained

$$\begin{aligned} R_{Y_n Y_n}(\tau) &= \mathbf{E}[Y_n(t)Y_n(t-\tau)] \\ &= R_{X_n X_n}(\tau) + R_{Z_n Z_n}(\tau) + R_{X_n Z_n}(\tau) + R_{Z_n X_n}(\tau) \\ &= R_{X_n X_n}(\tau) + R_{Z_n Z_n}(\tau) \end{aligned} \quad (6.5)$$

where the last equality stems from the assumption that the process $X_n(t)$ and the noise $Z_n(x)$ are uncorrelated (and have zero mean). Thus when the response and the noise are uncorrelated the available ACF $R_{Y_n Y_n}(\tau)$ is a sum of their individual contributions.

In the case of the CCF between two measured response processes $Y_1(t)$ and $Y_2(t)$ with uncorrelated noise,

$$\begin{aligned} Y_1(t) &= X_1(t) + Z_1(t) \\ Y_2(t) &= X_2(t) + Z_2(t) \end{aligned} \quad (6.6)$$

the result is even more attractive as it is seen that,

$$\begin{aligned} R_{Y_1 Y_2}(\tau) &= \mathbf{E}[Y_1(t)Y_2(t-\tau)] \\ &= R_{X_1 X_2}(\tau) + R_{Z_1 Z_2}(\tau) + R_{Y_1 Z_2}(\tau) + R_{Z_1 Y_2}(\tau) \\ &= R_{X_1 X_2}(\tau) \end{aligned} \quad (6.7)$$

which shows that the noise theoretically will cancel out and that the CCF of the measured processes equals that of the true response processes unaffected by the measurement noise.

For an ACF, however, as shown in Eq. (6.5) the noise Z_n will have an effect due to its contribution to the rms level of the measured response, $Y_n(t)$, which will contribute at $\tau = 0$.

Due to finite responses, for real measurements, both the ACF and the CCF estimates involving a noise process will add some uncertainty (random error) on the CFs at all lag values. As an example it can be shown that for a sufficiently long white noise process $Z(t)$ the variance of its CF estimate $\hat{R}_{ZZ}(\tau)$, which mean is zero for $\tau > 0$, will equal the inverse of the total duration of the finite process [12]. This was also observed in [13] on simulated data, where it was shown empirically that increasing the level of added noise to the responses did not affect the estimated natural frequencies and damping ratios estimated by SSI, however without giving any plausible reason for this attractive property.

A commonly used method for introducing measurement noise in simulations of OMA responses is to add white noise sequences to the responses. The rms level of the noise is typically scaled so that it is, for example, 10% of that of the responses. However, ideally, a white noise sequence is, due to its definition, only correlated with itself at $\tau = 0$ (its ACF is a delta function), where it equals the power of the sequence (std squared, σ_z^2)

$$R_{zz}(\tau) = \int_{-\infty}^{\infty} \sigma_z^2 \exp(j2\pi\tau f) df = \sigma_z^2 \delta(\tau) \quad (6.8)$$

As an example, as defined in Eq. (6.5), let a noise process $Z(t)$ have a rms level of 10% of the true response (corresponding to a SNR of 20 dB). The ACF of the noise process will then take a value of approximately 1% of the ACF of true process, at lag zero ($\tau = 0$).

In a real measurement the frequency range is limited and thus for a white noise sequence, its auto CF will take the form of a *sinc* function rather than a delta function [10, 12]. However it will decrease rapidly and can be assumed to be close to a delta function [12]. If the measurement noise was pure white noise it could easily be removed for the MPE by disregarding the first lag ($\tau = 0$) of the CF. In a real case with limited frequency range, instead disregarding the first few time lags will make the influence of measurement noise insignificant.

Furthermore, the assumption of white measurement noise is not realistic. Typical cascade noise from a sensor-DAQ chain (electronic noise, from op-amps. etc.) decays as $1/f$ and is referred to as pink noise or flicker noise (-10 dB/decade) [14]. In the case of pink noise ($1/f$) its corresponding ACF equals the cosine integral

$$R_{zz}(\tau) = \int_0^{\infty} \frac{\cos(2\pi\tau f)}{f} df \quad (6.9)$$

derived by the Wiener-Khinchine relation. Asymptotically it goes towards zero for $\tau \rightarrow \infty$, however, in the context of OMA it is the first part around $\tau = 0$ that is of interest. As can be seen in Fig. 6.2a pink measurement noise in the responses results in a decaying offset (bias) of the correlation function by maximum 1% at ($\tau = 0$) and after 20 s in the present case decreases to 0.32%. Assuming an equal combination of pink and white noise with the same noise level (10% true signals rms) the offset is lower and already after 1 s has decreased to approx. 0.25% of the response's correlation function. This latter combination of pink and white noise is suggested as a realistic noise characteristics of the sensor-DAQ chain, see e.g. Chapter 7 in [15] and in [16] where experimental investigations have been reported.

6.4 Influence on Modal Parameter Estimation: Simulation

In Sect. 6.3 it was shown that the first part of the CF should be disregarded when measurement noise is present; how much depends on the nature of the noise.

Most modern time domain algorithms are taking advantage of Singular Value Decomposition, e.g. the Multi-reference Ibrahim Time Domain method (MITD) [3] and the Stochastic Subspace Identification (SSI) methods [7, 17]. In the authors' experience these two methods give similar results. In the following the MITD method has been applied for MPE. Other time domain methods using CFs for modal parameter estimation work in a similar way as MITD and SSI, see e.g. [18]. The following suggested handling of broad band measurement noise are therefore expected to be similar for other methods, although not shown in the present work.

The response of a SDOF system, with natural frequency $f_0 = 1$ Hz and damping ratio $\zeta_0 = 1.5\%$, has been simulated 1000 times using independent realizations of Gaussian distributed white noise excitation with a sampling frequency of 8 Hz and response durations of 9600 s, which is assumed to be sufficient to neglect the influence of measurement time (that is outside the scope of the present work). The simulation was performed by the time domain method described in Section 6.5 in [19].

In order to show that the influence of noise can be handled well with proper use of the CF, combined pink and white noise has been added to the responses, having a rms level of 10% with respect to the rms level of the responses. The ratio of pink and white noise was equal in contribution to the rms level and new realizations of the noise were generated for each simulation.

The natural frequency and damping ratio were estimated for each simulation using a variable duration of the ACF, from 1.25 to 25 s in steps of 0.25 s (two lags). The number of disregarded lags in the ACF have been varied, from 1 to 30 in steps of a single lag, which corresponds to disregarding 0–3.75 s of the ACF. The estimates are evaluated at a model order of two, that is, using the two largest singular values from the SVD [3], allowing the estimation of a single mode.

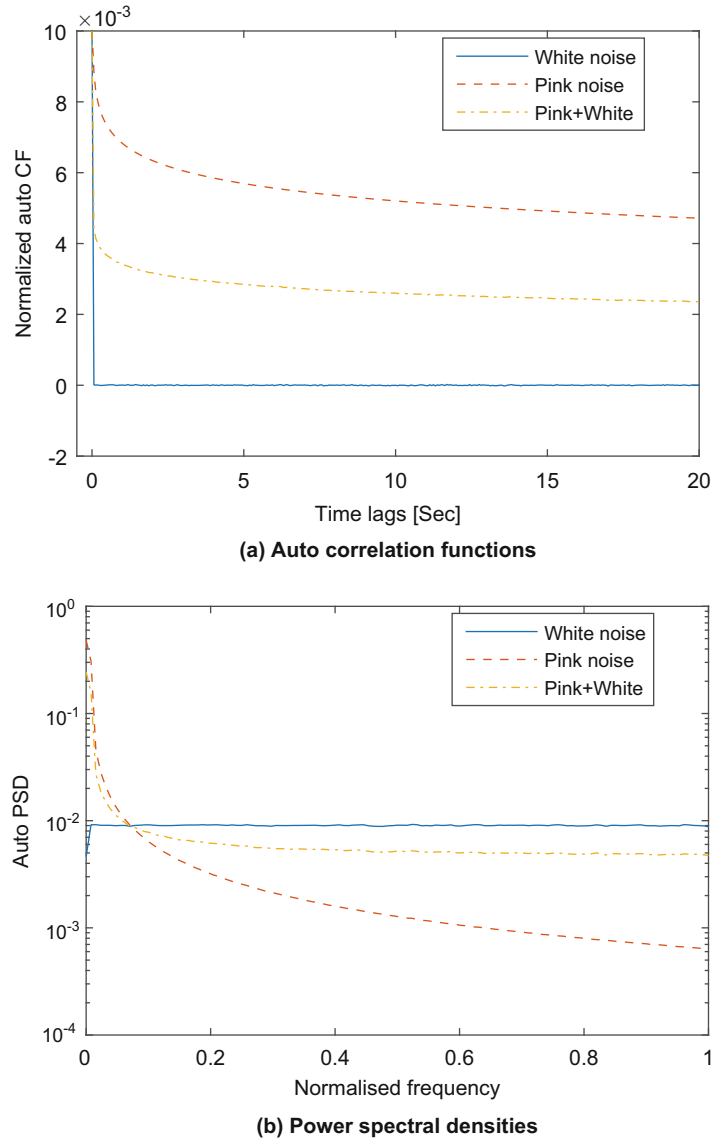


Fig. 6.2 (a) Auto correlation functions of a white, pink and combined pink + white noise processes $R_{Z_n, Z_n}(\tau)$ from synthetically generated data, normalized by the variance of a noise-free response $R_{X_n, X_n}(0)$. Hence $R_{Z_n, Z_n}(\tau)/R_{X_n, X_n}(0)$. The rms level of the noise processes $Z_n(t)$ is 10% of the rms level of the noise-free response $X_n(t)$. (b) The corresponding auto power spectral densities of the noise processes

The average of the estimated natural frequency and damping ratio with respect to the duration of the ACF used, and the start in the ACF are shown in Fig. 6.3.

In Fig. 6.3b a bias error can be observed on the damping estimate for all start lags, but in the current case disregarding the first three lags reduces this bias significantly. Increasing the portion of the ACF used, the bias error gets smaller and for the present response duration of 9600 s, the bias error is rather low. By evaluating the estimates using different portions of the CFs the effect of this choice is visualized, however a study of how to find the optimal portion is outside the scope of the present work. Again, adding noise to the responses and disregarding the first three lags the bias errors change insignificantly by less than 0.1% and shows the robustness of using CFs, e.g. compared to free-decays as it was shown in [20]. The SNR has an insignificant influence on the damping estimates from CF if disregarding the first few lags. Using free-decays the SNR has a significant influence on the modal parameters, whereas it only has a small influence when using CFs, as Eq. (6.5) suggest. This robustness was also observed in [13] using SSI, where no effect of adding white noise to the responses was reported.

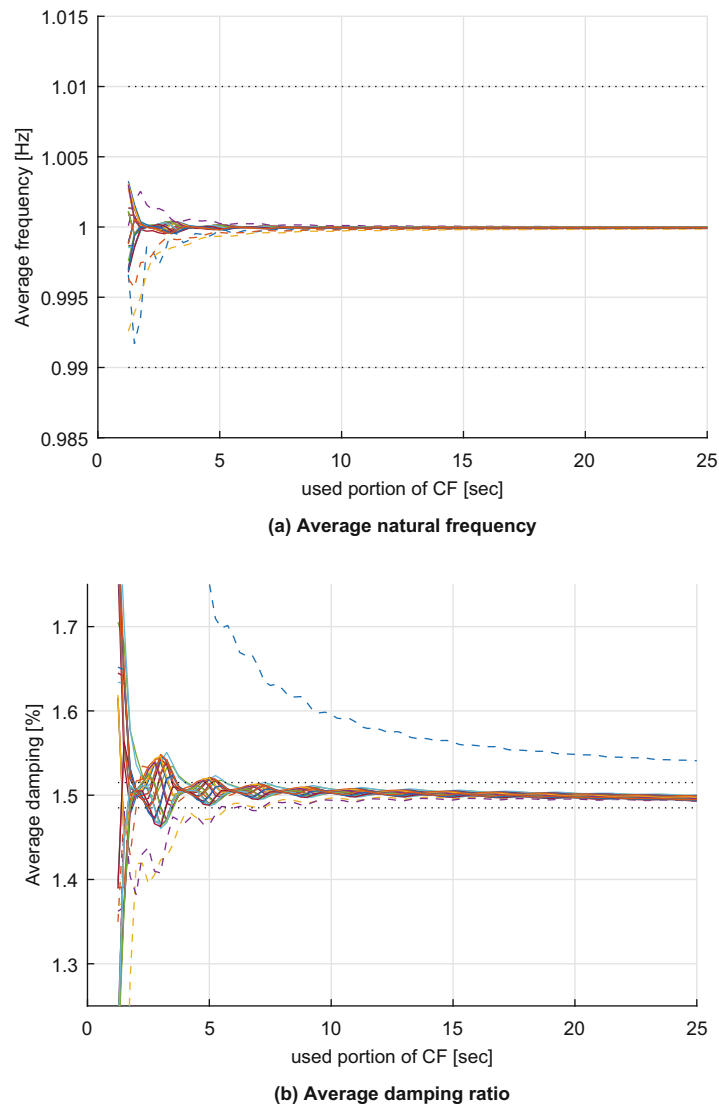


Fig. 6.3 Average of estimated natural frequency **(a)** and damping ratio **(b)** based on 1000 realizations of the SDOF system with response duration of 9600 s. The two dotted lines indicates the $\pm 1\%$ interval around the true values. Results are shown for increasing start lag, see text for details, the dashed lines highlight the first four lags as start, hereafter distinguishing the curves of increasing start lag is not crucial but it shows the bias error caused by using the first lags. Especially the upper dashed line with is the estimates using the very first lag ($\tau = 0$) of the ACF

6.5 Experimental Data

In the following experimental data from a Plexiglas plate are used to illustrate the handling of broad band noise. The Plexiglas (PMMA) plate that has been experimentally tested is shown in Fig. 6.4a. The dimensions of the plate are $533 \times 321 \times 20$ mm. The plate is similar to the so-called IES-Plate proposed in [21], although, for practical reasons, the plate thickness was chosen slightly different from the IES-Plate, by choosing 20 mm thickness, which is a standard thickness in Europe.

The measurement grid consisted of 35 DOFs distributed uniformly out of plane on the plate as shown in Fig. 6.4b and responses from all DOFs were measured simultaneously. The accelerometers and cables significantly mass load the structure, and it is also possible that there will be additional damping added. The present experiments are, however, designed so that it is the combined structure together with the instrumentation that is investigated. See [22] for more details.

A total of 300 s of data were acquired for the OMA test from all DOFs simultaneously. The excitation was applied by gently tapping the tip of a pencil randomly around the plate. The idea of tapping rather than scratching is to minimize the interaction with the plate as much as possible. It has been experienced that scratching the present plate will influence its dynamics in a detectable way.

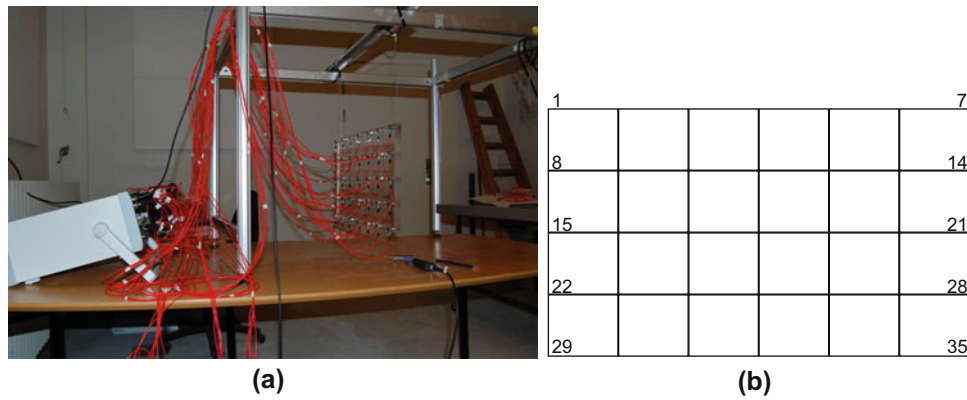


Fig. 6.4 (a) The experimental setup: plexiglas plate suspended vertically in two springs with 35 accelerometers mounted. The impact hammer seen in the photo was not used for the present data. (b) Measurement grid on the plate consisting of 35 measurement points with a separation of 75×85 mm. The full dimensions of the plate are 533×321 mm and thickness 20 mm

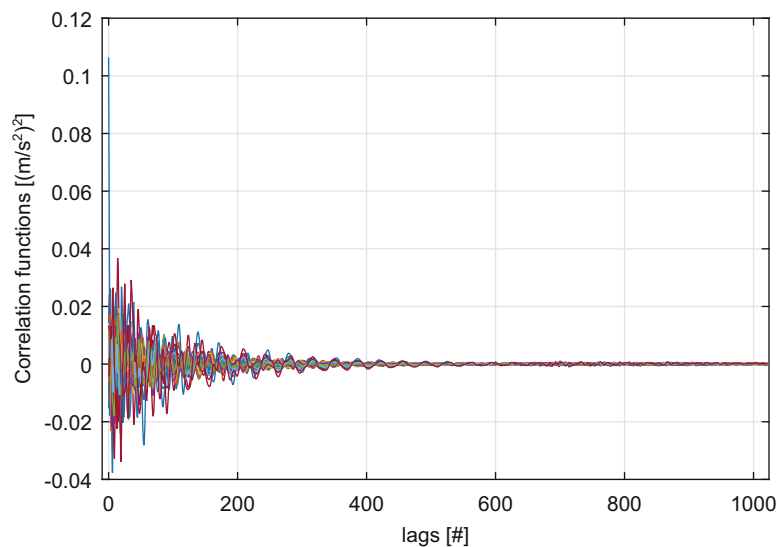


Fig. 6.5 Correlation functions estimated for all responses with the response of DOF1 as reference

The CFs between the responses were estimated by the Periodogram approach, see [11]. The CFs with DOF 1 as reference are plotted overlaid in Fig. 6.5, giving an impression of the ‘memory’ of the plate, hence which amount of the CFs that should be expected to contain useful information for the estimation of modal parameters. An observation from Fig. 6.5 is that at the first lag value one of the CFs shows a significantly higher value than the rest. This is the ACF, here for the response of DOF 1. For all of the following results in this paper only the first ten modes are estimated, these all fall below 1 kHz, and unless else stated the estimates of the natural frequencies and damping ratios are the average values of the stable modes evaluated (manually selected) from the stabilization diagram. The maximum model size used allows up to 80 poles, corresponding to 40 modes.

The natural frequencies and damping ratios have been estimated by disregarding up to the first 29 lag values and in order to take into account the unknown dependency on the used number of lags included in the estimation, three different amounts have been included here with 100, 200 and 300 number of lags respectively. The estimated natural frequencies are shown in Fig. 6.6 and the damping ratios in Fig. 6.7, the values shown are the average of at least 23 estimates (see Sect. 6.5). As it was expected, using the first few lags of the CFs for estimation of the modes gives a significantly different result compared to disregarding these. This is most distinguished for the damping ratios. Disregarding the first five lags, in the current case, the estimates of both natural frequency and damping ratio can be observed to converge to a ‘stable’ value and this observation is independent of the amount of lags used. This is believed to verify that the effect of measurement noise is negligible in the MPE if a proper number of the first lags are disregarded from the CFs.

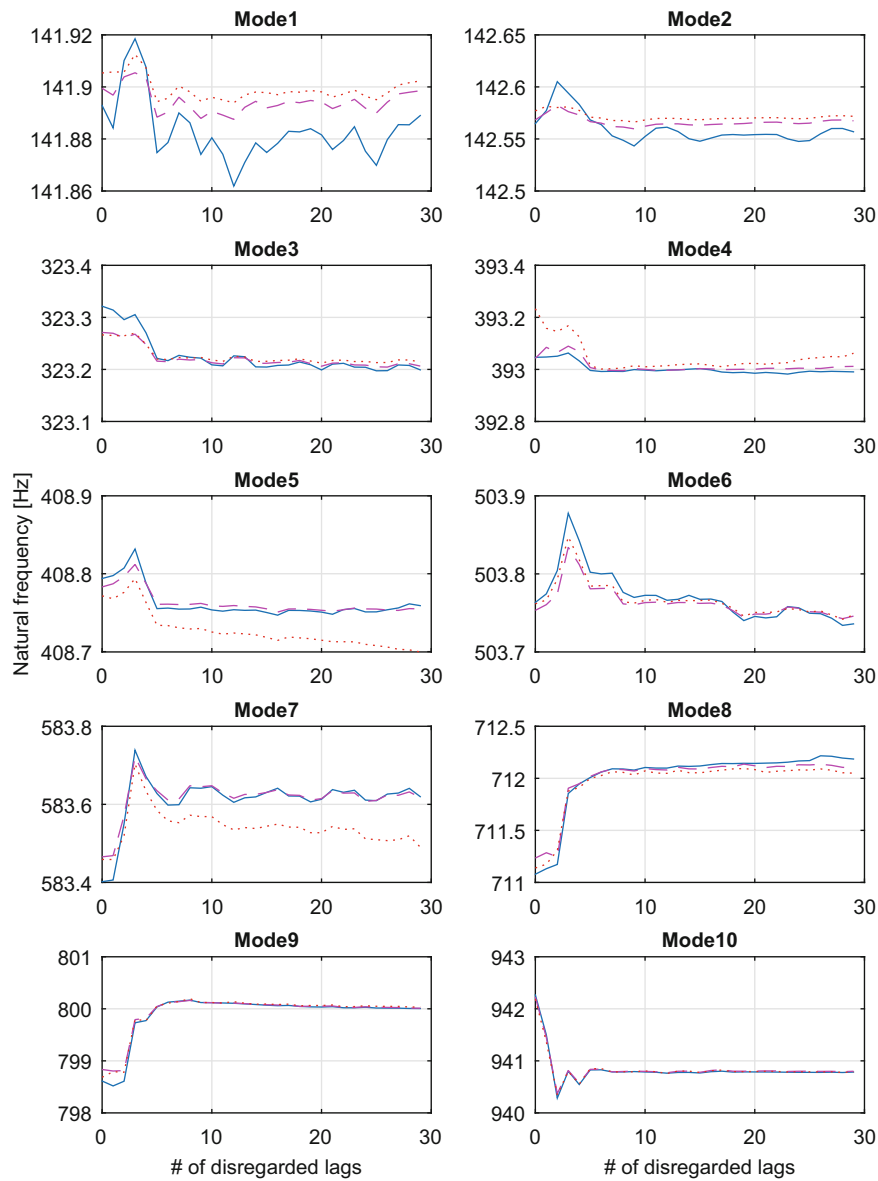


Fig. 6.6 Natural frequencies estimated for the first ten modes of the plate, disregarding an increasing number (#) of lags of the correlation functions. Three lines are shown representing the usage of 100 (solid), 200 (dashed) and 300 lags (dotted) of the correlation function, respectively

6.6 Conclusions

Although there is still a lot more to be investigated, in the authors' opinion the usage of CFs in OMA has several attractive properties. CFs are simple to estimate and influence of broadband measurement noise can be reduced easily.

It has been shown theoretically that broadband noise on the response signals will affect only the first few lags of the CFs and thus the signal-to-noise ratio is not a serious concern when normal experimental considerations about sensors, measurement techniques, etc. are followed. This is true under the assumption that the noise is uncorrelated with the true responses of the structure.

The effect of neglecting the first few lags of the CFs have been demonstrated first on simulated data of a SDOF system with added broadband noise. Here it was shown how the added noise gives a bias error on the damping estimate, if no lags are neglected. Following it has been validated using an experimental dataset, from which it was shown that disregarding the first few lag values of the CFs significantly reduced the influence of broadband measurement noise. Disregarding these first few

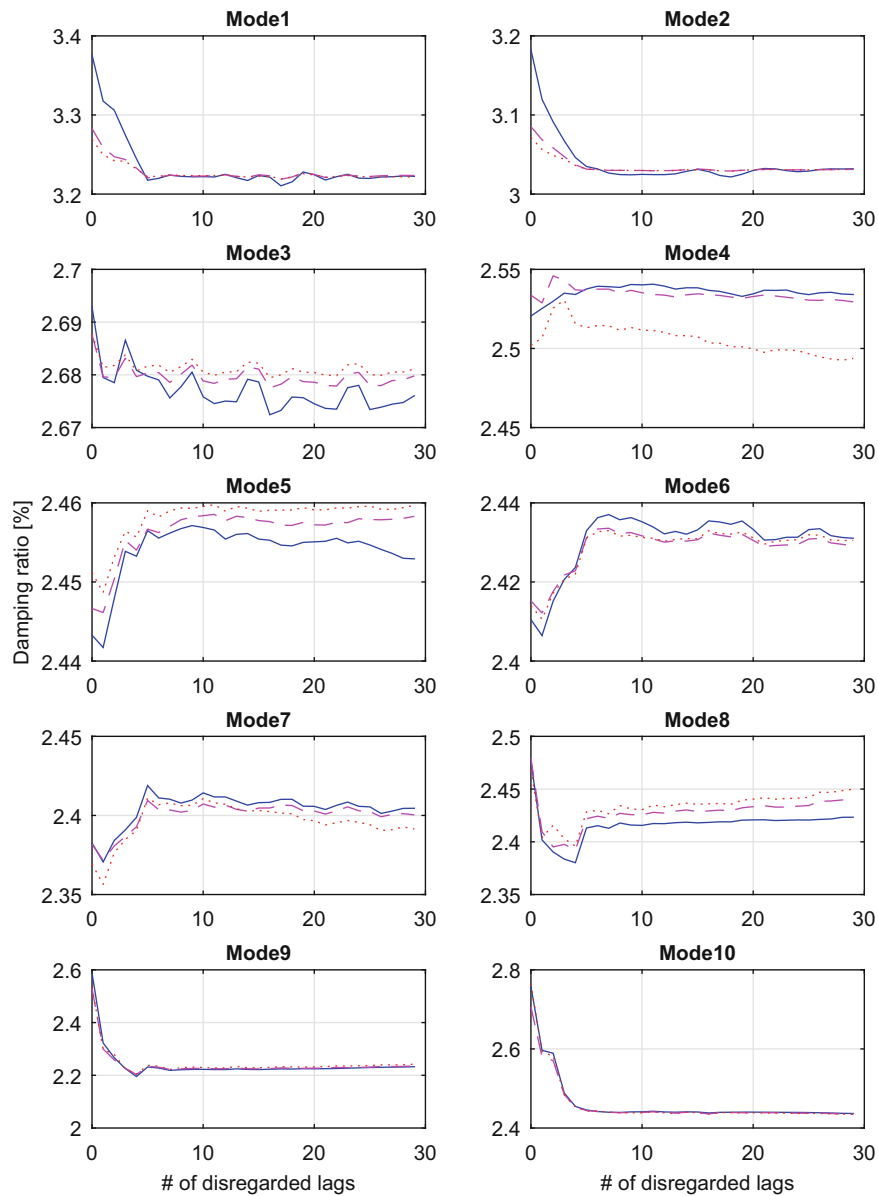


Fig. 6.7 Damping ratios estimated for the first ten modes of the plate, disregarding an increasing number (#) of lags of the correlation functions. Three lines shown are representing the usage of 100 (solid), 200 (dashed) and 300 lags (dotted) of the correlation function, respectively

lag values the damping ratio estimates converged and increasing the number of disregarded lags the damping estimates were found to stabilize, which is seen as an indication of reliable estimates. When not disregarding these first lags the estimated damping ratio was significantly different.

Acknowledgements The work presented has been partly supported by the INTERREG 4 A program in Southern Denmark and Schleswig-K.E.R.N, Germany with funding from the European Fund for Regional Development.

References

1. Ewins, D.J.: Modal Testing: Theory, Practice and Application, 2nd edn. Research Studies, Baldock (2000)
2. Maia, N.M.M., Silva, J.M.M. (eds.): Theoretical and Experimental Modal Analysis. Research Studies, Taunton (1997)
3. Allemang, R., Brown, D.: Experimental modal analysis and dynamic component synthesis – volume 3: modal parameter estimation. Technical report, USAF (1987)

4. Reynders, E.: System identification methods for (operational) modal analysis: review and comparison. *Arch. Comput. Meth. Eng.* **19**, 51–124 (2012)
5. Lauwagie, T., Van Assche, R., Van der Straeten, J., Heylen, W.: A comparison of experimental, operational, and combined experimental-operational parameter estimation techniques. In: *Proceedings of Conference on Noise and Vibration Engineering, Leuven* (2006)
6. Carden, E.P., Mita, A.: Challenges in developing confidence intervals on modal parameters estimated for large civil infrastructure with stochastic subspace identification. *Struct. Control Health Monit.* **18**, 53–78 (2009)
7. Overschee, P.V., Moor, B.D.: *Subspace Identification for Linear Systems*. Kluwer Academic Publishers, Boston (1996)
8. James, G.H., Carne, T.G., Lauffer, J.P.: The natural excitation technique (next) for modal parameter extraction from operating structures. *Int. J. Anal. Exp. Modal Anal.* **10**, 260–277 (1995)
9. Jenkins, G.M., Watts, D.G.: *Spectral Analysis and Its Applications*. Holden-Day, San Francisco (1968)
10. Bendat, J., Piersol, A.G.: *Random Data: Analysis and Measurement Procedures*. Wiley Interscience, New York (1986)
11. Orlowitz, E., Brandt, A.: Influence of correlation estimation methods on damping estimates. In: *Proceedings of 5th International Operational Modal Analysis Conference, Guimaraes* (2013)
12. Priestly, M.B.: *Spectral Analysis and Time Series*, vol. 1. Academic, London (1981)
13. Giraldo, D.F., Song, W., Dyke, S.J., Caicedo, J.M.: Modal identification through ambient vibration: comparative study. *J. Eng. Mech.* **135**, 759–770 (2009)
14. Ott, H.W.: *Noise Reduction Techniques in Electronic System*. Wiley, Singapore (1988)
15. Levinzon, F.: *Piezoelectric Accelerometers with Integral Electronics*. Springer, Cham (2014)
16. Tondreau, G., Deraemaeker, A.: Numerical and experimental analysis of uncertainty on modal parameters estimated with the stochastic subspace method. *J. Sound Vib.* **333**, 4376–4401 (2014)
17. Peeters, B., De Roeck, G.: Reference-based stochastic subspace identification for output-only modal analysis. *Mech. Syst. Signal Process.* **13**, 855–878 (1999)
18. Allemang, R.J., Brown, D.L.: A unified matrix polynomial approach to modal identification. *J. Sound Vib.* **211**(3), 301–322 (1998)
19. Brandt, A.: *Noise and Vibration Analysis – Signal Analysis and Experimental Procedures*. Wiley, New York (2011)
20. Pappa, R., Ibrahim, S.: A parametric study of the ibrahim time domain modal identification algorithm. *Shock Vib. Bull.* **51**, 43–72 (1981)
21. Smallwood, D., Gregory, D.: A rectangular plate is proposed as an ies modal test structure. In: *Proceedings of International Modal Analysis IV, Los Angeles* (1986)
22. Orlowitz, E., Brandt, A.: Comparison of experimental and operational modal analysis on a laboratory test plate. *Measurement* **102**(Supplement C), 121–130 (2017)

Chapter 7

Comparison of Two (Geometric) Algorithms for Auto OMA

Martin Juul, Peter Olsen, Ole Balling, Sandro Amador, and Rune Brincker

Abstract In this paper we compare two geometric algorithms for automatic Operational Modal Analysis(OMA). The compared algorithms are the Shortest Path Algorithm (SPA) that considers shortest paths in the set of poles and the Smallest Sphere Algorithm (SSA) that operates on the set of identified poles to find the set of smallest spheres, containing physical poles. Both algorithm are based on sliding filter stability diagrams recently introduced by Olsen et al. We show how the two algorithms identify system parameters of a simulated system, and illustrate the difference between the identified parameters. The two algorithms are compared and illustrated on simulated data. Different choices of distance measures are discussed and evaluated. It is illustrated how a simple distance measure outperforms traditional distance measures from other Auto OMA algorithms. Traditional measures are unable to discriminate between modes and noise.

7.1 Extended Abstract

7.1.1 Sliding Filter Stability Diagram

The work in this paper is based on a simulation a 5 Degree Of Freedom (DOF) system using the FFT simulation technique explained by Brincker and Ventura [1]. The sampling rate was chosen to be $f_s = 1000$ Hz, the mode shapes were chosen at random and orthogonal and the system was sampled for 200 s, giving a total of 200,000 samples in each channel. After simulation 90 dB sensor noise was added to the signal. The singular values of the simulation is shown in Fig. 7.1 First the correlation function is calculated for the dataset using Welch averaging with a block size of $N_{welch} = 4096$. The resulting correlation function is pass band filtered in bands of $B_w = 130$ Hz, with a guard band of 8 Hz. The filtered dataset is sent through the TDPR system identification algorithm [1], and the identified poles are saved. This process is repeated many times where the band pass filter is slit over the entire frequency band of the dataset. The sliding filter process is done by starting the filter $B_w/2$ Hz before the start of the frequency band, and sliding it $B_w/2$ Hz past the Nyquist frequency to ensure an even density of estimated poles over the entire band. Thus the effective band width is $B_{eff} = f_s/2 + B_w = 630$ Hz. It was chosen to have $N_{filt} = 200$ different filter positions in the stability diagram, giving a filter step size $\Delta f = B_{eff}/(N_{filt} + 1) = 3.1343$ Hz. Since a pole is estimated each time the sliding filter contains the pole frequency the effective number of estimations of each pole is about $N_{est} = [B_w/\Delta f] - 1 = 40$ where $[\cdot]$ is rounding to nearest integer. The results of the algorithm are shown in Fig. 7.2.

7.1.2 Identification Algorithms

Automated Operational modal Analysis (AOMA) is done using two algorithms named the Smallest Sphere Algorithm(SSA) and the Shortest Path Algorithm (SPA). The SSA is described by Juul et al. [2]. The SPA considers the set of poles from the stability diagram a Directed Acyclic Graph (DAG) and finds the shortest paths in this graph using proven techniques from graph theory [3]. The SPA finds distances between graph-nodes using a distance function in the same way as the SSA, and

M. Juul (✉) · P. Olsen · O. Balling
Department of Engineering, Aarhus University, Aarhus, Denmark
e-mail: mj@eng.au.dk

S. Amador · R. Brincker
Department of Civil Engineering, Technical University of Denmark, Kongens Lyngby, Denmark

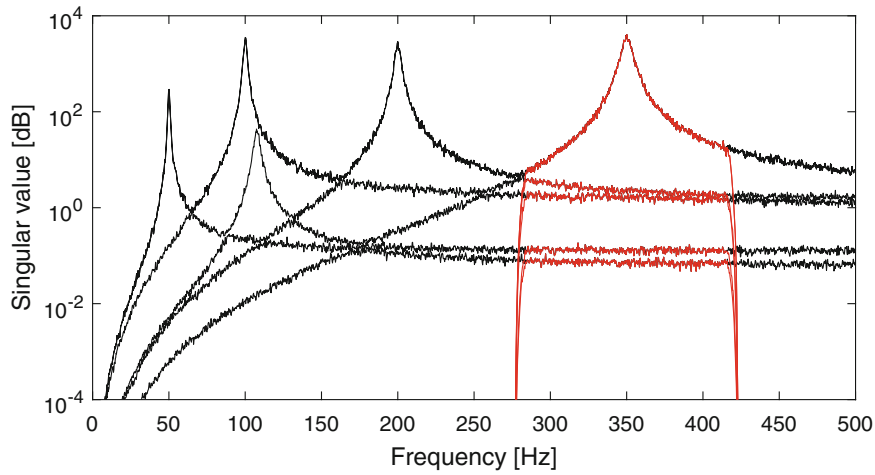


Fig. 7.1 Singular values for the spectral density of the simulated system. The red part of the frequency band illustrates the width of the sliding filter, for building the stability plot in Fig. 7.2

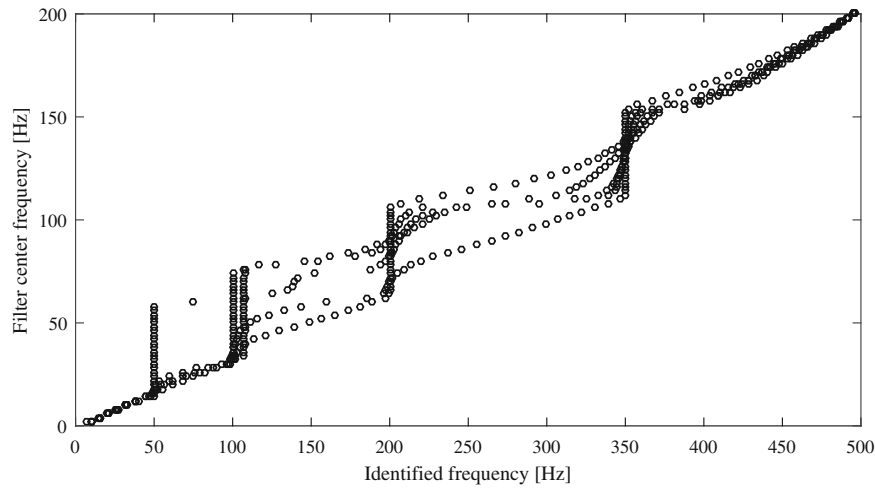


Fig. 7.2 Sliding filter stability diagram for the simulated system and the sliding filter technique described above

the shortest paths contains as many nodes as there are repeated estimation of the pole in the sliding filter stability diagram. If a path intersects a shorter path, the long path is removed, in the same way that bigger spheres are removed when overlapping a smaller sphere in the SSA in [2].

For the identified poles in the sliding filter diagram we consider distances between identifications using a distance measure. Each identified pole p_i consists of frequency f_i , damping ζ_i , mode shape b_i and possibly a participation vector γ_i . We can write $p_i = (f_i, \zeta_i, b_i, \gamma_i)$. A distance between two poles p_i and p_j is a non-negative function $d(p_i, p_j) \geq 0$. We have chosen to use distance functions that are linear combinations of frequency difference between identified modes, and the MAC value. The MAC value is the squared cosine of the generalized angle between b_i and b_j [4]. Using this distance measure with the SSA and the SPA gives the modes shown in green in the stability diagram in Fig. 7.3. An alternative way to measure distance is found in [5] and [6]. Here the frequency difference is scaled relative to the mean of the two absolute frequencies. This technique is common in machine learning, to ensure that the learning algorithm converges [7]. There is however no reason to believe that feature scaling will be of value to the SSA and SPA identification algorithms. To test this hypothesis we have tested the feature scaled distance measure.

Doing identification on the system shown in Fig. 7.4 using the unscaled distance measure both the SSA and the SPA algorithm identifies the modes correctly. If we use the scaled distance measure the five smallest spheres of the SSA are as shown in Fig. 7.5. This illustrates that the scaled distance measure have a tendency to not penalize horizontal parts of the clusters enough to prefer the weak vertical mode around 450 Hz. This tendency to accept horizontal spheres is illustrated by the sixth sphere, that is the first bad sphere. This is shown in Fig. 7.6. Both the SSA and the SPA will fail identifying

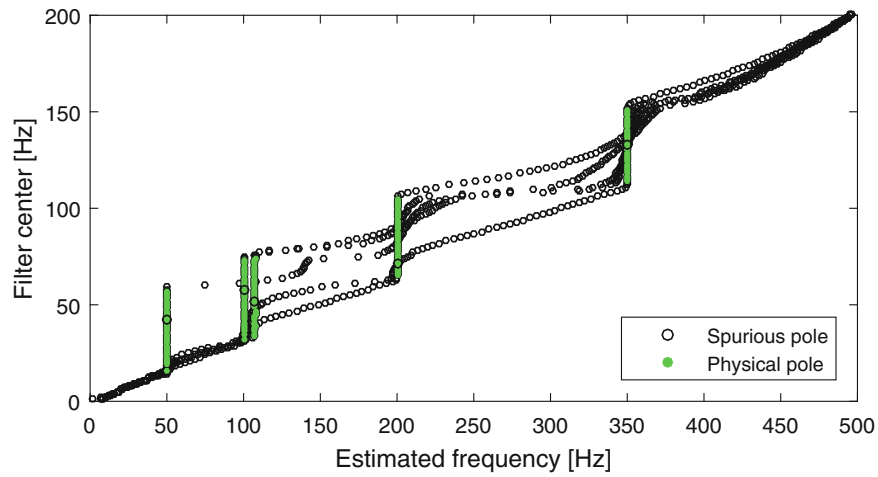


Fig. 7.3 Plot of sliding filter stability diagram with all poles from the remaining five smallest spheres from the SSA shown in green. The shortest paths from the SPA are almost identical

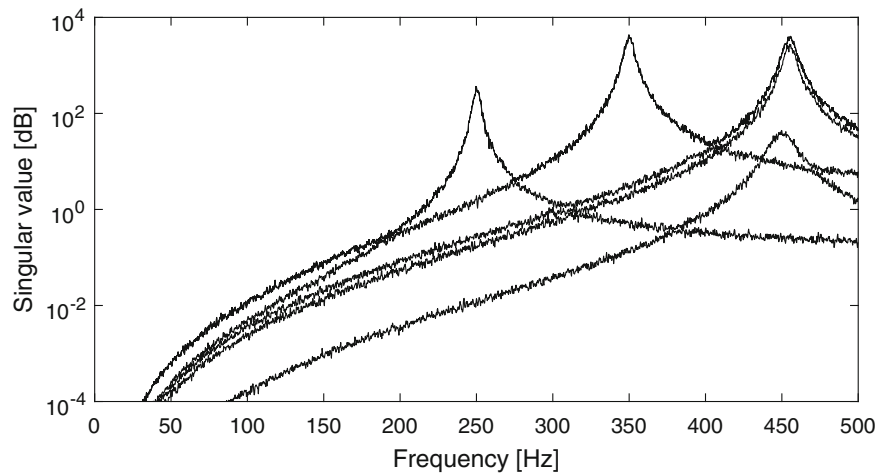


Fig. 7.4 Singular value plot for a simulated system with modes at high frequencies

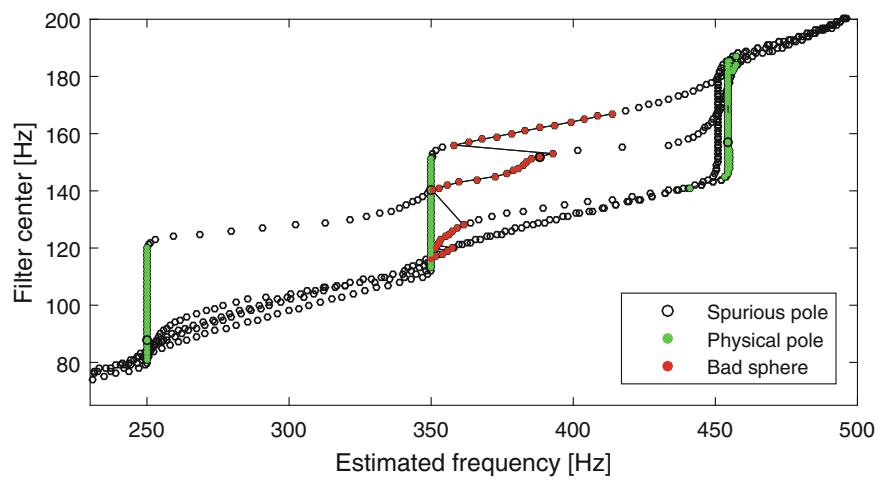


Fig. 7.5 Stability plot of the system in Fig. 7.4

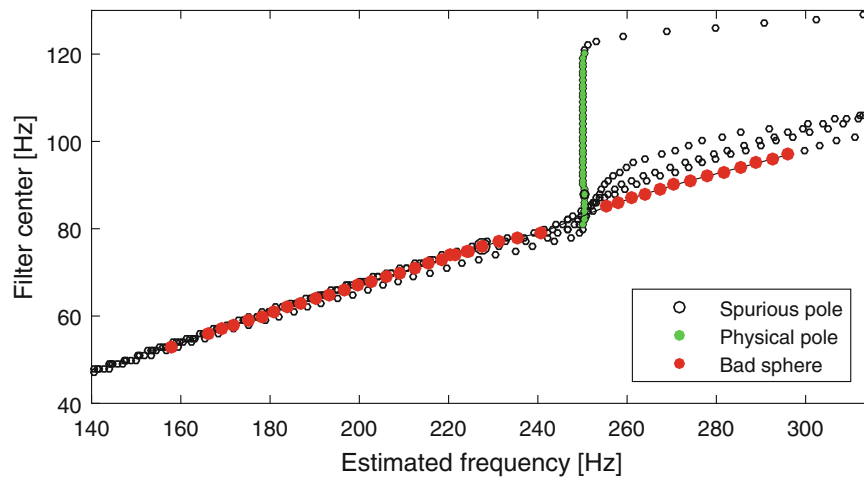


Fig. 7.6 Zoom into the sliding filter stability diagram shown in Fig. 7.5 illustrating the sixth smallest sphere in red. This sphere tends to be horizontal due to the scaling in the distance measure

poles correctly using the scaled distance measure. The main difference in results between the two algorithms is that a cluster can exist where the frequency of the identified poles jumps between two frequencies. As long as these frequencies are close together the radius of the sphere can be small. The SPA will eliminate this path since many changes between frequencies will give a long path. This makes the SPA the more robust of the two algorithms.

Acknowledgements This contribution is partly based upon work done in the INNOMILL project supported by the Innovation Fund Denmark, contract number 54-2014-3.

References

1. Brincker, R., Ventura, C.: Introduction to Operational Modal Analysis. Wiley, New York (2015). ISBN:9781118535158
2. Allemang, R.J., Brown, D.L.: Operational modal analysis on wind turbine hub. In: Proceedings of the 36th International Modal Analysis Conference (IMAC). SEM, Orlando (2018)
3. Cormen, T.H., Leiserson, C.E., Rivest, R.L.: Introduction to Algorithms. MIT Electrical Engineering and Computer Science. The MIT Press (1990). ISBN:0262530910
4. Allemang, R.J., Brown, D.L.: A correlation coefficient for modal vector analysis. In: Proceedings of the 1st International Modal Analysis Conference (IMAC), vol. 1, pp. 110–116. SEM, Orlando (1982)
5. Neu, E., Janser, F., Khatibi, A.A., Orifici, A.C.: Fully automated operational modal analysis using multi-stage clustering. *Mech. Syst. Signal Process.* **84**, 308–323 (2017)
6. Reynders, E., Houbrechts, J., De Roeck, G.: Fully automated (operational) modal analysis. *Mech. Syst. Signal Process.* **29**, 228–250 (2012)
7. Raschka, S.: Python Machine Learning. Packt Publishing Ltd, Birmingham (2015)

Chapter 8

Operational Modal Analysis on Wind Turbine Hub

Martin Juul, Ole Balling, and Rune Brincker

Abstract In this paper we present a dataset for Operational Modal Analysis (OMA) on a Vestas V112 wind turbine hub and illustrate how reliable Automatic OMA (AOMA) can be done on this structure. The chosen AOMA algorithm is called the Smallest Sphere Algorithm (SSA), and is based on the sliding filter stability diagram recently introduced by Olsen et al. We show how the SSA is able to identify all modes of the hub dataset reliable, including many closely spaced modes. The algorithm also successfully identifies two triple modes automatically. We show how a set of manually identified mode shapes compares to the Finite Element (FE) model. In this context it is discussed how the phenomenon of closely spaced modes is handled by rotating the identified modes into a basis defined by the FE model. A method for mode shape merging for multi setup testing is discussed.

Nomenclature

In this work we use the notation from Brincker and Ventura [1], where mode shapes are column vectors in matrices.

- A** Matrix with mode shapes as columns
- B** Matrix with Finite Element mode shapes as columns

8.1 Introduction

In this paper we present results from a vibration dataset collected as part of the INNOMILL project. INNOMILL is a cooperation between Danish industry partners, universities and the Danish Advanced Manufacturing Research Center (DAMRC). The project goal is to construct a small CNC machining cell for working on large cast iron workpieces.

In the project we have worked on the Vestas hub shown in Fig. 8.1. A Finite Element (FE) model was constructed to effectively model the hub and an open question was how well the FE model matched the actual structure. To verify the quality of the FE model a modal test was performed. From the beginning the project has focused on being able to do modal analysis and potential model update on the fly during the machining process. Thus it has been of interest to be able to do modal analysis fast and under operational conditions, either based on excitation signals directly from the milling process, or based on external exciters. Therefore Operational Modal Analysis (OMA) has been the focus of attention for all modal analysis. Initial results for doing OMA on the hub can be found in [2] where many open questions remains.

M. Juul (✉) · O. Balling
Department of Engineering, Aarhus University, Aarhus, Denmark
e-mail: mj@eng.au.dk

R. Brincker
Department of Civil Engineering, Technical University of Denmark, Kongens Lyngby, Denmark



Fig. 8.1 Vestas V112 hub placed on Polyurethane blocks for vibration isolation. The blocks effectively isolates the hub from the surroundings

8.2 The Hub Experiment

To do Operational Modal Analysis (OMA) on the wind turbine hub in Fig. 8.1 it was placed on Polyurethane (PU) blocks. These blocs ensure that the hub is effectively isolated from the floor, and the hub can be considered as having a free boundary.

For the experiment Brüel and Kjær 4508B-002 modal testing accelerometers were placed at 63 positions on the hub as shown in Fig. 8.2. Data was collected using the National Instruments (NI) CompactDAQ system with NI9234 modules. The OMA test was performed as five different tests with 6 reference and 14 roving sensors [1]. Excitation of the structure was done by dragging two 2 kg hammers over the surface of the hub duration of the test. A singular value plot of the resulting data is shown in Fig. 8.3. In this figure more than 80 modes can be seen.

The effect of the PU blocks can be seen from Fig. 8.3 where the rigid body modes are clearly visible at very low frequencies below 0.2 Hz. The first structural mode appears at about 1 Hz, or about five times that of the rigid body modes.

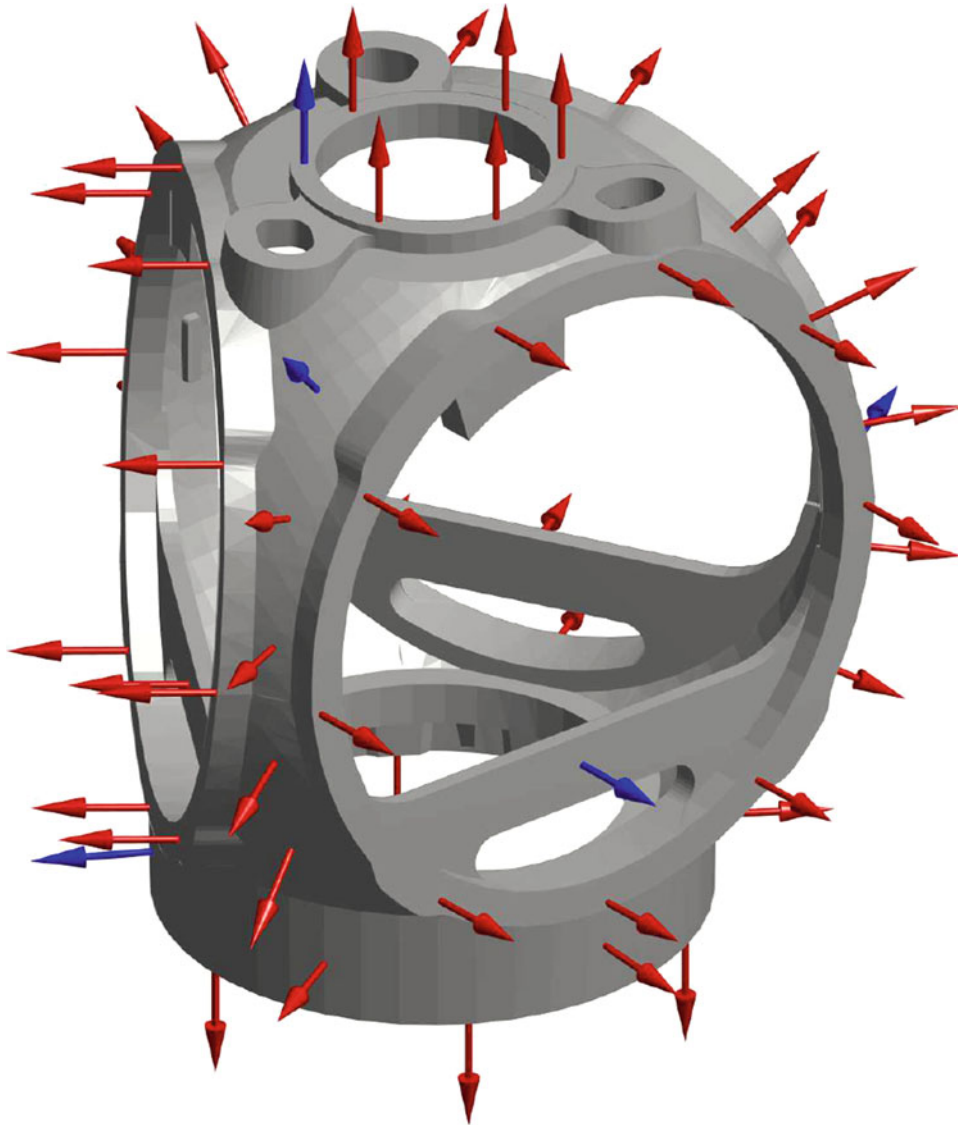


Fig. 8.2 Sensor positions and direction for the OMA test on the hub shown in Fig. 8.1

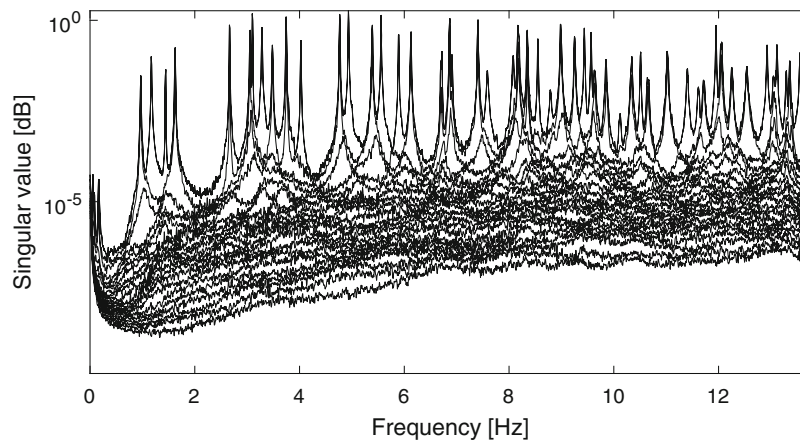


Fig. 8.3 Singular value plot of the data from the wind turbine hub in Fig. 8.1. More than 80 modes are visible in the band. The frequency axis is rescaled to place the first structural mode at about 1 Hz

8.3 Automatic Identification Algorithm

System identification is done using the least squares algorithm TDPR [1] in small frequency intervals of bandwidth B_w where frequencies outside the band are removed using a band pass filter with guard band B_g . This filter is slid over the entire band, in small steps of Δf . In each band identification is done and the identified poles are saved in a data structure.

When the sliding filter process is done the identified poles can be plotted in a stability plot with identified frequency on the horizontal axis and the filter center on the vertical axis. The technique is described by Olsen et al. in [3]. As is evident from Fig. 8.4 physical poles are re-estimated many times by the technique generating vertical lines in the stability diagram.

8.3.1 Automated OMA

When the sliding filter has produced the set of identified poles for all filter pass bands, the vertical lines are detected. This detection is done using an algorithm called the Smallest Sphere Algorithm (SSA). This algorithm iterates over all poles, and for each pole the distance to all other poles is calculated using a distance measure. The distance between two identified poles is created by using the frequency difference between poles and the MAC [4] value between the mode shapes corresponding to the poles. Each pole is estimated approximately a fixed number of times, N_{est} , determined by the filter width and the step size of the sliding filter. For each pole the closest N_{est} poles are used to create a local N_{est} -sphere around each pole, containing the N_{est} closest poles. The sphere with the smallest radius is marked, and bigger overlapping spheres are removed. After this the smallest un-marked sphere is marked and again bigger overlapping spheres are removed. Iterating in this way until all remaining spheres are marked gives a set of smallest spheres. The remaining spheres have increasing radius, and at some point the radius may get so big that the sphere can be ignored. The smallest spheres detects the vertical lines perfectly for all physical poles, even the closely spaced modes.

In Fig. 8.5 the low frequency part of the stability diagram is shown. This illustrates how well the physical poles are separated from the spurious poles. The corresponding singular values are shown in Fig. 8.6. Zooming even further around the first structural mode at about 1 Hz gives Fig. 8.7.

The radii of the spheres is shown in Fig. 8.8. A large jump is seen in the graph from sphere number 83 to sphere number 84, indicating that after mode number 83 the radii of the spheres starts to get much bigger. This is an indication of bad or spurious modes.

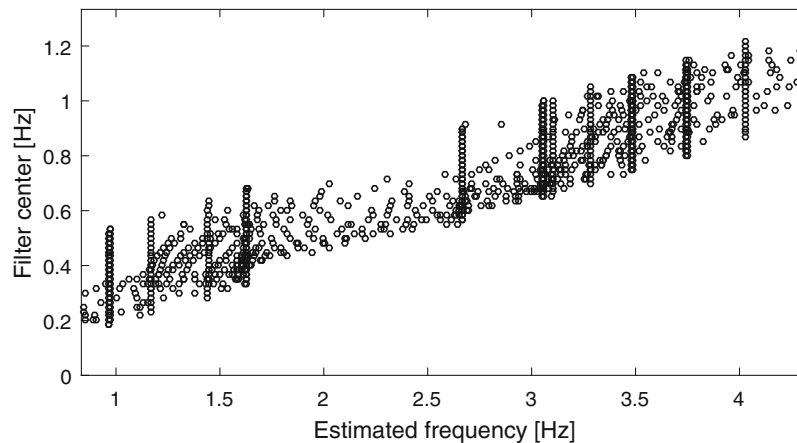


Fig. 8.4 Low frequency region of the sliding filter stability diagram

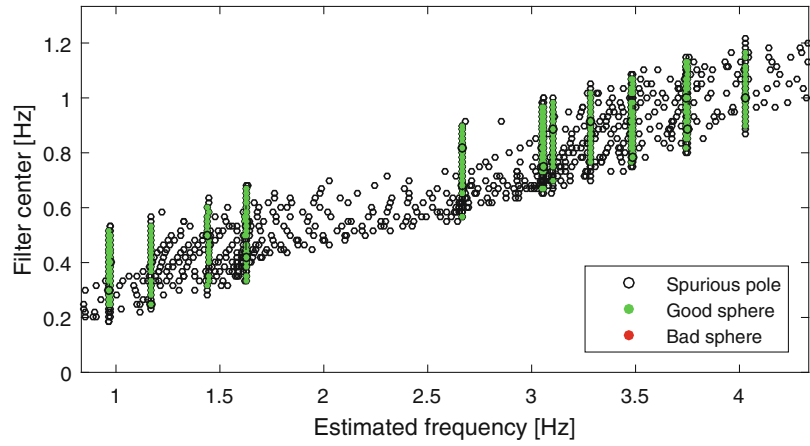


Fig. 8.5 Identified modes in Fig. 8.4. This plot illustrates separation of physical poles from spurious poles. The physical poles are shown in green

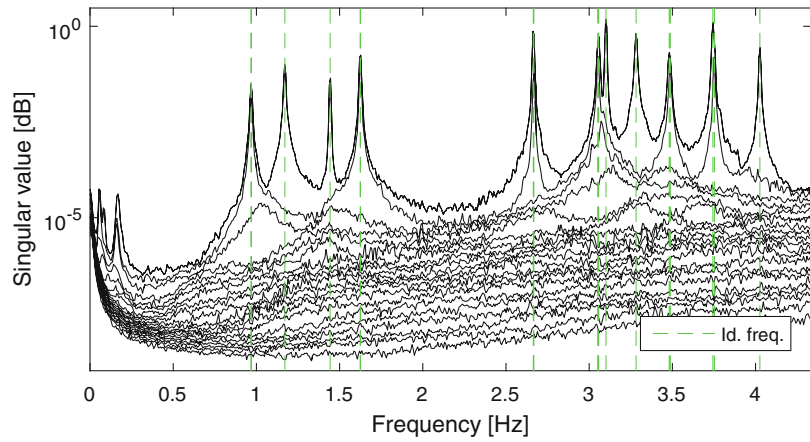


Fig. 8.6 Singular values corresponding to the stability diagram shown in Fig. 8.5. The identified poles are shown as vertical green dashed lines

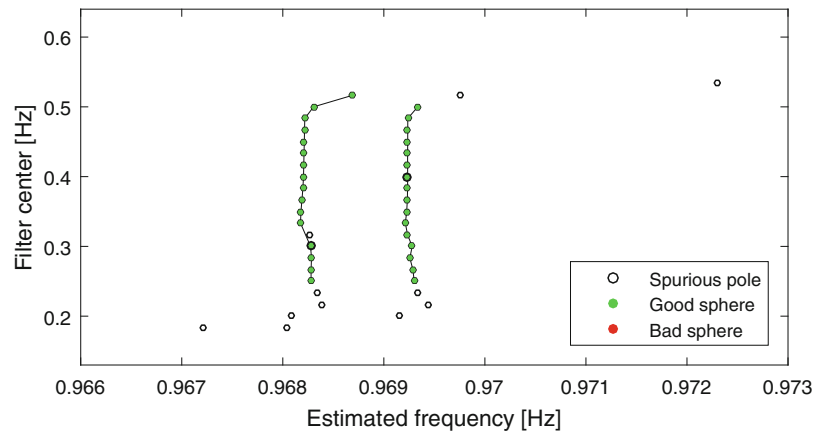


Fig. 8.7 Zoom into the stability diagram around the first two closely spaced modes in Fig. 8.5. This figure illustrates successful identification of closely spaced modes

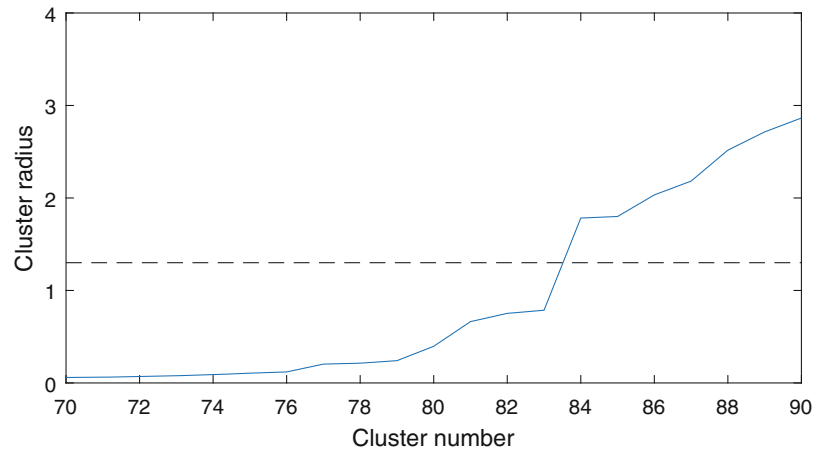


Fig. 8.8 Plot of the radii of the spheres of the SSA. A significant jump is clearly visible from mode 83 to mode 84, indicating that from mode 84 and up, the spheres become much larger. Spheres with lengths above the dashed line are discarded

8.4 Identification with FDD and Projection

In Fig. 8.9 the first 6 mode shapes from the Finite Element (FE) model is compared to the identified test modes from Artemis Modal [5]. These modes show large deviations from the ideal MAC matrix that would have ones on the diagonal. If the closely spaced mode shapes are rotated into the comparable FE closely spaced subspaces the MAC matrix will change into the MAC matrix shown in Fig. 8.10.

These mode shapes were identified with Artemis [5] so merging of the sub modes shapes from the individual tests has already been done. If identification is done on only one test the merging procedure is avoided. Figure 8.11 shown how the mode shapes of the first 6 modes from test 1 compare to the FE model. If the closely spaced modes of this test are rotated into the subspaces of the closely spaced modes of the FE model we get the MAC matrix shown in Fig. 8.12. For mode 1, 2, 5 and 6 there is an improvement over Fig. 8.10.

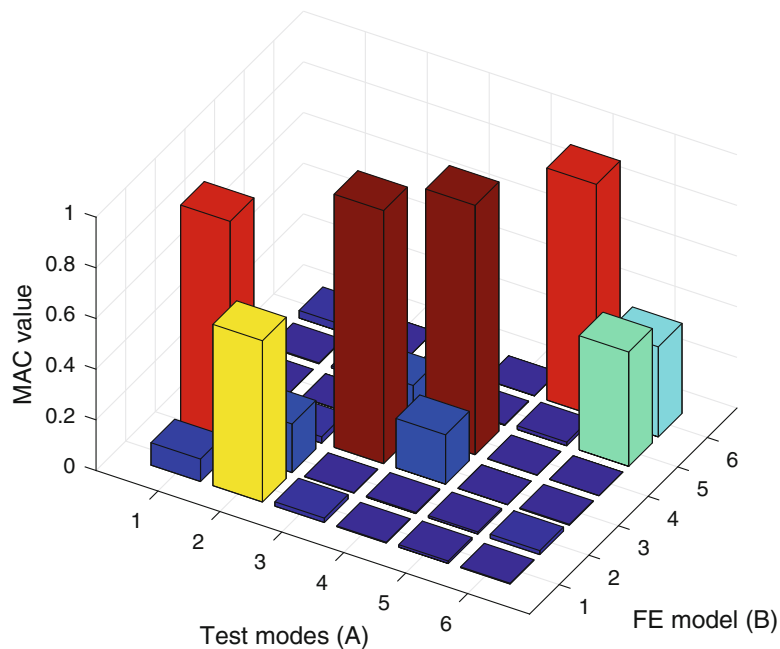


Fig. 8.9 MAC value between the first 6 mode shapes of length 34 from FE model and the test mode shapes identified by Artemis Modal

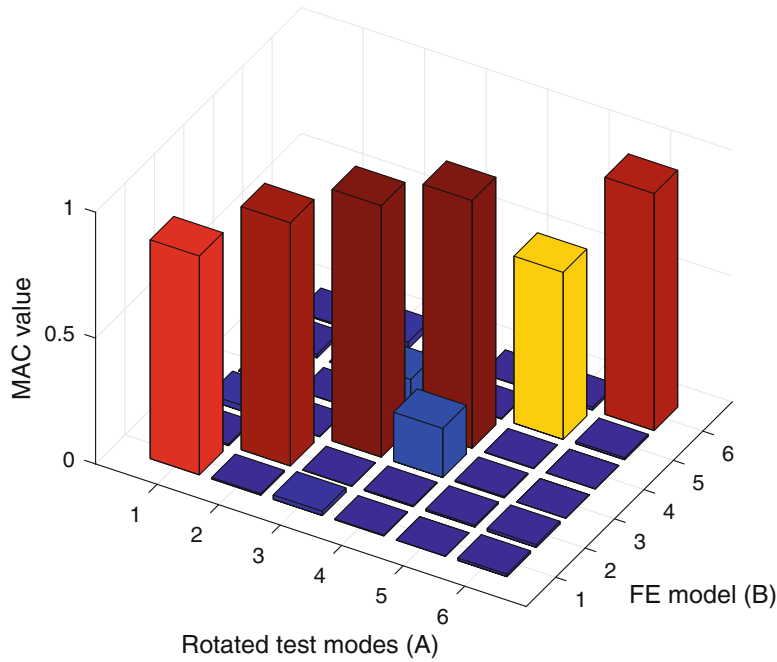


Fig. 8.10 MAC value between the first 6 mode shapes of length 34 from FE model and the rotated test mode shapes

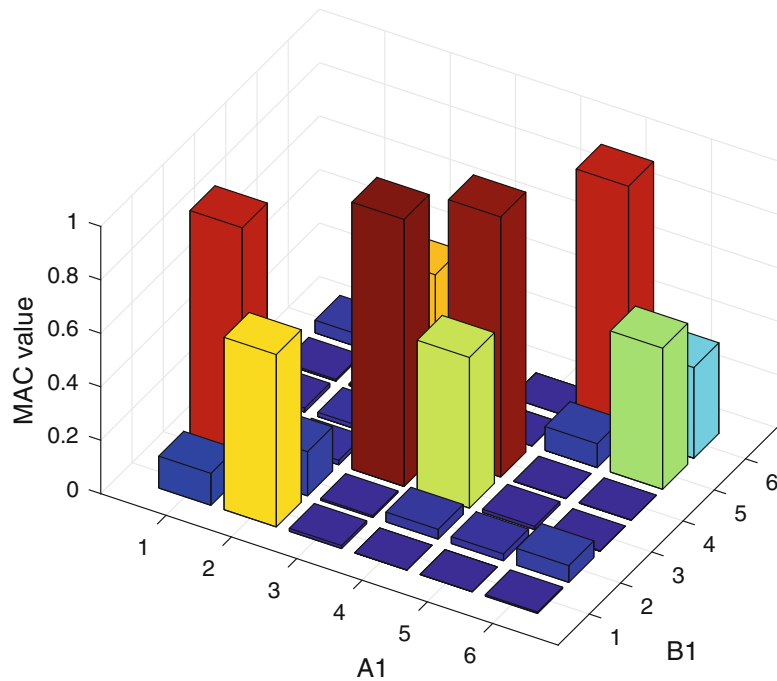


Fig. 8.11 MAC value between the first 6 mode shapes of length 20 from FE model and the mode shapes from the first test

If the closely spaced mode shapes of both test 1 and 2 are rotated into the subspaces of the closely spaced FE mode shapes, and mode shape merging is done after this rotation, the result is as shown in Fig. 8.13. Merging is done as described in [1]. This procedure shows improved results over the MAC of the mode shapes in Fig. 8.10, for all modes.

We conclude that for closely spaced modes, rotating the mode shapes into the mode shape basis defined by the FE model before merging will give a notable improvement over traditional merging. Defining this basis from a singular value decomposition of the test mode shapes on the reference sensor positions only, will give comparable results, and give an algorithm that does not rely on the FE model [6].

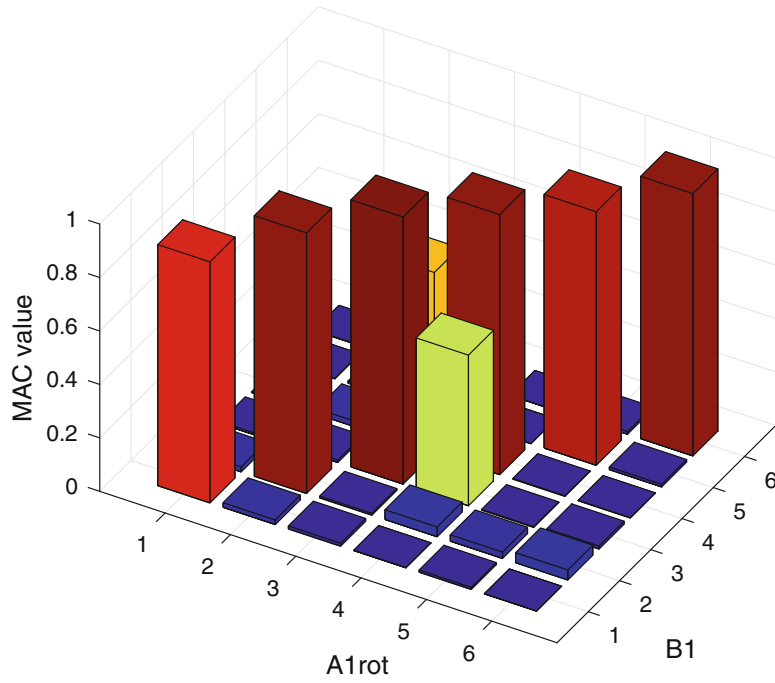


Fig. 8.12 MAC value between the first 6 mode shapes of length 20 from FE model and the rotated mode shapes from the first test

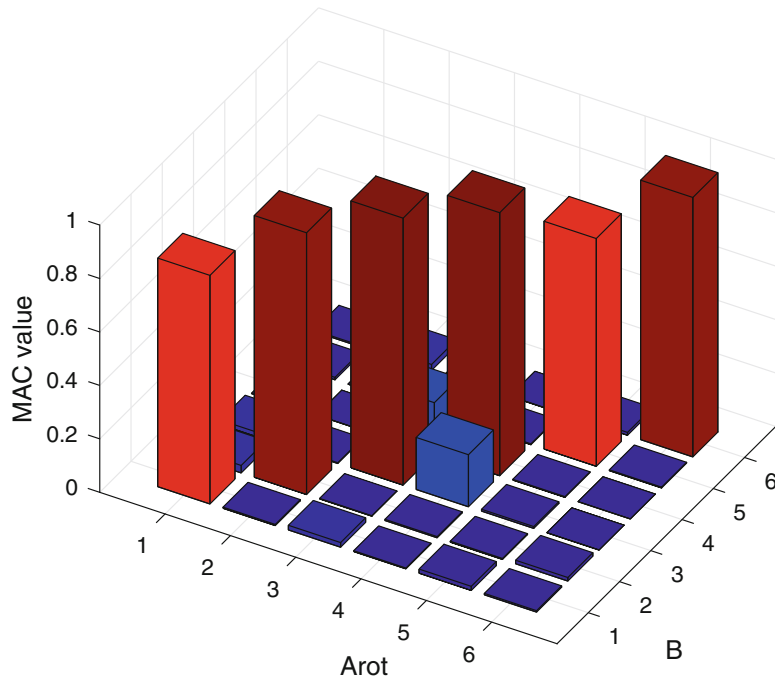


Fig. 8.13 MAC value between the first 6 mode shapes of length 34 from FE model and the rotated and re-merged test mode shapes

8.5 Conclusion

In this work it has been illustrated how operational modal analysis can be automated using the sliding filter stability diagram and a new clustering technique called the Smallest Sphere Algorithm. It has been shown that this algorithm will identify closely spaced modes and that the algorithm successfully identifies 83 modes on the structure. It has been shown that multi setup operational modal analysis can be done on a highly axial symmetric structure, by showing that closely spaced modes can be handled by subspace rotation.

Acknowledgements This contribution is partly based upon work done in the INNOMILL project supported by the Innovation Fund Denmark, contract number 54-2014-3.

References

1. Brincker, R., Ventura, C.: Introduction to Operational Modal Analysis. Wiley (2015). ISBN:9781118535158
2. Juul, M., Kovacs, E., Brincker, R., Balling, O.: OMA identification of a wind turbine rotor hub for monitoring purpose. In: International Conference on Noise and Vibration Engineering, ISMA (2016)
3. Olsen, P., Juul, M., Tarpø, M., Brincker, R.: Stabilization diagrams using operational modal analysis and sliding filters. In: 7th International Operational Modal Analysis Conference (IOMAC) (2017)
4. Allemang, R.J., Brown, D.L.: A correlation coefficient for modal vector analysis. In: Proceedings of the 1st International Modal Analysis Conference (IMAC), vol. 1, pp. 110–116. SEM, Orlando (1982)
5. Structural Vibration Solutions A/S (SVS): Artemis modal 4.0 (2015). <http://www.svibs.com/>
6. Juul, M., Ringgaard, K., Balling, O., Brincker, R.: Closely spaced modes in multi setup operational modal analysis. Manuscript submitted for publication (2017)

Chapter 9

The Influence of Edge Boundary Conditions and Cracks on Vibrational Modes of Multilayer Ceramic Capacitors

Jonel Ortiz, Giuliana Davis, Kevin Troyer, and Paul Heyliger

Abstract Electrical failure of layered capacitors is often a limiting factor in the design of many important electronic devices. Manufacturing processes, soldering, and service conditions have been shown to induce cracks in the dielectric material of the capacitor, providing conductive pathways that result in electrical leakage. In addition to the crack itself, edge boundary conditions can cause modal stress concentrations in a particular region of the capacitor that can initiate new cracks or propagate existing ones. Small but potentially damaging cracks can be very difficult to detect, and their presence may only become evident when they grow large enough to impact the capacitor's performance. Recent experimental studies have demonstrated that cracks in layered capacitors can be detected nondestructively by measuring a shift in the resonant frequency of the structure via ferroelectric transduction. This study seeks to extend these recent findings by developing finite element models of layered capacitors in order to determine the level of influence that cracks and edge boundary conditions have on their frequency spectrum and their localized stress fields. Of particular interest is determining if ferroelectrically excited modes will be sensitive to cracks that can commonly appear near either restrained or traction-free corners. Computational investigation is intended to supplement future experiments on these structures, with the eventual goal of merging and analyzing the results from theoretical predictions and physical measurements. Specifically, three different crack types were simulated (endcap crack, inner crack, corner crack) along with three boundary conditions (free-free, fixed surface, and soldered). Results indicated that a fractured capacitor yielded lower natural frequency values in comparable modes to an uncracked capacitor, and that this shift in natural frequency values could be magnified depending on the applied boundary conditions. This finding is an important contribution toward the effort of non-destructively detecting cracks in the MLCCs and for future research to confidently utilize MLCCs in future applications.

9.1 Introduction and Background

Multilayer ceramic capacitors (MLCCs) provide a small-dimension yet high capacitance alternative to other existing operational capacitors. Although these components have proven to be advantageous as they help reduce electrical circuit size, predicting their reliability still remains a challenge due to hidden fractures. External damage in MLCCs can often be detected visually. However, the capacitors often fail due to subsurface cracks that cannot be seen on the outer layers of the MLCC resulting in unanticipated failure. Finite element (FE) modeling of multilayer ceramic capacitors (MLCCs) has proven to be an effective way of modeling damage such as cracks of various sizes in different regions of the capacitor. Some common cracks found in MLCCs include interior flexure (or flex) cracks through the layers and cracks that form in the inner corner through the dielectric layer known as corner cracks. A flex crack (Fig. 9.1) and a corner crack (Fig. 9.2) can both form during manufacturing, soldering, or operation of the capacitor. Previous studies [1] have found that the addition of endcap material does not have a significant impact on the natural frequencies of the capacitor. This conclusion also extends to cracks that form on the interface of the endcap material and alternating layers of electrodes. Therefore, cracks of this nature are ignored in this paper. It should be noted that these cracks may still have significant effects on the reliability of the capacitor;

J. Ortiz (✉)

Texas A&M University, College Station, TX, USA

e-mail: jaortiz16@tamu.edu

G. Davis

University of New Mexico, Albuquerque, NM, USA

e-mail: davisg@unm.edu

K. Troyer · P. Heyliger

Colorado State University, Fort Collins, CO, USA

e-mail: kevin.troyer@colostate.edu; prh@engr.colostate.edu

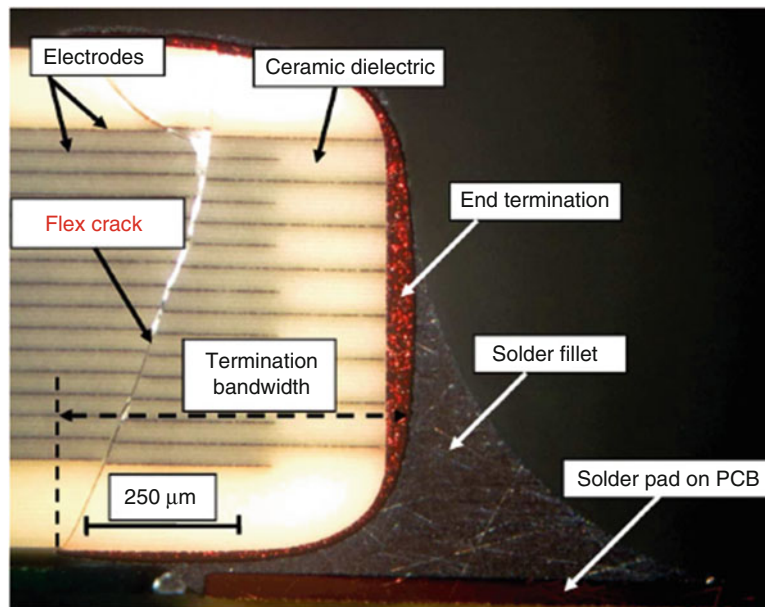
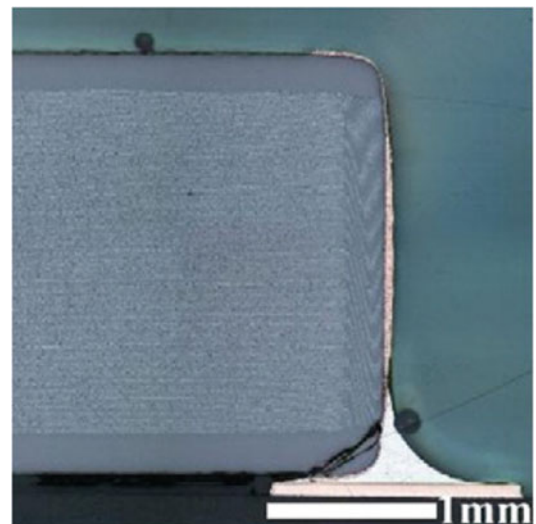


Fig. 9.1 A flex (interior) crack through multiple layers of a capacitor (Adapted from Keimasi et al. [3])

Fig. 9.2 A corner crack on the bottom right edge of a capacitor mainly cutting through the dielectric material (Adapted from Andersson et al. [6])



however, they are not good candidates for cracks that can be detected relatively easily using acoustic techniques. A flex crack is the easiest crack to detect through electrical methods since it penetrates through multiple electrode layers and thus can have a rather significant impact on the capacitor's electrical performance. Corner cracks in the capacitor often occur where the endcap terminates with the dielectric material due to stress concentrations near the edge boundary. Cracks that form in the corner of the capacitor in the dielectric layer are of interest since they are particularly difficult to detect via capacitance measurements due to the fact that the electrode layers remain intact. While a crack in the dielectric layer may not cause initial capacitor failure, propagation of that crack can eventually penetrate the electrode section and cause an electrical shortage [2]. Corner cracks can form due to bending stresses transmitted by the circuit board during operation, transportation, or storage.

The impacts that each type of crack can have on the magnitude of the natural frequencies of the capacitors vary in the sense of the magnitude of their shift. When a large frequency shift is detected, it can indicate a flaw within the capacitor. To overcome these obstacles, a FE model of the capacitor was developed to replicate several types of cracks and the natural frequencies were measured and compared to uncracked capacitors with similar boundary conditions.

9.2 Methods

9.2.1 Geometry and Mesh

In order to model the different types of cracks in the capacitor, an uncracked MLCC model was first constructed to validate the model against previously published data and to identify natural frequency shifts between the uncracked and cracked models. The model was constructed in ABAQUS using dimensions similar to those reported by Peterson et al. [1] The overall dimensions of the capacitor without endcaps are 3.04 mm in length, 2.474 mm in width and 1.414 mm in height (Fig. 9.3). The dimensions of the capacitor with endcaps are 3.102 mm in length, 2.536 mm in width, and 1.476 mm in height (Fig. 9.4). Contrary to the model published by Peterson et al., the current model does not use symmetry conditions to reduce the size of the model. Rather, it is a full capacitor model, which, while being more computationally expensive, provides more flexibility in introducing cracks of various lengths and angles throughout the domain.

Development of the computational model required several geometric simplifications to allow the construction of a higher quality mesh. The first simplification was to assume there were no fillets on the edges and corners of various features of the capacitor. The second assumption was to use a nominal termination length of 0.48 mm given by Vishay Intertechnologies for a set of type-1210 MLCCs with a model number of VJ1210Y474KXAAT¹. The termination length can be visualized in

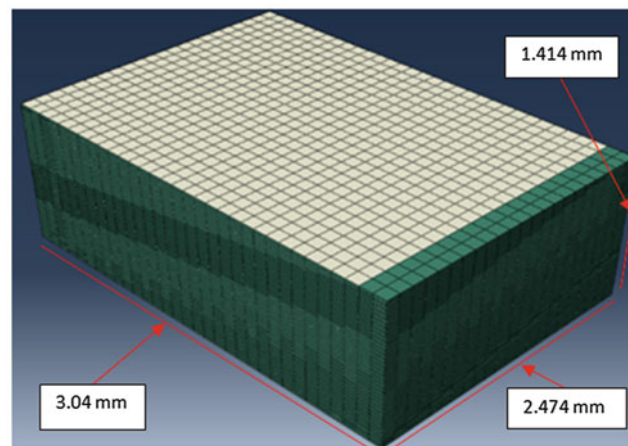


Fig. 9.3 FE model of MLCC without endcaps

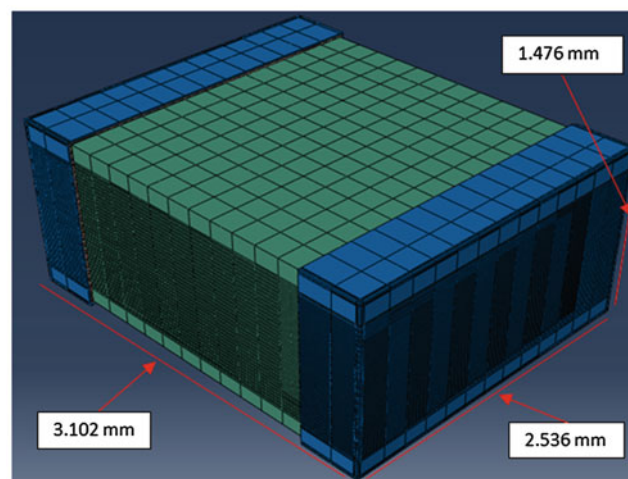


Fig. 9.4 FE model of MLCC with endcaps added

¹Identification of this commercial product is provided solely for the purpose of technical completeness and does not reflect an endorsement.

Fig. 9.1 which is referred to as the “termination bandwidth”, and is the same for both the bottom and the top surfaces of the capacitor.

The endcaps consisted of three consecutive metallic layers (inner, middle, outer) that each have a uniform thickness wrapping over the capacitor. As shown in Fig. 9.4, the outermost layer of the endcaps is shown by the blue layer, on either side of the capacitor. From the innermost layer to the outermost layer, the thickness of each metallic layer was taken to be $7\ \mu\text{m}$, $9\ \mu\text{m}$, and $15\ \mu\text{m}$ respectively [1]. Figure 9.5 shows the circuit board that was constructed in ABAQUS and used as one of the boundary conditions for the capacitor FE model. The circuit board consists of Arlon 85, gold, and solder, with the properties given in Table 9.2. In practice, circuit boards will typically have a thin polymer coating on the top surface. This thin layer was omitted for this study since it should not greatly affect the natural frequencies while keeping the number of elements to a manageable size.

9.2.2 Material Properties

The material properties used in the MLCC FE model are shown in Table 9.1.

Table 9.2 shows the material properties used to model the circuit board model.

The material used for the bulk of the circuit board was Arlon 85. Additionally, the solder material was chosen as one that is versatile and not directly specified from a data sheet. The circuit board material is modeled as an isotropic material although in reality are considered to be orthotropic. The model reduction was used to reduce computational time, and the premise of this assumption is that it is more crucial to study how the capacitor interacts with the solder rather than refining the material model for the underlying circuit board.

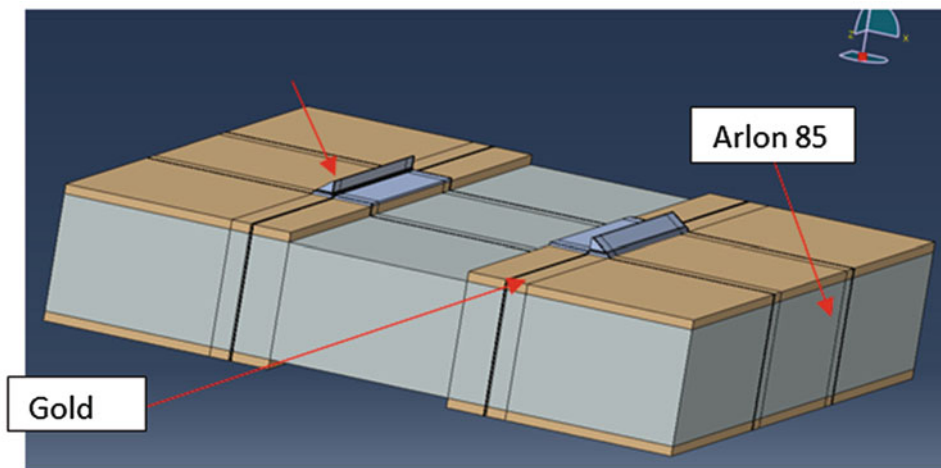


Fig. 9.5 Circuit board geometry

Table 9.1 Material properties of MLCC

Material	E (MPa)	ν	ρ (kg/m^3)
BaTiO ₃ , ceramic electrode layer	149,800	0.324	6050
Sn, middle endcap layer	47,883	0.252	7297
Ag, dielectric layer & inner endcap layer	82,405	0.364	1050
Ni, outer endcap layer	220,608	0.202	8909

Table 9.2 Material properties of circuit board

Material	E (MPa)	ν	ρ (kg/m^3)
Arlon 85	22,063	0.15	1840
Au	77,200	0.42	19,320
Solder (Sn63-Pb37)	43,225	0.38	8520

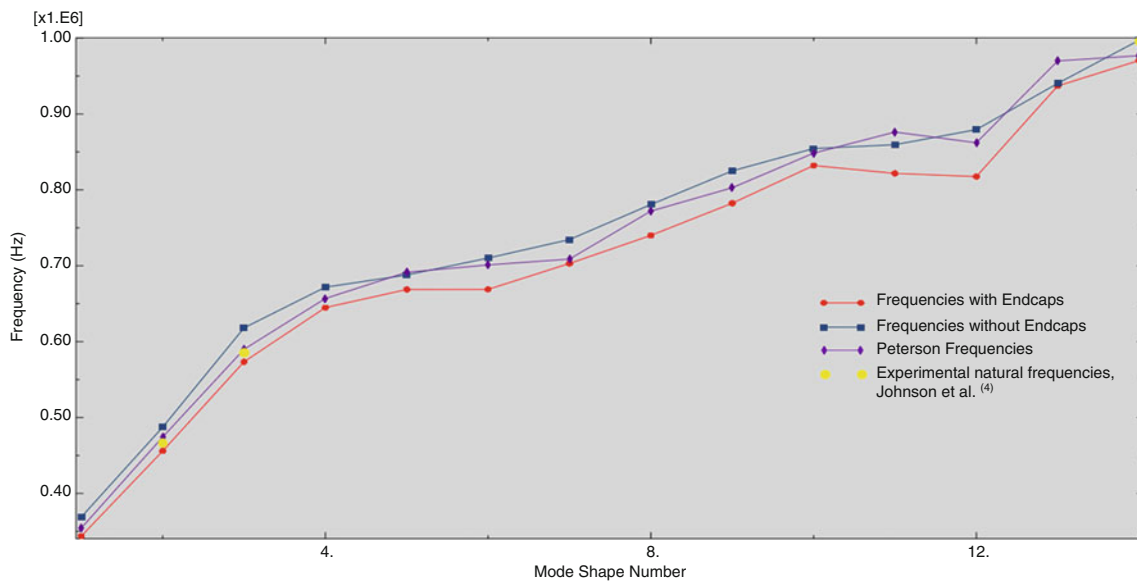


Fig. 9.6 Comparative calculations for validation, natural frequencies with and without endcaps along with Peterson calculations and data points from Johnson et al. [4]

9.2.3 Model Validation

To ensure that the model was a valid and accurate representation of real MLCCs, calculations of natural frequency from the uncracked model were compared with published calculations of Peterson et al. [1], which used the same material properties but slightly different physical dimensions that more accurately represented MLCCs studied experimentally [2]. The average percent difference between each of the modes produced from the current model and the previously published model is 2.7%. This slight variation can be attributed to the assumptions and idealizations made for the full-scale model in order to preserve mesh quality and keep the model tractable. A plot of the natural frequencies for the capacitor with and without endcaps when compared to the published calculations is provided above in Fig. 9.6, along with values taken from Johnson et al. characterizing “as received” (AR) natural frequencies of similar capacitors [4].

In Fig. 9.6, the middle line (represented by purple diamonds) with data points represents the published natural frequency values while the top and bottom lines describe the current model without and with endcaps, respectively. As mentioned above, the average difference between the published data and the model with endcaps in this paper is 2.7%, which indicates that the assumptions made in geometry, material properties, and the addition of endcaps increases the natural frequencies by an expected but negligible amount and therefore validates the model.

9.3 Analysis Methods

9.3.1 Cracks and Boundary Conditions

We simulated three primary types of cracks: a crack on the capacitor/endcap interface (endcap crack), a flex crack (Fig. 9.1), and a corner crack (Fig. 9.2). Based on results obtained throughout the analysis and current research interests, an emphasis will be placed on the corner crack. Corner cracks can occur due to thermal shock or board flexure during the solder reflow process that is employed to attach the MLCCs to the circuit boards [4]. Overall, corner cracks prove to be most difficult to detect because damaging the dielectric layer by itself may not cause failures, but can lead to crack propagation ultimately resulting in penetration of the electrode layer causing electrical leakage and capacitor failure. Subsequently, detecting these cracks through non-destructive methods such as acoustic excitation would prove to be a powerful method in determining a faulty or fatiguing capacitor where capacitance/voltage based metrics fall short. Detecting cracks like these before they propagate becomes especially useful when the capacitors are going to be in an environment where they cannot be replaced once they are put into operation (e.g. medical devices and spacecraft).

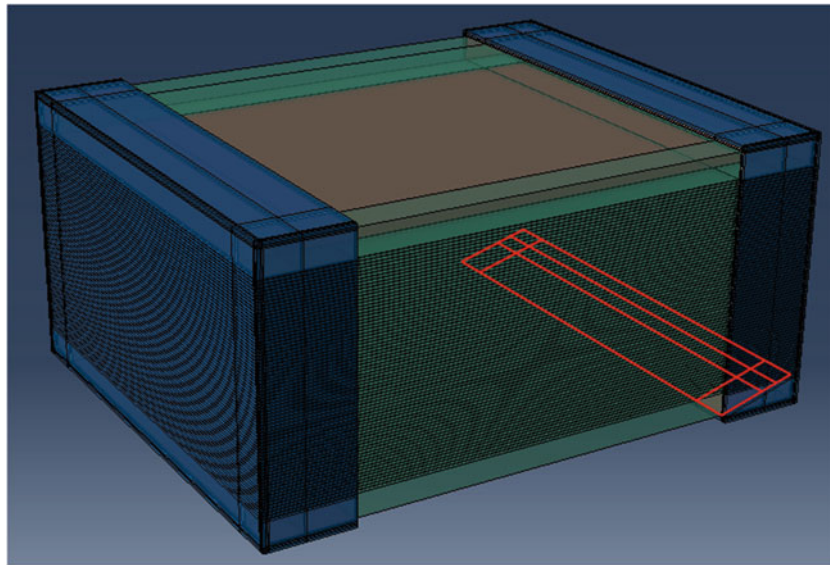


Fig. 9.7 Corner crack implementation

An example of a corner crack implementation in the FE model is shown in Fig. 9.7, in which the crack does not cut through any electrode layers and resides solely in the dielectric material with an orientation consistent with experimental studies [6]. The crack in the model is extended across the entire width (2.474 mm) of the capacitor in order to obtain upper-bounded metrics of frequency shifts. The corner crack was implemented in the FE model through node ties, which is a way of releasing part of the solid material in the mesh so that nodes on an interface are free to experience discontinuous displacement. At the red interface shown in Fig. 9.7, all nodes connecting the portion of the capacitor to the rest of the capacitor are untied except for the nodes on the end to attach that section to the capacitor.

Of particular interest were boundary conditions that could be used to exaggerate these shifts in natural frequency to make them easier to detect experimentally. In total, there were three boundary conditions implemented: a capacitor in free space, a capacitor fixed on the bottom surface adjacent to the circuit board, and a capacitor kinematically tied to the soldered portion of the circuit board introduced in Fig. 9.5. All three of these boundary conditions are shown in Fig. 9.8. Modeling the capacitor on the circuit board provides a more compliant boundary condition as opposed to fully fixed, which would be more difficult to realize experimentally. Additionally, some applications of the MLCCs require multiple capacitors on one circuit board and therefore would be extremely tedious to remove each capacitor individually [4].

9.3.2 Modal Analysis

A modal analysis was performed on both the uncracked and cracked capacitors across all boundary conditions in order to investigate any shifts in natural frequencies. Overall, it was expected that the natural frequencies would drop as cracks were implemented, relative to an uncracked capacitor. This assumption is derived from the capacitor undergoing a decrease in stiffness while maintaining the same mass, with the same mass being guaranteed as a result of how the crack was initiated in the computational model.

Since the modal analysis assumes linear response of the capacitor, the contact on the crack interfaces was not captured. This assumption helped to bound the problem in terms of the magnitude of shift to expect in the natural frequencies of the cracked and uncracked capacitors. It also allowed for a relatively coarse mesh to be tractably used on the capacitor, which helped in quickly completing a mesh convergence study. The frequency range of interest was determined by the modes that were excited experimentally [4], and was found to be near 1 MHz. There are, however, other experimental studies that have reported natural frequencies as high as roughly 12 MHz, such as Erdahl et al. [5]. To ensure the capturing of the modes of interest, the frequency range of interest was set to 0 Hz to 1.5 MHz.

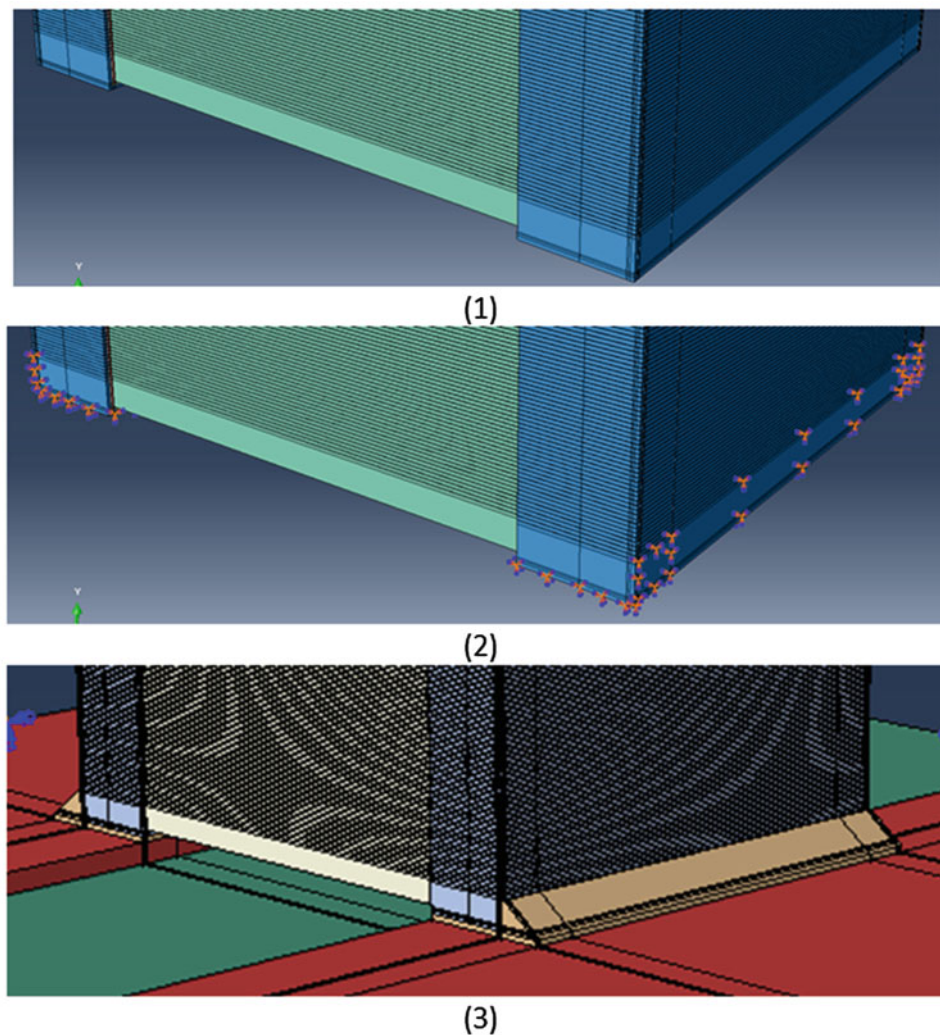


Fig. 9.8 Capacitor boundary conditions: (1) free boundary condition, (2) fixed boundary condition, (3) soldered boundary condition

9.3.3 MAC Plots for Modal Comparison

While comparing mode shapes between cracked and uncracked capacitors, it became evident that implementing cracks caused additional modes (in the frequency range of interest) with acoustic stress fields often localized near the cracks. These modes are referred to as *local modes*, and modes that are shared between cracked and uncracked capacitors are referred to as *global modes*. Local modes produce shifts in natural frequencies but show no resemblance to any uncracked mode shapes for a given boundary condition, and therefore cannot be used when comparing similar mode shapes and subsequently quantify the frequency shift for a cracked and uncracked capacitor. Figure 9.9 illustrates an example of a local mode found in a corner crack analysis. This figure shows how the crack completely dominates the mode shape which implies that this mode shape would not be found in the modal analysis of an uncracked capacitor.

The presence of local modes in the spectra is intriguing, with respect to the possibility of such modes serving as a basis for nondestructively detecting the presence of cracks, since local modes are completely absent in uncracked MLCCs. Johnson et al. [4] reported no extra modes in cracked MLCCs with ferroelectric excitation. However, the types of cracks in that study (induced by thermal quenching) may have included only near-surface cracks with no local modes in the measured frequency range. The question of whether typical corner cracks could be detected with resonant ferroelectric excitation warrants further study, but this subject is beyond the scope of the current work.

Considering the overall objective of detecting cracks non-destructively is to compare natural frequencies of similar modes, these local modes were neglected and only similar modes between an uncracked and cracked capacitor were compared.

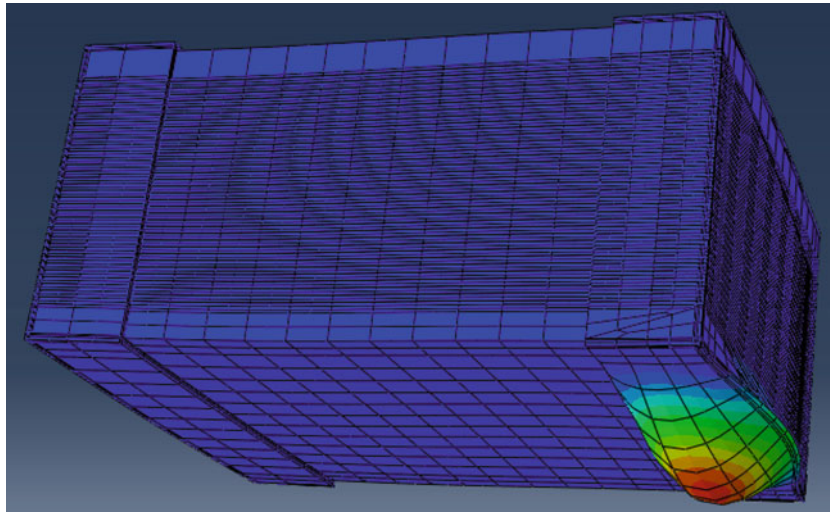


Fig. 9.9 Illustration of a local mode present in a corner cracked capacitor in free space. The magnitude of displacements are emphasized with a color scale ranging from red (highest) to blue (lowest). The crack is modeled as extending along the entire depth of the capacitor in the lower right corner (except for nodes on the surface)

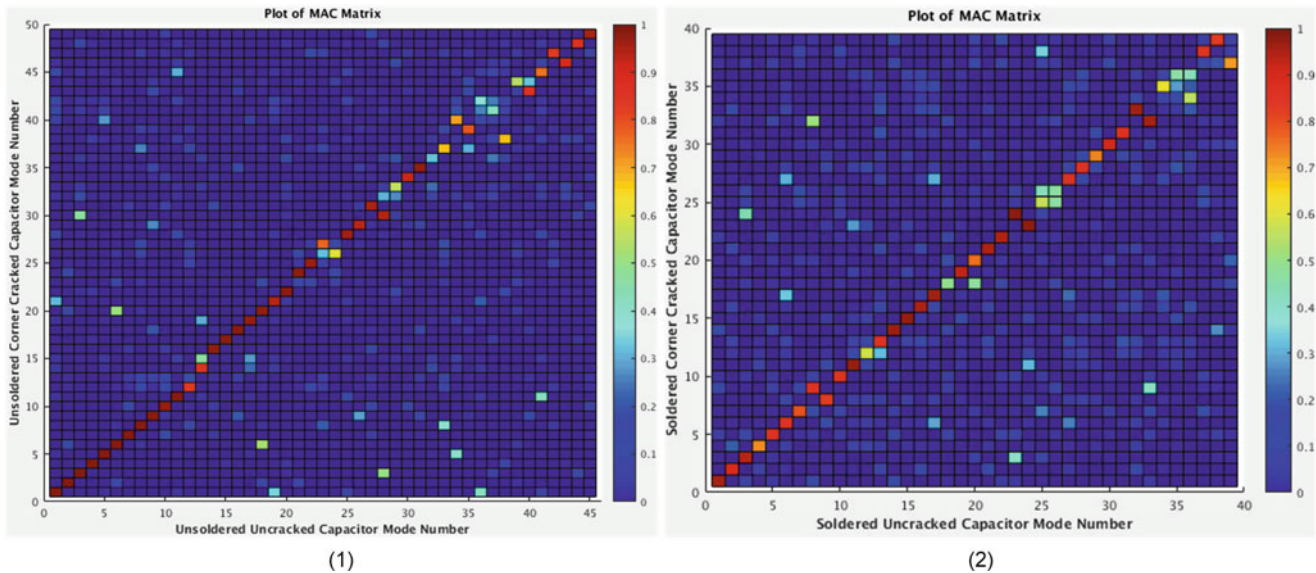


Fig. 9.10 MAC plots of (1) unsoldered and (2) soldered boundary conditions

Although Fig. 9.9 shows a clear local mode, some local modes are less obvious to discern visually. In order to confidently compare modes, the use of a Modal Assurance Criterion (MAC) plot was implemented. The plot compares the mode shapes (i.e., eigenvectors) of an uncracked capacitor on the x-axis to mode shapes of a cracked capacitor on the y-axis. Two modes that have a high correlation will be indicated with a dark red square, whereas blue squares indicate that there is a low correlation between the two modes. For the purposes of this study, a correlation of 0.8–1 was used to confidently compare modes for both the free and fixed boundary conditions. For the circuit board boundary conditions, the correlation cutoff was increased to 0.99 in order to eliminate higher-order modes that were mistakenly being compared with their lower-order counterparts.

Figure 9.10 shows two MAC plots of two different comparative cases. The first MAC plot shows a unsoldered (free-free) case comparing an uncracked and a corner cracked capacitor, and the second plot shows the same comparison but for a soldered case. Both plots show a strong linear correlation between modes of the comparative cases. A high correlation simply makes it easier to compare and record data between the modes. Using the MAC plots presented above, comparative modes were inspected to determine the shift in their natural frequencies before and after suffering from a fracture.

Table 9.3 Comparing the natural frequencies for the capacitor in free space, with and without cracks, for modes that have a MAC index of 0.8 or above

Uncracked mode number	Frequency (Hz)	Corner cracked mode number	Frequency (Hz)	% Difference between frequencies
1	3.44E + 05	1	3.43E + 05	0.079
2	4.56E + 05	2	4.55E + 05	0.115
3	5.73E + 05	3	5.73E + 05	0.078
4	6.45E + 05	4	6.45E + 05	0.052
5	6.69E + 05	5	6.67E + 05	0.219
6	6.69E + 05	6	6.68E + 05	0.103
7	7.03E + 05	7	7.02E + 05	0.104
8	7.40E + 05	8	7.38E + 05	0.277
9	7.82E + 05	9	7.81E + 05	0.166
10	8.17E + 05	10	8.16E + 05	0.232

Table 9.4 Comparing the natural frequencies for the fixed capacitor, with and without cracks, for modes that have a MAC index of 0.8 or above

Uncracked mode number	Frequency (Hz)	Corner cracked mode number	Frequency (Hz)	% Difference between frequencies
1	2.55E + 05	1	2.23E + 05	12.78
2	3.37E + 05	2	2.95E + 05	12.45
3	3.66E + 05	3	3.34E + 05	8.78
5	4.22E + 05	5	3.85E + 05	8.90
6	6.05E + 05	6	5.09E + 05	15.79
8	7.05E + 05	9	6.91E + 05	2.00
9	7.19E + 05	8	6.90E + 05	4.02
10	7.91E + 05	10	7.48E + 05	5.35
11	8.04E + 05	11	7.83E + 05	2.61
13	8.65E + 05	13	8.51E + 05	1.69

Table 9.5 Comparing the natural frequencies for the capacitor on the circuit board, with and without corner cracks, for modes that have a MAC index of 0.99 or above

Uncracked mode number	Frequency (Hz)	Corner cracked mode number	Frequency (Hz)	% Difference between frequencies
1	1.12E + 05	1	1.10E + 05	1.96
2	1.43E + 05	2	1.40E + 05	2.31
4	1.91E + 05	4	1.87E + 05	1.95
5	2.29E + 05	5	2.25E + 05	1.66
6	2.42E + 05	6	2.38E + 05	1.72
7	3.75E + 05	7	3.74E + 05	0.28
9	4.08E + 05	9	4.07E + 05	0.16
19	4.63E + 05	19	4.61E + 05	0.44
20	4.68E + 05	20	4.68E + 05	0.07
25	5.03E + 04	25	5.02E + 04	0.04

The MAC plots show a correlation between more than ten modes; however, the table above shows only the first ten comparable modes to show the general trend that all comparable modes for the free-free boundary condition did not seem to show any significant shifts in their natural frequencies. For the free-free boundary condition, the first six natural frequencies will correspond to the six rigid body modes and therefore are omitted from Table 9.3. Upon comparing all the natural frequency shifts for the different mode shapes, the largest shift found between the undamaged and damaged capacitors in free space was found to be 2 kHz, or 0.277%, in the 8th mode.

The second MAC plot gives the natural frequencies in Table 9.4 above for the uncracked versus corner cracked case with the fixed boundary condition applied. The fixed condition is much more interesting because it shows a greater shift in frequencies. The largest shift in frequency is almost 16% in mode 6 of each case, which results in a shift of 96 kHz.

The final boundary condition to be analyzed computationally was enforced by kinematically attaching the capacitor to a circuit board. In a fashion similar to Tables 9.3, 9.4, and 9.5 above describes the shifts in natural frequencies that were encountered for this boundary condition. Notably, the peak shift in the natural frequency corresponds to the mode shape that was encountered for the fixed boundary condition (mode 6). This is consistent with the response found for the fixed boundary

condition. As expected, the shift in the natural frequency is considerably less, given that the boundary condition is now much more compliant than the fully fixed boundary condition. An observation unique to this boundary condition was the need to increase the requirement on the modal assurance criterion from 0.8 to 0.99. This adjustment was required due to the much higher number of mode shapes, over 500, once the circuit board material was included. For brevity, the number of mode shapes present for this boundary condition is also why the MAC plot was not included for this case. Comparison of mode shapes using 0.8 as the cut off criterion was mistakenly including higher order modes (such as bending, torsion, breathing, etc.) to lower order ones (of the same type) and considering it to be a dramatic shift in natural frequency. However, upon further inspection, it became clear that the cutoff criterion needed to be significantly increased to eliminate these scenarios. Upon doing so, the list of comparable mode shapes was greatly reduced, and the first ten frequency comparisons are shown in Table 9.5, in which the peak shift in natural frequency was found to be 4.16 kHz, or 15.79%, in mode shape number 6.

9.4 Conclusions

In order to confidently detect a crack, a shift in natural frequency larger than roughly 2–5 kHz is required in order to be outside of the variation present in the manufacturing of the capacitors [4]. This frequency shift is roughly 0.01%, which shows that even a small variance in the natural frequencies can prove to be detectable. Therefore, any shifts found to be larger than that range can be indicative of the presence of a corner crack. The corner crack in the FE model was particularly sensitive to the soldered (fixed) boundary condition and circuit board boundary condition most likely because of the proximity of the crack to the edge of the capacitor where the boundary conditions were applied and changed.

Upon studying the shifts in natural frequencies that were obtained in both the soldered and unsoldered cases, much larger shifts are found in the soldered case. As an example, the largest shift found for the unsoldered corner crack case was 0.277% which is less than 2 kHz, at the 8th mode. By comparison, the largest frequency shift found for the soldered corner cracked case was 15.79% which was slightly less than 100 kHz, in the 6th mode. Furthermore, the shifts are not only more pronounced for the soldered corner crack case but are actually not feasibly detectable for the unsoldered corner crack case due to the range of detectable frequencies mentioned above [4].

One interesting observation is the peak shift in natural frequency was for the same mode shape for both the fixed and circuit board conditions. A depiction of the similar mode shape is given below in Fig. 9.11, with the circuit board boundary condition on the left and the fixed boundary condition on the right. This observation leads to an interesting conclusion in that the apparent stiffness of the boundary condition can help in exaggerating the shift in natural frequency a corner crack would have on a MLCC thus making it easier to detect.

The data presented herein indicate that corner cracks are a good candidate for detection through acoustic excitation methods. However, it would not be enough to simply excite them acoustically and measure their shifts in natural frequency.

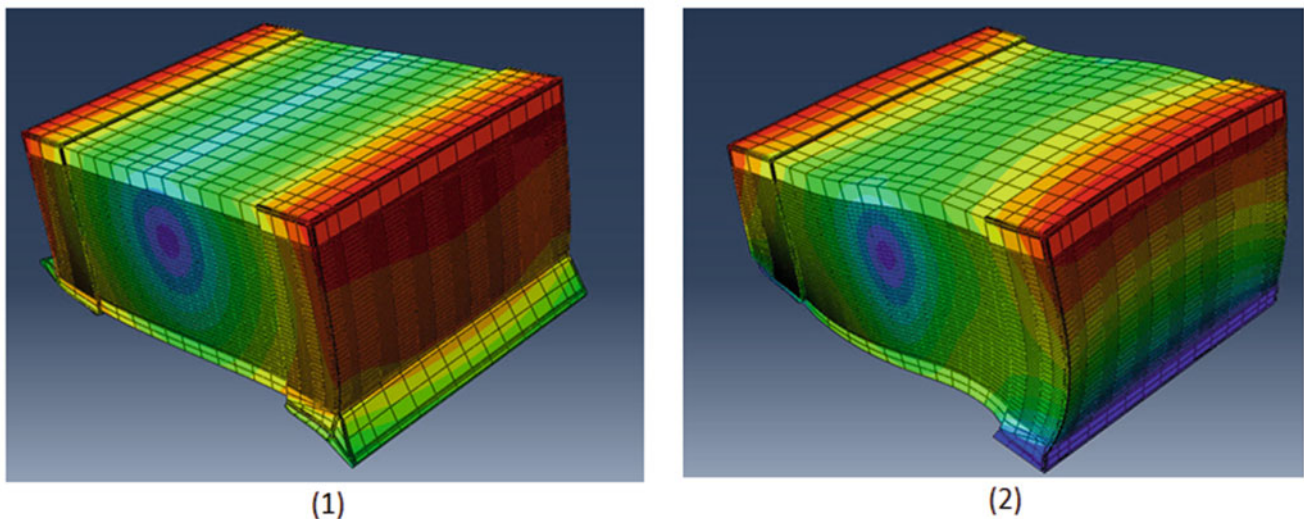


Fig. 9.11 Sixth mode shape for (1) circuit board boundary condition and (2) fixed boundary condition

Overall, boundary conditions may be used to exaggerate the effects that the corner crack had on the natural frequencies of the capacitor, thus making their presence easier to detect when compared to other performance metrics.

Acknowledgements The authors would like to thank Ward Johnson at the National Institute of Standards and Technology (NIST) for his support in many aspects of the work presented here. This research was conducted at the 2017 Nonlinear Mechanics and Dynamics (NOMAD) Research Institute supported by Sandia National Laboratories. Sandia National Laboratories is a multi-mission laboratory managed and operated by National Technology and Engineering Solutions of Sandia, LLC., a wholly owned subsidiary of Honeywell International, Inc., for the U.S. Department of Energy's National Nuclear Security Administration under contract DE-NA-0003525. SAND #: SAND2017-11498 C.

References

1. Peterson, K.L., et al.: Vibrational modes of multilayered ceramic capacitors. *Finite Elem. Anal. Des.* **116**, 1–11 (2016)
2. Johnson, W.L., et al.: Nonlinear resonant acoustic detection of cracks in multilayer ceramic capacitors. In: *Ultrasonics Symposium (IUS), 2014 IEEE International IEEE* (2014)
3. Keimasi, M., Azarian, M.H., Pecht, M.G.: Flex cracking of multilayer ceramic capacitors assembled with Pb-free and tin-lead solders. *IEEE Trans. Device Mater. Reliab.* **8**(1), 182–192 (2008)
4. Johnson, W.L., et al.: Resonant acoustic frequency shifts associated with cracks in multilayer ceramic capacitors. *IEEE Trans. Device Mater. Reliab.* **17**(2), 316–323 (2017)
5. Erdahl, D.S., Charles Ume, I.: Online-offline laser ultrasonic quality inspection tool for multilayer ceramic capacitors-part II. *IEEE Trans. Adv. Packag.* **28**(2), 264–272 (2005)
6. Andersson, C., et al.: Detection of cracks in multilayer ceramic capacitors by X-ray imaging. *Microelectron. Reliab.* **64**, 352–356 (2016)

Chapter 10

The Cross Spectrum in Multiple Input Multiple Response Vibration Testing

Norman F. Hunter, Kevin R. Cross, and Garrett Nelson

Abstract Random vibration tests have been conducted for over 5 decades using vibration machines which excite a test item in uniaxial motion. With the advent of multi shaker test systems, excitation in multiple axes and/or at multiple locations is feasible. For random vibration testing, both the auto spectrum of the individual controls and the cross spectrum, which defines the relationship between the controls, define the test environment. This is a striking contrast to uniaxial testing where only the control auto spectrum is defined.

In a vibration test the energy flow proceeds from drive excitation voltages to control acceleration auto and cross spectral densities and finally, to response auto and cross spectral densities. This paper examines these relationships, which are encoded in the frequency response function. Following the presentation of a complete system diagram, examination of the relationships between the excitation and control spectral density matrices is clarified. It is generally assumed that the control auto spectra are known from field measurements, but the control cross spectra may be unknown or uncertain. Given these constraints, control algorithms often prioritize replication of the field auto spectrum. The system dynamics determine the cross spectrum. The Nearly Independent Drive Algorithm, described herein, is one approach.

A further issue in Multi Input Multi Response testing is the link between cross spectrum at one set of locations and auto spectra at a second set of locations. The effect of excitation cross spectra on control auto spectra is one important case, encountered in every test. The effect of control cross spectra on response auto spectra is important since we may desire to adjust control cross spectra to achieve some desired response auto spectra. The relationships between cross spectra at one set of locations and auto spectra at another set of locations is examined with the goal of elucidating the advantages and limitations of using control cross spectra to define response auto spectra.

10.1 Introduction

Most environmental vibration tests are conducted using a single vibration machine which excites the test item in a single direction. Three sequential tests, one in each of the X, Y, and Z axes are considered sufficient to ensure that a test item will survive the relevant field vibration environment. Test requirements, derived from field vibration data, are used to derive the test specifications. In the context of random vibration these specifications are typically auto spectral densities. Auto spectral densities define the squared magnitude of the vibration level (usually accelerations) as a function of frequency. This methodology is mature, a product of refinement over the last 70 years. It has always been recognized that there are significant limitations to the “single axis” excitation approach. Field environments inherently excite a test body in multiple axes simultaneously and, in addition, field environments sometimes involve multiple, simultaneously active, vibration sources. Multiple degrees of freedom and the multiple source issues encouraged development of vibration systems using multiple actuators to simultaneously excite a test item. Methodologies developed over the past three decades have matured to the point where multiple excitation, multiple control point vibration tests are readily conducted [1–3]. These tests utilize either a “rigid body” fixture, like the Team Corporation “Tensor” systems [1], or a distributed set of vibration machines [4]. The rigid

Sandia National Laboratories is a multimission laboratory managed and operated by National Technology and Engineering Solutions of Sandia, LLC, a wholly owned subsidiary of Honeywell International, Inc., for the U.S. Department of Energy’s National Nuclear Security Administration under contract DE-NA0003525

N. F. Hunter (✉) · K. R. Cross · G. Nelson
Vibration/Acoustics Simulation, Sandia National Laboratories, Albuquerque, NM, USA
e-mail: nfhunte@sandia.gov

fixture approach seeks to excite the test item simultaneously in three to six degrees of freedom, while the distributed exciter approach seeks to meet the multiple vibration source requirement in addition to exciting the body in at least several degrees of freedom.

Random vibration test control requires the replication of a specified auto spectral densities at one or more points on the test body. These points are referred to as “control locations”. Random voltages applied to vibration exciters are acted on by the exciter, fixture, and system dynamics to produce the control auto spectra. For a single input, single control point test, the auto spectrum is all that is required.¹ Multiple Input-Multiple Response Tests have a set of auto spectra, each defining the magnitude profile of a response as a function of frequency at a specific location and/or degree of freedom. With multiple control auto spectra, the relationships between the control auto spectra, called cross spectra, are of vital importance. These relationships are defined by the relevant cross spectral densities. The result is a spectral density matrix, whose diagonal terms are auto spectra and whose cross terms are the cross spectra. The number of cross spectra terms grows rapidly with the number of control points. For two controls there is a single cross spectrum. For three control locations there are three cross spectra (1–2, 1–3, and 2–3). In general, for n control locations, there are $(n^2 - n)/2$ independent cross spectra.

When the voltage excitation signals are independent random processes, the control cross spectra are created by the system dynamics. The relevant dynamics includes the vibration machines, fixtures, and test item. By artificially relating the voltage excitation signals new, “artificial” dynamics are introduced, and these dynamics interact with the system dynamics to produce a modified test environment. Different excitation cross spectra can thus expose the test item to profoundly different environments.

At present, the typical single control axis vibration test is conducted using an auto spectrum composed of straight line segments on a log amplitude-log frequency scale. Multiple axis- multiple control location tests might be able to use this type of specification for the auto spectra, but it may not be practical for cross spectra specifications. The problem has been clearly elucidated by Daborn [4]. As we proceed through this paper some of the issues related to specification of cross spectra will be clarified.

The development of a reasonable laboratory replication of the field environment must deal with a set of issues, the primary ones including:

1. Test item boundary conditions usually differ between field and laboratory.
2. The measured field environment is known through a limited set of measurements and will differ between similar field events.
3. The field and laboratory test items exhibit different, though similar, dynamics.

All of these issues influence the environmental specification process and the definition of auto and cross spectral densities.

This document systematically examines issues related to the transfer of energy from independent excitations, to coupled excitations (drives), thence to control locations and ultimately to response locations. The objective is an understanding of the relationships between excitations, drives, controls, and responses. The drives interact with the drive to control frequency response function (FRF) to produce the control spectra. In a similar manner, the control spectra react with the control to response FRF to produce the response spectra. Moving from the domain of spectra to that of spectral density, the interactions between controls are defined by the control cross spectral densities. In the same manner, the interactions between responses are described by response cross spectral densities.

Section 10.2 examines how independent or coupled drives interact with the Frequency Response Function to produce the control spectra and the control spectral density. A central issue here is the relationships between the excitations and the frequency response function. Together these generate the control spectra and the control spectral density matrix.

There are no inherent mathematical constraints on the auto spectral density. At each frequency and each control location the ASD is simply a real number. The situation is different with the cross spectral densities. In the first place, the magnitudes of the cross spectral terms are bounded by the relevant auto spectra. Further (as if this wasn't already enough), all physically realizable spectral density matrices are positive definite. This positive definite character is examined in Sect. 10.3.

Specifying the cross spectra for a laboratory vibration test is a significant issue. Cross spectral magnitudes and phases quantify the relative motions between control locations. When the excitation platform is a rigid body like the Team Tensor Table [1], the magnitudes and phases of the cross spectrum couple motions in each degree of freedom. For example, motion in the x direction could be independent of, or correlated with, motion in y. The dynamics of the rigid table does not “favor” one cross spectral configuration over another. The situation is quite different when motions of a dynamically active test item are considered. In the field the test item moves in a pattern defined by the interactions of the field excitation, the boundary

¹Random vibration tests are conducted using vibration with a Gaussian Probability Density. These signals are readily generated given a required auto spectral density.

conditions, and the linear and nonlinear dynamics of the complete assembly. Points on the test body move in unison, with phase and magnitude relationships defined by the dynamics, at system modal frequencies. Reproducing this motion in the laboratory, requires that the dynamics of the laboratory test body play a significant role in the definition of the cross spectrum.

In a manner, analogous to the excitation-control relationship, the controls react with the system FRF to produce the response spectra and the corresponding response auto and cross spectra. Like the excitation to control situation, the control to response relationship involves both the coupling between the controls (control cross spectra) and the coupling encoded in the FRF.

The above relationships, while mathematically reasonably straightforward, can be confusing. Herein the following issues are examined:

1. The equations relating excitation spectra to the control spectral density matrix and then, the equations relating control to response spectral densities.
2. To be physically realizable, a spectral density matrix must be positive definite.
3. Implications of strongly coupled controls (high cross spectral relationships).
4. The Nearly Independent Drive Algorithm.
5. When Independent Drives Fail.

10.2 Spectra, Spectral Density, and Frequency Response for MIMO Systems

Consider the multiple-excitation multiple response system depicted in Fig. 10.1. N vibration machines excite a test item and associated fixture. The response is controlled at M locations on the item.

Figure 10.1 illustrates the complete path from excitation spectra to response spectral densities. N drive voltages, each representing a band limited random process, excite the system. The corresponding time domain voltages are $x_i(t)$ and the Fourier Spectra are $X_i(t)$. Input excitations are coupled through a coupling matrix C and these coupled drives CX are applied to the power amplifier driving the vibration machines. For a linear system, the frequency response function H_{mn} maps the

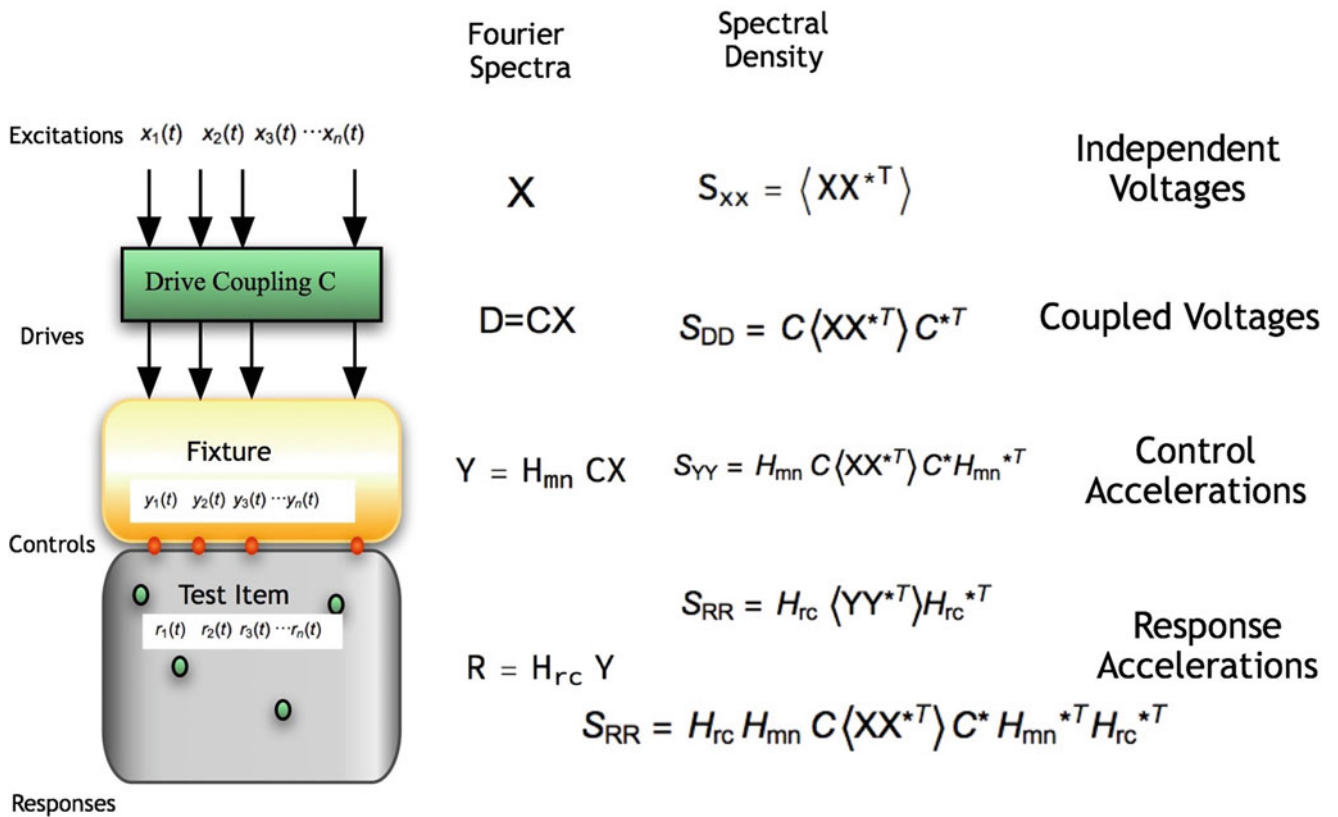


Fig. 10.1 A General multiple input multiple response system illustrating the path from excitations X to responses R

frequency domain drive voltages to the frequency domain control accelerations $Y(f)$. The frequency response function H_{rc} maps the control accelerations $Y(f)$ to the Response Accelerations $R(f)$. The equations are shown, in both the spectral and spectral density domains, in Fig. 10.1. The vector of excitation spectra is:

$$X = \{X_1, X_2, \dots, X_N\} \quad (10.1)$$

Using Expected Values, the corresponding Diagonal Excitation Spectral Density Matrix is:

$$S_{xx} = \langle X^H X \rangle \quad (10.2)$$

where $\langle X \rangle$ indicates expected values and the X^H is the conjugate transpose (Hermitian).

The coupling matrix C allows linear combinations of the drives to be used as excitations.

$$C = \begin{bmatrix} c_{11} & 0 & 0 & 0 \\ c_{12} & c_{22} & 0 & 0 \\ \vdots & \vdots & \ddots & \vdots \\ c_{n1} & c_{n2} & \cdots & c_{nm} \end{bmatrix} \quad (10.3)$$

The frequency response or transfer function matrices couple the drives CX to the controls Y .

$$Y = H_{mn}CX \quad (10.4)$$

Or, in the format of spectral densities

$$S_{yy} = H_{mn}CS_{xx}C^H H_{mn}^H \quad (10.5)$$

In a similar manner, the controls are coupled to the responses.

$$S_{rr} = H_{rc}S_{yy}H_{rc}^H \quad (10.6)$$

Equations (10.1, 10.2, 10.3, 10.4, 10.5, and 10.6) define the spectral and spectral density relationships linking excitations, drives, controls, and responses. In a typical test, at least the diagonal of the control spectra, i.e., the auto spectra at the control locations, is defined based on field data. The control cross spectra may or may not be defined from field data.

10.3 Properties of the Spectral Density Matrix

Spectral density matrices are formed from the expected value of a vector or matrix product of the form:

$$S_{rr} = \langle A^H A \rangle \quad (10.7)$$

This matrix product has several important properties. First, S_{rr} is symmetric. Second, S_{rr} is positive definite. For a positive definite matrix A the product:

$$X^H A X \geq 0 \quad (10.8)$$

For any vector X . If, for some X the equality is true, the matrix A is positive semi-definite. Properties of positive definite matrices include:

1. All eigenvalues of a positive definite matrix are positive.
2. All pivots of a positive definite matrix are positive.
3. All leading minors of a positive definite matrix are positive.

4. If $\mathbf{A} \in n \times n$ is positive definite and $\mathbf{X} \in n \times k$ has rank k then $\mathbf{X}^H \mathbf{A} \mathbf{X}$ is also positive definite.
5. For symmetric positive definite matrices, like the spectral density matrix, the eigenvectors are orthogonal, and the eigenvalues are real.

The diagonal terms of $\mathbf{A}^H \mathbf{A}$ are the squared magnitudes of the corresponding rows (or terms, if \mathbf{A} is a vector) of \mathbf{A} . The off diagonal terms quantify the degree to which one row (or term) of \mathbf{A} resembles another. The cross, or off diagonal terms, as dot products have magnitudes bounded by:

$$a_{ij} = \sqrt{|a_{ii}| |a_{jj}|} \quad (10.9)$$

In the spectral density context, \mathbf{A} is a complex matrix, and each off diagonal term has a real and imaginary part or, equivalently, a magnitude and phase. The off diagonal terms of \mathbf{A} are of the form:

$$a_{ij} = e^{i\theta_{ij}} \sqrt{\gamma^2 |a_{ii}| |a_{jj}|} \quad (10.10)$$

where γ^2 is the ordinary “coherence” between row i and row j and its maximum value is unity. θ_{ij} is the angle between the complex quantities in rows i and j .

If the candidate control spectral density matrix \mathbf{S}_{yy} is created from some compilation of measured field vibration data, there is no a priori assurance that the construction is positive definite. Of course, if the field measurement itself is either a set of Fourier spectra or a spectral density matrix then the requirement is satisfied. But field data are often noisy, modified, or enveloped. In these cases, it is easy to violate the positive definite requirement.

Given a non-positive definite symmetric candidate matrix a “hopefully nearby” positive definite matrix can be constructed by first performing an eigenvalue decomposition, setting the negative (hopefully only one small) eigenvalue to a small positive number, and reconstructing the matrix. The new matrix is positive definite by construction and is in some sense the “closest” positive definite matrix to the candidate. Other approaches are also possible, Smallwood [5] recommends decreasing the coherence in the cross terms by a few percent until the result gives a positive definite matrix.

10.4 General Approaches to Specification of Cross Spectral Density

As noted above, the proposed Control Spectral Density Matrix must be symmetric, positive definite, with off diagonal terms whose magnitudes are bounded by Eq. (10.10). Ideally, the CSD (control spectral density) matrix could be entirely derived from field data, but there are significant issues.

Field data are often limited to estimated auto spectra at a set of predetermined measurement locations. Relative phase between locations may or may not be available. For single input tests the auto spectral control (perhaps with limiting) is specified for nearly all random vibration tests. It is natural to extend this procedure to MIMO tests by specifying the auto spectrum at $3 \leq n \leq 6$ control locations. If good field measurements of cross spectra are available this argument can be extended to specification of the cross spectra, but there are deeper issues which can make this difficult to implement in practice. Typically, auto spectra are specified as a suite of straight line values on a log-log plot. These straight lines in some sense “envelope” the field data and also, optimistically, attempt to allow some leeway to account for different dynamics of the field and laboratory test systems. The combined effects of this enveloping and a probable difference between laboratory and field boundary conditions forces the laboratory control force to unrealistic levels at test item resonant frequencies because the vibration machine, unlike most field structures, is capable of imparting very high force levels even when the mechanical impedance of the test item is low. To mitigate this issue, response auto spectra are limited at various judiciously selected locations.

Extending vibration testing to multiple degrees of freedom exacerbates this problem. There are significant differences in the dynamics of nominally identical test items, and the test items are subjected to very different boundary conditions in the field and laboratory. Additionally, of course, nothing in the field produces straight line spectra. Both Daborn [4] and Smallwood [5], have addressed this issue, albeit from somewhat different viewpoints.

There is no universal way of addressing these issues. Their resolution depends on details of the specific system. However, there are some viable general approaches. These include:

1. Control the auto spectra at designated control locations and let the system dynamics determine the cross spectra. The Nearly Independent Drive Algorithm, described in more detail below, is one embodiment of this approach.
2. Control the auto spectra at designated control locations and adjust the cross spectra for minimum excitation voltages. This is Smallwood's minimum drive algorithm [5]. In practice, minimum drive and nearly independent drives achieve similar results.
3. Control both auto and cross spectra to measured field levels. This is best achieved in situations where motion, at the control locations, in each degree of freedom, are nearly independent, and implies low cross spectral coherence. This is approximately true for some component configurations. Daborn [4] describes successful application of this technique in some example cases.
4. Control auto spectra and cross spectra coherence (no phase control) to field levels. In this framework, the control system works to achieve the desired coherence between controls and allows the phase to be determined by the natural system dynamics. This has been achieved recently with some success, although not all control systems have this capability.
5. Force all control cross spectra to be near zero.
6. Don't control cross spectra directly, rather, specify, for say, n drives, auto spectral control at more than n control locations. The cross spectra "adapt" to produce the specified auto spectra. Daborn [4] also describes an application of this approach. Since auto spectra are often known at a fair suite of field locations and auto spectral control avoids the rather messy difficulty of specifying cross spectral phase, this is an attractive approach, though it is somewhat limited as noted below.

The Nearly Independent Drive Algorithm and the effect of cross spectra on response auto spectra are now examined in more detail.

10.5 The Nearly Independent Drive Algorithm

Consider a MIMO system described by $Y = HX$. The auto spectral terms in S_{yy} are specified, but not the cross spectra. Excite the system with independent drives. The response auto spectrum is the sum of the contributions from each of the independent drives conditioned by the appropriate term in H .

$$\begin{aligned} S_{yyd} &= H_d H_d^H S_{xxd} \\ S_{xxd} &= (H_d H_d^H)^{-1} S_{yyd} \end{aligned} \quad (10.11)$$

Where the d subscript indicates that we are dealing only with the diagonal terms. Using Eq. (10.11), solve for S_{xxd} . If all of the S_{xxd} are positive, then the independent drive magnitudes are simply the square root of the respective diagonal auto spectra in S_{xxd} . However, some S_{xxd} terms may be negative. This means that the requested auto spectra S_{yyd} cannot be achieved with independent drives. In essence too much interaction between drives is encoded in H for fully independent drives to work. Set the drive corresponding to negative auto spectrum to zero and compute a new trial S_{yy0} from

$$\begin{aligned} Y_0 &= HX_{d0} \\ S_{yy0} &= Y_0 Y_0^H \end{aligned} \quad (10.12)$$

Where X_{d0} are the independent drives corresponding to S_{xxd} with the negative drive values set to zero. Some of the diagonal values in S_{yy0} will be too large. Scale these values using a diagonal matrix of real valued scaling constants S_c

$$S_c = \sqrt{\frac{S_{yy0}}{S_{yyd}}} \quad (10.13)$$

Such that

$$\hat{Y} = S_c Y_0 \quad (10.14)$$

The new response spectral density

$$\begin{aligned} S_{yyc} &= \hat{Y} S_c^2 \hat{Y}^H \\ X_d &= H^{-1} S_c \hat{Y} \end{aligned} \quad (10.15)$$

has the desired auto spectral values in S_{yy} and the drives X_d are coupled. Either the inverse of \mathbf{H} or the pseudo inverse are used in Eq. (10.15) as appropriate. This process from Eqs. (10.11, 10.12, 10.13, 10.14, and 10.15) couples the drives “just enough” to achieve the desired S_{yyd} .

10.6 An Example of Nearly Independent Drives in a 3 × 3 System

Consider a three by three system described by the transfer function matrix in Eq. (10.16).

$$\mathbf{H} = \begin{bmatrix} e^{i\theta_{11}} h_{11} & e^{i\theta_{12}} h_{12} & e^{i\theta_{13}} h_{13} \\ e^{i\theta_{21}} h_{21} & e^{i\theta_{22}} h_{22} & e^{i\theta_{23}} h_{23} \\ e^{i\theta_{31}} h_{31} & e^{i\theta_{32}} h_{32} & e^{i\theta_{33}} h_{33} \end{bmatrix} \tag{10.16}$$

Now, if the cross terms $h_{ij} \forall i \neq j$ are small relative to the diagonal terms then fully independent drives work. Consider the case in which a single cross term, say h_{32} , is significant. The revised \mathbf{H} matrix is:

$$\mathbf{H} = \begin{bmatrix} e^{i\theta_{11}} h_{11} & 0 & 0 \\ 0 & e^{i\theta_{22}} h_{22} & 0 \\ 0 & e^{i\theta_{32}} h_{32} & e^{i\theta_{33}} h_{33} \end{bmatrix} \tag{10.17}$$

Application of the nearly independent drive algorithm yields drives:

$$\mathbf{X}_d = \begin{bmatrix} \frac{\sqrt{S_{yy1}}}{h_{11}} \\ \frac{\sqrt{S_{yy2}}}{h_{22}} \\ -\frac{e^{i\theta_{32}-i\theta_{33}} h_{32} \sqrt{S_{yy2}}}{h_{22} h_{33}} + \frac{e^{i\theta_{32}-i\theta_{33}} \sqrt{S_{yy3}}}{h_{33}} \end{bmatrix} \tag{10.18}$$

Drives one and two, X_{d1} and X_{d2} , are independent. Drive three, X_{d3} , is coupled to drive two through the last term, in red, in Eq. (10.18). The situation is depicted graphically in Fig. 10.2.

The coupling term, shown by the orange arrow, means that drive two induces more response at control location three than $\sqrt{S_{yy3}}$. To alleviate this coupling, drive three is modified by the circled term, which effectively cancels the coupling from drive two. The drive and response spectral densities are:

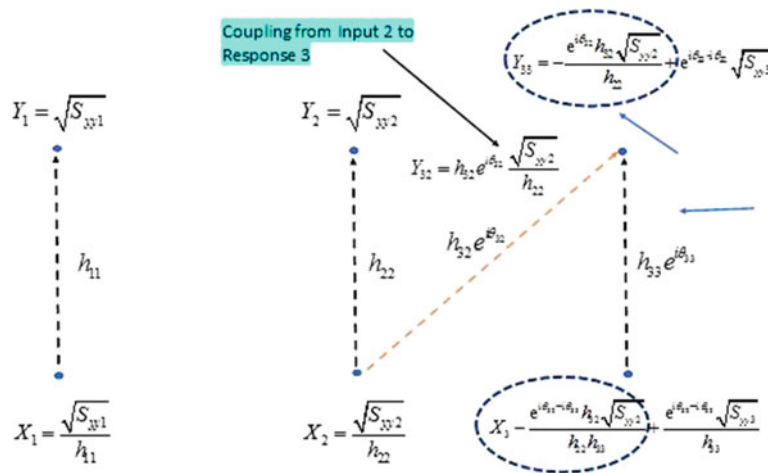


Fig. 10.2 Coupled drives compensate for system dynamics

$$\mathbf{S}_{xx} = \begin{bmatrix} \frac{S_{yy1}}{h_{11}^2} & \frac{\sqrt{S_{yy1}}\sqrt{S_{yy2}}}{h_{11}h_{22}} & -\frac{e^{-i(\theta_{32}-\theta_{33})}\sqrt{S_{yy1}}(h_{32}\sqrt{S_{yy2}}-h_{22}\sqrt{S_{yy3}})}{h_{11}h_{22}h_{33}} \\ \frac{\sqrt{S_{yy1}}\sqrt{S_{yy2}}}{h_{11}h_{22}} & \frac{S_{yy2}}{h_{22}^2} & \frac{e^{-i(\theta_{32}-\theta_{33})}\sqrt{S_{yy2}}(h_{32}\sqrt{S_{yy2}}-h_{22}\sqrt{S_{yy3}})}{h_{22}^2h_{33}} \\ -\frac{e^{i(\theta_{32}-\theta_{33})}\sqrt{S_{yy1}}(h_{32}\sqrt{S_{yy2}}-h_{22}\sqrt{S_{yy3}})}{h_{11}h_{22}h_{33}} & -\frac{e^{i(\theta_{32}-\theta_{33})}\sqrt{S_{yy2}}(h_{32}\sqrt{S_{yy2}}-h_{22}\sqrt{S_{yy3}})}{h_{22}^2h_{33}} & \frac{(h_{32}\sqrt{S_{yy2}}+h_{22}\sqrt{S_{yy3}})^2}{h_{22}^2h_{33}^2} \end{bmatrix} \quad (10.19)$$

And

$$\mathbf{S}_{yy} = \begin{bmatrix} S_{yy1} & e^{i(\theta_{11}-\theta_{22})}\sqrt{S_{yy1}}\sqrt{S_{yy2}} & e^{i(\theta_{11}-\theta_{32})}\sqrt{S_{yy1}}\sqrt{S_{yy3}} \\ e^{-i(\theta_{11}-\theta_{22})}\sqrt{S_{yy1}}\sqrt{S_{yy2}} & S_{yy2} & e^{i(\theta_{22}-\theta_{32})}\sqrt{S_{yy2}}\sqrt{S_{yy3}} \\ e^{-i(\theta_{11}-\theta_{32})}\sqrt{S_{yy1}}\sqrt{S_{yy3}} & e^{-i(\theta_{22}-\theta_{32})}\sqrt{S_{yy2}}\sqrt{S_{yy3}} & S_{yy3} \end{bmatrix} \quad (10.20)$$

In Eq. (10.20) the diagonal (auto spectral) terms are just as desired. Now the cross spectral terms are nonzero, and, in fact, have unity coherence.

There is a fundamental relationship here. The magnitudes of the diagonal terms of \mathbf{S}_{yy} are defined by the requested control auto spectral values. The cross spectral terms, have magnitudes defined by the various combinations of auto spectra and phases defined by the dynamics in \mathbf{H} . The drives are no longer independent, and their coupling is defined by the dynamics.

Note the “phase sensitive” character of the excitation via the term $e^{i(\theta_{32}-\theta_{33})}$. Phase sensitive excitations are not typical in single axis random vibration tests though they are present in single axis transient waveform control. The phase sensitive excitation here implies that, for Multiple Input Multiple Output systems the effect of nonlinearity on control is likely to be more strident than in the single axis case because nonlinear behavior can easily contaminate the precise, rapidly changing phase relationships generated by linear resonances.

When is coupling between off diagonal drives and responses likely? The most significant coupling occurs at modal frequencies. At modes, the various control locations are coupled through the dynamics of the structure, which includes the test item, fixture, and vibration machines. Of course, at low frequencies, for some configurations, rigid body motions could also induce coupling. For a relatively small test item affixed to a large rigid table, as may often be the case with the Team Tensor, coupling between drives at the table-test item interface is unlikely. If the table is the control location, then independent drives should work well. The situation is quite different for a test item in a nearly free-free configuration excited by smaller vibration machines. In this case, structural modes can strongly couple motions at control locations.

10.7 Controlling Response Auto Spectra Using Cross Spectra Between Control Locations

With specified control auto spectral densities, the control cross spectra can be adjusted to effect the response auto spectral densities. To some degree this relationship can allow control of response auto spectra by modifying control cross spectra because the relative phases between the controls have a sometimes dramatic effect on response spectra and spectral density.

There are numerous possibilities. Consider three cases:

1. The independent drive algorithm is utilized. Via the algorithm control auto and cross spectral densities are defined so response spectral density is determined by the FRF from control to response, \mathbf{H}_{rc} .
2. Based on field measurements, auto and cross spectra are controlled. Again, the response spectral density is determined by \mathbf{H}_{rc} .
3. Control Auto spectra are specified. Control cross spectra are adjusted so that a combination of the control cross spectral densities and \mathbf{H}_{rc} determine response auto spectra.

Here we are interested in case 3. It is quite likely, given field measurement considerations, that auto spectra at control points are known along with auto spectra at some response points. Cross spectra are not available. It is desirable to adjust the control cross spectral densities to approximate the response auto spectra.

The dynamics of the test body interact with the control auto and cross spectra. Consequently, cross spectra adjustment produces a range of auto spectral responses. Not all response auto spectra are achievable. Even what seem to be “reasonable” values may not be achievable. An equally serious issue, noted in Sect. 10.1, is the differing, albeit similar, dynamics of field and laboratory test items. The equations relating control and response spectra and spectral density are:

$$\begin{aligned} \mathbf{Y}_r &= \mathbf{H}_{rc} \mathbf{X}_c \\ \mathbf{S}_{rr} &= \mathbf{H}_{rc}^H \mathbf{S}_{cc} \mathbf{H}_{rc} \end{aligned} \quad (10.21)$$

We can imagine diverse situations. If we are driving a small component excited by the Team Tensor System where a large mass is excited by 12 vibration machines, we are exciting the test system with rigid body motion in six degrees of freedom. \mathbf{H}_{rc} then describes how the test body responds to motions in these various degrees of freedom. For example, $\mathbf{H}_{rc}(1, 2)$ could describe the relationship between the Y response at a given point on the test item to an excitation in X . When the test item is a rigid body, as it is at low frequency, motion in Y is independent of motion in X so no adjustment of phase between X and Y is going to change the test item response in X or Y . At very high frequencies test item response is likely decoupled from control in either X or Y so again the phase between X and Y control is moot. In the intermediate frequency range, the test body dynamics often “couples” motion between different degrees of freedom. The coupling between degrees of freedom is responsible for the “cross motion” in single axis vibration tests.

Note that the case for rotations is somewhat different. Rotations about the origin do not couple to translations. However, if the rotational accelerations are large and the test item is sizeable, rotation does induce linear motion. So, rotation about the Z axis, for example, will produce a gradient in the X accelerations. This may be significant and does induce coupling between translational and rotational degrees of freedom. It is also worth noting that the space of rotations and translations of a rigid body is a non-Euclidian 6 manifold.

The linear acceleration gradient induced by rotations and the test item dynamics are the major avenues driving the off diagonal terms in \mathbf{H}_{rc} . When the control in one degree of freedom is related to the control in another degree of freedom the off diagonal terms and the corresponding dynamics play a role in determining auto spectral response. Otherwise, they do not. This tells us that we cannot just casually set some straight-line response auto spectral density and expect to achieve it through adjustment of the control cross spectra. Unless there are relevant dynamics, the coupling is just too small to make this achievable. In a different venue, the “Controllability” between the control cross spectrum and the response auto spectrum is just not significant. Conversely, at frequencies where the test item dynamics couple degrees of freedom, the cross spectra can have dramatic effects on the auto spectral response.

The general form of the auto spectral response due to a single cross spectral term is of the form shown in Eq. (10.22), where a simplified case of interaction between two controls y_1 and y_2 is considered.

$$S_{rr1} = h_{11}^2 y_1^2 + h_{12}^2 y_1^2 \alpha^2 + 2h_{11}h_{12}y_1^2 \alpha \cos[\gamma_2 - \theta_{11} + \theta_{12}] \quad (10.22)$$

S_{rr1} = auto spectrum at response location 1

$h_{11}^2 y_1^2$ = auto spectrum at response location 1 induced by drive 1

$h_{12}^2 y_1^2 \alpha^2$ = auto spectrum at response location 1 induced by drive 2

$2h_{11}h_{12}y_1^2 \alpha \cos[\gamma_2 - \theta_{11} + \theta_{12}]$ = auto spectrum at response location 1 achieved thru adjustment of the phase γ_2 between drives 1 and 2

Consider each of the terms in Eq. (10.22). $h_{11}^2 y_1^2$ is the response due to drive 1. $h_{12}^2 y_1^2 \alpha^2$ is the response from drive 2. The phase sensitive interaction between the drives is $2h_{11}h_{12}y_1^2 \alpha \cos[\gamma_2 - \theta_{11} + \theta_{12}]$. The control auto spectral terms are fixed by the specified control levels. The system dynamics fixes h_{11} and h_{12} . The magnitude of the cross spectral term, α is adjustable as is the phase of the cross term γ_2 . The effect of the cross spectral phase is dependent on the product of h_{11} and h_{12} . Both terms must have significant magnitude for the cross spectral phase to affect the response auto spectrum. Consider three bounding cases:

1. h_{11} is large, h_{12} small. In this case the cross spectral phase has minimal effect and the response is a function of $y_{11}h_{11}$.
2. h_{12} is large, h_{11} small. The cross spectral phase has minimal effect and the response is a function of $\alpha h_{12}y_1$.
3. h_{11} and h_{12} have similar magnitudes. This case is illustrated in Fig. 10.3 for $\alpha = 1$. The effect of phase is substantial, especially if both h_{11} and h_{12} are large.

Figure 10.3 illustrates the induced auto spectrum as a function of the magnitudes of h_{11} and h_{12} with $\alpha = 1$.

In Fig. 10.3 the response auto spectrum in the vertical axis is plotted as a function of the FRF terms h_{11} and h_{12} .

Along the h_{11} axis, coming out of the page, h_{12} is small and the cross spectrum has no effect on the response auto spectrum. Conversely, along the h_{12} axis, h_{11} is small, and again the cross spectrum has no effect. Only when both h_{11} and h_{12} are large does the cross spectrum have a strong effect. This effect is evident along the 45 degree line where h_{12} is equal to h_{11} . Of course the effect of cross spectral adjustment is very system dependent. An example of the range of response auto spectral values achievable for a system composed of six interconnected masses with two excitations is illustrated in Fig. 10.4.

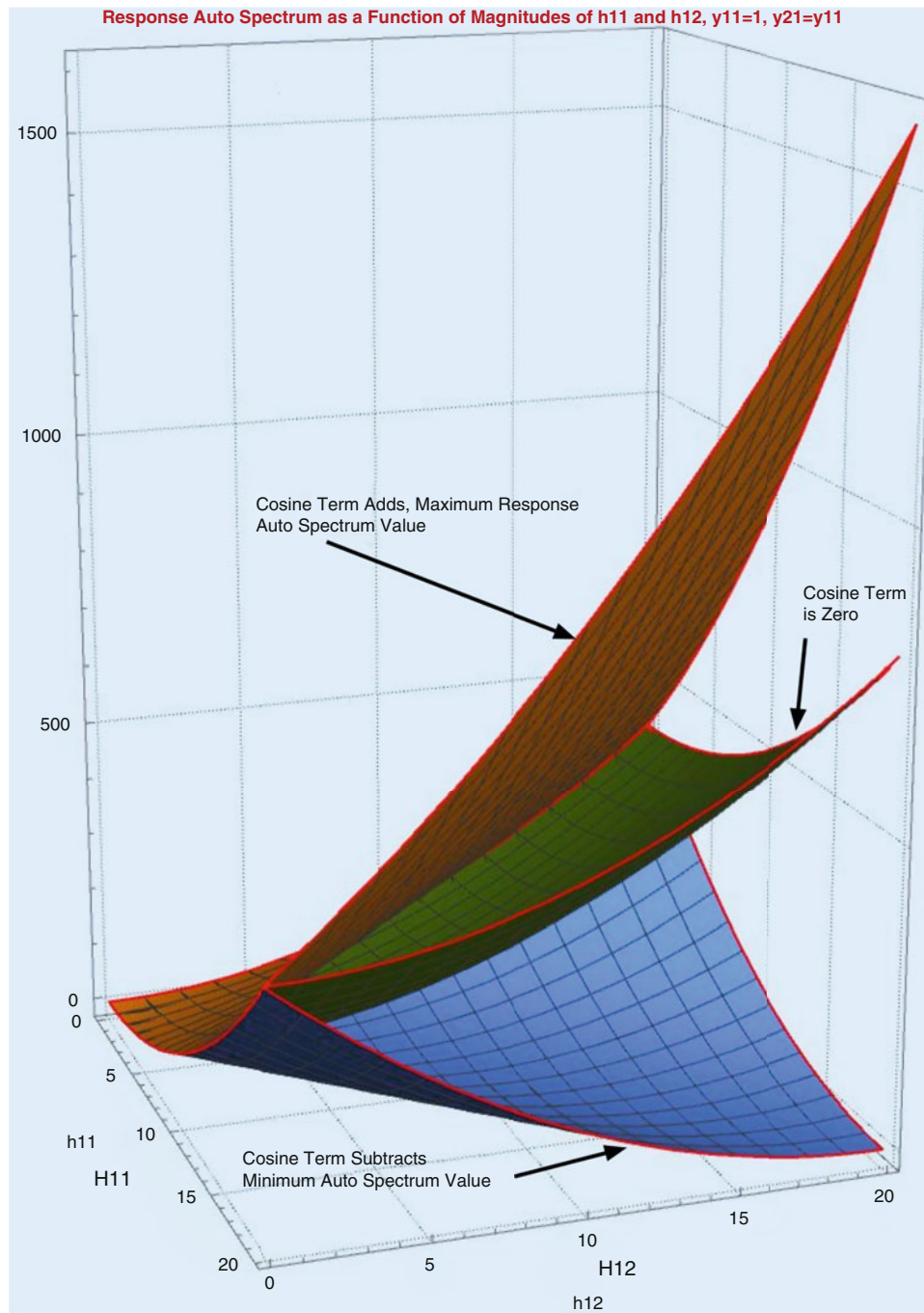


Fig. 10.3 Induced response auto spectrum as a function of H magnitudes

From Fig. 10.4 it is evident that in some frequency ranges (below 50 Hz and above 1000 Hz.) the cross spectra has negligible effect. However, in the range of active dynamics between 100 Hz. and 600 Hz. the cross spectrum can have dramatic effect.

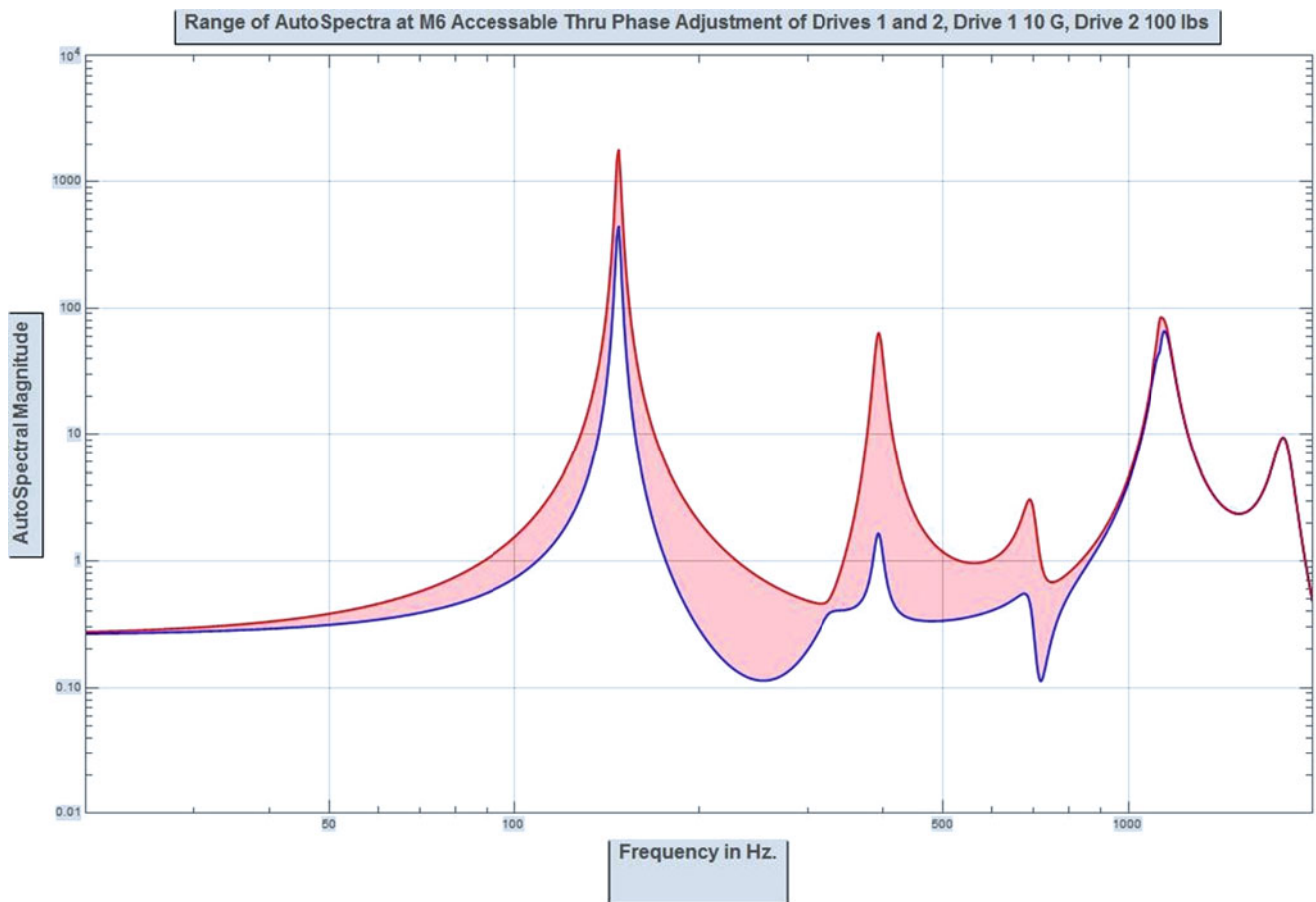


Fig. 10.4 Range of response auto spectra achieved by adjusting cross spectra for a six mass, two excitation system

10.8 Conclusions

MIMO testing adds a degree of complexity and of versatility far exceeding that of single axis vibration testing. The major contrasts between, on the one hand, field and laboratory dynamics, and on the other, field and laboratory boundary conditions, are more critical in MIMO tests. No single approach is going to suffice for realistic replication of multiple degree of freedom field environments. In general, several cases can be considered.

First, a smaller component (perhaps up to several feet on a side), can readily be tested in multiple degrees of freedom using a massive vibration table such as the Team Tensor. With this type of system, the excitation in each of the translational and rotational degrees of freedom are mostly independent, at least in regards to vibration about the control axes. The standard procedure of testing with independent control spectra in each degree of freedom is reasonable and practical. Measured field data can serve as a guide to input specifications. Independent drives and controls should be possible over most of the frequency range. Note that the system geometry means that various linear combinations of the vibration drives are independent, not the individual shaker excitations.

There is a tendency to approximate a set of measured response field auto spectra at numerous locations using the 6DOF tensor as excitation. See, for example, Jacobs et al. [6]. This can work well when, as in Jacobs [6], the inverse of the laboratory transfer function is used to derive the input in each degree of freedom. This approach is most effective for a component where the excitation is reasonably approximated by base rigid body motion in the relevant degrees of freedom.

System tests are another matter. In a system test, there may be several physically separated excitation sources and each source may operate in several degrees of freedom. Attempting to simulate this environment with a single base excited system in the laboratory is a pretty gross approximation, even when the base excitation has multiple degrees of freedom. In this case excitation from several sources is warranted. Daborn [3], has also shown excellent results with multiple, physically separated excitation sources.

The most striking issue, and one which demands further investigation, is the reconciliation of the different, but related, dynamics evidenced by field and laboratory test bodies. Use of straight line spectra to approximate field inputs, as is typical for single axis testing is a very questionable approach. A new approach, one which considers the dynamics of the specific test item, is needed.

The effects of coupling between drives or controls is through the FRF matrix H . This sort of coupling is not evident in single axis tests. Significant coupling between degrees of freedom requires adjustment of the excitations to reduce the response, especially at resonances, by putting in energy that cancels some of the resonant response. The nearly independent drive algorithm described shows just how this operates.

Adjustment of the cross spectra is often proposed as a method of producing response auto spectra within a desired range. This is indeed possible, but the bounds are strongly influenced by the dynamics of the test item. Enhancing or damping existing system resonances is quite possible and reasonable, but arbitrary formulation of response auto spectra is not achievable.

References

1. Hoksbergen, J.: Team corporation, bringing broadband 6-DOF field vibration environments into the lab- Tensor 18kN vibration test system, 83 shock and vibration symposium, New Orleans, La. (2012)
2. Smallwood, D.O.: Multiple shaker random control with cross-coupling. Proceedings of the Institute of Environmental Sciences, pp. 341–347 (1978)
3. Underwood, M.A.: Multi-exciter testing applications: theory and practice. Proceedings of the Institute of Environmental Sciences and Technology, pp. 1–10 (2002)
4. Daborn, P.M., Ind, P.R., Ewins, D.J.: Enhanced ground-based vibration testing for aerodynamic environments. Mech. Syst. Signal Process. **49**, 165–180 (2014)
5. Smallwood, D.O.: A proposed method to generate a spectral density matrix for multiple input, multiple output (MIMO) vibration test. Shock. Vib. **14**(2), 107–132 (2007)
6. Jacobs, L., Ross, M., Tipton, G., Nelson, G., Cross, K., Hunter, N., Harvie, J.: 6DOF Shaker Test Input Derivation from Field Test. IMAC, Orlando, Florida (2016)

Norman F. Hunter Jr. Sandia Labs Affiliate, 2010-present. Consultant, 2003-2010., Engineer at Los Alamos National Labs, 1979-2003, Engineer at Sandia Labs, 1964-1975. B.S. Electrical Engineering 1964, Mississippi State University, M.S. Electrical Engineering 1966, University of New Mexico. His current work is in signal processing and Multi Input Multi Response Vibration Testing.

Kevin R. Cross Mechanical Engineer R&D S&E, Sandia National Labs 2011-Present. R&D Engineer at Remington Arms, 2007-2011. M.S. Mechanical Engineering 2007 & B.S. Mechanical Engineering 2005, Clarkson University, A.S. Engineering Science 2003, Hudson Valley Community College. His current work is in vibration testing, vibration test technique development, and Multiple Input Multiple Response Vibration Testing.

Garrett Nelson received his PhD in Mechanical Engineering and MS in Aerospace Engineering in October 2015 from the University of Minnesota in Minneapolis, MN. After holding a position as a Postdoctoral Appointee in the Vibration and Acoustic Simulation group at Sandia National Laboratories, he has since transitioned to a role as a Senior Member of the Technical Staff. His current research focus is in the area of multi-axis vibration control and the surrounding theory/applications.

Chapter 11

A Systematic Evaluation of Test Specification Derivation Methods for Multi-axis Vibration Testing

Garrett Nelson

Abstract In the past decade, multi-axis vibration testing has progressed from its early research stages towards becoming a viable technology which can be used to simulate more realistic environmental conditions. The benefits of multi-axis vibration simulation over traditional uniaxial testing methods have been demonstrated by numerous authors. However, many challenges still exist to best utilize this new technology. Specifically, methods to obtain accurate and reliable multi-axis vibration specifications based on data acquired from field tests is of great interest. Traditional single axis derivation approaches may be inadequate for multi-axis vibration as they may not constrain profiles to adhere to proper cross-axis relationships—they may introduce behavior that is neither controllable nor representative of the field environment. A variety of numerical procedures have been developed and studied by previous authors. The intent of this research is to benchmark the performance of these different methods in a well-controlled lab setting to provide guidance for their usage in a general context. Through a combination of experimental and analytical work, the primary questions investigated are as follows: (1) In the absence of part-to-part variability and changes to the boundary condition, which specification derivation method performs the best? (2) Is it possible to optimize the sensor selection from field data to maximize the quality/accuracy of derived multi-axis vibration specifications? (3) Does the presence of response energy in field data which did not originate due to rigid body motion degrade the accuracy of multi-axis vibration specifications obtained via these derivation methods?

11.1 Introduction

The first shaker system dates back to the 1930's and owes its origins to demands in the auto industry to reliably produce vibratory motion on small components in a lab setting. Shakers have since become an integral tool in the auto industry and have found widespread usage in most other engineering industries. In aerospace applications, they are relied on heavily for product verification and qualification testing and to simulate the harsh environmental conditions that are anticipated during both ground and air transportation of a given system. If not properly mitigated, the vibration loads encountered in these environments can cause costly failures [1].

The vast majority of product life-cycle and environmental vibration tests are currently conducted on uniaxial vibration test platforms. These tests have been established as a method to detect part failures and predict the effects of service loads without the need of costly and time consuming field testing. The most widely referenced standard for these tests, MIL-STD-810G, specifies the use of sequential single axis tests in each of three orthogonal axes to characterize and validate the performance of both components and assemblies [2]. Comparable methods are provided by the U.S. Navy in NAVMAT P-9492 and the electronics industry's JESD22-B103B [3, 4]. Per the guidance given by these standards, the device is first tested along a single axis and then rotated 90° about the appropriate axis, with a test conducted after each rotation.

In the past few decades, advances in multi-axis testing hardware and software solutions have increased the application of multi-axis testing at both the system and component level. Vibration systems capable of multi-axis simulation have been successfully incorporated in both research and development labs across the U.S. in universities, government labs, and industry alike [5–10]. Their increased prevalence is motivated by a growing body of evidence which indicates shortcomings

Sandia National Laboratories is a multimission laboratory managed and operated by National Technology and Engineering Solutions of Sandia LLC, a wholly owned subsidiary of Honeywell International Inc. for the U.S. Department of Energy's National Nuclear Security Administration under contract DE-NA0003525.

G. Nelson (✉)

Vibration/Acoustics Simulation, Sandia National Laboratories, Albuquerque, NM, USA

e-mail: gdnelso@sandia.gov

in conventional single axis testing [11]. In many environments, the effects of cross-axis excitation can have large impacts on the resulting dynamics of a structure [12]. Accordingly, it has been found that the combined loading effects caused by these multi-axis excitations can result in different stress states [13–15], failure modes [16], and rates of damage accumulation [17–19]. Thus, it is no surprise that multi-axis testing has been shown to produce loading conditions that more closely simulate real world environments [20, 21]. This has motivated a dramatic increase in research on multi-axis test methods and the tools and analysis techniques necessary to make this testing possible. One key research area, and the focus of the present discussion, is the development of specifications for multi-axis testing.

In general, multi-axis vibration test specifications require the definition of a desired energy level and distribution for each axis as well as a definition for the relationship between each pair of axes. For random vibration tests, the specification for each independent axis is most commonly defined by an auto spectral density (ASD). As a function of frequency, the ASD specifies the level of energy in units of g^2/Hz . For a multi-axis specification, the relationship between each pair of axes can be defined by the cross power spectral density (CPSD). For convenience and increased physical understanding, this relationship is often presented as a frequency dependent coherence and phase. Collectively, the ASDs and CPSDs fully define the desired input conditions for the test.

Traditional multi-axis testing is conducted by developing a control scheme based on rigid body acceleration at the base of a component, assembly, or fixture [22]. Unfortunately, due to limits on the number of channels available for data acquisition during field tests, it is rare to have sufficient instrumentation such that six degree of freedom (6-DOF) inputs can be directly derived at either the system or component level. Specifically, the coherence and phase between axes are not adequately quantified and little to no data is available for rotational acceleration measurements. This has led to the development of various methods to derive test specifications and inputs by pairing field data with analysis on a dynamic model of the system of interest. Depending on the availability of a high fidelity finite element model of the unit under investigation, alternate experimental model techniques may be employed.

A recent field test conducted by Sandia National Laboratories on a critical system level assembly was instrumented specifically such that these multi-axis inputs could be directly measured. In addition to providing an input signal which could be used directly for multi-axis testing, this set of field data also provided the unique opportunity to benchmark the performance of other methods for deriving 6-DOF test inputs from field data with limited instrumentation. This was possible by comparing the results of tests conducted with input signals derived from only response channels which would have been available during a standard field test to those conducted with the “true” input signals which were directly measured. In addition to comparing the estimate of input signal obtained from each method, the dynamic response of the test article to these derived inputs were experimentally obtained on a shaker system and compared to measurement response data from the original field test [23, 24].

Although the combination of data from both field and lab testing was informative, a truly unbiased and objective measure of the specification derivation methods was not possible. The analysis and subsequent conclusions were limited by key uncontrolled factors:

1. The use of a different (albeit very similar) test article in the field and lab test sequences
2. Changes to the assembly dynamics between field and lab testing caused by differing boundary conditions
3. Minimal redundancies with measured acceleration levels on the assembly

Additionally, a common but unverified critical assumption was made during all of the explored specification derivation methods: All of the observed dynamics in the field response data can be explained by rigid body dynamics at the base. This assumption may be valid on components with approximately rigid boundary attachments within subassemblies, but may not be applicable in a wider context.

In attempt to address each of these limitations, a series of well controlled lab tests were proposed. By design, the experiments can enable a true and accurate comparison of the specification derivation methods. Based on these results, it will be possible to re-explore the more general case as was originally attempted.

As was done in the initial study, four different multi-axis input specification derivation methods were explored: (1) using the pseudo-inverse of the transmissibility function, (2) the output spectral density method, (3) a scaled output spectral density method, and (4) an iterative spectral density method with Tikhonov regularization. Objective measures of the performance of each method were based on time and frequency domain characteristics of the input specification and response data.

In Sects. 11.2 and 11.3 respectively a description of the test article/instrumentation and details of the multi-axis shaker system which was employed are provided. Subsequently, in Sect. 11.4 an explanation of each of the input derivation methods is provided. Lastly, experimental and analytical results and a detailed analysis of each method are given in Sect. 11.5.

Fig. 11.1 “Can” test article

11.2 Test Article Selection/Instrumentation

The hardware considered in this study is the bolted aluminum structure shown in Fig. 11.1. This structure has been the subject of a number of previous research activities aimed to understand its dynamics in a multi-axis test environment. The hardware is “can like” with an outer diameter of 6.65in, a hollow interior, and 3/8in wall thickness. The bottom piece of the can has a flange for mounting to a shaker table or adapter plate. The top piece of the can is connected to the lower piece through a series of 36 radial bolts along a lap joint. A cylindrical plate was also bolted to the top of the structure for added mass. The entire assembled structure has an 8in square footprint with a height of 10 in.

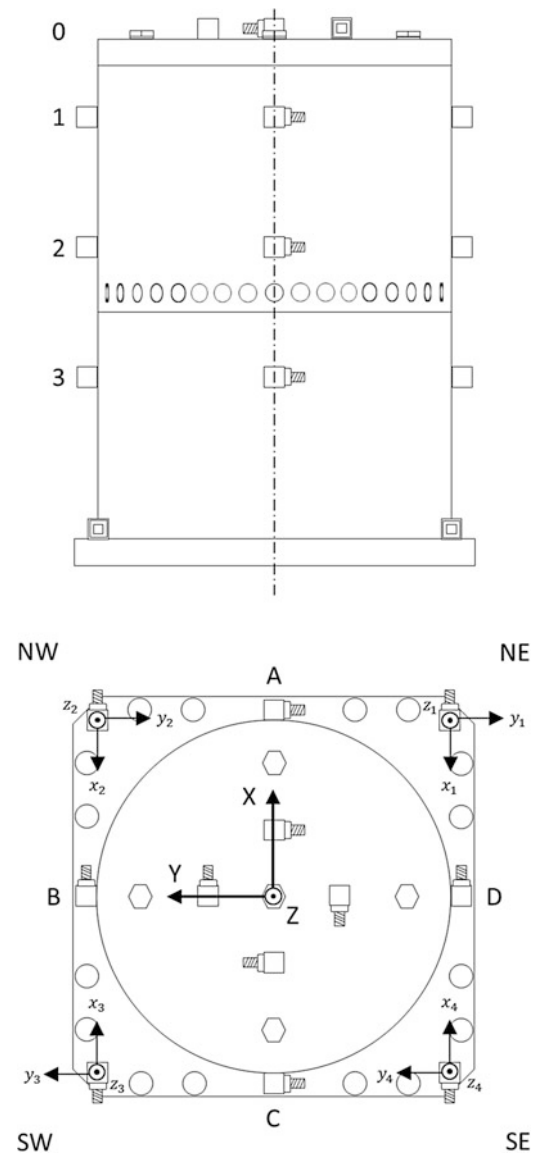
For response monitoring, the assembly was instrumented with a radial array of tri-axial accelerometers on a 90-degree pattern. Three rings of tri-axial accelerometers were placed on the outer surface of the main diameter with an additional ring on the top of the upper plate. In total, 16 response accelerometers were employed. Although this is greatly “over instrumented” in comparison to a typical field test, the increase in instrumentation was desired to enable future research into the effects of sensor selection/configuration on the specification derivation methods under investigation. The reference sensor arrangement was selected in part based on the expected dynamics of the test article. Therefore, any change to the test article behavior should be observable in the response data. In order to capture the base rigid body motion, four tri-axial accelerometers were mounted to the base plate which serves as an interface between the assembly and the shaker system used for testing. In a square pattern, the base accelerometers collectively enable full characterization of the base rigid body translation and rotation. A schematic of the sensor configuration is provided in Fig. 11.2.

11.3 Experimental Multi-axis Shaker System

There are currently two multi-axis shaker systems in service at Sandia National Laboratories, the Tensor 900™ and the Tensor 18kN™. For the proposed research, the smaller of the two systems—Team Corporation’s Tensor 900 (TE-900) multi-axis high frequency vibration test system (see Fig. 11.3)—was employed. This system was selected because it requires fewer resources when running a test sequence and enables quick turnaround between alternate test configurations.

The system is equipped with 12 independent electrodynamic shakers which together enable full six degree of freedom vibration testing. Four shakers are aligned along each of three orthogonal axes with opposing pairs of shakers positioned on either horizontal side of the base fixture and four vertical shakers positioned on the bottom of the fixture. By controlling the relative amplitude and phase of each shaker, it is possible to achieve the desired translational and rotational accelerations of the base fixture. At its maximum payload, this system can achieve 10 g acceleration with 200 lbf (900 N) along each primary axis from 10 Hz to 5 kHz. Additional details about the performance of this system can be found in papers by other authors [8, 25].

Fig. 11.2 Test article sensor configuration



11.4 Specification Derivation Methods

Irrespective of the control scheme employed, multi-axis random vibration test specifications require the definition of the desired auto spectrum for each axis. Additionally, it is required to define the relationship between each pair of axes or target response locations. The methods by which these inter-axis relationships are developed is of present interest.

For a single axis specification, the vibration level is most commonly defined by the auto spectral density (ASD), $P_{xx}[k]$. As a function of frequency, this metric specifies the level of energy in units of g^2/Hz . These specifications are routinely derived from time domain data obtained from field environments. The desired levels are estimated by using the Welch power spectral density algorithm.

In order to develop a multi-axis specification, it is necessary to define an additional function, the cross power spectral density (CPSD). Again using Welch's method, an estimate of the CPSD, $P_{xy}[k]$, between a pair of discrete signals can be obtained. For convenience and increased physical understanding, this relationship is most often presented as a frequency dependent coherence, $C_{xy}[k]$, and phase, $\phi_{xy}[k]$.

The relationship between an input and output is generally defined by a transfer function between the input and output. By construction, this relationship is assumed to be linear mapping between the input x and output y as defined in the frequency domain. Denoting the frequency dependent transfer function as $T_{xy}[k]$, the relationship between the input and output Fourier transforms is given by



Fig. 11.3 Tensor 900 multi-axis vibration test system

$$Y[k] = T_{xy}^*[k] X[k] \quad 1 \leq k \leq K \quad (11.1)$$

When working with power spectral densities, this relationship can equivalently be defined as follows:

$$P_{yy}[k] = T_{xy}^*[k] P_{xx}[k] T_{xy}[k] \quad 1 \leq k \leq K \quad (11.2)$$

In the case of multi-input multi-output (MIMO) systems, these relationships are combined in matrix form in what are commonly referred to as cross spectral density matrices (CSDMs). If you define $P_{x_i y_j}[k]$ as the frequency dependent cross spectral density between input x_i and output y_j for $1 \leq i \leq q$ and $1 \leq j \leq r$, the CSDM $P_{XY}[k] \in \mathbb{C}^{q \times r}$ can be defined as:

$$P_{XY}[k] = \begin{bmatrix} P_{x_1 y_1}[k] & P_{x_1 y_2}[k] & \cdots & P_{x_1 y_r}[k] \\ P_{x_2 y_1}[k] & P_{x_2 y_2}[k] & \cdots & P_{x_2 y_r}[k] \\ \vdots & \vdots & \ddots & \vdots \\ P_{x_q y_1}[k] & P_{x_q y_2}[k] & \cdots & P_{x_q y_r}[k] \end{bmatrix} \quad 1 \leq k \leq K \quad (11.3)$$

Similarly, the auto spectral densities for the inputs and outputs can each be combined in matrix form as

$$P_{XX}[k] = \begin{bmatrix} P_{x_1 x_1}[k] & P_{x_1 x_2}[k] & \cdots & P_{x_1 x_q}[k] \\ P_{x_2 x_1}[k] & P_{x_2 x_2}[k] & \cdots & P_{x_2 x_q}[k] \\ \vdots & \vdots & \ddots & \vdots \\ P_{x_q x_1}[k] & P_{x_q x_2}[k] & \cdots & P_{x_q x_q}[k] \end{bmatrix} \quad 1 \leq k \leq K \quad (11.4)$$

$$P_{YY}[k] = \begin{bmatrix} P_{y_1 y_1}[k] & P_{y_1 y_2}[k] & \cdots & P_{y_1 y_r}[k] \\ P_{y_2 y_1}[k] & P_{y_2 y_2}[k] & \cdots & P_{y_2 y_r}[k] \\ \vdots & \vdots & \ddots & \vdots \\ P_{y_r y_1}[k] & P_{y_r y_2}[k] & \cdots & P_{y_r y_r}[k] \end{bmatrix} \quad 1 \leq k \leq K \quad (11.5)$$

Where $P_{XX}[k] \in \mathbb{C}^{q \times q}$, $P_{YY}[k] \in \mathbb{C}^{r \times r}$, and both ASDMs are hermitian (i.e. $P_{XX} = P_{XX}^*$, $P_{YY} = P_{YY}^*$ where $[\cdot]^*$ denotes the matrix conjugate transpose).

Of present interest is a method by which the input cross spectral density matrix can be estimated from knowledge of both the transfer matrix and output cross power spectral density matrix. In general, we have the following known and unknown variables (Table 11.1):

Table 11.1 Known and unknown variables of interest in lab and field tests

	Lab test	Field test
Known	T_{XY} : Transfer Matrix between Input & Output X : Fourier Transform of Input Y : Fourier Transform of Output P_{XX} : Spectral Density Matrix of Input P_{YY} : Spectral Density Matrix of Output P_{XY} : Cross-Spectral Density Matrix	Y : Fourier Transform of Output P_{YY} : Spectral Density Matrix of Output
Unknown		T_{XY} : Transfer Matrix between Input & Output X : Fourier Transform of Input P_{XX} : Spectral Density Matrix of Input P_{XY} : Cross-Spectral Density Matrix

In previous work, three main PSD based methods were investigated. Each relies on an initial estimate of the transfer function based on data obtained in the lab.

$$\widehat{T}_{XY}[k] = P_{XX}^{-1}[k] P_{XY}[k] \quad 1 \leq k \leq K \quad (11.6)$$

where the \widehat{T} symbol is used to indicate an estimated quantity.

Specifically, the four primary methods which will be explored as a part of this paper are:

1. Moore-Penrose Pseudo-Inverse (PINV Method)
2. Scaled Moore-Penrose Pseudo-Inverse (SPINV Method)
3. Tikhonov Regularization (TR Method)
4. Iterative Phase & Coherence Matched Tikhonov Regularization (IPCMTR Method)

In the sections which follow, a detailed explanation of each method is provided. For convenience and clarity of exposition, the frequency dependence of all variables will be omitted.

11.4.1 Method 1: Moore-Penrose Pseudo-Inverse (PINV Method)

In general, we seek the solution to the problem where we have r outputs and q inputs, $r > q$. Therefore, we have an overdetermined set of equations and the transfer matrix cannot be inverted directly. Accordingly, we can implement the Moore-Penrose Pseudo-Inverse and find the so-called “best fit” or least squares solution to the system of linear equations.

$$\widehat{P}_{XX} = \left(\widehat{T}_{xy}^*\right)^{-\dagger} P_{YY} \widehat{T}_{XY}^{-\dagger} \quad (11.7)$$

Where $[\cdot]^{-\dagger}$ represents the Moore-Penrose generalized inverse of the matrix.

11.4.2 Method 2: Scaled Moore-Penrose Pseudo-Inverse (SPINV Method)

In practice, the output CSDM can be very ill-conditioned—the condition number (ratio of largest to smallest singular value) is very large. This can cause severe loss of precision in solving the given equations for the input CSDM. In these cases, it is suitable to apply a transformation to increase the condition number of the problem. Accordingly, define scaling (i.e. preconditioning) matrices, $S_1 \in \mathbb{R}^{r \times r}$ and $S_2 \in \mathbb{R}^{r \times r}$ to scale the output CSDM as follows:

$$P_{YY,S} = S_1 P_{YY} S_2 \quad (11.8)$$

Then, the scaled input CSDM can be obtained as

$$\widehat{P}_{XX,S} = \left(\widehat{T}_{XY}^*\right)^{-\dagger} P_{YY,S} \widehat{T}_{XY}^{-\dagger} \quad (11.9)$$

Now, to scale the input CSDM back one must use the following relation

$$\widehat{P}_{XX} = \left(\widehat{T}_{XY}^*\right)^{-\dagger} S_1^{-1} \widehat{T}_{XY}^* \widehat{P}_{XX,S} \widehat{T}_{XY} S_2^{-1} \widehat{T}_{XY}^{-\dagger} \quad (11.10)$$

By substituting back into the original equations, one can verify that in the absence of numerical errors, the input CSDM estimated by the PINV and sPINV Methods reduce to the same answer.

$$\widehat{P}_{XX} = \left(\widehat{T}_{XY}^*\right)^{-\dagger} S_1^{-1} \widehat{T}_{XY}^* \left(\widehat{T}_{XY}^*\right)^{-\dagger} S_1 P_{YY} S_2 \widehat{T}_{XY}^{-\dagger} \widehat{T}_{XY} S_2^{-1} \widehat{T}_{XY}^{-\dagger} \quad (11.11)$$

$$\widehat{P}_{XX} = \left(\widehat{T}_{XY}^*\right)^{-\dagger} S_1^{-1} S_1 P_{YY} S_2 S_2^{-1} \widehat{T}_{XY}^{-\dagger} \quad (11.12)$$

$$\widehat{P}_{XX} = \left(\widehat{T}_{XY}^*\right)^{-\dagger} P_{YY} \widehat{T}_{XY}^{-\dagger} \quad (11.13)$$

There exist a wide variety of choices for how to scale the output CSDM (i.e. the choice of scaling matrices S_1 and S_2). In the previous work done on this subject, the scaling matrices were defined as follows:

$$S_1 = S_2 = \begin{bmatrix} \sqrt{P_{y_1 y_1}} & 0 & 0 & 0 \\ 0 & \sqrt{P_{y_2 y_2}} & 0 & 0 \\ 0 & 0 & \ddots & 0 \\ 0 & 0 & 0 & \sqrt{P_{y_r y_r}} \end{bmatrix}^{-1} \quad (11.14)$$

When scaled in this way, the scaled output CSDM has ones along the diagonal but preserves the phase and ordinary coherence. Specifically, the magnitude of the off diagonals squared is the ordinary coherence and the phase of these off diagonals is the phase of the original CSDM.

11.4.3 Method 3: Tikhonov Regularization (TR Method)

Recalling that we seek the solution to the overdetermined problem of estimating q inputs given r outputs where $r > q$, there exists multiple solutions. In the general form, we seek a solution to the following equation.

$$Ax = b \quad (11.15)$$

The Moore-Penrose Pseudo-Inverse method chooses the solution which minimizes the sum of square residuals

$$\widehat{x} = \arg \min_x \|Ax - b\|_2^2 \quad (11.16)$$

where $\|\cdot\|_2$ is the Euclidean norm. Tikhonov regularization is a method by which we can choose an alternate solution which has some desirable properties. The solution is steered towards this new solution by a suitably chosen Tikhonov matrix, L . If the Tikhonov matrix is chosen as the identity matrix, the solution is steered to those with smaller norms. With the Tikhonov matrix, our estimate is given by the solution to the following:

$$\widehat{x} = \arg \min_x \left\| \begin{bmatrix} A \\ \lambda L \end{bmatrix} x - \begin{bmatrix} b \\ 0 \end{bmatrix} \right\|_2^2 \quad (11.17)$$

$$\widehat{x} = \arg \min_x \left(\|Ax - b\|_2^2 + \lambda^2 \|Lx\|_2^2 \right) \quad (11.18)$$

The explicit solution for this minimization is given as the solution to the following:

$$(A^T A + \lambda^2 L^T L) \hat{x} = A^T b \quad (11.19)$$

Thus,

$$\hat{x} = (A^T A + \lambda^2 L^T L)^{-1} A^T b \quad (11.20)$$

Returning to our original problem formulation, we have the following relation:

$$T_{XY}^* P_{XX} T_{XY} = P_{YY} \quad (11.21)$$

By using the vector operation on the original matrix product, this equation can be reduced to the standard form whereby on a single stage of Tikhonov regularization need be applied. First, apply the vector operation to both sides of the original equation

$$vec [T_{XY}^* P_{XX} T_{XY}] = vec [P_{YY}] \quad (11.22)$$

Then, by using Kronecker products, this can be rearranged as follows:

$$(\overline{T_{XY}} \otimes T_{XY}^*) vec [P_{XX}] = vec [P_{YY}] \quad (11.23)$$

Where $\overline{[\cdot]}$ denotes matrix transposition (with no complex conjugation).

Thus, define:

$$\begin{aligned} A &= \overline{\widehat{T}_{XY}} \otimes \widehat{T}_{XY}^*, A \in \mathbb{C}^{qr \times qr} \\ x &= vec [P_{XX}], x \in \mathbb{C}^{q^2 \times 1} \\ b &= vec [P_{YY}], b \in \mathbb{C}^{r^2 \times 1} \end{aligned} \quad (11.24)$$

Now, substituting back into our original expression

$$vec [\widehat{P}_{XX}] = \left\{ (\overline{\widehat{T}_{XY}} \otimes \widehat{T}_{XY}^*)^T (\overline{\widehat{T}_{XY}} \otimes \widehat{T}_{XY}^*) + \lambda^2 L^T L \right\}^{-1} (\overline{\widehat{T}_{XY}} \otimes \widehat{T}_{XY}^*)^T vec [P_{YY}] \quad (11.25)$$

Similarly, by using properties of the Kronecker product, this can be written in the form

$$vec [\widehat{P}_{XX}] = \left\{ (\overline{\widehat{T}_{XY} \widehat{T}_{XY}^*} \otimes \widehat{T}_{XY} \widehat{T}_{XY}^*) + \lambda^2 L^T L \right\}^{-1} (\overline{\widehat{T}_{XY}} \otimes \widehat{T}_{XY}^*)^T vec [P_{YY}] \quad (11.26)$$

11.4.4 Method 4: Iterative Phase & Coherence Matched Tikhonov Regularization (IPCMTR Method)

Although the Tikhonov regularization seeks to minimize the residual error between the field response and output estimate, it is possible that the resulting estimate is not compatible with the transfer function matrix obtained during the lab test. With this in mind, an additional step can be added into the input estimation algorithm to assure this compatibility. Specifically, this process iteratively modifies the off-diagonal terms of the target output power spectral density used in the derivation to assure that both the phase and coherence are compatible with the current test setup.

Let \widehat{P}_{XX} be the regularized solution of the first iteration using the Tikhonov regularization from the previous section. Then, an estimate of the output CSDM can be obtained as follows:

$$\widehat{P}_{YY} = \widehat{T}_{XY}^* \widehat{P}_{XX} \widehat{T}_{XY} \quad (11.27)$$

By defining

$$\widehat{P}_{y_i y_j} = \begin{cases} \widehat{P}_{y_i y_j} & i = j \\ |P_{y_i y_j}| \sqrt{\frac{\widehat{P}_{y_i y_i} \widehat{P}_{y_j y_j}}{P_{y_i y_i} P_{y_j y_j}}} e^{-i \angle \widehat{P}_{y_i y_j}} & i \neq j \end{cases} \quad (11.28)$$

the phase and coherence of the original \widehat{P}_{YY} are copied over to the new synthetic output, \widehat{P}_{YY} , while maintaining the original auto-spectral densities (diagonals of the CSDM). Subsequently, the new synthetic output is used to generate a new regularized solution.

$$vec[\widehat{P}_{XX}] = \left\{ \left(\widehat{T}_{XY} \otimes \widehat{T}_{XY}^* \right)^T \left(\widehat{T}_{XY} \otimes \widehat{T}_{XY}^* \right) + \lambda^2 L^T L \right\}^{-1} \left(\widehat{T}_{XY} \otimes \widehat{T}_{XY}^* \right)^T vec \left[\widehat{P}_{YY} \right] \quad (11.29)$$

The process is repeated until the desired level of convergence has been achieved. For the purposes of this paper, 10 iterations were performed.

11.5 Proposed Test Sequence

The proposed testing was broken into two primary phases, each with different measured outcomes. In order to isolate the specific objectives of this research and avoid confounding of results, each phase was completed in its entirety before proceeding to the next. A detailed discussion of specific test and analysis sequence is provided in the sub-sections which follow.

11.5.1 Phase I

The first phase of the research consisted of a series of multi-axis vibration tests based on scaled and modified vibration profiles from MIL-STD-810G Method 514.6. A scaled test level was selected to ensure that all testing remains within the normal operating envelope of the equipment. In addition to ensuring that subsequent tests are repeatable, a nominal test level was desired to ensure that secondary derived specifications (with or without numerical errors) would also remain within the normal operating envelope of the equipment.

Due to equipment constraints, the specification coherence and phase relationships between the axes were determined experimentally for the “truth” data. Once the test article was instrumented, a variety of different phase relationships were attempted until yielding a set of specifications which produced well-controlled yet meaningful—sufficiently interesting—results.

For all tests, the response data was acquired in the time domain and processed via each of the four specification derivation methods. For the portion of research completed at this time, each method was attempted with the full data set. As future work, the same investigation will be repeated with a reduced subset of the available data to explore the variability due to sensor selection and sensor redundancy—or lack thereof. For each method, the derived specifications were compared to the measured test control input (based on a transformation of the four base accelerometers). An analysis of the agreement between the derived and actual specification was based on both auto and cross-spectral density magnitudes. In order to capture global agreement, no weighting scheme was used to evaluate each axis despite their difference in relative magnitude. For future research, the global error method proposed by Hoksbergen may be explored [26].

Until proven otherwise, it was assumed that it was possible that the solution for the specification was not unique and deviations in the input specification may still have produced comparable response data. Therefore, in addition to direct comparisons of the input specification, the output spectral density was estimated by propagating the estimated input through the system dynamics analytically. Then, the response of the test article to this new derived specification was compared to that of the original tests conducted.

11.5.2 Phase II

Leveraging the results of the first phase, testing and evaluation proceeded to the second phase of this research. After having assessed the performance of the different derivation methods in a very well controlled lab setting, an attempt was made to relax these conditions and evaluate the methods in less “ideal” settings.

The vast majority of vibration test specifications are designed with a level of conservatism. The primary intent of these traditional tests is to excite a system with sufficient energy at the desired frequencies. The load path observed in the field may differ drastically from that of “representative” lab tests, but as long as the right amount of energy is provided to the test article at the right frequencies, the objective of these tests are met. When making the move from single to multi-axis, these details must be carefully considered. For multi-axis vibration testing, a specification developed based on field tests must both capture the environment and be physically realizable given the constraints of the equipment on which it will be tested. In a typical field environment, the test article is subjected to complex loads that originate from a variety of different sources. Some, but not all, of these loads may manifest as rigid body motion. If the load path of any source differs significantly from that of the lab tests, it will be difficult to obtain concurrence between lab and field tests.

In order to simulate this physical scenario, a new set of simulated field tests were conducted on the 6DOF system with an additional load path provided by acoustic excitation. Simultaneous inputs provided by both the rigid body base acceleration of the shaker system and direct field acoustic exposure were desired to produce data that is inherently different from that obtained in Phase I.

To provide acoustic excitation, speakers were arranged in pairs along a 2ft radial pattern every 45 degrees surrounding the test article (16 total). The lower speaker of each pair was in-line with the test article. The upper speakers were aligned at a 30° angle such that they were directed at the test article. Although averaged acoustic control was implemented, an independent control microphone was used to provide a control signal for each pair of speakers. A picture of the final test set-up which shows the speaker/microphone arrangement relative to the test article on the shaker system is provided in Fig. 11.4.

The acoustic profile selected for testing was designed to induce sufficient dynamics in the test structure at frequencies overlapping with the original six degree of freedom vibration profiles. Due to the averaged control approach selected, all speaker/microphone pairs utilized the same reference profile. The selected profile. A single unified control system was employed for both the vibration and acoustic sources.

The same input specification derivation methods were used to process the multi-source response data and test the hypothesis that specifications derived from this field data will differ drastically from those obtained from 6DOF only field test simulations. Without further modifications, each of the methods distribute the acoustic response energy across the six rigid body degrees of freedom. However, the coherence and phase of this portion of the response differs from that of the original environment. This may largely degrade the quality of the specifications—produce physically unrealizable input specifications. As was done previously, the derived specifications were used to calculate predicted response data and compared to the original response data.

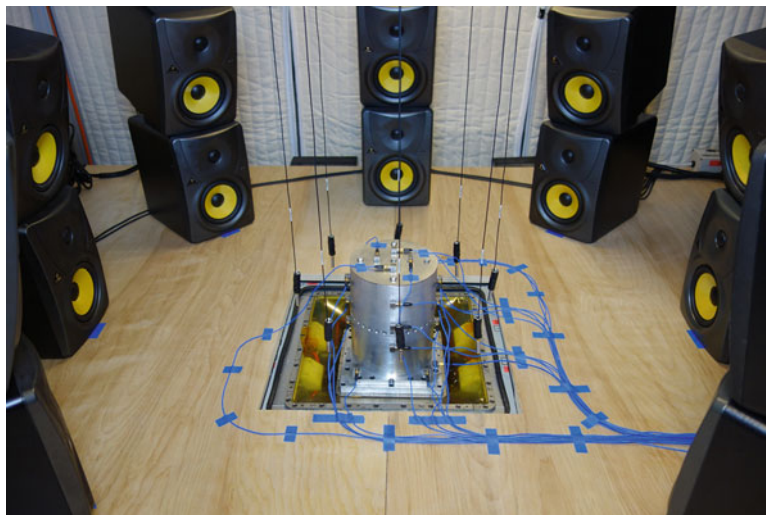


Fig. 11.4 Speaker and microphone configuration for simultaneous six degree of freedom vibration and direct field acoustic testing

11.6 Results

11.6.1 Phase I

As a preliminary assessment of the different methods, the derived input specifications were compared to the measured test control input (based on a transformation of the four base accelerometers). Although data was collected with various input energy levels and combinations of axes, the present discussion will focus only on the 3-axis translational and 6 degree-of-freedom test cases. For the 3-axis translational tests, the transfer function and input estimate were both limited to the 3 translational degrees of freedom. Data from a flat spectrum random test with uncorrelated inputs was used for transfer function estimation. Subsequently, data from the tests controlled to the specified environment were processed in the input estimation algorithms. The resulting input auto spectral density estimates for each method are shown in Figs. 11.5 and 11.6 for the 3-axis translational and 6DOF cases respectively.

As expected, due to the quality of the data obtained in this well controlled laboratory environment, all methods performed well in both the cases. However, it can be noted that even in these simple test cases all methods did not perfectly estimate the input.

To more clearly illustrate the performance or limitations of each method, it is beneficial to compare the predicted responses from each estimate to the original target responses. Numerically, this was accomplished by running each input estimate through the transfer function obtained experimentally. As it is difficult to compare each gauge location simultaneously, previous authors have used the cumulative ASD—sum of the ASDs for all response locations—as a reliable metric for performance assessment. Although less intuitive, the same can be done to produce the cumulative CSD (magnitude only)—sum of the magnitude of the CSDs between all response locations. For the cumulative CSD, only the upper right triangle of the CSDM was employed. An error in the summed responses is obtained as follows:

$$E_{YY,ASD} = 10\log_{10} \left(\sum_i |\hat{P}_{y_i y_i}| \right) - 10\log_{10} \left(\sum_i |P_{y_i y_i}| \right) \quad (11.30)$$

$$E_{YY,CSD} = 10\log_{10} \left(\sum_i \sum_{j>i} |\hat{P}_{y_i y_j}| \right) - 10\log_{10} \left(\sum_i \sum_{j>i} |P_{y_i y_j}| \right) \quad (11.31)$$

The results for the 3-axis translational and 6DOF cases are shown respectively in Figs. 11.7 and 11.8.

When shown in this way, the errors clearly indicate that the scaled pseudo inverse result over estimates the response. For this set of experimental data, the error in this estimation method is attributed to numerical errors caused by excessive scaling. In a general case, the proposed scaling method can improve the condition of the output spectral density matrix. However, in the case of well-conditioned output spectral densities, the effect of aggressively scaling large numbers down and small

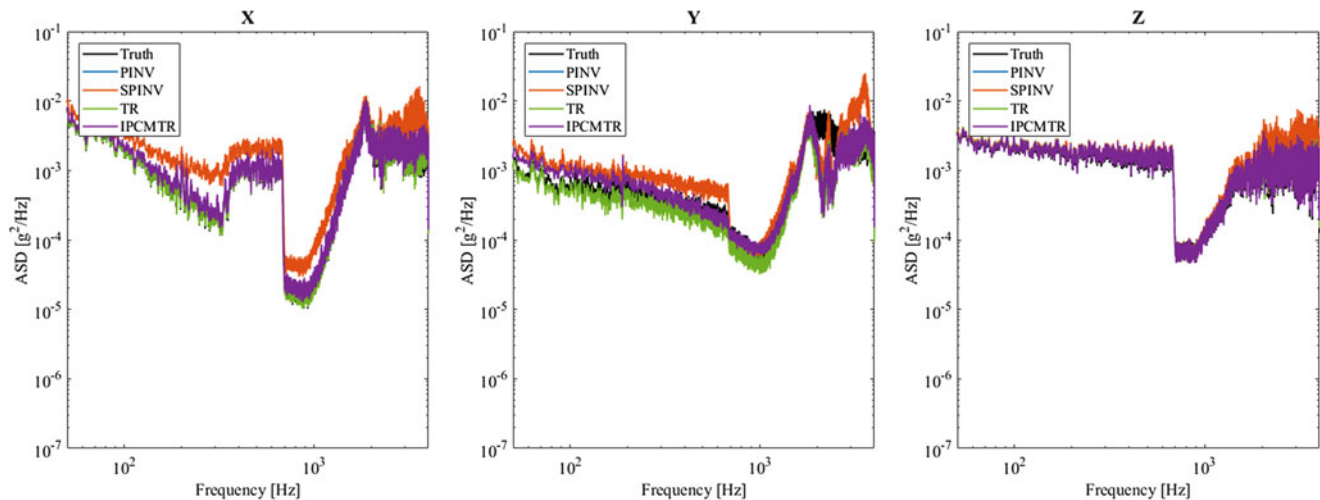


Fig. 11.5 Estimated input auto-spectral density for each method based on a 3-axis translational “truth” test

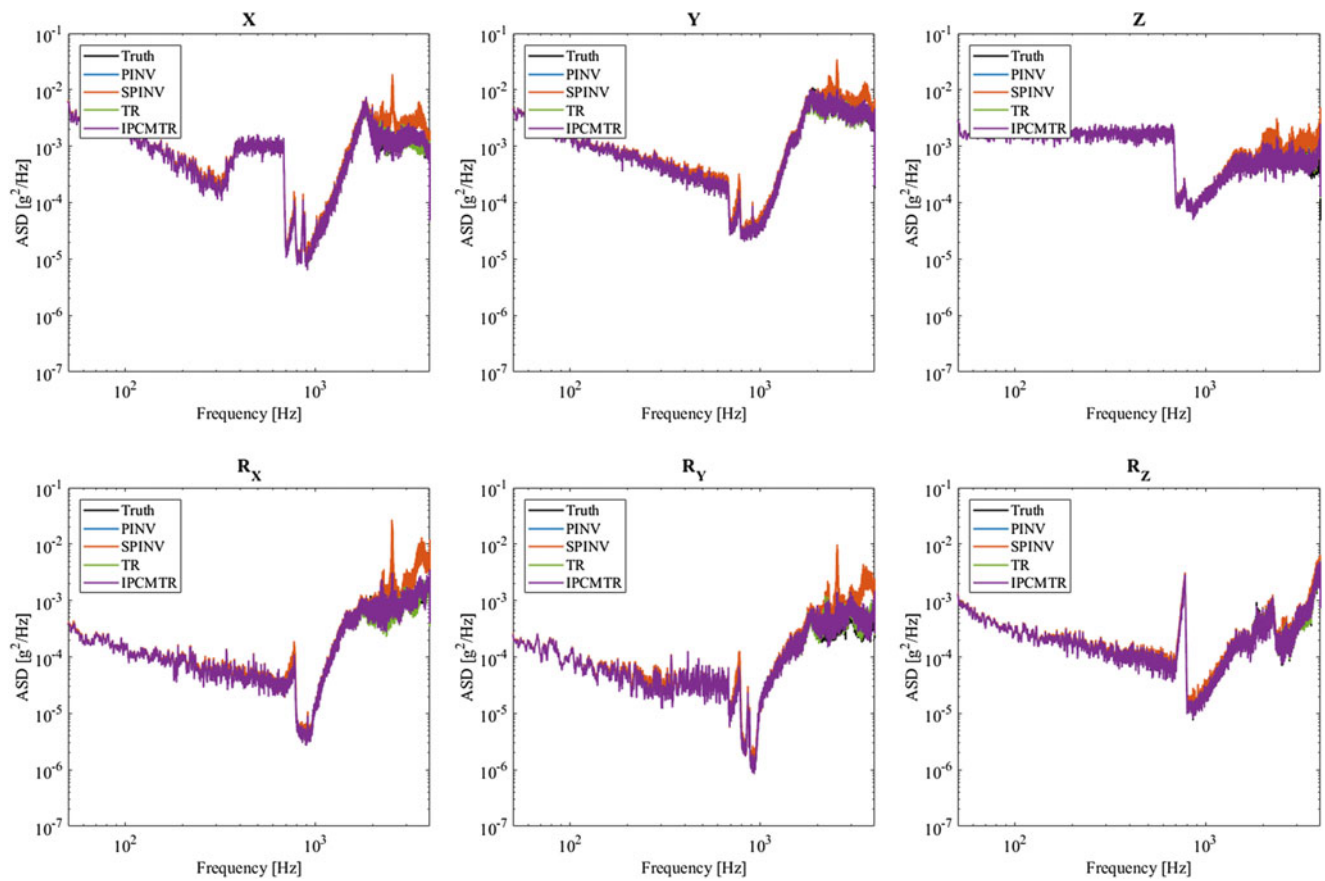


Fig. 11.6 Estimated input auto-spectral density for each method based on a 6DOF “truth” test

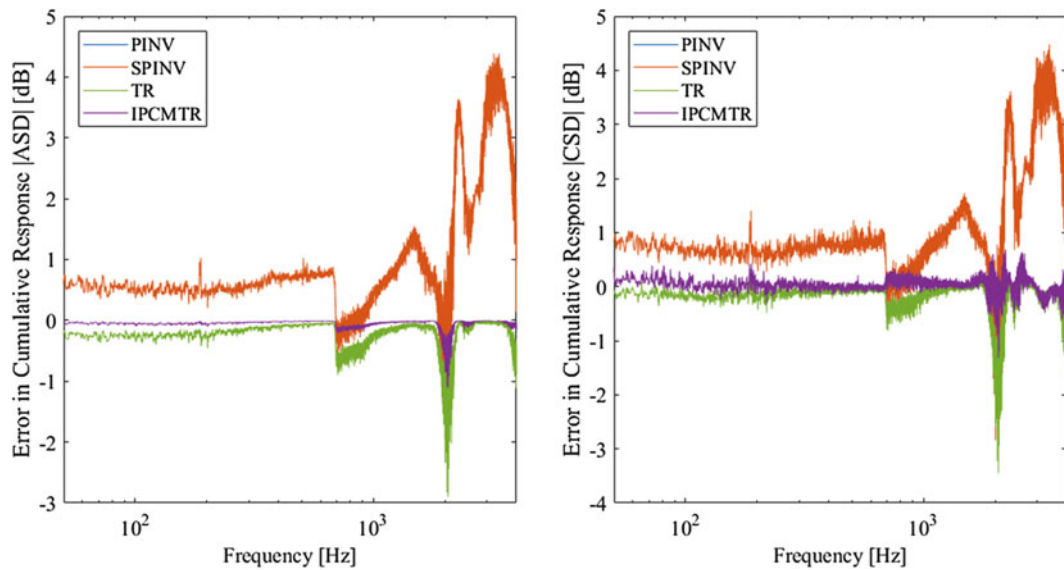


Fig. 11.7 Error in the cumulative response for each method based on a 3-axis translational “truth” test

numbers up introduces new numerical errors. In these cases, a less severe scaling matrix would be preferred. In both sets of data, the Tikhonov regularization solution and the standard pseudo-inverse solution yielded the same result. Across the bandwidth of interest, these methods achieved a cumulative response that deviated no more than 3 dB from the true output response. In the case of the 6DOF data, these errors are reduced even further.

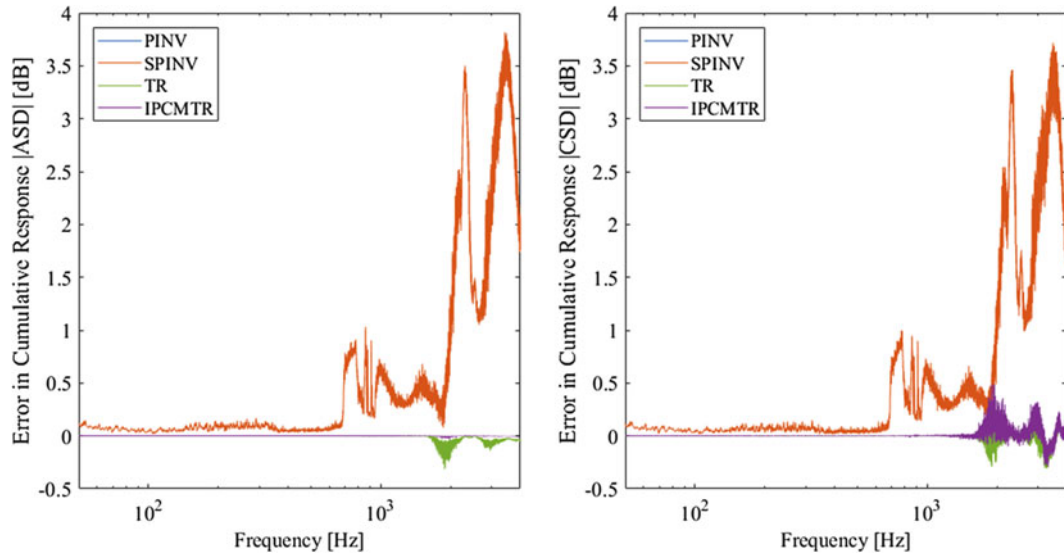


Fig. 11.8 Error in the cumulative response for each method based on a 6DOF “truth” test

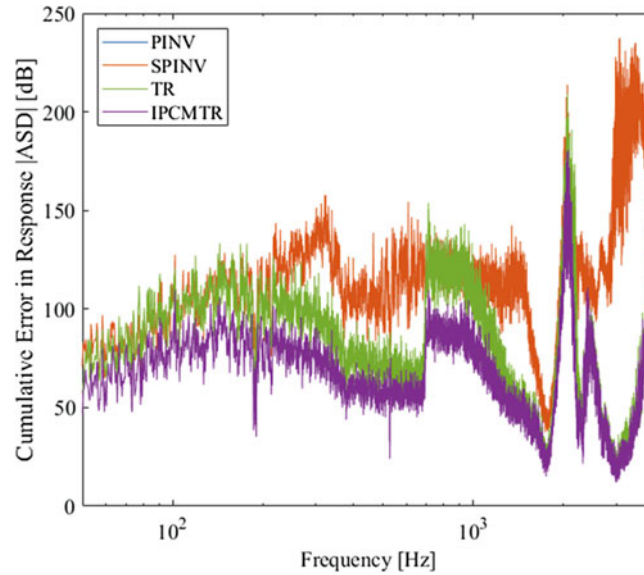


Fig. 11.9 Cumulative error in the response for each method based on a 3-axis translational “truth” test

For both the 3-axis translational and 6DOF test cases, the iterative phase & coherence matched Tikhonov regularization method performed the best. As shown in the error in cumulative ASD response plot in Fig. 11.8, this method almost perfectly matched the output response energy. Stated alternatively, the iterative method guarantees that the total response energy in the resulting estimate will match that of the target response data.

Although these plots demonstrate agreement in the sense of the overall response, they do not clearly demonstrate the error on a location by location basis. For this purpose, an additional error metric can be defined—the cumulative absolute error in response ASDs.

$$\bar{E}_{YY,ASD} = \sum_i \left| 10 \log_{10} \left(\left| \hat{P}_{y_i y_i} \right| \right) - 10 \log_{10} \left(\left| P_{y_i y_i} \right| \right) \right| \quad (11.32)$$

The results for both test cases are shown respectively in Figs. 11.9 and 11.10.

These results demonstrate that on a location by location basis, the iterative method still yields the best results. For the 6DOF test case, the improvement of this method over the standard pseudoinverse and Tikhonov regularization are less pronounced.

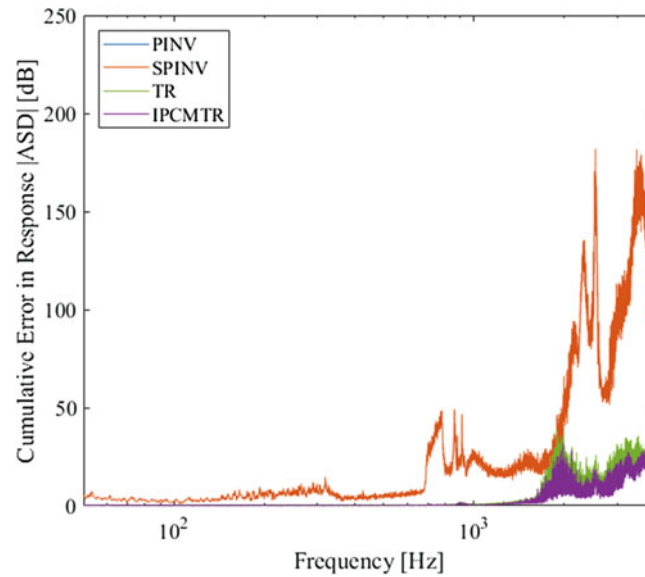


Fig. 11.10 Cumulative error in the response for each method based on a 6DOF “truth” test

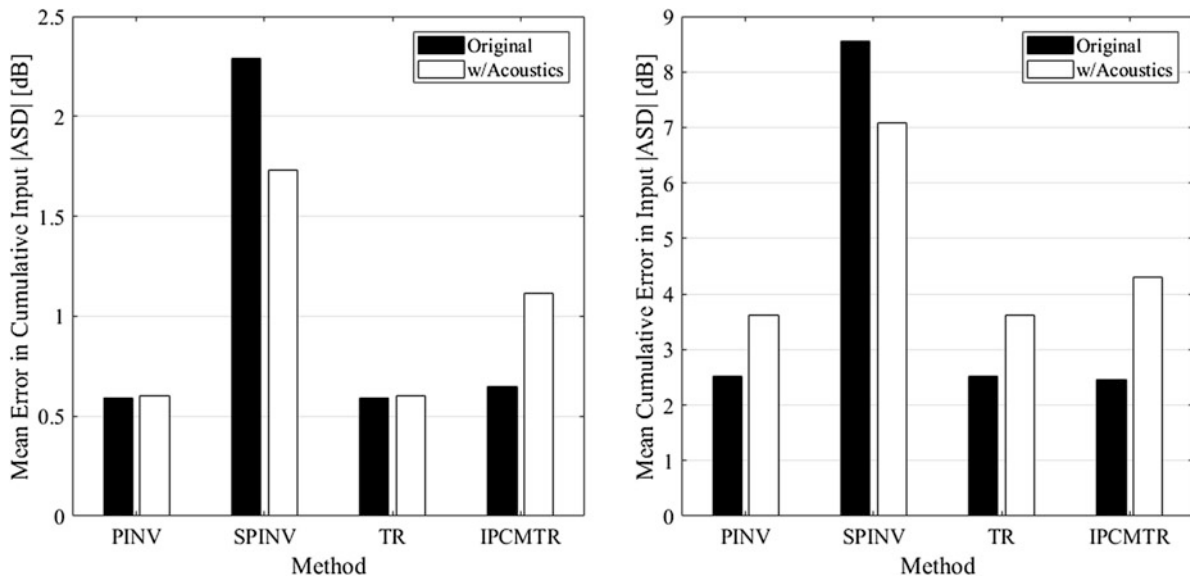


Fig. 11.11 Error in the cumulative response for each method based on a 3-axis translational “truth” test

11.6.2 Phase II

In order to extend the analysis and results into more complex test scenarios, the same experiments were repeated for the Phase 2 test cases in which additional acoustic excitation was supplied during the “truth” test. For all derivation approaches, no knowledge of the acoustic energy was assumed. Thus, the acoustics appear as noise during in the input derivation process. For both the 3-axis translation and 6DOF cases, the error in the cumulative input ASD as well as the cumulative error in the individual input’s ASDs were calculated. Shown in Figs. 11.11 and 11.12 are the mean errors across the test bandwidth for each test case and error metric.

As can be seen in the plots, the presence of additional acoustic energy in the “truth” test generally degrades the quality of the input estimate. Additionally, none of the current methods appears to handle this problem better than the other.

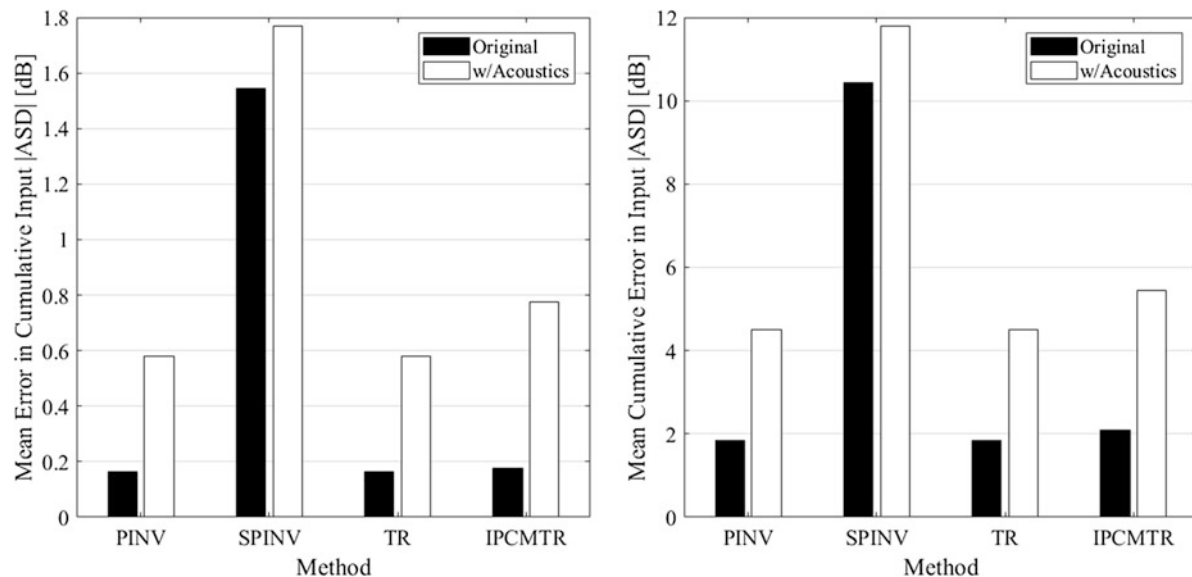


Fig. 11.12 Error in the cumulative response for each method based on a 6DOF “truth” test

11.7 Conclusions

This paper explores the use of four different derivation methods to develop input specifications for multi-input multi-output vibration testing. The response of the system in the lab setting “truth” test was compared to predictions generated from the results for each method. The test set-up and method were well controlled to minimize the uncontrolled variables in the investigation and obtain a true baseline comparison of each of the proposed methods.

The predicted responses confirm that the iterative phase and coherence matched Tikhonov regularization method produces the least amount of error in the predicted response. Contrary to a previous investigation, the results also demonstrate that the scaling method must be used with caution as it may introduce undesirable numerical errors. Although not discussed elsewhere, each method produced positive semi-definite input CSDM estimates—physically realizable specifications. It is possible that by some combination of these methods, greater results may have been possible. Additionally, alternate choices of a scaling matrix and optimized selection of regularization parameters may improve performance.

By using an acoustic input in the simulated test cases, it was possible to confirm that the presence of response energy in field data which did not originate due to rigid body motion can significantly degrade the accuracy of multi-axis vibration specifications. Further research is required to investigate methods by which these effects and be minimized or mitigated.

References

1. Sater, J.M., Crowe, C.R., Antcliff, R., Das, A.: An assessment of smart air and space structures: demonstrations and technology. Institute for Defense Analyses, Alexandria (2000)
2. U.S. Department of Defense: Environmental engineering considerations and laboratory tests (2008)
3. U.S. Navy: Manufacturing screening test standards (1979)
4. Joint Electron Device Engineering Council: JEDEC standard: vibration variable frequency (2006)
5. Choi, C., Al-Bassiyouni, M., Dasgupta, A., Osterman, M.: PoF issues in multi-dof vibration testing. In: Shakers, E.D., Shakersq, R.S. (eds.) IEEE accelerated stress testing and reliability conference. IEEE ASTR09 Workshop, Cham (2009)
6. Shafer M.J., Wilson D.R., Johnson R.V.: New ICBM shock and vibration test capabilities at OOALC’s Survivability and Vulnerability Integration Center, in Proceedings Joint Services Data Exchange Conference (1994)
7. Chen, M., Wilson, D.: The new triaxial shock and vibration test system at hill air force base. *J. IEST.* **41**(2), 27–32 (1998)
8. Smallwood, D.O., Gregory, D.: Evaluation of a six-DOF electrodynamic shaker system, in Proceedings of the 79th Shock Vibration Symposium, Orlando, FL (2008)
9. McIntosh, K., Davis, J.: Multi-axis testing of under wing and ground vehicle weapons systems, Aerospace Testing International, July (2002)
10. Füllekrug, U., Sinapius, M.: Simulation of multi-axis vibration in the qualification process of space structures, in International Symposium. Environmental Testing for Space Programmes, Noordwijk, Netherlands (1993)

11. Whiteman, W.E., Berman, M.S.: Fatigue failure results for multi-axial versus uniaxial stress screen vibration testing. *Shock. Vib.* **9**(6), 319–328 (2002)
12. Habtour, E., Connon, W., Pohland, M.F., Stanton, S.C., Paulus, M., Dasgupta, A.: Review of response and damage of linear and nonlinear systems under multiaxial vibration. *Shock. Vib.* **21**(4), (2014)
13. Gregory, D., Bitsie, F., Smallwood, D.O.: Comparison of the response of a simple structure to single axis and multiple axis random vibration inputs, in Proceedings of the 79th Shock Vibration Symposium, Orlando, FL (2008)
14. Loychik, N.E., Pan, J.: Achieving reliability goals for an EFV LRU through laboratory testing, in Proceedings Annu. Reliability Maintainability Symposium, Lake Buena Vista, FL (2011)
15. Ling, H., Shichao, F., Yaoqi, F.: Effect of multi-axis versus single-axis vibration test on the dynamic responses of typical spacecraft structure, in Proceedings of the 25th International Conference Noise Vibration Engineering, Leuven, Belgium (2012)
16. French, R.M., Handy, R., Cooper, H.L.: A comparison of simultaneous and sequential single-axis durability testing. *Exp. Tech.* **30**(5), 32–37 (2006)
17. Himelblau, H., Hine, M.J., Frydman, A.M., Barrett, P.A.: Effects of triaxial and uniaxial random excitation on the vibration response and fatigue damage of typical spacecraft hardware, in Proceedings of the 66th Shock Vibration Symposium, Biloxi, MS (1995)
18. Ernst, M., Habtour, E., Dasgupta, A., Pohland, M., Robeson, M., Paulus, M.: Comparison of electronic component durability under uniaxial and multiaxial random vibrations. *J. Electron. Packag.* **137**(1), 011009 (2015)
19. Peterson, C.: Time-to-failure testing using single- and multi-axis vibration. *Sound Vibration.* **47**(3), 13–16 (2013)
20. Harman, C., Pickel, M.B.: Multi-axis vibration reduces test time. *Eval. Eng.* **45**(6), 44 (2006)
21. Aykan, M., Celik, M.: Vibration fatigue analysis and multi-axial effect in testing of aerospace structures. *Mech. Syst. Signal Process.* **23**(3), 897–907 (2009)
22. Underwood, M.A., Hale, M.: MIMO testing methodologies, in Proceedings of the 79th Shock Vibration Symposium, Orlando, FL (2008)
23. Jacobs, L.D., Ross, M., Tipton, G., Cross, K., Hunter, N., Harvie, J., Nelson, G.: Experimental execution of 6DOF test derived from field tests, in International Modal Analysis Conference, Los Angeles (2017)
24. Ross, M., Jacobs, L. D., Tipton, G., Nelson, G., Cross, K., Hunter, N., Harvie, J.: 6-DOF shaker test input derivation from field test, in International Modal Analysis Conference, Los Angeles (2017)
25. Hoksbergen, J.: Advanced high-frequency 6-DOF vibration testing using the tensor. *Sound Vibration.* **43**(3), 6–12 (2013)
26. Hoksbergen, J.: Defining the global error of a multi-axis vibration test. *Sound Vibration.* **48**(9), 8–13 (2014)

Chapter 12

Designing Hardware for the Boundary Condition Round Robin Challenge

David E. Soine, Richard J. Jones, Julie M. Harvie, Troy J. Skousen, and Tyler F. Schoenherr

Abstract Qualification of products to their vibration and shock requirements in a laboratory setting consists of two basic steps. The first is the quantification of the product's mechanical environment in the field. The second is the process of testing the product in the laboratory to ensure it is robust enough to survive the field environment. The latter part is the subject of the "Boundary Condition for Component Qualification" challenge problem. This paper describes the challenges in determining the appropriate boundary conditions and input stimulus required to qualify the product. This paper also describes the steps and analyses that were taken to design a set of hardware that demonstrates the issue and can be used by round robin challenge participants to investigate the problem.

12.1 Introduction

Fixture design strategies for many component level shock and vibration tests remain as they were in the middle of the last century. The traditional approach attempts to provide rigid boundary conditions (or "infinite impedance") at the component interface locations. The literature refers to two general ideas for rigid fixture guidance. The first, more strict, guidance is to design a fixture to have a first participating mode at a frequency at least four times the maximum test frequency. A second more general guidance is for the frequency of the first participating mode of the fixture to be higher than the maximum test frequency. Analogous guidance based on pulse duration can be found for shock testing. Unfortunately environment specifications, component attachment interfaces, and environmental test fixtures are generally not developed as a cohesive package; they are often independently developed by different engineering groups. Component shock and vibration tests can be specified to (higher) frequencies or (shorter) durations, without considering the component fixture design at all, making it essentially impossible to design a rigid fixture according to the guidance – the dynamic modes of the fixture (and likely the test system to which it is attached) will be excited.

The structural dynamics and environmental testing communities have long recognized the shortcomings of the rigid fixture approach. Once the test envelope has moved out of the rigid body motion regime, it has been shown that dramatic under- and over-testing can occur due to the structural dynamics of *both* the next assembly and the lab test system itself. Scharton [1] documented potential approaches to address the issue, including consideration of modal density of the vehicle assembly

The Department of Energy's Kansas City National Security Campus is operated and managed by Honeywell Federal Manufacturing & Technologies, LLC under contract number DE-NA0002839.

Sandia National Laboratories is a multimission laboratory managed and operated by National Technology and Engineering Solutions of Sandia, LLC, a wholly owned subsidiary of Honeywell International, Inc., for the U.S. Department of Energy's National Nuclear Security Administration under contract DE-NA0003525.

© Copyright Honeywell Federal Manufacturing & Technologies LLC, 2017.

Notice: This manuscript has been authored by Honeywell Federal Manufacturing & Technologies under Contract No. DE-NA-0002839 with the U.S. Department of Energy. The United States Government retains and the publisher, by accepting the article for publication, acknowledges that the United States Government retains a nonexclusive, paid-up, irrevocable, world-wide license to publish or reproduce the published form of this manuscript, or allow others to do so, for United States Government purposes.

D. E. Soine (✉) · R. J. Jones
Kansas City National Security Campus, Kansas City, MO, USA
e-mail: dsoine@kcp.com

J. M. Harvie · T. J. Skousen · T. F. Schoenherr
Sandia National Laboratories, Albuquerque, NM, USA

as a tool to guide fixture and test design, followed later by Edwards [2] who outlined the potential of partial next-assembly style test fixtures. Various military and space testing standards have evolved to deal with the issue, focusing on full- and sub-assembly level or large component test articles. They mention dynamically representative test fixtures, and give guidance on other techniques such as force limiting to manage the risk of overtest, but specific design guidance for component level fixtures is minimal. Daborn [3] has proposed techniques that utilize a large portion of the next assembly as the test fixture, and Mayes [4] has been developing substructuring methods that could be useful to evaluate test fixture design.

12.1.1 The Component Qualification Process

The basic goal of the challenge problem is to design an environmental shock and vibration test fixture for a component. The term component implies that it is a part of a whole – components are built up into sub-assemblies and sub-assemblies are combined to create a full vehicle assembly. The means by which the components are attached to the next assembly varies and includes weldments, bolted joints, potting, clamping systems, adhesive joints, and other methods. Historically, some of the most challenging components to test have multiple connection points to the next assembly.

Shock and vibration testing at the component level is carried out to demonstrate (1) that an individual component will survive and function correctly throughout the expected life of the component, and (2) that the manufacturing process is being carried out correctly on an ongoing basis. Component shock and vibration specifications in many aerospace applications are derived from actual flight tests of some full vehicle assembly. The derivation of the specifications can involve a substantial amount of data analysis, modeling, test time compression techniques, ground tests of sub-assemblies, and other engineering processes. The goal is to deliver an environment that can be applied in the test lab that reflects the expected field loading of the component and exercises the same failure modes.

12.1.2 Inception of the Challenge Problem

Faced with an expanding test environments envelope and an aggressive production schedule, engineers at the Kansas City National Security Campus proposed a research project to harness emerging additive manufacturing technologies for environmental test fixture design and fabrication. It was expected that topology optimization would play a significant role in the effort, and the team realized that understanding the criteria for success – the objective function for the optimization – might be non-trivial. This work aligned with ongoing research at Sandia National Lab and teams from both organizations began collaborating in 2016. The combined team recognized that input from the wider aerospace testing industry as well as the structural dynamics community would be needed to make lasting and significant progress. This led to the idea of a common test bed or round-robin challenge problem to make it easy for researchers and small teams to engage the issue.

12.1.3 Hardware Goals, Concepts, and First Demonstration

As the research team considered the scope of the process and envisioned a hardware model, several goals were formed:

1. The model would include a full assembly, to enable direct formulation of an environment and to provide a “truth” test.
2. The model would have a simple component that can be easily detached from the assembly and tested individually.
3. The full assembly will be low cost and simple to fabricate or acquire.
4. The component would be small enough to test on a small environmental shaker system or shock machine.
5. The component response should be non-trivial. Single axis inputs result in multi-axis motions.
6. The component and assembly interact dynamically.
7. The under- and over-test problem would manifest if a rigid fixture approach was used.

After a brief review of objects already in use for research and round-robin testing, the team brainstormed on potential structures for the full assembly and the component. Use of an assembly that could be sourced locally or purchased at retail was strongly considered but the team could not locate an assembly with the required simplicity. Review of materials from the product list of McMaster-Carr was carried out and several schemes for bolted assemblies were proposed. The square tube section was conceptualized and the team recognized it might have the right combination of simplicity and structural dynamics for the project.

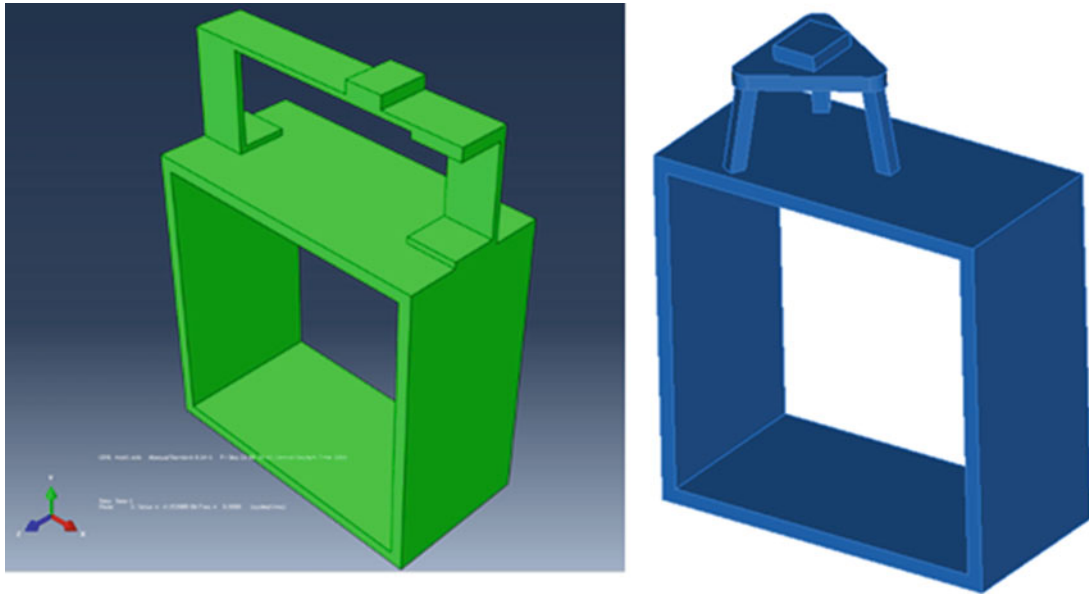


Fig. 12.1 Component concepts: C-channel vs. three-leg designs

Regarding component design, the desire for non-trivial component response drove the team to consider a three leg design. The challenge with the three-leg design was in how to attach it to the assembly. A competing proposal was to use a simple beam along with some short sections of C-channel. A finite element model and additively manufactured plastic prototypes were created for both proposals, and because of its immediate availability, hardware was ordered for the C-channel design (Fig. 12.1).

12.1.4 Prototype Development

The first prototype was constructed of steel, and six inch square steel tube was only available with rounded corners. The model was updated to reflect the rounded corners, and a presentation demonstrating the component boundary condition problem was generated, elements of which are shown in Figs. 12.2, 12.3, and 12.4, and Table 12.1. Figure 12.2 shows, from left to right, the assembly stress field with a flat random vibration Acceleration Spectral Density (ASD) of $0.001 \text{ g}^2/\text{Hz}$ from 100 Hz to 2000 Hz on the bottom surface of the assembly. In this assembly, the vertical direction ASD was measured at one of the feet of the component and used as the input spectrum in the component test configuration (middle graphic). Note that the stress fields of the component differ between the assembly and the component test configuration. To exercise the same damage mechanism between the two configurations, the stress fields should be similar to each other. The graphic on the right shows the vertical ASD response of a point on the top of the component in the assembly and the component test configuration. The differences in the responses are concerning. Figure 12.3 shows the differences in the modes of the assembly and the component test configuration graphically by mode. Figure 12.4 shows the MAC of the two configurations at select points on the component, which indicates how closely related different modes between the configurations are. Table 12.1 lists the modes of the two configurations.

Upon fabrication of the steel hardware, some problems became apparent. The flatness of the walls of the steel tube section was inadequate. The faces of the steel c-channel were not square (this could have been due to fabrication), and the internal faces of the c-channel were not parallel to the outer faces. As a result of these dimensional issues, the flat bar stock on the top of the component showed a substantial curvature when the parts were assembled, and if the assembly was bolted together, the bolts would have to provide a clamping load on surfaces that were not parallel.

The team decided to try an assembly made of aluminum, and ordered raw material of the same nominal dimensions as the steel prototype. The hardware was better dimensionally and the team decided to use aluminum instead of steel. Fabrication of the first aluminum prototype was completed prior to the IMAC 35 Structural Dynamics Conference, and the team brought the aluminum prototypes and a presentation that demonstrated the component testing boundary condition problem to the conference.

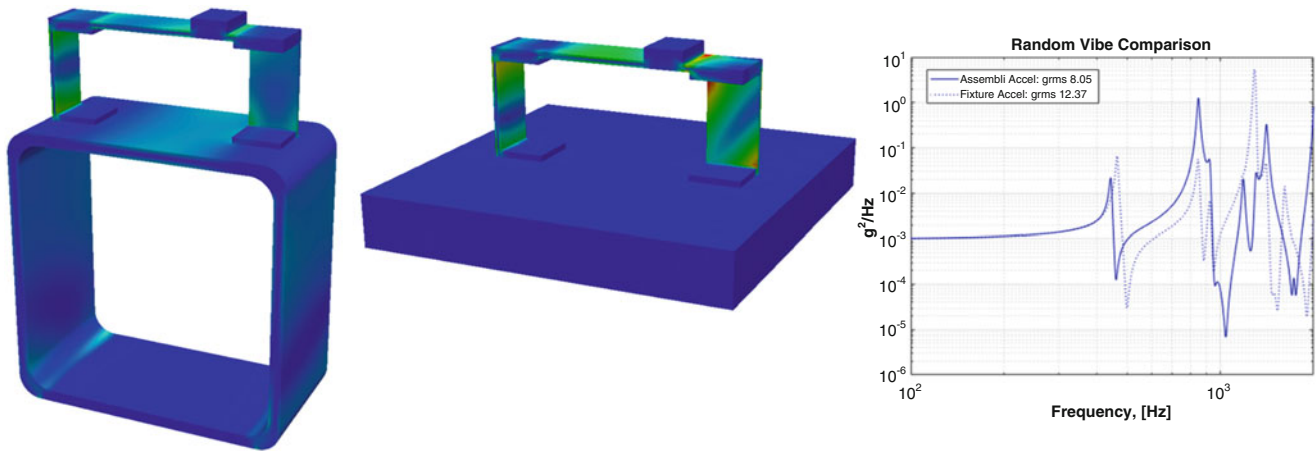


Fig. 12.2 Component testing boundary condition problem, random vibration (simulation) example. Stress field from random input to the base of the assembly (l.). Component stress field from acceleration input at the base of the component, derived from the assembly response (center.) Assembly response vs component response on fixture, derived using traditional techniques (r.). From the presentation at IMAC 35

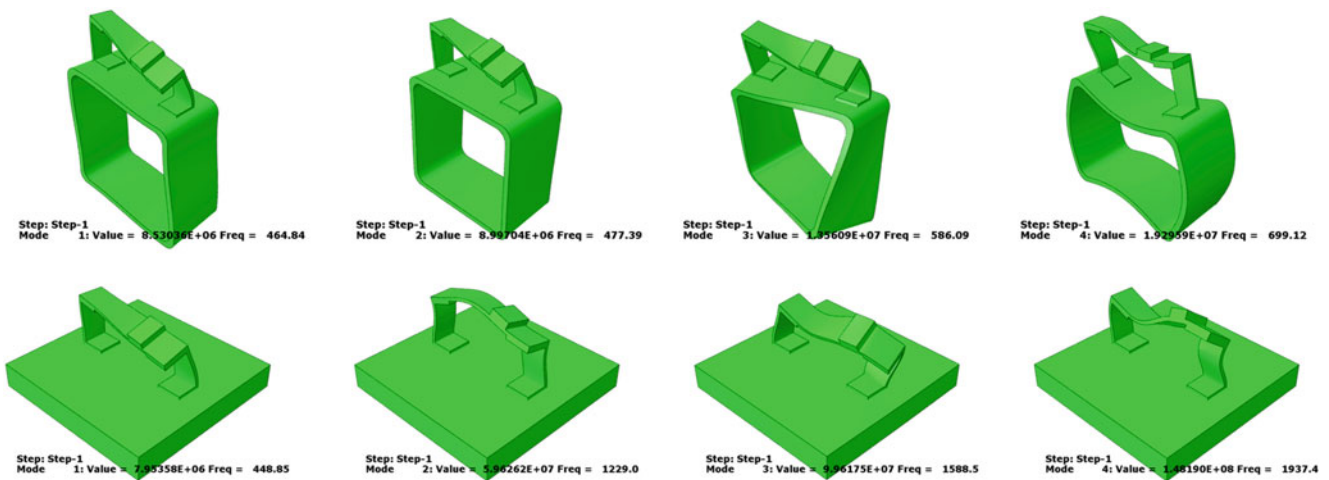


Fig. 12.3 First four flexural modes from Finite Element Models of the component-in-assembly and component-on-fixture configurations, steel, free boundary conditions

12.2 Component Attachment

The goal of simple assembly and disassembly drove a demand for bolted joints in the hardware. The original C-channel design had one bolt at each interface. In discussions following a meeting on the boundary condition problem at the IMAC 35 conference, an experienced dynamicist suggested four bolts at each interface. Reluctant to increase the system complexity and cost, the team decided to try a four-bolt approach at the component interface. Prototype parts were fabricated and a simple impact survey done to determine the effect the four bolt interface would have on test-to-test variability when the component was detached and re-attached to the assembly. The survey showed that the peaks of the acceleration Frequency Response Functions (FRFs) of the four-bolt configuration exhibited less variability than those of the single-bolt configuration. The team accepted the survey results and adopted the four-bolt configuration to attach the component to the fixture. Photos from the survey and a comparison of FRFs are shown in Figs. 12.5 and 12.6.

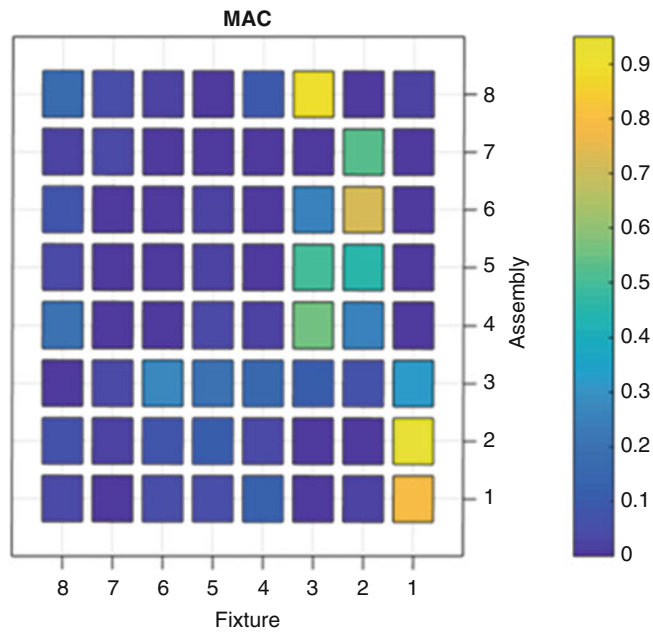


Fig. 12.4 MAC from selected points on the component

Table 12.1 List of modes – steel models

Mode number	Mode frequency (Hz)	
	Steel component+assembly model	Steel component+fixture model
1	465 ^a	449 ^a
2	477 ^a	1229 ^a
3	586	1588 ^a
4	699	1937 ^a
5	1131	2415
6	1284 ^a	2878 ^a
7	1537	3404 ^a
8	1812 ^a	3681
9	1924	4476

^aModes dominated by local flexure of the component

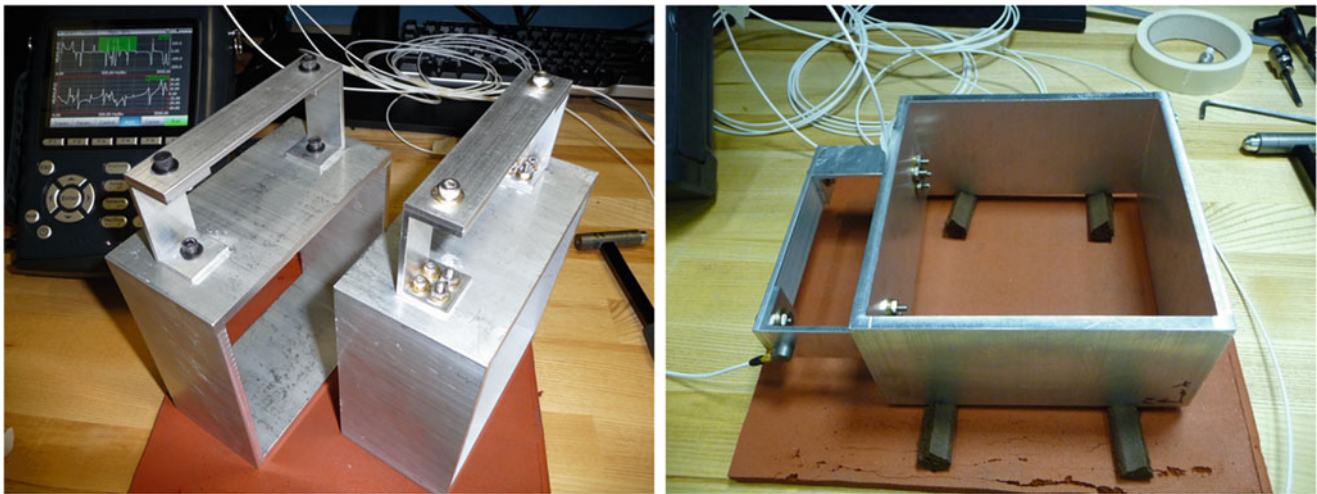


Fig. 12.5 Impact survey on Single vs Four bolt attachment

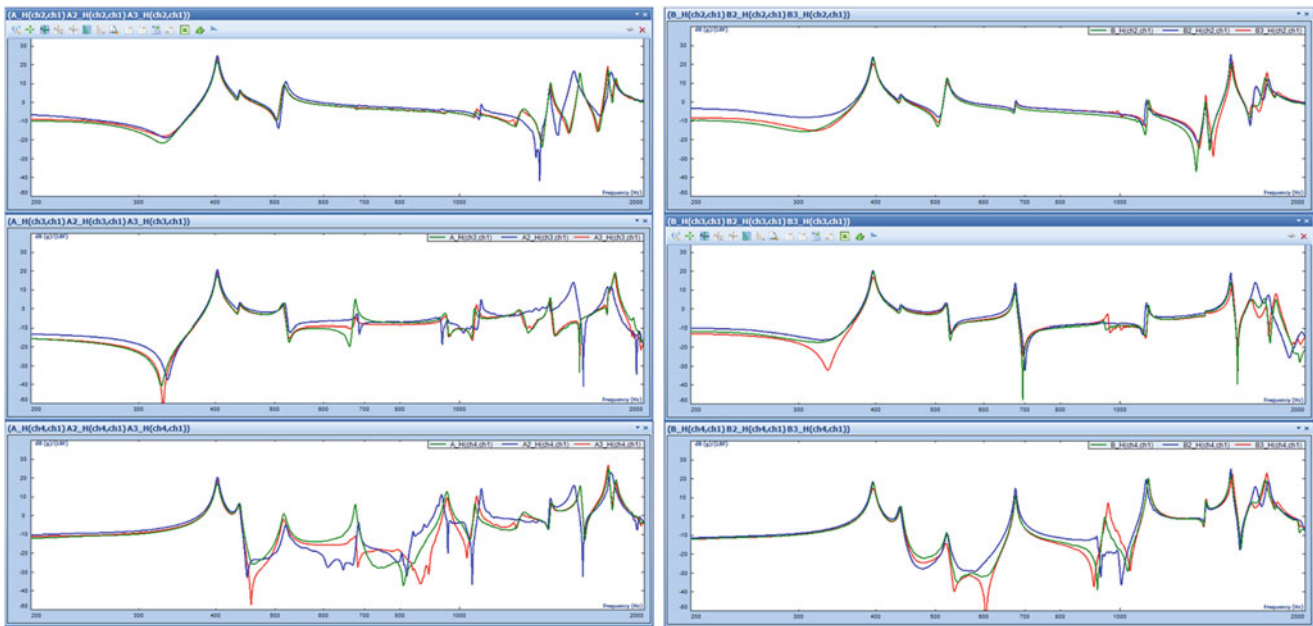


Fig. 12.6 Single bolt attachment (l.) vs. Four bolt attachment (r.) at a driving point (top plot) and two additional response locations. Once the initial data set was taken, the component was removed and re-attached to the assembly twice, with the same measurements repeated after each re-attachment

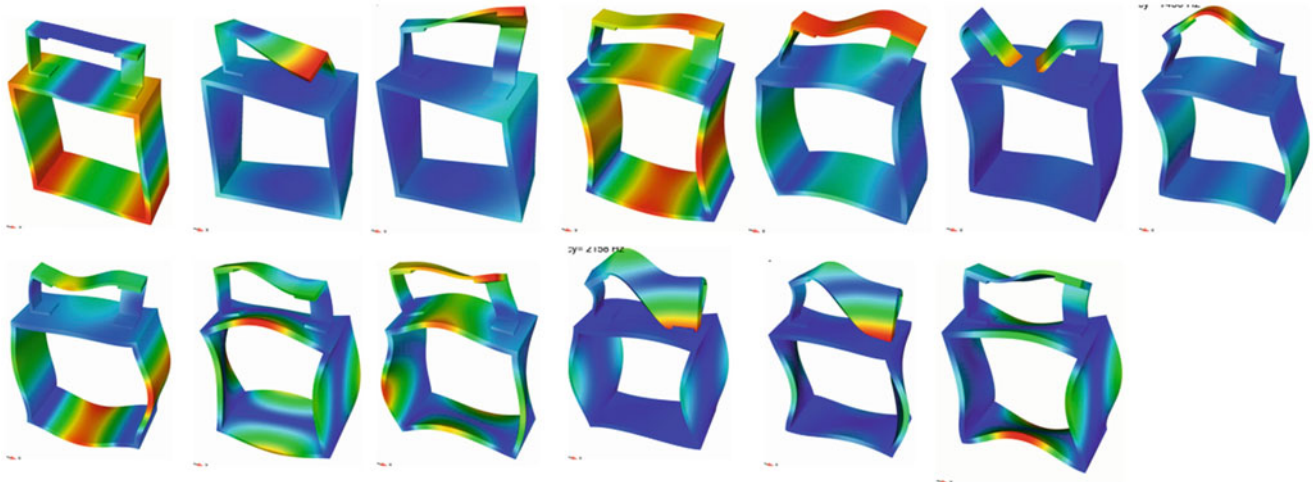


Fig. 12.7 Uncut aluminum box assembly flexural mode shapes from modeling

12.2.1 Progression to the Final Design

The last changes to the design were motivated by a desire to have the component and the rest of the assembly interact dynamically, and to have more assembly modes present below 2000 Hz. Modes of the original aluminum assembly model are shown in Fig. 12.7. The team felt the component and assembly did not interact enough. A cut, between the component attachment locations and through the box section was modeled, resulting in an assembly in which the component plays a much larger role in the system dynamics. The natural frequency of the first flexural mode was lowered dramatically. The team decided to keep the cut in the box section, anticipating that the fixture design problem will directly address the issue of mismatched dynamic impedance between the test fixture and the next level assembly. Modes of the cut system are shown in Fig. 12.8, and tables of modes and frequencies of various models and tests are in Table 12.2 (Fig. 12.9).

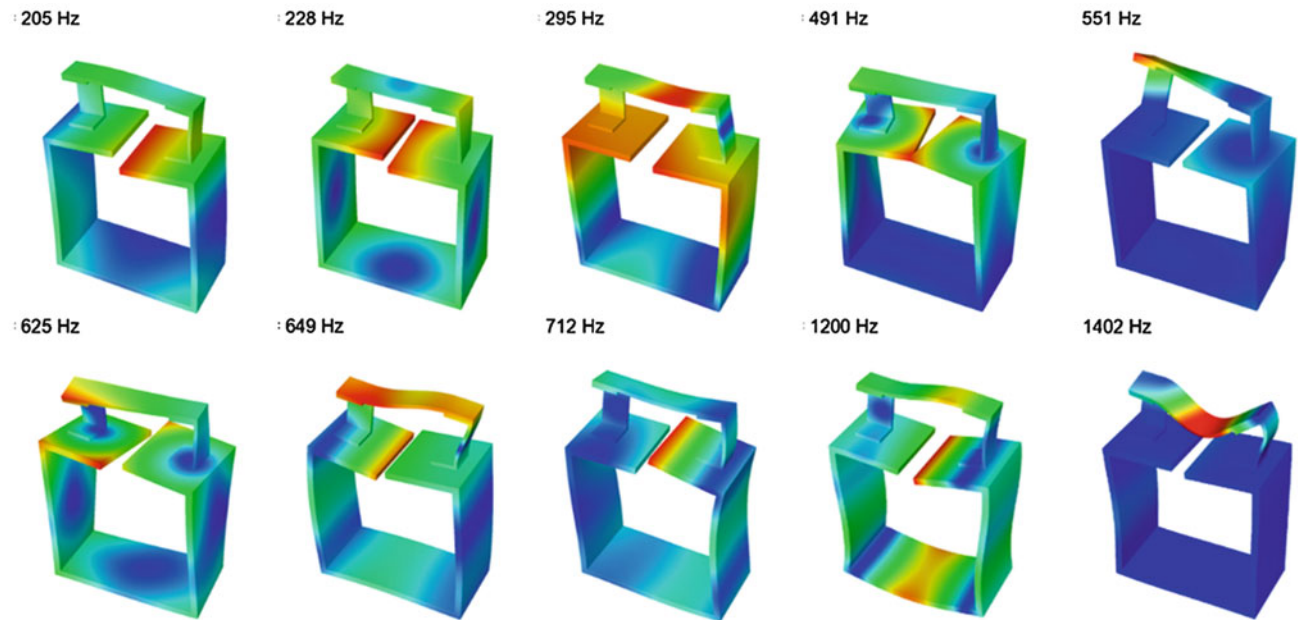


Fig. 12.8 Flexural mode shapes of the final design, from a finite element model

Table 12.2 Natural frequencies from modeling and testing

Mode number	Natural frequency (Hz)		
	Uncut aluminum box assembly FEM model	Uncut aluminum box assembly test	Cut aluminum box assembly FEM model
7	416	398	205
8	521	443	228
9	590	528	295
10	714	679	491
11	1150	963	551
12	1350	1116	625
13	1450	1381	649
14	1603	1517	712
15	1879	1635	1200
16	2021	1736	1402
17	2158	1799	1619
18	2245		1732
19	2347	1944	1947
20			2111

12.2.2 Summary

The hardware for the boundary condition challenge has matured. The research team looks forward to more interaction with structural dynamics modeling and test communities, as we strive to develop performance criteria and design guidance for creation of high fidelity component test fixtures and testing methods (Fig. 12.10).

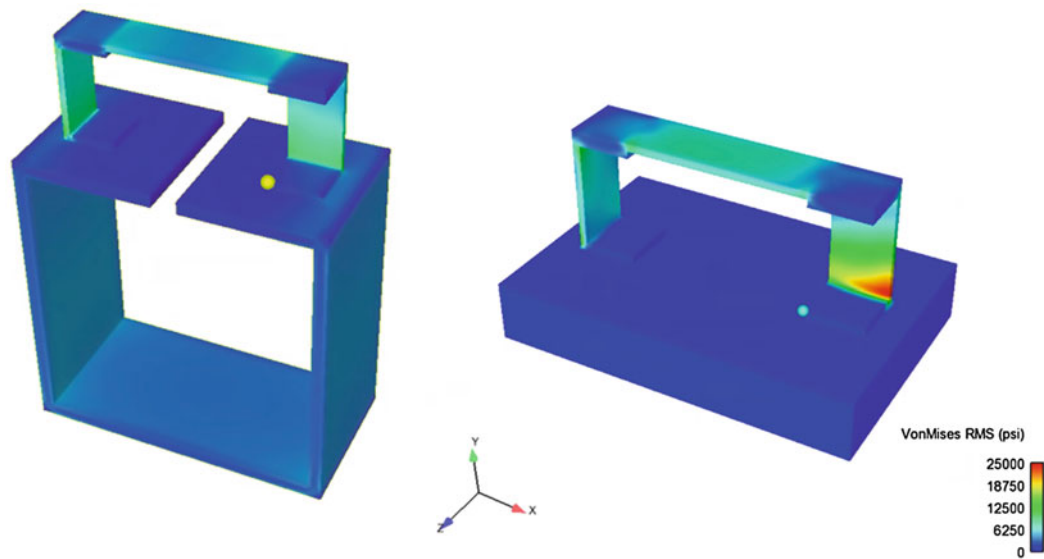


Fig. 12.9 Component testing boundary condition problem simulation for random vibration. Random acceleration input was applied to the base of the assembly. The stress field (color contours) and response at the component base (indicated by a yellow dot) was calculated (l.). Component stress field from acceleration input at the component base (indicated by a green dot), derived from the assembly response (r.)

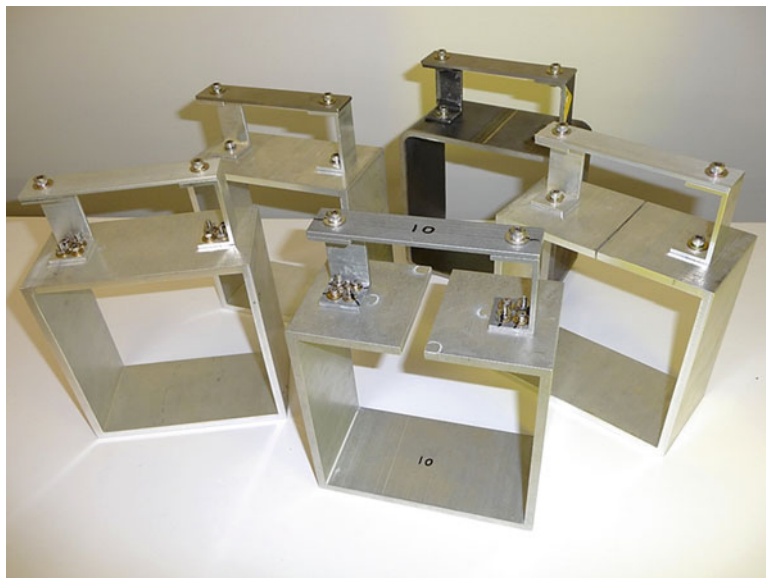


Fig. 12.10 Development prototypes, and the final version (front) of the box and bench test bed for the component test boundary condition problem

References

1. Scharon, T.D.: Impedance simulation vibration test fixtures for spacecraft tests. *Shock Vibr Bull.* **40**(3), 230–256 (1969)
2. Edwards, T.S.: The effects of boundary conditions in component-level shock and vibration testing, publication details unknown (2007)
3. Daborn, P.M.: Scaling up of the Impedance-Matched Multi-Axis Test (IMMAT) technique. In: Proceedings of the 35th International Modal Analysis Conference, Garden Grove, CA, Feb (2017)
4. Mayes, R.L.: A modal Craig-Bampton substructure for experiments, analysis, control and specifications. In: Proceedings of the 33rd International Modal Analysis Conference, Orlando, FL, Feb (2015)

Chapter 13

Modal Comparison of Stock and Performance Brake Rotors

Kaitlin Spak

Abstract Although generally similar in appearance, automobile brake rotors vary widely in terms of cost, material, and quality. Modal analysis was conducted on a variety of stock and performance used and new brake rotors to determine whether vibration analysis could be an effective method for evaluating quality, performance, and/or remaining life of a given brake rotor. Regular and slotted performance brake rotors were tested using an impact hammer and tri-axial accelerometer, and natural frequencies were evaluated up to 12,000 Hz. Testing methodology was varied to determine what parameters were most effective to highlight differences between rotors. The overall finding was that the most significant difference between rotors was due to the reduced mass of a used rotor; i.e., different types of rotors for the same vehicle showed greater similarity in dynamic response than a new rotor and a used rotor of the same type. Additionally, comparison of new and used rotors can show a correlation between remaining rotor life and dynamic response. While simple mass measurement of the rotor could provide similar information, vibration data can be taken with the brake rotor in place on the vehicle, and could provide information about the amount of brake rotor used in high performance driving events during the event, as well as the condition of the rotor. Testing is ongoing, and may also include identification of dynamic response for cracked rotors. Further testing is required to verify the differences in rotor wear for rotors installed on the vehicle.

13.1 Introduction

Brake rotors are the large disc of a disc brake assembly, in which brake pads are pressed against the rotor to stop a vehicle using the friction between the brake pads and the brake rotors. Brake rotors range widely in cost, from about \$25 for a single rotor to over \$150 each for an aftermarket high performance rotor. High performance rotors are made to withstand higher temperatures experienced during performance driving, which involves heavy braking from high speeds. Many high performance rotors are cross drilled or slotted, to allow gases that build up between the brake pad and brake rotor to dissipate, allowing the brake to run cooler and more effectively. While brake rotors on a normal passenger car may be replaced only once or twice in the car's lifetime (depending on use, size of the brakes, and vehicle weight), high performance brake rotors see significantly more use, and are subject to replacement not just for wear, but for possible damage such as through-cracking, surface cracking, and uneven wear. This investigation was conceived to reduce the disassembly required for inspection of brake rotors in between and following high performance driving event (HPDE) sessions.

13.2 Background

The brake system of a performance vehicle consists of a brake rotor, brake pads, and brake calipers. The brake calipers apply hydraulic pressure to the brake pads to squeeze the brake rotor, using friction to slow and stop the car. Much of the literature available regarding modal analysis of brake rotors is related to combating the problem of "brake squeal."^{1 2} However, in

¹Kharate, N.K., Chaudhari, S.S., "Investigation of Natural Frequency and Modal Analysis of Brake Rotor Using Fea and Ema", International Journal of Innovative Research in Science, Engineering and Technology, Vol. 3, Issue 10, October 2014.

²Parra, C., Olazagoitia, J.L., Biera, J., "Application of testing, modal analysis and numerical methods to the detection, prediction and avoidance of squeal noise in automotive brake systems," Proceedings of ISMA 2010 Including USD2010, 2010.

K. Spak (✉)
Exponent, Menlo Park, CA, USA
e-mail: kspak@exponent.com

performance driving, brake squeal is not an issue compared to brake performance. In high performance driving, which may involve braking from speeds in excess of 100 mph to less than half that in as short a distance as possible, rotors wear out, become warped or uneven, crack, or otherwise become unusable in just a few performance driving sessions. Manufacturers of performance brake rotors recommend that “All disc rotors should be inspected during and after track day events. This involves removing the rotor from the vehicle and inspecting for heat checking (surface cracking) and severe cracks from fatigue on the pad surfaces . . . Users need to be mindful that in most motorsport applications, the rotor can be deemed to have reached its usable life due to stress cracking well before it reaches minimum thickness at which point the rotor must be discarded.”³ In an effort to determine whether modal analysis could contribute to the estimation of rotor life, modal analysis was conducted on a variety of rotors from two 2010 SS Chevrolet Camaros used in HPDEs.

13.3 Procedure

The ultimate goal of this investigation is to determine brake rotor wear or damage without removing the rotors from the vehicle. Therefore, the first step was to examine the frequency response of individual rotors to identify differences in the rotor response in a free condition, where the rotor is not mounted or otherwise constrained. When the rotors are mounted, lug nut torque must be considered, as the boundary conditions of the rotor will affect the frequency response. The free condition work provides a baseline understanding to support the ultimate goal of mounted rotor condition monitoring based on modal analysis. The rotors investigated were used and new rotors used on the front wheels of two 2010 Camaros for high performance driving events; the cars are distinguished by their engines, an LS3 and an L99. The cars are identical in frame and weight. The rotors used are pictured in Fig. 13.1 and include:

1. A used Disc Brakes Australia (DBA) brand 4000 series T3 slotted rotor. Used for one high performance track event and parked with brakes engaged while hot, resulting in uneven surface. Attempted turning (resurfacing of the rotor face) resulted in gouges along the outer edge of the rotor surface. This rotor was used for less than 1000 miles on the L99 Camaro.
2. A used Disc Brakes Australia (DBA) brand 4000 series T3 slotted rotor. Used for one high performance track event and parked while hot, resulting in uneven surface. No attempt was made to turn this rotor. This rotor was used for less than 1000 miles on the L99 Camaro.
3. A used OEM (stock) rotor originally installed on the LS3 Camaro. This rotor was used in aggressive daily driving for approximately 70,000 miles.
4. A used OEM (stock) rotor originally installed on the L99 Camaro. This rotor was used in daily driving for approximately 40,000 miles.
5. A new Disc Brakes Australia (DBA) brand 4000 series T3 slotted rotor. This rotor was never installed on a vehicle.

As vibration response is highly dependent on mass, each rotor was weighed. Figure 13.2 shows weight measurement of the Used DBA rotor (#2). Rotor weights are listed in Table 13.1; weights ranged from 24.10 pounds for the Gouged DBA rotor (#1) to 24.90 pounds for the new DBA rotor (#5). Rotor thickness was also measured at several locations around the rotor circumference, and total face to face average thickness for each rotor are also listed in Table 13.1. Weights and thickness correlated as expected, with the heavier rotors having the greatest remaining thickness. The gouging of rotor 1 removed mass without affecting the thickness, explaining the differing weights for the pair of similarly used DBA rotors.

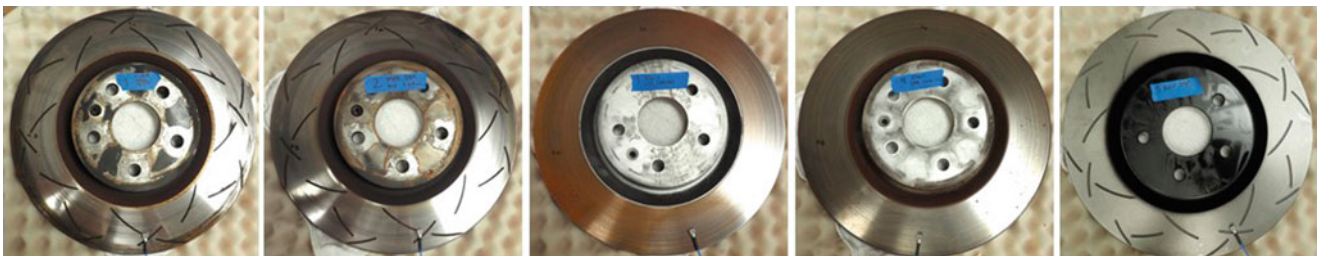


Fig. 13.1 Rotors 1 through 5 from left to right: Gouged DBA, Used DBA, OEM LS3, OEM L99, and New DBA

³Disc Brakes Australia, “Motorsport – important information”, https://www.dba.com.au/wp-content/uploads/2013/02/DBA_PROFILE.pdf accessed 10/2/2017.



Fig. 13.2 Weight measurement of rotor 2

Table 13.1 Rotor weight and average rotor thickness for each rotor

Rotor number	Rotor 1	Rotor 2	Rotor 3	Rotor 4	Rotor 5
Rotor weight (pounds)	24.1	24.3	24.8	24.3	24.9
Face to face thickness (inches)	1.24	1.24	1.25	1.21	1.26

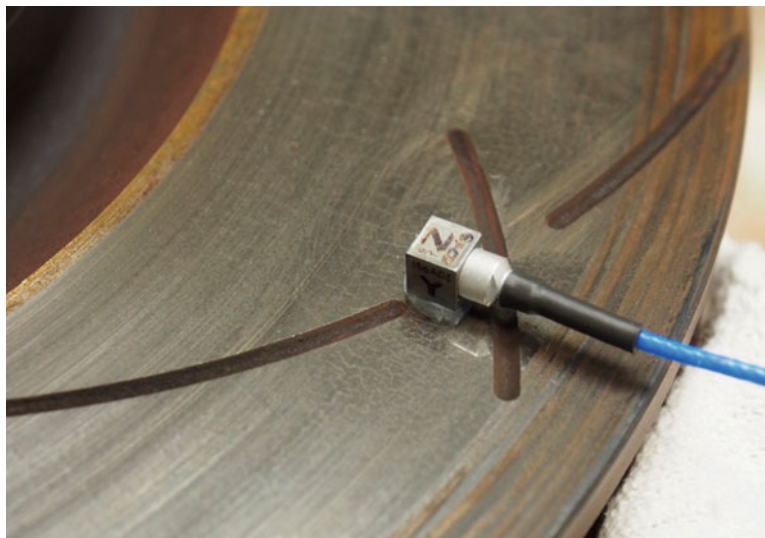


Fig. 13.3 Location of accelerometer for testing

For modal testing, rotors were set on two layers of egg crate foam to represent a free boundary condition. A tri-axial PCB 356A03 accelerometer weighing less than 0.04 ounces was mounted with wax at a location 1 inch radially inward from the edge of the rotor as pictured in Fig. 13.3. A modal hammer was used to tap the rotor at locations A and B labeled on the rotor, identified in Fig. 13.4.

For data collection, a variety of hammer tips were used and rotors were struck in either location A or B. Response was recorded and the transfer function evaluated and compared as described below.

13.4 Results

Rotor data showed good coherence and agreement between trials and test conditions. Figure 13.5 shows two representative comparisons for the frequency response functions (FRFs) between 0 and 2600 Hz for the five rotors tested with excitation at location A; one comparison shows excitation with the plastic hammer tip and the other comparison shows excitation with the



Fig. 13.4 Test set up for Used DBA rotor (#2) showing modal hammer, foam base, accelerometer location, and hammer locations A and B

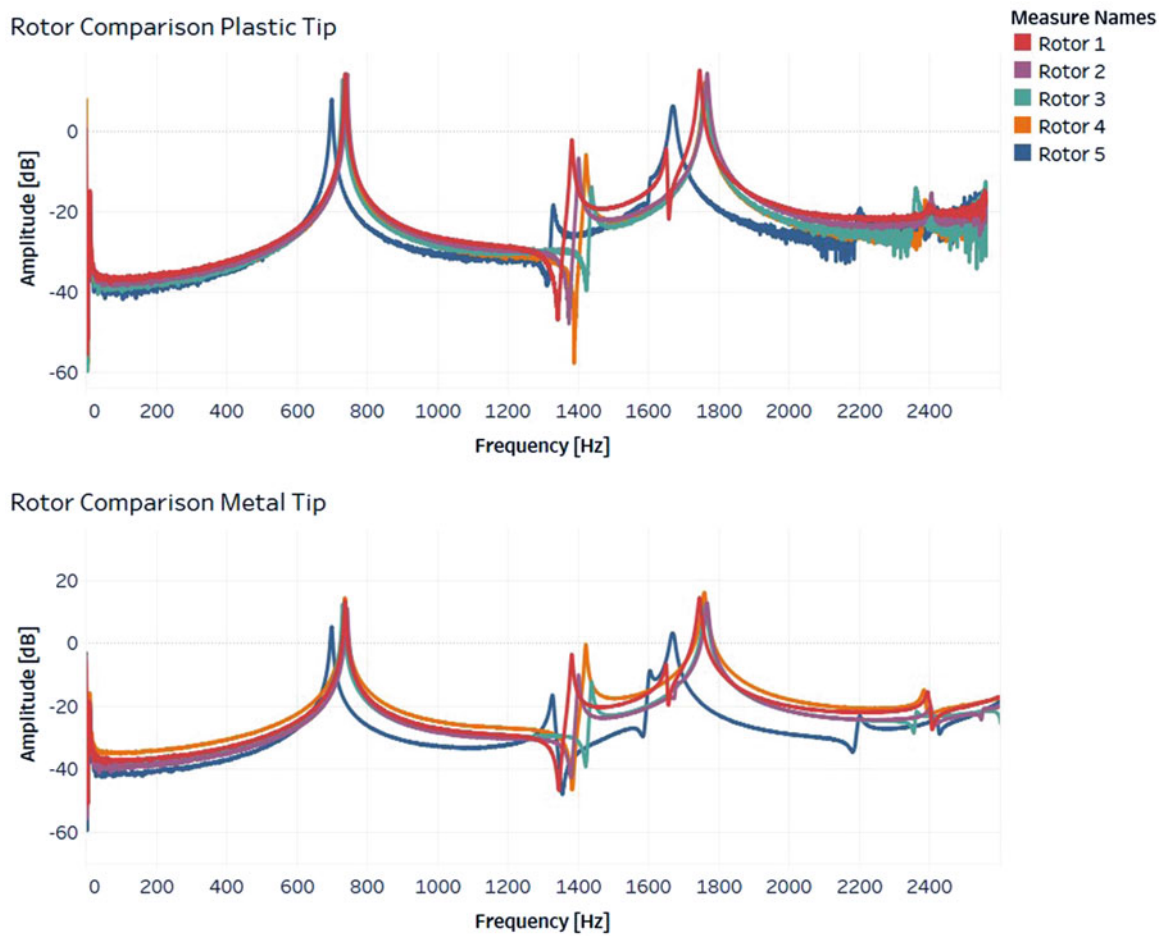
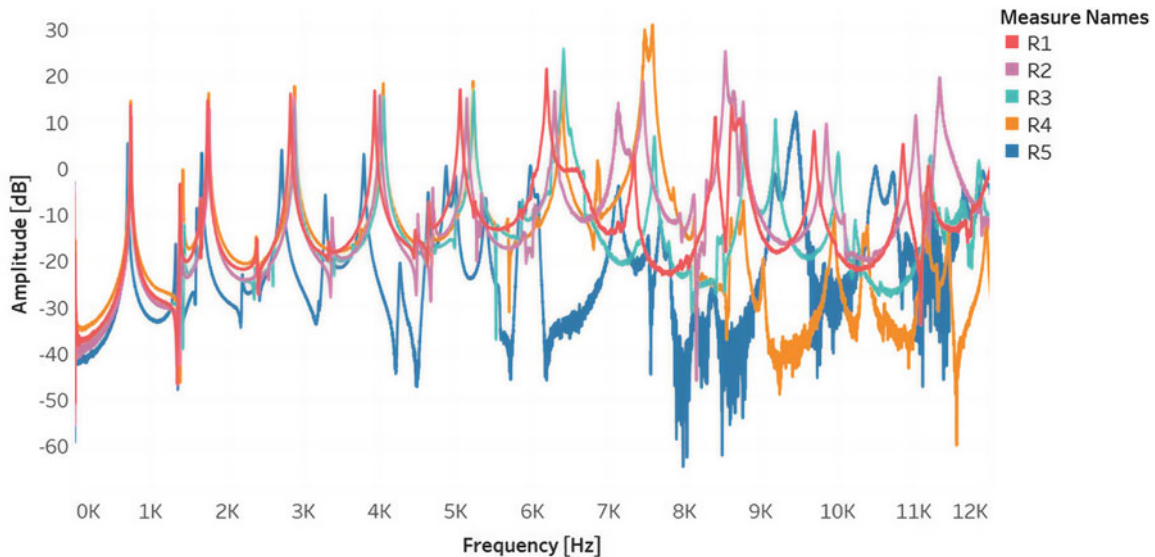


Fig. 13.5 Representative frequency response functions FRFs for the five tested rotors

Table 13.2 Rotor description, weight, and first few natural frequencies

Rotor number	Description	Rigid body mode (Hz)	Frequency 1 (Hz)	Frequency 2 (Hz)	Frequency 3 (Hz)	Frequency 4 (Hz)
1	Gouged DBA	11	737	1381	1650	1745
2	Used DBA	11	742	1400	1674	1766
3	OEM LS3	11	730	1437	–	1759
4	OEM L99	11	736	1422	–	1759
5	New DBA	11	698	1328	1606	1669

**Fig. 13.6** Frequency response comparison of five rotors with significant differences in the higher frequency range

metal hammer tip. The hammer tip type did not affect frequency response, although the metal hammer tip provided cleaner signal for higher frequency data. All of the rotors had a rigid mode at 11 Hz. The first observed natural frequency occurred around 740 Hz and the second between 1320 and 1430 Hz. The DBA rotors showed a natural frequency around 1600 to 1680 Hz that was not shown by the OEM rotors. The new DBA rotor had the greatest mass and the lowest frequencies. Table 13.2 lists the rotor description and natural frequencies observed for the rotors as tested with the plastic hammer tip at location A. There was sufficient variation between the rotors, as well as good repeatability of the trials of the same rotor at varying locations, to warrant further consideration of vibration analysis for rotor condition evaluation.

The frequencies between 700 Hz and 2600 Hz showed differences between the different rotors, but for more points of comparison, Fig. 13.6 shows FRF comparisons of the five rotors for frequencies up to 12,000 Hz. The differences become much more pronounced above 6000 Hz, with the exception of the brand new DBA rotor (#5), which showed decreased amplitude and lower frequencies from the very first natural frequency. Figure 13.7 shows the FRFs for the DBA rotors only; the gouged rotor (#1) showed only slight frequency shifts from the used DBA rotor (#2) until around 6000 Hz, at which point differences are more apparent. The gouges in rotor #1 are located along the edges of the rotor, and may not accurately represent the condition of a cracked rotor, so a fully cracked rotor will be tested in further study. The two OEM rotors were used on the same make and model of car, and despite more miles on rotor 4 corresponding with less mass and less overall rotor thickness, the frequency response function was similar; Fig. 13.8 shows the two OEM rotor responses with peak locations in the same place across the entire frequency range examined.

Trials were repeated multiple times to evaluate variability between trials. Figure 13.9 shows the agreement between three trials of the gouged DBA rotor (#1), showing minimal variation in frequency and amplitude between trials.

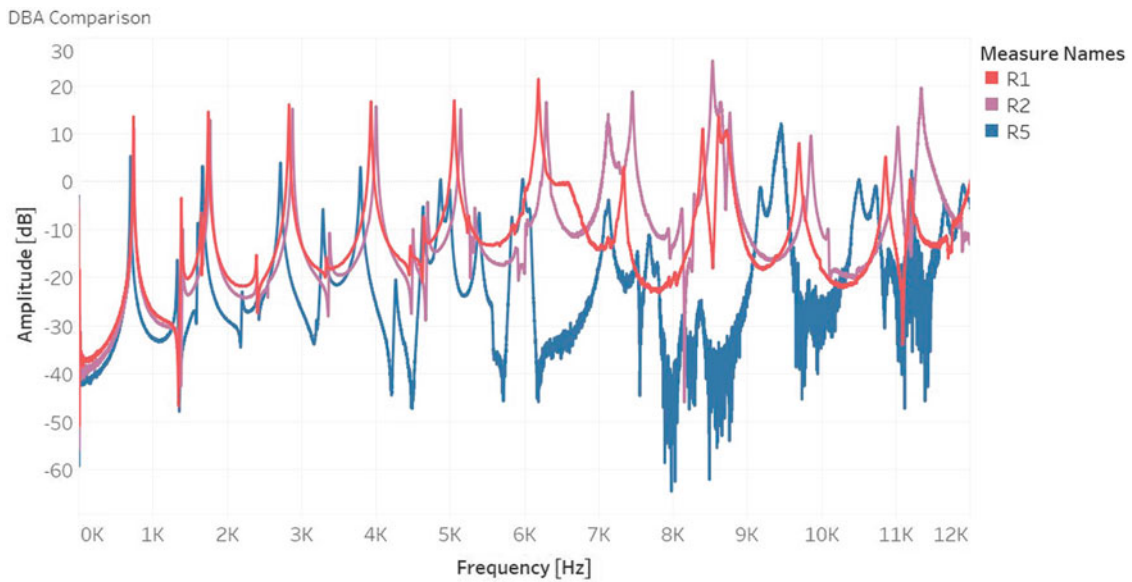


Fig. 13.7 Frequency response functions for used and new DBA rotors

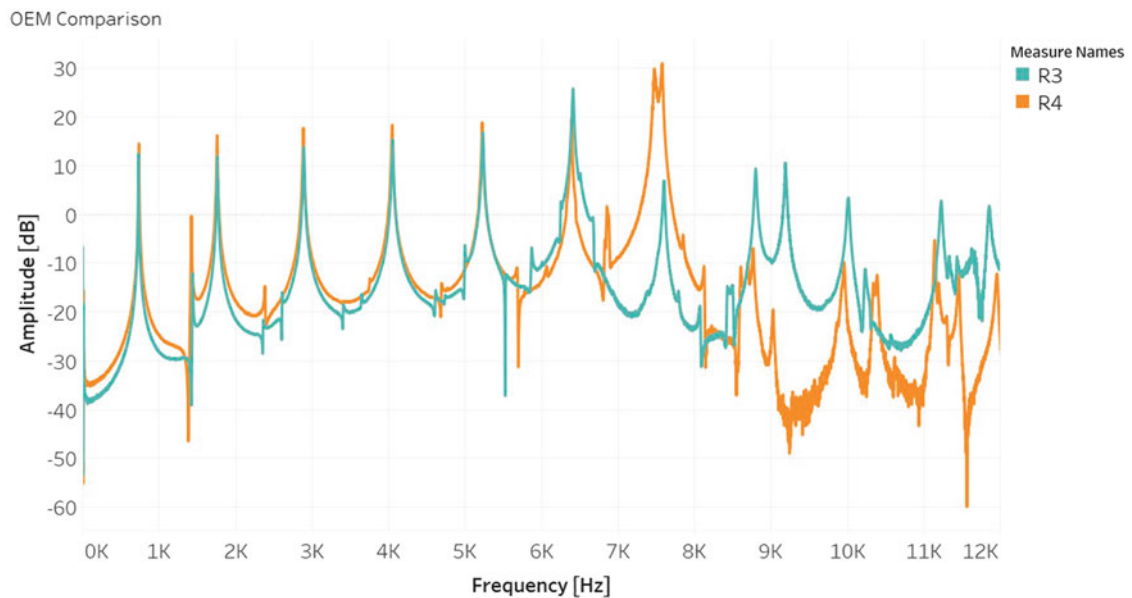


Fig. 13.8 Frequency response functions for used OEM rotors showing similar peak locations through 12 kHz

Note that this author attempted to compare the natural frequency results to other rotor modal tests, but rotor frequency response is dependent on rotor mass and size, which was not reported in other publications. The performance rotors tested by this author were intended for a nearly 4000 pound sporting vehicle so they were large in swept area, diameter, and thickness, resulting in a lower first frequency than reported by others. For instance, the first natural frequency for the rotor pictured on the left in Fig. 13.10 occurred at 1526 Hz, while the DBA rotors (such as the one pictured on the right) and OEM Camaro rotors had a first natural frequency close to 740 Hz. In the figure below, the accelerometer appears to be a similar model with the same cabling, showing the size (and corresponding mass) difference of the two rotors. This highlights the importance of running a baseline test on a new rotor to establish the frequency response for that particular rotor size and mass, since rotors vary in size for different applications. Additionally, different rotors have different arrangements of rib vanes between the surfaces, resulting in varying stiffness and further affecting the frequency response.

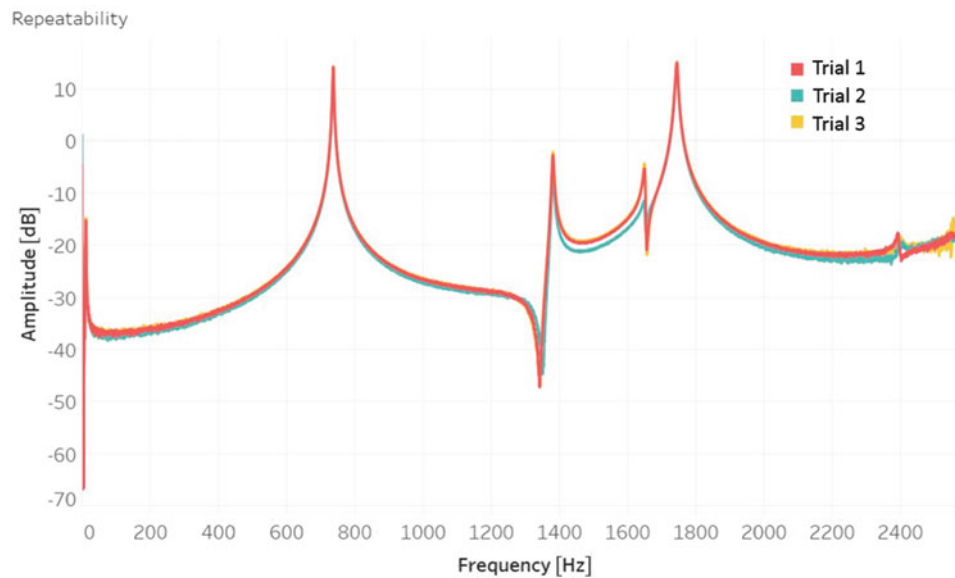


Fig. 13.9 Three representative trials of rotor 1 tested at the A location with the plastic hammer tip

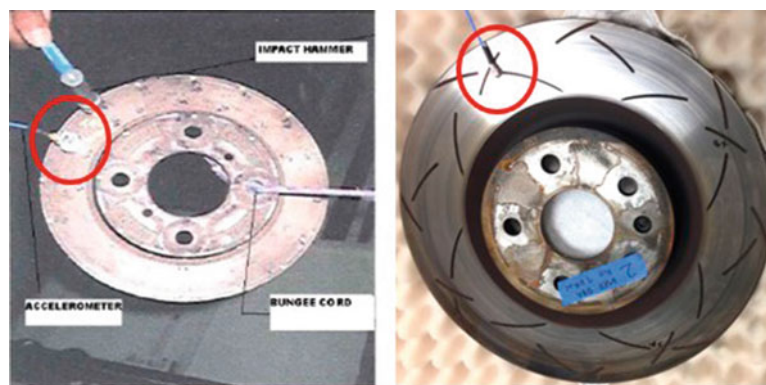


Fig. 13.10 Rotor with first natural frequency of 1526 Hz on left, (Kharate, N.K., Chaudhari, S.S.: Investigation of natural frequency and modal analysis of brake rotor using Fea and Ema. *Int. J. Innov. Res. Sci. Eng. Technol.* **3**(10), 2014) while larger rotor on right has first natural frequency of 740 Hz. Accelerometers on each rotor are circled in red

13.5 Conclusion and Future Work

The ultimate goal of the brake rotor modal testing investigation is to reduce the need to remove wheels and rotors for inspection between and following HPDE sessions by substituting vibration analysis for disassembly and visual inspection. As a first step, this investigation tested different types of rotors with varying amounts of wear by exciting with a modal hammer and measuring the frequency response with an accelerometer. Differences in location of hammer tap or hammer tip did not affect the frequency response, and the results were repeatable. Two types of rotors were tested, with two or three levels of wear for each type of rotor.

The unused DBA rotor showed greater FRF differences from the used DBA rotors than were observed between the used DBA rotors and used OEM rotors. This verifies that the mass removed from the rotor through use is the most significant driver of the FRF. The stiffness of the rotor, corresponding to rotor type and possible damage, is secondary. Thus, it would be necessary to evaluate the rotors shortly after their installation on the vehicle to establish a baseline rather than testing the rotors before use. Of course an installed rotor would also have significantly different boundary conditions, so comparison with lug nuts torqued to specification and equal brake caliper and pad contact on the rotors would be necessary and comparisons could not be directly made to these initial tests.

The benefit of the proposed evaluation is in eliminating the removal of the rotors from the vehicle. Thus, the next step for this testing is to test the various rotors on a vehicle. An accelerometer can be mounted to the installed rotor with easily removable wax and tapped with the hammer to provide data for comparison from baseline.

Although differences are apparent in the different rotor types and levels of wear, it is necessary to verify that the observed changes correspond to levels of wear, and that true damage, such as a crack, can be identified. In addition to testing of rotors on the vehicle as described, additional testing should be conducted on a cracked rotor of the same type as tested here, and testing on rotors that are used and tested a few times, so that additional wear is characterized on the same rotor.

Chapter 14

On the Veering Phenomenon Potential in High Speed Gears Design

Carlo Rosso, Elvio Bonisoli, and Fabio Bruzzone

Abstract In modern industry, the design process of most mechanical components is aimed at reducing their mass and increasing the performance, especially in weight-critical applications like aero-space engines. This approach often results in components that can have resonances in the operative range that could cause excessive vibrations and a consequential reduction of the life of the component itself. For this reason, a modal analysis check is always performed and the design process is iterated until also the dynamic behavior is acceptable. However, this approach is non-optimal, as not all resonances are excited during operation. Hence a design process that aims also to reduce the real dynamic response is proposed in this paper. By changing the geometry of thin-webbed high speed helical gears the dynamic response is altered to modify the mode shapes to obtain ones that are non-excitable by the external forces in the operative range, thus greatly improving its dynamic response. The original contribution of the paper relies on the improvement of the dynamic design process by means of the optimal balance between geometrical parameters and dynamic behavior governing phenomena like veering and crossing. Due to the high flexibility of these components, the design process is developed considering the stress-stiffening effect of the centrifugal force on the resonance frequencies and also the high influence of gyroscopic effects. To prove the effectiveness of this approach, a test case is presented with the main rotation-induced phenomena considered and the results obtained highlight the importance of the veering phenomenon in the switching between different mode shapes, and the great reduction in the response of the component.

14.1 Introduction

In the previous paper [1], the authors suggest and prove the possibility to use the veering phenomenon as a design strategy. Until this point the veering phenomenon has only been regarded as analytical and experimental curiosity of modal interactions varying a parametric structure [2, 3] or such as an undesired occurrence that can cause large problems in both civil, mechanical and aerospace field [4–6]. More related to gyroscopic systems, veering phenomena are taken into account in bladed discs and brake squeal [7–9]. Purpose and scope of this paper is hence to show that veering can be used to substitute in the stationary operative range an excitable mode shape with a non-excitable one or at least less sensitive, by simply adjusting some geometrical parameters, with a considerable reduction in the dynamic response and thus also improving fatigue life and noise levels. In the specific case the application of this methodology to thin-webbed helical gears will be investigated and the parameters variations will induce a veering towards modes that are not excitable by the meshing interaction. In particular this paper is focalized on the potential of such idea applied to very high speed gears, characterized by frequency variation due to the gyroscopic effects.

14.2 The Idea

As depicted in the previous paper [1], the proposed idea is to consider veering as a design condition. As demonstrated in the previous paper, by changing the face width of the gear it is possible to reduce the gear dynamic response in a certain frequency range. In the present paper, the gyroscopic effect is taken into account in order to validate the idea also for high speed gears.

C. Rosso (✉) · E. Bonisoli · F. Bruzzone
Department of Mechanical and Aerospace Engineering, Politecnico di Torino, Torino, Italy
e-mail: carlo.rosso@polito.it

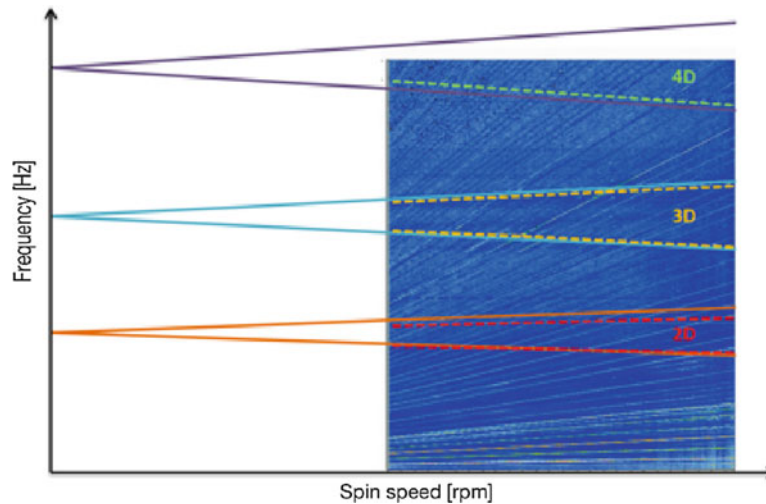


Fig. 14.1 Experimental Campbell diagram of a very high speed gear with superimposed computed one

14.3 Rotordynamics Influence on Gear Dynamics

Up until now the gear and its dynamics have been considered as static [10, 11], that is no effect of rotation has been taken into account. This is a huge assumption since gears require rotation in order to transfer power and motion. The main forces that have to be included in order to correctly model the rotation of a gear are the centrifugal force and its effects on stresses and strain in the material and more importantly the gyroscopic and Corioli's effects, which directly influence the dynamics of the body. Closed form solutions of this kind of rotor-dynamic problems are only available for a handful of very simple rotor geometries and therefore a finite element approach has been adopted. In Fig. 14.1 it is possible to highlight the importance of the phenomena, by observing an experimental Campbell diagram.

As in [12–14], in order to study the rotordynamic effect on the gears, the stressing effect of the centrifugal field has to be taken into consideration by performing a preliminary static analysis with the centrifugal load: the stresses and the deformations of the body are then applied as starting conditions for the subsequent modal analysis. This process is repeated for different rotational speeds and the results are finally combined to form a Campbell diagram, as depicted in Fig. 14.1.

14.4 Model Description

In order to highlight the possible occurrence of veering, a parametric model has been built using the Ansys Parametric Design Language (APDL) Finite Element solver suite. The gear geometry used for this example is visible in Fig. 14.2. The hub length is 60 mm, while its thickness is 7.5 mm. To simplify the geometry generation and the meshing procedures the crown of teeth has not been modelled, but it has been cut at the pitch circle which has a diameter of 281.94 mm, which corresponds to a gear with module $m = 2.54$ mm with $z = 111$ teeth. The web thickness is 2.54 mm, while the thickness of the rim is 12 mm. The parameter that varies for each different case is the face width, which has values ranging from 14 to 30 mm, with a step-by-step increase of 2 mm. The generation of the parametric geometry is tasked to a Matlab script, which writes an input file for Ansys APDL. Each model cross-section has been initially meshed with 4-node MESH200 element type, with a mesh size of 2 mm. Then the 2D mesh has been revolved forming 72 sectors of 5° each and creating 8-node SOLID185 solid elements. The number of 3D elements ranges from 18,360, for the case with the lowest value of face width, to 21,456, for the highest one. The inner surface of the hub has been constrained in the axial and tangential directions.

Then a modal analysis is performed at each rotational velocity (Ω) of interest also taking into account the gyroscopic effects, thus the damped solver of the code is employed. Then using specifically created macros the resulting complex conjugated eigenvalues and eigenvectors of each case, at each rotational velocity, were written for further processing and analysis. In order to easily observe the evolution of the different mode shapes, a hybrid Matlab-Ansys double mode tracking algorithm is integrated in the process, whose flowchart is visible in Fig. 14.2. This algorithm uses an extension of the Modal Assurance Criterion (MAC) [15] for complex eigenvectors. The Complex Modal Assurance Criterion (MACx) [16] is here

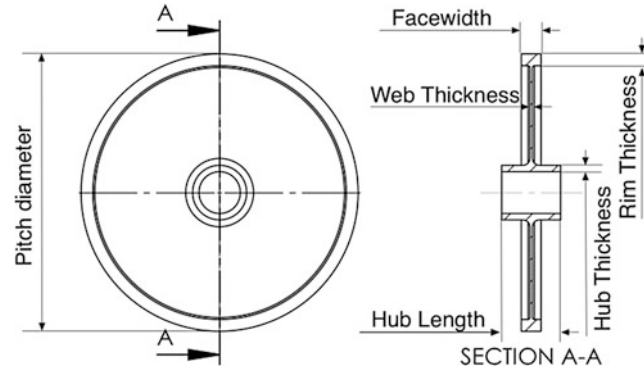


Fig. 14.2 Main parameters of the gear geometry

adopted to ensure the correct coupling of the same mode shape at the different rotational velocities, categorising them by the number of Nodal Diameters (ND) and by the number of Nodal Circumferences (NC). The definition of MACx results:

$$MACx_{r,s} = \frac{(|\Phi_r^H \Phi_s| + |\Phi_r^T \Phi_s|)^2}{(\Phi_r^H \Phi_r + |\Phi_r^T \Phi_r|) (\Phi_s^H \Phi_s + |\Phi_s^T \Phi_s|)} \quad (14.1)$$

where T and H are respectively the transpose and the Hermitian (complex conjugate transpose) operators.

This index is suitable to measure the likeness of two complex eigenvectors r and s of two different gears according to a corresponding nodes pattern and their degrees of freedom. This criterion alone is used to correlate the natural frequencies of the different designs of gears with varying facewidth. Furthermore, to correctly distinguish between the forward (FW) and backward (BW) whirling modes at the different rotational velocities in the same gear design, the results of the MACx have been weighted with an exponential function of the corresponding eigenvalues s difference (setting the arbitrary parameter $k = 0.5$):

$$Err_{r,s} = \exp \left[-k \frac{2 (|s_r| - |s_s|)}{(|s_r| + |s_s|)} \right] \quad (14.2)$$

This allows to correctly track the frequency evolution of each whirling mode automatically and robustly, and to plot this evolution due to the gyroscopic effect in the Campbell diagrams for each face width value. Firstly, Matlab generates the input files changing the face width parameter at each iteration. This input file is read and processed by Ansys, which builds the model, performs the modal analysis and stores the obtained results at each rotational speed, which are fed back to Matlab. Then the eigenvectors of the same design at the different velocities are compared to each other using the weighted MACx to correctly track the frequency evolution of each mode. Lastly, having the complex eigenvectors reordered in the same way for each face width value, the complex eigenvectors of each design are compared to follow their evolution with the variation of the face width parameter. The described algorithm is visible in Fig. 14.3.

14.5 Results

By referring to the results of [1], the presence of veering is underlined for mode ND4 (4 nodal diameters) and ND4, NC1 (4 nodal diameters, 1 nodal circumference), at a face width of 20 mm as shown in Fig. 14.4.

The variational analysis is shown for all the modes in Fig. 14.4 where each mode is followed according to MACx criteria. A lot of other modes present crossing phenomena, without any coupling. This is valid at a spin speed equal to zero. As the spin speed increases, the modes change. In Fig. 14.5 the Campbell diagram of the gear with a face width of 20 mm can be observed.

As depicted in Fig. 14.5, the mode opening affects the dynamic behaviour of the system, so it is expected that also veering phenomenon is affected by gyroscopic effects. In order to evaluate this, for some discrete face widths, ranging from 14 mm to 30 mm, the Campbell diagram is computed in order to highlight the gyroscopic effect on veering.

In Fig. 14.6 it is possible to see the envelope of all the Campbell diagrams and in particular the two modes of interest (red and green surfaces). In that figure, it is highlighted the different behaviour from backward and forward modes, through the

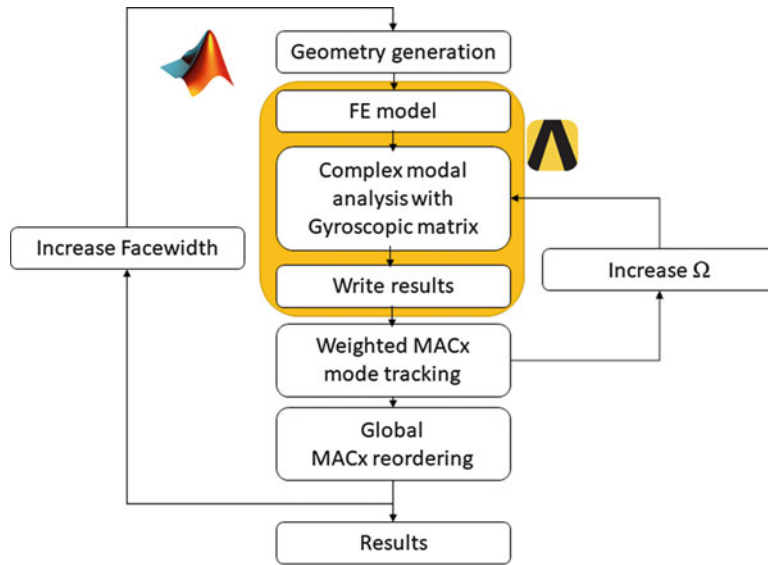


Fig. 14.3 Hybrid Matlab-Ansys algorithm

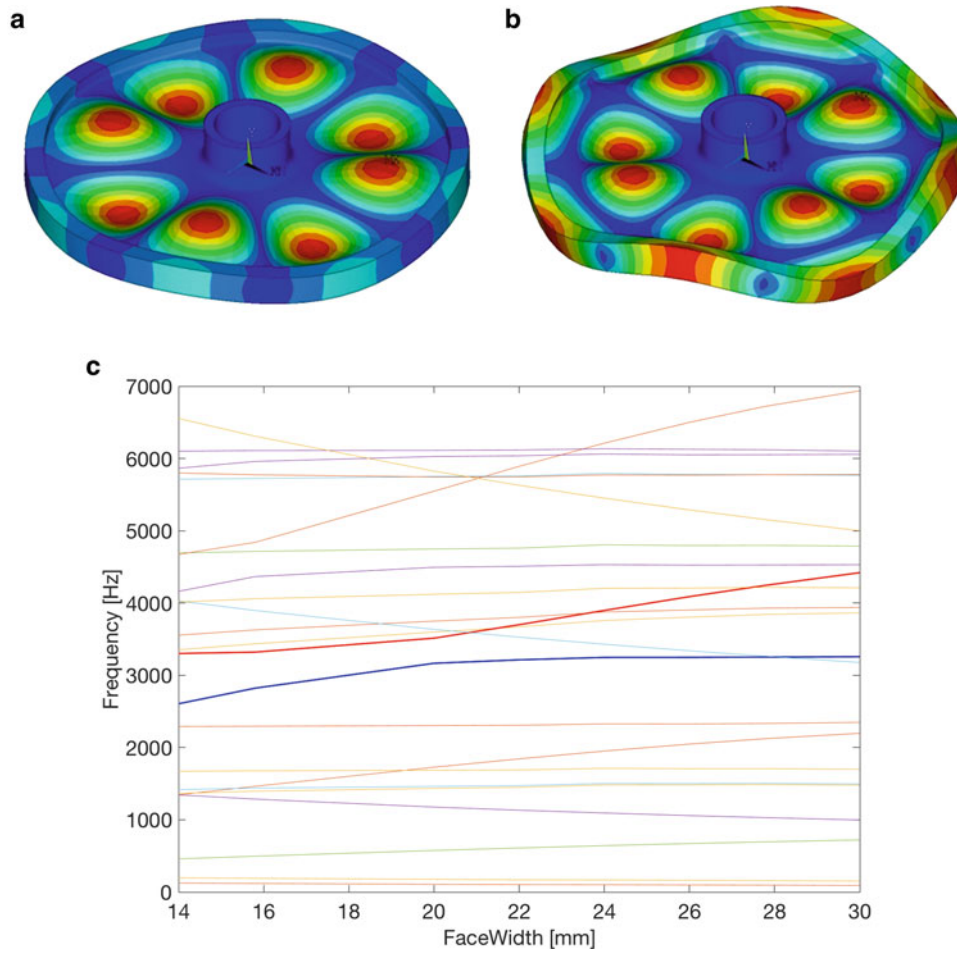


Fig. 14.4 Veering mode shapes for (a) ND = 4, NC = 1 at 3153 Hz and (b) ND = 4 at 3501 Hz for face width = 20 mm (c) Plot of the mode changes with respect to the geometric parameter modification

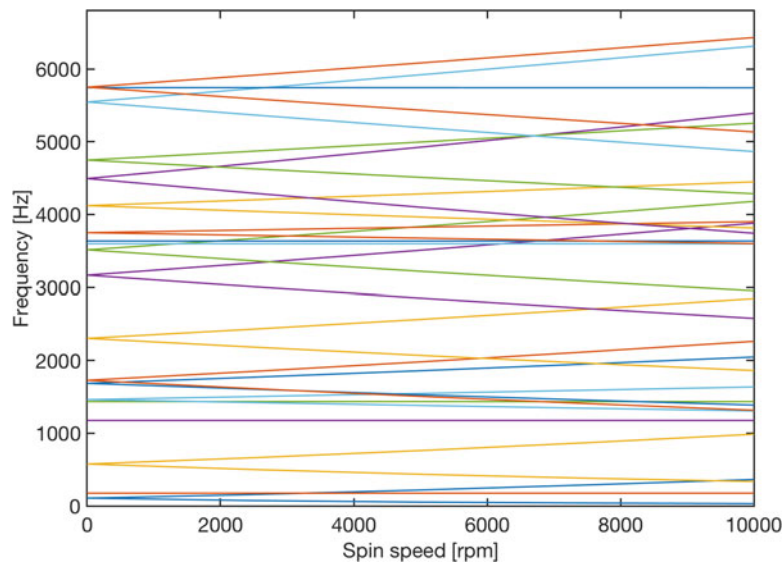


Fig. 14.5 Campbell diagram of the gear with a face width of 20 mm, with spin speed ranging from 0 to 10,000 rpm

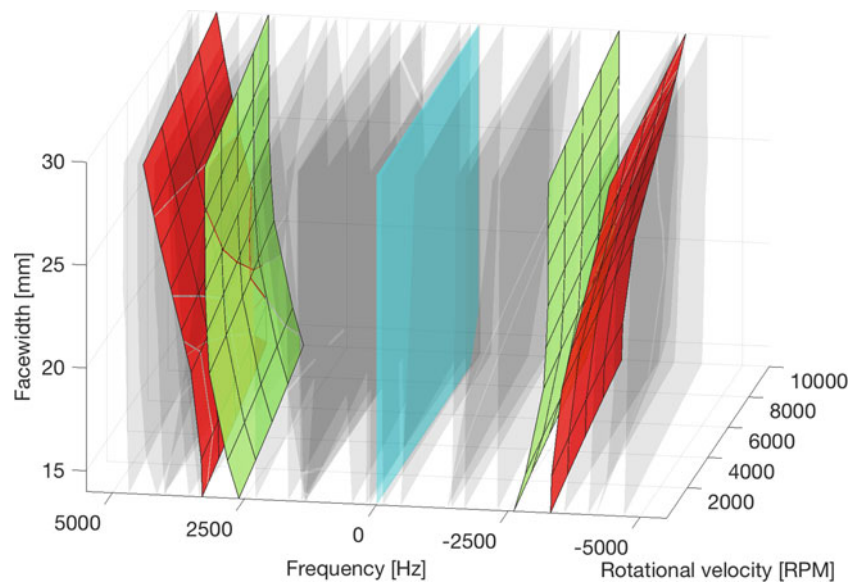


Fig. 14.6 Campbell diagram with BW and FW modes of the gear parametrically with respect to face width and rotational velocity from 0 to 10,000 rpm

azure zero plane. It is possible to notice that the veering effect is still present. The backward (BW) and the forward (FW) modes have the same trend.

If the modes are displayed in absolute frequency axis, a different conclusion can be drawn. In Fig. 14.7, the trend of BW and FW mode is superimposed. It is possible to see an intersection between the surface representing the ND4 FW mode and the ND4,NC1 BW mode. In gear dynamics, it is known that the backward mode can be excited in the same manner of the forward mode, because of the nature of the engagement. So, this seems to predict that no beneficial effect can be expected over certain spin speed (around 4000 rpm). In order to evaluate this possibility, the envelope of all possible FRF is performed.

The model is the same of [1], but in this case the gyroscopic effects are taken into account, see Fig. 14.8 for details. A great computational effort is required, in order to keep it to the minimum, just some discrete spin speeds are evaluated for some discrete values of the face width. In Fig. 14.9 it is possible to observe the trend.

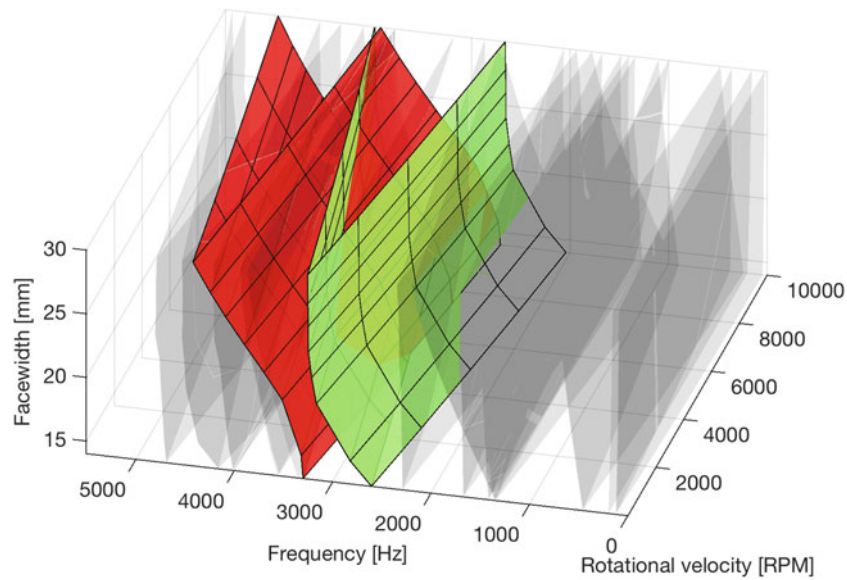


Fig. 14.7 Campbell diagram with absolute values of the gear parametrically with respect to face width and rotational velocity from 0 to 10,000 rpm (see Fig. 14.1 for comparison)

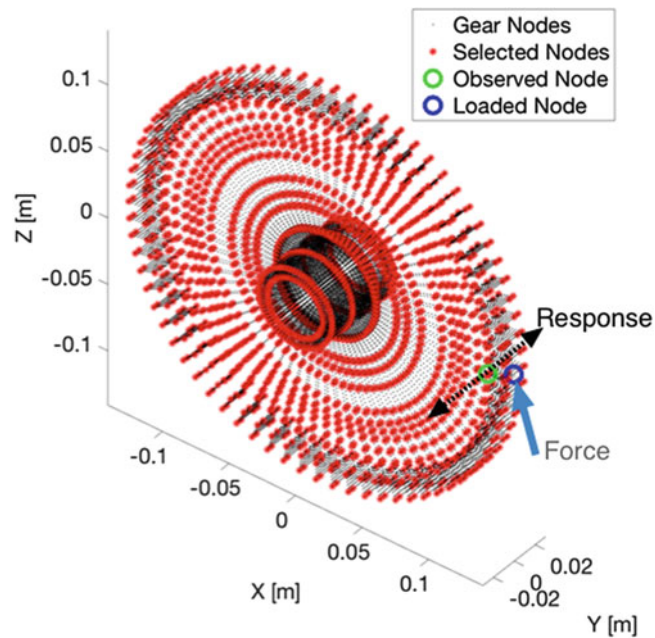


Fig. 14.8 Gear nodes, excitation position and response evaluation

By observing the results of Fig. 14.9, it is possible to note that with a face width of 24 mm and more, the displacements in the field of interest (3000–3500 Hz) are lower than for initial value of face width. This means that the indication coming from a parametric analysis of veering phenomenon can be used also regarding the gyroscopic effect, as a matter of fact, the spin speed forces the face width to grow in order to reduce the vibration amplitude, but the phenomenon still persists.

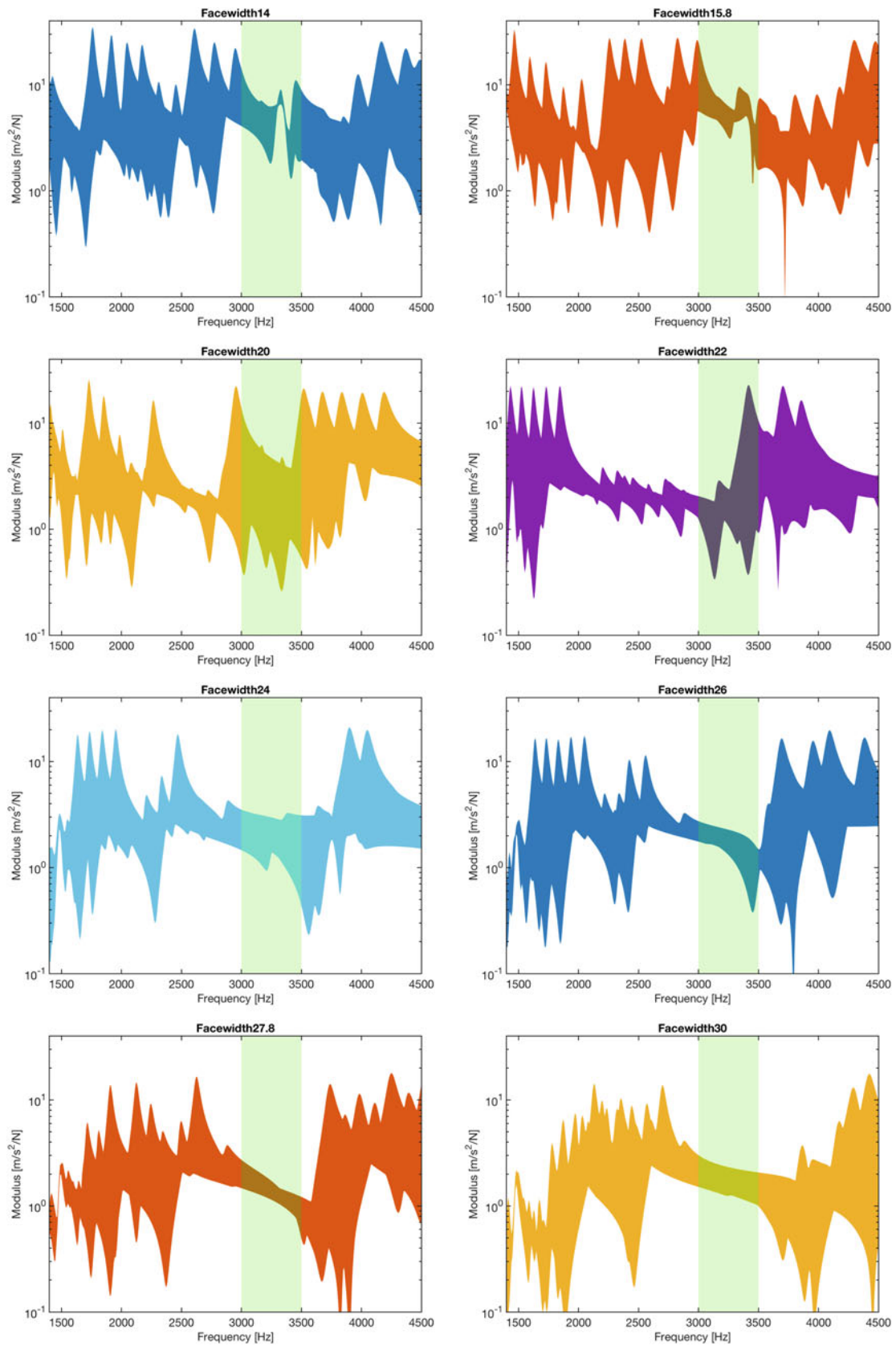


Fig. 14.9 Envelope FRF of the 8 investigated face widths

14.6 Conclusions

In the present paper, the veering phenomenon is considered as a degree of freedom for better designing a gear. As demonstrated previously, this approach is valid for non-rotating components. In this paper, the concept is extended to a rotating element. The gear is studied in combination of different spin speeds and face widths. The mode opening due to gyroscopic effects increases the distance between modes, but does not change the veering phenomenon. By considering the FRF of the different gears, it can be appreciated that modifying the face width can reduce the amplitude of the dynamic response, confirming what demonstrated for non-rotating conditions.

The idea to use veering as a design methodology proves to be effective for rotating gears. It has to be also checked considering other design parameters, such as rim and web thickness, and also checked on conical gears. Anyway it seems to be a good approach to have a proper dynamic design of a gear.

References

1. Rosso, C., Bonisoli, E., Bruzzone, F.: Could the veering phenomenon be a mechanical design instrument? In: Topics Modal Anal Test, vol. 10, pp. 85–95. Springer, New York (2017)
2. Balmès, E.: High modal density, curve veering, localization: a different perspective on the structural response. *J. Sound Vib.* **161**(2), 358–363 (1993)
3. du Bois, J.L., Adhikari, S., Lieven, N.A.J.: Eigenvalue curve veering in stressed structures: an experimental study. *J. Sound Vib.* **322**(4–5), 1117–1124 (2009)
4. Chen, X., Kareem, A., Matsumoto, M.: Multimode coupled flutter and buffeting analysis of long span bridges. *J. Wind Eng. Ind. Aerodyn.* **89**(7–8), 649–664 (2001)
5. Lin, J., Parker, R.G.: Natural frequency veering in planetary gears. *Mech. Struct. Mach.* **29**(4), 411–429 (2001)
6. Bae, J.S., Inman, D.J., Lee, I.: Effects of structural nonlinearity on subsonic aeroelastic characteristics of an aircraft wing with control surface. *J Fluids Struct.* **19**(6), 747–763 (2004)
7. Chan, Y.J., Ewins, D.J.: Management of the variability of vibration response levels in mistuned bladed discs using robust design concepts. Part 1: parameter design. *Mech. Syst. Signal Process.* **24**, 2777–2791 (2010)
8. Chan, Y.J., Ewins, D.J.: Management of the variability of vibration response levels in mistuned bladed discs using robust design concepts. Part 2: tolerance design. *Mech. Syst. Signal Process.* **24**, 2792–2806 (2010)
9. Akay, A., Giannini, O., Massi, F., Sestieri, A.: Disc brake squeal characterization through simplified test rigs. *Mech. Syst. Signal Process.* **23**, 2590–2607 (2009)
10. Hotait, M.A., Kahraman, A.: Experiments on the relationship between the dynamic transmission error and the dynamic stress factor of spur gear pairs. *Mech. Mach. Theory.* **70**, 116–128 (2013)
11. Li, S., Kahraman, A.: A tribo-dynamic model of a spur gear pair. *J. Sound Vib.* **332**, 4963–4978 (2013)
12. Geradin, M., Kill, N.: A new approach to finite element modelling of flexible rotors. *Engg Comput.* **1**(1), 52–64 (1984)
13. Nelson, H.D., Mc Vaugh, J.M.: The dynamics of rotor-bearing systems using finite elements. *ASME J Manufact Sci Engg.* **1**, 52–64 (1976)
14. Rosso, C., Bruzzone, F.: Benchmark of the rotordynamics capabilities of the most prominent finite element method software. *Int J Mechanics Control.* **17**(2), 11–18 (2016)
15. Allemang R.J., Brown D.L.: A correlation coefficient for modal vector analysis. In: Proceeding of the I IMAC, pp. 110–116 (1982)
16. Vacher P., Jacquier B., Bucharles A.: Extensions of the MAC criterion to complex modes. In: Proceeding of ISMA, pp. 2713–2725 (2010)

Chapter 15

Modal Truncation in Experimental Modal Analysis

Marius Tarpø, Michael Vigsø, and Rune Brincker

Abstract Some methods in experimental modal analysis rely on a finite set of modes and they neglect the higher modes. However, this approach causes a truncation of the modal decomposition and the modal truncation introduces errors of unknown magnitude. In this paper the effect of modal truncation is investigated on a test specimen in the laboratory. It is found that the system response is dependent of the frequency and the distribution of the load. Modal truncation can introduce significant errors if the set of mode shapes does not efficiently span the spatial distribution of the load.

15.1 Introduction

The modal decomposition describes the structural dynamic response where the mode shapes of the system uncouple the dynamic response into the modal coordinates. When we truncate the modal decomposition to only include the first number of modes, we have a smaller set of modal coordinates to describe the system. This simplifies the structural response and it is frequently used to ease the calculation in structural dynamics. In experimental modal analysis, we identify a number of modes and we use them with experimental techniques for different purposes like; full field response estimation, fatigue analysis, load estimation, damage detection etc.

Normally, the truncated set of mode shapes provides good results however it might result in significant errors in certain instances where omitted modes contribute to the response [1–7]. The gross behaviour of structures is generally captured by the modes that are located in the frequency range of the load [3, 8]. However, higher modes might influence the localised behaviour by their non-trivial contribution. Therefore, a truncation of the modal decomposition can lead to errors of the representation of the response [1, 5, 7, 8]. This is also the case for experimental techniques that uses a truncated set of mode shapes to represent the structural response.

The phenomenon of modal truncation is described in structural computation and finite element modelling. Generally, these fields of research state that we can calculate the response as a combination of the dynamic responses of the lower modes and a correction term, which is based on the quasi static response of the remaining modes. Two types of corrections are created; static residual and residual vectors. The static residual uses static correction terms to adjust for the modal truncation. Whereas the other method make use of residual modes, also called “assumed modes” or “pseudo modes”, combined with the mode shapes [9].

This paper showcases the potential problem of the modal truncation in an experimental setting. We find that the required number of modes in a modal decomposition depends on the frequency range and the spatial distribution of the loading.

M. Tarpø (✉) · M. Vigsø
Aarhus University, Aarhus, Denmark
e-mail: martar@eng.au.dk; mvigso@eng.au.dk

R. Brincker
Department of Civil Engineering, Technical University of Denmark, Kongens Lyngby, Denmark

15.2 Theory

15.2.1 Truncation of the Modal Decomposition

The modal decomposition says that any response from a linear system is a linear composition of its mode shapes. This means that the response of a linear structure is located in the subspace of its mode shapes.

$$\mathbf{y}(t) = \sum_{i=1}^N \boldsymbol{\phi}_i q_i(t) \quad (15.1)$$

where $\mathbf{y}(t) \in \mathbb{R}^{N \times 1}$ is system response, $\boldsymbol{\phi}_i \in \mathbb{R}^{N \times 1}$ is the mode shape, $q_i(t)$ is the modal coordinate for mode i and N is the degree of freedom for the system.

Let us say that we only use K modes in the modal decomposition then we have a smaller set of modes to describe the system. Hence, we have introduced an error in our representation of the structural response due to the modal truncation. This error is often referred to as the residual effect.

$$\boldsymbol{\varepsilon}(t) = \sum_{i=K+1}^N \boldsymbol{\phi}_i q_i(t) \quad (15.2)$$

As long as this error is insignificant then the truncation of the modal decomposition is acceptable. However, it is hard to estimate the magnitude of this error. We will look at the modal coordinates to get a better understanding of the truncation error. We calculate the modal response in the frequency domain.

$$Q_i(\omega) = H_i(\omega) \boldsymbol{\phi}_i^T \mathbf{X}(\omega) \quad (15.3)$$

where $\mathbf{X} \in \mathbb{R}^{N \times 1}$ is the load in the frequency domain, $H_i(\omega)$ is the frequency response function for the i th mode.

$$H_i(\omega) = \frac{1}{m_i (-\square + j2\zeta_i \omega_i \omega + \omega_i^2)} \quad (15.4)$$

where m_i is the modal mass, ω_i is natural frequency and ζ_i is the damping ratio for mode i .

In the following, we will look at two types of loading: random or fixed spatial distribution of the load. A load with a fixed spatial distribution can be separated like

$$\mathbf{X}(\omega) = \mathbf{F}S(\omega) \quad (15.5)$$

where $\mathbf{F} \in \mathbb{R}^{N \times 1}$ is the spatial distribution of the load and $S(\omega)$ is the scalar function defining the temporal variation of the load. Therefore, we can rewrite the expression for the modal coordinates in the frequency range, Eq. (15.3), if the load has a spatial distribution.

$$Q_i(\omega) = H_i(\omega) S(\omega) \boldsymbol{\phi}_i^T \mathbf{F} \quad (15.6)$$

We see that the contribution of each mode is dependent of the scalar product of frequency response function and the frequency range of the load. However, it is also dependent on the inner vector product between the given mode shape and the spatial distribution of the load. This tells us that a modal coordinate is given both by the frequency range and the spatial distribution of the load. But if the load has a random spatial distribution then the modal response only depends on the frequency range of the load. Therefore, the residual effect depends on frequency range and spatial distribution of the load.

15.2.1.1 Modal Truncation of the Quasi Static Contribution

Often, the omitted modes are located above the frequency range of the load when we truncate the modal decomposition. When the load frequency is located way before the natural frequencies of the modes then the omitted modes act quasi static.

We will show this by an example where the frequency range of the load is restricted and we omit all modes outside this range. Here we assume that the first omitted mode n and all higher modes have much higher natural frequencies, ω_n , than the highest load frequency, ω_x . This means; $\omega_x \ll \omega_n$. So we can rewrite the frequency response function, Eq. (15.4), for the truncated modes when we roughly approximate that any term in denominator with ω is insignificant compared with the term ω_n^2 . Then the modal coordinates for truncated modes are

$$\tilde{Q}_n(\omega) \approx \begin{cases} \frac{1}{m_n \omega_n^2} S(\omega) \phi_n^T \mathbf{F} & 0 \leq \omega \leq \omega_x \\ 0 & \omega > \omega_x \end{cases} \quad (15.7)$$

We see on Eq. (15.7) that the modal coordinates is no longer a dynamic response but a quasi static response. Therefore, we approximate the residual effect as

$$\tilde{\boldsymbol{\varepsilon}}(t) \approx s(t) \sum_{n=K+1}^N \frac{\phi_n \phi_n^T \mathbf{F}}{m_n \omega_n^2} \quad (15.8)$$

This is a quasi static error, which depends on the inner vector product between the mode shape and spatial distribution of the load and the modal mass and frequency. So a truncation of higher modes might give a amplitude error of the system response because we have removed a quasi static contribution from the residual modes.

15.2.2 Reduction of Subspace

We would like to be able to remove the influence of certain modes from a measured system response in order to access the effect of modal truncation. In order to do this we will use a linear transformation, which we base on the modal decomposition. The estimated modal coordinates for K modes is found when we project the system response onto the subspace of the mode shapes.

$$\hat{\mathbf{q}}(t) = \Phi_K^+ \mathbf{y}(t) \quad (15.9)$$

where $\hat{\mathbf{q}}(t) \in \mathbb{R}^{K \times 1}$ is the estimated modal coordinate matrix and $\Phi_K \in \mathbb{R}^{N \times K}$ is the truncated modal matrix, which contains the applied mode shape as columns. Then we can find the truncated system response.

$$\hat{\mathbf{y}}(t) = \Phi_K \hat{\mathbf{q}}(t) \quad (15.10)$$

where $\hat{\mathbf{y}}(t) \in \mathbb{R}^{N \times 1}$ is the truncated system response with a reduced subspace. This transformation projects the response onto the column space of the modal matrix and thereby it reduces the subspace of the response to only include the given modes.

15.2.3 Quality Measurements

It is useful to access the difference between a measured and the equivalent truncated response so we know the errors of a modal truncation. To assess the difference, we utilise the coefficient of determination, $R_{t,i}^2$, from model validation in both time and frequency domain [10].

$$R_{t,i}^2 = 1 - \frac{\sum_{k=1}^N (y_i(t_k) - \hat{y}_i(t_k))^2}{\sum_{k=1}^N (y_i(t_k) - \mathbf{E}[y_i(t)])^2} \quad (15.11)$$

$$R_{f,i}^2 = 1 - \frac{\sum_{k=1}^N (|Y_i(f_k)| - |\hat{Y}_i(f_k)|)^2}{\sum_{k=1}^N (|Y_i(f_k)| - \mathbf{E}[|Y_i(f)|])^2} \quad (15.12)$$

where $E[X]$ is the expected value of X , $y_i(t)$ & $\hat{y}_i(t)$ are the measured and truncated response for sensor i and $Y_i(f)$ & $\hat{Y}_i(f)$ are the Fourier transformed measured and truncated response for sensor i .

15.3 Case Study

We will show the effect of modal truncation on a small structure in the laboratory. The test specimen is a T-shaped steel structure, which is fixed with claps, see Fig. 15.1. In this case study, we will assume that we are only interested in the first 100 Hz of the system. We will identify the modes located inside this frequency region and we will project the response onto the column space of the mode shapes using Eq. (15.10). By projecting the response onto the subspace of the used mode shapes, we remove the contribution of the higher modes and all noise that are perpendicular to this subspace. This is to illustrate the effect of neglecting the contribution of the others modes in an experimental setting.

In this paper, we will call the modes located in given frequency range for the “*dynamic modes*” and we will define the modes located outside this range as “*residual modes*”. So we will look at the truncation error by using the dynamic modes that are located in the given frequency range. Then we will add one and then two residual modes to the modal decomposition from outside this frequency range and calculate the truncation error. This is in order to see if modes outside the frequency range will have a contribution to the system response.

15.3.1 Set Up

Ten uniaxial accelerometers with a sensitivity of 100 mV/g and two geophones are applied to the structure as seen on Fig. 15.2. The geophones work as shakers when we apply a current to them. Compressed air excites the structure from 3 directions and this loading creates turbulence around the structure and the excitation resembles white Gaussian noise. One set of data is acquired where the geophones are idle and this data set is used to identify the modal parameters using operational modal analysis [11].

A time length of 300 s is used with a sampling frequency of 1651 Hz for each data set. The data is decimated to a new frequency of 825.5 Hz [11]. We bandpass filter the data sets from 5 to 100 Hz, see Fig. 15.3. The low frequency cut-off is applied to remove noise from DC.

Fig. 15.1 Photo of the test specimen in the lab

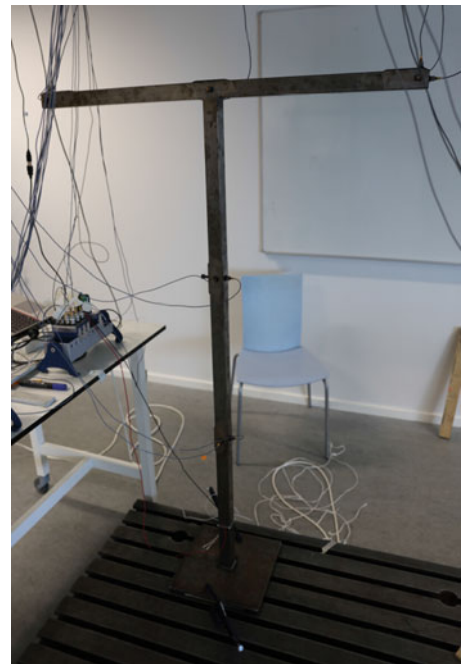


Fig. 15.2 Position of sensors, red arrows are for uniaxial accelerometers and blue arrows are the geophones

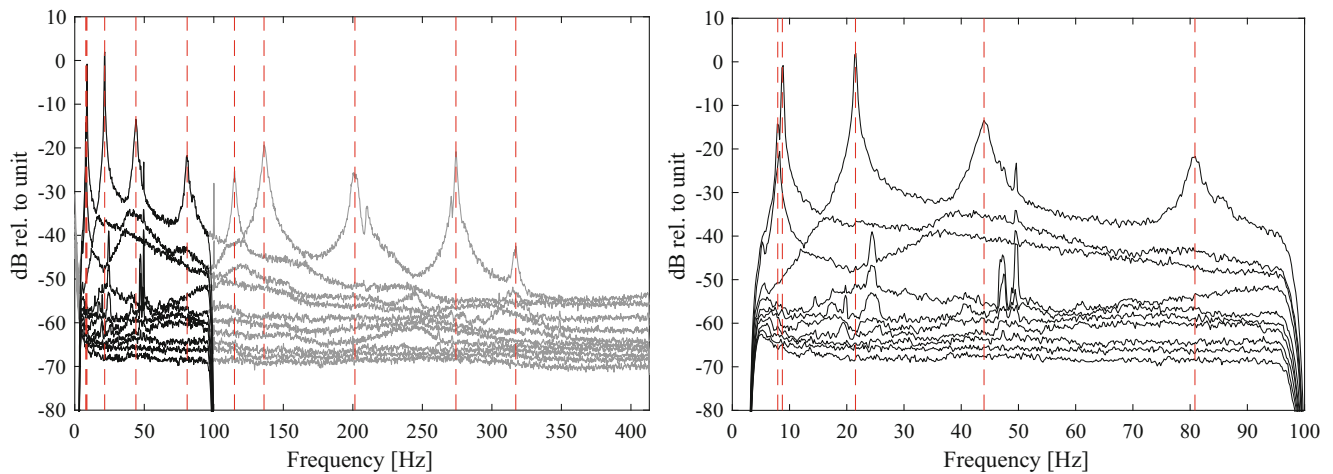
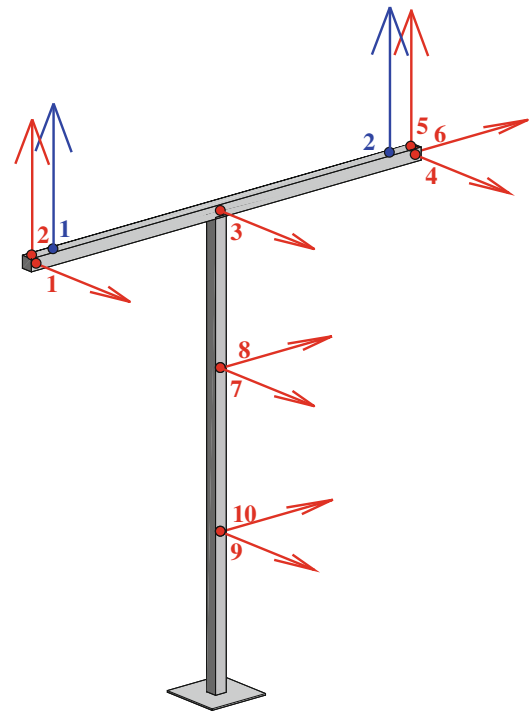


Fig. 15.3 Case 1, singular value decomposition of the spectral density matrix

An Operational Modal Analysis is performed where the *Frequency Domain Decomposition* is used to identify the modes [12]. We found five dynamic modes in the frequency region and five residual modes outside this range, see Figs. 15.3 and 15.4.

15.3.2 Case 1

In this case, the geophones are idle and only compressed air is used as excitation and therefore the load has no defined spatial distribution. The measured response is projected onto the subspace of the five dynamic modes using Eq. (15.10). Afterwards, we add one and then two residual modes to the modal decomposition. We calculate the coefficient of determination in time and frequency domain for each version of the modal decomposition, see Table 15.1.

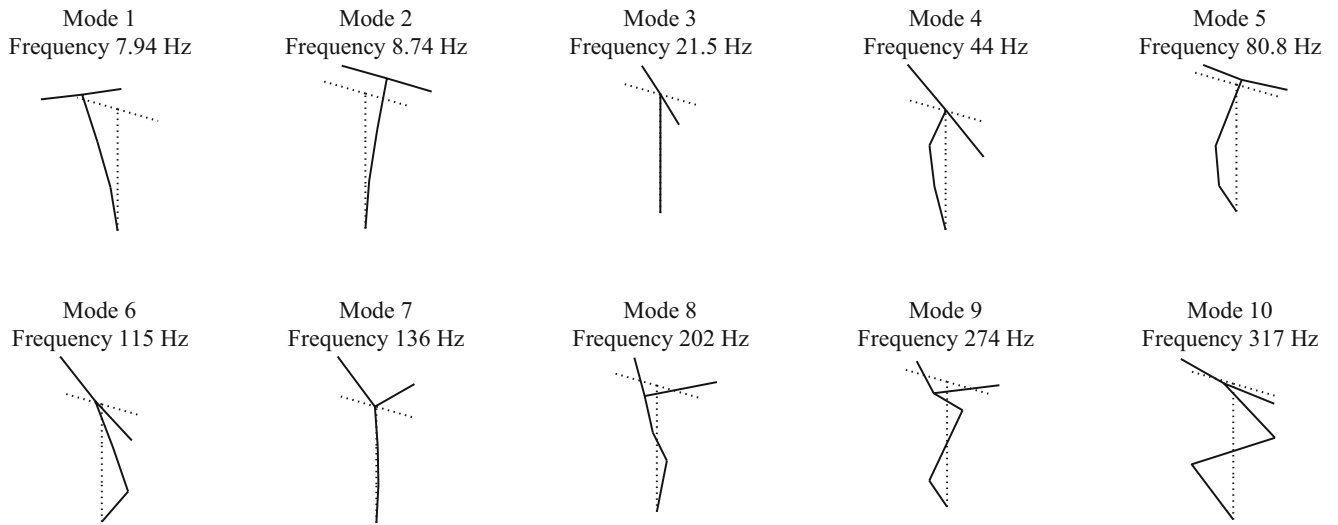


Fig. 15.4 Identified experimental mode shapes

Table 15.1 Quality measurements for case 1

		Sensor 1	Sensor 2	Sensor 3	Sensor 4	Sensor 5	Sensor 6	Sensor 7	Sensor 8	Sensor 9	Sensor 10
Dynamic modes	R_t^2	1.0000	0.9916	0.9990	1.0000	0.9919	0.9958	0.9997	0.9969	0.9977	0.9850
	R_f^2	1.0000	0.9955	0.9995	1.0000	0.9975	0.9977	0.9998	0.9979	0.9985	0.9866
Dynamic modes + 1 residual mode	R_t^2	1.0000	0.9924	0.9990	0.9999	0.9917	0.9992	0.9997	0.9986	0.9977	0.9973
	R_f^2	1.0000	0.9960	0.9995	1.0000	0.9974	0.9995	0.9998	0.9991	0.9985	0.9984
Dynamic modes + 2 residual modes	R_t^2	1.0000	1.0000	0.9990	1.0000	1.0000	0.9996	0.9997	0.9986	0.9977	0.9978
	R_f^2	1.0000	1.0000	0.9995	1.0000	1.0000	0.9997	0.9998	0.9991	0.9985	0.9986

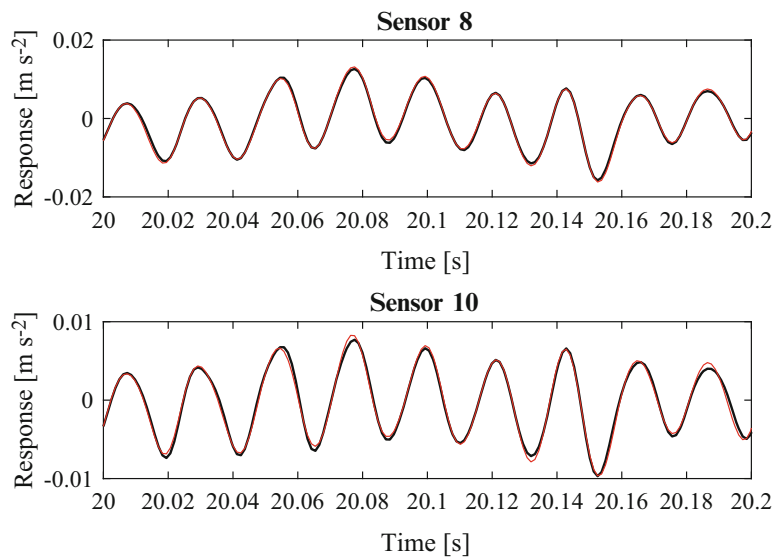


Fig. 15.5 Case 1, only dynamic modes: response of truncated response, black is the measured and red is the truncated response

Generally, we do not achieve a better representation of the response by adding residual modes to the modal decomposition. The two worst truncated responses are sensor 8 & 10 and the recorded acceleration for these two sensors plotted on Figs. 15.5 and 15.6 for the scenario with dynamic modes only.

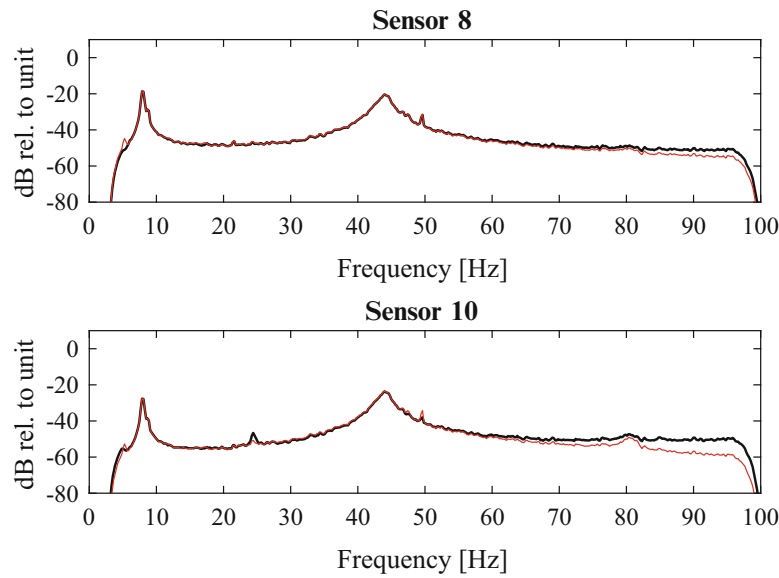


Fig. 15.6 Case 1, only dynamic modes: spectrum of truncated response, black is the measured and red is the truncated response

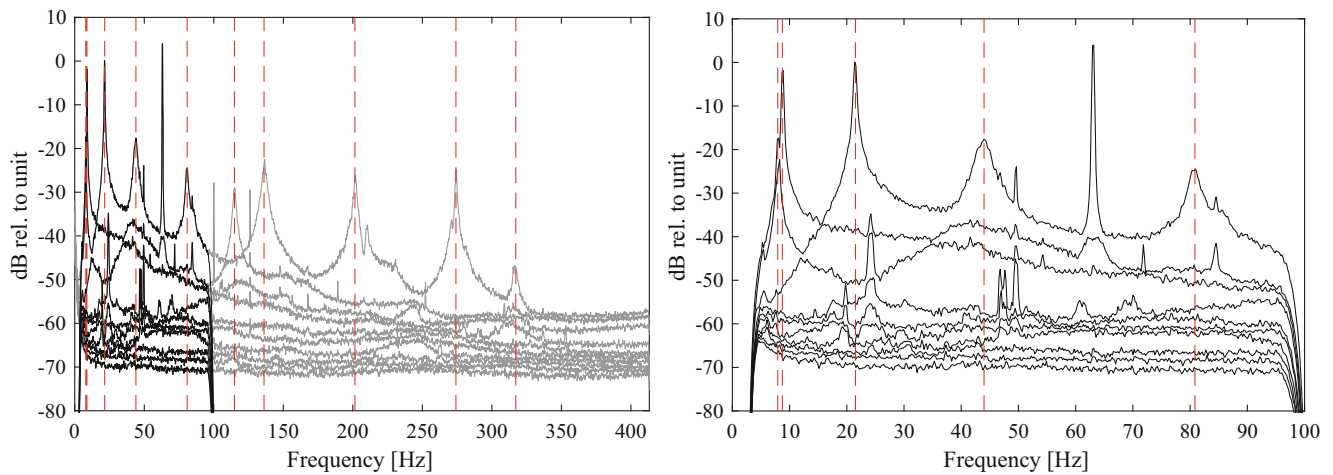


Fig. 15.7 Case 2, singular value decomposition of the spectral density matrix

15.3.3 Case 2

In the next case, we excite the structure with compressed air. Additionally, we apply a current to the second geophone so it excites the structure at a frequency of 64 Hz, see Fig. 15.7 for spectral density plot. This means that a significant part of the load has a fixed spatial distribution in this case.

Like in Case 1, the five dynamic mode shapes are used for the projection of the subspace using Eq. (15.10). Next, we add one and two residual modes from outside the frequency region. Then the coefficients of determination are calculated for the time and frequency domain, see Table 15.2.

Generally, the truncated response using only the dynamic mode has a high correlation with the measured response but a few sensors deviate. The two worst channels are for sensor 5 & 6 and the responses for the sensors have wrong amplitudes, see Figs. 15.8 and 15.9. By adding residual modes, we see an increase in the quality measurements, which is especially evident for sensor 5 & 6. The quality fit for sensor 6 increases with more than 0.1 by adding one residual mode. Whereas, sensor 5 needs two residual modes to have a quality fit above 0.93. The response for sensor 5 & 6 using two residual modes are plotted in Figs. 15.10 and 15.11.

Table 15.2 Quality measurements for case 2

		Sensor 1	Sensor 2	Sensor 3	Sensor 4	Sensor 5	Sensor 6	Sensor 7	Sensor 8	Sensor 9	Sensor 10
Dynamic modes	R_t^2	0.9999	0.9759	0.9991	0.9999	0.9236	0.8625	0.9991	0.9947	0.9976	0.9745
	R_f^2	0.9999	0.9759	0.9996	0.9999	0.9227	0.8565	0.9991	0.9947	0.9984	0.9745
Dynamic modes + 1 residual mode	R_t^2	0.9999	0.9709	0.9991	0.9999	0.9300	0.9718	0.9994	0.9990	0.9977	0.9993
	R_f^2	0.9999	0.9708	0.9995	1.0000	0.9293	0.9706	0.9995	0.9991	0.9985	0.9994
Dynamic modes + 2 residual modes	R_t^2	1.0000	1.0000	0.9990	0.9999	1.0000	0.9977	0.9997	0.9989	0.9978	0.9989
	R_f^2	1.0000	1.0000	0.9995	1.0000	1.0000	0.9977	0.9998	0.9990	0.9985	0.9990

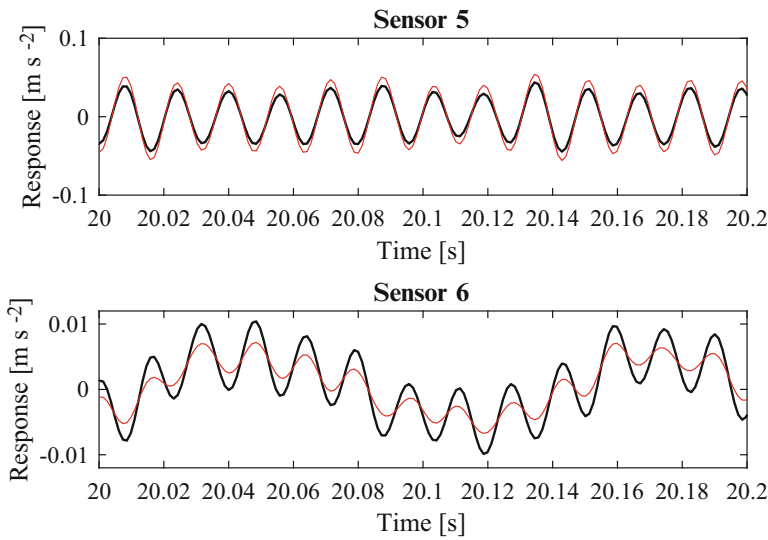


Fig. 15.8 Case 2, only dynamic modes: response of truncated response, black is the measured and red is the truncated response

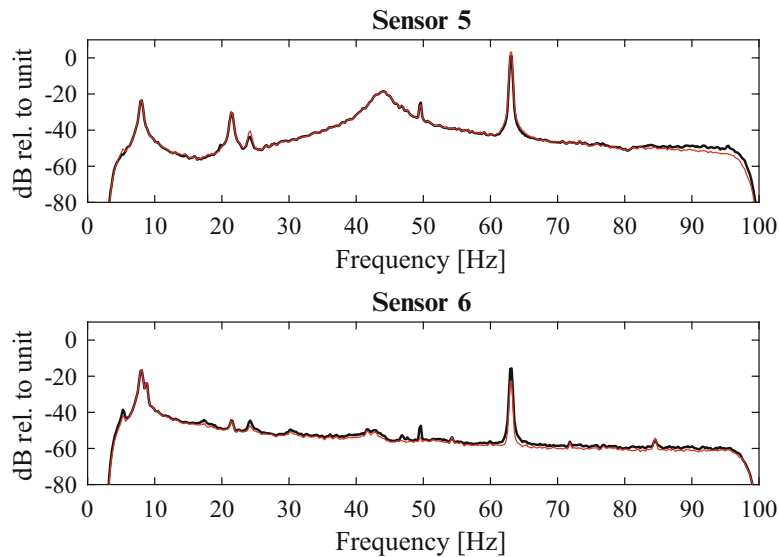


Fig. 15.9 Case 2, only dynamic modes: spectrum of truncated response, black is the measured and red is the truncated response

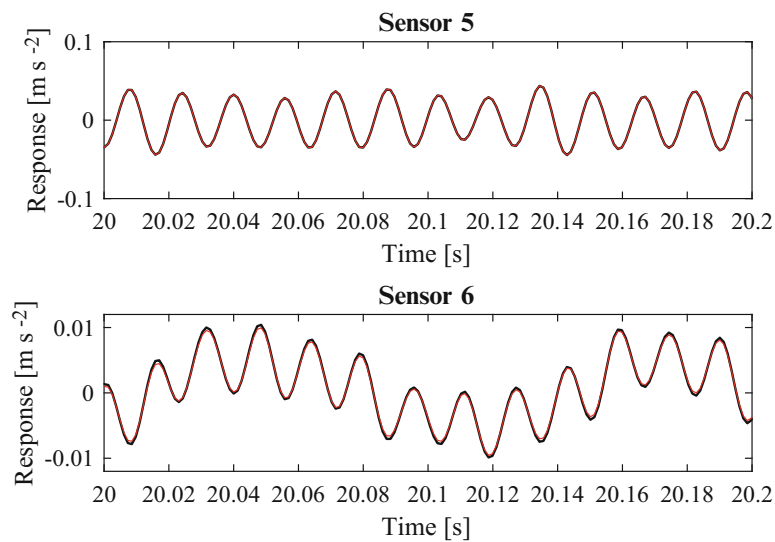


Fig. 15.10 Case 2, dynamic modes + 2 residual modes: response of truncated response, black is the measured and red is the truncated response

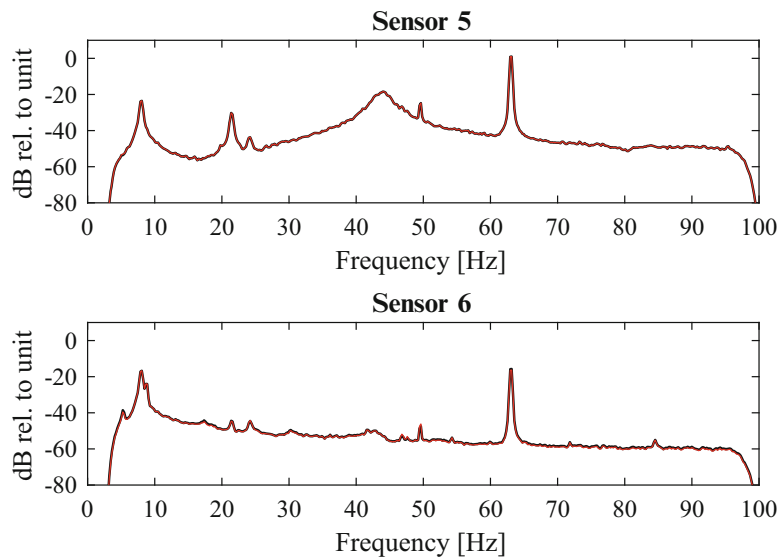


Fig. 15.11 Case 2, dynamic modes + 2 residual modes: spectrum of truncated response, black is the measured and red is the truncated response

15.4 Discussion

First, we should note that the projection onto a fixed number of mode shapes removes noise and modal response alike if their subspaces are orthogonal to the new subspace of the projection. Therefore, we will remove noise and this reduction of noise will affect the quality measurements since we are using a signal with noise as reference. The resolution of the experimental mode shapes also has an influence on the assumption that we can reduce the subspace. However, we will assume that these errors are insignificant.

Overall the modal truncation has a low error and most sensors maintain the same response as measured when we use the five dynamic mode shapes. In Case 1, the first five dynamic mode shapes were sufficient to span the measured response but in Case 2 we needed additional mode shapes to accurately span the measured response for a few of the sensors. Here sensor 5 & 6 are less precise in Case 2 where a part of the load had a defined load pattern. By observing Fig. 15.2, we can see that the excitation by the second geophone primarily results in responses for sensor 2, 5 & 6. Furthermore, we can observe in Fig. 15.4 that the first five mode shapes do not span this movement. The sixth and seventh mode shapes add more information to better span the response that is caused by the geophone.

In these tests, we see that an excitation with a fixed spatial distribution has a higher residual effect compared with an excitation with a random load pattern. This is in accordance with the theory of the residual effects. The theory suggests that a fixed spatial distribution of the load causes contributions from modes outside the frequency of load. Therefore, a fixed load pattern seems to activate quasi static response of the higher modes even-though the frequency of the load is located before the natural frequencies of these modes. These modes should be included in the lower frequency region if we want a proper representation of the response for localised behaviour.

15.5 Conclusion

In this paper we have shown the possible errors caused by truncating the modal decomposition in experimental modal analysis. Often this truncation error is insignificant but it is pronounced if a significant part of load has a fixed spatial distribution. The magnitude of the error is hard to estimate but localised structural behaviour seem to be highly affected by this residual effect. This means that experimental techniques that use a truncated set of modes to describe the response might introduce errors in localised behaviour.

To sum up, we cannot rely purely on the frequency range to choose the number of modes in an experimental modal analysis since the combination of higher modes may contribute to the response. Therefore, modal truncation introduces errors in response representation if the set of mode shapes inefficiently span the spatial distribution of the load.

Acknowledgements The authors acknowledge the funding received from Centre for Oil and Gas – DTU/Danish Hydrocarbon Research and Technology Centre (DHRTC).

A special thanks to Jannick Balleby Hansen for helping with the experimental tests.

References

1. Lui, D.C., Chung, H.L., Chang, W.M.: The errors caused by modal truncation in structure dynamic analysis. In: IMAC XVIII – 18th International Modal Analysis Conference, pp. 1455–1460 (2000)
2. Maddox, N.R.: On the number of modes necessary for accurate response and resulting forces in dynamic analysis. *J. Appl. Mech. ASME* **42**(2), 516–517 (1975)
3. Vugts, J.H., Hinesm, I.M., Nataraja, R., Schumm, W.: Modal superposition vs. direct solution techniques in the dynamic analysis of offshore structures. In: BOSS'79, Proceedings of the Second International Conference on Behaviour of Off-Shore Structures, pp. 23–29 (1979)
4. Léger, P., Ricles, J.M., Robayo, L.J.: Reducing modal truncation error in wave response analysis of offshore structures. *Commun. Appl. Numer. Meth.* **6**(1), 7–16 (1990)
5. Léger, P., Wilson, E.L.: Generation of load dependent ritz transformation vectors in structural dynamics. *Eng. Comput.* **4**(4), 309–318 (1987)
6. Dickens, J.M., Nakagawa, J.M., Wittbrodt, M.J.: A critique of mode acceleration and modal truncation augmentation methods for modal response analysis. *Comput. Struct.* **62**(6), 985–998 (1997)
7. Hansteen, O.E., Bell, K.: On the accuracy of mode superposition analysis in structural dynamics. *Earthq. Eng. Struct. Dyn.* **7**, 405–411 (1979)
8. Avitabile, P., Pingle, P.: Prediction of full field dynamic strain from limited sets of measured data. *Shock Vib.* **19**(5), 765–785 (2012). <https://doi.org/10.1155/2012/408919>
9. Roy, N., Girard, A.: Impact of residual modes in structural dynamics. In: Proceedings of the European Conference on Spacecraft Structure, Materials and Testing (2005)
10. Hansen, P.C., Pereyra, V., Scherer, G.: Least Squares Data Fitting with Applications. Johns Hopkins University Press, Baltimore (2013). ISBN:9781421408583; 1421408589; 9781421407869; 1421407868
11. Brincker, R., Ventura, C.: Introduction to Operational Modal Analysis. Wiley, Chichester (2015). ISBN:9781119963158
12. Brincker, R., Zhang, L.M., Andersen, P.: Modal identification of output-only systems using frequency domain decomposition. *Smart Mater. Struct.* **10**(3), 441–445 (2001)

Chapter 16

Combined Mechanical Environments for Design and Qualification

Brian C. Owens and Julie M. Harvie

Abstract Aerospace systems and components are designed and qualified against several operational environments. Some of these environments are climatic, mechanical, and electrical in nature. Traditionally, mechanical test specifications are derived with the goal of qualifying a system or component to a suite of independent mechanical environments in series. True operational environments, however, are composed of complex, combined events. This work examines the effect of combined mechanical shock and vibration environments on response of a dynamic system. Responses under combined environments are compared to those under single environments, and the adequacy/limitations of conventional, single environment test approaches (shock only or vibration only) will be assessed. Test integration strategies for combined shock and vibration environments are also discussed.

16.1 Introduction

Aerospace systems and components are designed and qualified against several operational environments. Some of these environments are climatic, mechanical, and electrical in nature. Mechanical environments include shock, vibration, acceleration, and spin. Traditionally, test specifications are derived with the goal of qualifying a system or component to a suite of environments in series, on an individual per axis basis [1–3]. This test methodology favors ease of testing and repeatability, and is especially attractive in the production process. True operational environments, however, are composed of complex, combined events with multi-axis loading.

Conventional mechanical testing and test specifications neglect combined effects. Indeed, traditional test specifications can be excessively conservative to overcome these shortcomings. Such an approach may lead to overly conservative, low performance designs because of limited, but conservative testing methodologies. Furthermore, combined mechanical environments can elicit remarkably different system responses. This can lead to significantly different failure modes and expose a qualification program to undue risk if testing fails to predict probable failures under operational environments.

The combined effects of certain types of environments are widely acknowledged and regularly tested. For example, many vibration test labs are equipped to simultaneously expose parts to both vibration and thermal loading. Additionally, most vibration control software includes an option for sine-on-random testing. Other types of combined loading are not tested as regularly, presumably due to increased complexity in test execution.

Previous research has examined avenues for improved qualification through development of advanced physical and analytical simulation capabilities. One example of advanced capabilities includes Sandia's "vibrafuge" which combines centrifuge inertial acceleration and mechanical vibration testing [4, 5]. Furthermore, Sandia's "superfuge" combines centrifuge inertial acceleration, spin, and mechanical vibration. These two physical simulation capabilities provide an avenue to simulate realistic, combined operational environments. Currently, experimental capabilities are complemented by research to enhance analytical capabilities such as combined inertial and mechanical vibration to simulate system dynamics under pre-load effects.

Sandia National Laboratories is a multimission laboratory managed and operated by National Technology and Engineering Solutions of Sandia, LLC, a wholly owned subsidiary of Honeywell International, Inc., for the U.S. Department of Energy's National Nuclear Security Administration under contract DE-NA0003525.

B. C. Owens (✉) · J. M. Harvie
Engineering Sciences Center, Sandia National Laboratories, Albuquerque, NM, USA
e-mail: bcowens@sandia.gov

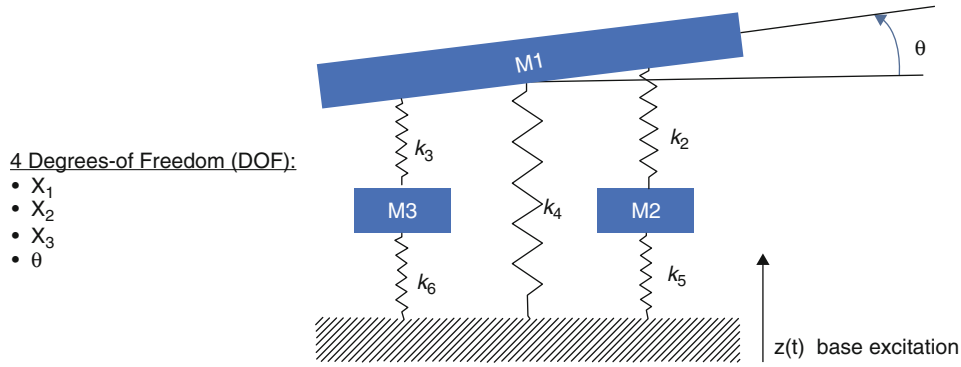


Fig. 16.1 Schematic of 4DOF example system

Other research efforts have addressed the multi-axis nature of mechanical inputs through 6 degree-of-freedom shock and vibration testing and analysis [6–8]. Furthermore, research in structural-acoustic environments and response and resulting multi-axis inputs [9] has highlighted the limitations of conventional, single-input testing.

This work will examine the effect of combined mechanical environments, specifically combined shock and vibration environments. The impact of combined environments will be assessed by examining the responses of a simple dynamic system. Responses under combined environments will be compared to those under single environments, and the adequacy of conventional, single environment test approaches (shock only or vibration only) will be assessed. Test integration considerations will also be discussed including identifying/extracting shock and vibration environments from combined environment measurements, development of combined environment test specifications, and testing methodologies for physical simulation of combined environments.

First, the dynamic system employed in this study and the modal response of this system will be discussed. Next, the combined shock and vibration environments considered in this study are presented followed by system response under the combined shock and vibration environments. After assessing the impact of combined environments, test implementation considerations associated with combined environments are addressed. Finally, conclusions are made on outcomes of this study and potential avenues for future work are discussed.

16.2 Description of System

The system considered in this study is a relatively simple 4 degree of freedom (DOF) dynamic system shown in Fig. 16.1. The system is composed of three masses, all of which can undergo translation in one dimension, and one (m_1) which can undergo in-plane rotation. Therefore, the degrees of freedom of this system are $x_1(t)$, $x_2(t)$, $x_3(t)$, and $\theta(t)$. The system will undergo a prescribed base motion $z(t)$. Specifically, a prescribed acceleration, $\ddot{z}(t)$.

This a simple spring-mass system. Damping mechanisms are not explicitly accounted for in the system definition, but modal damping will be prescribed after the structural dynamics modes of the system are determined. This choice was made for simplicity in analysis of the system, but future work could consider other damping mechanisms. The equations of motion of the system are shown below:

$$[M] \ddot{\vec{x}}(t) + [K] \vec{x}(t) = \vec{F}(t) \quad (16.1)$$

$$M = \begin{bmatrix} m_1 & 0 & 0 & 0 \\ & m_2 & 0 & 0 \\ & & m_3 & 0 \\ SYM & & & \frac{1}{12} m_1 L^2 \end{bmatrix} \quad (16.2)$$

$$K = \begin{bmatrix} k_2 + k_3 + k_4 & -k_2 & -k_3 & 2(k_2 - k_3)/L \\ & k_2 + k_5 & 0 & -2k_2/L \\ & & k_3 + k_6 & 2k_3/L \\ SYM & & & (k_2 + k_3)L^2/4 \end{bmatrix} \quad (16.3)$$

Table 16.1 System parameter values

Parameter	Value	Parameter	Value
m_1	0.3 lbs-m	k_2	20e4 lb/in
m_2	1.2 lbs-m	k_3	30e4 lb/in
m_3	1.2 lbs-m	k_4	5e4 lb/in
L	1 in	k_5	20e4 lb/in
		k_6	14e4 lb/in

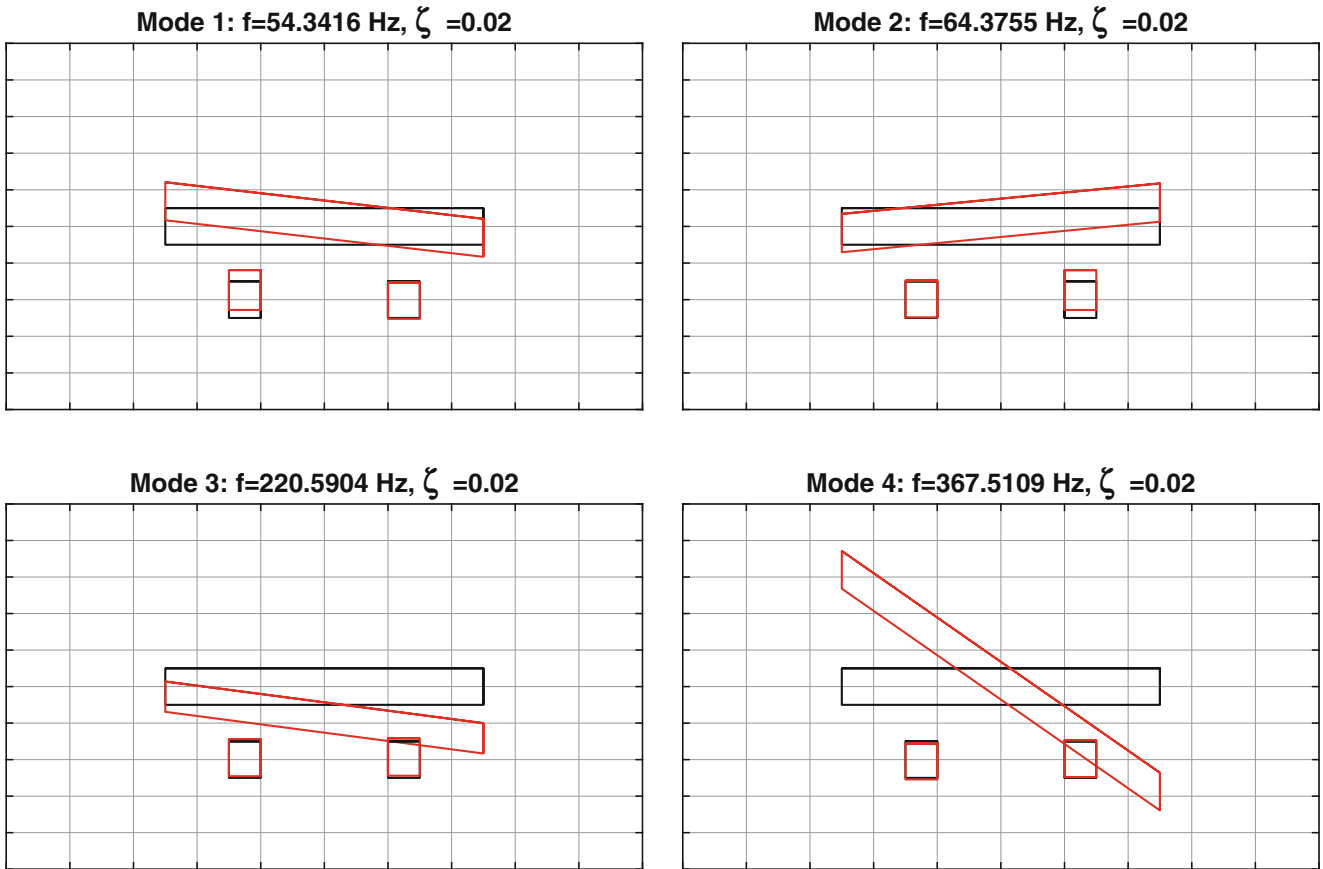


Fig. 16.2 Structural dynamic mode shapes and natural frequencies of 4 DOF system

$$\vec{F}(t) = \begin{bmatrix} -m_1\ddot{z}(t) \\ -m_2\ddot{z}(t) \\ -m_3\ddot{z}(t) \\ 0 \end{bmatrix} \tag{16.4}$$

$$\vec{x}(t) = \begin{bmatrix} x_1(t) \\ x_2(t) \\ x_3(t) \\ \theta(t) \end{bmatrix} \tag{16.5}$$

The parameter values for the system are shown in Table 16.1. The structural dynamic modes of this system are shown Fig. 16.2. There are two similar modes with natural frequencies around 60 Hz with a plunging of either m_2 or m_3 and the associated rotation of m_1 . Note that there appears to be minimal translation of m_1 . A third mode exists at 220 Hz, with a mode shape depicting translation and rotation of m_1 . The fourth mode is at 370 Hz, with a mode shape depicting primarily rotation of m_1 . Note that 2% modal damping on all modes will be considered in subsequent modal transient analysis.

16.3 Description of Example Combined Shock and Vibration Environment

This section describes the combined shock and vibration environment considered in this preliminary study of the subject. For simplicity, a 3.1 grms flat random vibration environment is considered with an acceleration spectral density (ASD) of $0.01 \text{ g}^2/\text{Hz}$ from 10 Hz to 1000 Hz. This will provide a uniform input across all natural frequencies of the system as described in Sect. 16.2. Next, a simple decayed sine shock is considered. The shock has a single frequency of 60 Hz and a decay rate of $1.5e-2$. This shock will primarily excite the first two modes of the system. The amplitude of the shock is a parameter of this study and is prescribed as multiples of the acceleration root mean square (RMS) value of the baseline random vibration environment considered in this study. In this way, the level of the shock is related to a characteristic level of the vibration environment. Five different shock levels were considered: 1, 3, 6, 9, and 12 times the RMS value of the vibration environment.

In this study, the combined environment is constructed through superposition of the time series of the baseline random vibration input and the time series of the shock input. The time realization of the random vibration ASD is created using Sandia's in-house signal processing toolbox, Graflab. Figures 16.3 and 16.4 show the time realization of the random vibration environment and shock environments respectively.

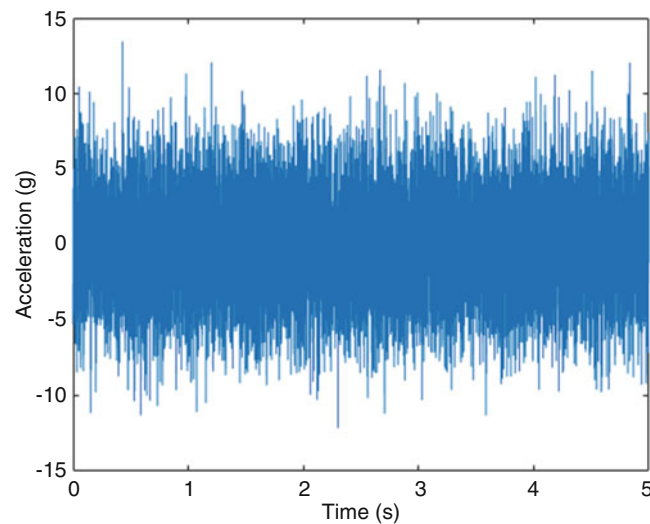


Fig. 16.3 Time series realization of random vibration environment (3.1 grms)

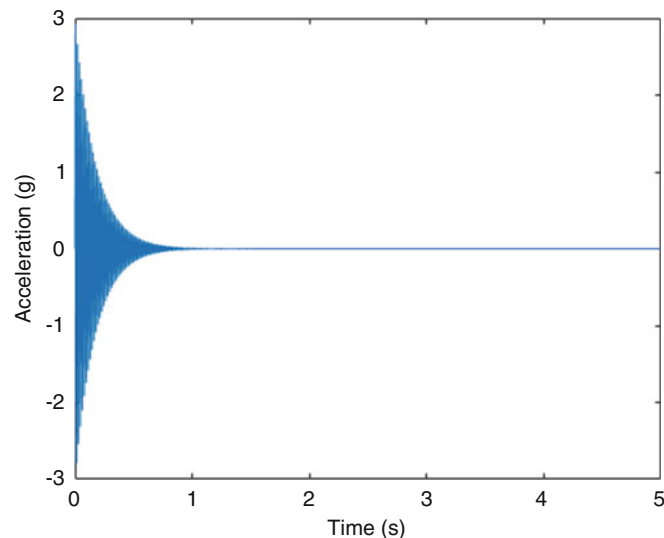


Fig. 16.4 Time series of 60 Hz shock decayed sine shock environment (3.1 g amplitude)

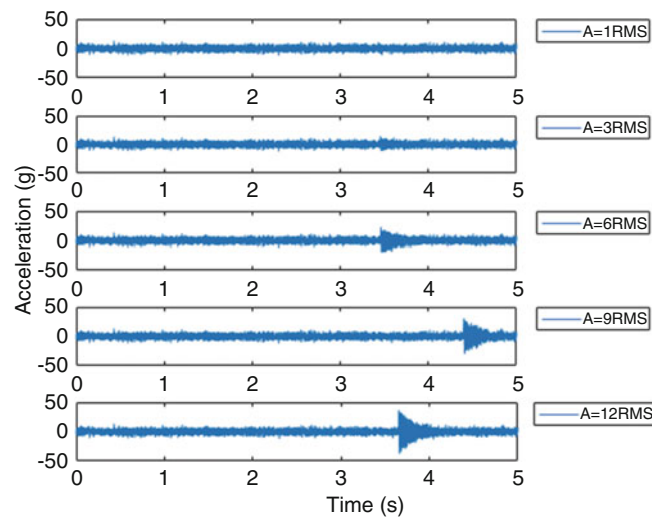


Fig. 16.5 Examples of combined shock and vibration environments at various levels of shock amplitude with random insertion of the shock signal

The timing of the combined shock and vibration environment is likely to be stochastic in nature. Therefore, the shock environment is superposed on the vibration environment at a random point in time. Specifically, 50 uniformly sampled random insertion points between 0.5 T and 0.75 T (T being the length of the vibration signal, 5 s in this case), to create 50 unique combined shock and vibration environments for each of the 5 shock levels considered. Therefore, a total of 250 combined shock and vibration environments were created.

Examples of these realizations are shown in Fig. 16.5. As one familiar with random vibration would expect, it is difficult to see the presence of a shock environment until the shock level exceeds an amplitude of 3 times the RMS value of the vibration signal alone. This important observation will be revisited later in the paper.

Future work may consider more complicated shock and vibration environments with specific inputs varied around the natural frequencies of the system. This will provide a further understanding of the interplay of combined mechanical environments on the response of a system.

16.4 System Response to Combined Shock and Vibration Environment

The system described in Sect. 16.2 was excited under the various combined environments described in Sect. 16.3. A modal transient analysis was used to simulate the system response under environments. A time step of $1e-4$ s was employed in an implicit Newmark-Beta time integration solver, and 2% modal damping was assumed on all modes. These simulations generated response time series for 4 DOFs under 250 environments.

There are many potential quantities of interest (QOIs) to examine, such as acceleration, velocities, displacement, spring forces, etc. Specific QOIs may be dictated by known or speculated failure modes (structural or functional) or the desire to produce environmental specifications from system responses. For simplicity, peak absolute acceleration values will be the QOI for this study. Although, future studies may consider other QOIs.

After simulation of the dynamic system response to combined environments, the peak accelerations of the DOFs were extracted for all simulation results. These peak accelerations were then processed to determine the mean peak acceleration and the standard deviation of the peak acceleration across the 50 shock time lags. Furthermore, the responses of the system under random vibration input and shock input alone were also computed for comparison against combined environments.

Figure 16.6 shows the peak acceleration responses for translation of m_1 , m_2 , and m_3 . The circle marker denotes the mean peak acceleration for the combined environments and the “error bars” denote the 3σ value for peak acceleration. The star markers denote the peak acceleration under shock alone (no combined vibration) and the dashed line denotes the peak acceleration under vibration alone (no combined shock).

Upon first inspection of Fig. 16.6, it is notable that the peak acceleration for shock input alone is typically very close to the mean peak acceleration. This makes sense, because the expected/mean value of the random vibration signal is zero.

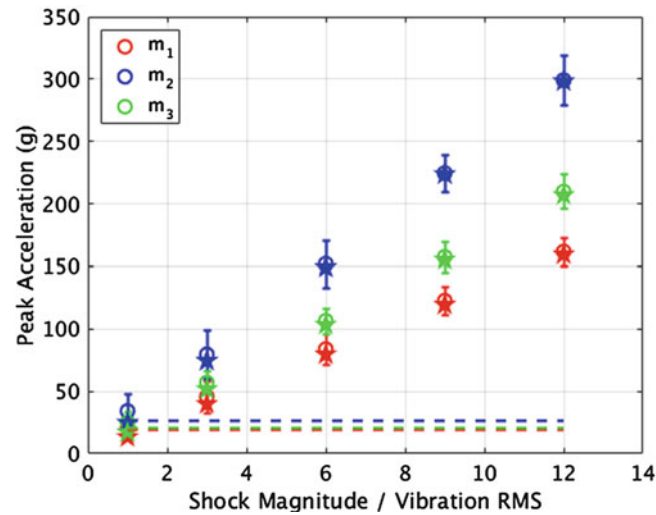


Fig. 16.6 Summary of responses under combined and single environments

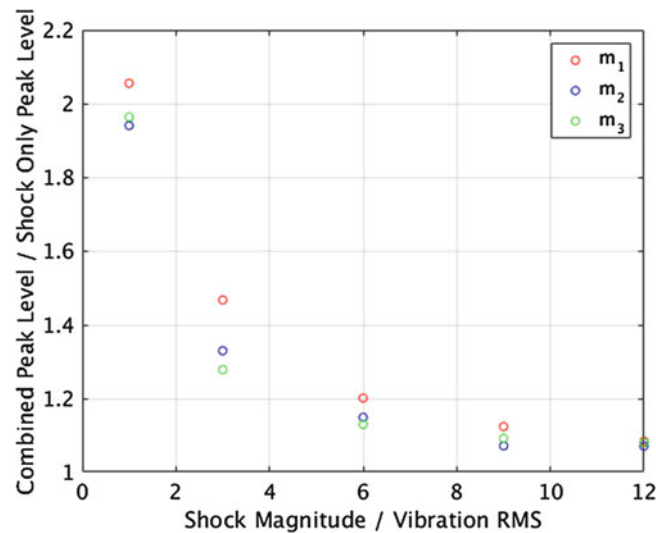


Fig. 16.7 Ratio of peak acceleration response under combined environment to that under shock alone

Therefore, it is statistically likely that the shock will be superposed near a zero-valued vibration level. While this is the case on average, the 3σ value gives a better characterization of the potential combined response.

While Fig. 16.6 presents a wealth of information on system response to combined and single-environment inputs it doesn't answer some critical questions regarding system response combined environments. These questions are:

1. When do shock environments dominate the response relative to concurrent vibration environments?
2. When do vibration environments dominate the response relative to concurrent shock environments?

To address Question 1, the peak acceleration response (mean + 3σ) under combined environments was normalized by peak acceleration response under shock alone and is depicted in Fig. 16.7. For this specific system and environments, combined environments with shock amplitudes greater than or equal to 6 times the RMS value of the vibration environment appear to be well characterized by shock input alone. For example, peak responses are within 20% of the combined environment. This relatively small difference would likely be accounted for by conservatism in environmental specifications, test specifications, and test implementation.

To address Question 2, the peak acceleration response (mean + 3σ) under combined environments was normalized by peak acceleration response under vibration alone and is depicted in Fig. 16.8. As one would expect, the vibration only input cannot adequately predict responses of combined environments with shock amplitudes greater than or equal to 3 times

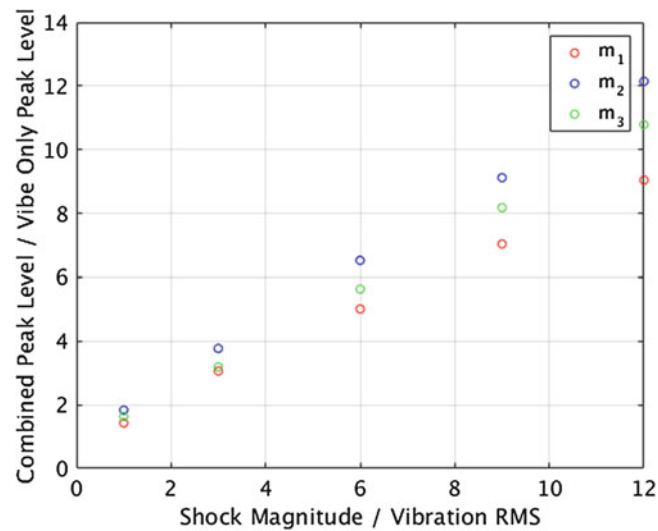


Fig. 16.8 Ratio of peak acceleration response under combined environment to that under vibration alone

the RMS value of the vibration signal. Furthermore, there appear to be differences in response (anywhere from 50% to 100%) for combined environments with shock amplitudes of 1 RMS compared to response under vibration alone. For this specific study, it appears shocks with amplitudes <1 RMS of the concurrent vibration signal would be required before the vibration response dominates. This conclusion is in the context of the current QOI, peak acceleration. For systems sensitive to fatigue damage, the shock component would likely contribute less to fatigue response.

Perhaps of most concern is the detection of a shock environment in the “noise” of a random vibration signal. Re-examination of Fig. 16.5 shows that shocks are readily observable (but perhaps not identifiable) in combined environments with shock amplitudes greater than 3 times the RMS value of the underlying vibration signal. However, it isn’t necessarily evident that a combined environment exists for shock amplitudes less than or equal to three times the RMS value of the vibration signal. This example problem, however, reveals that lower amplitude shocks can have significant effect on response when combined with vibration environments. For example, revisiting Fig. 16.8 shows that the response to a vibration environment alone results in a 50–300% under prediction relative to a combined environment. This observation motivates the development of more advanced techniques to extract shock and vibration environments from complex, combined environments.

It is noted that the observations and conclusions of this section may be strongly dependent on this sample problem and selected environments. Furthermore, the significance of these observations may be reduced in a qualification program that incorporates large amounts of conservatism (or time compression) into environmental and test specifications. Nevertheless, these observations may be a key consideration for design and qualification of functional hardware that seeks to perform functional testing under combined environments with realistic operational environments (e.g. environments with minimal conservatism or time compression).

16.5 Implementation of Combined Shock and Vibration Environment Testing

This section will discuss test integration aspects of combined shock and vibration environments specifically, it will consider:

- Extraction of environmental specifications from combined environment data
- Development of test specifications for combined shock and vibration testing
- Test hardware for combined shock and vibration testing

16.5.1 Extraction of Environmental Specifications from Combined Environment Data

Data from combined environments should be decomposed into the individual underlying components prior to post-processing and test specification development to ensure proper characterization of the environment. If each component cannot be accurately extracted, the individual environment characterizations will likely be overestimated due to contributions from the other environments.

Certain types of environments are more straightforward to extract from combined exposure than others. In general, stationary signals (sine or random vibration) are easier to extract than non-stationary signals (shock) because time-invariant properties can be observed in stationary signals.

An ideal random vibration signal will exhibit several properties that can be useful in identification of its environment type. The ideal random signal will be stationary, ergodic, and Gaussian. In particular, these properties mean that the statistical properties of the signal will not change over time. Thus, a change in the statistical properties over time suggests that an additional loading, perhaps a shock, has occurred.

The running RMS and running kurtosis are recognized as useful properties and are compared between the random vibration environment and a combined environment, as shown in Fig. 16.9. The pure random vibration signal exhibits around 3 grms of response consistently across the time record. The kurtosis of the random vibration signal is around 3 across the time record, as expected for a Gaussian signal. For the combined environment, the shock is apparent in both the running RMS and kurtosis as a spike around 3.5 s. Thus, the usefulness of both running RMS and kurtosis for identifying shocks in combined environments is established.

Although the running kurtosis has more variance than the running RMS, the running kurtosis can be particularly useful in applications for large data sets because the running kurtosis should be close to 3 for all Gaussian signals, whereas the running RMS is dependent upon the actual environment.

An estimate of the random vibration in this combined environment is then determined by extracting the portion of data where the running RMS is a constant value and the running kurtosis is a constant value of 3, both with some variation.

ASDs were calculated for the combined environment, reference vibration environment, and vibration extracted from the combined environment [10]. This comparison is shown in Fig. 16.10. As seen, the ASD of the original combined environment is higher than the reference around 60 Hz due to the shock content. However, the segmented environment produces an ASD close to the reference, with some slight differences due to a smaller time record with less averages. Although this example is very basic, the technique has proven promising for actual flight data applications.

Similarly, it is desired to extract the shock from the combined environment. Extraction of the shock environment is notably more difficult than the random vibration, and an accurate method has not been discovered to date. Various time and frequency domain techniques were attempted unsuccessfully. Additional information about the shock character is required to fully extract the shock pulse.

Nonetheless, a very basic shock extraction technique was performed by segmenting the shock pulse from the combined environment, as identified using the running RMS and kurtosis described above. Note that this does not completely isolate the shock pulse, as the random vibration is still superimposed.

The 3% Maxi-Max Shock Response Spectra (SRS) were calculated for the combined environment, reference shock, and the shock segmented from the combined environment. This comparison is shown in Fig. 16.11. As seen, the SRS of the original combined environment contains significant noise due to the random vibration content. By segmenting the combined environment to only include the shock portion, there is a reduction in noise on the SRS, especially at low frequencies. However, the approximation is still conservative at higher frequencies and additional techniques need to be investigated for shock characterization.

16.5.2 Development of Test Specifications for Combined Shock and Vibration Testing

There are certain cases where the data captured during a combined shock and vibration environment may represent the worst-case scenario, and the time domain signal can be used directly in the subsequent laboratory test using waveform replication. However, this is not typically the case.

Development of test specifications for the individual underlying environments should likely include similar processes as traditional single environment testing (incorporating variabilities, uncertainties, scaling to worst case, etc.). Combined environments testing also requires an additional parameter to be specified – relative timing of environments.

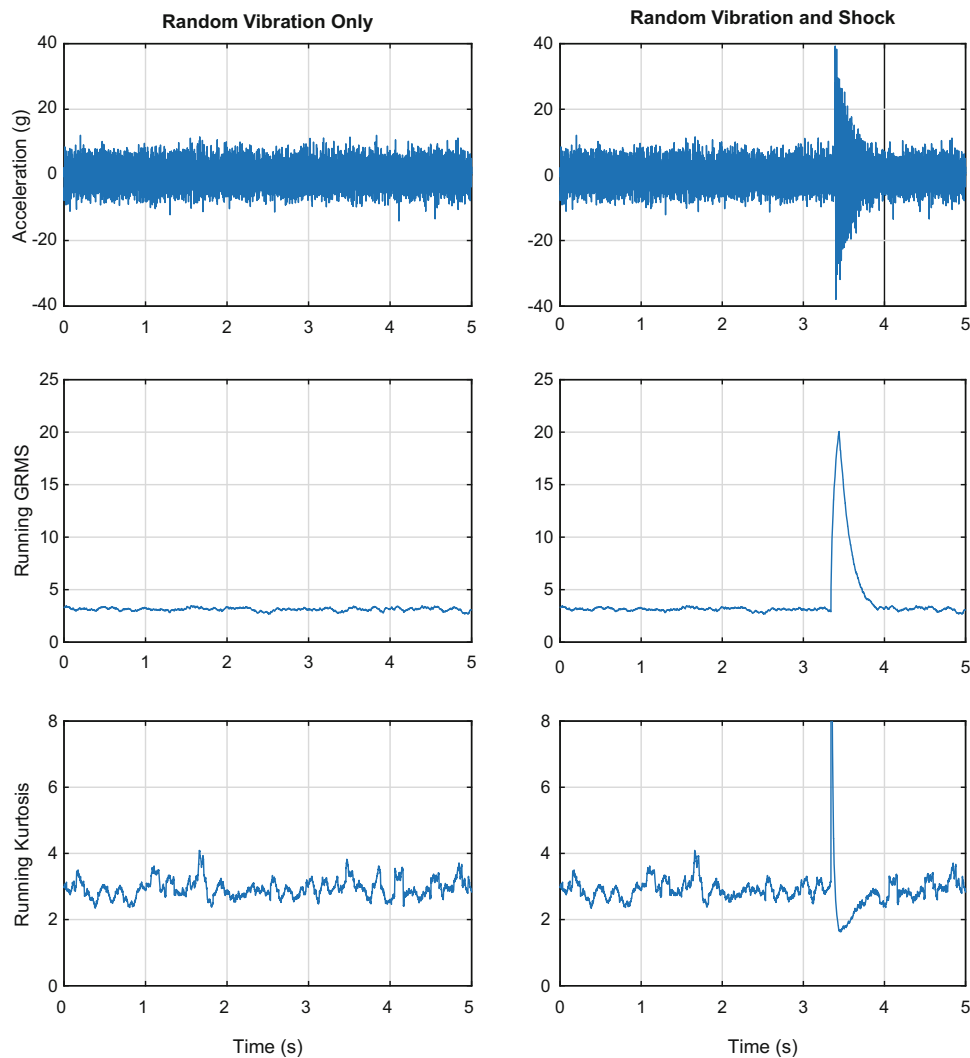


Fig. 16.9 Running RMS and kurtosis for vibration signal and combined environment signal

There are several methods for defining the timing of the shock during the combined environments test. Ideally the expected timing of the shock during the combined environment in the field exposure would be well characterized and used to define the timing of the shock in the laboratory test. In the absence of well characterized field data, there are a few options. An accurate analytical model could be used to determine the sensitivity of the device under test to changes in the timing of the shock, as was done in the earlier sections of this paper. If a model is not available, it may be prudent to run the combined test with the shock applied at several different times.

16.5.3 Test Hardware for Combined Shock and Vibration Testing

The concept of applying a shock load at some instance in a vibration test seems relatively simple, but some unique considerations must be made. Random vibration testing is typically performed using a closed loop controller to achieve the desired input at a control location. A lower level input of the desired vibration specification is applied and the input is updated to achieve the target response at the control location. The input level is then stepped up until the full level specification is reached. A similar approach can be taken for shock synthesis via decayed sine shocks on a traditional shaker table.

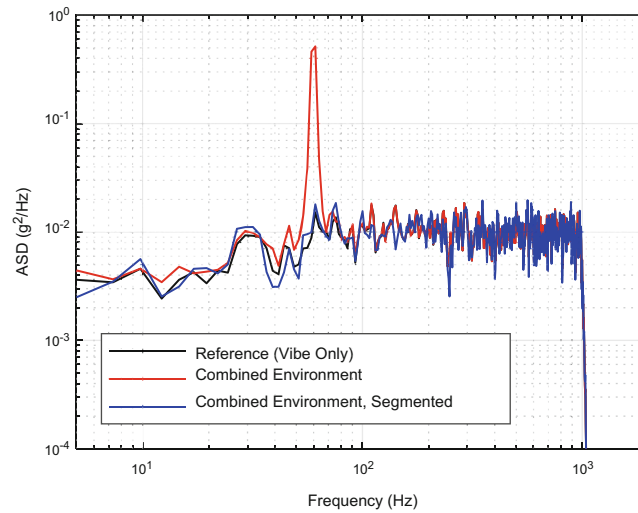


Fig. 16.10 Contamination of ASD from combined environment and proposed random vibration extraction

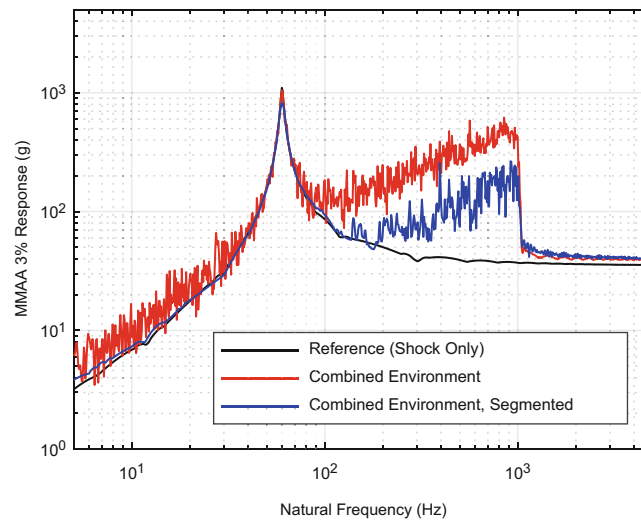


Fig. 16.11 Contamination of SRS from combined environment and proposed shock extraction

Using this conventional approach to simulate a combined shock and vibration environment would be difficult because the controller may suppress the shock input as it controls the vibration input. Therefore, some modifications to the test implementation are proposed to account for the unique requirements of combined shock and vibration testing.

First, the experimental facility needs to be modified. It is proposed that piezoelectric actuators be used to apply the vibration input, while the traditional shaker table is used to apply decayed sine shock input. This results in the experimental set-up depicted in Fig. 16.12. The piezoelectric actuators are installed between the shaker table and test article. The required number of actuators is driven by force requirements as dictated by test article mass and the vibration specification.

The following testing process is proposed:

1. Apply vibration only through the piezoelectric actuators using feedback control until the desired vibration specification is achieved at the control location.
2. Record the input vibration signal achieved in #1 for the desired vibration test duration.
3. Apply shock only through the shaker table using feedback control until the desired shock specification is achieved at the control location.
4. Record the input shock signal achieved in #3.
5. Input the recorded signal obtained in #2 without feedback control on the piezoelectric actuators.
6. At the desired instance(s) in time apply the pre-determined shock obtained in #4, no feedback control should be used on the shaker table.

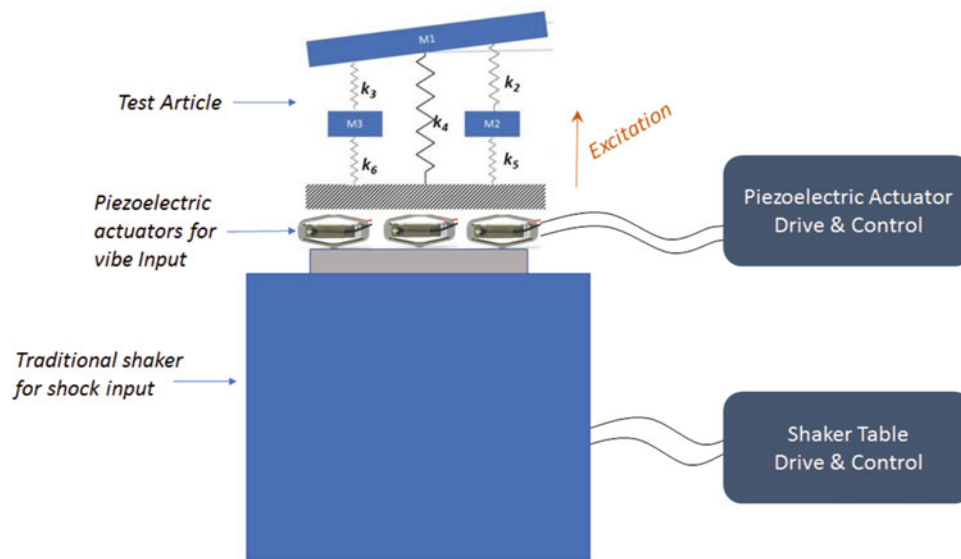


Fig. 16.12 Illustration of test set-up for combined shock and vibration testing

Note that some practical considerations may be required to account for this unique test set-up, but this is beyond the scope of this work.

16.6 Conclusions

This paper has explored the effect of combined mechanical shock and vibration environments on a simple dynamic system. The peak acceleration response of the system was compared to that of the system under shock and vibration environments alone and some interesting trends were observed. As one might expect, for shock environments with amplitudes greater than some representative level of the vibration signal (e.g. RMS) the response to the shock environment dominates. For shock environments with amplitudes less than the vibration environment (i.e. $1 \times \text{RMS}$ in the current study), the vibration response dominates. Perhaps most noteworthy though, is the difficulty in observing a concurrent shock and vibration environment unless the shock amplitude is significantly greater (greater than $3 \times \text{RMS}$) than the underlying vibration signal. The current study has revealed a system in which the combined effect of shock and vibration significantly influences dynamic response, but in a case where the combined environment is not necessarily observable. This may be the case for other systems, and this should be considered in future work.

Considering this outcome, test integration and implementation strategies for combined mechanical shock and vibration environments were explored. Strategies for extracting shock and vibration environments from combined environment measurements were examined and applied with some success. Approaches for extracting vibration environments appeared promising. There were, however, limitations in accurately extracting shock environments and shock extraction methodologies require future work. This paper also discussed the development of combined shock and vibration test specifications. Furthermore, a test set-up for combined shock and vibration testing was proposed.

Finally, it is emphasized that this work has examined the response of a specific system to combined mechanical shock and vibration within the context of a specific quantity of interest (peak acceleration response). Although the effect of combined shock and vibration environments has been clearly demonstrated for the study at hand, this study should be extended to other systems and quantities of interest. Specifically, future studies should consider the effect of combined environments on fatigue as well as responses representing non-structural failures (i.e. functional failures). Future work should also frame the sensitivity of responses to combined environments against the conservatism present in a test integration program.

Acknowledgements The authors wish to thank Rich Jepsen of Sandia National Laboratories for his input and helpful discussions related to this work.

References

1. U.S. Department of Defense Environmental Engineering Considerations and Laboratory Tests, MIL-STD-810G (2008)
2. U.S. Navy Manufacturing Screening Test Standards, NAVMAT P-9492 (1979)
3. JEDEC standard: Vibration variable frequency, JESD22-B103B (2006)
4. Jepsen, R., Romero, E., Vangoethem, D.: Flight and re-entry test simulation in combined acceleration and vibration environments: part I. *Crit. Technol. Shock Vib.* **6**(1) (2011)
5. Jepsen, R., Romero, E.: Flight and re-entry test simulation in combined acceleration, vibration, and spin environments: part II. *Crit. Technol. Shock Vib.* **6**(2) (2011)
6. Gregory, D.L., Bitsie, F., Smallwood, D.O.: Comparison of the response of a simple structure to single axis and multiple axis random vibration inputs. In: *Proc. 80th shock and vibration symp., San Diego* (2009)
7. Smallwood, D.O., Gregory, D.L.: Evaluation of a 6-DOF electrodynamic shaker system. In: *Proc. 79th shock and vibration symp., Orlando* (2008)
8. Owens, B.C., Tipton, D.G., McDowell, M.: 6 Degree of freedom shock and vibration: testing and analysis. In: *Proc. 86th shock and vibration symposium, Orlando* (2015)
9. Mayes, R.L., Rohe, D.P.: Physical vibration simulation of an acoustic environment with six shakers on an industrial structure. In: *Proc. 34th international modal analysis conference, Orlando* (2016)
10. Engelhardt, C., Baker, M., Mouron, A., Vold, H.: Separation of sine and random components from vibration measurements. *Shock. Vib. Mag.*, 6–11 (June 2012)

Chapter 17

Comparing Free-Free and Shaker Table Model Correlation Methods Using Jim Beam

James Ristow, Kenneth Wayne Smith, Jr., Nathaniel Johnson, and Jackson Kinney

Abstract Finite element model correlation as part of a spacecraft program has always been a challenge. For any NASA spacecraft, a Coupled Loads Analysis (CLA) is used to predict the coupled system response of the spacecraft and launch vehicle. The accuracy of the CLA is highly dependent on the precision of the frequencies and mode shapes extracted from the spacecraft model. NASA standards require the spacecraft model used in the final Verification Loads Cycle to be correlated by a modal test. Due to budgetary and time constraints, most programs opt to correlate the spacecraft dynamic model during the environmental qualification test, conducted on a large shaker table.

For any model correlation effort, the key has always been finding a proper definition of the boundary conditions. This paper is a correlation case study to investigate the difference in responses of a simple structure using a free-free boundary, a “fixed” boundary on the shaker table, and a base-drive vibration test, all using identical instrumentation. The NAVCON Jim Beam test structure, featured in the IMAC XXVII round robin modal test of 2009, was selected as a simple, well recognized and well characterized structure to conduct this investigation.

First, a free-free impact modal test of the Jim Beam was done as an experimental control. Second, the Jim Beam was mounted to a large 22,000 lbf shaker, and an impact modal test in this pseudo-fixed configuration was conducted. Lastly, a vibration test of the Jim Beam was conducted on the shaker table. The free-free impact test, the “fixed” impact test, and the base-drive test were used to assess the effect of the shaker modes, evaluate the validity of fixed-base modeling assumptions, and compare final model correlation results between these boundary conditions.

17.1 Background and Motivation

Launching a spacecraft into space is a costly endeavor. As a product of the current budget constraints, spacecraft programs are continually looking for ways to cut costs. There is a very tangible push to reduce expensive system level testing, and this has led many spacecraft programs to omit expensive full-scale modal tests from their schedule and rely solely on the system level environmental qualification test for model verification. This approach has two primary drawbacks [1]: (1). Data collected from a system level vibration test for correlation is limited compared to a full-scale modal test. (2). Spacecraft model correlation is not complete until very late in the launch campaign, which may pose a schedule risk to the program.

NASA’s Launch Services Program (LSP) has minimum correlation criteria for spacecraft opting to correlate the spacecraft model during environmental qualification test. A Frequency Response Function (FRF) derived from a basedrive analysis of the spacecraft stack Finite Element Model (FEM) must envelope the levels observed during test; primary modes should match test frequencies within 5%, and secondary modes should match within 10% [1]. The analytical basedrive is typically conducted using the classic method of adding a rigid seismic mass to the base of the model and driving the system. Inherently, this analysis fixes the base of the spacecraft and assumes that there is no flexibility in the table.

J. Ristow (✉)
NASA Kennedy Space Center, Orlando, FL, USA
e-mail: james.a.ristow@nasa.gov

K. W. Smith, Jr.
Georgia Institute of Technology, Atlanta, GA, USA

N. Johnson
University of Oklahoma, Norman, OK, USA

J. Kinney
University of Alabama Huntsville, Huntsville, AL, USA

It has been this author's observation that it is difficult to achieve good correlation of modes beyond the first two bending modes and first axial mode. Further hampering model correlation efforts is the difference in accelerometer placement during an environmental qualification test from a modal test. For a qualification test, accelerometers are placed at a component's center of mass or its interface to ensure proper vibration levels are achieved, not necessarily at locations that would lend themselves to capturing frequencies and mode shapes for model validation. Model correlation is usually a secondary objective to the primary programmatic requirement of reaching the required qualification levels for the interface acceleration.

As stated by Mayes [2], there is a need for Finite Element validation using a fixed base condition, typical of payloads on a delivery system. This study investigates the difference in responses of a simple structure in a free-free boundary condition and "fixed" to a shaker table using identical instrumentation. Both tests are used to validate the FEM, and the results of each correlation are compared. Throughout this paper, the term "fixed" test will be used to refer to the impact modal test data taken of the Jim Beam while bolted to a stationary powered-off shaker table. The term "fixed" will remain in quotes, as this paper will demonstrate what the intuitive reader already knows: this boundary condition is not truly fixed.

17.2 Can a Shaker Table Be Used to Correlate a FEM?

There are many publications available which give insight into some of the challenges of correlating a FEM on a shaker table and some of the techniques employed to address this unique boundary condition; a few of them are highlighted here. Aerospace Corporation has several papers on the subject, but most notably has reported the bending mode frequency of a spacecraft was 25% lower than the frequency derived from modal test of the same spacecraft. The difference was traced to the flexibility of the table [3]. Sandia National Labs reported modes attributable to the base-shake table, which violates the assumed theoretical boundary condition of zero motion at the attachment point, except for the prescribed input [4]. This finding is of particular interest to this study, as it essentially invalidates the fixed base modeling assumption inherent in a seismic basedrive analysis. Sandia has since done additional work to identify the effects of the shaker table itself by using a separate small modal shaker to characterize the table and update the extracted FRFs and match modal mass [2]. This is likely one of the more robust ways to characterize the table, however, characterizing the table itself is beyond the scope of this paper, as typically very little characterization, if any, is done on shaker tables during spacecraft qualification testing.

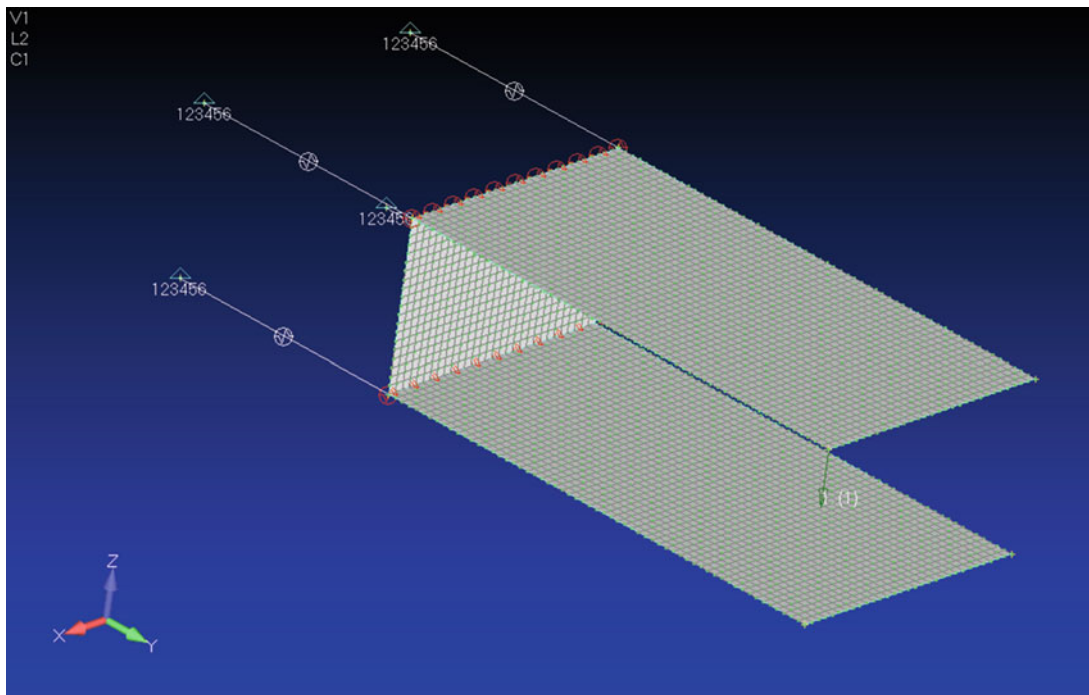
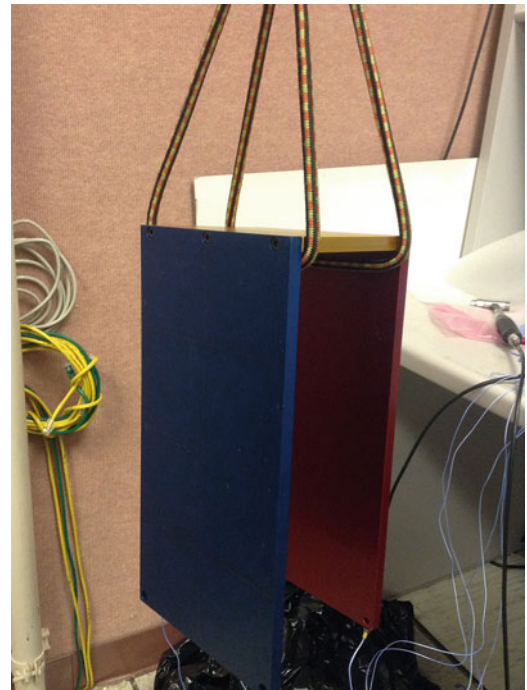
17.3 Meet Jim Beam

The goal of this paper is to illustrate the effect of three separate boundary conditions on model correlation using a simple structure. The simple structure chosen for this investigation was the NAVCON Jim Beam, a simple three plate structure that was featured as part of the 2009 IMAC XXVII round-robin modal test. The Jim Beam has been tested well over 900 times by industry and academia, lending itself to being an ideal "experimental control". It is a simple, well recognized and well characterized structure to conduct this investigation. The Jim Beam is comprised of three aluminum plates and six screws, and weighs approximately 6.5 lbs (Fig. 17.1).

Modeling of the Jim Beam was done in FEMAP and analyzed using NX Nastran. Approximately 26,000 plate elements were used to model the three plates. This mesh size was driven by sizing studies conducted in support of modal testing done on each of the plates individually, and was required to capture the high frequency modes of the gold plate. The most sensitive part of the model was the joints. Trying to model the joint between the center gold plate and each of the other plates with only three bolt locations proved to be inadequate to capture the joint dynamics; instead, 11 "stiff" CBUSH spring-elements were used along the plate connections to simulate the joint compliance. For the free-free modal test model, four soft CBUSH spring-elements were used to simulate the bungees suspending Jim Beam (Fig. 17.2).

From this point forward to avoid confusion, the six bolts connecting the three plates of the Jim Beam will be referred to as the *connection* bolts, while the six bolts at the interface between the Jim Beam and shaker table will be referred to as the *interface* bolts.

For the "fixed" base modal test, it was found that fixing only a single node at each of the six interface bolts was insufficient to capture the stiffness of the Jim Beam interface with the table. Therefore, the center node of each bolt was fixed in all six Degrees-Of-Freedom (DOF) using a Nastran SPC card, and rigid Nastran RBE2 "spiders" were used to connect that center node to the nine adjacent nodes surrounding it. Additionally, it was found this constraint alone still allowed too much compliance between the Jim Beam and the flat shaker table interface, as the physical test setup constrained the gold plate from bending. Therefore, in the analysis the entire gold plate was constrained in the Axial Y-direction (DOF 2) to better

Fig. 17.1 Jim Beam test article**Fig. 17.2** Jim Beam Bungee configuration model

match mode shape animations (Fig. 17.3). As noted previously, modeling the Jim Beam interface in this manner incorrectly assumes a fixed interface, as if the test article was mounted to a rigid modal plate.

The model used for the “fixed” modal test was modified to simulate a seismic baseshake. The Y-direction constraint was removed, and a seismic mass (Nastran CONM2) was added to the center of the gold plate. The SPC constraint at the center node of each interface bolt was removed in lieu of an additional rigid RBE2 “spider” connecting the center of each bolt to the seismic mass (Fig. 17.4).

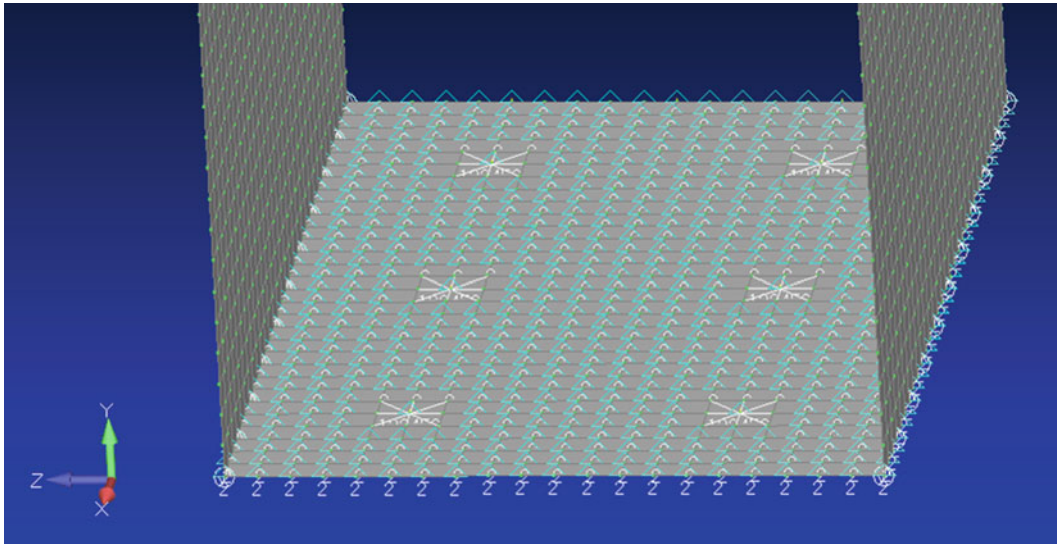


Fig. 17.3 Jim Beam fixed boundary

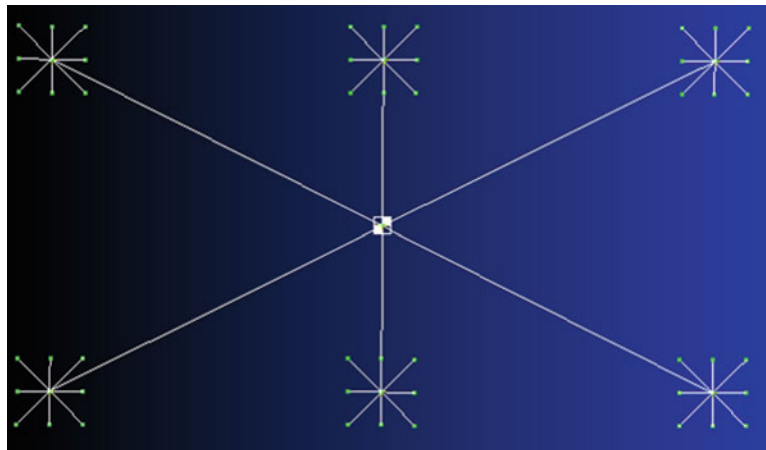


Fig. 17.4 Jim Beam Seismic mass boundary

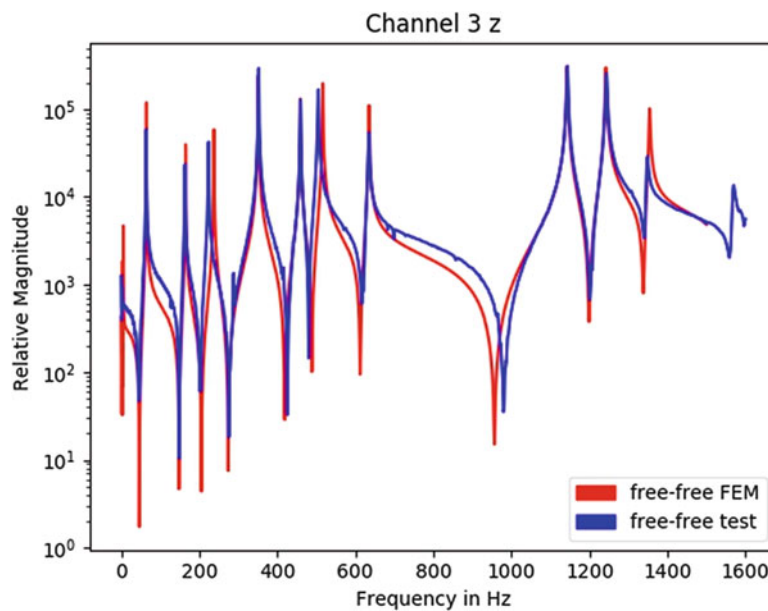
17.4 The Free-Free Test

The first boundary condition investigated was the classic free-free condition, where the Jim Beam was hung by bungees and modal impact data was taken (Fig. 17.1). One of the focal points of the original Jim Beam round-robin testing was varying torque from 30 in-lbs to 60 in-lbs on the six connection bolts between the three plates and observing the effect on the modal test results. As the effect of bolt torque was not a focus of this paper, the torques of these six connection bolts was kept constant at 60 in-lbs, and verified before each of the three different tests were conducted. Results of the Jim Beam free-free modal test were compared with free-free results published by ATA [5] as a “truth test” to verify the test methodology and data processing. Results are compared below in Table 17.1:

Overall, the frequency comparison between ATA and KSC is rather good considering the variability of lab equipment, analysts, and bungeed boundary conditions. The first mode shows the largest difference, likely due to slight differences in how KSC and ATA suspended the Jim Beam, and Mode 3 was a torsion mode that was difficult to excite and capture with impact modal testing. Having verified the test methodology, the FEM was correlated to the KSC test data to act as the baseline verified model for the “fixed” test and shaker test. NX Nastran Solution 111 was used to synthesize modal hammer impulse excitations, and post processing of the results was completed using Python software to generate FRF comparisons. A FRF comparison between the modal test and the correlated FEM are given in Fig. 17.5. Channel 3Z, located at the tip of the red plate, was chosen for test vs FEM comparisons, as this single channel captured the majority of clean system modes.

Table 17.1 Frequency comparison ATA vs KSC

Free-free modal test frequency comparison			
Mode	ATA [5]	KSC	% Diff
1	59	64	8.47
2	159	164	3.14
3	209	224	7.18
4	346	352	1.73
5	446	460	3.14
6	494	505	2.23
7	601	635	5.66
8	1126	1144	1.6
9	1216	1244	2.3
10	1332	1348	1.2

**Fig. 17.5** FRF of Free-Free Test vs FEM

17.5 The “Fixed” Test

Following completion of the free-free test, the Jim Beam was modified for vibration table fixturing. Six half-inch holes with two-inch spacing were drilled into the gold plate of the Jim Beam (Fig. 17.6) to interface with an existing 1x1x1 foot vibrate table adaptor Cube, weighing approximately 107 lbs. The Cube was mounted to an Unholtz-Dickie T1000 22,000 lbf shaker. The same data acquisition system, computer, accelerometers, accelerometer locations and impact points as the free-free test were used, with the exception of nine impact points on the bottom of the gold plate that were inaccessible due to the new mounting configuration.

As with the free-free test, NX Nastran Solution 111 was used to synthesize modal hammer impulse excitations, and post processing of the results was completed using Python software. Channel 3 was once again used for FRF comparisons between FEM and test (Fig. 17.7). Observing differences between the free-free and “fixed” base plots (Figs. 17.5 and 17.7) immediately reveals that while the “fixed” base FEM follows the test response, the comparison is not nearly as good as the correlation achieved with the free-free boundary condition. It was quite difficult to obtain clean modal impact data and mode shapes mounted to the shaker table, as impacts on the blue plate could not transfer enough energy through the bolted interface to excite the red plate, and vice versa. If the vibrate table were a perfect fixed interface as it was modeled, there would be zero motion in the red plate when the blue plate was excited. The fact that any motion at all was captured in the red plate during the modal test is indicative of an imperfect fixation. It is also important to note that the table was powered off for the “fixed” test, which means the air bearings within the vibrate table were not active. Practically, this means that there was

Fig. 17.6 Jim Beam six interface bolts

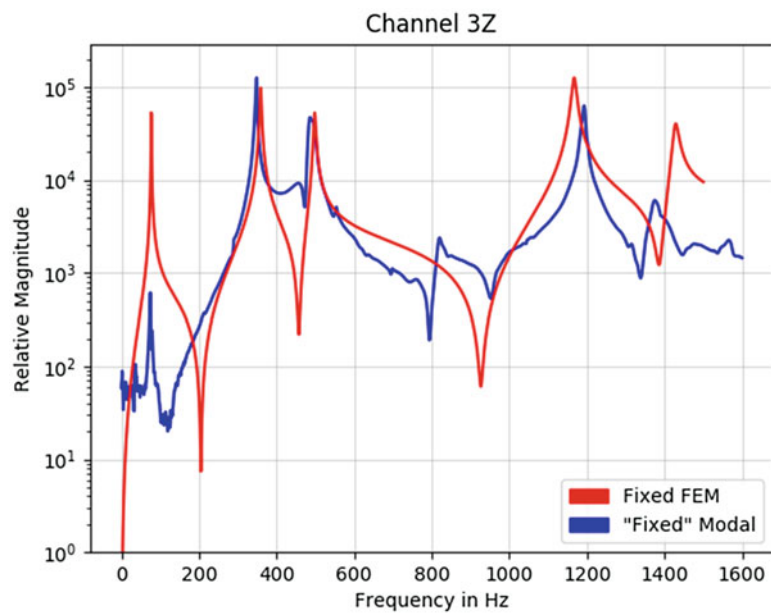
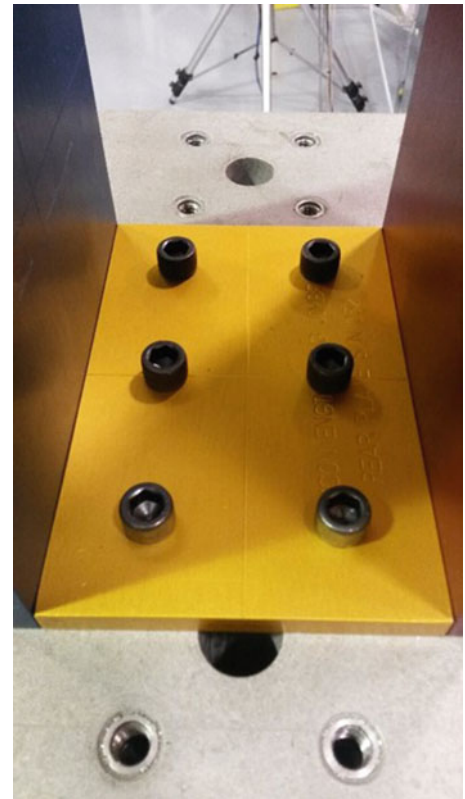


Fig. 17.7 FRF of "Fixed" modal test vs. FEM

some undetermined compliance in the shaker head/armature. A good shove on the interface Cube could induce noticeable oscillation of the Cube with the attached Jim Beam. This is likely why the first mode was difficult to resolve during the "fixed" modal test, and why a model correlated in the free-free realm was no longer correlated on this quasi-fixed shaker boundary condition.

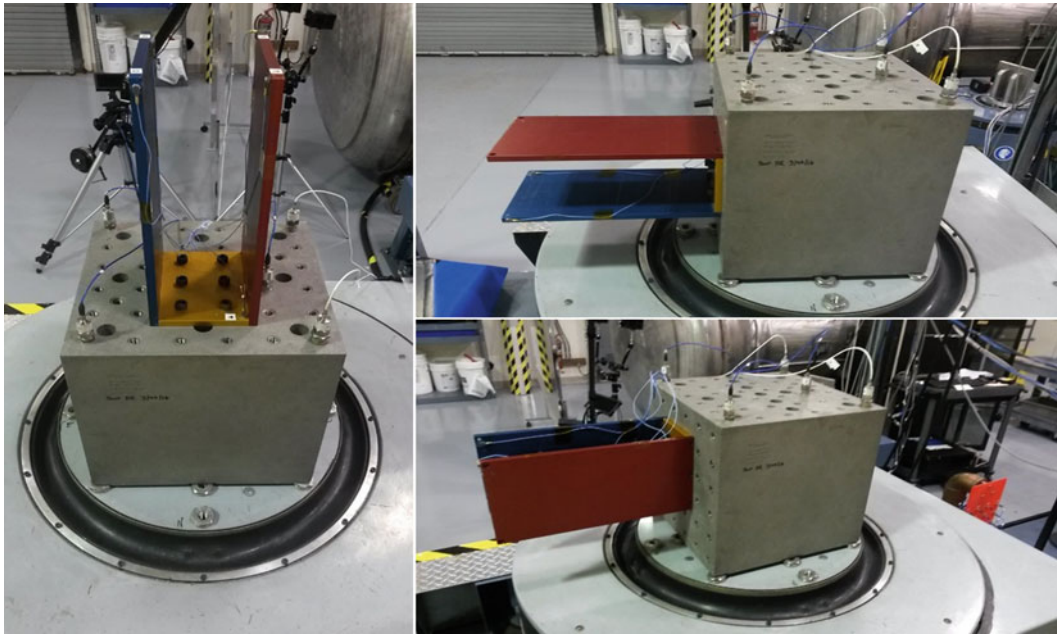


Fig. 17.8 Jim Beam Vibe table test configurations. Clockwise from bottom right: X-Axis, Y-Axis, Z-Axis

17.6 The Sine Vibration Test

Once the “fixed” modal test was complete, the shaker was powered on for the sine vibration test. For this test, the KSC vibration lab’s ten channel data acquisition system was used, as it interfaces with the shaker table control system. The same five teardrop accelerometers on the Jim Beam were kept at the same locations as for the previous two modal tests, and five additional single-axis accelerometers were added to the Cube; one close to the Jim Beam interface to be used as the control channel, and one at each of the four corners of the Cube. This was to capture any rotations present in the Cube, especially during the lateral runs where the Jim Beam was cantilevered off the side of the Cube (Fig. 17.8).

Sine sweeps were run in all three axes (XYZ) from 5 Hz to 3000 Hz at quarter-G and half-G levels, sweeping at two octaves/min. The Jim Beam was rotated on the Cube after each test to drive the next test axis. No frequency shifts were observed between the quarter-G and half-G testing, as the Jim Beam is a very simple and linear structure.

The effect of directionality on the fixed-base modes of the Sine Vibe results is clear from Fig. 17.9 – all three test axes are required to capture all the fixed base modes. By contrast, a single reference accelerometer could be used to capture all of the free-free modes.

NX Nastran Solution 111 was used to synthesize seismic basedrive responses, and post processing of the results was completed using Python software to generate Frequency-Response-Function (FRF) comparisons, given in Fig. 17.10.

It is clear from the data that the sine vibration test is picking up something that the analytical basedrive did not. In particular, the X-Axis test data does not show clean modes between 400 Hz and 600 Hz, and an additional mode appears around 800 Hz in the X-Axis that wasn’t seen during the free-free test. One might surmise that these effects are due to the cantilevered test configuration, however, upon further inspection, the 800 Hz mode can also be seen in the “fixed” modal test data, which was taken while the Jim Beam was bolted upright in the Y-Axis. Additionally, the analysis shifts the high frequency modes above 1100 Hz. Given that the analysis was conducted using a correlated FEM, the only new element is the unknown compliance of the shaker table. However, without an a-priori correlation, and just the sine vibration data, would this model be considered uncorrelated? Would time and effort be spent changing the model to match shaker table effects, which do not actually reflect the test article or the flight interface?

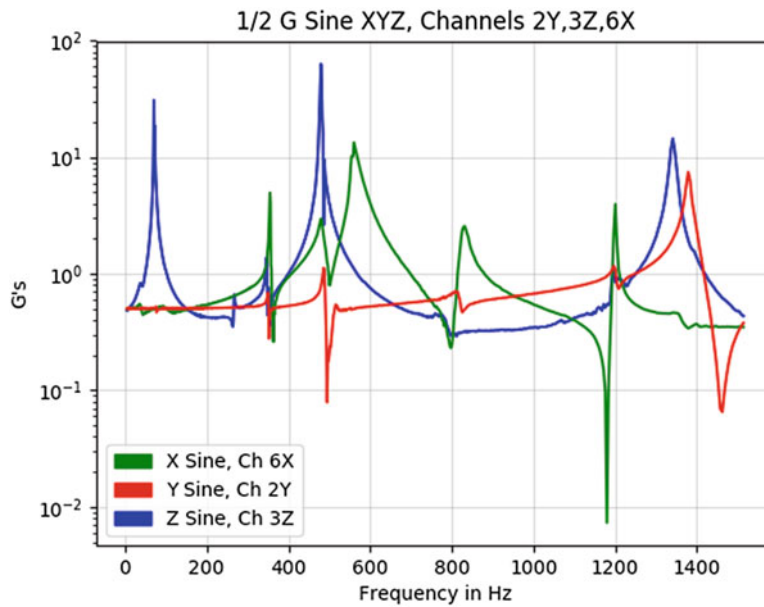


Fig. 17.9 Sine vibration test, Channels 6X, 2Y, and 3Z

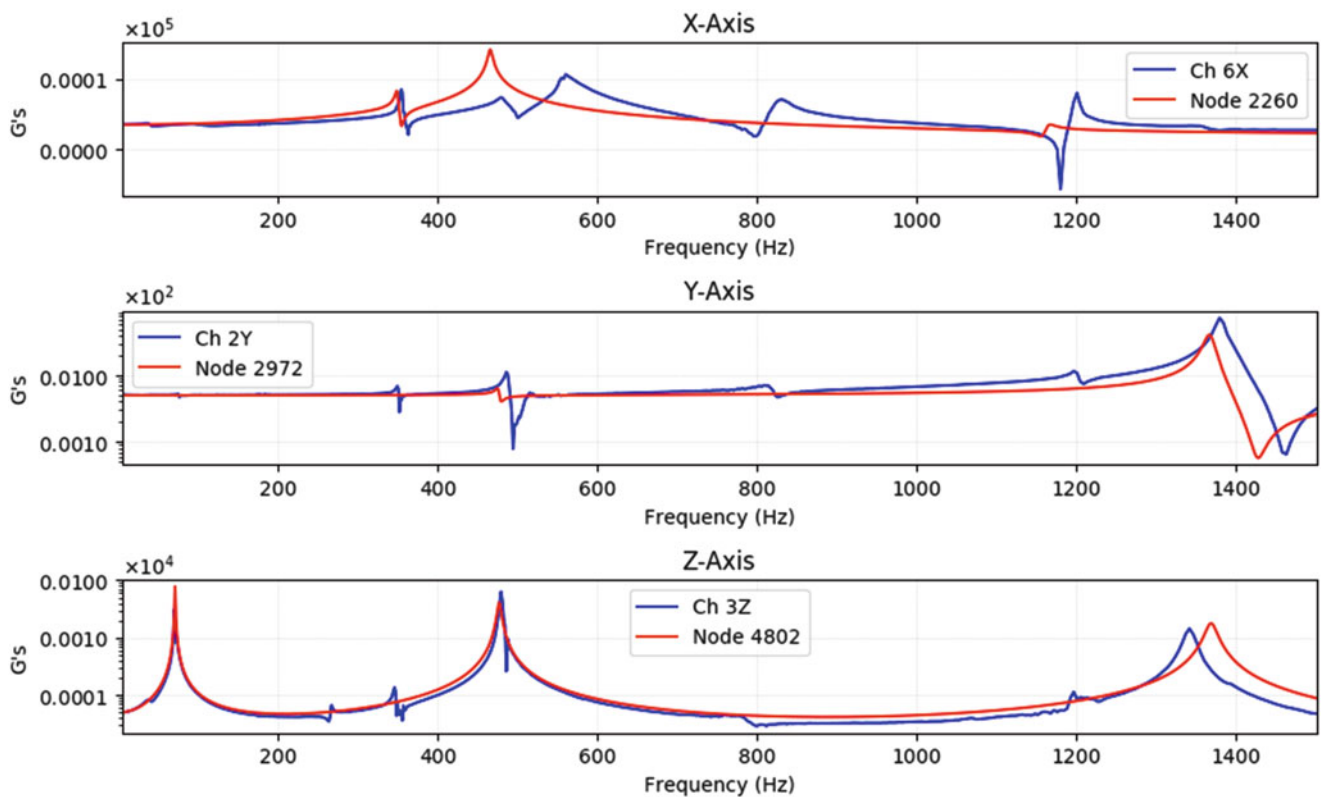


Fig. 17.10 Comparison of each test axis with its respective accelerometer

17.7 Conclusions

The ability to capture the boundary conditions of the test in the model dictate the success of the correlation. Thus most modal tests control the boundary by using a modal plate to assume a fixed boundary condition or very soft springs such as bungees or airbags to assume a free-free boundary condition. The difficulty in using a sine vibration test for model correlation is

the definition of the shaker boundary, as there is compliance in the system that cannot be accounted for in the model with a classic seismic basedrive, which is an industry standard practice. The results presented here validate the supposition of Carne [4] that the shaker table cannot be assumed to have zero motion at the interface point, as a seismic basedrive implies. In this study, it was easy to model bungees as light springs and produce excellent correlation results, where most of the time and effort spent on model correlation was devoted to updating the Jim Beam FEM. To achieve similar correlation results with the sine vibration test, most time and effort would be spent accounting for the shaker boundary condition, not the Jim Beam model itself. In this case, the sine vibration test was completed on a correlated Jim Beam FEM, highlighting the poor definition of the shaker boundary. The luxury of a correlated FEM going into sine vibration testing is not afforded to most spacecraft, as the vibration test may be the only opportunity to obtain empirical data for model correlation.

Acknowledgements The authors would like to thank NAVCON Engineering for providing a Jim Beam for study, and KSC Vibrations Lab Test Director Mark Hamilton for time in the vibration lab.

Bibliography

1. Abdallah, A.: Verification of Spacecraft Dynamic Models for Coupled Loads Analysis. Kennedy Space Center/NASA, Orlando (2007)
2. Bridgers, D.L., Mayes, R.L.: Extracting Fixed Base Modal Models from Vibration Tests on Flexible Tables. Sandia National Laboratories, Albuquerque (2009)
3. Lollock, J.A.: A Comparison of Base-Shake and Mode Survey Test Based Model Correlation Techniques. The Aerospace Corporation, Los Angeles (2004)
4. Carne, T.G., Martinez, D.R., Nord, A.R.: A Comparison of Fixed-Base and Driven-Base Modal Testing of an Electronics Package. Sandia National Laboratories, Albuquerque (1989)
5. Hoople, G.: Jim Beam Testing & Results. IMAC XXVII, Orlando (2009)

Chapter 18

Real-Time Hybrid Testing: Challenges and Experiences from a Teaching Point of View

Markus J. Hochrainer

Abstract Hybrid simulation techniques, which combine real physical models with virtual simulation models, have developed significantly in the last decades. Continuing scientific work and steady progress in simulation and modeling techniques together with powerful automatic code generation tools have pushed this development. For an engineer, this technology offers the possibility of significant savings, faster product development, reduced design uncertainties and reliable component testing without any risk. Due to these advantages there is an increased industrial acceptance and consequently the integration in engineering education is required. From a scientific point of view, hybrid testing demands advanced knowledge in the fields of modeling and simulation, real-time integration, model-order reduction, measurement and signal processing. Furthermore, since coupled systems generally result in a closed loop structure, profound understanding of control theory as well as sensors and actuators is essential. In order to manage this diversity of requirements, several experiments of varying complexity have been developed for illustration of the theoretical background. The laboratory experiments presented comprise dynamic absorber testing and hybrid testing of mechatronic systems like a quadcopter during complex flight operations. The aim is a basic understanding of hybrid testing, its challenges and potentials, and the ability recognize and implement possible application in science and industry.

18.1 Introduction

The constant development of experimental techniques has resulted in very powerful and sophisticated methods with a high level of acceptance in the engineering community. In parallel, numerical simulation techniques have reached incredible progress in almost any field, up to a point, where the substitution of physical models by virtual components has become every day routine. However, physical testing of components is still required, particularly for mechatronic systems due to their complexity and demanding real world interactions. Nevertheless, with the slow but steady emergence of hybrid simulations a method has come into focus, which has the potential to fundamentally extend the possibilities of conventional testing. The simple and captivating idea is to couple an existing physical model with a real-time simulation model (virtual model) to test the physical component under most realistic conditions. The fascinating approach of combining experimental and numerical techniques, thus merging the advantage of both disciplines, has been very attractive for the scientific community for a long time [1–3]. Finally, hybrid simulation techniques have become popular and acknowledged in industrial developments and commercial applications. Its acceptance is increased by tools supporting model based design, physical modeling and automatic code generation (ACG). Today, there are several commercial products for real-time simulation on the market, providing solutions for off the shelf hardware components, without the need for special knowledge in the areas of programming or hardware architecture.

Furthermore, popular and wide spread low-cost embedded systems meet the basic demands for real-time simulation, and consequently, the necessity for using expensive, dedicated real-time hardware has been reduced. In addition, the development time for real-time hybrid simulation decreases when using ACG tools, and the simulation models remain almost hardware-independent. Consequently, hybrid simulation techniques have attracted increased attention and can be found in almost any field of experimental testing. Product development becomes faster, with less uncertainty, and the possibility of testing components prior to the accessibility of a prototype is particularly attractive. Commonly, only a limited number of engineers can work with real prototypes, and in addition, their availability is usually just a fraction of the development time. Hybrid simulation techniques compensate this drawback by virtual prototypes and allow experimental testing even in an early development stage. In addition, they offer all advantages of conventional simulation, including significantly reduced costs for

M. J. Hochrainer (✉)

University of Applied Sciences, Wiener Neustadt, Austria

e-mail: markus.hochrainer@fhwn.ac.at

testing and analysis, repeatability of experiments with precisely defined boundary conditions, analysis of difficult to maintain or dangerous system conditions or settings, and, with respect to the simulated model, trouble free modifications and even substitution by a different or more accurate model.

Depending on the advance of a design process, a hierarchy of “in the loop” methods has been established. Model in the loop (MIL) describes the simulation in an early stage, when both, the physical component and its environment (virtual component) are simulated as computer model. The interface/communication is modelled by simulated sensor and bus signals. This approach is commonly denoted “computer simulation”. If the physical component is converted into automatically generated code, which is still running on the simulation computer, the experiment is called software in the loop (SIL). Assuming that the physical component is an embedded system, e.g. an electronic control unit (ECU), then the target hardware does not even have to be defined at this stage. Next, when the automatically generated code is running correctly on the selected target hardware without any physical peripherals, with all sensor and communication signals still simulated, a processor in the loop (PIL) simulation is performed. Finally, when a real physical hardware is connected to virtual simulation models under most realistic conditions, we are talking about real-time hybrid simulation. Differing from this classification, some HIL experiments are just described by their primary purpose, e.g. steering in the loop, vehicle in the loop, airplane in the loop. Furthermore, the different “in the loop” levels (MIL, SIL, PIL, HIL) are sometimes summarized as XIL approach, where X denotes a model, software, processor or real physical hardware.

The salient features mentioned have made real-time hybrid simulations very attractive for all areas with a complex interaction between physical and virtual components. Depending on the scientific discipline, the combination of numerical and experimental techniques is known as (real-time) hybrid simulation (RTHS), real-time hybrid testing, dynamic hybrid substructuring, hardware in the loop (HIL) or cyber physical testing. Due to the multidisciplinary nature of projects linking numerical and experimental methods, hybrid simulation has become rather demanding for experimentalists: modeling and simulation, real-time integration, model-order reduction, basic control theory or signal measurement and processing are fundamental for successful hybrid testing. Nevertheless, the requirements and challenges of real-time hybrid simulations vary considerably, because they are strongly dependent on the actual application. Historically, quasi-static methods have been used first for hybrid testing of nonlinear structural elements, whereas for applications in noise and vibration analysis, steady state conditions are quite often sufficient. Generally, real-time hybrid testing is performed without such limiting constraints, which is particularly true if a system’s electronic control unit (ECU) is tested. Potential data transmission, digital interfaces, timing aspects, possible control loops as well as analog filtering go far beyond the possibilities of quasi-static or steady state testing. Although control theory is a crucial component for HIL applications, there are significant differences in the objectives of the respective disciplines. Control theory aims at the analysis and improvement of system dynamics (stability) to get a desired performance. Hybrid simulations, on the other side, focus on testing real physical components in a virtual environment, commonly emphasizing aspects of reliability, fault injection/tolerance or test management and automation. Because many initial challenges of RTHS have been solved, and a much deeper understanding of hybrid simulations has been developed, the method is ready for a wide spread use. Although the method has been developed into a robust, reliable tool, the need for full scale testing of the entire system is only reduced, and not eliminated yet.

18.2 System modelling and Simulation

In modelling and simulation of dynamic systems, there has been a strong tendency to model-based approaches in recent years. The system and its functionality forms the center of the development process, beginning from the definition of requirements up to implementation and final testing. Since the virtual component is executable all the way through the development process, simulations can always be used to ensure a desired behavior and proper operation. Furthermore, hard- or software requirements, like fixed-point or timing performance, can be included for proper code generation and real-time system verification.

With respect to the modelling process, two fundamentally different approaches must be distinguished: mathematical modeling and physical system modeling (PS). The former represents a fundamental part of university education, is well established in engineering and has been used since the development of modern science. The latter has emerged from analyzing complex and multiple domain systems, and is supported by modeling languages like modelica [4]. It offers an intuitive way of modelling systems of real components organized in a physical network. The PS elements (blocks) are arranged and connected according to the real world situation. Once a description of the model is completed, it is translated into a mathematical model, mostly differential algebraic equations, and solved by proper solution algorithms. In contrast to an abstract mathematical description, a close relationship between reality and model is always maintained. Since all PS blocks are linked by physical connections, the level of detail of the simulation can be increased by substituting simple components

Table 18.1 Flow and potential variables from common domains [4]

Domain	Flow	Potential
Electrical	Current (A)	Voltage (V)
Mechanical (translational)	Force (N)	Velocity (m/s)
Mechanical (rotational)	Torque (Nm)	Angular velocity (rad/s)
Hydraulic	Flow rate (m ³ /s)	Pressure (N/m ²)
Heat conduction	Heat flow (W/m ²)	Temperature (K)

by more complex ones. A hierarchy of different component models is often readily available from comprehensive, multiple domain component libraries.

Contrary to conventional modeling based on signal flow diagrams, PS is also known as “acausal modeling”, because there is no explicit specification of a systems input and output, and thus no flow direction. The way the mathematical model is derived, optimized and solved is not determined by the engineer, and consequently no signal flow is needed during the model layout. For acausal formulations it is vital to identify the flow (through variables) as well as the potential (across variables). The latter denotes a driving force, whereas the former represents the flow of some conserved quantities. For an electrical system the respective quantities are voltage and current, as well as velocity and force in case of mechanical systems, see Table 18.1. The product of flow and potential quantities naturally has the unit of power.

Another very common technique in modeling and simulation is the system description by signal flow diagrams (signal flow graphs), known from popular and wide spread environments like Simulink, Scicos or LabVIEW. The entire system’s behavior is described by a network of basic elements, generally blocks with defined inputs and outputs. The way these elements are connected determines how information is processed. Consequently, there is a clear and well-defined signal flow and the method is referred to as “causal modeling”. It is every day routine for the experienced engineer to derive a signal flow model or a mathematical description for a specific problem, even if there is a large number of degrees of freedom. Still, the required mathematical transformations and manipulations are tedious and error prone and minor modifications, e.g. changes in boundary conditions often require considerable modifications of the signal flow diagram.

Before the wide spread availability of graphical tools, engineers had to work with abstract mathematical model descriptions and text-based programming. With this traditional approach model development and simulation is time consuming, error prone and needs trial and error to obtain a final model. Furthermore, this process must be repeated whenever the mathematical models changes during the various stages of the design process. There again, graphical tools aim to avoid unnecessary revisions by structuring the model complexity into different design blocks and providing ACG.

Finally, however, it must be pointed out that all methods discussed (text-based description, signal flow models and physical system modeling) can be interpreted as different levels of modeling. When properly used, their results are identical, and hence all system descriptions are equivalent. In order to understand the challenges of HIL experiments each representation has individual benefits. A rigorous mathematical representation is essential for model order reduction, the requirements of real-time integration are easily demonstrated and understood with signal flow models, and the implementation of complex multiple domain systems is best performed with physical modeling.

There is, however, another efficient and quite productive way of model development. If the virtual model has a physical representation (an already existing prototype), then all methods established in system identification can be applied to find the virtual counterpart. This approach is well established in structural dynamics and known as modal testing. However, it is rarely used as a hybrid simulation technique. Nevertheless, modal identification directly renders a mathematical model by a process which is almost fully automated and performed on a computer. If it is possible to derive a consistent mathematical model based on physical measurements, this is a very attractive alternative to model derivation based on physical principles only. However, due to the restrictions of most system identification methods, the approach will be limited to systems with predominant linear behavior.

18.3 Real-Time Simulation

Because a HIL experiment requires the simulation model to run in real time, techniques for model acceleration must be considered. The mathematical representation of the simulation model is often given by ordinary differential equations or differential algebraic equations, and a solution is obtained from time integration. Common explicit solver use variable integration step sizes for a solution with a specified accuracy. Consequently, the solution will not be real-time any more, if small integration steps are required. The same is true for implicit solver with superior stability properties but an unknown

number of iterations. Accordingly, explicit fixed step solver are widely used for real-time integration, because the solution is obtained in a predetermined period of time. To understand the challenges of fixed step integration the numerics of ordinary differential equations must be studied. However, for explicit, fixed step integration schemes (of the Runge-Kutta type), a desired unconditional stability does not exist, and the critical step size depends on both, the system dynamics and the integration method, respectively. For a given integration method and linear system dynamics, the critical integration time step h is dependent on the fastest system pole λ_{fast} . This is particularly important since HIL applications often use components described by stiff equations, for which explicit numerical methods are known to be numerically unstable, unless the step size is extremely small. Although it is difficult to formulate a precise definition of stiffness, it is commonly accepted that a linear system is stiff, if there is a large ratio between the fastest and the slowest pole, $|Re(\lambda_{fast})|/|Re(\lambda_{slow})| \gg 1$. A graphical representation of the relation between stability, step size and pole location is given in stability charts.

As just described, the drawback of explicit approaches is the dependence of the step size (and thus the stability limit) on the fastest pole. For moderately complex systems the required time-step is likely to be much too small for real-time integration on the target hardware. For linear systems, there are two common ways to deal with this situation. Firstly, a state model of order n

$$\begin{aligned}\dot{\mathbf{x}}(t) &= \mathbf{A}\mathbf{x}(t) + \mathbf{B}\mathbf{u}(t) \\ \mathbf{y}(t) &= \mathbf{C}\mathbf{x}(t) + \mathbf{D}\mathbf{u}(t)\end{aligned}\quad (18.1)$$

can be converted from continuous to discrete time

$$\begin{aligned}\mathbf{x}_{k+1} &= \mathbf{A}_d\mathbf{x}_k + \mathbf{B}_d\mathbf{u}_k \\ \mathbf{y}_k &= \mathbf{C}_d\mathbf{x}_k + \mathbf{D}_d\mathbf{u}_k\end{aligned}\quad (18.2)$$

with the sampling time T_S selected to fulfill all real-time requirements. The most common discretization methods include zero order hold, first order hold, impulse invariant discretization or the bilinear method, see e.g. Ref. [5]. From a numeric point of view, time discrete models are favorable as long as the rounding errors are small. The time discretization is a very powerful and highly underestimated method of circumventing integration difficulties. Secondly, a model order reduction (MOR) can be performed to eliminate superfluous but numerically critical system states. MOR is an essential technique for systems with a large number of degrees of freedom. Since both methods complement each other, the different approaches should be combined for optimal real-time performance with minimal hardware requirements. In any case, the concept of MOR is necessary if the system model is derived from finite element modeling (FEM). This popular and well-established numerical method renders very large linear systems, typically in the order of millions of degrees of freedom, and MOR is inevitable for real-time applications. In the field of modal analysis, MOR and modal decomposition are extensively used and highly researched, even for nonlinear applications. Generally, however, the method is restricted to linear problems, e.g. vibrations (structural modes), heat conduction (thermal modes), electromagnetic phenomena (waveguide modes) or optics (laser modes). Given a linear system of order n in state space, a modal transformation can be performed by diagonalization of the system dynamics matrix \mathbf{A} such that the system is given in Jordan (diagonal) form,

$$\mathbf{A} = \begin{pmatrix} \lambda_1 & 0 & \cdots & 0 \\ 0 & \lambda_2 & \cdots & 0 \\ \vdots & \vdots & \ddots & \vdots \\ 0 & 0 & 0 & \lambda_n \end{pmatrix}, \quad \mathbf{B} = \begin{pmatrix} \mathbf{b}_1^T \\ \mathbf{b}_2^T \\ \vdots \\ \mathbf{b}_n^T \end{pmatrix}, \quad \mathbf{C} = (\mathbf{c}_1 \ \mathbf{c}_2 \ \cdots \ \mathbf{c}_n). \quad (18.3)$$

with λ_i ordered so that $|\lambda_1| < |\lambda_2| < \cdots < |\lambda_n|$. If the state vector \mathbf{x} is partitioned into $\mathbf{x}^T = (\mathbf{x}_1^T \ \mathbf{x}_2^T)$, where \mathbf{x}_1 contains the k relevant states, and \mathbf{x}_2 the $n - k$ states to be removed, the state space equations become

$$\begin{aligned}\dot{\mathbf{x}}_1 &= \mathbf{A}_{11}\mathbf{x}_1 + \mathbf{A}_{12}\mathbf{x}_2 + \mathbf{B}_1\mathbf{u} \\ \dot{\mathbf{x}}_2 &= \mathbf{A}_{21}\mathbf{x}_1 + \mathbf{A}_{22}\mathbf{x}_2 + \mathbf{B}_2\mathbf{u} \\ \mathbf{y} &= \mathbf{C}_1\mathbf{x}_1 + \mathbf{C}_2\mathbf{x}_2 + \mathbf{D}\mathbf{u}.\end{aligned}\quad (18.4)$$

In modal truncation all states and dynamics associated with \mathbf{x}_2 is discarded, $\mathbf{x}_2 = \dot{\mathbf{x}}_2 = \mathbf{0}$. When residualizing \mathbf{x}_2 instead, the second state space equation is set $\dot{\mathbf{x}}_2 = \mathbf{0}$. Solving for \mathbf{x}_2 in terms of \mathbf{x}_1 and \mathbf{u} renders, after back substitution, the reduced order system

$$\begin{aligned}\dot{\mathbf{x}}_1 &= (\mathbf{A}_{11} - \mathbf{A}_{12}\mathbf{A}_{22}^{-1}\mathbf{A}_{21})\mathbf{x}_1 + (\mathbf{B}_1 - \mathbf{A}_{12}\mathbf{A}_{22}^{-1}\mathbf{B}_2)\mathbf{u} \\ \mathbf{y} &= (\mathbf{C}_1 - \mathbf{C}_2\mathbf{A}_{22}^{-1}\mathbf{A}_{21})\mathbf{x}_1 + (\mathbf{D} - \mathbf{C}_2\mathbf{A}_{22}^{-1}\mathbf{B}_2)\mathbf{u}.\end{aligned}\quad (18.5)$$

This procedure is known as static condensation in structural engineering. An important property of the residualization is the preservation of the static gain, whereas the modal truncation retains the behavior at infinite frequency. So far, the modal reduction is based on the assumption that the fastest modes should be removed, without considering the excitation input matrix \mathbf{B} and the output matrix \mathbf{C} , respectively. From a control point of view, the balanced realization is a much better state space representation, since the observability and controllability Gramians $\mathbf{P} = \mathbf{Q} = \text{diag}(\sigma_1, \sigma_2, \dots, \sigma_n)$ are diagonal with $\sigma_1 \geq \sigma_2 \geq \dots \geq \sigma_n$. The realization is called balanced, because the size of each σ_i , which is only associated with the i -th state, is a relative measure of the input-output behavior of the system. Consequently, if $\sigma_i \gg \sigma_j$ then x_i effects the input-output behavior much more than x_j . After balancing a system, each state is just as controllable as it is observable, but the system matrix \mathbf{A} is no longer diagonal. After residualization or truncation an error measure can be given by the singular values discarded [6, 7]

$$\|\mathbf{G}(s) - \mathbf{G}_r(s)\|_\infty \leq 2(\sigma_{k+1} + \sigma_{k+2} + \dots + \sigma_n), \quad (18.6)$$

where $\mathbf{G}(s)$ and $\mathbf{G}_r(s)$ denote the transfer function of the original and the reduced order system, respectively. Relation 18.6 can be used to determine the number of states k necessary to stay below a given error bound. In control theory, the concept of balanced truncation or residualization has been developed, because optimal control designs based on model state observers like linear quadratic Gaussian (LQG) or \mathcal{H}_∞ produce controller of an order at least equal to that of the model, often higher because of the inclusion of weights. Consequently, the motivation for MOR in control is the same as in hybrid simulation, and the concepts and methods developed in control theory are directly applicable to RTHS.

For FEM models (with thousands of degrees of freedom) the concept of balanced residualization is difficult to implement within numerical matrix computation environments, because of memory and matrix size limitations. Since many FEM software packages support modal analysis, it is, in any case, favorable to decompose the numerical model before trying to export the relevant system parameters. If, however, there is no option to export the data directly, it is still possible to obtain reduced order model by applying the methods of system identification to FEM simulated time responses or frequency domain data, e.g. impulse responses or Bode diagrams. Although this approach is not favorable when compared to modal truncation or balanced residualization it will, very probably, produce acceptable models with a high level of model reduction. Finally, with an accurately reduced order system model, a stable, explicit, fixed step real-time integration is most likely possible on a suitable target hardware.

18.4 Interfaces and System-Coupling

Independent of all topics already discussed, another key issue in RTHS is the selection of the interface between virtual and physical model. Often, this is the most demanding task when setting up a HIL experiment, because at a physical interface all (dynamic) equilibrium conditions must be met. According to the substructuring methodology, the physical component is excited through its interface degrees of freedom, and consequently all interface constraints must be met for a correct RTHS with meaningful results. Independent from the physical domain considered, the dynamic substructuring approach requires all flow and potential constraints to be fulfilled. Because optimal interface conditions are very difficult to establish and maintain, an inner feedback control loop is commonly used for correct operation. Typically, all actuating, sensing and control elements needed to couple physical and virtual models are referred to as transfer system. Before designing the inner feedback control, the input and output quantities must be defined. In a lumped interface model of a mechanical subsystem either the interaction force, or the component velocity can be prescribed by a control algorithm, whereas the remaining other quantity is only depending on the mechanical impedance of the structure and must be known (measured) for updating the simulation model. For transient dynamics, the interface control is very demanding and limited to a frequency band of interest, [8–11]. If, however, the analysis of the stationary behavior is sufficient, a much slower, adaptive control process can be applied to meet the steady state equilibrium conditions see e.g. Ref. [12]. The above discussion clearly shows, that direct physical coupling is challenging and a common source of errors. Therefore, if possible, the system boundaries should be extended to a signal or data bus to circumvent direct physical coupling. For this reason, the substructure interface should always be selected accordingly, as in the first example presented in this work.

Apart from special application areas like HIL experiments, active feedback control is primarily used to change, modify or improve the dynamic system behavior. In principle, this is possible by injecting or absorbing energy by regulating the system

input according to the control law. Consequently, active control can stabilize dynamic processes by energy dissipation, which is quite favorable when dealing with noise or vibration problems. However, in case of RTHS energy dissipation is rather annoying, because it conflicts with the principle of energy conservation within the simulation setup. Even worse is the opposing effect of energy injection, since it has the potential to destabilize models. This property is well known and understood, but is still a very demanding topic because for lightly or almost undamped structures any additional time delay will result in instability. Even if the actuator energy supply is limited or too small to damage or destroy the setup, any change of relevant stability properties will lead to results, which are no longer meaningful. Therefore, the primary goal is to ensure that the overall system stability is described correctly. Due to various sources of delay, e.g. the actuator delay, the low pass characteristics of sensing devices or sampling and processing times the compensation of time delays has become a crucial aspect in HIL.

18.5 Applications

The principles of hybrid simulation are illustrated by two representative applications with varying demands in terms of system modeling, real-time simulation and interfaces. In the first example, the IMU (inertial measurement unit) of a quadcopter is tested by hybrid simulation to analyze its undesired dynamic flight performance.

The most important requirement for successful HIL testing is a well-defined interface between virtual and experimental components. The latter (quadcopter ECU) includes the IMU sensor evaluation, the control unit, power amplifiers, BLDC engines and the remote control. In this experiment, the systems are separated at a digital interface, avoiding all problems with physical coupling. The virtual model transmits simulated sensor values to the physical quadcopter ECU and engine control commands are returned to the virtual flight model running on the real-time PC, see Fig. 18.1. The host-PC configures and controls the experiment, and in addition the simulated flight is visualized by a virtual reality quadcopter model. The ECU is based on an embedded system (Microchip PIC 24FJ256GB106) and already set up to perform both, the calculation of the direction in space and the stabilization of the inherently instable quadcopter. In addition, the ECU is responsible for the communication with the remote control unit, and UART communication necessary for the HIL setup.

The salient feature of quadcopters is the simple and robust design with rigid rotors directly attached to independently operated engines. Due to their geometry, most quadcopters are instable, and feedback control based on local IMU measurements is obligatory. In this study, the simulation model is obtained from mechanical principles, assuming that the quadcopter of mass m is rigid with all moments of inertia collected in the tensor \mathbf{J} . Under these assumptions, there are only six degrees of freedom, thus, no need for FEM or PS modelling. The external forces are the rotor thrusts \mathbf{F}_i , $i = 1..4$, their corresponding reaction torques \mathbf{M}_i , the gravitational force \mathbf{F}_g , and the aerodynamic drag $\mathbf{F}_A = \mathbf{v}|\mathbf{v}|k$, with \mathbf{v} and k denoting the velocity and the drag constant, respectively. Newton's law of inertia for moving reference frames renders an equation of motion in the moving reference frame (local coordinates superscript b)

$$m\dot{\mathbf{v}}^b + m\boldsymbol{\omega}^b \times \mathbf{v}^b = \sum \mathbf{F}_i^b + \mathbf{F}_g^b + \mathbf{F}_A^b, \quad (18.7)$$

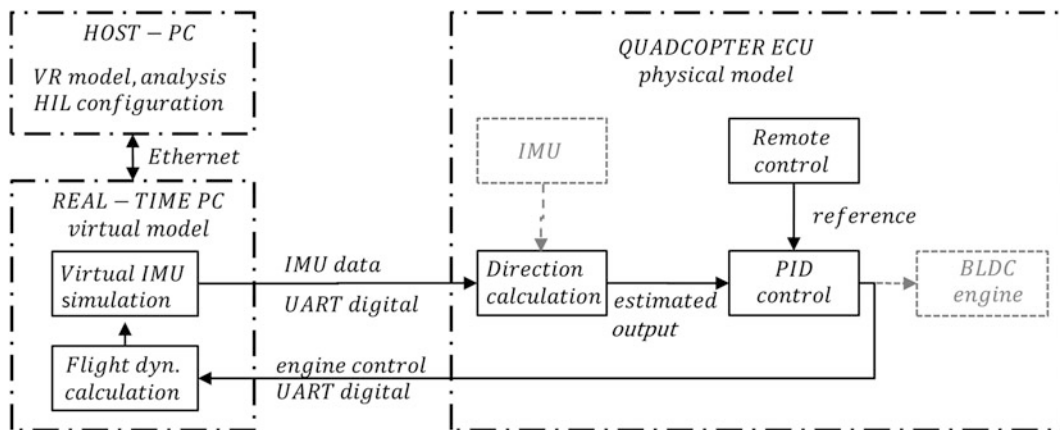


Fig. 18.1 Schematics of HIL quadcopter experiment [13]

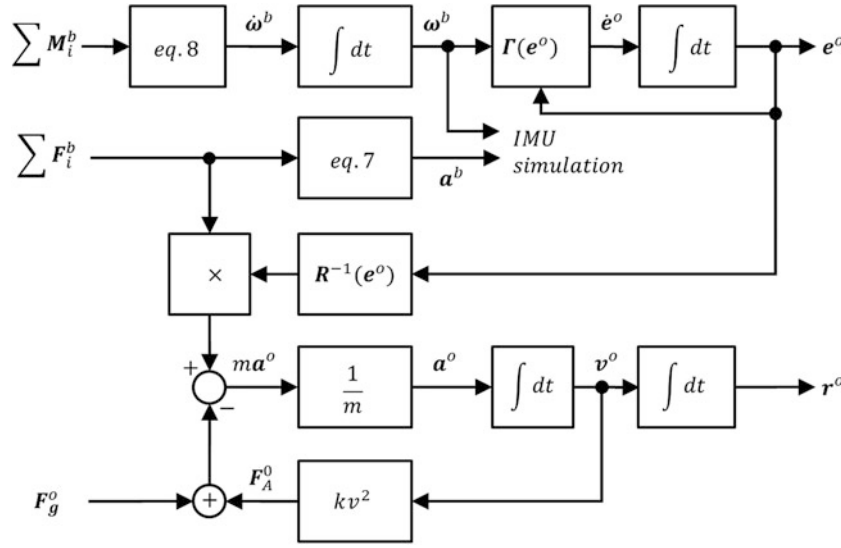


Fig. 18.2 Signal flow diagram of real-time flight simulation [13]

with $\omega^b = (\dot{\phi}_x^b, \dot{\phi}_y^b, \dot{\phi}_z^b)^T$ representing the angular velocity vector, and $\mathbf{r}, \mathbf{v} = \dot{\mathbf{r}}, \mathbf{a} = \ddot{\mathbf{r}}$ describing the position, velocity and acceleration vector, respectively. The conservation of angular momentum renders another nonlinear differential vector equation,

$$\mathbf{J}^b \dot{\omega}^b + \omega^b \times \mathbf{J}^b \omega^b = \sum \mathbf{M}_i^b. \quad (18.8)$$

Given the individual engine thrusts, $\mathbf{F}_i^b = (0, 0, f_i)^T$, the equations of motion 7-8 can be solved by explicit fixed step integration. Apparently, the position should be given in absolute coordinates (global coordinates, superscript o). The transformation of vectors between different frames of reference is performed by multiplication with the orthogonal rotation matrix $\mathbf{R}(\mathbf{e})$, with the rotation vector $\mathbf{e}^o = (\phi, \theta, \psi)^T$ containing the Euler angles. Since the equations of motion are given in local coordinates the time dependent relation between the angular velocity vector ω^b and the Euler angles \mathbf{e}^o

$$\dot{\mathbf{e}}^o = \begin{pmatrix} 1 & \sin \phi \tan \theta & \cos \phi \tan \theta \\ 0 & \cos \phi & -\sin \phi \\ 0 & \sin \phi / \cos \theta & \cos \phi / \cos \theta \end{pmatrix} \omega^b = \mathbf{\Gamma}(\mathbf{e}) \omega^b \quad (18.9)$$

is required for the numerical integration of the equations of motion. For details on the required transformations, see Refs. [13, 14, 15]. The signal flow diagram of the simulation model is given in Fig. 18.2. For simulated IMU measurements the determination of ω^b is straightforward, but the calculation of \mathbf{a}^b requires the correction of centrifugal forces, and both vectors must be scaled according to the datasheet's sensor hardware specification. All simulated sensor outputs can be superposed by various errors e.g. sensor noise, offset, temperature drift or nonlinearities.

Having derived the signal flow diagram, the implementation of the virtual model is straightforward. The numerical integration uses an explicit Runge-Kutta method of order four (RK4) with a constant integration step size of $T_S = 5$ ms. The model is compiled and transferred to the target hardware, a PC with a real-time operating system. All relevant system parameters (e.g. mass, inertia, thrusts) have been identified by experimental testing whereas the driveline dynamics has been identified using dynamic system identification (ARX model).

The calibrated HIL experiment allows simulating, validating and analyzing the quadcopter behavior in any possible flight conditions. Testing was focused on flight situations, which initially triggered the HIL testing: little stability margins during hovering, irregular crashes due to suspected engine shut downs as well as firmware bugs in signal processing. The inspection of the HIL flight performance has confirmed the shortcomings of the current ECU with respect to stability margins and limit cycle vibrations during stationary hover flight. Based on the hybrid simulation, it has been possible to identify and correct several sources of errors within the ECU. Figure 18.3 demonstrates the improvements achieved by comparing the system performance before and after error elimination and optimization. The quadcopter motion was triggered manually using the physical remote control unit.

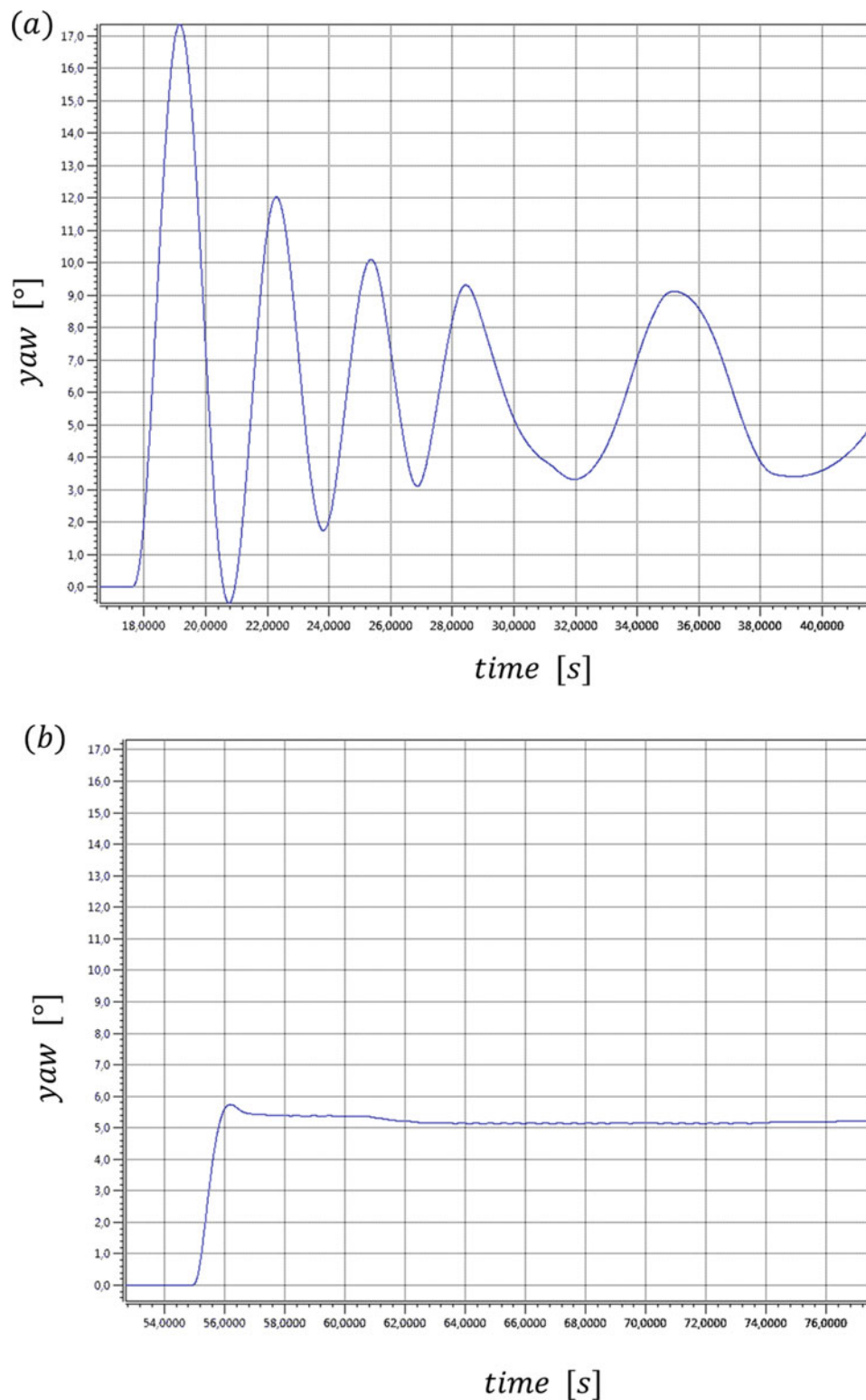


Fig. 18.3 HIL simulated yaw rotation of the quadcopter during hovering (a) original system (b) quadcopter performance after optimization and error elimination

The second example, developed for final year master classes, is intended to illustrate all major development steps when setting up a HIL experiment - including common challenges and complications. The hybrid simulation philosophy is used to investigate the vibration absorbing behavior of a tuned mass damper (experimental model) attached to the top floor of a virtual three story shear frame building (simulation model) under external force excitation, e.g. strong wind loading. The building

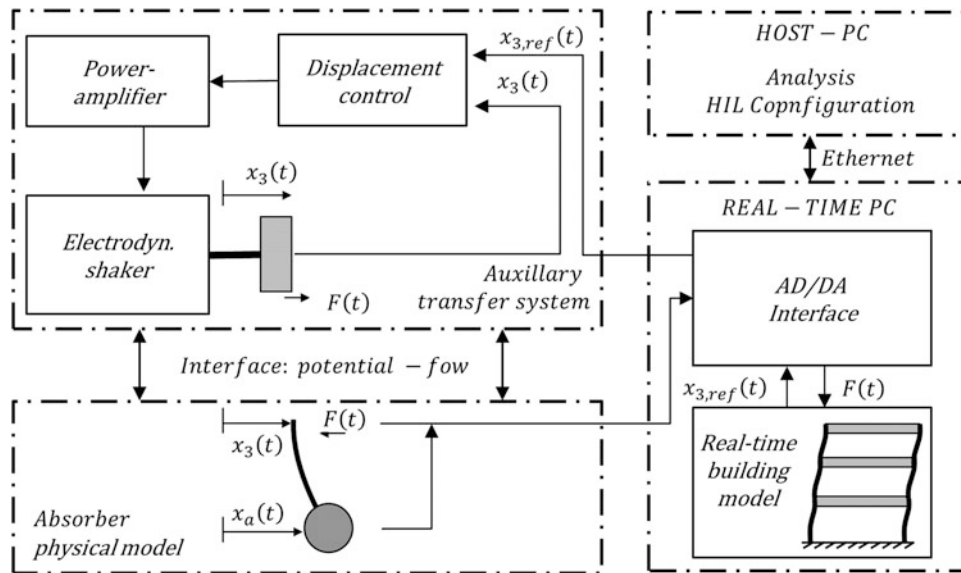


Fig. 18.4 Schematics of HIL absorber testing

model consists of rigid floors, which are connected by linear elastic columns. This time, the separation of the systems can only be done via a physical interface, with the corresponding mechanical quantities of velocity (flow) and force (potential). In principle, the top floor movement $x_3(t)$ of the virtually excited simulation model is transferred to the absorber under test which is attached to an electrodynamic shaker. The required interaction force $F(t)$ is measured, and instantaneously passed to the simulation model. In this setup, a transfer system is required for proper implementation of the interface constraints. It consists of an electrodynamic shaker and laser based displacement sensors in a feedback control configuration. For the schematics of the experiment, see Fig. 18.4.

Although the structural components tested are taken from small-scale experiments, a similar configuration is used in many large or full-scale test applications. In hybrid structural simulation the idea of substructuring is based on the experience, that nonlinear effects, typically plastic deformations, tend to be quite localized. Since the remaining part of the structure behaves linearly and thus quite predictable, it can be simulated, generally using FEM. Only structural member with nonlinear characteristics need to be tested experimentally, such as energy absorbing devices like braces, plastic hinges or vibration isolation elements.

The real time model used in the presented work is derived from a FE model. However, to avoid commercial FEM tools and tedious data exchange procedures, a small FE model of the frame is provided in the simulation environment. It is derived from beam elements with approximately 700 degrees of freedom (DOF) and is already arranged as state space model according to Eq. 18.1. Due to high frequency modes, even this extremely simple FE model is difficult to simulate in real time, and therefore, MOR must be applied. Examination of the top floor transfer function indicates, that the first three modes of vibration (6 DOF) are sufficient to determine the horizontal displacement $x_3(t)$. Having transferred the state model into a balanced realization, the same result is obtained from inspection of the singular values σ_i , which are required to define the MOR error bound, Eq. 18.6. The fact, that three modes of vibration describe the building dynamics sufficiently accurate, is certainly no surprise for an engineer. However, from a teaching point of view, it is definitely much better to get this result by a general and structured approach instead of using experience or engineering intuition. Furthermore, it is even debatable whether a single mode would be sufficient for the experiment. Certainly, this question can only be answered if the absorber parameter, and thus the tuning frequency is known. Because a 6 DOF linear system can easily be simulated in real-time, the reduced order model is appropriate. Again, ACG tools are used to generate real-time code running on the target hardware. The required integration time step T_S is dependent on the virtual model, the frequency content of the excitation and the absorber dynamics. To accurately simulate the structural response, a step size (sampling time) of $T_S \leq 10$ ms and an explicit Runge-Kutta integration method (RK4) are appropriate.

For the development of the auxiliary transfer system, the electrodynamic shaker, the power amplifier and the laser based displacement sensors must be considered. Because the excitation system is not force or displacement controlled, and sensitive to dynamic interaction forces, a linear, empirically tuned regulator is controlling the transfer system. The closed loop performance is just sufficient for hybrid simulation, see Fig. 18.5 for a sine sweep time response. It is important to note, that the controller is used for all types of excitation signals, hence, it is not optimized for steady state performance applying, e.g. parameter adaption. Apparently, the dynamics of the transfer function is not perfect, with both, phase and amplitude errors.

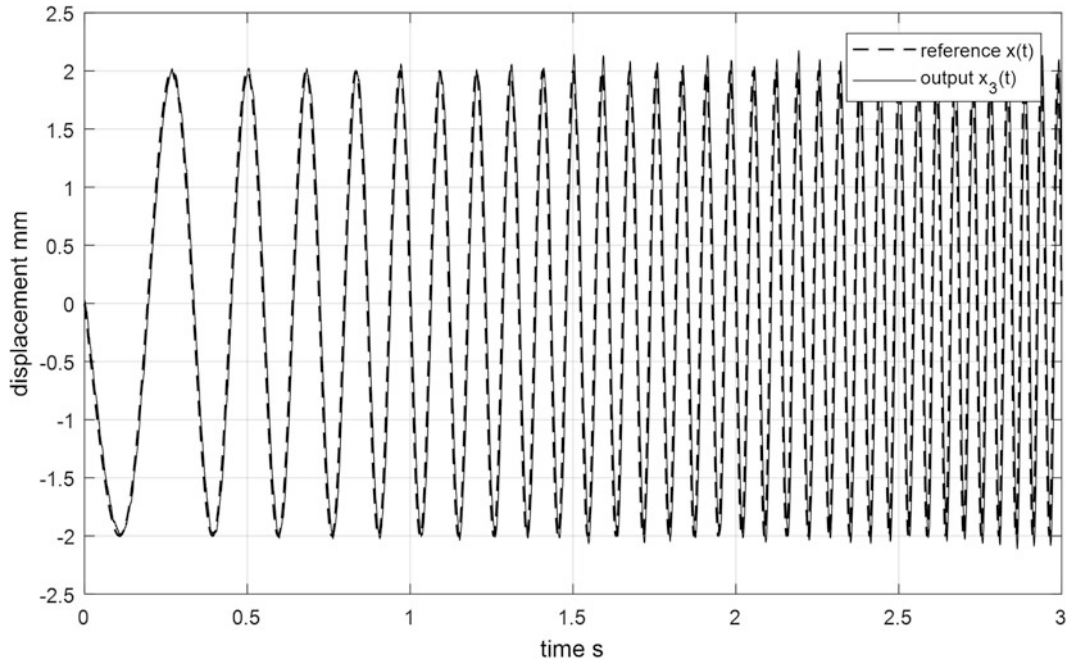


Fig. 18.5 Time response of the feedback controlled transfer system in the relevant frequency range

In addition, there is significant measurement noise, and the actual displacement $x_3(t)$ differs slightly from its reference $x_{ref}(t)$. The control algorithm is again implemented on the real-time PC, however with a different, faster, sample rate of $T_S = 1$ ms. Thus, deviating from the schematics of Fig. 18.4, both, the virtual model and the inner feedback loop are running on the target hardware.

Instead of measuring the shaker-absorber interaction force directly, it is estimated from the relative deformation, assuming the absorber to be linear elastic, $F = k(x_a - x_3)$, with the stiffness k identified by the absorber's natural frequency. This way, the required interaction force is determined with sufficient accuracy. Having defined and set up all relevant elements, first hybrid simulations can be conducted. However, it turned out that depending on the structural damping parameter, the experiment has a tendency to become unstable due to time delays within the system. They are in the order of several milliseconds, see again Fig. 18.5, and arise mainly from imperfect dynamics of the transfer system. From a control point of view, the effect reduces the stability margin, and by looking at the Nyquist stability criterion, it follows that time delay in lightly damped systems effectively introduces negative damping. Failure to correct for the delay will result in inaccurate and possibly unstable simulations. There are three accepted methods to compensate for system delays: increasing the damping of the virtual model, improving the dynamics of the transfer system and predicting the model output. The first approach works satisfactorily with the drawback, that the damping properties of the simulation model do not reflect the damping of its physical counterpart. The second option, the improvement of the transfer system, is important for any HIL application, even though it will never be possible to create the perfect transfer system. The third option, the prediction of future model outputs is, in general, a quite demanding task, but in the actual setup straightforward. Since the dynamics of the virtual model is dominated by inertia effects, the future system state can be predicted assuming free decay time response, thereby neglecting all external forces. For a discrete time state model and a prediction horizon of n steps, \mathbf{x}_{k+n} is defined by the repeated application of Eq. 18.2,

$$\mathbf{x}_{k+n} = \mathbf{A}_d^n \mathbf{x}_k. \quad (18.10)$$

This relation can be used to define a modified output matrix C_d , and thus the existing model can be used without any further modifications. Having compensated the time delay, the hybrid simulation performs well, and it can be used to explain all basic phenomena and principles of dynamic vibration absorption, see e.g. Fig. 18.6a for the frequency response function of the HIL experiment and Fig. 18.6b for an almost perfect absorption in the time domain.

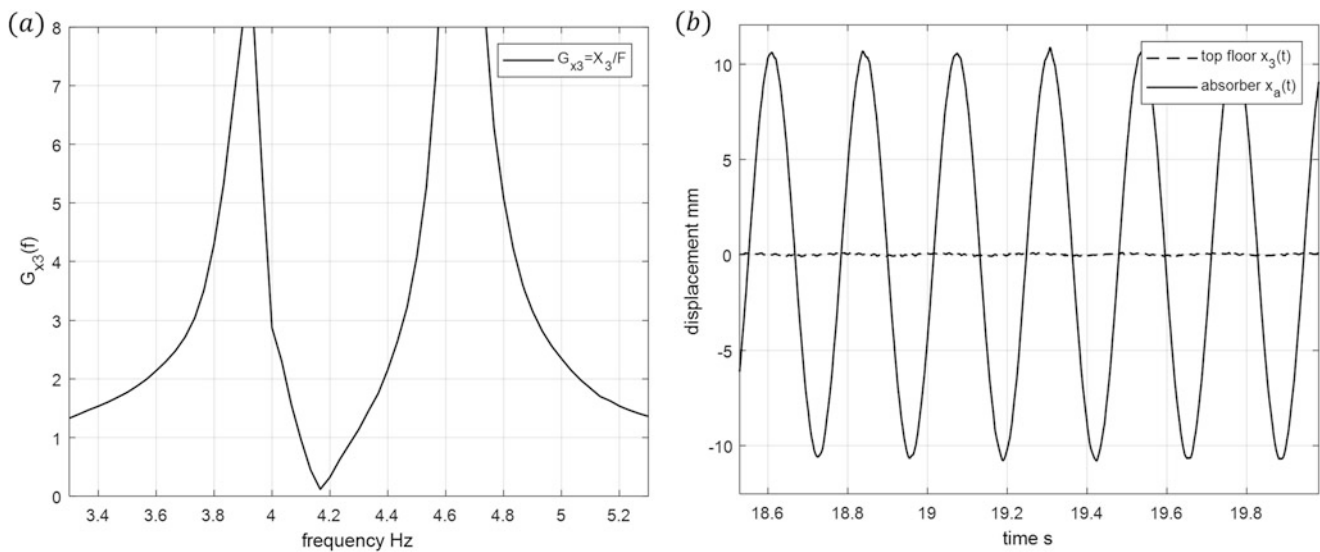


Fig. 18.6 Hybrid simulation results. (a) Frequency response function of top floor (b) almost perfect absorption of first mode vibration for harmonic excitation

Since all components are taken from small-scale models available in the dynamics laboratory, the HIL results can be immediately verified by attaching the absorber (used in hybrid testing) to the physical building model and investigate the overall system performance. From a didactic point of view, it is very satisfying to discover that the hybrid simulation reproduces the behavior of the real system reliably.

18.6 Conclusions

The idea of real-time hybrid simulation has been around for a long time, but the required hardware together with actuating and sensing devices has become available about 20 years ago. Since then, the method has attracted the attention of all engineering disciplines because it permits reliable testing of individual components while taking into account the complex interaction with the overall system. For an engineer, this technology offers the possibility of significant savings, faster product development, reduced design uncertainties and reliable component testing without any risk. On the other side, it requires basic knowledge in the fields of modeling and simulation, real-time integration, model-order reduction, measurement and signal processing. This work introduces the basic concepts and discusses common challenges and complications. The laboratory applications presented comprise dynamic absorber testing and hybrid testing of a quadcopter. Both experiments have been developed to illustrate relevant steps in the development of hybrid simulation. The goal is to identify possible applications in science and industry and to recognize challenges, limits and potentials of the HIL technique. The examples given provide excellent results and underline that the method presented enables developments, which are hardly possible with traditional methods, or only at the price of a significantly greater effort.

References

1. Saouma, V., Sivaselvan, M. (eds.): Hybrid Simulation: Theory, Implementation and Applications. Taylor & Francis Ltd Leiden, The Netherlands (2008)
2. Bursi, O.S., Wagg, D.: Modern Testing Techniques for Structural Systems, Dynamics and Control, vol. 502. CISM International Centre for Mechanical Sciences. Springer, New York (2008)
3. Williams, M.S.: Real-time hybrid testing in structural dynamics. 5th Australasian Congress on Applied Mechanics, ACAM 2007, 10–12 December 2007, Brisbane (2007)

4. Tiller, M.: Introduction to Physical Modelling with Modelica. Kluwer Academic Publishers, London (2001)
5. Ogata, K.: Discrete-Time Control Systems, 2nd edn. Prentice Hall, International (UK) Limited, London (1994)
6. Skogestad, S., Postlethwaite, I.: Multivariable Feedback Control: Analysis and Design, 2nd edn. Wiley, Chichester, England (2005)
7. Moore, B.: Principal component analysis in linear systems: controllability, observability, and model reduction. *IEEE Trans. Autom. Control.* **AC-26**, 17–31 (1981)
8. Darby, A.P., Blakeborough, A., Williams, M.S.: Improved control algorithm for real-time substructure testing. *Earthq. Eng. Struct. Dyn.* **30**(3), 431–448 (2001)
9. Darby, A.P., Williams, M.S., Blakeborough, A.: Stability and delay compensation for real-time substructure testing. *J. Eng. Mech.* **128**(12), 1276–1284 (2002)
10. Ahmadizadeh, M., Mosqueda, G., Reinhorn, A.M.: Compensation of actuator delay and dynamics for real-time hybrid structural simulation. *Earthq. Eng. Struct. Dyn.* **37**(1), 21–42 (2008)
11. Chen, C., Ricles, J.M.: Analysis of actuator delay compensation methods for real-time testing. *Eng. Struct.* **31**(11), 2643–2655 (2009)
12. Bartl, A., Mayet, J., Karamooz Mahdiabadi, M., Rixen, D.J.: Multi-DoF interface synchronization of real-time-hybrid-tests using a recursive-least-squares adaption law: a numerical evaluation. *Proceedings of the 34th IMAC, A conference and exposition on structural dynamics* (2016)
13. Hochrainer, M., Schattovich, P.: Real-time hybrid simulation of an unmanned aerial vehicle, dynamics of coupled structures. *Conference proceedings of the society for experimental mechanics series*. https://doi.org/10.1007/978-3-319-54930-9_4 (2017)
14. Schattovich, P.: Hardware in the loop studies of an unmanned aircraft, in german, Master Thesis, University of Applied Sciences, Wiener Neustadt (2016)
15. Fu, K.S., Lee, C.S.G., Gonzales, G.C.: Robotics, Control, Sensing, Vision and Intelligence. McGraw-Hill International Editions, Singapore (1987)

Chapter 19

Comparison of Computational Generalized and Standard Eigenvalue Solutions of Rotating Systems

Ali Tatar, Loic Salles, Alexander H. Haslam, and Christoph W. Schwingshackl

Abstract Modal analysis is regularly used to compute natural frequencies and mode shapes of structures via eigenvalue solutions in vibration engineering. In this paper, the eigenvalue problem of a 6 degrees of freedom rotating system with gyroscopic effects, including axial, torsional and lateral motion, is investigated using Timoshenko beam theory. The main focus thereby is the investigation of the computational time and the numerical errors in generalized and standard eigenvalue solutions of rotating systems. The finite element method is employed to compute the global stiffness, mass and gyroscopic matrices of the rotating system. The equations of motion is expressed in the state space form to convert the quadratic eigenvalue problem into the generalized and standard forms. The number of elements in the finite element model was varied to investigate the convergence of the natural frequencies and the computational performance of the two eigenvalue solutions. The numerical analyses show that the standard eigenvalue solution is significantly faster than the generalized one with increasing number of elements and the generalized eigenvalue solution can yield wrong solutions when using higher numbers of elements due to the ill-conditioning phenomenon. In this regard, the standard eigenvalue solution gives more reliable results and uses less computational time than the generalized one.

19.1 Introduction

Dynamic analysis of rotating systems has attracted much interest over the last decades since rotor systems are present in many engineering applications, such as electrical machines, turbo machines, combustion engines and wind turbines. The first known basic rotor model consisting of a flexible rotating shaft, a rigid disk and bearings was defined by Föppl and Jeffcott in 1895 and 1919 respectively, which is known as Jeffcott rotor today [1]. Carrying out modal analysis on the Jeffcott rotor is relatively simple compared to complex rotor systems, because such systems require solution of an eigenvalue problem with large matrices. The finite element and transfer matrix methods [2–6] are widely known methods to compute mass, stiffness, damping and gyroscopic matrices of large scale rotor systems. In the past, transfer matrix method was the preferred method for the solution of large scale rotor dynamics problems, but recently the finite element method has become more widely used because it provides better computational performance compared to the other methods [2, 4].

In large scale eigenvalue problems, matrices could have special properties; they may be symmetric, skew-symmetric, non-symmetric or Hermitian [7]. For example, the gyroscopic matrix for rotating systems is normally skew-symmetric, but the addition of damping leads to the loss of this property [8]. Therefore, the eigenvalue problem of the damped or undamped gyroscopic systems often require special numerical methods for the correct solution such as eigenvalue shifting techniques [9, 10]. Various numerical methods and software tools have been developed to solve large-scale quadratic eigenvalue problems [7, 11–13]. There are also existing studies investigating the solution of non-symmetric eigenvalue problems [14]. The Linear Algebra Package (LAPACK) [15] is one of the most well-known pieces of software used to solve eigenvalue problems including those with non-symmetric matrices. Another important development in the solution of eigenvalue problems has been algorithm reduction techniques, allowing calculation of only certain eigenvalues such as largest or smallest in magnitude [7]. Algorithm reduction is a convenient tool for reducing the computation time.

Eigenvalue problems can be formulated in two forms, (i) the standard eigenvalue problem (SEP) and (ii) the generalized eigenvalue problem (GEP). Inman [16] states that the standard eigenvalue solution is faster than the generalized eigenvalue solution in terms of computational performance. Hereby, it can be inferred that the standard eigenvalue solution is more advantageous than the generalized one in terms of computational time. The matrices can sometimes be badly conditioned, which can lead to wrong solutions to the eigenvalue problem. Kannan et al. [17] emphasize the severity of ill conditioning in

A. Tatar (✉) · L. Salles · A. H. Haslam · C. W. Schwingshackl
Imperial College London, Department of Mechanical Engineering, London, UK
e-mail: a.tatar16@imperial.ac.uk

structural finite element method and state that modelling beam elements with large sections or small lengths can cause these kinds of problems. Although, there are studies about the numerical accuracy of eigenvalue solutions, the numerical accuracy of the generalized and standard eigenvalue problems has not yet been compared.

In this paper, a 6 degrees of freedom 1-D rotating Timoshenko beam with gyroscopic effects is investigated using the finite element method. Generalized and standard eigenvalue solutions are sought using the global stiffness, mass and gyroscopic matrices obtained by the finite element method. The main aim of this study is to compare the standard and generalized eigenvalue solutions of rotating systems in terms of their computational performance and numerical accuracy by increasing the number of beam elements in the finite element model. This paper is organised as follows; a short literature review and the main objective of the study are introduced in the first section. Modal analysis of rotating systems is then discussed to provide theoretical background in the second chapter. Numerical analyses carried out on a rotating beam using the standard and generalized eigenvalue solutions are presented in the third chapter, including studies into the convergence and computational effort. Finally, the main findings and concluding remarks are presented in the fourth section.

19.2 Modal Analysis of Rotating Systems

19.2.1 Dynamic Modelling of Rotating Beams with Finite Element Method

Rotating systems can mathematically be represented with mass, stiffness, damping and gyroscopic elements using lumped parameter, continuous system, or finite elements models. The latter discretises the structure into small elements based on the selected mesh sizes [2]. For each element, mass, stiffness, damping and gyroscopic matrices are formulated based on their material and geometry properties. After the computing element matrices, the connectivity between each element is defined by a topology matrix which allows the assembly of the global matrices. Finally, boundary conditions are imposed on the global matrices. Having obtained the updated global mass, stiffness, gyroscopic and damping matrices, the equations of motion for the free response of a six degrees of freedom system can be written as [2];

$$[M] \ddot{q}(t) + ([C] + \Omega [G]) \dot{q}(t) + [K] q(t) = 0 \quad (19.1)$$

where M , C , G and K represent the mass, damping, gyroscopic and stiffness matrices respectively. Ω is the rotating speed of the rotor, and $q(t)$ is the generalized coordinate for a six degree of freedom (DOF) system;

$$q_i = [x_i, y_i, z_i, \theta_{x_i}, \theta_{y_i}, \theta_{z_i}] \quad (19.2)$$

The mass, stiffness and gyroscopic matrices of the flexible rotating shaft can be computed using two beam theories: Timoshenko or Euler – Bernoulli. They are used for the finite element formulations of flexible shafts in rotor dynamics. The main difference between the two theories is that shear deflections and rotational inertia effects are taken into account in Timoshenko beam theory [18, 19].

19.2.2 Quadratic Eigenvalue Problem of Gyroscopic Systems

The modal analysis of a rotating system is slightly different from a static one since gyroscopic moments acting on the rotating systems affect their modal parameters in terms of natural frequencies and mode shapes, and causes them to vary with the rotor speed. Similar to the damping terms, the gyroscopic terms introduce a term involving the first derivative of the generalized coordinate to the equation of motion. Therefore, the rotordynamics problem becomes a quadratic eigenvalue problem [20, 21]. In order to obtain the eigenvalues and eigenvectors, quadratic eigenvalue problem can be expressed using the state space representation which yields a first order eigenvalue problem [22–24]. However, this also doubles the sizes of the matrices in the eigenvalue problem, leading to an increase in computational time.

As mentioned in the introduction, there are two forms of eigenvalue problem, known as standard and generalized eigenvalue problem. There is one input matrix in the standard eigenvalue problem, whereas there are two input matrices in generalized eigenvalue problems. In MATLAB, generalized and standard eigenvalue problems can be solved using the `eig` or `eigs` functions. The `eig` function computes all the eigenvalues whereas the `eigs` function computes a subset of eigenvalues such as the smallest or largest eigenvalues, using algorithmic reduction techniques. MATLAB uses LAPACK

routines to calculate the eigenvalues; and the eigenvalue solution algorithm is determined based on whether the input matrices are real or complex, symmetric or non-symmetric, Hermitian or non-hermitian; or positive definite [25, 26].

There are currently three rotor dynamics software suites based on the finite element method, written in MATLAB. They are developed by Bucher [27], Genta [28] and Friswell et al. [29], called RotFE, DynRot and Rotordynamics respectively. Among these software, Bucher [27] uses the generalized eigenvalue problem in his RotFE code whereas Friswell et al. [29] use the standard eigenvalue problem in their rotor dynamics software.

19.2.2.1 Generalized Eigenvalue Problem of Gyroscopic Systems

The generalized eigenvalue problem of gyroscopic systems [2] can be derived by first expressing the equations of motion from Eq. (19.1) in state space form as shown below:

$$\begin{bmatrix} C + \Omega G & M \\ M & 0 \end{bmatrix} \begin{Bmatrix} \dot{q} \\ \ddot{q} \end{Bmatrix} + \begin{bmatrix} K & 0 \\ 0 & -M \end{bmatrix} \begin{Bmatrix} q \\ \dot{q} \end{Bmatrix} = \begin{Bmatrix} 0 \\ 0 \end{Bmatrix} \quad (19.3)$$

Then, the equation can be rewritten using state vectors $x = \begin{Bmatrix} q \\ \dot{q} \end{Bmatrix}$ and $\dot{x} = \begin{Bmatrix} \dot{q} \\ \ddot{q} \end{Bmatrix}$ as,

$$A\dot{x} + Bx = 0 \quad (19.4)$$

The size of the eigenvalue problem is now $2n$ as can be seen from the matrix equations. Therefore, $2n$ eigenvalues and eigenvectors are obtained with the eigenvalue solution. Half of the eigenvalues and eigenvectors are the complex conjugates of the other half. The eigenvalue and eigenvector matrices are denoted by $[\lambda]_{2n \times 2n}$ and $[\phi]_{2n \times 2n}$ respectively where λ is also defined as;

$$\lambda_n = \omega_n^2 \quad (19.5)$$

In order to evaluate the accuracy of the generalized eigenvalue solution, parity check can be done with residual value calculation as defined below;

$$residual = B \times \phi + A \times \phi \times \lambda \quad (19.6)$$

After the calculation of the residual values in matrix form, the matrix norm can be computed using the `norm` function in MATLAB. Residual value calculation is a useful tool to quantify the numerical errors.

19.2.2.2 Standard Eigenvalue Problem of Gyroscopic Systems

The vibration problem of gyroscopic systems defined in Eq. (19.1) can be reformulated using inverse matrix operation as below [16];

$$\ddot{q}(t) + M^{-1}(C + \Omega G)\dot{q}(t) + M^{-1}Kq(t) = 0 \quad (19.7)$$

With the state vectors $x = \begin{Bmatrix} q \\ \dot{q} \end{Bmatrix}$ and $\dot{x} = \begin{Bmatrix} \dot{q} \\ \ddot{q} \end{Bmatrix}$, standard eigenvalue problem in matrix form is expressed as;

$$\begin{Bmatrix} \dot{q} \\ \ddot{q} \end{Bmatrix} = \begin{bmatrix} 0 & I \\ -M^{-1}K & -M^{-1}(\Omega G + C) \end{bmatrix} \begin{Bmatrix} q \\ \dot{q} \end{Bmatrix} \quad (19.8)$$

where I represents the identity matrix. The matrix equation for the standard eigenvalue problem becomes

$$\dot{x} = Ax \quad (19.9)$$

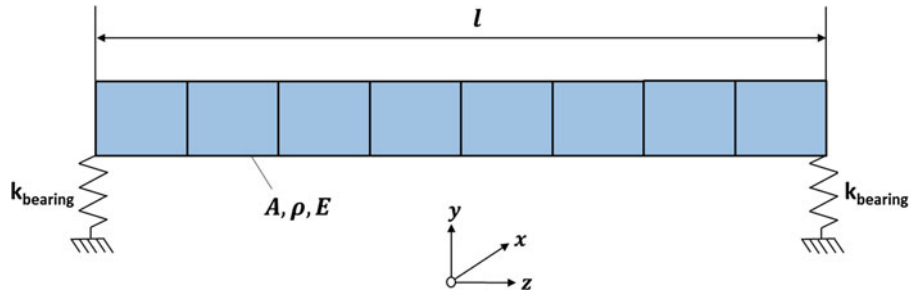


Fig. 19.1 A rotating beam model with finite element model

where A is called state matrix. As with the generalized eigenvalue problem, the size of the standard eigenvalue problem is $2n$ and half of them are the complex conjugates of the other half, but only one matrix needs to be computed for Eq. (19.9) instead of two for Eq. (19.4). Similar to the parity check of the generalized eigenvalue solution, a residual value formula can be defined for the standard eigenvalue solution as;

$$residual = A \times \phi - \phi \times \lambda \quad (19.10)$$

19.2.3 Modal Assurance Criteria

Independent of the chosen approach to compute the eigenvalue solutions, the Modal Assurance Criteria (MAC) [30] will be used to compare the resulting eigenvectors quantitatively. The formula of the modal assurance criteria is defined as [30, 31];

$$MAC(X, A) = \frac{|\{\phi_X\}_r^T \{\phi_A\}_q|^2}{(\{\phi_X\}_r^T \{\phi_X\}_r) (\{\phi_A\}_q^T \{\phi_A\}_q)} \quad (19.11)$$

where ϕ_X represents the “x” data set eigenvectors and ϕ_A represents “a” data set eigenvectors. Practically, ϕ_X and ϕ_A can be considered as data sets of experimental and analytical results. In this study, the main aim of the using the MAC is to compare mode shapes of the generalized and standard eigenvalue solutions.

19.3 Numerical Analysis of a Rotating Beam

A rotating beam was modelled using the finite element method with Timoshenko beam elements, each with 6 DOF. The beam is supported by bearings at each end as shown in Fig. 19.1.

In Fig. 19.1, $k_{bearing}$ represents bearing stiffness, and A , ρ , E and l represent cross sectional area, mass density, Young’s modulus and length of the beam. Bearing elements of the rotating beam have stiffness in lateral and axial directions as defined below;

$$k_{bearing} = \begin{bmatrix} k_{xx} & 0 & 0 & 0 & 0 & 0 \\ 0 & k_{yy} & 0 & 0 & 0 & 0 \\ 0 & 0 & k_{zz} & 0 & 0 & 0 \\ 0 & 0 & 0 & k_{Q_{xx}} & 0 & 0 \\ 0 & 0 & 0 & 0 & k_{Q_{yy}} & 0 \\ 0 & 0 & 0 & 0 & 0 & 0 \end{bmatrix} \quad (19.12)$$

No damping was included in the rotating beam or the bearings to enhance the effect of the gyroscopic matrix. The global mass, stiffness and gyroscopic matrices of the rotating beam were computed via a finite element code written in MATLAB. Generalized and standard eigenvalue solutions of the rotating beam were found for an increasing number of beam elements,

Table 19.1 Parameters of the rotating beam model

Parameter	Value
Length of the beam [m]	5
Cross sectional area of the beam [m ²]	0.0314
Density of the beam [kg/m ³]	7810
Young modulus of the beam [GPa]	211
Shear modulus of the beam [GPa]	81.2
Rotating beam speed [rpm]	8000
Bearing Stiffness k_{xx} [N/m]	10^8
Bearing Stiffness k_{yy} [N/m]	10^8
Bearing Stiffness k_{zz} [N/m]	10^8
Bearing Stiffness $k_{Q_{xx}}$ [Nm/rad]	10^6
Bearing Stiffness $k_{Q_{yy}}$ [Nm/rad]	10^6

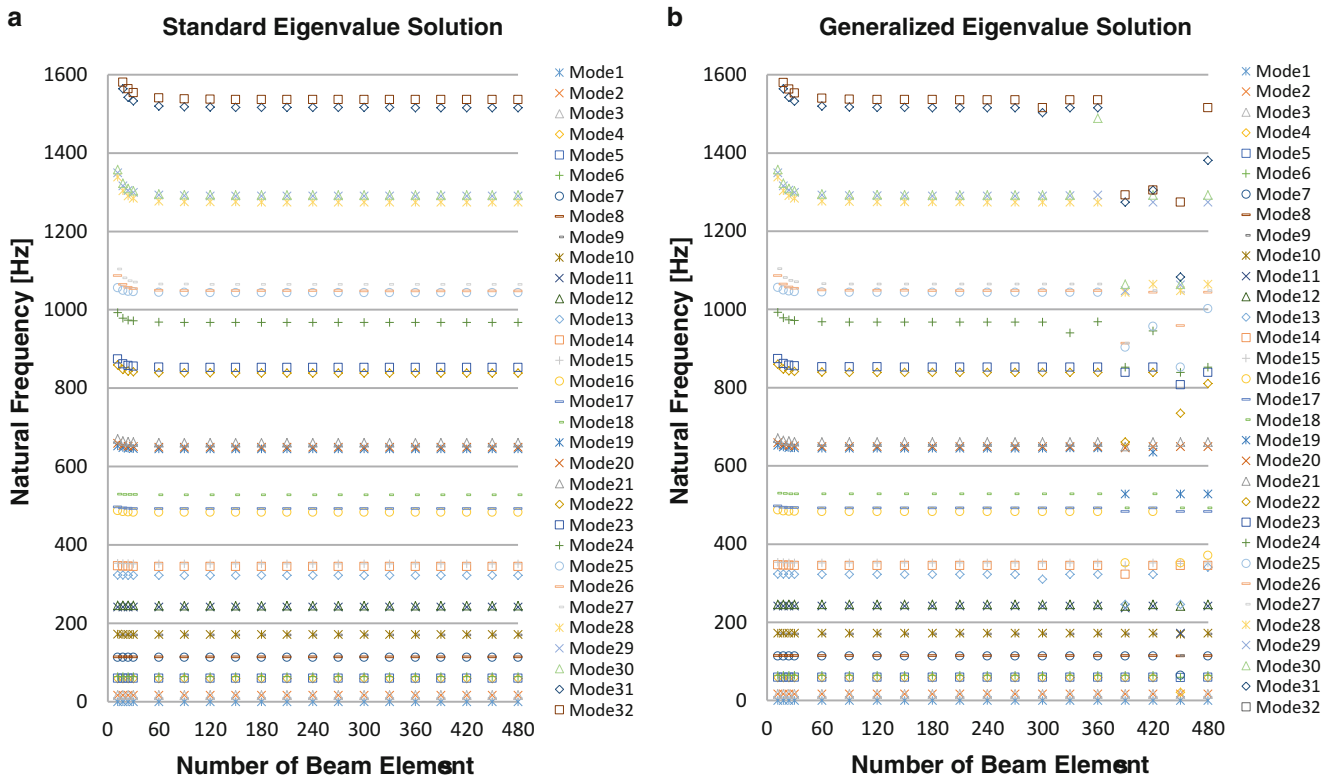


Fig. 19.2 Natural frequency comparison of (a) standard eigenvalue solution and (b) generalized eigenvalue solution

ranging from 6 to 480. For each number of beam elements, the natural frequencies, mode shapes and computation time were calculated using the two methods. The parameters of the rotating beam with its bearings are shown in Table 19.1.

19.3.1 Eigenvalue Solution Results

The finite element convergence studies were done by increasing the number of beam elements from 6 to 480 for both standard and generalized eigenvalue solutions in MATLAB. Eigenvalues and eigenvectors were computed using standard and generalized eigenvalue solutions. Natural frequency and mode shape comparison of the two methods are shown for the first 32 modes in Figs. 19.2 and 19.3 respectively.

Natural frequencies obtained from standard and generalized eigenvalue solutions were plotted with respect to the number of beam elements as seen in Fig. 19.2. It is clearly seen that generalized eigenvalue solution does not give stable results after 300 beam elements while standard eigenvalue solution gives the correct and stable results for each number of beam

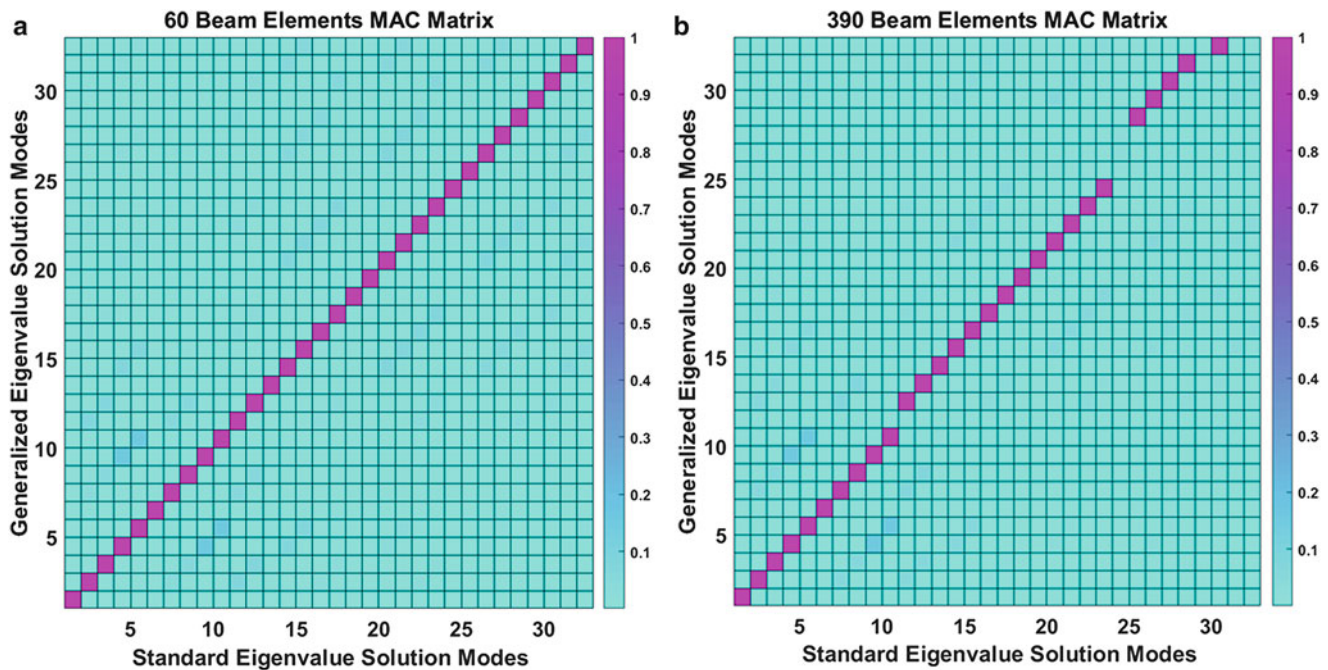


Fig. 19.3 MAC comparison of standard and generalized eigenvalue solution, (a) 60 beam elements, (b) 390 beam elements

Table 19.2 Norm of the residual values of generalized and standard eigenvalue solutions

Eigenvalue solution method	60 beam elements	390 beam elements
Generalized eigenvalue solution	0.0043	0.2901
Standard eigenvalue solution	0.0000246	0.0030

elements. In particular, for the generalized eigenvalue solution, the natural frequencies were wrongly calculated to be 236 Hz for the 11th mode, 902 Hz for the 25th mode, 912 Hz for the 26th mode and 912 Hz for the 27th mode when using 390 beam elements.

The MAC values of the two eigenvalue solutions are shown for 60 and 390 beam elements in Fig. 19.3. As can be expected from the natural frequency plot in Fig. 19.2, generalized and standard eigenvalue solutions give fully consistent mode shapes for 60 beam elements. On the other hand, distorted correlation between the standard and generalized eigenvalue solutions for 390 beam elements is observed due to the wrongly calculated 11th, 25th, 26th and 27th modes by the generalized eigenvalue solution. These modes were also determined as torsional modes.

To check the quality of the eigenvalue computation and identify the source of the observed discrepancies, the norm of the residual values, which were defined in Sect. 19.2.2, were calculated for both standard and generalized eigenvalue solutions for 60 and 390 beam elements. The resulting norm of the residuals in Table 19.2 show significant residual differences between the standard and generalized eigenvalue solutions, where the latter leads to high residual values for both the 60 and 390 beam element case. Particularly very large norm of the residual values were observed for the 390 element beam.

As described in reference [17], ill-conditioning can lead to wrong results in structural finite element models. In our specific rotating system problem with gyroscopic effects, this phenomenon occurred in the generalized eigenvalue solution, but it did not happen in the standard eigenvalue solution. Based on these findings, it may be concluded that generalized eigenvalue solution is not the best tool for the modal analysis of rotating systems due to its increased sensitivity towards ill-conditioning which can be introduced by the gyroscopic matrix for larger systems. Standard eigenvalue solution on the other hand gives correct and stable results and can be recommended for the analysis of rotating structures.

19.3.2 Computational Cost

A final comparison of the two eigenvalue solution approaches is based on their computational performance since any finite element analysis needs to find the right balance between accuracy and computational cost. A standard desktop PC with an

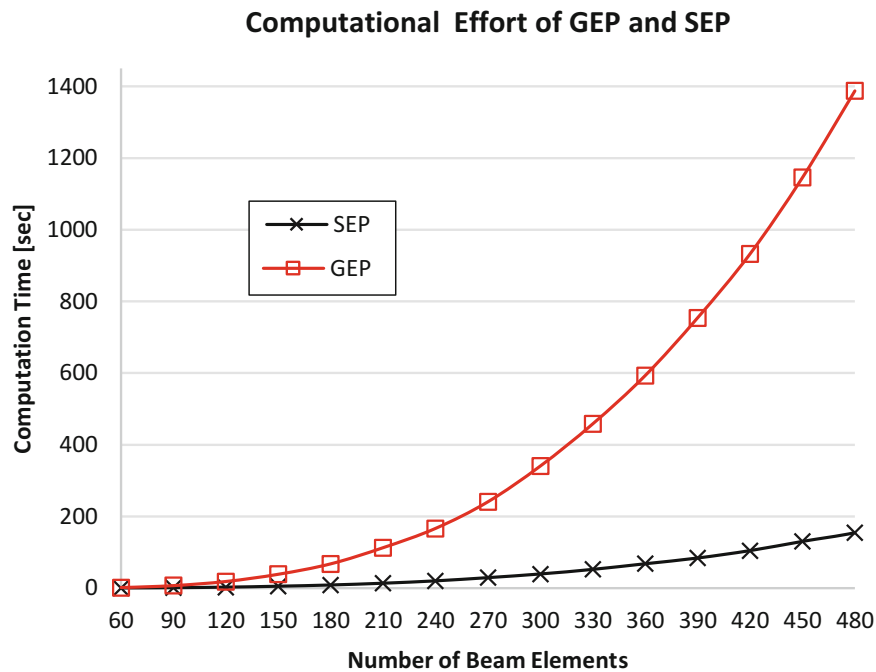


Fig. 19.4 Computational cost of generalized (GEP) and standard (SEP) eigenvalue problem

Intel® Core™ i7-6700 processor which has 3.40 GHz CPU and 16 GB random access memory (RAM) was used to compute the previously presented eigenvalues and eigenvectors in MATLAB R2016a.

In Fig. 19.4, it is clearly seen that the computation time difference between standard and generalized eigenvalue solutions increases with the number of beam elements. At lower numbers of beam elements, their computational performance is close to each other. However, there is a large computation time difference between them at higher mesh densities. It is numerically proven that the standard eigenvalue solution is faster than the generalized one. Based on the results in Fig. 19.4, the standard eigenvalues solution can be recommended for the fast computation of rotating systems with gyroscopic effects.

19.4 Conclusion

An evaluation of the accuracy and computational efficiency of the standard and generalized eigenvalue solutions for rotating beam elements with gyroscopic effects was presented. A finite element code written in MATLAB was used for this purpose. Natural frequencies and mode shapes were obtained using both eigenvalue solution methods. Then, the accuracy of the two methods was investigated using their eigenvalues, eigenvectors and residual values.

With an increase in the number of beam elements (>300), the generalized eigenvalue solution started to introduce inaccurate eigenvalues and eigenvectors whereas the standard eigenvalue solution provided consistent results. High residual values were also computed with generalized eigenvalue solutions while low residual values were obtained from standard eigenvalue solution. This suggests that the generalized eigenvalue solution may not be reliable when using higher number of beam elements. Moreover, this calls into question the reliability of LAPACK, the numerical solver employed by MATLAB for eigenvalue problems. It was also found that the standard eigenvalue solution is significantly faster than the generalized eigenvalue solution for higher numbers of elements.

Based on these findings, the standard eigenvalue solution is recommended for modal analysis of rotating systems with gyroscopic effects, and particular care is required when using the generalized eigenvalue solution with fine meshes. It is recommended that the residual values should be checked for the eigenvalue solutions to ensure the problem has been solved to the required level of accuracy. It can be concluded that the standard eigenvalue solution gives more reliable results than generalized eigenvalue solution and it is faster than the generalized eigenvalue solution.

Acknowledgment This study was funded by Republic of Turkey, Ministry of National Education. The authors are grateful to the Turkish Government for the financial support.

References

1. Nelson, F.C.: Rotor dynamics without equations. *Int. J. COMADEM*. **10**(3), 2–10 (2007)
2. Friswell, M.I.: *Dynamics of Rotating Machines*. Cambridge University Press, Cambridge (2010)
3. Muszynska, A.: *Rotordynamics*. CRC Press, Boca Raton (2005)
4. Rao, J.S.: *History of Rotating Machinery Dynamics*. Springer Science & Business Media, Dordrecht
5. Genta, G.: *Dynamics of Rotating Systems*. Springer Science & Business Media, New York (2007)
6. Yamamoto, T., Ishida, Y.: *Linear and Nonlinear Rotordynamics: a Modern Treatment with Applications*. A Wiley-Interscience publication, Wiley, Hoboken (2001)
7. Golub, G.H., Van der Vorst, H.A.: Eigenvalue computation in the 20th century. *J. Comput. Appl. Methods*. **123**(1), 35–65 (2000)
8. Zheng, Z., Ren, G., Williams, F.W.: The eigenvalue problem for damped gyroscopic systems. *Int. J. Mech. Sci.* **39**(6), 741–750 (1997)
9. Ferng, W.R., Lin, W.-W., Wang, C.-S.: Numerical algorithms for undamped gyroscopic systems. *Comput. Math. Appl.* **37**(1), 49–66 (1999)
10. Qian, J., Lin, W.W.: A numerical method for quadratic eigenvalue problems of gyroscopic systems. *J. Sound Vib.* **306**(1–2), 284–296 (2007)
11. Kerner, W.: Large-scale complex eigenvalue problems. *J. Comput. Phys.* **85**(1), 1–85 (1989)
12. Kressner, D.: *Numerical Methods for General and Structured Eigenvalue Problems*. Springer-Verlag Berlin Heidelberg, Berlin (2005)
13. Saad, Y.: *Numerical Methods for Large Eigenvalue Problems: Revised Edition*. SIAM, Philadelphia (2011)
14. Bai, Z.: Progress in the numerical solution of the nonsymmetric eigenvalue problem. *Numer. Linear. Algebra. Appl.* **2**(3), 219–234 (1995)
15. Anderson, E., et al.: LAPACK: A portable linear algebra library for high-performance computers. In: *Proceedings of the 1990 ACM/IEEE Conference on Supercomputing*, pp. 2–11, New York, USA (1990)
16. Inman, D.J.: *Engineering Vibration*, 4th edn. Pearson, Prentice Hall, London (2008)
17. Kannan, R., Hendry, S., Higham, N.J., Tisseur, F.: Detecting the causes of ill-conditioning in structural finite element models. *Comput. Struct.* **133**, 79–89 (2014)
18. Thomas, D.L., Wilson, J.M., Wilson, R.R.: Timoshenko beam finite elements. *J. Sound Vib.* **31**(3), 315–330 (1973)
19. Nelson, H.D.: A finite rotating shaft element using Timoshenko beam theory. *J. Mech. Des.* **102**(4), 793 (1980)
20. Tisseur, F., Meerbergen, K.: The quadratic eigenvalue problem. *SIAM Rev.* **43**(2), 235–286 (2001)
21. Berhanu, M.: *The Polynomial Eigenvalue Problem*, Ph.D. Thesis, University of Manchester, Manchester, UK (2006)
22. Gutiérrez-Wing, E.S., Ewins D.J.: Modal characterisation of rotating machines. *Proceedings of the 19th International Modal Analysis Conference*, Orlando, Florida (2001)
23. Lee, C.: A complex modal testing theory for rotating machinery. *Mech. Syst. Signal Process.* **5**(2), 119–137 (1991)
24. Bucher, I., Ewins, D.J.: Modal analysis and testing of rotating structures. *Philos. Trans. R. Soc. Lond. A Math. Phys. Eng. Sci.* **359**(1778), 61–96 (2001)
25. Anderson, E., et al.: *LAPACK Usersguide: Release 1.0*. Argonne National Lab, Chicago, Illinois, USA (1992)
26. Moler, C.: “Matlab incorporates LAPACK,” Increasing the speed and capabilities of matrix computation. *MATLAB News & Notes–Winter* (2000)
27. Bucher, I.: *RotFE 2.1 The finite element rotor analysis package*. Faculty of mechanical Engineering, Technion, Haifa, Israel (2000)
28. Genta, G., Bassani, D., Delprete, C.: *DYNROT: A Matlab Toolbox for Rotordynamics Analysis*, Polytechnic University of Turin, Turin, Italy (1994)
29. Friswell, M.I., Penny, J.E.T., Garvey, S.D., Lees, A.W.: *Dynamics of Rotating Machines Rotordynamics Software Manual*, pp. 1–19. Cambridge University Press, Cambridge (2010)
30. Pastor, M., Binda, M., Harčarik, T.: Modal assurance criterion. *Procedia Eng.* **48**, 543–548 (2012)
31. Ewins, D.J.: *Modal Testing: Theory, Practice and Application*, Research Studies Press, Baldock, (2000)

Chapter 20

Residual States for Modal Models Identified from Accelerance Data

Mladen Gibanica, Thomas J. S. Abrahamsson, and Randall J. Allemang

Abstract Residual stiffness and mass terms are often employed in frequency response synthesis to compensate for outside band eigenmodes in the identification of modal models from test data. For structures that have strongly participating modes above the test frequency band, it has been observed that in particular direct accelerances with strong outside-band modal contribution tend to render modal models that give poor fit to test data. For such problems it may be insufficient to just add residual mass and stiffness terms to the accelerance modal series to get a sufficiently improved fit. For accelerance, such residual terms are constant and quadratic in frequency. Another, residual term that is quasi-linear over the frequency range of interest has been found to augment the identified model. In this paper that complementary term is added to the constant and quadratic terms in a state-space model identification with a subspace state-space identification method. A comparison is performed to an alternative residualisation method. The methods' results are compared on simulated finite element test data from of an automotive component.

20.1 Introduction

System identification [1] is used in many academic disciplines and industries that rely upon dynamical models derived from experimental data. In structural dynamics, and related fields, it is commonly denoted experimental modal analysis (EMA) [2] due to the end goal of obtaining experimental modal models. The use of EMA is widespread in aerospace, civil engineering and automotive industries, to name a few. In the automotive industry, and more specifically in the noise, vibration and harshness (NVH) field, EMA is used to identify models from experiments which can be used to validate finite element (FE) models [3, 4]. Therefore, very good identified models are essential. Another use is in experimental analytical dynamic substructuring, where experimental and FE models are coupled [5–7]. In most cases accelerances are measured because of the ease of use and cost benefits of using accelerometers for vibration testing. These involve direct accelerances (acceleration related to force at the same location and orientation) that are typically of high interest in coupling applications. Therefore, it is of particular interest to include also the direct accelerances in the identified model.

Many methods exist for modal analysis, out of which some common methods are briefly mentioned here. In the automotive industry the polyreference least-squares complex frequency-domain method, known as PolyMAX [8], is commonly used. A related method is the rational fractional polynomial (RFP) method [9] that has been extended to the rational fractional polynomial-Z domain (RFP-Z) method [10, 11]. In the control community other methods are more prevalent, such as the prediction error method (PEM) [1] and subspace state-space identification (N4SID) methods [12, 13]. Selection of the identification method is many times based on tradition and their availability to the user.

In frequency based system identification a frequency range of interest is under study. For structures tested on soft supports, exhibiting quasi-rigid body modes at low frequencies, the identified model is often augmented with the addition of a residual mass term compensating for the low frequency modes, at frequencies that are usually smaller than the cut-on frequency of the range in test [2]. Similarly, for continuous systems with infinitely many modes, most high-frequency modes will not be

M. Gibanica (✉)
Mechanics and Maritime Sciences, Chalmers University of Technology, Göteborg, Sweden

Volvo Car Corporation, Göteborg, Sweden
e-mail: mladen.gibanica@chalmers.se

T. J. S. Abrahamsson
Mechanics and Maritime Sciences, Chalmers University of Technology, Göteborg, Sweden

R. J. Allemang
Structural Dynamics Research Laboratory, Department of Mechanical Engineering, University of Cincinnati, Cincinnati, OH, USA

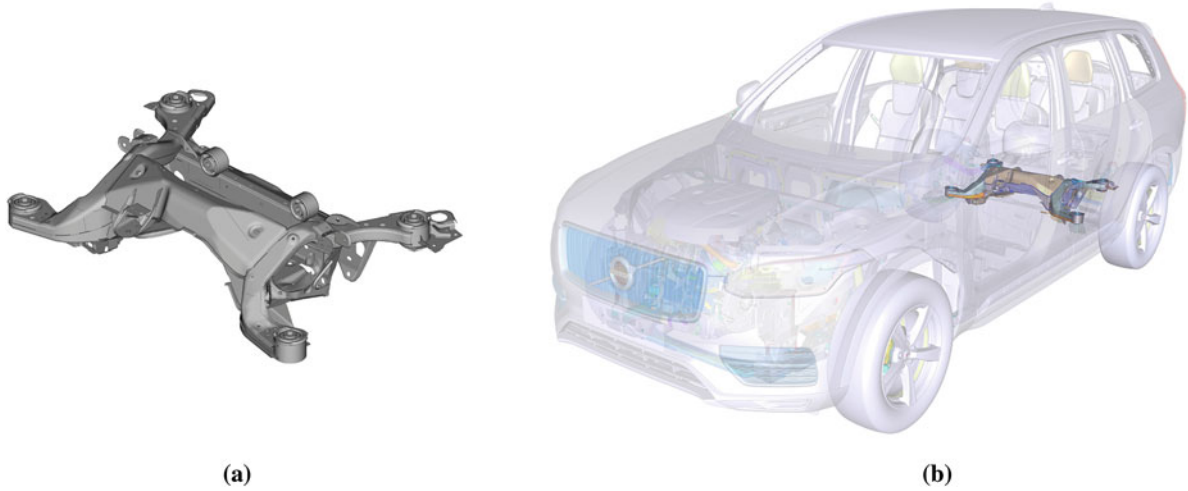


Fig. 20.1 The rear subframe connects the suspension link arms and the car body, and is thus an important part from a vibration perspective. (a) Rear subframe. (b) Rear subframe location in the car. Figure from [17]

clearly visible in test data but will give some quasi-static contribution in the frequency range of interest. These modes are compensated for in the identified model by addition of a residual stiffness term [2]. However, for structures with strong local modes just outside the tested frequency range, it has been observed that direct accelerances are estimated poorly even with the inclusion of the two residual mass and stiffness terms.

In this paper the frequency based version of the system identification method N4SID is used [12] and compared with the outcome of the RFP-Z method [10, 11]. A procedure is proposed for identification of models with a classical residual mass and a non-classical stiffness term, both consistent with a state-space description, including a third residual term that compensates for strong local modes just above the frequency range of interest that can easily be embedded in a state-space description. It has been found that the inclusion of a third residual significantly improves the model's direct accelerance while the cross-accelerances mostly remain unaffected. Two strategies for the residual pole placement problem are proposed. The first depends on the availability of experimental data well above the frequency range of interest and the other maximises the identifiability of the introduced residual from data only in the frequency region of interest. The proposed method's performance is compared to the RFP-Z method [10, 11] that uses another residualisation strategy. Simulated test data from an FE model from 47 to 854 Hz is used from a rear subframe of the Volvo XC90 (2015). In Fig. 20.1 the FE model of the subframe is shown along with its location in the car.

The theory behind the proposed procedure is presented in Sect. 20.2. In Sect. 20.3 the problem is described in detail, along with a description of the FE model. The results are presented in Sects. 20.4 and 20.5 concludes the paper.

20.2 Proposed Method

The N4SID method is flexible in its pole placement and the identified poles are not constrained to lie in the frequency range of test data [12]. However, with noisy frequency response functions (FRFs) the method tends to identify spurious noise modes within the range rather than out of range modes. Therefore, residual modes with poles outside the range can be used to approximate the out of range behaviour, see Ewins [2] for a thorough explanation. A receptance FRF matrix $\mathbf{H}^R(\omega) \in \mathbb{C}^{n_y \times n_u}$ of an undamped system for a frequency ω , with n_y and n_u the number of outputs and inputs, can be expressed in modal parameters as

$$H_{jk}^R(\omega) = \sum_{r=1}^N \frac{R_{jk}^{(r)}}{\omega_r^2 - \omega^2} = \sum_{r=1}^N \frac{R_{jk}^{(r)}/(2\omega_r)}{\omega_r - \omega} + \frac{R_{jk}^{(r)}/(2\omega_r)}{\omega_r + \omega} \quad \text{for } j = 1, \dots, n_y \quad \text{and } k = 1, \dots, n_u, \quad (20.1)$$

where ω_r is the eigenfrequency of the r th mode in ordered sequence, $R_{jk}^{(r)}$ the residue factor for mode r and N is the modal order of the system. For continuous systems $N = \infty$. The series in Eq. (20.1) can be split into

$$H_{jk}^R(\omega) = \sum_{r=1}^{n_1-1} \frac{R_{jk}^{(r)}}{\omega_r^2 - \omega^2} + \sum_{r=n_1}^{n_2} \frac{R_{jk}^{(r)}}{\omega_r^2 - \omega^2} + \sum_{r=n_2+1}^N \frac{R_{jk}^{(r)}}{\omega_r^2 - \omega^2} \quad (20.2)$$

with n_1 and n_2 corresponding to the lowest and highest eigenfrequency inside of the frequency range of interest, respectively. The first term is generally identified as the contribution from low frequency modes and the third term as the contribution from high frequency modes. For frequencies ω inside the frequency range of interest the series may be approximated [2] as

$$H_{jk}^R(\omega) \approx -\frac{1}{\omega^2 M_{jk}^R} + \sum_{r=n_1}^{n_2} \frac{R_{jk}^{(r)}}{\omega_r^2 - \omega^2} + \frac{1}{K_{jk}^R} \quad (20.3)$$

where M_{jk}^R and K_{jk}^R are the mass and stiffness residuals, respectively. This formulation is related to a state-space description (the state-space formulation is explained further below) with state \mathbf{x} , input \mathbf{u} and output \mathbf{y}

$$\begin{aligned} \dot{\mathbf{x}} &= \mathbf{A}\mathbf{x} + \mathbf{B}\mathbf{u} \\ \mathbf{y} &= \mathbf{C}\mathbf{x} + \mathbf{D}\mathbf{u} \end{aligned} \quad (20.4)$$

with the stiffness residual being represented by the direct throughput matrix \mathbf{D} . Such direct throughput from loading \mathbf{u} to displacement output \mathbf{y} is not justified from physical reality in which displacement needs to be integrated from acceleration via velocity. To be more consistent with physical reality, the terms with fast modes may instead be approximated with $Q_{jk}^R(\omega)$ such that

$$H_{jk}^R(\omega) \approx -\frac{1}{\omega^2 M_{jk}^R} + \sum_{r=n_1}^{n_2} \frac{R_{jk}^{(r)}}{\omega_r^2 - \omega^2} + Q_{jk}^R(\omega). \quad (20.5)$$

The stiffness residualisation is possible since

$$\sum_{r=n_2+1}^N \frac{R_{jk}^{(r)}}{\omega_r^2 - \omega^2} \approx \sum_{r=n_2+1}^N \frac{R_{jk}^{(r)}}{\omega_r^2} \triangleq \frac{1}{K_{jk}^R} \quad (20.6)$$

for eigenfrequencies $\omega_r \gg \omega$. An alternative residualisation is possible by introducing $\omega_K \gg \omega$ leading to

$$\sum_{r=n_2+1}^N \frac{R_{jk}^{(r)}}{\omega_r^2 - \omega^2} = \sum_{r=n_2+1}^N \frac{(\omega_K^2 - \omega^2) R_{jk}^{(r)}}{(\omega_r^2 - \omega^2)(\omega_K^2 - \omega^2)} \approx \sum_{r=n_2+1}^N \frac{\omega_K^2}{\omega_r^2} \frac{R_{jk}^{(r)}}{\omega_K^2 - \omega^2} \triangleq \frac{R_{jk}^{(K)}}{\omega_K^2 - \omega^2}. \quad (20.7)$$

We propose that the fast mode term $Q_{jk}^R(\omega)$ is approximated with a two term residual series as

$$Q_{jk}^R(\omega) \approx \frac{R_{jk}^{(S)}}{\omega_S^2 - \omega^2} + \frac{R_{jk}^{(K)}}{\omega_K^2 - \omega^2} \quad (20.8)$$

where the first term is associated with an introduced mode at ω_S with residue factors $R_{jk}^{(S)}$. The introduced mode is at frequency $\omega_S > \bar{\omega}$ such that the corresponding term for accelerance is quasi-linear in frequency over the frequency range of interest $[\underline{\omega}, \bar{\omega}]$. The pole placement strategy is presented in Sect. 20.2.1. The second term approximates the residual stiffness with residue factors $R_{jk}^{(K)}$ and $\bar{\omega} \ll \omega_K < \infty$ which will render the term approximately constant over $[\underline{\omega}, \bar{\omega}]$ and consistent with

a state-space description with states for a mode at very high frequencies ω_K . Hence, the system's FRFs can be approximated with the series

$$H_{jk}^R(\omega) \approx -\frac{1}{\omega^2 M_{jk}^R} + \sum_{r=n_1}^{n_2} \frac{R_{jk}^{(r)}}{\omega_r^2 - \omega^2} + \frac{R_{jk}^{(S)}}{\omega_S^2 - \omega^2} + \frac{R_{jk}^{(K)}}{\omega_K^2 - \omega^2}. \quad (20.9)$$

The proposed method will be derived for accelerance FRFs, and it is trivial to show its counterpart for receptance FRFs. The receptance FRFs in Eq. (20.9) can be brought to accelerance form $H_{jk}^A(\omega)$ as

$$H_{jk}^A(\omega) = \frac{1}{M_{jk}^R} - \sum_{r=n_1}^{n_2} \frac{\omega^2 R_{jk}^{(r)}}{\omega_r^2 - \omega^2} - \frac{\omega^2 R_{jk}^{(S)}}{\omega_S^2 - \omega^2} - \frac{\omega^2 R_{jk}^{(K)}}{\omega_K^2 - \omega^2}. \quad (20.10)$$

It can be seen that the mass residual term is constant and the stiffness residual term (fourth term) is approximately quadratic in frequency when $\bar{\omega} \ll \omega_K$ while the third term has a significantly different frequency behaviour when ω_S is just above $\bar{\omega}$.

The experimental accelerance FRFs of the generally damped system will here be denoted $\underline{H}^A(\Omega_m) \in \mathcal{C}^{n_y \times n_u}$. Note that discrete frequencies $\Omega_m \in [\underline{\omega}, \bar{\omega}]$ for $m = 1, \dots, M$ are used here. A real-valued model without the influence of the identified modal parameters, denoted here the low order model $\hat{H}^{A, \text{low}}(\Omega_m) \in \mathcal{R}^{n_y \times n_u}$, can be found from the real part of the experimental accelerance FRFs $\underline{H}^{A, \text{Re}}(\Omega_m) = \mathcal{R}(\underline{H}^A(\Omega_m)) \in \mathcal{R}^{n_y \times n_u}$. Hence, the residue factors $\sigma = 1/M_{jk}^R$, $\mu = R_{jk}^{(S)}$ and $\eta = R_{jk}^{(K)}$ need to be determined, which can be done in a linear least squares sense [14]

$$\hat{\theta}_{jk} = \arg \min_{\theta_{jk}} \left\| \underline{H}_{jk}^{A, \text{Re}} - \mathbf{E} \theta_{jk} \right\|_F \in \mathcal{R}^{3 \times 1} \quad \text{for } j = 1, \dots, n_y \quad \text{and } k = 1, \dots, n_u, \quad (20.11)$$

with $\|\cdot\|_F$ the Frobenius norm [15] and $\theta_{jk} = [\sigma, \mu, \eta]^T$ the parameter vector. Note that $\underline{H}_{jk}^{A, \text{Re}} \in \mathcal{R}^{M \times 1}$ is a vector containing one channel from the FRF matrix along the frequency dimension. Define the observation matrix

$$\mathbf{E} = \begin{bmatrix} 1 & \Omega_1^2/(\omega_S^2 - \Omega_1^2) & \Omega_1^2/(\omega_K^2 - \Omega_1^2) \\ 1 & \Omega_2^2/(\omega_S^2 - \Omega_2^2) & \Omega_2^2/(\omega_K^2 - \Omega_2^2) \\ \vdots & \vdots & \vdots \end{bmatrix} \in \mathcal{R}^{M \times 3}. \quad (20.12)$$

The solution $\hat{\theta}_{jk}$ to Eq. (20.11) is given by

$$\hat{\theta}_{jk} = (\mathbf{E}^T \mathbf{E})^{-1} \mathbf{E}^T \underline{H}_{jk}^{A, \text{Re}}. \quad (20.13)$$

The estimated FRF matrix $\hat{H}^{A, \text{low}}(\Omega_m)$ can be obtained for each channel $\hat{H}_{jk}^{A, \text{low}} \in \mathcal{R}^{M \times 1}$ individually as

$$\hat{H}_{jk}^{A, \text{low}} = \mathbf{E} \hat{\theta}_{jk}. \quad (20.14)$$

The low order model's contribution $\hat{H}^{A, \text{low}}(\Omega_m)$ can now simply be subtracted from the experimental data $\underline{H}^A(\Omega_m)$ for each frequency Ω_m

$$\bar{H}^A(\Omega_m) = \underline{H}^A(\Omega_m) - \hat{H}^{A, \text{low}}(\Omega_m) \in \mathcal{C}^{n_y \times n_u} \quad (20.15)$$

to obtain the augmented data $\bar{H}^A(\Omega_m)$ without the undamped residual model's contribution. The N4SID method, implemented in MATLAB's System Identification Toolbox [12], is used on this data to obtain the quadruple $\bar{\Sigma} = \{\bar{A}, \bar{B}, \bar{C}, \bar{D}\}$ which represent the identified model on first order form.

$$\begin{aligned} \dot{\bar{x}} &= \bar{A} \bar{x} + \bar{B} \bar{u} \\ \bar{y} &= \bar{C} \bar{x} + \bar{D} \bar{u} \end{aligned} \quad (20.16)$$

Here, $\bar{\mathbf{A}} \in \mathcal{R}^{\bar{n} \times \bar{n}}$ is the system matrix, $\bar{\mathbf{B}} \in \mathcal{R}^{\bar{n} \times n_u}$ is the input matrix, $\bar{\mathbf{C}} \in \mathcal{R}^{n_y \times \bar{n}}$ is the output matrix, $\bar{\mathbf{D}} \in \mathcal{R}^{n_y \times n_u}$ is the direct throughput matrix, $\bar{\mathbf{x}} \in \mathcal{R}^{\bar{n} \times 1}$ the state vector, $\bar{\mathbf{u}} \in \mathcal{R}^{n_u \times 1}$ the input vector and $\bar{\mathbf{y}} \in \mathcal{R}^{n_y \times 1}$ the output vector, with \bar{n} denoting the number of system states.

It is also possible to find a state-space representation of system $\hat{H}_{jk}^{A, \text{low}}(\Omega_m = -is_m) = \mathbf{E}(\Omega_m) \hat{\theta}_{jk}$, with $i = \sqrt{-1}$ the imaginary number, by writing the transfer functions on zero-pole gain form

$$\hat{H}_{jk}^{A, \text{low}}(s_m) = q_{jk} \frac{(s_m - z_{jk,1})(s_m - z_{jk,2})(s_m - z_{jk,3})(s_m - z_{jk,4})}{(s_m - i\omega_S)(s_m + i\omega_S)(s_m - i\omega_K)(s_m + i\omega_K)} \quad (20.17)$$

where s_m is the Laplace variable, q_{jk} is the channel gain and $z_{jk,v}$ its zeros, with $v = 1, 2, 3, 4$. Note that the system poles are the same for all channels. From the system zeros, poles and gains a state-space system $\Sigma^{\text{low}} = \{\mathbf{A}^{\text{low}}, \mathbf{B}^{\text{low}}, \mathbf{C}^{\text{low}}, \mathbf{D}^{\text{low}}\}$ can be found [16]. Note that $\mathbf{A}^{\text{low}} \in \mathcal{C}^{n_{\text{low}} \times n_{\text{low}}}$, $\mathbf{B}^{\text{low}} \in \mathcal{R}^{n_{\text{low}} \times n_u}$, $\mathbf{C}^{\text{low}} \in \mathcal{R}^{n_y \times n_{\text{low}}}$ and $\mathbf{D}^{\text{low}} \in \mathcal{R}^{n_y \times n_u}$, and the number of residual system states is here $n_{\text{low}} = 4$, due to 3 residuals being included in the low order model Σ^{low} , where the mass residual is modelled in \mathbf{D}^{low} .

To obtain a system describing the original FRFs $\underline{H}^A(\Omega_m)$ the system Σ^{low} is connected to $\bar{\Sigma}$ in parallel producing the system $\Sigma = \{\mathbf{A}, \mathbf{B}, \mathbf{C}, \mathbf{D}\}$

$$\begin{aligned} \dot{\mathbf{x}} &= \mathbf{A}\mathbf{x} + \mathbf{B}\mathbf{u} \\ \mathbf{y} &= \mathbf{C}\mathbf{x} + \mathbf{D}\mathbf{u} \end{aligned} \quad (20.18)$$

with

$$\mathbf{A} = \begin{bmatrix} \bar{\mathbf{A}} & \mathbf{0} \\ \mathbf{0} & \mathbf{A}^{\text{low}} \end{bmatrix}, \quad \mathbf{B} = \begin{bmatrix} \bar{\mathbf{B}} \\ \mathbf{B}^{\text{low}} \end{bmatrix}, \quad \mathbf{C} = [\bar{\mathbf{C}} \quad \mathbf{C}^{\text{low}}], \quad \mathbf{D} = \bar{\mathbf{D}} + \mathbf{D}^{\text{low}} \quad (20.19)$$

Here the system matrix $\mathbf{A} \in \mathcal{R}^{n \times n}$ with the number of system states $n = \bar{n} + n_{\text{low}}$. The system input $\mathbf{B} \in \mathcal{R}^{n \times n_u}$, output $\mathbf{C} \in \mathcal{R}^{n_y \times n}$ and direct throughput $\mathbf{D} \in \mathcal{R}^{n_y \times n_u}$ matrices are not minimal [1] for the new system Σ and therefore need to be re-estimated. Writing the system Σ in Eq. (20.18) on transfer function form

$$\mathbf{H}^{A, \Sigma}(\Omega_m) = [\mathbf{C}(i\Omega_m \mathbf{I} - \mathbf{A})^{-1} \mathbf{B} + \mathbf{D}] \in \mathcal{C}^{n_y \times n_u} \quad (20.20)$$

it can be realised that, given that \mathbf{A} and \mathbf{B} are fixed, the problem in Eq. (20.20) is linear in \mathbf{C} and \mathbf{D} . It is also linear in \mathbf{B} if \mathbf{A} , \mathbf{C} and \mathbf{D} are fixed. It is therefore possible to iteratively re-estimate \mathbf{B} , \mathbf{C} and \mathbf{D} using a sequence of linear least squares solutions until convergence is reached. Such iterations are used here to improve the fit to test data.

20.2.1 Optimal Residual Pole Selection Strategies

Selecting a proper pole location ω_S of the residual term that best represent outside range modes is not obvious. In this paper two approaches are proposed.

20.2.1.1 Strategy 1

This strategy is based on the relative ease of obtaining experimental data above the frequency range of interest. In a controlled EMA test such data are usually obtained using impact or broadband excitation. In a single input multiple output (SIMO) test it

is usually easy to identify, with reasonable accuracy, an eigenfrequency ω_r of any strong local mode just outside the frequency range of interest from the direct accelerance, if there should be one (or more). The eigenfrequency ω_r may substitute as the location for the residual state at ω_S .

20.2.1.2 Strategy 2

If data are not available for frequencies above $\bar{\omega}$ but the asymptotic behaviour of data indicate that a strong local mode is present above $\bar{\omega}$, another strategy is proposed here. The additional residual is assumed to contribute as a quasi-linear term, and hence the pole placement ω_S can be sought such that the linear independence between the three residual terms resembles, in some sense, the linear independence between the first three terms in a polynomial series in ω

$$\mathcal{P} = \{\alpha, \beta\omega, \gamma\omega^2\} \quad (20.21)$$

as much as possible. The Gram matrix determinant (Gramian) [15] can be used to quantify the linear independence between these functions over a range. For continuous real valued functions $f(\omega)$ the Gram matrix elements are

$$G_{jk} = \langle v_j, v_k \rangle = \int_{\underline{\omega}}^{\bar{\omega}} f_j(\omega)f_k(\omega)d\omega. \quad (20.22)$$

The normalised Gramian $\det(\mathbf{G})$ will here be used as a measure of linear independence with assumptions that all variables are real valued, $\omega > 0$ and $\underline{\omega} = 0$. The polynomial coefficients $\{\alpha, \beta, \gamma\}$ are given by the normalising relation

$$G_{jj}^{\mathcal{P}} = \langle v_j, v_j \rangle = 1. \quad (20.23)$$

Note that $0 < \det(\mathbf{G}) < 1$, where 0 indicate a singular Gram matrix and 1 an orthogonal set of functions over $[\underline{\omega}, \bar{\omega}]$. The normalised Gramian of the polynomial series \mathcal{P} can be shown to be independent of the upper frequency bound $\bar{\omega}$ and is

$$\mathbf{G}^{\mathcal{P}} = \begin{bmatrix} 1 & -\frac{\sqrt{3}}{2} & -\frac{\sqrt{5}}{3} \\ -\frac{\sqrt{3}}{2} & 1 & -\frac{\sqrt{15}}{4} \\ -\frac{\sqrt{5}}{3} & -\frac{\sqrt{15}}{4} & 1 \end{bmatrix} \quad (20.24)$$

and its determinant is

$$\det(\mathbf{G}^{\mathcal{P}}) = \frac{1}{144}. \quad (20.25)$$

The same procedure is carried out on the accelerance residual series in ω

$$\mathcal{A} = \left\{ \alpha, \frac{\beta\omega^2}{\delta^2\bar{\omega}^2 - \omega^2}, \gamma\omega^2 \right\} \quad (20.26)$$

for which the Gramian $\det(\mathbf{G}^{\mathcal{A}})$ is a complicated expressions that is dependent on the frequency multiplier δ . A δ that renders the residual series to be of the same level of linear independence as the polynomial series, in the Gramian sense, can be found from

$$\det(\mathbf{G}^{\mathcal{A}}) = \det(\mathbf{G}^{\mathcal{P}}) \quad (20.27)$$

for which the scaling factor δ is found by numerical procedures to be

$$\delta \approx 1.4279 \quad (20.28)$$

which indicates that a good choice for ω_S is that $\omega_S = 1.4279\bar{\omega}$.

20.3 FE Model and Problem Description

The data used in this paper was generated from an FE model of the Volvo XC 90 (2015) rear subframe with simulated noise. The FE model has been extensively studied in [17] where experiments have also been performed. The same sensor placement is used in this paper, which can be seen in Fig. 20.2. It has been observed in both experimental data and simulated FE model data that a very strong local mode is present near the excitation position. The mode is shown in Fig. 20.3a and is at 1265 Hz. The direct accelerance FRF is shown in Fig. 20.3b for the FE model with low damping and experimental data from [17]. It can be seen that the two data sets have a very similar trend, i.e. a very strong local mode is present around 1250 Hz in both sets.

The identification of models using N4SID [12] from experimental data on this subframe has consistently rendered models with a poor direct accelerance. This observation has been similar for true test data and simulated FE data alike. Working with FE model data instead of true experimental data has the clear advantage that it allows for absolute knowledge of the underlying model, and it will be shown that even the identified model with the correct number of states but without the additional residual give a poor direct accelerance model.

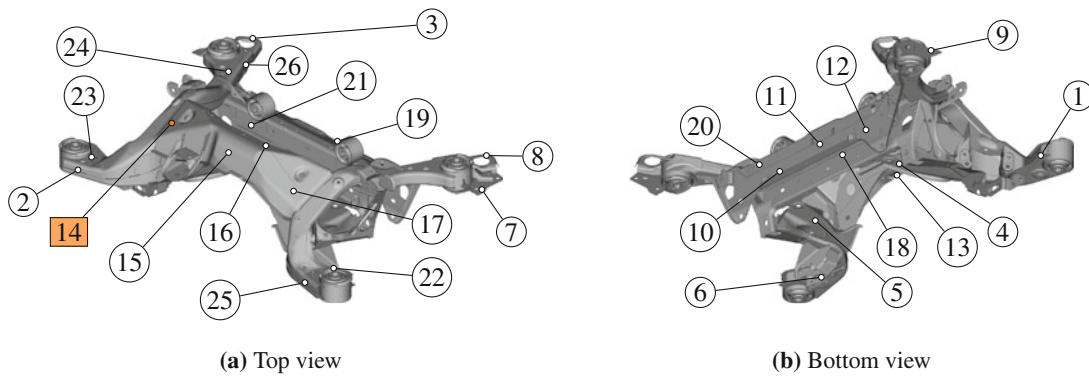


Fig. 20.2 Top view of rear subframe in (a) and bottom view in (b). Circle markings indicate accelerometer locations and the rectangular marking indicate the input force position. The force was normal to the surface, with a direct accelerance accelerometer sensor configuration. Figure from [17]

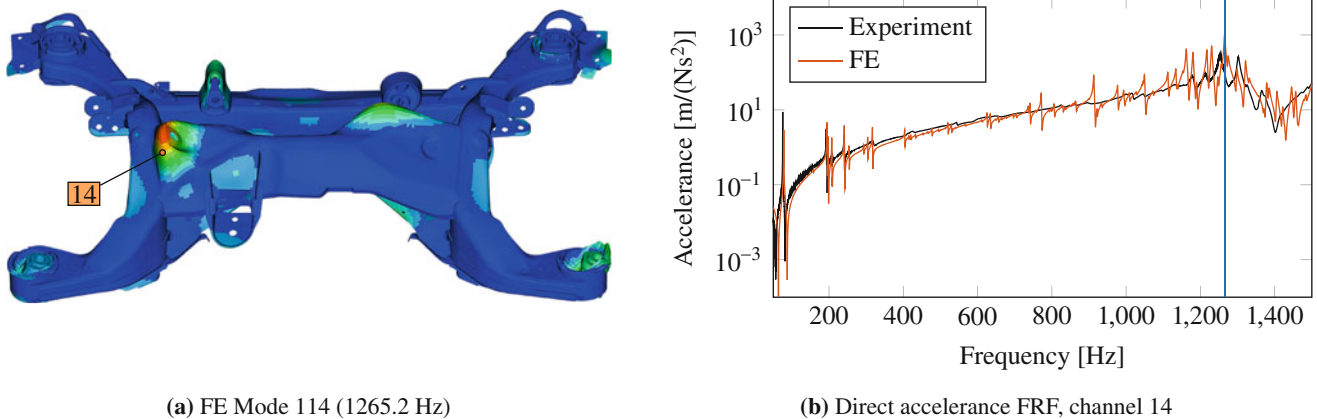


Fig. 20.3 Modeshape (red domain indicate strong motion, blue indicate insignificant motion) of the local strong mode (a) visible in the FRF of the direct accelerance channel 14 (b). True experimental data and FE model data shown. The blue line in (b) indicate the local strong mode location in FE model data

20.4 Results

Identified models using the proposed method, with three residual terms, are denoted $N4SID_A$ and $N4SID_R$ for identification on accelerance and receptance data, respectively. The third residual pole is placed according to strategy 2 in Sect. 20.2.1, i.e. at $\omega_S \approx 1220$ Hz since the frequency range of interest here ends at 854 Hz. This is very close to the true location of the locally strong mode at 1265 Hz, and hence strategy 1 need not be used. Identified models with the proposed method, but with only mass and stiffness residuals are denoted $N4SID_{A,2}$ and $N4SID_{R,2}$ for accelerance and receptance data, respectively. Models identified using RFP-Z are denoted simply RFP-Z. The RFP-Z model is identified from receptance data by identifying two models from a split data set into a low and high frequency part. The two models are then synthesised and five residuals added to the model. All models were identified with 14 modes on the same data in the frequency range of interest, between 47 and 854 Hz, with 0.5 Hz spacing in data. The performance of the models will be measured by the normalised root mean squared error (NRMSE) [1] and the frequency response assurance criterion (FRAC) [18, 19] for each channel. The NRMSE is magnitude dependent and is defined as

$$\xi_{jk} = 1 - \frac{\|\underline{\mathbf{H}}_{jk} - \mathbf{H}_{jk}^\Sigma\|_2}{\|\underline{\mathbf{H}}_{jk} - \text{mean}(\underline{\mathbf{H}}_{jk})\|_2} \in \mathcal{R} \quad (20.29)$$

with $\mathbf{H}_{jk}^\Sigma \in \mathbb{C}^{M \times 1}$ the identified system on accelerance or receptance form, $\underline{\mathbf{H}}_{jk} \in \mathbb{C}^{M \times 1}$ the experimental data on accelerance or receptance form, $\text{mean}(\underline{\mathbf{H}}_{jk}) \in \mathbb{C}$ the mean value of the experimental data and $\|\cdot\|_2$ the 2-vector norm. It should be pointed out that the NRMSE value is bounded between $-\infty < \xi_{jk} < 1$, where 1 indicate perfect fit, $-\infty$ bad fit and 0 no better fit than a constant \mathbf{H}_{jk}^Σ matching $\underline{\mathbf{H}}_{jk}$. The FRAC is magnitude independent and defined as

$$\rho_{jk} = \frac{|\underline{\mathbf{H}}_{jk}^H \mathbf{H}_{jk}^\Sigma|^2}{(\underline{\mathbf{H}}_{jk}^H \underline{\mathbf{H}}_{jk}) (\mathbf{H}_{jk}^{\Sigma H} \mathbf{H}_{jk}^\Sigma)} \in \mathcal{R} \quad (20.30)$$

where \cdot^H is the conjugate transpose [15]. The FRAC is bounded between $0 < \rho_{jk} < 1$, where 0 indicate that the vectors \mathbf{H}_{jk}^Σ and $\underline{\mathbf{H}}_{jk}$ are orthogonal while 1 indicate that they are co-directional.

In Fig. 20.4a the direct accelerance is shown for the $N4SID$ identified models. It can be seen that when only the mass and stiffness residuals are included, model $N4SID_{A,2}$, the channel is estimated very poorly, with $NRMSE=0.0543$ and $FRAC=0.5732$. For the model with three residuals $N4SID_A$ it can be seen that a much better estimate is obtained, with $NRMSE=0.9726$ and $FRAC=0.9996$. The $NRMSE$ for all channels of the $N4SID$ identified models is shown in Fig. 20.6a, where it can be seen that the remaining channels are mostly unaffected, but some improved. Similarly, the $FRAC$ for all channels is shown in Fig. 20.6c. Models identified on receptance data are shown in Fig. 20.4b. Here it can be seen that all models seem to match data quite good. However, in Fig. 20.5, which shows the cropped magnitude of Fig. 20.4b for clarity, it can be seen that the model with only two residuals $N4SID_{R,2}$ does not capture the direct receptance channel very well, even though its $NRMSE=0.7478$ and $FRAC=0.9840$, as seen in Fig. 20.6a. Furthermore, the RFP-Z model has a very good fit, $NRMSE=0.9503$ and $FRAC=0.9994$, with very slight deviations from the experimental data. However, the $N4SID_R$ model captures the direct receptance channel best with $NRMSE=0.9942$ and $FRAC \approx 1$ (above 0.9999). In Fig. 20.6b, d the $NRMSE$ and $FRAC$ are shown for all channels of the $N4SID_{R,2}$, $N4SID_R$ and RFP-Z models, respectively. It can be seen that the addition of the third residual in $N4SID_R$ affects the direct receptance the most, essentially making it perform on par with all other channels in terms of $NRMSE$ and $FRAC$. Most cross-receptances remain unchanged or slightly improved. The RFP-Z model is on par with $N4SID_R$ but estimates the direct receptance channel poorer than the other channels.

It is also interesting to compare the eigenfrequencies of the identified models, when the FE model's true eigenfrequencies are known. This is done in Table 20.1. It can be seen that the $N4SID_A$, $N4SID_R$ and RFP-Z models obtain very similar estimates of the eigenfrequencies. The highest error is 0.0329% for the third mode of the RFP-Z model. However, the fourth mode is estimated poorest in $N4SID_R$. Generally the third and fourth eigenfrequencies are estimated poorest, for all three models. Interestingly, the $N4SID$ identified model on accelerance data $N4SID_A$ estimates the eigenfrequencies better compared to the RFP-Z and $N4SID_R$ models.

In Fig. 20.7 the modal assurance criterion (MAC) [19, 20] is used to compare the identified models' eigenvectors. The fourth mode between $N4SID_R$ and RFP-Z show the lowest correlation, having a MAC value of 0.9688. All other MAC values

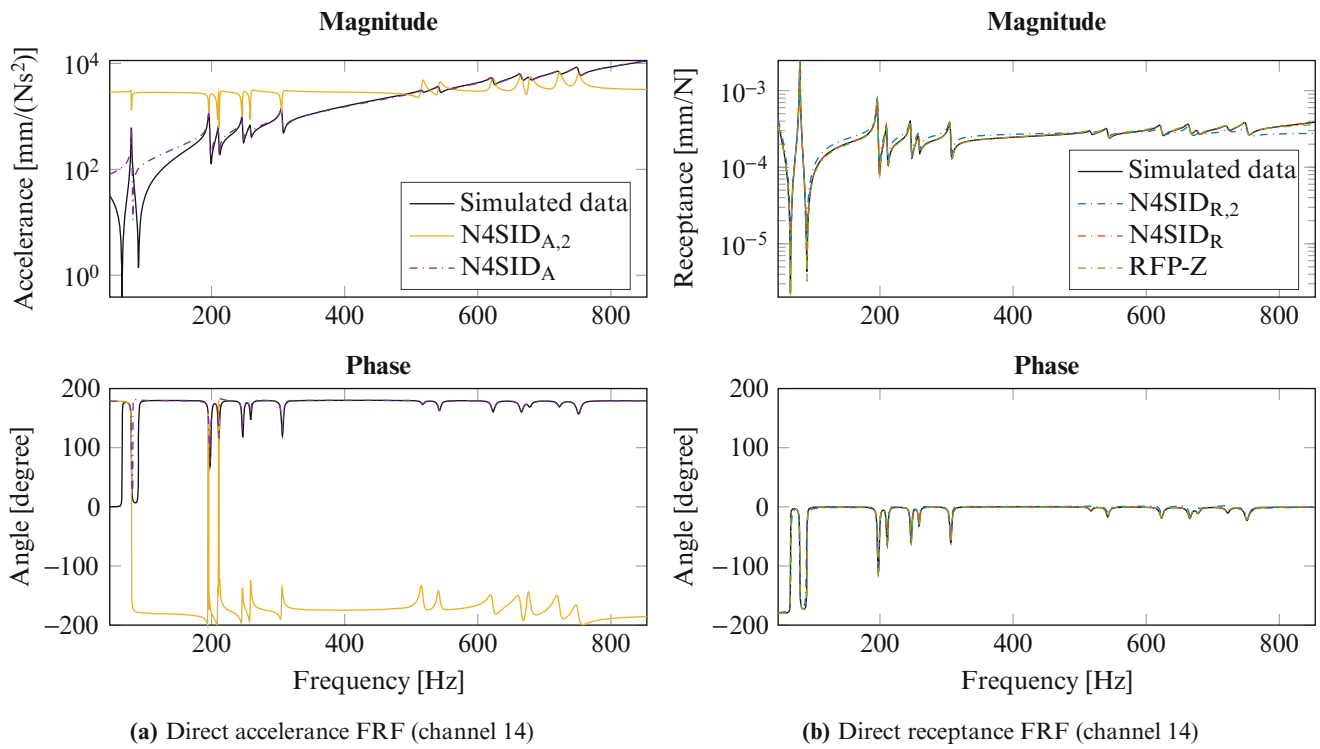


Fig. 20.4 Direct (a) acceleration and (b) receptance for the different methods

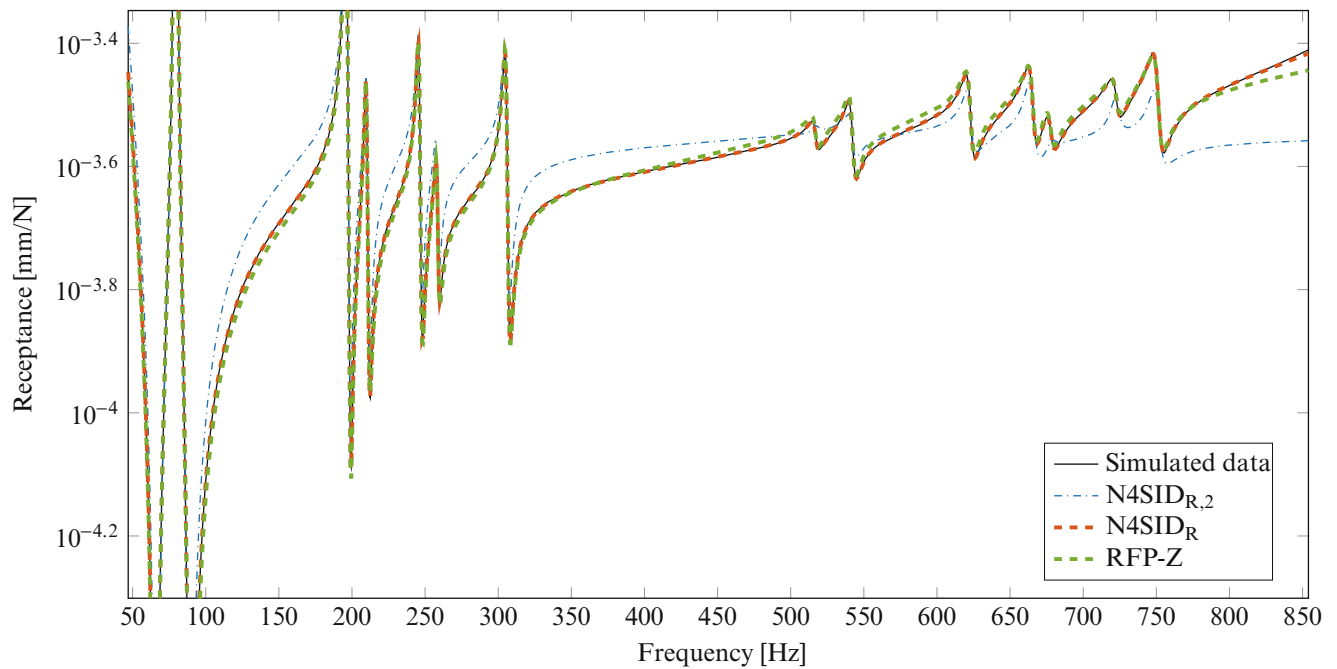


Fig. 20.5 Cropped direct receptance FRF (channel 14) between 47 and 854 Hz

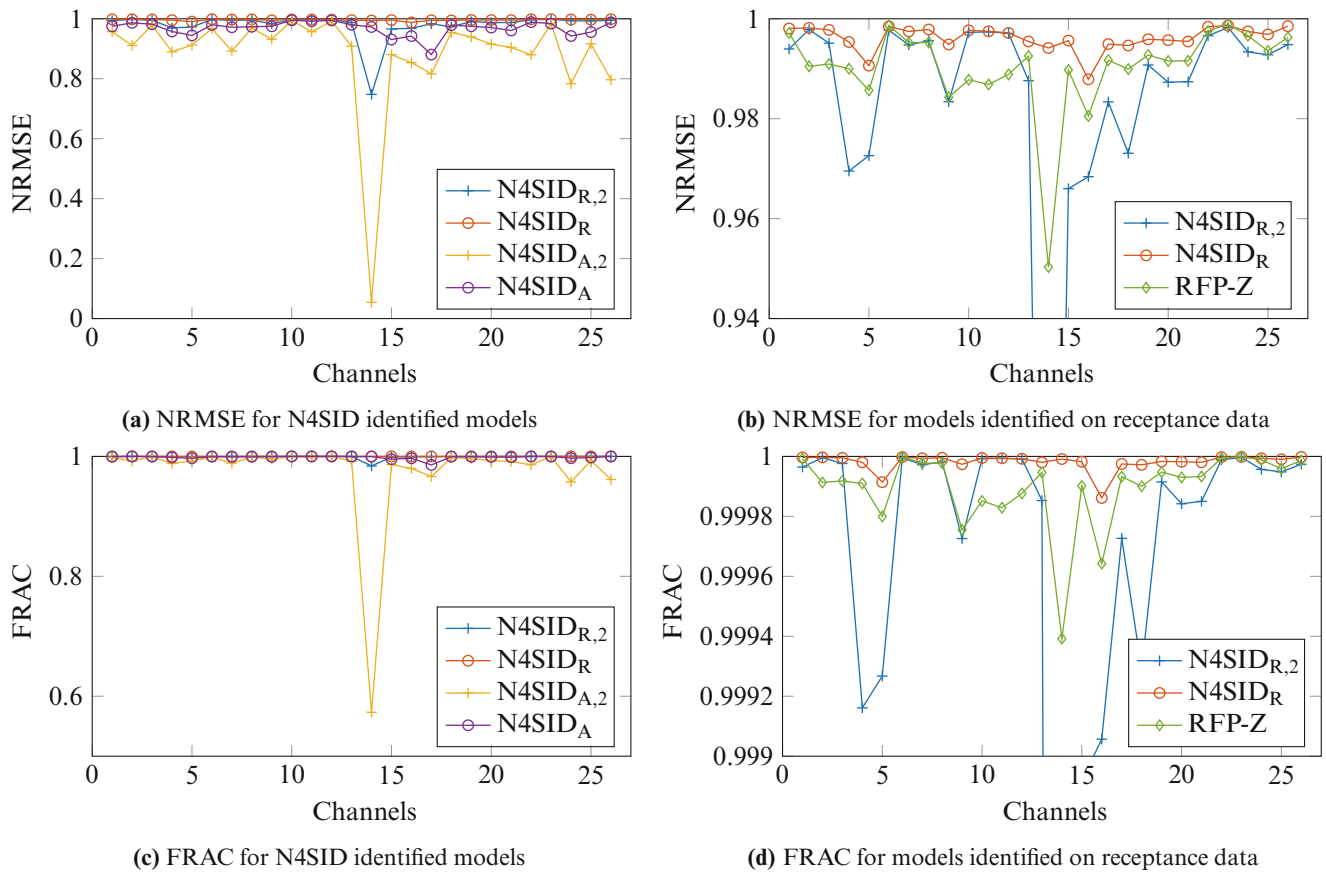


Fig. 20.6 NRMSE for all channels for models identified on (a) acceleration and (b) receptance data. FRAC for all channels for models identified on (c) acceleration and (d) receptance data

Table 20.1 Eigenfrequencies (Hz) of the FE model, N4SID identified models on acceleration N4SID_A and receptance N4SID_R and RFP-Z model. Relative error Δ (%) of the three identified models relative the FE model

Mode	FE model	N4SID _A	N4SID _R	RFP-Z	Δ N4SID _A	Δ N4SID _R	Δ RFP-Z
1	79.5	79.5	79.5	79.5	-0.0000	-0.0012	-0.0012
2	196.1	196.1	196.1	196.1	0.0003	-0.0001	-0.0032
3	210.0	210.0	210.0	210.1	-0.0000	-0.0026	0.0329
4	211.1	211.1	211.1	211.1	0.0033	-0.0112	-0.0057
5	246.0	246.0	246.0	246.0	0.0001	0.0001	-0.0029
6	258.4	258.4	258.4	258.4	-0.0003	-0.0007	-0.0031
7	305.5	305.5	305.5	305.5	0.0002	0.0004	-0.0020
8	516.8	516.8	516.8	516.9	-0.0001	-0.0007	0.0032
9	541.9	541.9	541.9	541.9	0.0001	0.0025	0.0053
10	622.5	622.5	622.5	622.5	-0.0002	-0.0025	0.0054
11	665.0	665.0	665.0	665.0	0.0002	-0.0002	0.0042
12	677.7	677.7	677.7	677.6	0.0000	0.0001	-0.0002
13	722.3	722.3	722.3	722.3	0.0002	0.0006	-0.0000
14	750.7	750.7	750.7	750.7	-0.0003	0.0065	0.0004

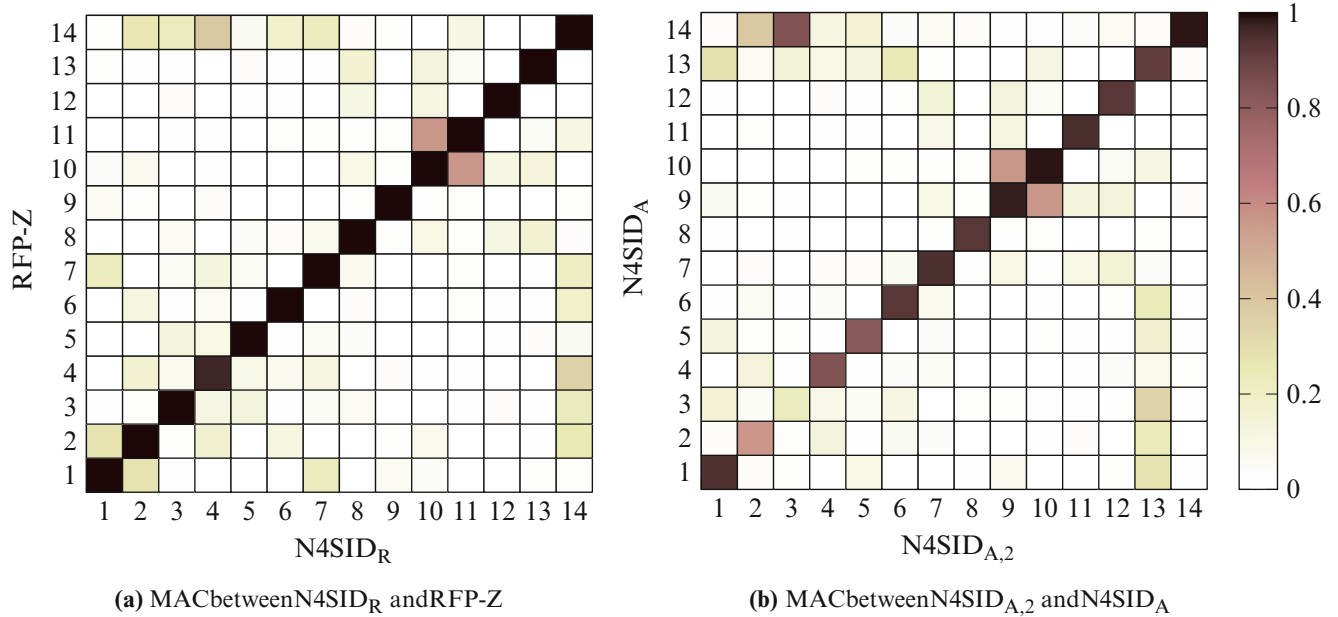


Fig. 20.7 MAC correlation (a) between $N4SID_R$ and RFP-Z and (b) $N4SID_{A,2}$ and $N4SID_A$

are over 0.9997. Interesting to note is that the MAC deviation between $N4SID_{A,2}$ and $N4SID_A$ is quite large, which was also evident in Fig. 20.4, for the direct accelerance. Hence, it can be seen that the third residual in $N4SID_A$ has a very large and positive impact on the identified system’s eigenvectors.

20.5 Conclusion

A method has been developed for identification of state-space models from frequency response data with residual compensation. In addition to mass and stiffness residuals a third residual term is added to compensate for strong local modes just outside the frequency range of interest. It has been shown that identification on accelerance data estimate poor direct accelerances without the third residual term. Similarly, for identification on receptance it has been shown that the direct receptance is significantly improved by inclusion of the third residual term, while remaining channels are relatively unaffected. The performance of the developed method has been compared to the RFP-Z method. Results indicate a very similar performance. Although the $N4SID_R$ model has a slightly better fit in terms of the NRMSE and FRAC for most channels. It is unclear how much the iterative re-estimation of the state-space system’s B , C and D matrices affect the performance of $N4SID_R$. It is likely that this step is responsible for the small improvements found in $N4SID_R$ over RFP-Z, but more research is necessary to draw a conclusion, which is left for future work. However, very similar MAC values are obtained between the RFP-Z and $N4SID_R$ models, and equally similar eigenfrequencies. Interestingly, it was found that the eigenfrequencies were slightly better estimated with the $N4SID_A$ model, although this model did not produce the best fit in terms of the NRMSE, FRAC or MAC. It is no clear why a frequency weighting (transformation of receptance to accelerance) results in a better estimate of the eigenfrequencies. Further research is necessary to understand this result.

The procedure’s performance remain to be tested on real experimental data. Also, the procedure presented here is planned to be tightly integrated with the $N4SID$ method [12], avoiding many separate least squares problems in series, hopefully gaining in efficiency and accuracy. Furthermore, it is possible that a better pole placement strategy for the pole in the third residual can be found, which is also left for future work. It is also interesting to investigate the identified model’s sensitivity to this pole placement.

Acknowledgements Volvo Car Corporation is gratefully acknowledged for providing the funding for this paper.

References

1. Ljung, L.: *System Identification: Theory for the User*, 2nd edn., p. 672. Prentice Hall, Upper Saddle River (1999)
2. Ewins, D.J.: *Modal Testing: Theory, Practice and Application*, 2nd edn., p. 576. Wiley-Blackwell, Philadelphia (2000)
3. Abrahamsson, T.J.S., Kammer, D.C.: Finite element model calibration using frequency responses with damping equalization. *Mech. Syst. Signal Process.* **6263**, 218–234 (2015)
4. Friswell, M.I., Motterhead, J.E.: *Finite Element Model Updating in Structural Dynamics*. Solid Mechanics and Its Applications, vol. 38. Springer Netherlands, Dordrecht (1995)
5. Sjövall, P., Abrahamsson, T.: Component system identification and state-space model synthesis. *Mech. Syst. Signal Process.* **21**(7), 2697–2714 (2007)
6. Liljehrn, A.: *Machine tool dynamics – a constrained state-space substructuring approach*. Doctoral thesis, Chalmers University of Technology (2016)
7. Klerk, D.D., Rixen, D.J., Voormeeren, S.N.: General framework for dynamic substructuring: history, review and classification of techniques. *AIAA J.* **46**(5), 1169–1181 (2008)
8. Peeters, B., Van der Auweraer, H., Guillaume, P., Leuridan, J.: The PolyMAX frequency-domain method: a new standard for modal parameter estimation? *Shock Vib.* **11**(3), 395–409 (2004)
9. Richardson, M.H., Formenti, D.L.: Parameter estimation from frequency response measurements using rational fraction polynomials. In: *Proceedings of the 1st IMAC International Modal Analysis Conference, Orlando*, pp. 167–186 (1982)
10. Allemang, R.J., Phillips, A.W.: The unified matrix polynomial approach to understanding modal parameter estimation: an update. In: *Proceedings of the ISMA International Conference on Noise and Vibration Engineering, Katholieke Universiteit, Leuven*, pp. 2373–2408 (2004)
11. Allemang, R.J., Brown, D.L., Phillips, A.W.: Survey of modal techniques applicable to autonomous/semi-autonomous parameter identification. In: *24th International Conference on Noise and Vibration Engineering, ISMA 2010, Including the 3rd International Conference on Uncertainty in Structural Dynamics, USD 2010, Leuven*, pp. 3331–3372 (2010)
12. McKelvey, T., Akcay, H., Ljung, L.: Subspace-based multivariable system identification from frequency response data. *IEEE Trans. Autom. Control* **41**(7), 960–979 (1996)
13. Van Overschee, P., De Moor, B.: N4SID: subspace algorithms for the identification of combined deterministicstochastic systems. *Automatica: Spec. Issue Stat. Signal Proces. Control* **30**(1), 75–93 (1994)
14. Kay, S.M.: *Fundamentals of Statistical Signal Processing, Volume I: Estimation Theory*, 1st edn., p. 625. Prentice Hall, Englewood Cliffs (1993)
15. Horn, R.A., Johnson, C.R.: *Matrix Analysis*, 2nd edn., p. 662. Cambridge University Press, New York (2012)
16. Kailath, T.: *Linear Systems*, 1st edn., p. 682. Prentice-Hall, Inc., Englewood Cliffs (1980)
17. Gibanica, M., Abrahamsson, T.J.S.: Parameter estimation and uncertainty quantification of a subframe with mass loaded bushings. In: Barthorpe, R., et al. (eds.) *Model Validation and Uncertainty Quantification, Volume 3. Conference Proceedings of the Society for Experimental Mechanics Series*, pp. 61–76. Springer International Publishing, Cham (2017)
18. Heylen, W., Lammens, S.: FRAC: a consistent way of comparing frequency response functions. In: *Proceedings of the Conference on Identification in Engineering Systems*, pp. 48–57 (1996)
19. Allemang, R.J.: The modal assurance criterion – twenty years of use and abuse. *Sound Vib.* **37**(8), 14–23 (2003)
20. Allemang, R.J., Brown, D.L.: A correlation coefficient for modal vector analysis. In: *Proceedings of the 1st IMAC International Modal Analysis Conference, Orlando*, pp. 110–116 (1982)

Chapter 21

Comparison of Time-Domain Objective Functions in Dynamic Fixture Optimization

Michael J. Starr and Timothy Walsh

Abstract Differences in impedance are usually observed when components are tested in fixtures at lower levels of assembly from those in which they are fielded. In this work, the Kansas City National Security Campus (KCNSC) test bed hardware geometry is used to explore the sensitivity of the form of the objective function on the adequate reproduction of relevant response characteristics at the next level of assembly. Inverse methods within Sandia National Laboratories' Sierra/SD code suite along with the Rapid Optimization Library (ROL) are used for identifying an unknown material (variable shear and bulk modulus) distributed across a predefined fixture volume. Comparisons of the results between time-domain based objective functions are presented. The development of the objective functions, solution sensitivity, and solution convergence will be discussed in the context of the practical considerations required for creating a realizable set of test hardware based on the variable-modulus optimized solutions.

21.1 Introduction

When performing ground-based component-level qualification testing it is common practice to use test fixtures that are effectively rigid across the frequency band of interest. It is also common practice to perform tests with single-axis inputs, with the understanding that the field inputs are much more complex. The implicit hope is that the process of deriving test inputs is adequately conservative to envelope all expected field responses. Although the manner in which component-level test environments are derived from field data typically supports the belief that they exceed field data, in general, there is no rigorous guarantee of that belief. Qualifying components at the next level of assembly could alleviate some of the issues associated with impedance mismatches observed when testing at lower levels of assembly, but still does not address issues related to multiple DOF inputs and boundary condition matching.

It is an axiomatic truth that if the field-level response characteristics of a component are preserved across all levels of assembly that any testing done will correctly inform any post-test assessments that need to be performed. For example, it is desired to gather correct evidence for qualifying components, calculating margin, assessing reliability, etc. Setting aside the philosophical discussion about whether reproducing field environments at the component-level is the actual goal of testing, if the intent is to reproduce actual field environments at a component, then it would be useful to characterize the effect of either optimizing applied input forces or optimizing test impedance subject to the appropriate test constraints. The latter optimization is explored here.

A purely numerical investigation is pursued to discover if there are mathematically-admissible solutions to a material inverse problem. Inverse methods within Sandia National Laboratories' Sierra/SD code suite [1, 2] along with the Rapid Optimization Library (ROL) [3] are used for identifying an unknown material (variable shear and bulk modulus) distributed across a predefined fixture volume. The KCNSC test bed hardware geometry [4] is used to explore how to construct time-domain objective functions that lead to material optimization solutions that preserve component response over multiple levels of assembly.

Sandia National Laboratories is a multimission laboratory managed and operated by National Technology and Engineering Solutions of Sandia, LLC., a wholly owned subsidiary of Honeywell International, Inc., for the U.S. Department of Energy's National Nuclear Security Administration under contract DE-NA-0003525.

M. J. Starr (✉) · T. Walsh

Sandia National Laboratories, Albuquerque, NM, USA

e-mail: mjstarr@sandia.gov; tfwalsh@sandia.gov

21.2 Problem Development

The goal of this work is to investigate the theoretical potential of deducing a mechanical filter, via a heterogeneous test fixture, that can reproduce the system-level responses (kinematic and stress) at a component, when that component is isolated from the system assembly. The boundary condition challenge geometry provided in [4] serves as the system-level assembly definition. The component defined in that assembly is used with a standard-sized, continuous plate to represent the component-level definition. Finite element representations of both levels of assembly are shown in Fig. 21.1.

All of the analysis is performed with Sandia National Laboratories' Sierra/SD code suite [1]. The first step of the analysis is to develop a set of "truth" data. This is achieved by exciting the system-level geometry (Fig. 21.1a) with an arbitrary 3-DOF shock transient and predicting the acceleration and stress responses throughout the component. A representative 3-DOF acceleration time history response at the component is then derived from the system-level forward simulation and used as the input into the component-level simulation geometry (Fig. 21.1b). In general, a forward simulation of the component-level geometry will not reproduce the responses observed in the system-level data, therefore, a solution will be sought by deducing a physically-admissible set of heterogeneous material properties across the elements of the discretized fixture in the component-level model. This is achieved by solving a time-domain inverse problem.

The time-domain inverse problem formulation is described in Ref. [2] and briefly summarized here. The solutions to the forward transient simulation are the measured acceleration histories (e.g. $\mathbf{a}_{m1} \dots \mathbf{a}_{mN}$, and N is the number of time steps in a fully discrete formulation) at all nodes of interest. These acceleration time histories are used in an objective function, J , as

$$J(\{\mathbf{a}\}, \{\mathbf{p}\}) = \frac{\kappa}{2} (\{\mathbf{a}\} - \{\mathbf{a}_m\})^T [Q] (\{\mathbf{a}\} - \{\mathbf{a}_m\}) - \mathfrak{R}(\{\mathbf{p}\}) \quad (21.1)$$

where \mathbf{p} is the parameter set of bulk and shear moduli distributed heterogeneously throughout the fixture, $[Q]$ is a general weight matrix (or a Boolean matrix to select a subset of measured degrees of freedom), κ is a scaling constant, and \mathfrak{R} is the regularization operator. In the above equation, the notation $\{\mathbf{a}\} = \{\mathbf{a}_0, \mathbf{a}_1, \dots, \mathbf{a}_N\}$ is used to describe the acceleration history. The material identification problem is defined as an optimization problem by

$$\underset{\{\mathbf{p}\}}{\text{minimize}} \tilde{J}(\{\mathbf{p}\}) \quad \text{subject to } g_i(\{\mathbf{p}\}) \leq 0, i = 1 \dots n \quad (21.2)$$

and subject to the governing system of equations at time t_{k+1}

$$[M(\{\mathbf{p}\})] \mathbf{a}_{k+1} + [C(\{\mathbf{p}\})] \mathbf{v}_{k+1} + [K(\{\mathbf{p}\})] \mathbf{u}_{k+1} = \mathbf{f}_{k+1} \quad (21.3)$$

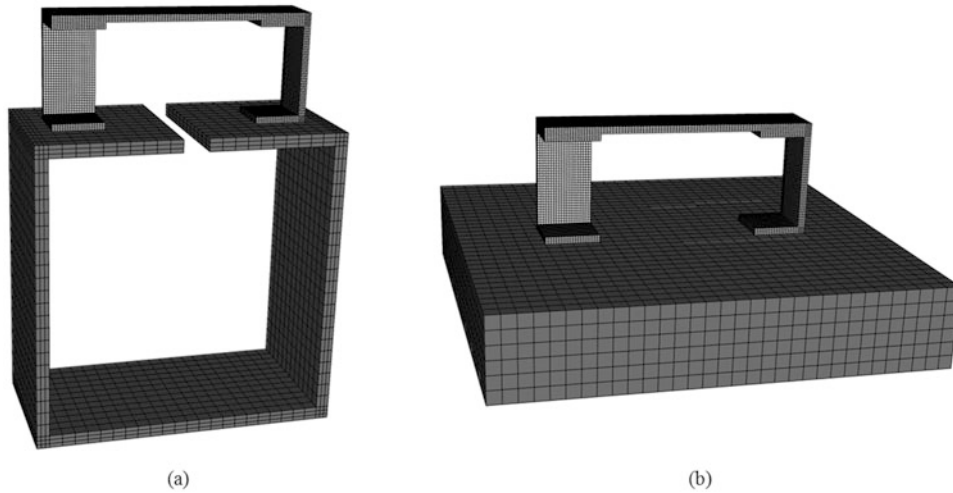


Fig. 21.1 Finite element model of the (a) boundary condition challenge system geometry and (b) boundary condition challenge component-level assembly on test fixture

with

$$\mathbf{u}_{k+1} = \mathbf{u}_k + \Delta t \mathbf{v}_k + \frac{\Delta t^2}{2} [(1 - 2\beta) \mathbf{a}_k + 2\beta \mathbf{a}_{k+1}] \quad (21.4)$$

$$\mathbf{v}_{k+1} = \mathbf{v}_k + \Delta t [(1 - \gamma) \mathbf{a}_k + \gamma \mathbf{a}_{k+1}] \quad (21.5)$$

where γ and β are user-defined parameters in the Newmark-beta transition equations. The solution to Eq. (21.2) is dependent on the number and spatial distribution of nodes that are retained in the objective function.

21.3 Discussion

For now, all of the practical matters of actually developing a test fixture that matches the theoretical distribution of material parameters have been ignored. Even if it were possible to do so using additive manufacturing or some other technique, a single fixture will not be adequate. The solution set, \mathbf{p} , is likely to have sensitive dependence on the input environments, so a unique fixture will be required for each unique input environment. The nature of the problem formulation and solution approach also guarantee non-uniqueness of the solutions. Since the solution converges only in the least squares minimization sense, there can be no expectation that the complicated field state can be reproduced closely enough to exercise the correct fatigue and damage mechanisms. The viability of this approach further relies on how faithfully the input environments can be produced within the constraints of current test capabilities. In the course of creating a more dynamically correct fixture have we sacrificed test repeatability and ease of test control?

The mathematical formulation given above was developed with respect to minimizing errors in local accelerations. Although acceleration is a common variable of interest for comparisons of environments and responses (along with other kinematic quantities, e.g. velocity and displacement), stress is a more natural variable when attempting to quantify fatigue, damage, consumed lifetime, or margin. The use of a stress-based objective function could be more appropriate for this type of optimization exercise. Such an objective function could also alleviate some of the concerns of matching the full-field kinematics. If certain regions are known, *a priori*, to be the primary locations of first failure, then satisfying the stress-state locally in those areas without regard to matching globally might be adequate (provided no induced stress states elsewhere shift where first failure occurs.)

References

1. Sierra Structural Dynamics User's Notes. Sandia National Laboratories, SAND2017-9470, Unlimited Release, Albuquerque (2017)
2. Walsh, T., Aquino, W., Ross, M.: Source identification in acoustics and structural mechanics using SIERRA/SD. Tech. Rep. SAND2013-2689, Sandia National Laboratories (2013)
3. Rapid Optimization Library (ROL): <https://trilinos.org/packages/rol> (2018)
4. Harvie, J.: Boundary conditions in environmental testing challenge problem. Memo (May 31, 2017)

Chapter 22

Advanced Hammer Excitation Technique for Impact Modal Testing on Lightweight Materials Using Scalable Automatic Modal Hammer

Tarun Teja Mallareddy, Sarah Schneider, and Peter G. Blaschke

Abstract Experimental Modal Analysis (EMA) on a lightweight material has proven to be very challenging in the recent past. The applications of these materials have increased invariably in various fields and so have a high demand for Research & Development (R&D). A lightweight material is very sensitive in terms of vibration. EMA on these materials in free - free boundary condition is very complicated as the hammer excitation becomes very difficult. In order to acquire valid results, the conditions are modified, and in consequence, obtain inaccurate dynamic characteristics.

Some of the major challenges faced are: (a) material getting displaced from its original position after every hit, (b) difficulties in obtaining a single hit, (c) reproducing the same excitation force level for averaging output response. Overcoming these crucial challenges can result in reducing the inaccuracies in the results. Scalable Automatic Modal hammer (SAM) is developed to overcome these challenges and enables the ability to reproduce the same force level of excitation. This advanced hammer excitation technique has the capability to avoid the double hit, adjust the repeatability of force level and automatizes the entire excitation process.

In this research paper, a light weight material is experimented under free-free boundary condition and the obtained results are analyzed. The input hammer excitation is provided by SAM and the output contactless response is measured by Scanning Laser Doppler Vibrometer (SLDV).

The conclusions provided will reflect the importance of repeatability and reproducibility of hammer excitation force level in order to acquire accurate results. The controlling of SAM, by changing various parameters, in order to precisely excite lightweight structures will be demonstrated.

Nomenclature

EMA	Experimental modal analysis
FEA	Finite element analysis
SAM	Scalable automatic modal hammer
SLDV	Scanning laser Doppler vibrometer
FRF	Frequency response function

22.1 Introduction

The R&D field of industrial productions is focusing on using advanced lightweight materials for increasing the fuel efficiency of modern automobiles and aircrafts while maintaining the safety and performance. Lighter objects have a great potential for multiplying the fuel efficiency. A 10% reduction in automobile vehicle weight can result in a 6–8% fuel economy improvement. Using lightweight components and high-efficiency engines enabled by advanced materials in one quarter

T. T. Mallareddy (✉) · S. Schneider
Technical University of Applied Sciences Wildau, Wildau, Germany
e-mail: mallareddy@th-wildau.de

P. G. Blaschke
Technical University of Applied Sciences Wildau, Wildau, Germany
NV Tech Design GmbH, Steinheim, Germany

of the U.S. fleet could save more than 5 billion gallons of fuel annually by 2030 (Office of US Department of Energy) [1]. The same standards of utilization of these materials also inspire engineers to consider it as an alternative in the field of construction.

As the world is advancing towards employing lightweight materials, the challenges in the field of testing and analysis have increased. Especially in the field of experimental testing, the results of which are utilized in the correlation process of the simulation results. The correlation and validation process envelopes the quality standards of analysis of lightweight materials. It is important to test and analyze a structure by the method of modal analysis, Experimental Modal Analysis (EMA) also termed as impact modal testing, where the structures dynamic characteristics/ modal parameters in terms of eigenfrequencies, damping and mode shapes are derived. The testing includes exciting the structure by using a modal hammer, recording the output vibrational response using an accelerometer or Lased Doppler Vibrometer (LDV) and analyzing the data to derive the dynamic modal parameters.

The greatest challenge experienced in this method is the process of excitation of the lightweight material. This research paper explains the challenges in detail and the way to overcome these challenges with the help of the SAM.

22.2 Challenges in Exciting a Lightweight Material

- (a) The greatest challenge in inducing vibrations in a lightweight material is the lightweight itself. Figure 22.1 shows a composite material that has a maximum mass of 20 g.

When a modal hammer is used to excite the structure (which has a maximum mass of 20 g) placing it on a foam mat (which is heavier than the material) to create free vibrational conditions, the material displaces from its starting position. The combination of the high stiffness, strength and lightweight properties of the material makes it very difficult to excite the structure without making it jump and displace from its original place. It requires an automatic technique to precisely control the velocity and the contact of the hammer tip to the surface, in order to enable a suitable force input without displacing it from its position.

- (b) A single contact of the modal hammer tip to the lightweight material surface is of high importance to derive an accurate vibrational response. The challenge is in overcoming multiple contacts of the modal hammer tip during an impact. This again demands a precise control over the modal hammer. The manual hand-held modal hammer is highly susceptible to varying control of velocity (resulting in material displacement) and the precise single-hit excitation of the structure (resulting in inaccurate results).
- (c) In order to derive a mode shape, a mesh of DOFs is analyzed and at each DOF a number of hits are given to average the result. For example, a mesh of 20 DOFs on a structure has to be analyzed and at each DOF an average of 10 hits is to be considered. This would demand a hammer excitation with the same repeated force level, precise point of excitations, single impact of a hammer hit and all of this for 200 points, in order to obtain the accurate results. If either the averages or the DOFs increase the number of excitations will multiply. For this level of accuracy of exciting a lightweight material, working with a manual hand-held hammer is next to impossible and highly time consuming.

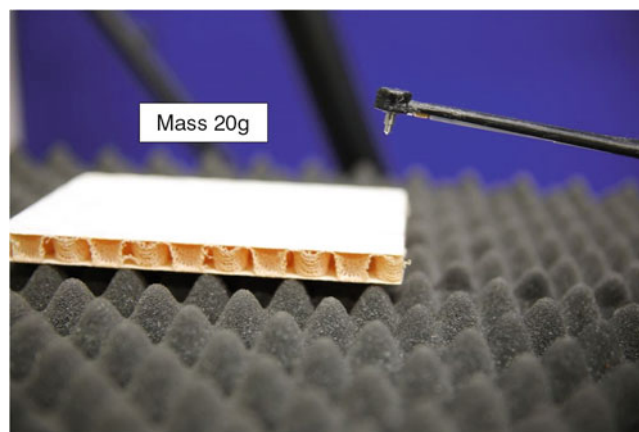


Fig. 22.1 Excitation of a light weight composite material using the SAM

In order to overcome the above mentioned challenges of testing by exciting a lightweight material, the advanced state of art automatic hammer excitation technique, the SAM, is utilized.

22.3 Materials and Methods

A composite material called Honeycomb structure (internal name) is used for the lightweight material excitation. The SAM (Noise-Vibration-Technology GmbH, Steinheim a.d. Murr, Germany) is instrumented with a mini impulse modal hammer tip model 086E80 (PCB Piezotronics Inc., Depew, NY, USA), and is used here for providing hammer excitations. The vibrational response is measured by the Scanning Laser Doppler Vibrometer (SLDV) ScanSet (Maul-Theet GmbH, Berlin, Germany) with laser head OFV-5000 (Polytec GmbH, Waldbronn, Germany). The SAM GUI v2.0 software is used to control the SAM and VLScanner and vModal from Maul Theet GmbH, Berlin, Germany, is used to acquire and analyze the data.

22.4 Results and Discussion

I. The challenge of the lightweight material excitation, where the 20 g composite material gets displaced with every hammer hit was outdistanced by using the SAM (Fig. 22.2)

The SAM is driven by an inbuilt stepper motor that is operated by SAM GUI v2.0 software (Fig. 22.3 - left), using which the input force can be adjusted and enables the control of the velocity of the hammer hit. The SAM is instrumented with a mini impulse modal hammer tip that has an in-built force sensor; this provides the force value of the excitation. The rotation is digitally controlled in distance and velocity via the stepper motor software and transmitted to the motor via USB. It is that the force input must be very low (the level which is just enough to excite the structure) in order not to displace the material from its original position. But how less a value must be the force input? The SAM has the capability of controlling the force input very precisely with its GUI. Figure 22.3 (right) shows the capability of the SAM system to adjust reproduce the repeatable input force value (shown in the box plot) according to the experiment requirements. The difference between the measurement results obtained due to good and varying force control is also shown in Fig. 22.3 (middle) [2].

II. The SAM GUI can precisely control the stepper motor to assist in eradicating the challenge of multiple hits by producing an accurate single hit. Figure 22.4 shows the measurement data of the composite material which consists of the vibrational output time signal, FFT data of the vibrational response, input force time signal, FFT data of the input force signal, coherence and FRF.

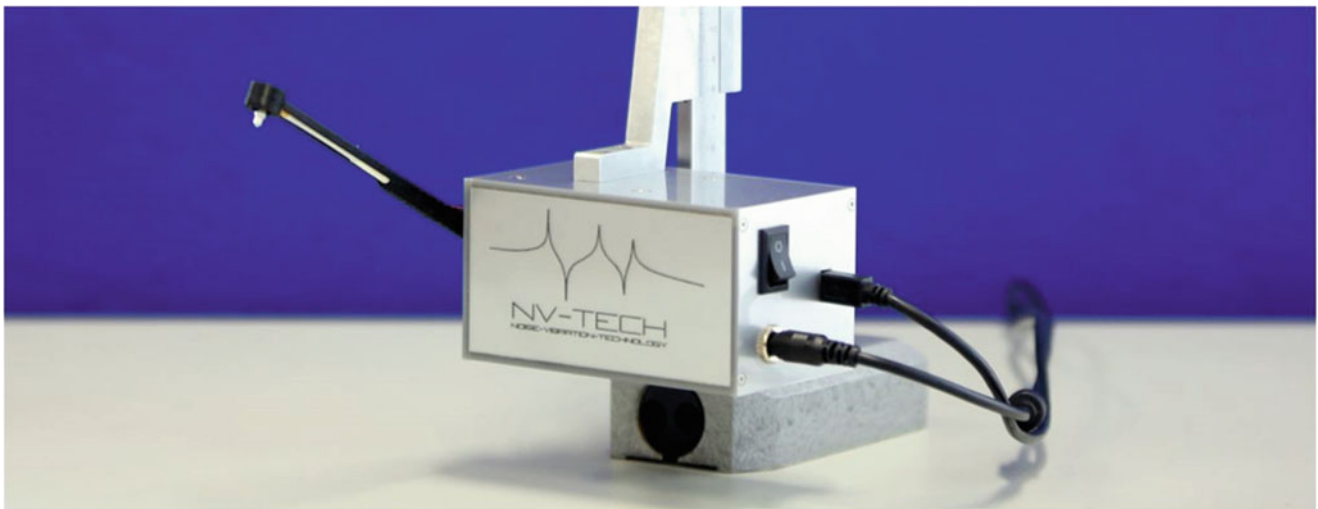


Fig. 22.2 The Scalable Automatic Modal Hammer (SAM) - Advanced state of art technique for hammer excitation

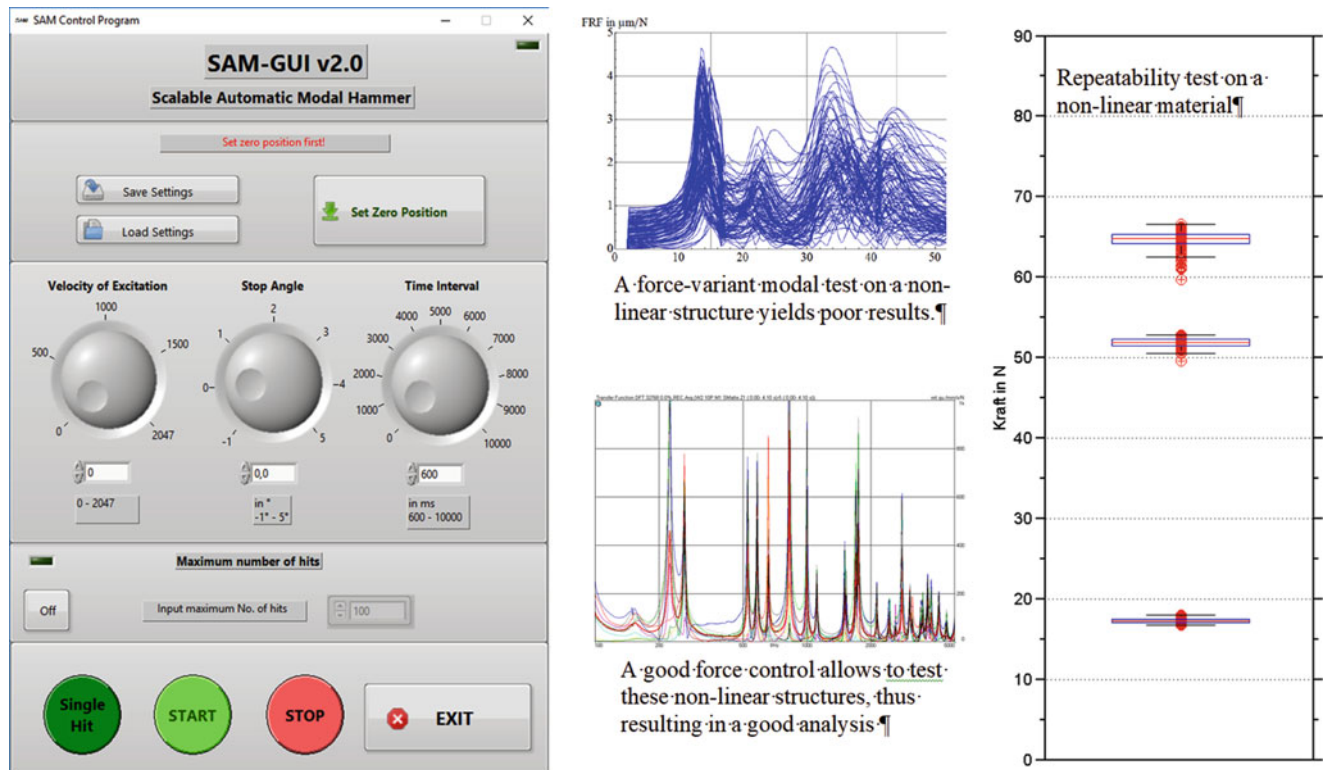


Fig. 22.3 The repeatability box plot of hammer excitations on a non-linear material and corresponding FRFs overlay (middle and right respectively) is displayed. The GUI of the SAM for controlling the precise force levels, acceleration, time interval etc., of the modal hammer is shown (left)

It can be seen that the force level is as low as 10 N. The vibrational response is acquired and due to the accurate structural excitation the frequency peaks can be very clearly identified in the graph of Frequency Response Function (FRF). The dynamic characteristics in terms of eigenfrequencies, damping and modeshapes are derived by analyzing the obtained FRFs.

III. As mentioned above, the SAM has the capability to reproduce the same force level repeatedly. If there is a structure that needs to be tested for 1000 DOFs with 10 averages at each DOF, the SAM can precisely excite the structures 10,000 times, with the same force level and at the excitation point. The composite material tested for obtained the dynamic characteristics was scanned at 50 DOFs using the SLDV. The input excitation force was consistently at a stable level of 8–10 N. The derived first 8 mode shapes in the frequency range of 0–8 kHz is shown in Table 22.1.

22.5 Conclusions

The application of the advanced hammer excitation technique, the SAM, on testing the lightweight composite material was successfully conducted and presented. The results in terms of mode shapes and eigenfrequencies were displayed. The high standard of automatizing the hammer excitation process with the assistance of SAM, has been a breakthrough in the field of impact modal testing of lightweight materials. The final word is stated as; it is possible to perform EMA on a lightweight material (as light as 20 g) by precisely exciting it using the SAM and deriving its dynamic characteristics by measuring the vibrations using LDV measuring techniques.

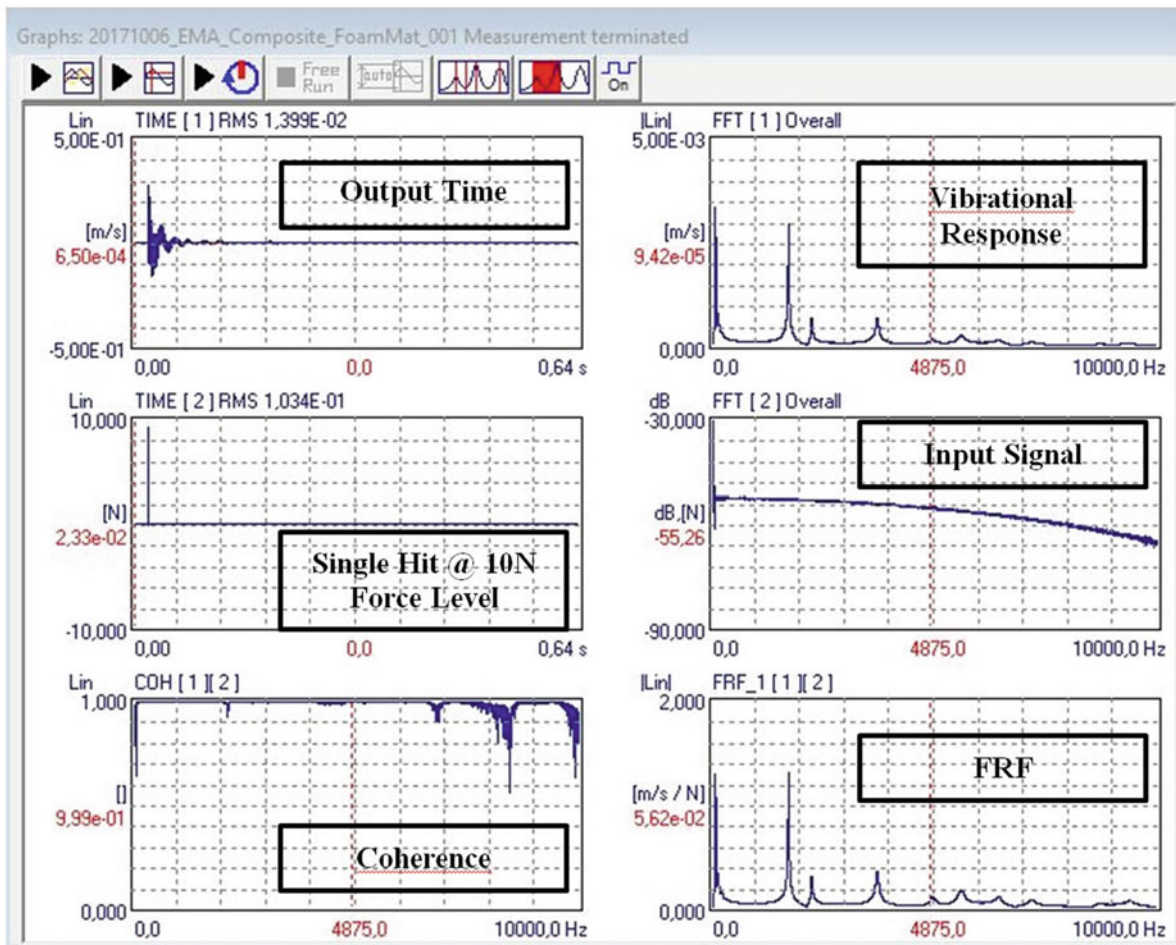
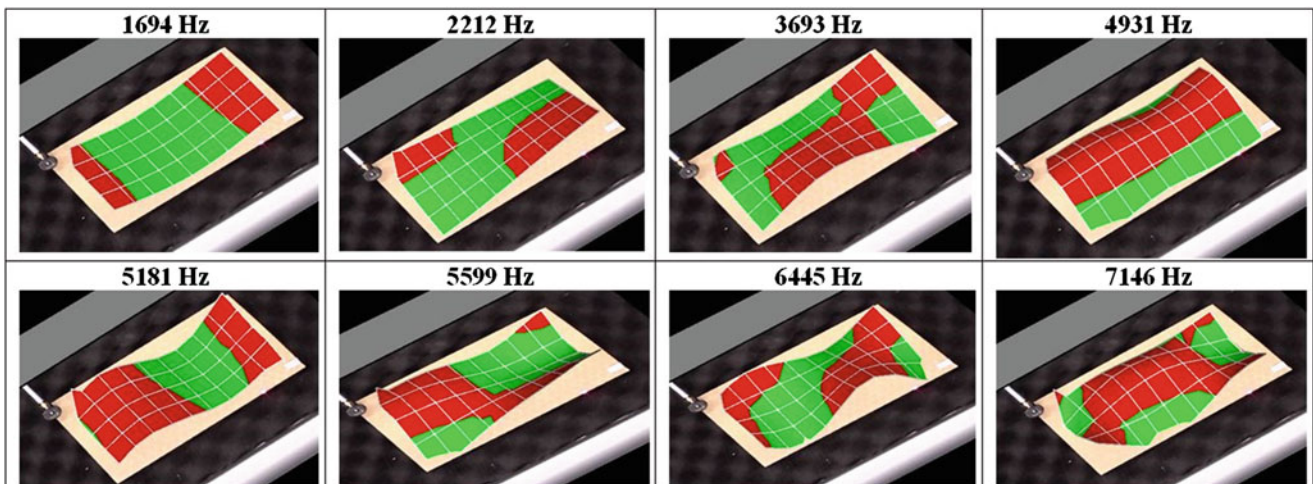


Fig. 22.4 Representation of measurement data of the tested composite lightweight material using SAM and SLDV

Table 22.1 Representation of first eight modeshapes and corresponding eigenfrequencies of the composite lightweight material tested using the SAM and SLDV



References

1. Office of Energy Efficiency and Renewable Energy, U. S. Department of Energy. Lightweight materials for Cars and Trucks. [Online resource] Available at <https://www.energy.gov/eere/vehicles/lightweight-materials-cars-and-trucks> (2014). Accessed 23 Sept 2017
2. Blaschke, P. et al.: Non-linearity identification of composite materials by scalable impact modal testing. In: Sensors and Instrumentation, Vol. 5, Conference Proceedings of the Society for Experimental Mechanics Series (2017)

Chapter 23

Evaluation of MIMO Input Derivations and Their Physical Context

Arup Maji

Abstract Multi-Input-Multi-Output (MIMO) vibration testing is considered to be more representative of the actual loads on many articles of interest. Since the derivation of MIMO inputs involve a matrix inversion process using $N \times M$ transfer functions corresponding to N input and M output locations, it is affected by both mathematical and physical parameters. The derived input loads can differ depending on the inversion and convergence algorithm used as well as on the accuracy of the underlying data.

A study was conducted using data from a benchtop MIMO test. The objective of the study was to understand how the convergence criteria and the underlying data used in MIMO algorithms affect the derived inputs. Two different input derivation methods were used. Of particular interest is the influence of the Tikhonov regularization used in the matrix inversion process and the consequence thereof in achieving the desired outputs as well as the input loads. The paper will present the results of these studies with the intent of providing a better understanding of their implications in tests and analyses associated with MIMO.

23.1 Test Article and Data Analysis Process

This study used a simple test article on a 6-DOF (6 Degrees of Freedom) shaker. The simplicity of this test article minimizes the relevant modes and allows one to focus on the errors associated with the MIMO inversion process that is the focus of this research. The test article (Fig. 23.1a) consisted of a solid block of aluminum mounted on the top of a threaded rod which was screwed on to an aluminum pedestal at the bottom end; the bottom block was screwed onto the 6-DOF shaker. A ‘Tensor’ 18kN capacity 6-DOF shaker was used (Fig. 23.1b); consisting of four shakers along each of the three axes allowing full 6-DOF vibration testing. ‘Signal Star Matrix’ software from ‘Data Physics’ was used, which utilizes frequency domain adaptive control to calculate the drive signals for each shaker. Four triaxial accelerometers can be seen in Fig. 23.1a attached to the bottom block; these were used to determine the movement of the pedestal which was assumed to equal the movement of the 6-DOF shaker (the pedestal was considered rigid). Eight triaxial accelerometers were mounted on the block. Four of these (12 channels; X, Y & Z vibration at each of four accelerometers) were used as targets for the MIMO derivation and the remaining four accelerometers (additional 12 channels) were used for additional validation. Data was acquired with a sample rate of 12,800 Hz with 294,912 data points per channel (≈ 23 s of vibration data).

The MIMO Implementation and analysis consisted of the following steps carried out independently at each frequency:

- Derivation of 6-DOF inputs using an optimized coordinate transformation that relate the 12 accelerometer channels on the pedestal to the 6-DOF Inputs (three translations and three rotations). This was based on the physical location of the accelerometers on the base pedestal [1].

Sandia National Laboratories is a multi mission laboratory managed and operated by National Technology and Engineering Solutions of Sandia, LLC., a wholly owned subsidiary of Honeywell International, Inc., for the U.S. Department of Energy’s National Nuclear Security Administration under contract DE-NA0003525.

A. Maji (✉)

Sandia National Laboratory, Albuquerque, NM, USA

e-mail: amaji@unm.edu

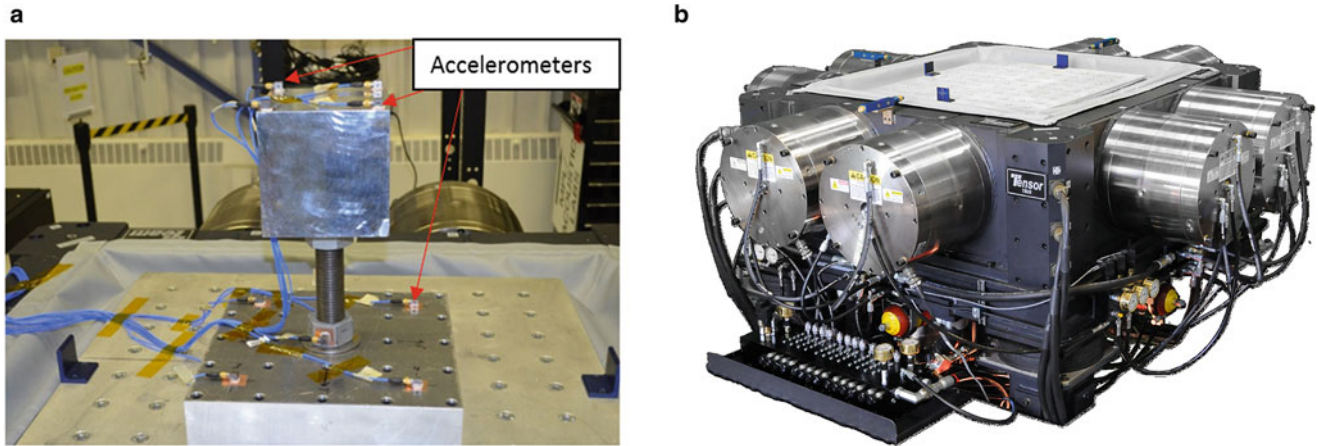


Fig. 23.1 (a) Test article with accelerometers. (b) 6-DOF shaker

- Determining the Auto-Spectral Densities (ASDs) of each of the six inputs and the Cross-Spectral Densities (CSD) corresponding to the 12 target accelerations from a 6-DOF test.
- Determining the Frequency Response Functions (FRF) ($12 \times 6 H$ matrix) connecting each of the 12 targets to each of the 6 inputs.
- Exploring different options of the matrix inversion process (and the Tikhonov regularization parameter) of determining inputs from the 12 target acceleration ASDs.
- Using the optimum derived inputs to compute new ASDs at the 12 targets and also at the remaining 24 channels.
- Examination of accuracy by comparing the derived input and resulting outputs with the original input and outputs from the 6-DOF test.

Using the 6-DOF test data, the 12×6 FRF matrix (H) was calculated as the ‘Output-Input CSD (P_{YX})’ divided by the ‘Input ASD (P_{XX})’ (* designates matrix multiplication):

$$[H]_{12 \times 6} = [P_{YX}]_{12 \times 6} / [P_{XX}]_{6 \times 6} \quad (23.1)$$

The output ASDs (P_{YY}) were also calculated to be used later as targets to derive the MIMO inputs as shown below. Since the 12×6 FRF matrix H is not square, the Moore-Penrose pseudo-inverse of H was obtained using the following equation (superscript T designates matrix transform, subscripts designate the size of each matrix) [2]:

$$[H]^{-1}_{6 \times 12} = ([H]^T * [H] + e * I)_{6 \times 6}^{-1} * [H]^T_{6 \times 12} \quad (23.2)$$

I is identity matrix and ‘ e ’ is the Tikhonov regularization parameter which prevents the very low values of the denominator from resulting in distorted (nearly singular) values in H^{-1} . The desired (MIMO) input ASD (P_{XXN}) that would result in the desired output ASD (P_{YY}) at the 12 target channels is then derived as:

$$[P_{XXN}]_{6 \times 6} = [H]^{-1}_{6 \times 12} * [P_{YY}]_{12 \times 12} * [H]^{-1T}_{12 \times 6} \quad (23.3)$$

New output auto-spectra (P_{YYN}) can then be derived from the MIMO-derived input auto-spectra (P_{XXN}) as:

$$[P_{YYN}]_{12 \times 12} = [H]_{12 \times 6} * [P_{XXN}]_{6 \times 6} * [H]^T_{6 \times 12} \quad (23.4)$$

The calculated input and output ASDs (P_{XXN}) and (P_{YYN}) can be compared with the original input and output ASDs (P_{XX}) and (P_{YY}) to examine the accuracy of the MIMO Inversion process.

23.2 Comparison Among Inversion Methods

Two different MIMO algorithms were used in the process of deriving MIMO inputs to match the desired outputs:

- The ‘ExtremeIO’ method is based on optimizing the ‘Trace’ (sum of the diagonal elements) of the Spectral Density matrix [3].
- The ‘IndDrive’ method attempts to keep the drives as independent as possible [4]; output is rescaled to desired output using iterative steps.

Analysis was conducted at each of 634 frequencies from 21.875 Hz to 2 kHz, using double-precision (64 bit) data. For easier comparison the results were rebanded to 6/octave frequency band from 20 Hz to 2 kHz (40 frequencies). Figure 23.2a, b compares the MIMO derived output ASDs (P_{YYN}) with the original target ASDs (P_{YY}) at the 12 targets (accelerometer 5, 6, 7, & 17). The ‘ExtremeIO’ method (Fig. 23.2a) is clearly more erroneous (errors >10DB) than the ‘IndDrive’ method (Fig. 23.2b) (errors <1 dB). Figure 23.3a shows the error (from ‘IndDrive’ method) in the remaining 12 channels that were not used as targets (accelerometers 8, 16, 18 & 19). As expected the error is larger in the remaining (non-target channels) than those in the target channels used to compute the input.

The data in Figs. 23.2a, b and 23.3a had been rebanded from the original linearly spaced frequencies to 6/octave frequency band. This smooths the data while preserving the energy in each frequency band. The error prior to rebanding is shown in Fig. 23.3b for comparison. Rebanding acts a smoothing operation and reduces the error. Rebanding at the beginning of the MIMO process (vs. at the end) did not produce better results than smoothing at the end. The significantly smaller number of frequencies reduces computation time without sacrificing accuracy.

Figure 23.4a, b compares the original inputs (black lines) to those derived from the MIMO inversion process (red lines) using ‘ExtremeIO’ and ‘IndDrive’ methods. The inputs derived using the ExtremeIO method (Fig. 23.4a) are all several orders of magnitude higher than the true inputs, these inputs are working against eachother to produce the desired output. The Inputs derived using IndDrive (Fig. 23.4b) are significantly higher at high frequencies for the translation motions and lower for the rotational motions. It is important to recognize that even though the iterative process of matching the outputs was effective at minimizing the error in outputs (Fig. 23.2b) the inputs that produced the desired outputs were at some frequencies several orders of magnitude different from the true inputs. Most often, in the absence of actual input data, this shortcoming of MIMO input derivation is overlooked.

Further analysis therefore focused on the ‘IndDrive’ method, in particular on the Tikhonov regularization parameter ‘ e ’ shown earlier in the matrix inversion process. It is well recognized that the matrix inversion process results in significant errors due to the ill-conditioning of the matrix being inverted. The ill-conditioning stems from several orders of magnitude differences in FRF values where a particular channel has a resonance or anti-resonance.

Figure 23.5a–c shows how the MIMO-derived response compares with the target using 3 different e values ($= 10^{-3}$, 10^{-5} & 10^{-7}). These are on original frequency (before rebanding to 6/octave). It is evident that reducing e from 10^{-3} to 10^{-5} improves the results while reducing it further to 10^{-7} greatly deteriorates the results. Figure 23.6 shows how the rms error (difference between actual and desired response) over all 24 channels (Full Response) and the 12 target channels as a function of ‘ e ’. Using $e = 10^{-4}$ seems to provide the best results. Figure 23.6 also shows that $e = 10^{-3}$ provides an improvement over $e = 10^{-5}$; which seems to contradict the earlier observation (examining Fig. 23.5a–c). This issue will be discussed later.

Figure 23.7 further explains how the choice of ‘ e ’ effects accuracy. The blue line in the top shows the Condition Number $C\#$ of the $[H]^T*[H]$ matrix on which the Tikhonov regularization is applied. The red arrows facilitate comparison for different regimes of $C\#$. The horizontal red line designates a $C\# = 10^3$. When the $C\#$ is low (left of 1st red arrow, between 2nd and 3rd red arrow and left of the 4th red arrow), inversion of the $[H]^T*[H]$ matrix is not prone to error and it is best to keep e low (lower than 10^{-4}). When the $C\#$ is high (at the resonances), matrix inversion is prone to error and a very low value of e is ineffective at minimizing errors and an optimum value of e (10^{-4} or 10^{-3}) is prudent. This is further illustrated in Fig. 23.8 which shows the same data for $e = 10^{-2}$, 10^{-6} and 10^{-7} . When $C\#$ is low Tikhonov regularization is unnecessary and adding $e = 10^{-2}$ results in a large error, and for all values of $e < 10^{-4}$ the error remains relatively unchanged. At resonances (see red arrows in Fig. 23.8) too low a choice of $e < 10^{-4}$ leads to progressively larger errors.

Figure 23.7 also helps understand why the overall grms error for $e = 10^{-3}$ was better than that for $e = 10^{-5}$ (Fig. 23.6). Although $e = 10^{-5}$ (red line in Fig. 23.7) had the lowest rms error through most of the frequencies, $e = 10^{-3}$ (blue line in Fig. 23.7) had the lowest rms error in regions where most of the vibration energy was concentrated (at higher resonant frequencies). Hence the overall rms error was lower for $e = 10^{-3}$.

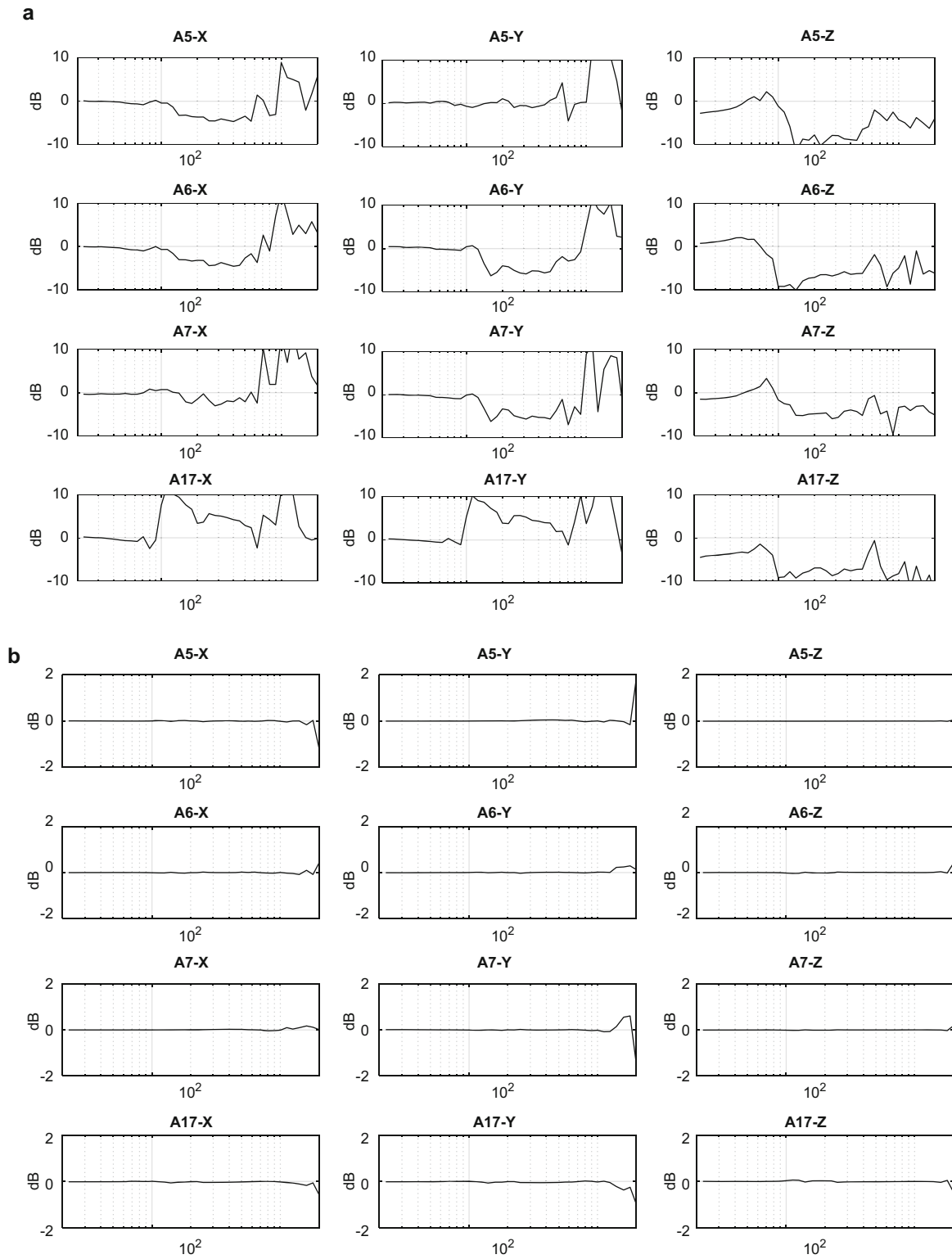


Fig. 23.2 (a) Error in target channel response using 'ExtremeIO'. (b) Error in target channel response using 'IndDrive'

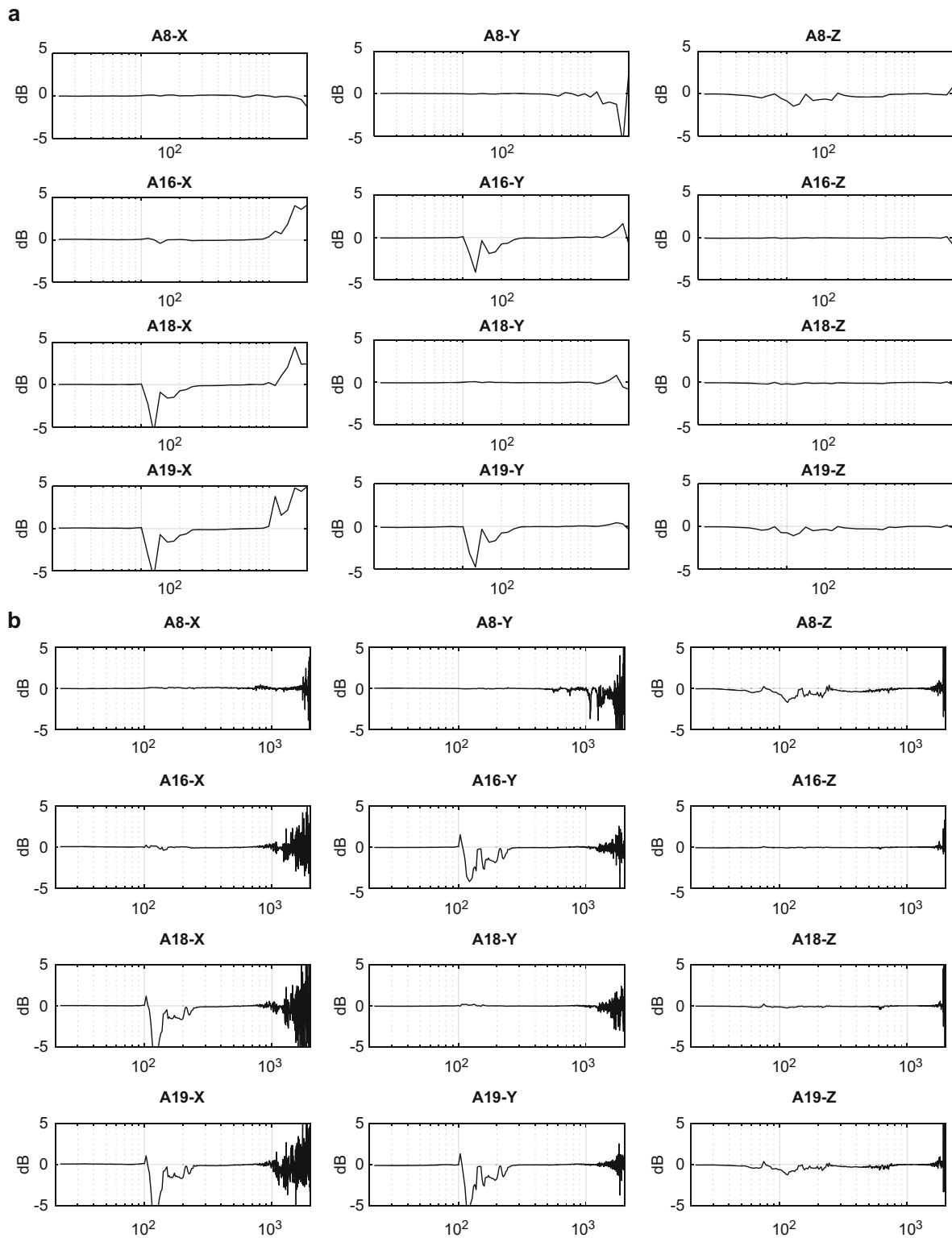


Fig. 23.3 (a) Error in non-target channel response using 'IndDrive'. (b) Error (prior to rebanding) in Non-target channel response using 'IndDrive'

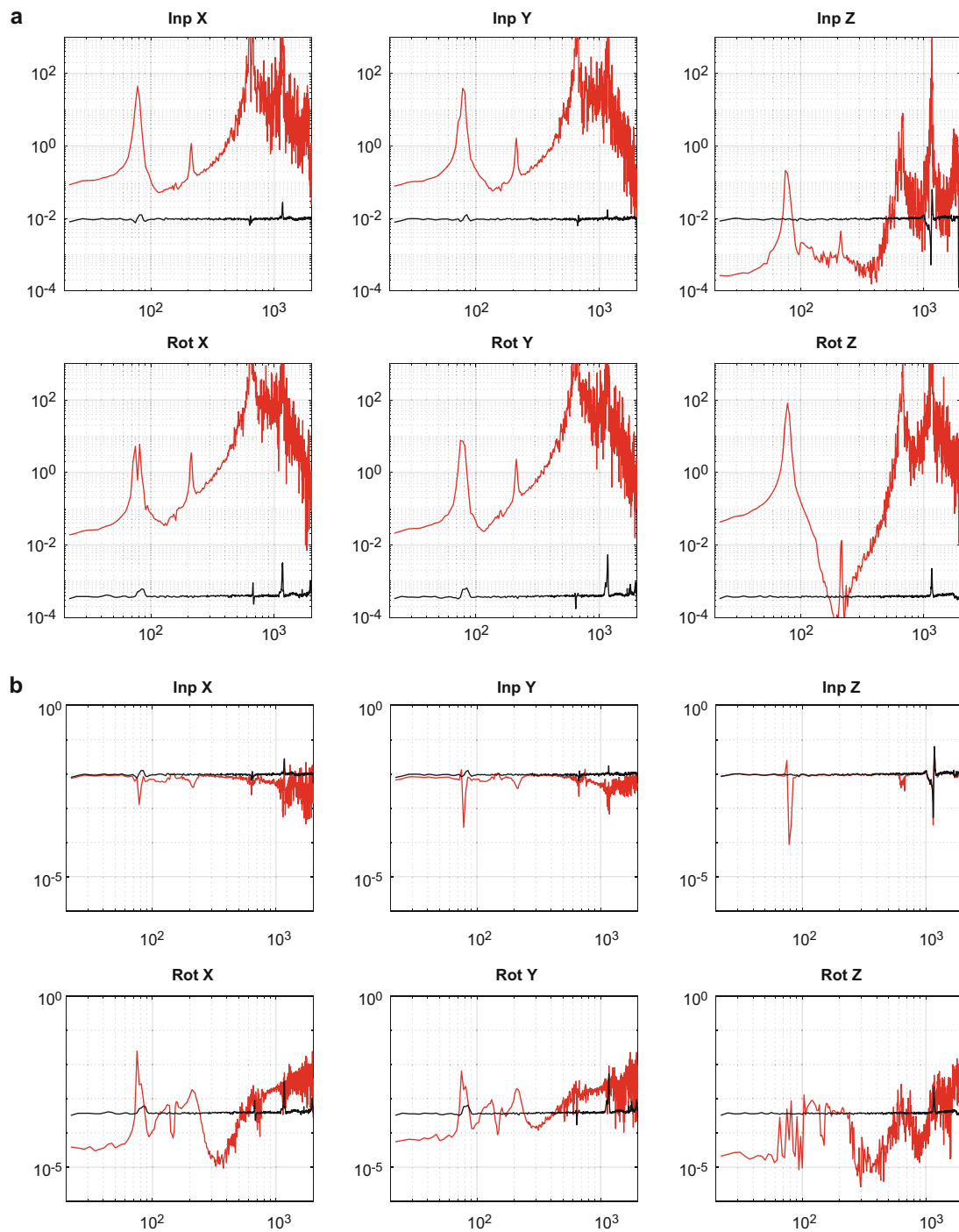


Fig. 23.4 (a) Comparison of actual (black) vs. MIMO-derived inputs using 'ExtremeIO'. (b) Comparison of Actual (black) vs. MIMO-derived Inputs (red) using 'IndDrive'

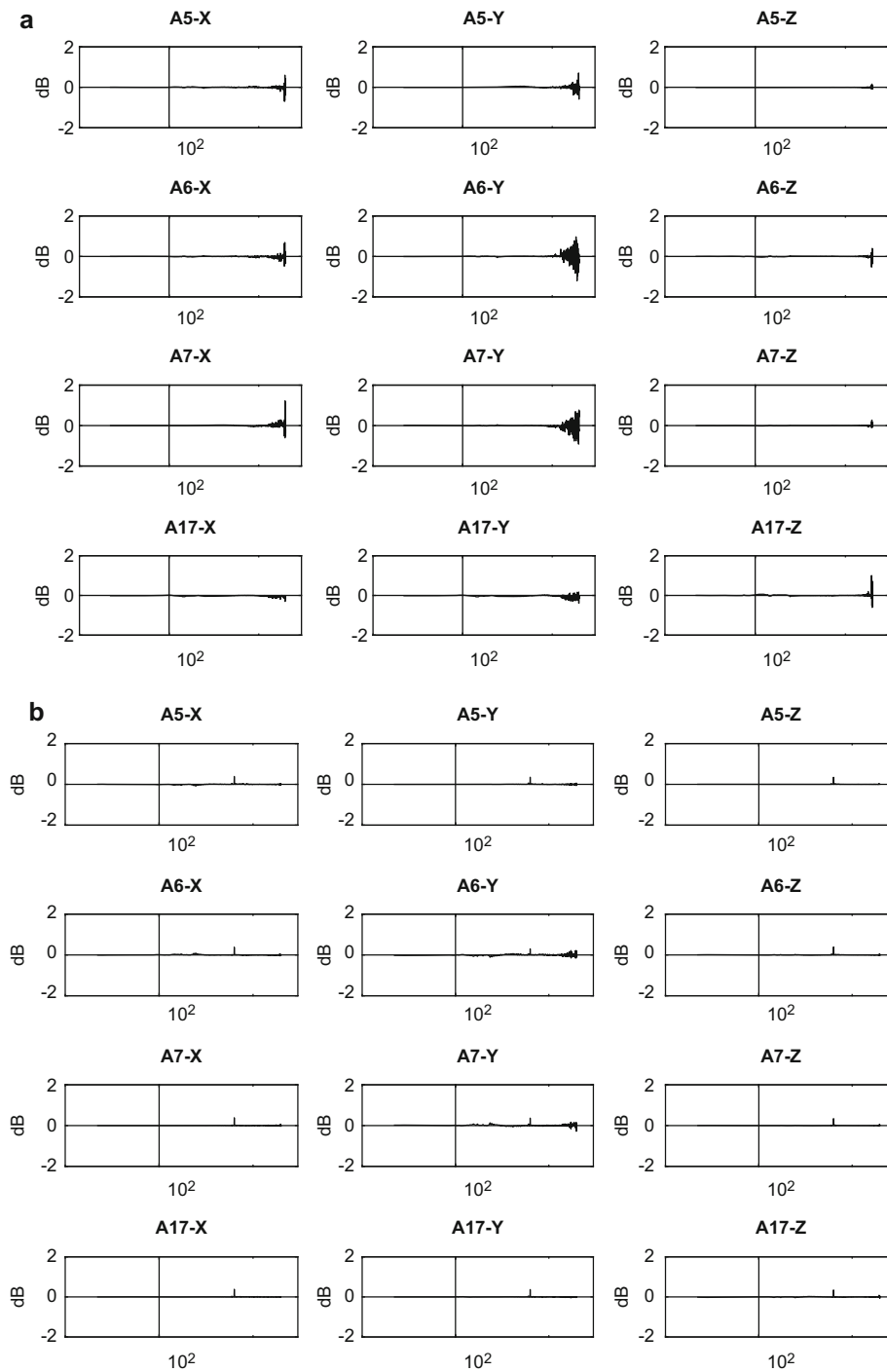


Fig. 23.5 (a) Ratio of MIMO/original target response using $\epsilon = 10^{-3}$. (b) Ratio of MIMO/original target response using $\epsilon = 10^{-5}$. (c) Ratio of MIMO/original target response using $\epsilon = 10^{-7}$

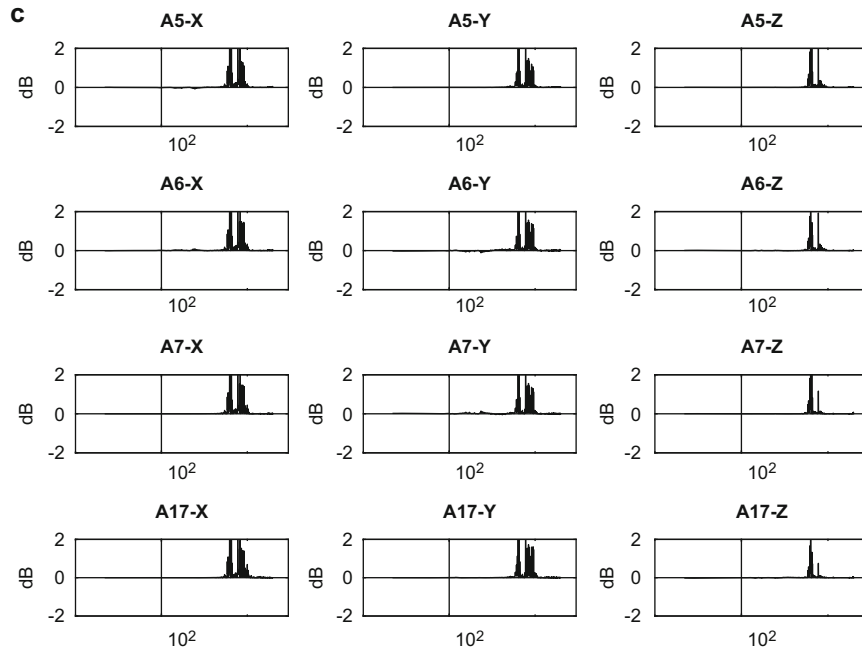


Fig. 23.5 (continued)

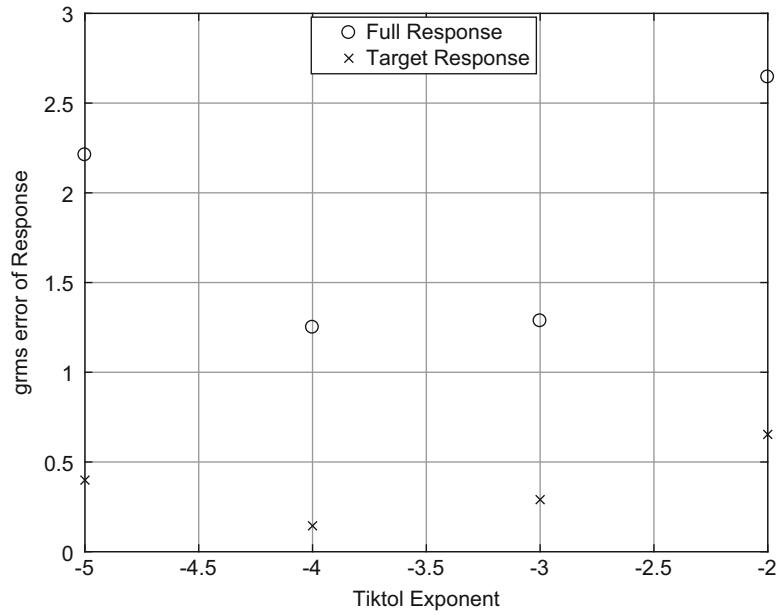


Fig. 23.6 grms of error in response with different Tikhonov tolerances (ϵ)

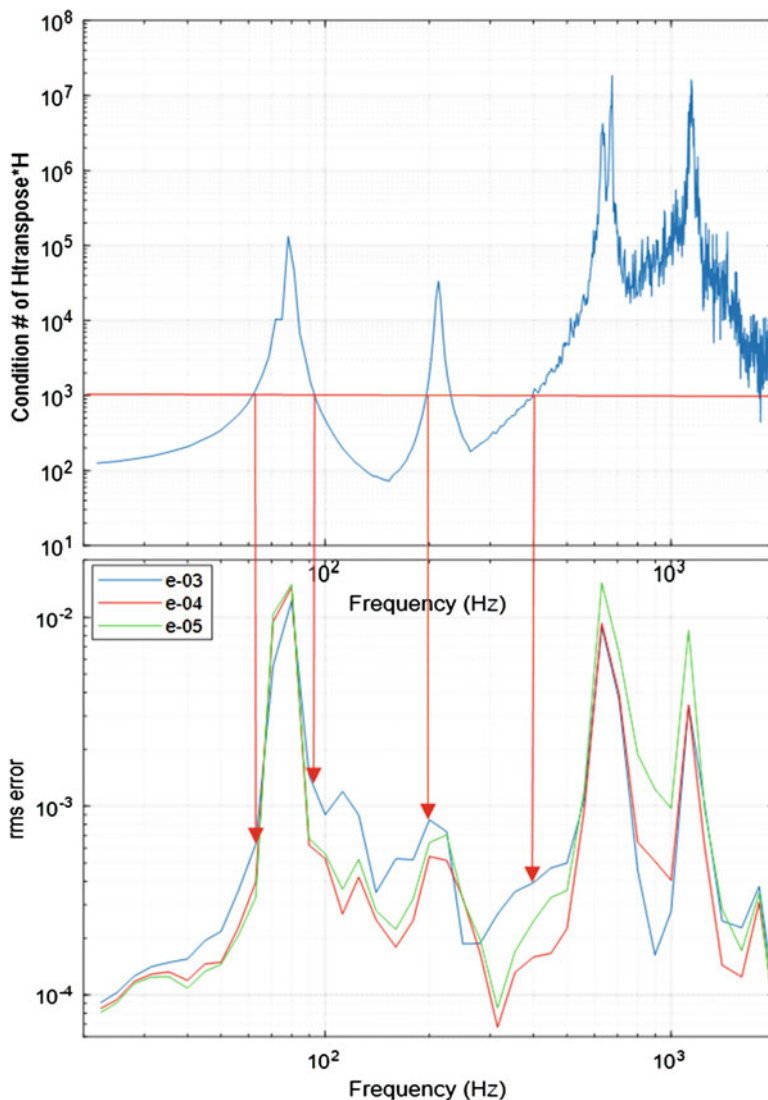


Fig. 23.7 Comparison of condition # with RMS error for 'e' = 10⁻³, 10⁻⁴, & 10⁻⁵

23.3 Conclusions

The 'IndDrive' method (independent individual inputs) of deriving MIMO inputs was superior to the 'ExtremeIO' method.

Rebanding to 6/octave frequency band after the MIMO inversion reduces the error via smoothing. Rebanding at the beginning of the MIMO process (vs. at the end) did not produce better results than smoothing at the end. The significantly smaller number of frequencies reduces computation time without sacrificing accuracy.

Further reduction in errors is possible using the appropriate Tikhonov regularization parameter (*e*). The appropriate value of *e* depends on the Condition number of the $[H]^T [H]$ matrix. It is therefore possible to minimize error by using frequency-specific *e* values.

Even when the iterative MIMO inversion process is effective at matching the outputs, the inputs producing the desired outputs can be very different from the true inputs. Most often, in the absence of actual input data, this shortcoming of MIMO input derivation is overlooked.

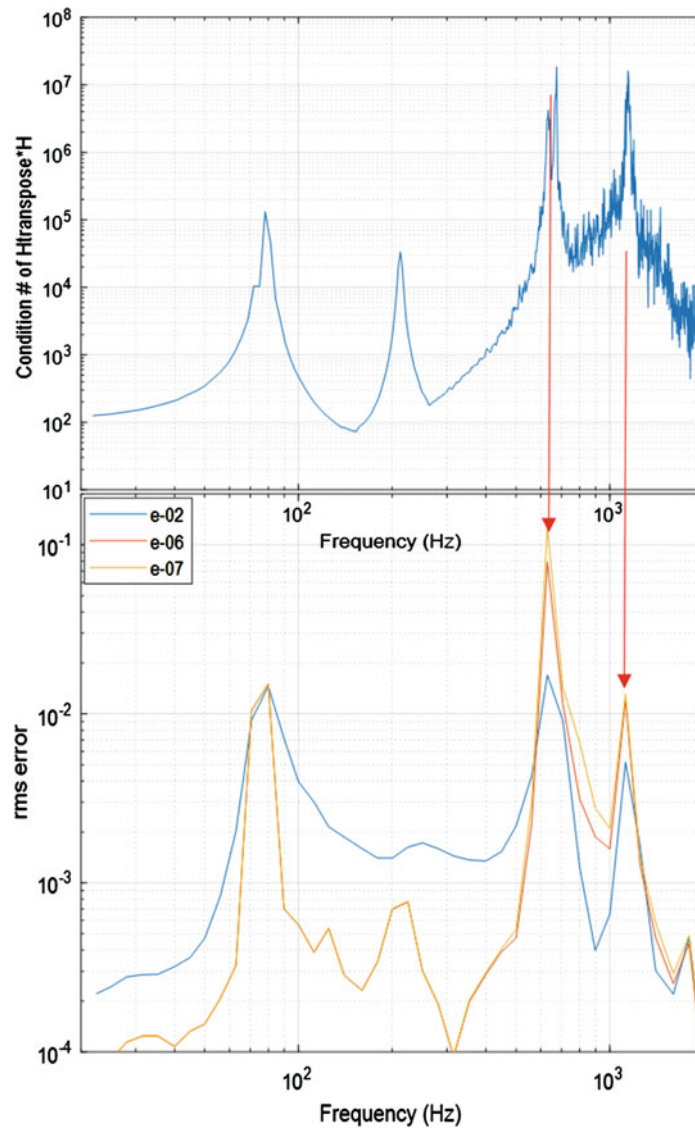


Fig. 23.8 Comparison of condition # with RMS error for ' e ' = 10^{-2} , 10^{-6} , & 10^{-7}

Acknowledgement The test data was provided by Garrett Nelson and the MIMO MatLab codes modified extensively by the author to conduct this study were originally written by David Smallwood and Jerry Cap.

References

1. Coy, N., Nagabhushan, V., Hale, M.: Benefits and challenges of over-actuated excitation systems. *Shock. Vib.* **17**, 285–303 (2010). <https://doi.org/10.3233/SAV-2010-0515>
2. Mayes, R.L., Rohe, D.P.: Physical vibration simulation of an acoustic environment with six shakers on an industrial structure. In: Proceedings of IMAC-34, Paper #122, (2016)
3. Smallwood, D.: Multiple-input multiple-output linear systems extreme inputs/outputs. *Shock. Vib.* **14**(2), 107–132 (2007)
4. Smallwood, D.: Minimum drive requirements for a multiple input multiple output linear system. In: IES 1986 Proceedings, pp. 295–301

Chapter 24

Using Modal Substructuring to Improve Shock & Vibration Qualification

Julie M. Harvie

Abstract Qualification of complex systems often involves shock and vibration testing at the component level to ensure each component is robust enough to survive the specified environments. In order for the component testing to adequately satisfy the system requirements, the component must exhibit a similar dynamic response between the laboratory component test and system test. There are several aspects of conventional testing techniques that may impair this objective. Modal substructuring provides a framework to accurately assess the level of impairment introduced in the laboratory setup. If the component response is described in terms of fixed-base modes in both the laboratory and system configurations, we can gain insight into whether the laboratory test is exercising the appropriate damage potential. Further, the fixed-base component response in the system can be used to determine the correct rigid body laboratory fixture input to overcome the errors seen in the standard component test. In this paper, we investigate the effectiveness of reproducing a system shock environment on a simple beam model with an essentially rigid fixture.

24.1 Introduction

The qualification of aerospace systems is a complex process that involves conducting tests, analyses, and inspections to demonstrate robustness of the products in the intended environments and satisfy design requirements with margin [1]. One aspect of the qualification process is consideration of the product's performance in mechanical environments such as random vibration, acoustics, and shock.

This evaluation is typically comprised of a combination of flight testing, laboratory testing, and analytical simulations. Flight testing has a major benefit over laboratory testing in that flight testing exposes the product to the true combined loading environment. However, flight testing is expensive, variable, and may not represent the worst case environments, and therefore must be supplemented with laboratory testing. Laboratory testing is cheaper, more repeatable, and lower risk than flight testing but suffers test equipment limitations such as lack of concurrent environment exposures, limited waveform replication options, and impedance differences. Analytical simulations are used to augment testing, providing a cost-effective method to predict responses at many locations on a structure in many scenarios. Analytical simulations tend to predict laboratory responses better than flight responses due to simplicity in the loading and boundary conditions.

In traditional laboratory testing, the test article is mounted to the test equipment (shaker, drop table, resonant plate) using a fixture to provide a single-axis shock or vibration input. Traditional guidance is to design a fixture that is stiff throughout the test bandwidth [2, 3] to ensure test repeatability and ease of test control. Typically, the test inputs are either derived from system-level response data near the component connection locations, if available, or from test standards [2, 3].

The differences between flight and laboratory testing, and specifically deficiencies of historical test techniques, have been recognized by many. There are several factors that may cause test articles to be either under- or over- stressed in the laboratory relative to the flight test. If a test article is unrealistically over-stressed in the laboratory without proper understanding of the cause, excessive funding will be wasted to ruggedize the design. If a test article is unrealistically under-stressed in the

Sandia National Laboratories is a multimission laboratory managed and operated by National Technology and Engineering Solutions of Sandia, LLC., a wholly owned subsidiary of Honeywell International, Inc., for the U.S. Department of Energy's National Nuclear Security Administration under contract DE-NA-0003525.

J. M. Harvie (✉)

Environments Engineering & Integration Department, Sandia National Laboratories, Albuquerque, NM, USA

e-mail: jharvie@sandia.gov

laboratory, true design flaws will not be exposed until the test article is used in service, causing immense hindrances to the qualification program.

As technology and analysis tools continue to mature, an emphasis has been placed on creating more realistic flight simulations both in the laboratory and modeling domains. Recent efforts have explored the effects of combined environments testing, particularly simultaneous acceleration and vibration exposure at Sandia's "vibrafuge" test facility [4, 5]. Replication of acoustic environments using shakers in the laboratory [6] and source inversion in finite element simulations [7] is also an area of promising research. There is an initiative in the dynamics community to better replicate multi-axis inputs in both the laboratory and finite element simulations [8–10]. Issues with impedance differences have been documented as early as the 1960s [11–13], and there is recently a renewed interest in exploring solutions [14–16].

All of these research areas strive to improve laboratory testing and analytical simulations. However, it is important to understand the magnitude of discrepancy between flight and laboratory testing on a component-by-component basis. While certain approximations may be adequate for testing certain families of components and subassemblies, those approximations may be inadequate for others. General practice does not require the test engineer or analyst to evaluate the component response dynamics in the laboratory test as compared to the system test.

One avenue for evaluation of component response is dynamic substructuring [17]. Dynamic substructuring provides a way to decouple and couple subsystems from a system. Both modal and frequency domain techniques may prove useful for different types of systems. This work will focus on the application of modal substructuring, while frequency domain techniques are being explored by other researchers [18].

Specifically, Mayes [19] has recently developed a specific form of modal substructuring that is particularly appealing for the situation identified here. The transformation decouples a system into the fixed-base modes of one component (the test article) and the free modes of the other component (the remaining system or fixture). Describing the environmental response of a component in terms of fixed-base motion is advantageous because it captures the damaging energy being exposed to the component while eliminating the non-damaging rigid motion. The methodology for extracting fixed-base modes from experimental data has become well-established [20–22]. Describing the remaining system in terms of free motion is useful in defining fixture control, especially for multi-axis testing, and understanding which fixture and system modes are being excited in a test. Note that this framework may need to be reassessed for cases where the motion of the remaining system cannot easily be described using its free mode shapes, for example if the component has a significant effect on the motion of the remaining system.

This modal substructuring theory has several applications within the realm of laboratory testing. Foremost, if the transformation is applied to a component both in a system in flight and in a fixture in the laboratory, the accuracy of the component excitation can be quantified. This will reveal whether or not the initial test setup adequately exercises the strain-inducing fixed-base modes of the component. If the fixed-base modes are not being excited properly, there are a few solutions to explore. The fixture can be redesigned to better match the impedance of the system, or the laboratory test inputs can be modified to excite the component modes properly. Each system may require a unique combination of these solutions, but input modifications are explored here.

24.2 Theory

The equations of motion can be written in modal space as

$$\mathbf{M}\ddot{\mathbf{q}} + \mathbf{C}\dot{\mathbf{q}} + \mathbf{K}\mathbf{q} = \mathbf{f} \quad (24.1)$$

where \mathbf{q} are the modal degrees of freedom (DOF), \mathbf{f} is a modal force, and \mathbf{M} , \mathbf{C} , and \mathbf{K} are the diagonal modal mass, damping, and stiffness matrices, respectively. The modal force \mathbf{f} and modal DOF \mathbf{q} are all vectors and will either be functions of time or frequency. The modal DOF are related to the physical DOF \mathbf{x} with

$$\mathbf{x} = \mathbf{\Phi}\mathbf{q} \quad (24.2)$$

where $\mathbf{\Phi}$ is the mode shape matrix. For a coupled system, it is desired to decouple the \mathbf{q} DOF into the DOF of the component and DOF of the remaining system. As mentioned above, we are specifically interested in transforming the coupled DOF

into the fixed-base motion of the component, p , and the free motion of the remaining system, s . Thus, we must develop the transformation matrix, T , to satisfy.

$$q = T \begin{Bmatrix} p \\ s \end{Bmatrix} \quad (24.3)$$

A simple relationship is used to relate the q coupled DOF and s fixture/remaining system DOF with.

$$\Phi_b q = \Psi_b s \quad (24.4)$$

where Φ_b contains the free mode shapes of the system at “b” DOF and Ψ_b contains the free mode shapes of the fixture/remaining system at “b” DOF. The “b” DOF should be chosen to capture enough modes to span the space of the problem. Note that the relationship in Eq. 24.4 will only be accurate for cases where the Φ_b modes can be fully described as a combination of the Ψ_b modes. This equation can then be rearranged to relate q to s as.

$$q = \Phi_b^+ \Psi_b s \quad (24.5)$$

where $^+$ denotes the Moore-Penrose pseudo inverse. This provides the second portion of the T matrix associated with the s DOF.

The first part of the transformation, where the coupled q DOF are transformed to fixed-base component p DOF, is achieved by analytically constraining the motion of all measurements not on the component, at “b” DOF. This relationship is given as.

$$q = L_{fix} \Gamma p \quad (24.6)$$

where L_{fix} is calculated with.

$$L_{fix} = null(\Psi_b^+ \Phi_b) \quad (24.7)$$

and Γ contains the eigenvectors resulting from pre- and post-multiplying Eq. 24.1 by L_{fix} . This part of the transformation is described more thoroughly in Refs. [19–22]. Equation 24.6 completes the rest of the transformation as.

$$T = [L_{fix} \Gamma \quad \Phi_b^+ \Psi_b] \quad (24.8)$$

Applying this transformation to Eq. 24.1 results in the following uncoupled modal equations of motion.

$$\begin{bmatrix} M_{pp} & M_{ps} \\ M_{sp} & M_{ss} \end{bmatrix} \begin{Bmatrix} \ddot{p} \\ \ddot{s} \end{Bmatrix} + \begin{bmatrix} C_{pp} & C_{ps} \\ C_{sp} & C_{ss} \end{bmatrix} \begin{Bmatrix} \dot{p} \\ \dot{s} \end{Bmatrix} + \begin{bmatrix} K_{pp} & K_{ps} \\ K_{sp} & K_{ss} \end{bmatrix} \begin{Bmatrix} p \\ s \end{Bmatrix} = \begin{Bmatrix} f_p \\ f_s \end{Bmatrix} \quad (24.9)$$

where the modal mass, damping, and stiffness now have non-zero off-diagonal terms. The physical significance of these coupling terms is still being investigated.

If the forcing function is known, Eq. 24.9 can be used to analytically calculate the system response in the decoupled space. However in most situations, the forces cannot directly be extracted from an environmental test. Instead, physical system responses can be transformed to modal system responses using Eq. 24.2 and then decoupled using Eq. 24.3. This is the process that would likely be used experimentally.

If the desired fixed-base component motion is known from a system test, the fixture motion required to induce the desired component motion can be calculated by rearranging the top portion of Eq. 24.9 as.

$$M_{pp}\ddot{p} + C_{pp}\dot{p} + K_{pp}p = -(M_{ps}\ddot{s} + C_{ps}\dot{s} + K_{ps}s) \quad (24.10)$$

Note that a typical system will have several s terms, both elastic and rigid body, acting on the p modes. A traditional fixture will only have rigid body s terms in the bandwidth of interest.

24.3 Models Developed

24.3.1 Physical Model Properties

A set of models were developed to study this problem. The intent is to have a component of interest that resides in a complicated system and is removed for qualification testing on a rigid fixture. A simple depiction of these two configurations is shown in Fig. 24.1. The red component of interest, Component A, is attached to the blue components, Component B, to create the system configuration, System AB. Then Component A is removed from System AB and attached to the green component, Component C, in the component laboratory test configuration, System AC.

These systems were modeled as beams in Matlab with 2 DOF per node, translation and rotation. A 2-DOF framework was chosen to maintain simplicity. All beams were modeled using aluminum material properties, and the cross-sectional properties of the beam elements were modified to control the flexibility of each component. Component A was modelled to be relatively flexible, while Component C (the fixture) was modelled to be relatively stiff, as is the case with typical fixture design today. All subcomponents in Component B had equivalent properties and were slightly less flexible than Component A.

All models utilized light springs to approximate a free-free boundary conditions and avoid a complex eigensolution. All joints were set to have an equivalent arbitrary stiffness (translation and rotation) that was relatively stiff but not completely rigid. Note that the joints between Component A and Component B must be similar to the joints between Component A and Component C in order for the proposed methodology to be effective.

24.3.2 System Input

A forcing function was designed using the sum of decaying sinusoids technique [23] to excite frequencies up to approximately 600 Hz. The forcing function is shown in Fig. 24.2 in both the time and frequency domains. This forcing function was used to excite System AB at a single arbitrary point near the mid-span of the base of Component B. The response of Component A to the forcing function in System AB provides the reference solution.

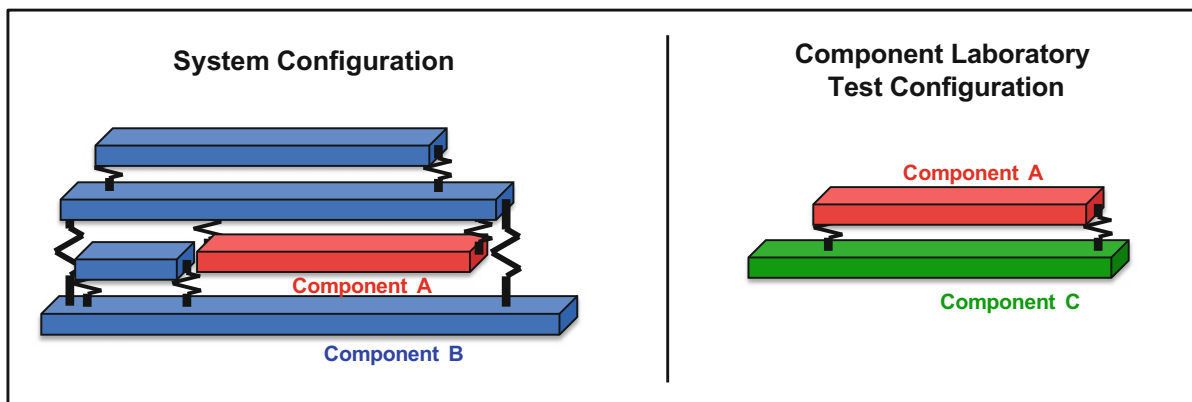


Fig. 24.1 Depiction of component of interest in system vs. laboratory test configuration

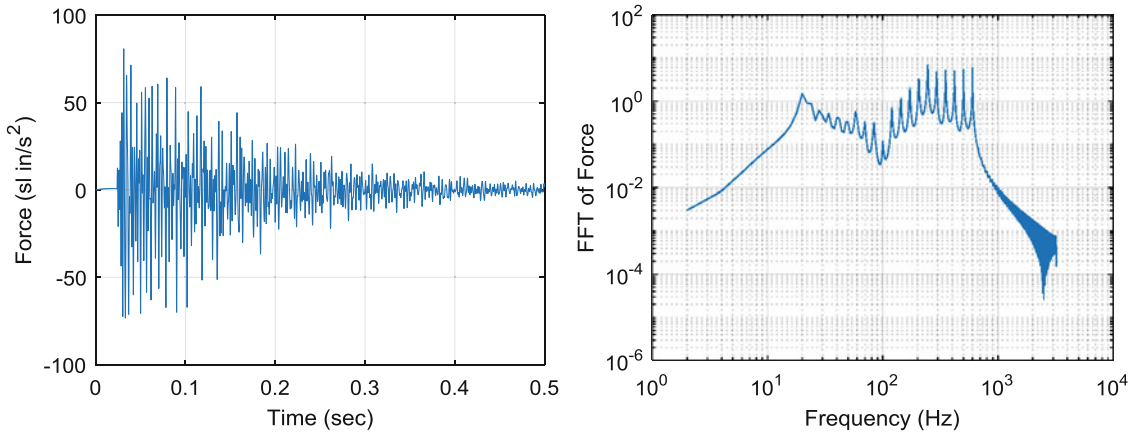


Fig. 24.2 Force input to system configuration

Table 24.1 Natural frequencies of both coupled systems

System AB Freq (Hz)	System AC Freq (Hz)
2.39	2.00
4.73	3.49
246.05	245.91
539.76	–
557.40	–
670.71	670.02
1005.90	–
1298.50	1293.43
1418.17	–

24.3.3 Substructured Model Properties

Both systems were transformed to a substructured space using the transformation developed in Eq. 24.4. To calculate this transformation matrix, one needs the free mode shapes of both the system (System AB or System AC) and the system without Component A. It is necessary to have some prior knowledge about the excitation bandwidth for this transformation to avoid truncation errors. As noted above, the forcing function was designed to excite frequencies up to 600 Hz, so modes up to around 1000 Hz were included in the transformation to ensure that truncation would not be an issue.

The natural frequencies of both systems are shown in Table 24.1. The modes included in the transformation are shown in black, while the higher modes are shown in gray. As seen, each system includes two rigid body modes near 0 Hz and several flexible modes. The modes with significant motion of Component A are highlighted in bold, and the table is arranged to easily compare Component A modes between the two configurations. As seen, System AB includes several modes that are not dominated by Component A motion, while all the modes in System AC are dominated by Component A motion in the bandwidth of interest. This is common for component qualification testing on a rigid fixture. Table 24.1 also suggests that the impedance mismatch between System AB and System AC is not particularly dramatic, as the modes dominated by Component A motion have not shifted significantly in frequency.

The natural frequencies of Component B and Component C are shown in Table 24.2. As seen, Component C only has rigid body modes in the bandwidth of interest, as desired for a fixture using historical methods.

The free-free mode shapes of System AB used in the transformation are shown in Fig. 24.3 and the corresponding free-free mode shapes of Component B are shown in Fig. 24.4. For all mode shape plots, the measurement locations are denoted with X's. Twenty-five measurements across Component B were used to capture six modes from System AB and four modes from Component B. While six system modes were used in the transformation, the frequency of the sixth mode is slightly higher than the 600 Hz input bandwidth. The sixth mode is primarily the second bending mode of Component A, but Fig. 24.3 shows that the second bending mode of Component A is also being excited in Modes 4 and 5. Thus, the forcing function may not excite the second bending mode of Component A directly, but it may be excited by the motion of Component B.

Table 24.2 Natural frequencies of components B and C

Comp. B Freq (Hz)	Comp. C Freq (Hz)
2.43	2.02
4.78	3.52
542.40	2020.59
559.86	5569.83
1010.29	10919.10
1418.12	18049.83

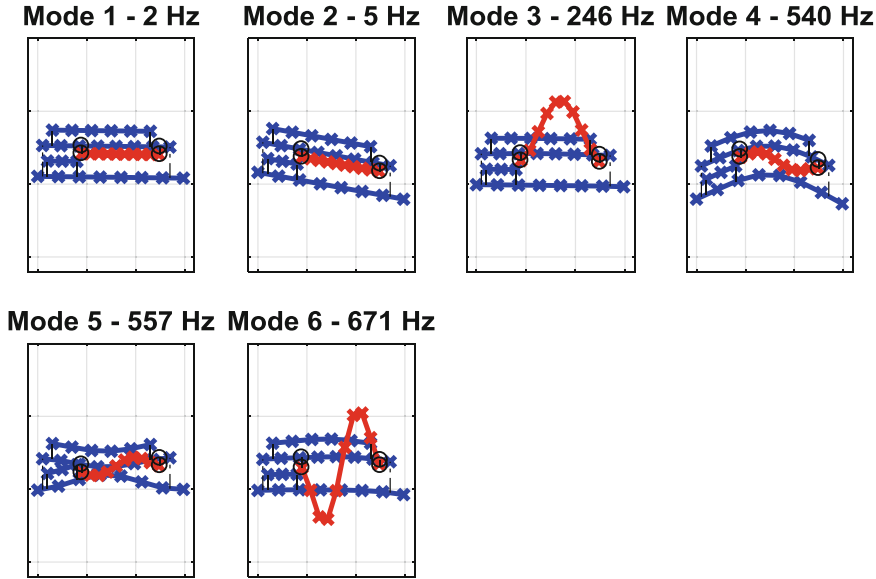


Fig. 24.3 System AB free-free modes

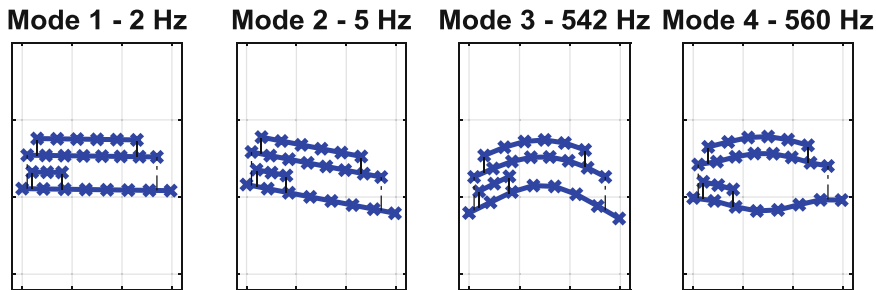


Fig. 24.4 Component B free-free modes

Figure 24.5 shows the original modal matrices for this system along with the transformed, decoupled modal matrices. As expected, the original modal matrices are diagonal while the decoupled matrices reflect the form of Eq. 24.9 and have coupling cross-terms. However, the cross-terms are all notably lower than the diagonal terms, which may suggest that there is little coupling between Component A and Component B.

Similarly, the free-free mode shapes of System AC used in the transformation are shown in Fig. 24.6 and the corresponding free-free mode shapes of Component C are shown in Fig. 24.7. As noted above, Component C only has rigid body modes in the bandwidth of interest. Ten measurements across Component C were used to capture four modes from System AC and two modes from Component C. Again, the frequency of the second bending mode of Component A is slightly higher than the input bandwidth. However, unlike System AB, System AC does not have any additional system modes within the input bandwidth that will excite the second bending mode of Component A.

Figure 24.8 shows the original modal matrices for this system along with the transformed, decoupled modal matrices. As expected, the original modal matrices are diagonal while the decoupled matrices reflect the form of Eq. 24.9 and have

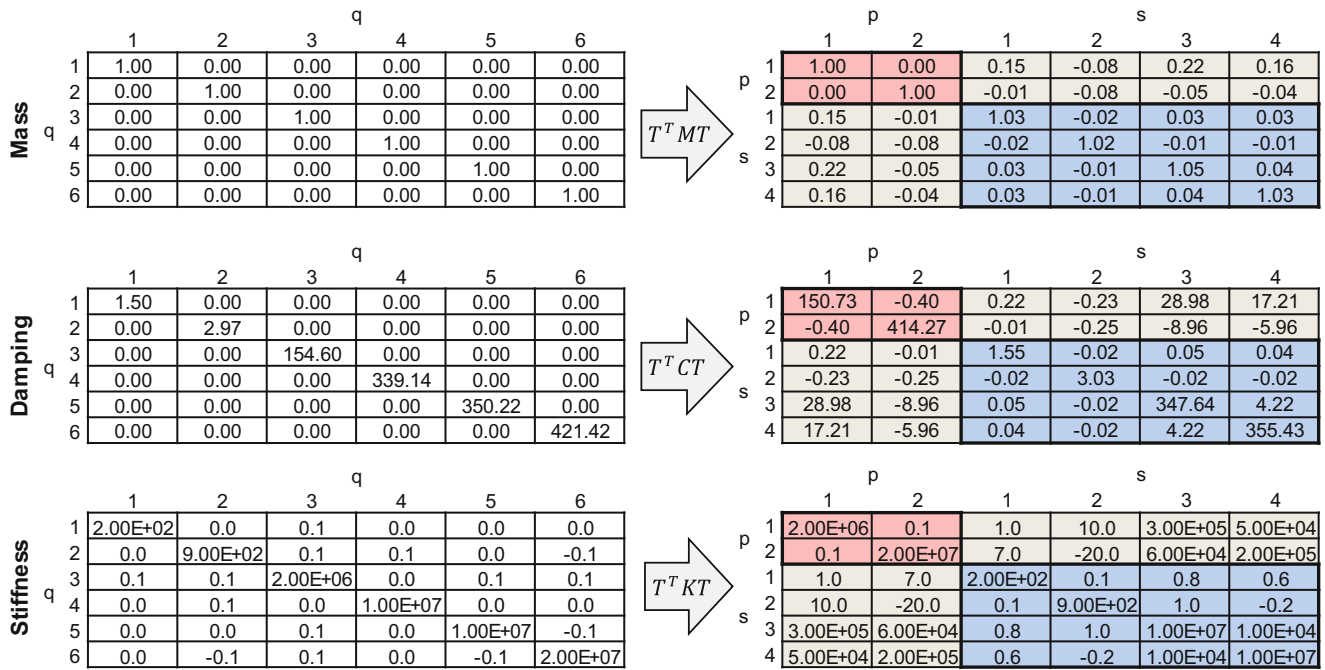


Fig. 24.5 Modal matrices for system AB, original and decoupled

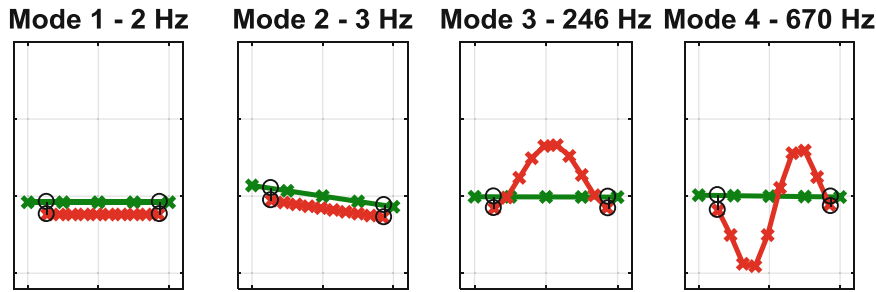
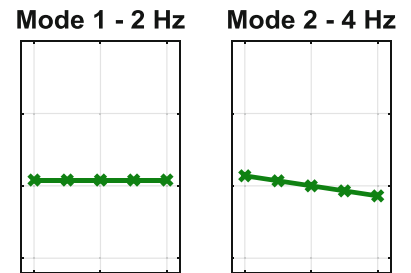


Fig. 24.6 System AC free-free modes

Fig. 24.7 Component C free-free modes



coupling cross-terms. Again, the cross-terms are all notably lower than the diagonal terms, which may suggest that there is little coupling between Component A and Component C.

24.4 Case Studies

The response of Component A in a laboratory test was studied with two different types of fixture inputs. First, a single acceleration measurement near the base of the component in the System AB configuration was used as a base acceleration input to the laboratory configuration, System AC. This process aligns with the typical methodology used for qualification

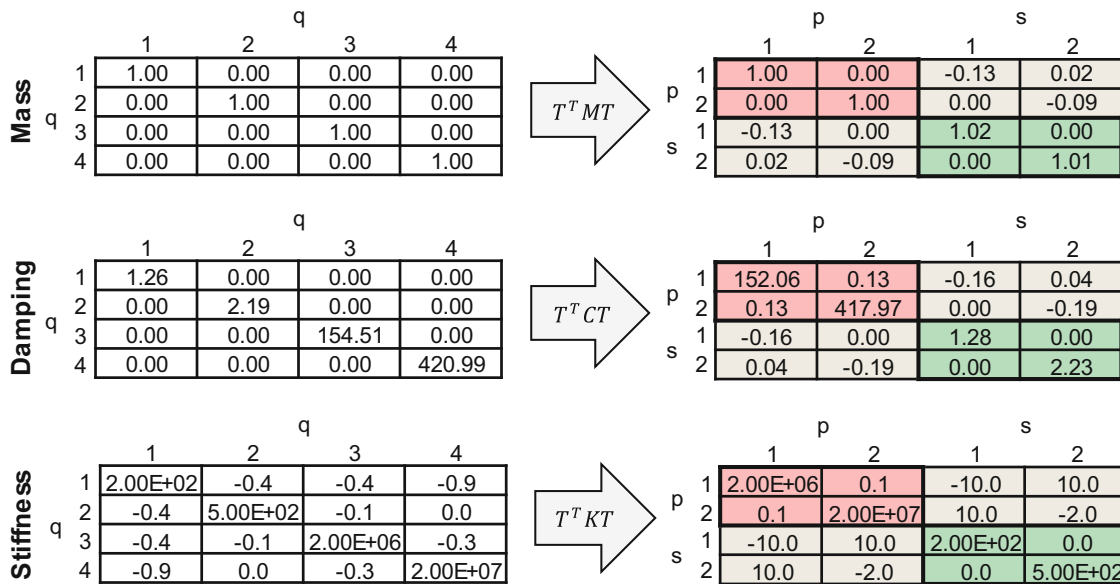


Fig. 24.8 Modal matrices for system AC, original and decoupled

testing today. Second, the inputs for the laboratory configuration, System AC, were derived to match the fixed-base Component A response from System AB. In both cases, the response of Component A in the laboratory test is compared to the response of Component A in the system test.

24.4.1 Evaluation of Traditional Methodology

The traditional methodology for developing laboratory test inputs is shown schematically in Fig. 24.9. Typically, a shock or vibratory force is induced on a system, and very few measurements are made to capture the system response. Accelerometers are primarily arranged on the system to measure the acceleration input to the components. The measured acceleration responses are then used to develop straight-line test specifications for the laboratory tests; this step is shown in gray because it has been omitted in these studies to limit sources of discrepancy. The specification is then input to the laboratory configuration, ideally as a rigid base acceleration input.

This methodology was used with the models described above. The shock was applied to the system and the response near a component attachment was used as the base acceleration input to the fixture. The response at an arbitrary location on the component is compared between configurations in Fig. 24.10. As seen, the response in configuration AC (on the fixture) is notably higher than the response in configuration AB (in the system). While only the displacement at an arbitrary location is shown here, similar results were seen at other locations and for other quantities (i.e. acceleration).

For most component testing, the component test setup is assumed to approximate the system configuration appropriately without any additional analysis. While a comparison like the one in Fig. 24.10 may suggest a conservative component test, as desired by many component designers, there is not a comprehensive understanding of the system dynamics. Using the methodology described above, we can decouple the response to analyze the fixed-base motion of the component of interest. The fixed-base modal response of Component A is compared between configurations in Fig. 24.11 for the two modes that are active. As seen, mode 1 is being over-excited in configuration AC as compared to configuration AB. However, mode 2 is being under-excited in configuration AC as compared to configuration AB. This is because mode 2 of Component A is excited in System AB through the Component B modes, while those dynamics are not present in System AC. Thus the rigid base acceleration of System AC is inappropriate to replicate this environment. Further, the fixture configuration is not necessarily conservative with respect to the system configuration, as hypothesized with the limited information in Fig. 24.10.

This case illustrates the usefulness of substructuring as an evaluation tool in component laboratory testing. Traditional measurements such as displacement or acceleration at a single point will likely not provide the complete picture of the system dynamics, and may even lead the analyst to draw incorrect conclusions about component margin. Using the framework

Traditional Methodology

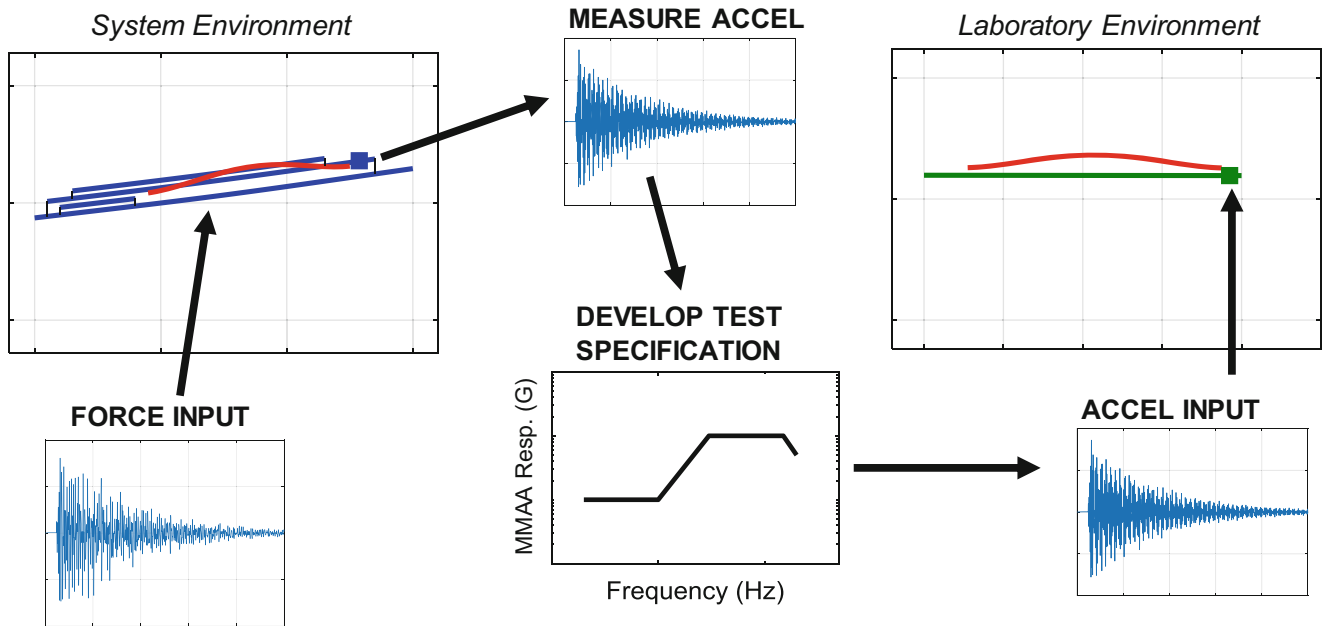


Fig. 24.9 Depiction of traditional test methodology

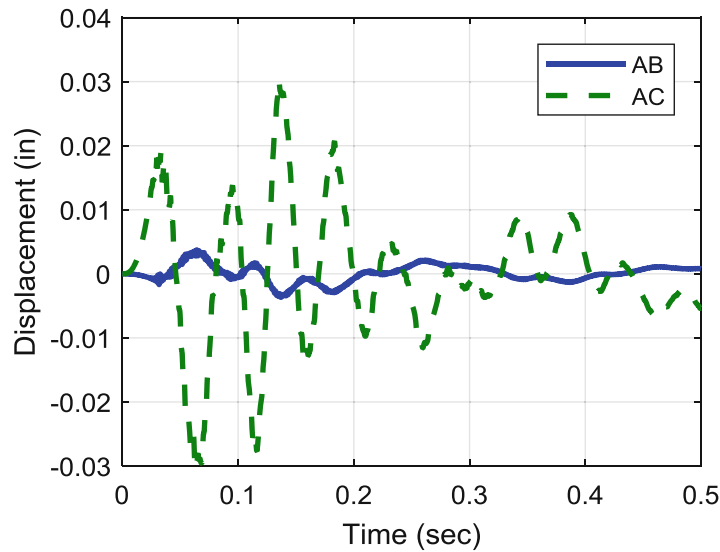


Fig. 24.10 Comparison of Component A physical response between configurations with historical input methodology

provided here, it is possible to assess the margin between the component test configuration and system configuration on a mode-by-mode basis.

24.4.2 Evaluation of Proposed Methodology

If a given test setup proves to be inappropriate for exercising the component dynamics accurately, this substructuring methodology can be used to determine the laboratory test inputs needed to excite the component correctly. The proposed

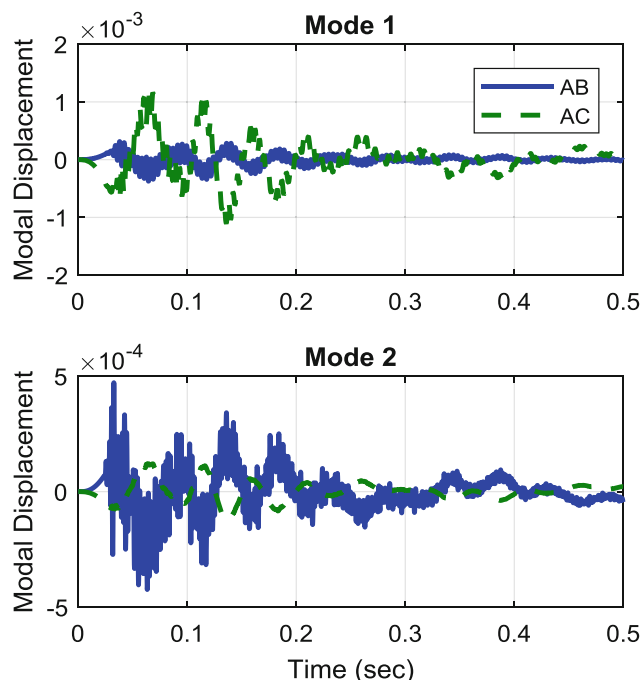


Fig. 24.11 Comparison of Component A fixed-base modal response between configurations with historical input methodology

methodology for developing laboratory test inputs is shown schematically in Fig. 24.12. Initially, more information is needed in the system environment than has been measured historically. Accelerometers are needed to capture all system modes that are excited in the environment. The increased quantity of measurements may be obtained either with advanced data capturing technology or by supplementing experimental data with analytical data.

These system dynamics are then transformed into decoupled responses. The test specification is developed in terms of fixed-base component modal response, although again this step is omitted in this study to limit sources of discrepancy. Then the free motion of the fixture is calculated that will excite the component fixed-base modes accurately. This may only be possible for cases where the impedance of the system doesn't have a critical effect on the component dynamics, or if the fixture and system have similar impedance.

The fixture motion required to excite Component A appropriately was calculated using Eq. 24.10 and applied to the system. The resulting fixed-base response of Component A is compared to the reference solution in Fig. 24.13. As seen, the component modal response to the updated inputs matches the reference solution notably well.

The modal motion of the fixture is shown in Fig. 24.14 for both the traditional and proposed approach. The traditional approach utilized a rigid base acceleration input, so the rotational mode of the fixture was not excited. The proposed approach utilizes both the translation and rotation mode of the fixture simultaneously to appropriately excite the Component A modes shown in Fig. 24.13. However, the inputs calculated using the proposed methodology resulted in notably higher modal displacements than with the traditional methodology. This difference may prove to be significant when defining physical test inputs and needs to be further investigated, as there are likely many solutions that meet the component exposure requirements within reason using the proposed methodology.

The improvement in component response seen here was achieved by improving the test specification derivation method. The substructuring methodology provided a convenient way to derive multi-DOF rigid base inputs to excite the fixed-base component modes accurately. For this case, the fixture impedance was similar enough to the system impedance that the component response could be corrected just by applying the correct multi-DOF rigid base inputs.

24.5 Conclusions

The current techniques used for component qualification testing typically assume that a rigid fixture will provide either accurate or conservative excitation to the component under test. This work showed that dynamic substructuring is an effective tool to assess whether or not this assertion is true. A simple Matlab model was used to investigate the response of a component

Proposed Methodology

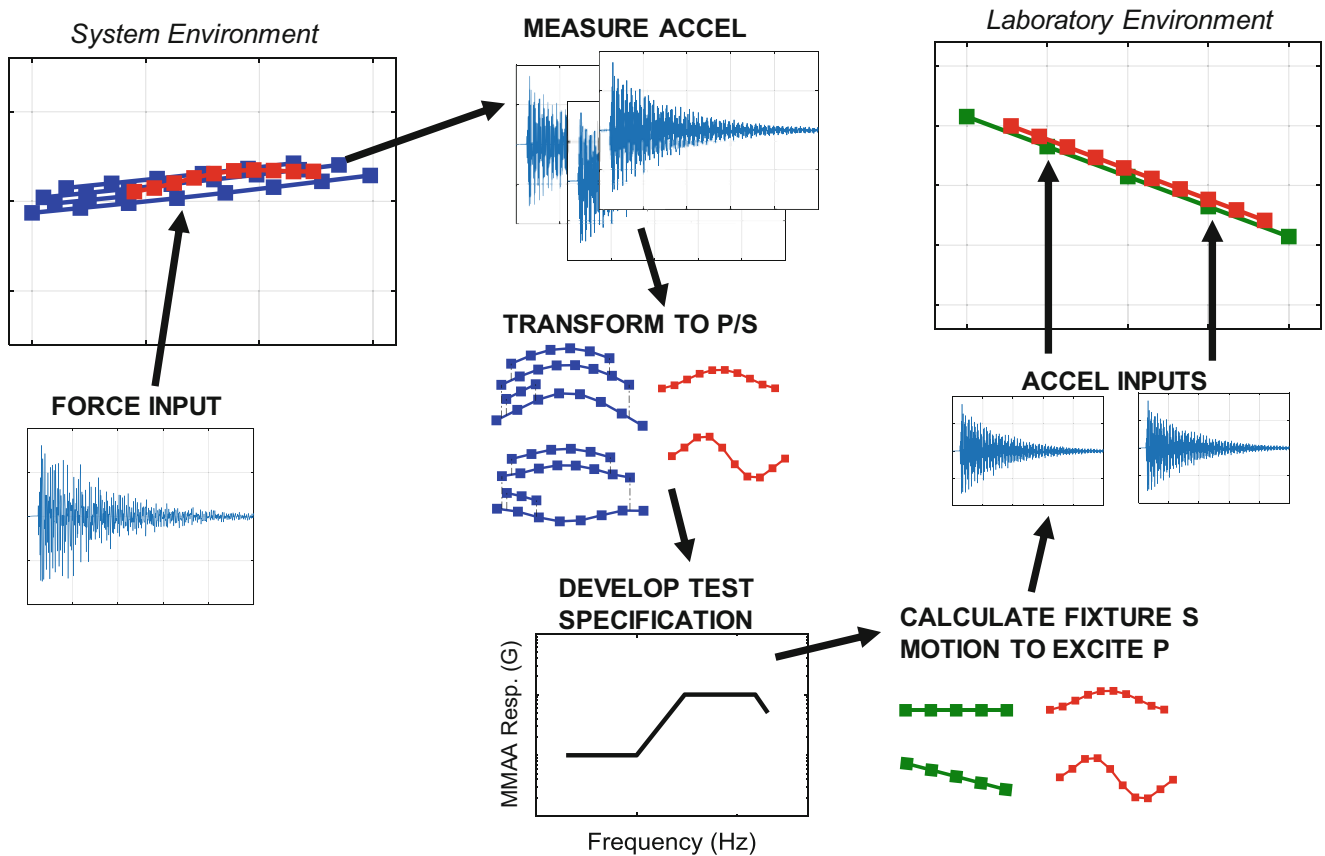


Fig. 24.12 Depiction of proposed test methodology using substructuring to define laboratory inputs

in a shock environment in both a system configuration and fixture configuration. The methodology was first used to evaluate current component testing techniques and identify a region of under-testing that the traditional metrics did not expose. Additionally, the methodology was used to determine fixture inputs that could correct for the differences and excite the component correctly. For this case, substructuring was used to derive multi-axis fixture motion to simulate the component response in the system. In other cases where impedance plays a bigger role in component response, it may also be necessary to use these tools to design fixtures with more realistic impedance. These cases showed very promising results for the future of dynamic substructuring within the environment qualification realm.

24.6 Future Work

The primary focus of future work is to determine the limitations of the proposed methodology and particularly what characteristics cause the transformation to break down. For example, the framework may not be suitable for cases where the component has a significant influence of the dynamics of the next assembly. Also, issues were encountered when trying to employ the proposed methodology to a much higher bandwidth where more complex dynamics were in play. These characteristics should be better understood before trying to implement the proposed technique on more advanced systems.

There are also several avenues to be researched prior to experimental execution of the methodology presented here. In this work, the fixture inputs were left as modal displacements, while they would need to be transformed to physical inputs for experimental implementation. The quantity and placement of accelerometers to control this type of test should be investigated. Ideally, the test inputs developed using this methodology would be defined in a similar way to traditional test inputs, allowing for an effortless revolution. Additionally, the methodology used to develop specifications in terms of fixed-base modal response will need to be considered.

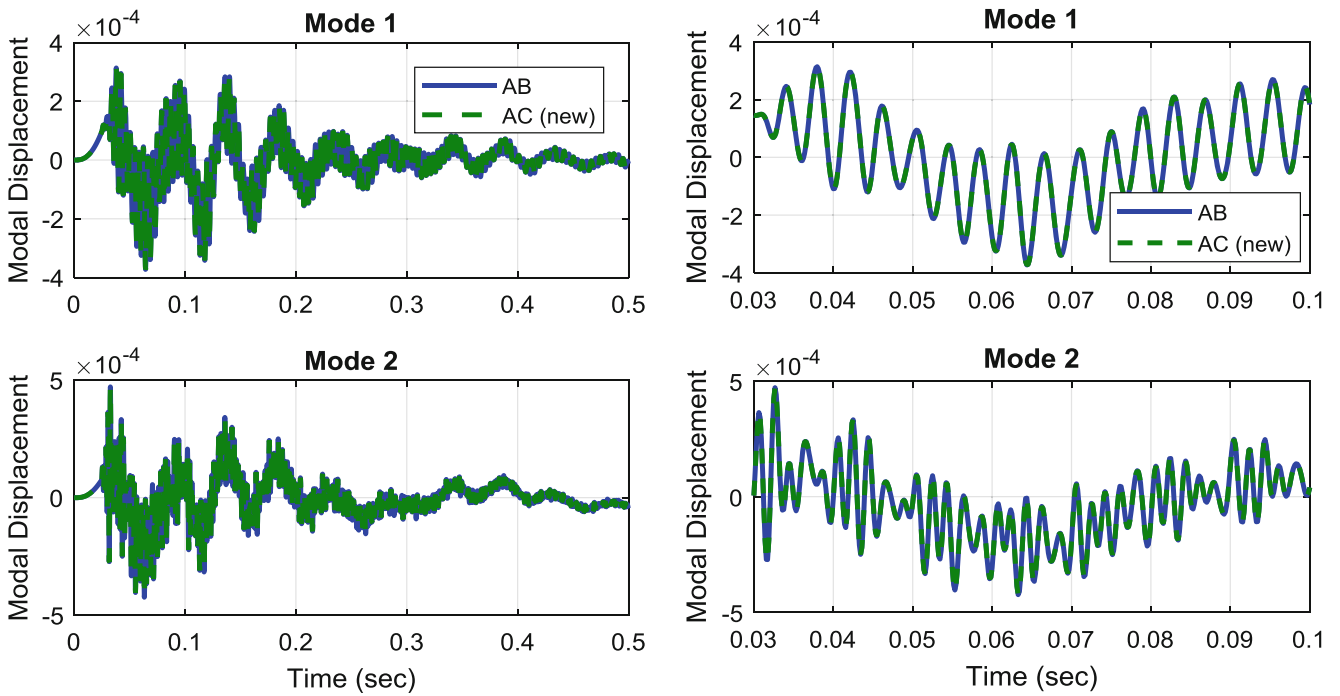


Fig. 24.13 Comparison of Component A fixed-base modal response between configurations with proposed input methodology

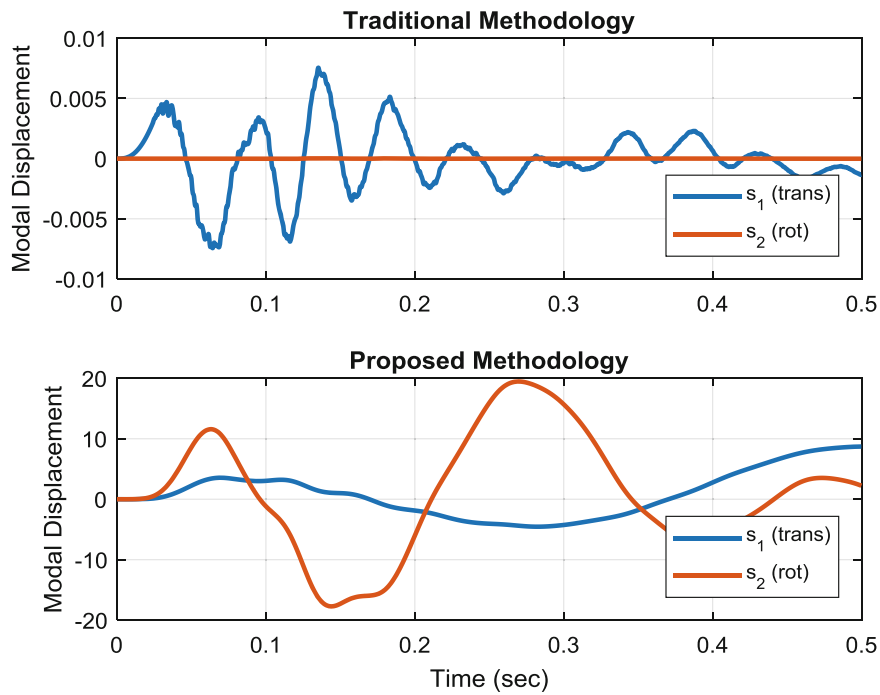


Fig. 24.14 Comparison of modal fixture motion for traditional and proposed methods

References

1. Welch, J.W.: Flight Unit Qualification Guidelines, Aerospace Report No. TOR02010(8591)-20 (2010). <http://aerospace.wpengine.netdna-cdn.com/wp-content/uploads/2015/04/TOR-20108591-20-Flight-Unit-Qualification-Guidelines.pdf>
2. Air Force Space Command.: Test Requirements for Launch, Upper-Stage and Space Vehicles. Space and Missile Systems Center Standard. SMC-S-016 (2014)
3. Department of Defense.: Environmental Engineering Considerations and Laboratory Tests. Test Method Standard, MIL-STD-810G (2008)
4. Jepsen, R., Romero, E., VanGoethem, D.: Flight and re-entry test simulation in combined acceleration and vibration environments: part I. In: Proc. of the 78th Shock and Vibration Symp., Philadelphia, PA (2007)
5. Jepsen, R., Romero, E.: Flight and re-entry test simulation in combined acceleration, vibration, and spin environments: part II. In: Proc. of the 79th Shock and Vibration Symp., Orlando, FL (2008)
6. Mayes, R.L., Rohe, D.P.: Physical vibration simulation of an acoustic environment with six shakers on an industrial structure. In: Proc. of the 34th International Modal Analysis Conference, Orlando, FL (2016)
7. Schultz, R., Walsh, T.: Evaluation of microphone density for finite element source inversion simulation of a laboratory acoustic test. In: Proc. of the 34th International Modal Analysis Conference, Orlando, FL (2016)
8. Gregory, D.L., Bitsie, F., Smallwood, D.O.: Comparison of the response of a simple structure to single axis and multiple axis random vibration inputs. In: Proc. of the 80th Shock and Vibration Symp., San Diego, CA (2009)
9. Smallwood, D.O., Gregory, D.L.: Evaluation of a 6-DOF electrodynamic shaker system. In: Proc. of the 79th Shock and Vibration Symp., Orlando, FL (2008)
10. Owens, B.C., Tipton, D.G., McDowell, M.: 6 Degree of freedom shock and vibration: testing and analysis. In: Proc. of the 86th Shock and Vibration Symposium, Orlando, FL (2015)
11. Scharton, T.D.: Impedance simulation vibration test fixtures for spacecraft tests. Shock Vib. Bull. **40**(3), 230–256 (1969)
12. Scharton, T.D.: Force limited vibration testing monograph. Jet Propulsion Laboratory, Pasadena (1997)
13. Sweitzer, K.A.: A mechanical impedance correction technique for vibration tests. Sound Vib. Mag. 30–34 (1988)
14. Daborn, P.M.: Smarter dynamic testing of critical structures. PhD Thesis, University of Bristol (2014)
15. Soine, D.E., Jones, R.J., Harvie, J.M., Skousen, T.J., Schoenherr, T.F.: Designing hardware for the boundary condition round robin challenge problem. In Proc. 36th International Modal Analysis Conference, Orlando, FL (2018)
16. Harvie, J.: Quantification of dynamic differences between boundary condition environment specification improvement. In: Proc. of the 34th International Modal Analysis Conference, Orlando, FL (2016)
17. de Klerk, D., Rixen, D.J., Voormeeren, S.N.: General framework for dynamic substructuring: history, review, and classification of techniques. AIAA J. **46**(5), 1169 (2008)
18. Reyes, J.M.: A study on the dynamic interaction of shock response fixtures and test payload. In: Proc. 34th International Modal Analysis Conference, Orlando, FL (2016)
19. Mayes, R.L.: A modal Craig-Bampton substructure for experiments, analysis, control and specifications. In: Proc. of the 33rd International Modal Analysis Conference, Orlando, FL (2015)
20. Allen, M.S., Kammer, D.C., Mayes, R.L.: Experimental based substructuring using a Craig-Bampton transmission simulator model. In: Proc. of the 32nd International Modal Analysis Conference, Orlando, FL (2014)
21. Allen, M.S., Gindlin, H.M., Mayes, R.L.: Experimental modal substructuring to estimate fixed-base modes from tests on a flexible fixture. J. Sound Vib. **330**(18–19), 4413–4428 (2011)
22. Allen, M.S., Mayes, R.L., Bergman, E.J.: Experimental modal substructuring to couple and uncouple substructures with flexible fixtures and multi-point connections. J. Sound Vib. **329**(23), 4891–4906 (2010)
23. Smallwood, D.O., Nord, A.R.: Matching shock spectra with sums of decaying sinusoids compensated for shaker velocity and displacement limitations. Shock Vib Bull. **44**(Part 3), 43–56 (1974)

Chapter 25

Off-Axis Input Characterization of Random Vibration Laboratory Data for Model Credibility

Jill Blecke, James Freymiller, and Michael Ross

Abstract The goal of this work is to build model credibility of a structural dynamics model by comparing simulated responses to measured responses in random vibration environments, with limited knowledge of the true test input. Oftentimes off-axis excitations can be introduced during single axis vibration testing in the laboratory due to shaker or test fixture dynamics and interface variation. Model credibility cannot be improved by comparing predicted responses to measured responses with unknown excitation profiles. In the absence of sufficient time domain response measurements, the true multi-degree-of-freedom input cannot be exactly characterized for a fair comparison between the model and experiment. Methods exist, however, to estimate multi-degree-of-freedom (MDOF) inputs required to replicate field test data in the laboratory Ross et al.: 6-DOF Shaker Test Input Derivation from Field Test. In: Proceedings of the 35th IMAC, A Conference and Exposition on Structural Dynamics, Bethel (2017). This work focuses on utilizing one of these methods to approximately characterize the off-axis excitation present during laboratory random vibration testing. The method selects a sub-set of the experimental output spectral density matrix, in combination with the system transmissibility matrix, to estimate the input spectral density matrix required to drive the selected measurement responses. Using the estimated multi-degree-of-freedom input generated from this method, the error between simulated predictions and measured responses was significantly reduced across the frequency range of interest, compared to the error computed between experimental data to simulated responses generated assuming single axis excitation.

Nomenclature

6DOF	6 degree-of-freedom
ASD	auto spectral density
dB	decibel
DOF	degree-of-freedom
FRF	frequency response function
$G_{yy}(\omega)$	output spectral density matrix
$H_{xy}(\omega)$	transmissibility matrix
λ	Tikhonov regularization parameter
MDOF	multi-degree-of-freedom
PSD	power spectral density
$S_{xx}(\omega)$	input spectral density matrix

25.1 Introduction

This work aims to build model credibility for a structural dynamics model of a mechanical component assembly. The model is intended to be used to aid in design decisions, provide confidence in understanding mechanical failure modes during development testing, and provide confidence in mechanical design changes that hardware will perform in specified, or

J. Blecke (✉) · M. Ross
Sandia National Laboratories, Albuquerque, NM, USA
e-mail: jblecke@sandia.gov

J. Freymiller
ATA Engineering, San Diego, CA, USA

changing, random vibration environments. In order for the computational structural dynamics model to serve in this capacity, the model must be shown to be capable of adequately predicting measured responses of the mechanical component assembly during random vibration environments. Oftentimes off-axis excitations can be introduced during single axis vibration testing in the laboratory due to shaker or test fixture dynamics and interface variation. Model credibility cannot be improved by comparing predicted responses to measured responses with differing excitation profiles. Ideally, the MDOF excitation frequency profile at the shaker reference accelerometer is one option for improved characterization of the acceleration applied to the base of the mechanical component assembly test fixture. Alternatively, time domain measurements can be recorded at various non-compliant locations such that solving the inverse problem provides the MDOF input required to drive the measured responses [1]. In the absence of this data and the inability to repeat testing due to financial or schedule constraints, the true MDOF input cannot be exactly characterized for a fair comparison between the model and experiment.

Methods exist, however, to estimate the MDOF inputs required to replicate field test data in the laboratory [2]. The work in this paper focuses on utilizing one of these methods to approximately characterize the off-axis excitation present during laboratory random vibration testing. The method selects a sub-set of the experimental output spectral density matrix degrees of freedom (DOFs), in combination with the experimentally- or model-derived system transmissibility matrix, to estimate the input spectral density matrix required to drive the selected measurement responses. Using the estimated MDOF input generated from this method, the error between simulated predictions and measured responses of the mechanical component assembly was significantly reduced across the frequency range of interest, compared to the error computed between experimental data to simulated responses generated assuming single axis excitation.

The remainder of this paper will first describe the test geometry, random vibration laboratory testing and computational model details. Next, the methodology used to estimate the MDOF test excitation will be discussed. Finally, results comparing the computational model predictions and experimental measurements will be provided.

25.2 Background

The mechanical component assembly consists of a cylindrical stainless-steel housing containing individual components assembled into the housing and then potted in a polyurethane foam. The mechanical component assembly is tested within a test fixture where the assembly rests on a test fixture plate and is “sandwiched” with a cellular silicone pad between the test fixture plate and the test fixture cover. A schematic representing the component assembly is illustrated in Fig. 25.1.

The nominal baseline random vibration test environment, for both longitudinal and transverse directions, is prescribed by the auto spectral density functions (ASDs) provided in Fig. 25.2. The test unit depicted in Fig. 25.1 is instrumented with six tri-axial accelerometers. This particular laboratory test recorded the power spectral density (PSD) response at the six sensor locations, relative to a uniaxial reference accelerometer located on the shaker base. The PSD response at each sensor location is to be compared to the response predicted by the computational structural dynamics model of the system.

The meshed computational model consists of 8-noded hexahedral elements and is solved in Sierra/SD [3] utilizing an *eigenvalue* solution case and a *modal random vibration* solution case [4]. Based on previous mesh studies of this mechanical

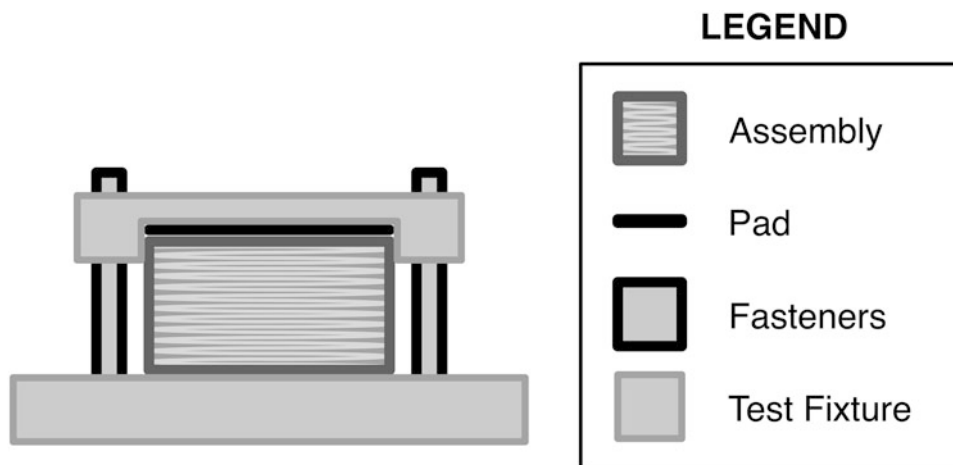


Fig. 25.1 Schematic of mechanical component assembly hardware as tested

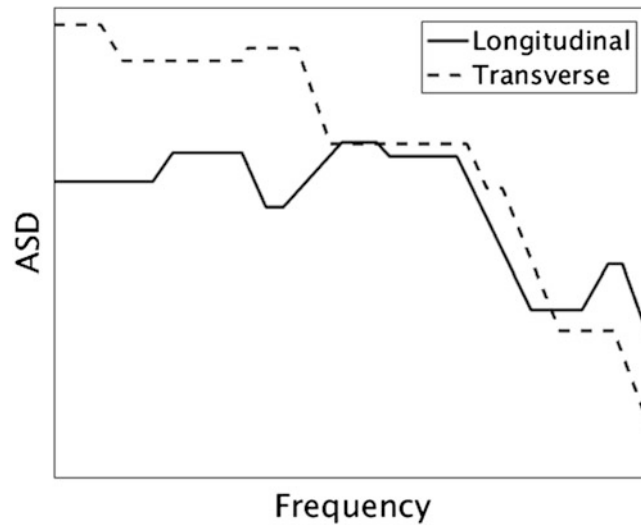


Fig. 25.2 Random vibration test environment input specification

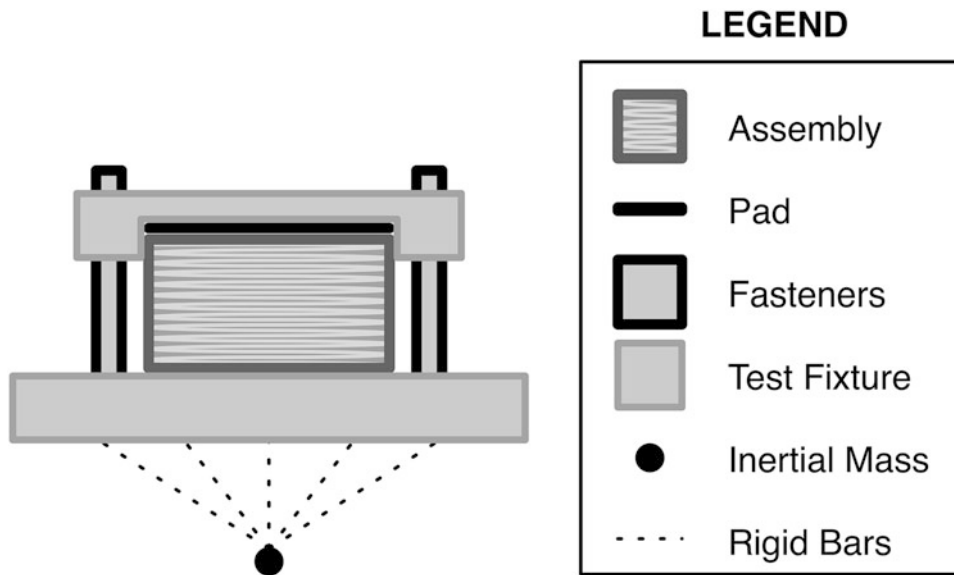


Fig. 25.3 Schematic of mechanical component hardware as simulated

component assembly, the mesh was determined to be satisfactory given the quantities of interest. The computational model assumes linear elastic materials with a 2% modal damping applied across all modes. The model is computationally excited through an applied force at an inertial mass, set to be at least 100 times larger than the mass of the modeled assembly. The inertial mass is connected to the modeled assembly via rigid bar elements and constrained in non-input DOFs. Figure 25.3 illustrates the as modeled component assembly geometry.

Initial comparisons between the in-axis responses predicted by the computational model, assuming a pure single DOF input, and the measured responses from the experiment resulted in significant error. As shown in Fig. 25.4, the measured responses contained significantly more dynamics relative to the model, resulting in significant errors (greater than 20 decibel (dB)), especially at higher frequencies. Upon further inspection of data recorded at the control accelerometer, the experimental data contained significant off-axis excitation (see Fig. 25.5), not captured in the simulation. Some off-axis response of the control accelerometer is expected in the test data as the control accelerometer is located on the top of the part, however, since off-axis data of the excitation profile at the reference accelerometer located at the base of the test fixture was not available, the magnitude of the measured off-axis response at the control accelerometer (multiple orders of magnitude greater than the in-axis test specification) was deemed significant enough to warrant further investigation. Ordinarily, time domain measurements recorded at various non-compliant locations near the base of the structure can be used to solve the

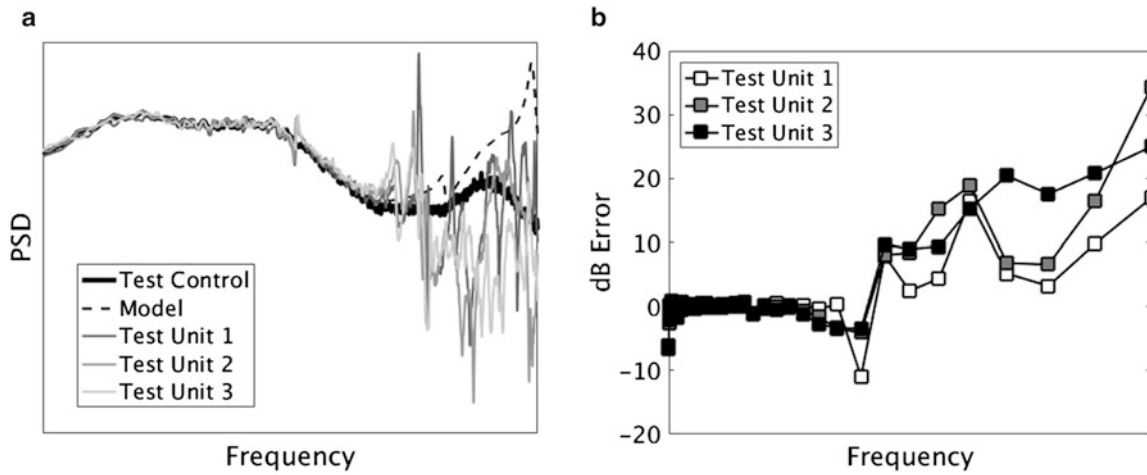


Fig. 25.4 Initial model-to-experiment comparison, assuming single-axis excitation, for (a) direct PSDs and (b) dB error relative to each of the three nominally identical test units

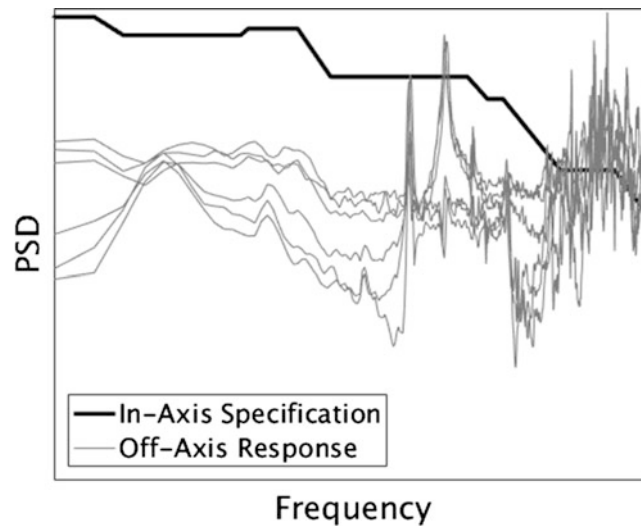


Fig. 25.5 Off-axis excitation as measured by the control accelerometer for a transverse excitation

inverse problem characterizing the 6DOF input required to drive the measured responses [1]. In the absence of the time domain measurements for this data set, yet a need for model credibility evidence, an alternative approach was developed.

25.3 Theory

The aim of this work is to utilize methodologies developed to generate 6DOF laboratory test specifications from measured field data. The approach, outlined in Sect. 3.4 of [2], is a modified version of the methodology presented in [5]. This approach involves first computing the transmissibility matrix, $H_{xy}(\omega)$, combined with a sub-set of the output-spectral density matrix, $G_{yy}(\omega)$, to estimate the input spectral density matrix, $S_{xx}(\omega)$, required to drive the selected measured responses. The process of identifying the input spectral density matrix, $S_{xx}(\omega)$, [2], involves solving Eq. (25.1),

$$H_{xy}^{T*}(\omega) S_{xx}(\omega) H_{xy}(\omega) = G_{yy}(\omega) \tag{25.1}$$

where $H_{xy}(\omega)$ is the transmissibility matrix ($[]^{T*}$ denotes the complex conjugate transpose), and $G_{yy}(\omega)$ denotes the output spectral density matrix. The reason this particular method was chosen is that this approach does not require knowledge of the off-diagonal terms of $G_{yy}(\omega)$ (not measured during the experiment due to uni-axial reference accelerometer), but maintains phase and coherence that is compatible with $H_{xy}(\omega)$ and, through an iterative process, $S_{xx}(\omega)$. For this work, the transmissibility matrix, $H_{xy}(\omega)$, is derived from the computational structural dynamics model of the mechanical component assembly using a *modal FRF* solution case in Sierra/SD. Ideally, this matrix would be experimentally-derived, however the test measured only the in-axis response at the reference accelerometer and thus, the model was utilized in lieu of this test data. Previous work calibrated the mode shapes and frequencies predicted by the computational model to experimental modal measurements within a limited frequency band. The model was calibrated to within approximately 5% of the measured data for both the mechanical component assembly in a free-free configuration as well as a fixed-base configuration within the test fixture. The diagonal terms of the output spectral density matrix, $G_{yy}(\omega)$, is measured directly from the experiment, leaving the only unknown variable in Eq. (25.1) to be the input spectral density matrix, $S_{xx}(\omega)$.

The input spectral density matrix, $S_{xx}(\omega)$, is solved for using a two-step Tikhonov regularization process [6]. Tikhonov regularization is commonly applied to ill-posed systems. Ultimately, the input spectral density matrix can be computed by Eq. (25.2), where λ represents the Tikhonov regularization factor and $D(\omega)$ is defined by Eq. (25.3). Further details on iteratively determining the off-diagonal terms of $G_{yy}(\omega)$ with compatible phase and coherence is provided in [2].

$$S_{xx}^{T*}(\omega) = [H_{xy}(\omega) H_{xy}^{T*}(\omega) - \lambda^2 I]^{-1} D^{T*}(\omega) \quad (25.2)$$

$$D(\omega) = [H_{xy}^*(\omega) H_{xy}^{T*}(\omega) - \lambda^2 I]^{-1} H_{xy}^*(\omega) G_{yy}(\omega) \quad (25.3)$$

There are two obvious shortcomings of using this approach. First, it is mathematically possible to generate a physically unrealizable excitation function. To mitigate this possibility, all estimations of the input spectral density matrix were screened for positive definiteness in order to be considered. The second, and more significant, shortcoming of this method is that model form error present in the simulation can be smeared out by deriving an input. For example, a mode of the system measured during testing may have less damping than the 2% modal damping assumed by the model. Using the measured response to estimate an excitation function could result in an input exceeding the physically real input in order to drive the model to the magnitude of the measured response.

Only a sub-set of the experimental DOFs are used to estimate the input spectral density matrix. In this work, sets of 3–5 sensors were used to estimate the input, resulting in 41 different realizations of the input spectral density matrix. An illustration of all 41 input spectral density matrix realizations, for the transverse environment, is displayed in Fig. 25.6. It should be noted that some of the estimated off-axis inputs exceed the test specification in the off-axis direction. This indicates frequency bands where off-axis modes are excited in the laboratory test but lack excitation in the model assuming pure 1DOF input. It should also be noted that some of the estimated in-axis inputs exceed the test specification in the in-axis direction as well. This indicates that there is potential for model form error that the estimated input is trying to compensate for, requiring additional investigation.

Next, the error between the predicted and measured response, at the remaining DOFs is computed, such that the estimated MDOF input resulting in the lowest maximum error relative to measured responses, across all remaining DOFs, is chosen as the “best” characterization of the input spectral density matrix. Figure 25.7 compares the measured and predicted responses of the mechanical component assembly at one DOF used to estimate the input spectral density matrix as well as one DOF not used in the estimation process. The estimated input clearly imparts additional dynamics into the simulation and the predicted responses are within family of the measured data.

25.4 Results

In order to more easily compare the measured and predicted responses, all DOFs were averaged in one-sixth octave frequency bands and the decibel error computed between each measured and predicted DOF, for each experimental test unit. The plot in Fig. 25.8 displays the average dB error, for all longitudinal DOFs, as a function of frequency. For this case, the simulated responses are, on average, within ± 3 dB of responses measured during laboratory testing, across the frequency range of interest. The viewgraph in Fig. 25.9 displays a similar plot for one of the transverse directions. For this case, the simulated responses are, on average, within ± 3 dB of the responses measured during laboratory testing, across much of the frequency range of interest except for a small frequency band.

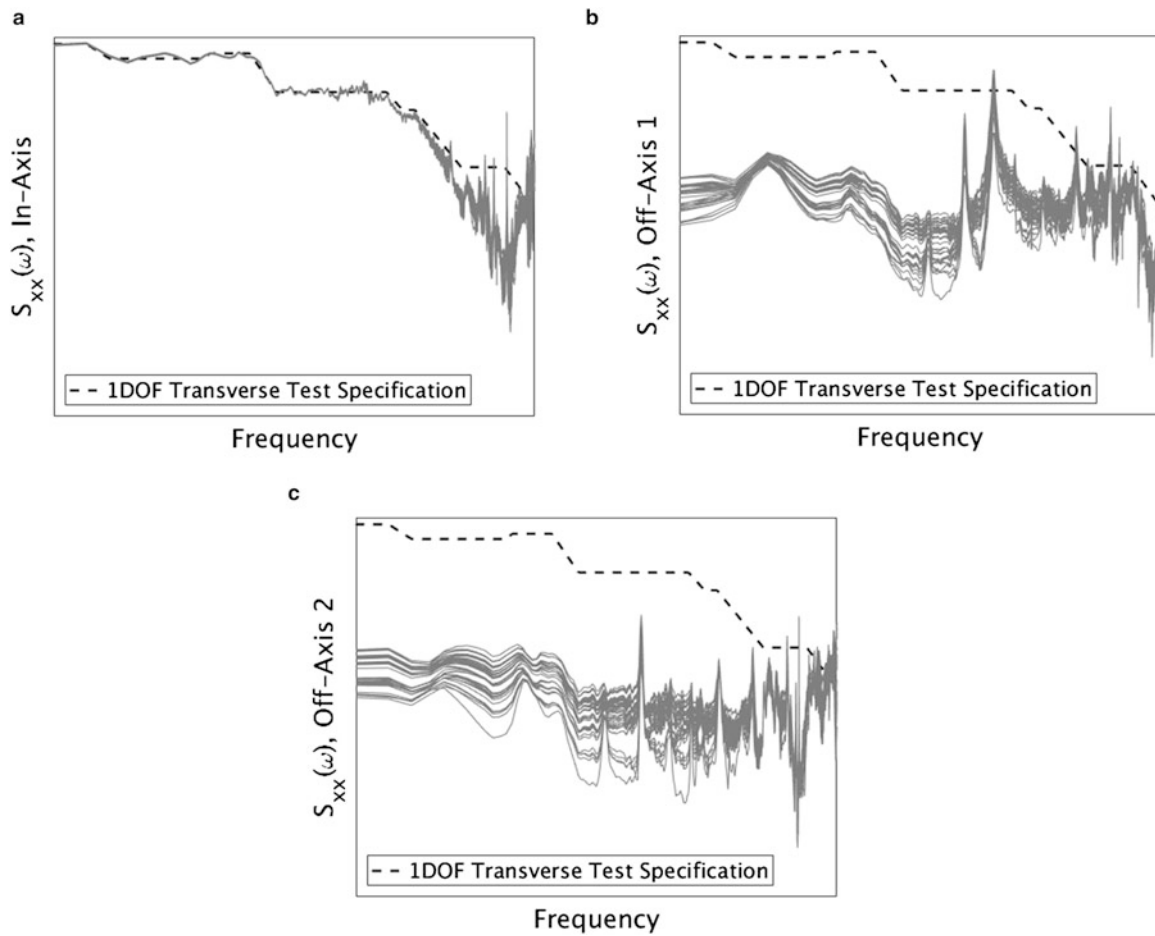


Fig. 25.6 Transverse input spectral density matrix, $S_{xx}(\omega)$, realizations for the (a) in-axis and (b, c) off-axis directions, where the dashed line represents the in-axis test specification

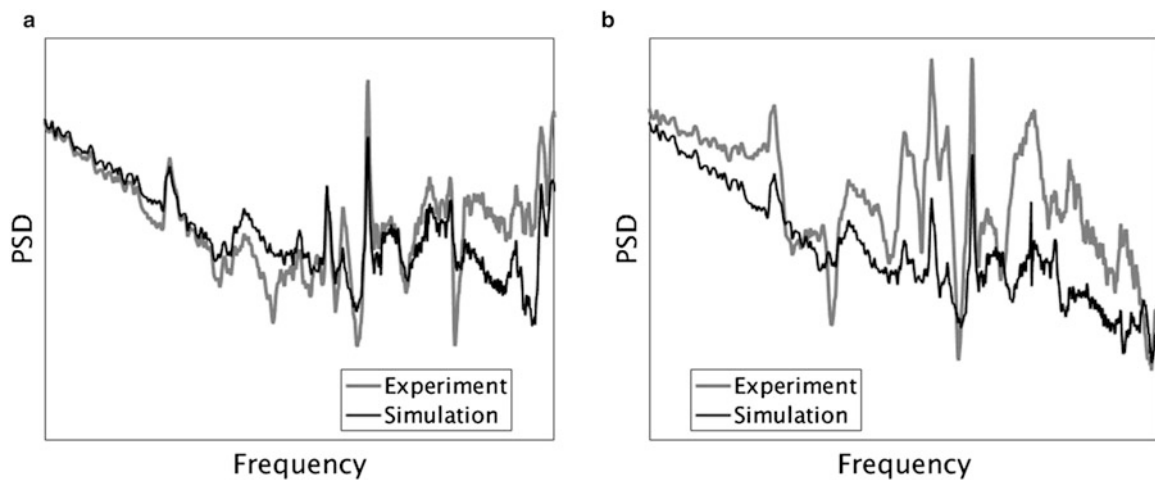


Fig. 25.7 Comparison of measured and predicted responses for (a) one DOF used to estimate the input spectral density matrix and (b) one DOF not used to estimate the input spectral density matrix

The frequency band where the model performs poorly for transverse environments is closely aligned with frequencies predicting various shear modes of the test fixture containing the mechanical component assembly. It is believed that these modes would be sensitive to the lateral stiffness of the test fixture bolts and the material stiffness of the cellular silicone

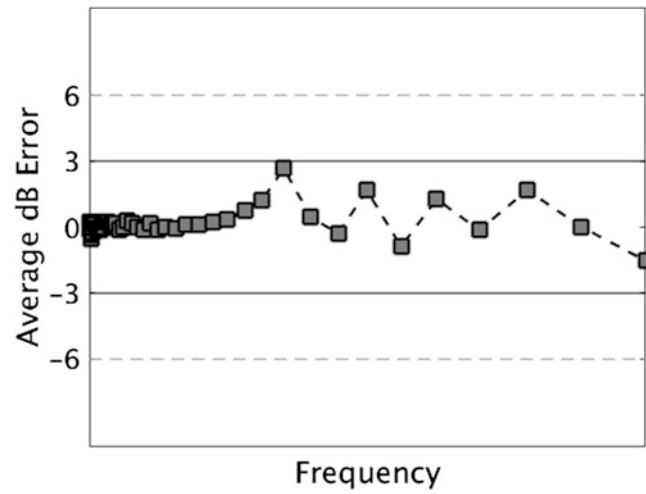


Fig. 25.8 Average dB error for all longitudinal degrees-of-freedom across the frequency range of interest

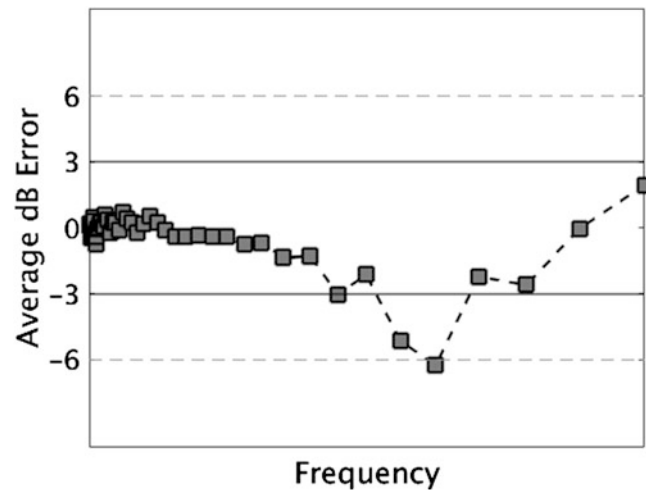


Fig. 25.9 Average dB error for all transverse degrees-of-freedom across the frequency range of interest

pad compressed between the unit and the test fixture. It is theorized that the current model is predicting the shear modes at different frequencies than recorded from the test hardware. Therefore, there is no derived input to match the measured responses adequately at this frequency. Current efforts to improve the prediction of this mode include altering the material and geometric properties of the cellular silicone pad and test fixture fasteners to more closely represent the experimental test set-up.

25.5 Summary

The goal of this work was to build model credibility of a structural dynamics model of a mechanical component assembly, despite limited knowledge of the true test input due to significant off-axis excitation, by comparing simulated responses to measured responses in random vibration environments. In the absence of sufficient time domain response measurements, the MDOF excitation profile was estimated utilizing methods developed for the generation of MDOF environment specifications in the laboratory from measured field test data. The method selected a sub-set of the experimental output spectral density matrix, in combination with the system transmissibility matrix, to estimate the input spectral density matrix required to drive the selected measurement responses. Using the estimated multi-degree-of-freedom input generated from this method, the error between simulated predictions and measured responses was significantly reduced across the frequency range of

interest, compared to the error computed between experimental data to simulated responses generated assuming single axis excitation. The simulated responses were, on average, within ± 3 dB of responses measured during laboratory testing, across the frequency range of interest for longitudinal DOFs. The simulated responses were, on average, within ± 3 dB of the responses measured during laboratory testing, across much of the frequency range of interest for transverse DOFs, except for a small frequency band where average error was extended to 6 dB. Efforts are ongoing to address deficiencies within the computational model for this frequency band as well as additional testing, including additional measurements to characterize the MDOF excitation, as scheduling permits.

Acknowledgements Sandia National Laboratories is a multimission laboratory managed and operated by National Technology and Engineering Solutions of Sandia LLC, a wholly owned subsidiary of Honeywell International Inc. for the U.S. Department of Energy's National Nuclear Security Administration under contract DE-NA0003525. SAND2017-11275 C.

References

1. Owens, B.C., Tipton, D.G., McDowell, M.D.: 6 degree of freedom shock and vibration: testing and analysis. In: Proceedings of the 86th Shock and Vibration Exchange, Orlando (2015)
2. Ross, M., Jacobs, L.D., Tipton, D. G., Nelson, G., Cross, K., Hunter, N., Harvie, J.: 6-DOF Shaker test input derivation from field test. In: Proceedings of the 35th IMAC, A Conference and Exposition on Structural Dynamics, Bethel (2017)
3. Sierra Structural Dynamics Development Team: Sierra Structural Dynamics – User's Notes, Sandia National Laboratories, Albuquerque, April (2015)
4. Sierra Structural Dynamics Development Team: Sierra/SD – Theory Manual SAND 2011–8272. Sandia National Laboratories, Albuquerque, April (2015)
5. Cap, J., Tipton, D. G., Smallwood, D.O.: The derivation of random vibration specifications from field test data for use with a six degree-of-freedom shaker test. In 80th Shock and Vibration Symposium. San Diego, Oct (2009)
6. Hansen, P.C.: Discrete Inverse Problems: Insight and Algorithms. Society for Industrial and Applied Mathematics, Philadelphia (2010)

Chapter 26

Modal Analysis of a Brake-Reuss Beam and Computational Modeling at the Undergraduate Level

Aaron J. Misla, Curtis J. O'Malley, and Siavash Norouzi

Abstract This paper outlines ongoing efforts to develop labs for undergraduate students at New Mexico Tech (NMT) from research projects sponsored by Sandia National Laboratories (SNL) [1, 2] to quantify the low frequency, high displacement damping characteristics of a Brake-Reuss beam.

26.1 Introduction

This paper outlines ongoing efforts to develop labs for undergraduate students at New Mexico Tech (NMT) from research projects sponsored by Sandia National Laboratories (SNL) [1, 2] to quantify the low frequency, high displacement damping characteristics of a Brake-Reuss beam.

The Brake-Reuss beam was chosen as the test article both to establish a connection with ongoing research and because it can be used to demonstrate the energy dissipation of bolted connections. The Brake-Reuss beam consists of a $1'' \times 1'' \times 28.38''$ stainless steel beam with a bolted lap splice at its center (Fig. 26.1). The labs include two types of experiments: one to conduct modal testing and one to establish hysteresis curves. The labs are part of two separate courses at NMT; the senior finite element analysis (FEA) class will conduct a modal test of a beam with a bolted connection to determine the beam's first two natural frequencies and mode shapes, while the sophomore mechanics of materials students will study the hysteresis curves of the same beam.

The senior FEA lab students build computer models, conduct modal experiments, and then compare the models to the experimental results. The key learning objectives for the lab are: learning to compare computational models and experiments, learning how to use experimental results to calibrate computational models, and understanding the impact of minor deviations in experimental techniques.

The sophomore mechanics of material students perform a quasi-static cyclic load test of a Brake-Reuss beam and process the results into hysteresis curves. The key learning objectives for the lab are: processing the hysteresis curve and computing the energy absorbed in the bolted connection.

26.2 Modal Analysis

The students use COMSOL to model a Brake-Reuss beam with free-free boundary conditions and conduct a computational modal analysis of the simulated structure to find its first two natural frequencies and associated mode shapes. The students next determine the first two natural frequencies and mode shapes using experimental data they collect from a physical modal analysis experiment. The students simulate the free-free boundary condition by suspending the Brake-Reuss beam from bungee cords. The beam is instrumented with eight single axis accelerometers equally spaced along the length. The students excite the beam with an impact hammer. They then are instructed on how to process the data into natural frequencies and mode shapes. Finally, they compare the results from the computational and experimental analyses and make recommendations.

The students are directed to determine critical parameters for use in processing the data. These parameters include: frequency bandwidth, time of impact, and identifying the natural frequency [1]. Figures 26.2 and 26.3 show the imaginary FRFs and the mode shape corresponding to the first natural frequency.

A. J. Misla (✉) · C. J. O'Malley · S. Norouzi
New Mexico Institute of Mining and Technology, Socorro, NM, USA
e-mail: aaron.misla@student.nmt.edu

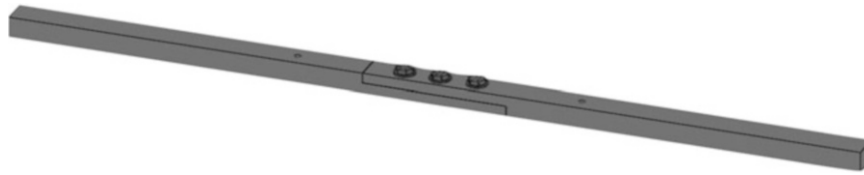


Fig. 26.1 Break-Reuss beam [2]

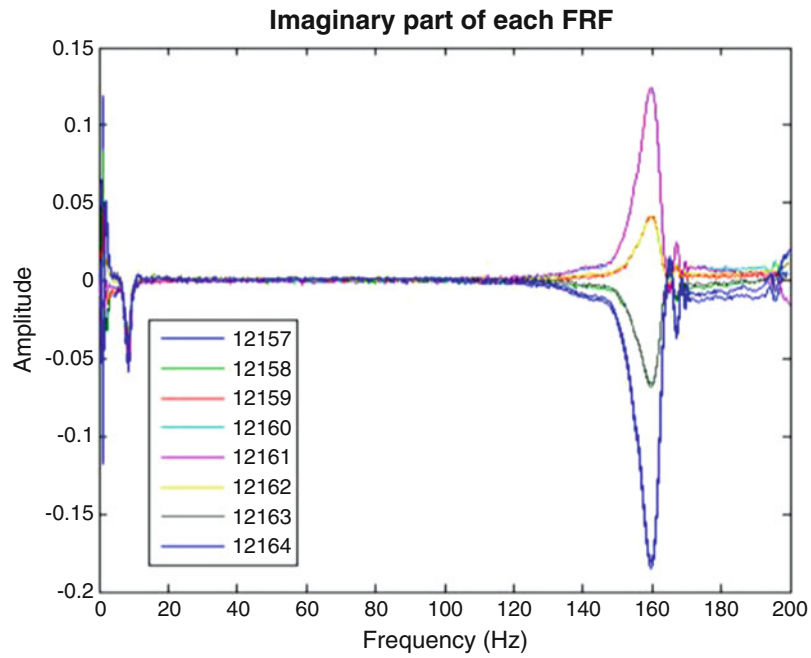


Fig. 26.2 Imaginary FRF of at first natural frequency [2]

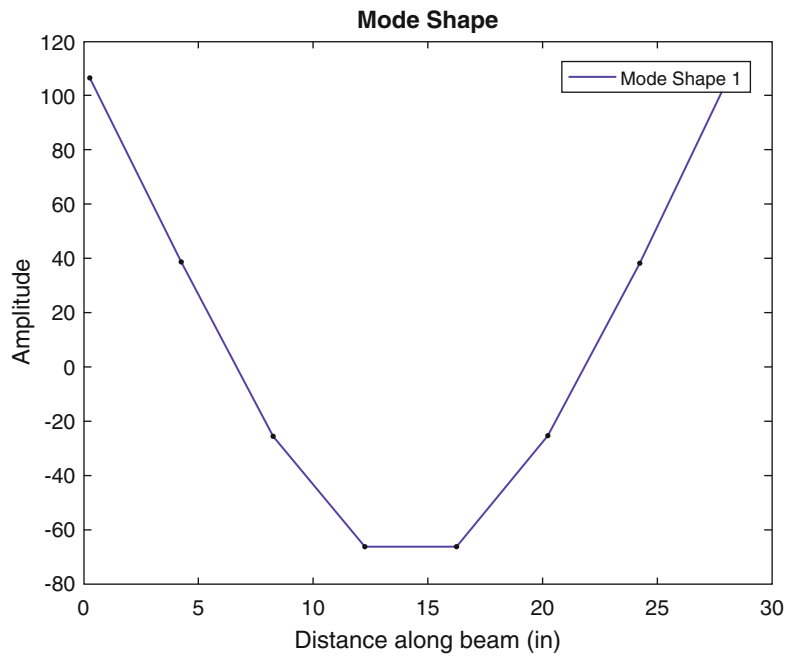


Fig. 26.3 First mode shape

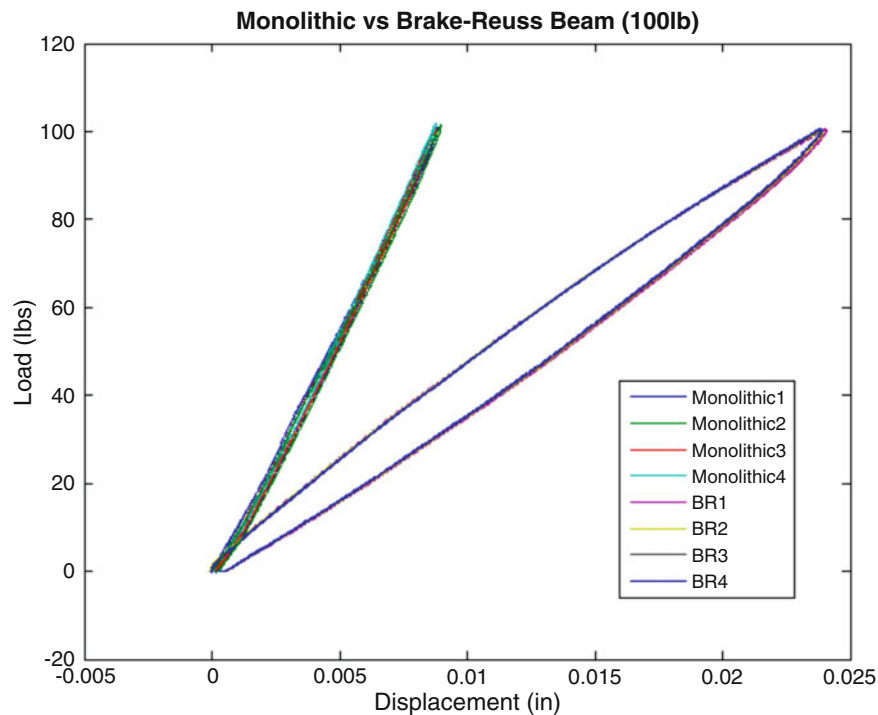


Fig. 26.4 Hysteresis curves of monolithic beam vs Break-Reauss beam (BR) [2]

26.3 Hysteresis Curves

The sophomore students conduct a three point bend test on a steel beam based on the mode shape of the first natural frequency as determined by the FEA class. The students cycle the load on the beam from 0 lbs to 100 lbs and back to 0 lbs 8 times, while recording the load and mid-span deflection. Plotting the data produces the hysteresis curves.

Figure 26.4 includes the hysteresis curves from the SNL study [2] of both the Brake-Reuss beam (BR1 to BR4) and from a monolithic beam. The lab procedure walk the student through reproducing the hysteresis plots for the Brake-Reuss beam and computing the energy dissipated in a bolted vs monolithic beam.

References

1. Mendoza, J.E.: The Development and Implementation of Modal Analysis Tools (2013)
2. Juarez, I., et al.: Modal Energy Dissipation for Bending Mode in Brake-Reuss Beam. Sandia National Labs, New Mexico Tech Department of Mechanical Engineering (2017)

Chapter 27

A Primer on Multiple Degree of Freedom Vibration Test for Aerospace and Military Applications

Luke A. Martin

Abstract The aerospace and military communities have performed vibration tests for decades using a single axis or single degree of freedom (SDOF) approach. In recent years, military standards have recognized a multiple exciter or multiple degree of freedom (MDOF) approach for conducting vibration testing. This primer on MDOF vibration testing serves to introduce the topic to the IMAC community and fits with IMAC-XXXVI's theme: Engineering Extremes.

This presentation will review how SDOF and MDOF vibration environmental definitions are obtained. The concept of *cloud plots* will be reviewed and approaches for determining acceptable test levels will be discussed. The common approach in the MIL-STD-810 community for accelerating testing using the Palmgren-Miner Hypothesis will be reviewed.

Next, the presentation will shift from the actual real-world vibration environment to the laboratory environment with special consideration reviewed such as: non-linearity effects, boundary conditions, controllability and observability.

Analogies between the power spectral density for an SDOF test and the spectral density matrix (SDM) for an MDOF test will be reviewed. The author's previous work will be adapted for illustrating how the SDM can take on a truly random nature for MDOF environments.

27.1 Extended Abstract

27.1.1 SDOF and MDOF Environmental Definitions

The raw time domain data measured during a vibration survey where two triaxial accelerometers are used, A1 and A2, at some distance apart can be represented in Eq. (27.1). $DATA_{SURVEY}$ represents a $6 \times 1 \times n$ matrix.

$$DATA_{SURVEY}(t) = \begin{bmatrix} A1_X(t) \\ A1_Y(t) \\ A1_Z(t) \\ A2_X(t) \\ A2_Y(t) \\ A2_Z(t) \end{bmatrix} \quad (27.1)$$

The Fourier Domain representation of a time domain accelerometer signal at location 1 in direction X is given in Eq. (27.2):

$$A1_X(f) = \text{fft}(A1_X(t)) \quad (27.2)$$

The SDM is then computed by multiplying the acceleration column vector by its conjugate transpose as shown in Eq. (27.3):

L. A. Martin (✉)

Naval Surface Warfare Center Dahlgren Division, Dahlgren, VA, USA

e-mail: Luke.a.martin@navy.mil

$$\begin{aligned}
SDM(f) &= \begin{bmatrix} A1_X(f) \\ A1_Y(f) \\ A1_Z(f) \\ A2_X(f) \\ A2_Y(f) \\ A2_Z(f) \end{bmatrix} [A1_X^*(f) \ A1_Y^*(f) \ A1_Z^*(f) \ A2_X^*(f) \ A2_Y^*(f) \ A2_Z^*(f)] \\
&= \begin{bmatrix} A1_X^2(f) & A1_X(f)A1_Y^*(f) & A1_X(f)A1_Z^*(f) & A1_X(f)A2_X^*(f) & A1_X(f)A2_Y^*(f) & A1_X(f)A2_Z^*(f) \\ A1_Y(f)A1_X^*(f) & A1_Y^2(f) & A1_Y(f)A1_Z^*(f) & A1_Y(f)A2_X^*(f) & A1_Y(f)A2_Y^*(f) & A1_Y(f)A2_Z^*(f) \\ A1_Z(f)A1_X^*(f) & A1_Z(f)A1_Y^*(f) & A1_Z^2(f) & A1_Z(f)A2_X^*(f) & A1_Z(f)A2_Y^*(f) & A1_Z(f)A2_Z^*(f) \\ A2_X(f)A1_X^*(f) & A2_X(f)A1_Y^*(f) & A2_X(f)A1_Z^*(f) & A2_X^2(f) & A2_X(f)A2_Y^*(f) & A2_X(f)A2_Z^*(f) \\ A2_Y(f)A1_X^*(f) & A2_Y(f)A1_Y^*(f) & A2_Y(f)A1_Z^*(f) & A2_Y(f)A2_X^*(f) & A2_Y^2(f) & A2_Y(f)A2_Z^*(f) \\ A2_Z(f)A1_X^*(f) & A2_Z(f)A1_Y^*(f) & A2_Z(f)A1_Z^*(f) & A2_Z(f)A2_X^*(f) & A2_Z(f)A2_Y^*(f) & A2_Z^2(f) \end{bmatrix} \quad (27.3)
\end{aligned}$$

The notation $A1_X^*(f)$ is used to represent the complex conjugate of $A1_X(f)$. When Eq. (27.3) is normalized by multiplying both sides by $1/\Delta f$, the auto-spectrums, which are found along the diagonal, assume the form of power spectral densities (PSD). A recommended sanity check is to compute the area under the spectral density function and compare to the root-mean-square of the original time signal to ensure they are equal.

The SDM will contain off-diagonal terms, which are referred to as the CSD terms. The CSD terms contain the relational information between the two measurements. From a modal analysis perspective, the CSDs can be viewed as the phase and coherence between respective signals. The CSDs found below the diagonal are the complex conjugates of the CSDs found mirrored above the diagonal.

In test specifications, generally one PSD is given to define a single degree of freedom (SDOF) test. This would be analogous to collapsing Eq. (27.3) to any one PSD, while ignoring all the information from other accelerometers. Furthermore, the one PSD given is rarely denoted as the mean value, 2 sigma value, maximum spectra, an envelope or other. The author recommends reporting test specification PSDs with respect to the greater environmental *cloud plot*. These details are essential to understanding the appropriateness of the test level. Traceability back to the environmental *cloud plot* is required, especially when the test level has been or will be accelerated using Palmgren-Miner's Hypothesis. Depending on the device under test and the device's lifecycle, the test level may need to be accelerated differently and without a traceable test specification, this change in test level is not possible. The rescaling equation from MIL-STD-810G Change Notice 1 requires this information.

27.1.2 Considerations for Laboratory Testing

Vibration tests conducted in a laboratory are rarely straight forward for the engineer or technician conducting the test and operating the vibration control system. This is especially true when test items are modally rich and/or large. Four common reasons why testing may be difficult to conduct are: non-linear effects, boundary conditions, controllability, and observability. Each of these should be carefully considered in test planning and setup.

Non-linearity can arise in two common ways. The first is when a vibration test is ramping up, for example, from -9 dB to 0 dB in 3 dB increments; this is a common ramp up sequence. Amplitude non-linearity can arise, during ramp up, causing the transfer function estimate to drastically change. When this occurs, the vibration controller may need longer time at one of the steps to equalize or may not be able to equalize. The second non-linearity can arise from test items or test setups which exhibit frequency non-linearity. This behavior has been observed when excessive energy exists in one frequency band and this energy feeds into other frequency bands. The vibration controller assumes frequency linearity and without a seasoned vibration operator, this non-linearity can be uncorrectable. When this arises, often times the reference profile may need to be adjusted to help the vibration controller obtain better estimates of the transfer function.

Differences between the in-service boundary conditions of a test item and the laboratory boundary conditions can cause the test item to exhibit modal responses in the laboratory, which defer from in-service modal responses. Ideally, operational deflection shapes would be measured for a test item in its in-service condition and then those operation deflection shapes would be matched in the laboratory.

The test laboratory is sometimes limited in driving down vibration levels and is thus limited in controllability of a test within the reasonable tolerance and goodness of a test defined by the test plan or military standards. Two examples which can contribute to the minimum level of vibration are: (1) the dynamic range of the vibration controller and (2) the ambient noise present in the test laboratory.

A common problem when conducting laboratory vibration test is the inability to observe all the mode shapes or operation deflection shapes. This shortcoming is often due to limitations in the quantity of sensors available to survey the vibratory event.

27.1.3 Power Spectral Density and the Spectral Density Matrix

Power spectral densities (PSDs) are to single degree of freedom testing what the spectral density matrices (SDMs) are to multiple degree of freedom testing. As vibration test expand into the multiple degree of freedom domain, the notion of test tolerances for SDMs needs to be understood by the testing laboratories, sponsors, and structural analysts. This understanding will include allowing test tolerances to be random for regions within the SDM.

Chapter 28

A Study on the Generation and Propagation of Traveling Waves in Strings

Isil Anakok, V. V. N. Sriram Malladi, and Pablo A. Tarazaga

Abstract Traveling and standing waves occurring in mechanical systems are the results of the interplay of excitation sources, locations, and boundary conditions. While traveling waves carry energy throughout a system, standing waves keep such energy within a located area associated with the modes of excitation. Depending on the desired characteristics of a system, it is crucial to understand the wave propagation and what parameters affect wave propagations. In the present work, one-dimensional string equations are studied with fixed-fixed boundary condition with the purpose of generating steady-state traveling waves. Two excitation forces at various frequencies of excitation are applied to a string near opposing boundaries to understand the generation and propagation of traveling and standing waves. The work focuses on how parameters affect the wave propagation on a string under the fixed-fixed boundary condition and their quality examined. Understanding the effects of these parameters on the wave propagation of a string can lead to better understanding of microorganism behaviors, such as the propulsion of flagella or biological counter parts such as the basilar membrane (2D string) in the ear's cochlea that exhibit non-reflective waves.

28.1 Introduction

Travelling waves carry energy throughout a system, and standing waves keep such energy within a located area associated with the modes of excitation. Waves have been widely studied on many mechanisms such as in mechanical and biological systems. In recent literature, there are multiple studies focusing on the generation of steady-state traveling waves in finite structures using multiple simultaneous forces. Avirovik et al. [1] studied steady-state mechanical waves in beams with different boundary conditions and showed the effects of control variables. Gabai et al. [2, 3] worked to answer how the forces should be applied through structures and wave characterization in 1D structures. Malladi et al. [4–8] studied the generation and propagation of waves, and followed a cost function approach to optimize the traveling waves generated in a beam with free-free boundary condition. In this study, a similar cost-function approach is adapted to study one-dimensional strings with fixed-fixed boundary conditions. In [4, 5] there are multiple approaches to determine the relative content of traveling waves and standing waves in the response of a 1D structure. In the present study, cost function approach is adopted based on the wave envelope approach [5].

28.2 Analytical Solution of Two Force Excitation of a String

This section summarizes the analytical solution to a fixed-fixed string of length L excited by two forces which are out of phase from each other. $F_1 = \cos(\omega t)$ and $F_2 = \cos(\omega t + \Phi)$ are applied to a string at equal distances from both ends of the string as shown in Fig. 28.1. There is a phase difference, Φ , between the two harmonic forces. The governing equation for the string is given by,

$$\frac{\partial^2 \omega}{\partial t^2} - c^2 \frac{\partial^2 \omega}{\partial x^2} = \frac{F_1}{\rho A} \cos(\omega t) \delta(x - l_1) + \frac{F_2}{\rho A} \cos(\omega t + \Phi) \delta(x - l_2), \quad (28.1)$$

I. Anakok (✉) · V. V. N. S. Malladi · P. A. Tarazaga
Vibration, Adaptive Structures and Testing Lab (VAST), Department of Mechanical Engineering, Virginia Polytechnic Institute and State University, Blacksburg, VA, USA
e-mail: ianakok@vt.edu

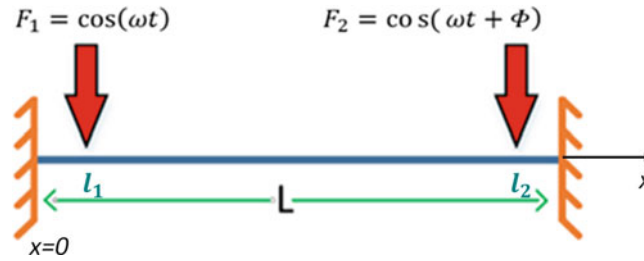


Fig. 28.1 The schematic of a string with two excitation forces and fixed-fixed boundary conditions

where $c = \sqrt{\tau/(\rho A)}$ is the speed of the wave in the string, A is the cross-sectional area of the string, ρ is the density of the string, τ is tension, ρA is the mass per unit length, and l_1 and l_2 are the location of the applied forces in the string and shown in Fig. 28.1.

A standard separation of variables approach is used to solve Eq. (28.1). Assuming that

$$w(x, t) = \sum_{n=1}^{\infty} X_n(x) T_n(t), \quad (28.2)$$

where $X_n(x)$ is the spatial part and $T_n(t)$ is the temporal part of separation of variables.

The solutions of the spatial component, $X_n(x)$, if given by the mode shapes of the string as,

$$x_n(x) = \sin \frac{n\pi x}{L}, \text{ for } n = 1, 2, 3, \dots, \infty \text{ and } x \in [0, L] \quad (28.3)$$

The temporal components $T_n(t)$ are calculated for each of the two forces applied to the string, and later superposed together for a total response. The temporal solution for the string is given by,

$$T_n^1(t) = T_1 \cos(\omega t - \theta_1) \quad (28.4)$$

$$T_n^2(t) = T_2 \cos(\omega t - \theta_2 + \Phi) \quad (28.5)$$

where $\theta_1 = \theta_2 = \tan^{-1}((2\zeta\omega_n\omega)/(\omega_n^2 - \omega^2))$, $T_1 = ((2/L\rho) \sin(n\pi l_1/L)) / \sqrt{(\omega_n^2 - \omega^2)^2 + (2\zeta\omega_n\omega)^2}$, $T_2 = ((2/L\rho) \sin(n\pi l_2/L)) / \sqrt{(\omega_n^2 - \omega^2)^2 + (2\zeta\omega_n\omega)^2}$, ω is the driving frequency, ω_n is the n th natural frequency, ζ is the damping ratio, and Φ , as described before, is the phase angle of between both forces. The natural frequency is given by $\omega_n = (n\pi/L) / \sqrt{\tau/(\rho A)}$.

28.3 Parametric Study of Two Force Excitation on a String

In this parametric study, a polyethylene string ($L = 1$ m, $A = 10 \text{ mm}^2$, $\zeta=0.001\%$) is excited with two forces that were applied at the $l_1 = L/20$ and $l_2 = L - L/20$ locations. The initial displacement is assumed to be zero and fixed-fixed boundary condition string case is considered for three different phase differences: 90° , 0° and 60° . The phase differences between the two forces results in traveling, standing and a hybrid combination of both waves accordingly. Figure 28.2 shows (from top to bottom) the plots of (i) the area swept by the string, (ii) the contour from a top view of the waves, and (iii) a three-dimensional plot of the waves. Red lines indicate the maximum envelope (w_{max}) and minimum envelope (w_{min}) of the waves in first row of Fig. 28.2. Additionally, the cost function (CF) for the one-dimensional string is defined according to [5]. The equation of the cost function by wave envelope is as follows

$$CF = \frac{w_{max} - w_{min}}{w_{max} + w_{min}}. \quad (28.6)$$

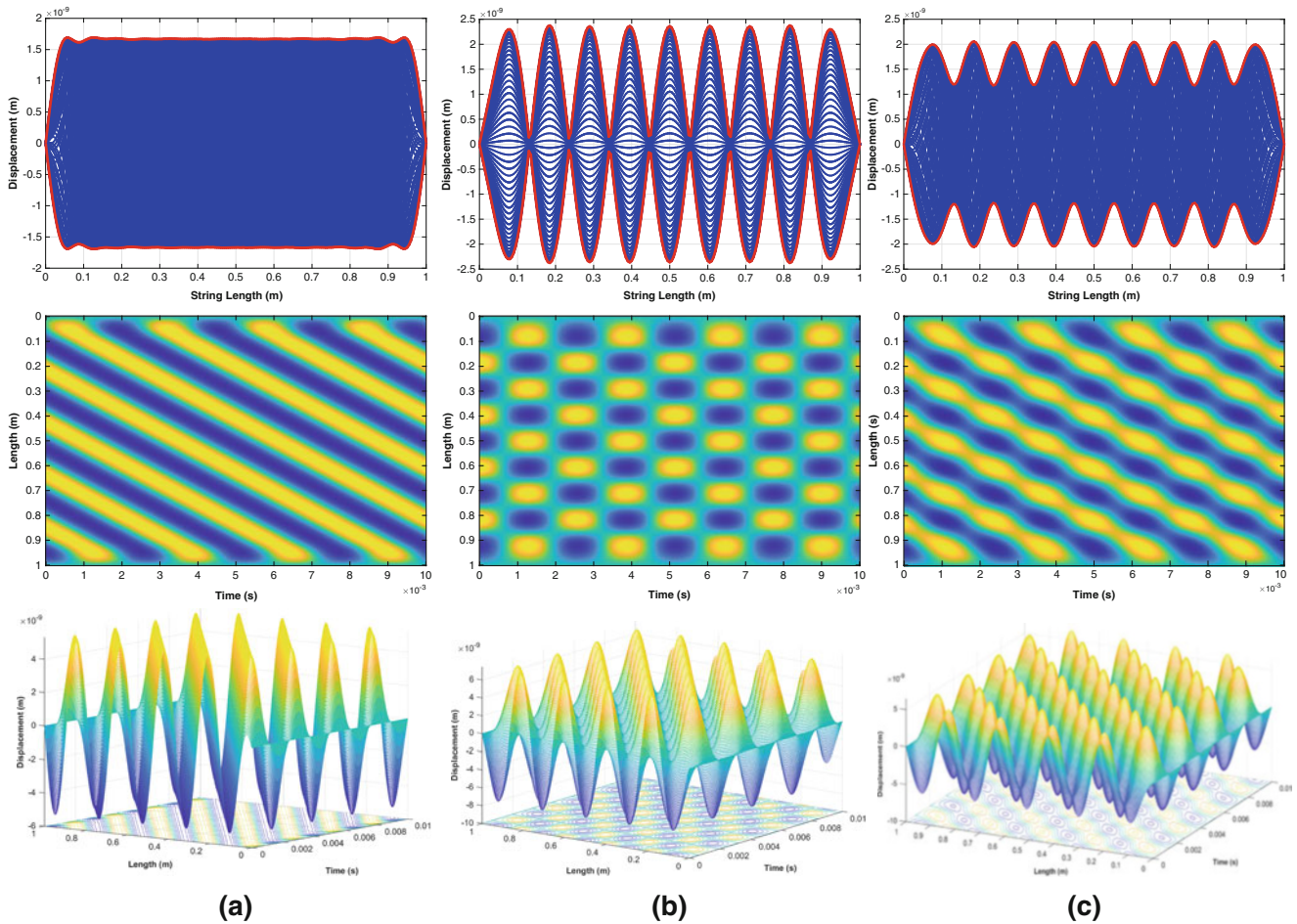


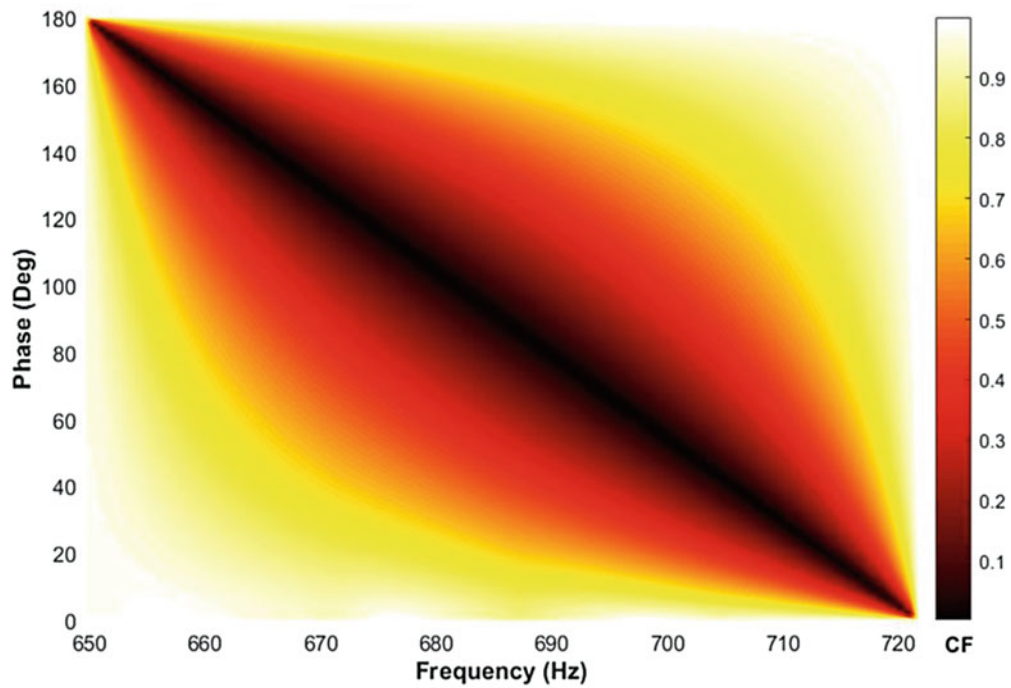
Fig. 28.2 The figures represent (a) traveling wave at 685.6 Hz, (b) standing wave at 685.6 Hz, (c) hybrid wave plots at 685.6 Hz

Equation (28.6) can be used to evaluate the wave quality at different phase angles with CF defined between 0 and 1. Zero valued CF represent pure traveling waves while a value of one represent pure standing waves. A hybrid wave gives rise to CF between zero and one. However, if the direction of the wave is considered, we can define a CF from -1 to 1 , where two waves traveling in opposite direction have positive and negative values of CF. Extending the specific phase angle cases addressed above (90° , 0° and 60°) an sweeping the angle yields all cases where the CF can be related to phase angle used for different frequencies. Figure 28.3 shows the cost function plots when the phase angle is varied from 0° to 180° in (a) and -180° to 0° in (b).

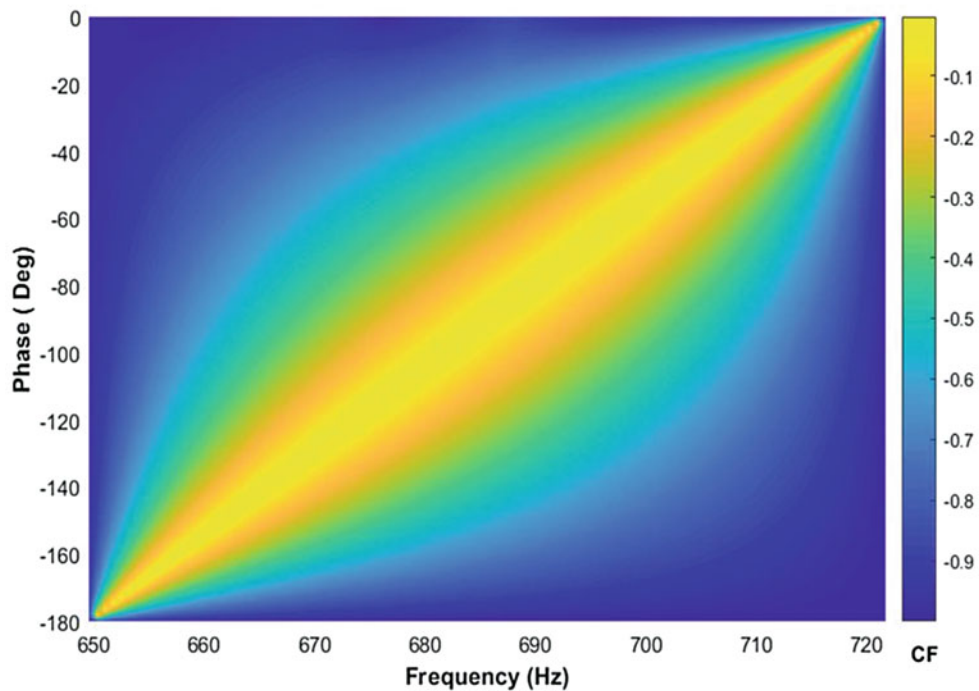
Both plots in Fig. 28.3 indicate that the direction of the waves are opposite due to the sign of cost function. It is also seen that we can determine an optimal traveling wave at a desired frequency by changing the phase angle value.

28.4 Conclusion

In this work, one-dimensional string equations are solved for a fixed-fixed boundary condition with the purpose of generating steady-state traveling waves. The work is successful at showing the non-control based approach to generate steady state traveling waves by using a two-force approach and optimizing the phase between the two forces. Traveling, standing and hybrid waves are represented herein for a string given the parameters used for excitation. To distinguish them a cost function is used to evaluate the quality of the waves that result and it is given by a value between 0 and 1, where 0 represent a pure traveling wave and 1 represents a standing wave. Based on the preliminary parametric study and results, the direction of traveling waves in strings can be manipulated by addressing the phase angle used. The work has shown that steady state waves can be generated using this two-force approach in different directions via a careful understanding of the phase angle. The work will further study location and different boundary conditions in the future.



(a)



(b)

Fig. 28.3 The schematic of cost function of a string with two excitation forces and fixed-fixed boundary conditions at phase angle (a) from 0° to 180° and (b) -180° to 0° at frequencies varying 650–720 Hz

Acknowledgment VVNS Malladi and P Tarazaga would like to acknowledge the support of the Air Force Office of Scientific Research through the Young Investigator Program (FA9550-15-1-0198). Dr. Tarazaga would also like to acknowledge the support through the John R. Jones III Faculty Fellowship. I Anakok would like to acknowledge the support of the Ministry of National Education of Turkey.

References

1. Avirovik, D., Sriram Malladi, V.V.N., Priya, S., Tarazaga, P.A.: Theoretical and experimental correlation of mechanical wave formation on beams. *J. Intell. Mater. Syst. Struct.* **27**(14), 1939–1948 (2016)
2. Gabai, R., Bucher, I.: Spatial and temporal excitation to generate traveling waves in structures. *J. Appl. Mech.* **77**(2), 021010 (2010)
3. Gabai, R., Bucher, I.: Excitation and sensing of multiple vibrating traveling waves in one-dimensional structures. *J. Sound Vib.* **319**(1), 406–425 (2009)
4. Malladi, V.V.N.S., Avirovik, D., Priya, S., Tarazaga, P.A.: Travelling wave phenomenon through a piezoelectric actuation on a free-free beam. In ASME 2014 Conference on Smart Materials, Adaptive Structures and Intelligent Systems, pp. V001T03A017–V001T03A017, Newport, Rhode Island, <http://www.asmeconferences.org/SMASIS2014/> (2014)
5. Malladi, V.V.N.S., Avirovik, D., Priya, S., Tarazaga, P.: Characterization and representation of mechanical waves generated in piezo-electric augmented beams. *Smart Mater. Struct.* **24**(10), 105026 (2015)
6. Malladi, V.V.N.S., Albakri, M., Tarazaga, P.A.: An experimental and theoretical study of two-dimensional traveling waves in plates. *J. Intell. Mater. Syst. Struct.* **28**(13), 1803–1815 (2017)
7. Malladi, V.V.N.S., Albakri, M., Musgrave, P., Tarazaga, P.A.: Investigation of propulsive characteristics due to traveling waves in continuous finite media. In: SPIE Smart Structures and Materials+Nondestructive Evaluation and Health Monitoring, pp. 101620O–101620O. International Society for Optics and Photonics, Bellingham, WA USA, <https://www.spiedigitallibrary.org/contact-us> (2017)
8. Malladi, V.V.N.S., Albakri, M.I., Gugercin, S., Tarazaga, P.A.: Application of projection-based model reduction to finite-element plate models for two-dimensional traveling waves. *J. Intell. Mater. Syst. Struct.* 1045389X16679295 (2016)

Chapter 29

A Color-Coded Complex Mode Indicator Function for Selecting a Final Mode Set

Randy L. Mayes and Daniel P. Rohe

Abstract Many test articles exhibit slight nonlinearities which result in natural frequencies shifting between data from different references. This shifting can confound mode fitting algorithms because a single mode can appear as multiple modes when the data from multiple references are combined in a single data set. For this reason, modal test engineers at Sandia National Laboratories often fit data from each reference separately. However, this creates complexity when selecting a final set of modes, because a given mode may be fit from a number of reference data sets. The color-coded complex mode indicator function was developed as a tool that could be used to reduce a complex data set into a manageable figure that displays the number of modes in a given frequency range and also the reference that best excites the mode. The tool is wrapped in a graphical user interface that allows the test engineer to easily iterate on the selected set of modes, visualize the MAC matrix, quickly resynthesize data to check fits, and export the modes to a report-ready table. This tool has proven valuable, and has been used on very complex modal tests with hundreds of response channels and a handful of reference locations.

29.1 Introduction and Motivation

It is quite common to test structures that are slightly nonlinear at Sandia National Laboratories. This nonlinearity can cause the modal frequency to shift slightly from one shaker input location to another, or one amplitude of excitation vs another. The slight frequency shift often is identified as a different mode with multi-reference matrix polynomial algorithms. In addition, if the system is nonlinear enough, the stabilization diagram may never really stabilize as the number of roots are increased because the algorithm generates computational roots attempting to compensate for the nonlinearity. At Sandia National Laboratories, the Synthesize Modes and Correlate (SMAC) [1] modal extraction algorithm is a mostly automated modal extraction algorithm. The SMAC algorithm has a time saving feature in that it does not develop computational roots for nonlinear systems as the matrix polynomial algorithms do. However, the algorithm is basically a single reference algorithm. Therefore, it generates modal parameter estimates from every reference. Many of these modes are duplicated from one reference to another, so some methodology is needed to pick out the “best” modes from each reference. An extension of the robust complex mode indicator function (CMIF) has provided a solution for this need.

The complex mode indicator function (CMIF) is an excellent multi-reference tool for determining if there are multiple closely spaced modes near a certain frequency. By collecting frequency response functions (FRFs) from multiple well-chosen shaker input locations and performing a singular value decomposition (SVD) of the FRF matrix at each frequency line, the number of active mode shapes at a frequency is usually apparent from the plot of the singular values vs frequency. There are other mode indicator functions that are designed to identify closely spaced modes from multi-input multi-output FRF data. However, we claim that the CMIF has one major advantage over some of these other mode indicator functions. Because the CMIF is based on a spatial filter instead of a frequency based estimator, it does not predict “false” modes as most other algorithms do in the common case of a slightly nonlinear test article. This resolves the issue of how many modes are active at any frequency, removing the annoyance of mode splitting. However the next step, if one desires to extract the closely spaced modes from a single reference, is to determine which reference would be the best one for the modal parameter extraction.

Sandia National Laboratories is a multimission laboratory managed and operated by National Technology and Engineering Solutions of Sandia LLC, a wholly owned subsidiary of Honeywell International Inc. for the U.S. Department of Energy’s National Nuclear Security Administration under contract DE-NA0003525.

R. L. Mayes · D. P. Rohe (✉)
Structural Dynamics Department, Sandia National Laboratories, Albuquerque, NM, USA
e-mail: dprohe@sandia.gov

Ideally this would be a shaker which excites the mode of interest but does not excite other modes. The first step in this situation is to determine which shaker location excites the mode of interest best. One approach would be a color-coding of the multiple plots in the CMIF that showed, by color, which shaker excites each shape best. How could this be achieved? This work uses the right singular vectors from the SVD to determine which shaker is most causal for a specific shape, and bases the color-coding of the different CMIF curves on that.

29.2 Desirable Features of the Algorithm

As a recap, we desire to be able to make accurate extractions of best fit modal parameters from slightly nonlinear data, especially in frequency bands with closely spaced roots. We require a method that will not split modes, or generate extra false roots, due to the nonlinearity. The SMAC modal extraction code used at Sandia National Laboratories satisfies this requirement. Because it utilizes spatial filtering to estimate the roots, it is not easily fooled by nonlinearity. However, since it is basically a single reference algorithm, we need additional help to identify which shaker is the best one to excite a particular mode shape in order to extract that particular root. The CMIF provides a robust indication of the true closely spaced roots, but in its well-known form, gives no insight as to which shaker is best for extracting a particular root. By associating each shaker with a color, the color-coded CMIF could provide us the information as to which FRF set to extract the root and shape from.

29.3 Theory of the Algorithm for Establishing the Best Shaker Through Color-Coded CMIF Curves

The CMIF algorithm was introduced by Shih et al. [2]. Basically, at each frequency line, the algorithm performs a SVD of the multiple sets of FRFs and plots the singular values. Relatively large singular values indicate that there are independent shapes associated with those singular values at that particular frequency. At a particular frequency line, the CMIF will come from the SVD that has the form of

$$\text{SVD}(\mathbf{H}(\omega)) = \mathbf{U}\mathbf{S}\mathbf{V}^T \quad (29.1)$$

where the \mathbf{S} matrix is a diagonal matrix of the singular values. These are the values that are plotted in the CMIF as a function of frequency. The FRF matrix \mathbf{H} is usually constructed so that rows are associated with the response measurements and columns are associated with the different shaker force inputs. The amplitude of the singular value shows how strongly a shape appears globally in the FRF data. The \mathbf{U} vectors show the approximate shapes at the frequency. The value of the \mathbf{V}^T matrix is that it shows which shapes are activated from a particular shaker. A column of the \mathbf{V}^T matrix will be associated with a particular shaker. By looking at the amplitude of the values in that column, one can see which mode is best excited by the shaker, which is second best and so on. The color-coded CMIF algorithm looks across the row of \mathbf{V}^T associated with the mode of interest and picks the shaker with the maximum value and applies the associated color to the CMIF singular value plot. Then the FRF data associated with that shaker can be processed in SMAC to obtain the root and shape estimate. An example of the color-coded CMIF plot from experimental data is given in Fig. 29.1.

29.4 User Interface to Automate the Features

If there are many modes to be extracted, the single reference algorithm of SMAC will possibly extract the number of modes in the bandwidth times the number of shaker locations. This can lead to an unwieldy number of “decisions” about which modes to utilize from which shaker input. A graphical user interface (GUI) was developed to make all these “decisions” and automate the modal extraction process with information from the SMAC algorithm and the color-coded CMIF. Prior to the development of the interface, modal test engineers kept track of the selected modes to keep from the various SMAC fits in a variety of ways, none of which were particularly robust. For example, a user may use indices (e.g. keep mode 1, 2, and 6 from dataset 1; mode 4 and 5 from dataset 2; etc.). This system is simple and it works well enough for simple structures. However, if the system is complex and the user determines that he or she needs to refit the data from dataset one for example

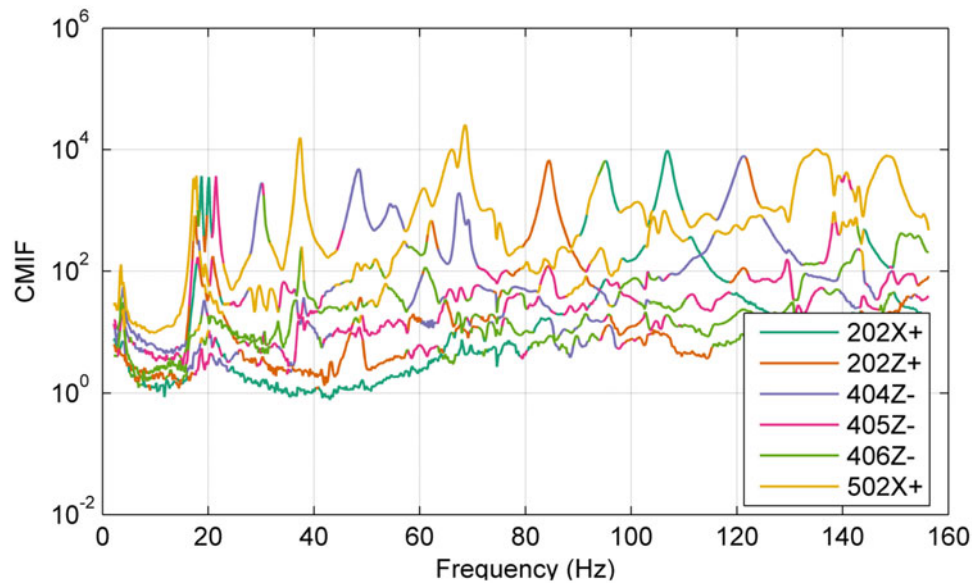


Fig. 29.1 The complex mode indicator function with colors to indicate which shaker best excites each shape

by adding a new mode, all of the indices into that dataset would thereafter be incorrect and need to be updated. An additional approach is to track modes by frequency (e.g. keep modes at 20.1, 22.5, and 30.0 Hz from dataset 1; modes at 25.3 Hz from dataset 2, etc.). This is slightly more robust to updates to fits in each dataset as the mode in question may not be modified by adding another mode. However, this can still be tedious to track, especially for large systems.

The goals of the interface were to directly utilize output from the existing SMAC tool to ease the burden on the users. While the current implementation relies directly on the Mayes-Hensley implementation [1] contained in ATA's IMAT MATLAB toolbox, it could be extended to interface directly with other tools and implementations. Another goal was to handle general modal tests, including where some degrees of freedom may not exist (for example if a drive point location were added midway through a test). It was designed to be flexible enough to enable easy re-fitting of data or updating of SMAC data files without losing progress, and also to provide tools to visualize modal fit quality, including resynthesizing data, plotting FRFs, CMIFs, and mode shapes. Finally, it was designed so that report-quality figures could be produced by the GUI without needing to pipe data to some other tool for plotting.

29.4.1 Interface Overview

An overview of the GUI is shown in Fig. 29.2. Key features are highlighted. The primary use of the GUI is to select modes from the data set. The left side of the GUI has a drop-down menu that allows the user to select the current dataset. This populates the list below with modes extracted from that dataset via SMAC. As datasets are added to the analysis, the color-coded CMIF is updated in the center of the screen. Modes are indicated on the figure, but are only drawn on the curves where the color of the curve corresponds to the dataset from which the mode was extracted. In this way, when a mode is selected from the figure it is automatically picked from the best reference as judged by the theory in Sect. 29.3. For many tests without repeated roots, the user needs only to travel along the top singular value curve and select the indicated modes on that curve. For tests with repeated roots, the user might need to go down to the second or lower singular value curves to select the modes corresponding to those repeated natural frequencies.

29.4.2 Changing Datasets

Many times during the course of fitting modes it may be decided that a certain mode wasn't fit quite right. In this case it would be advantageous to refit the data and reload it into the color-coded CMIF analysis. The GUI handles this gracefully,

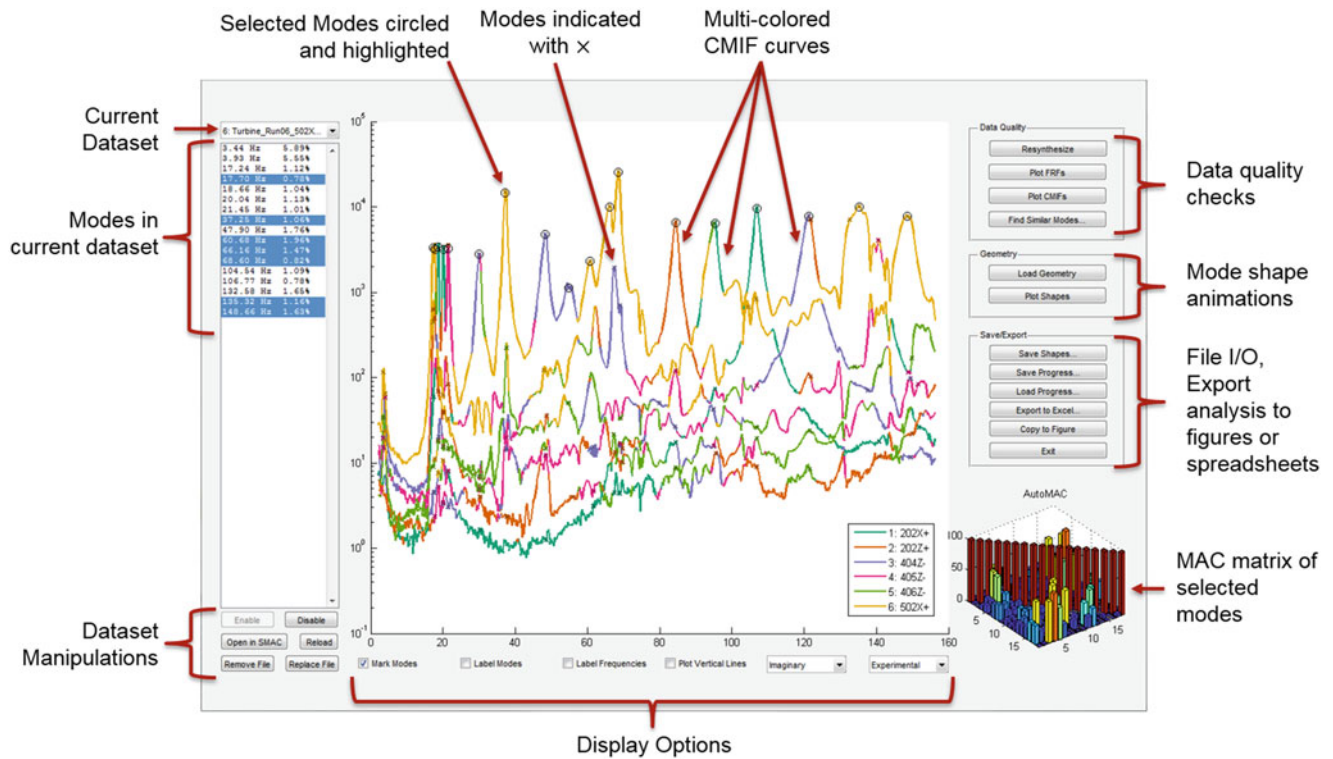


Fig. 29.2 Annotated view of the GUI

both with an option to directly open the dataset in the SMAC tool and with an option to reload or replace the dataset after it has been refit. In order to save progress so the user does not need to reselect modes from the dataset that they may have refit, the color-coded CMIF tool will use the mode shape information to correlate each mode in the original dataset to a mode in the new, refit data set. This way, a selected mode will remain selected even if its parameters change slightly. If the shape change is too large, however, no mode in the new dataset will be mapped to the original dataset; this is to prevent an original mode from being paired to a completely different mode if a mode doesn't exist in the new dataset.

29.4.3 Evaluating the Mode Set

Often in modal testing one mode can be excited and extracted from multiple shaker locations, and the shape from a weakly excited location may be just different enough to create a small peak in the next lower singular value curve. To aid in clarifying whether or not two selected modes are actually the same mode, the color-coded CMIF GUI includes a MAC matrix that is automatically updated whenever a new mode is selected. If a new mode is selected and the off-diagonal of the MAC matrix between that mode and another mode is very high, one might argue that those are the same mode and exclude one of them. Figure 29.3 shows an example where there is a relatively small peak (two orders of magnitude lower) in the second singular value curve directly underneath a large peak in the primary singular value curve, but the MAC matrix clearly shows these two as the same mode.

Alternatively, there may be two closely spaced modes at a given frequency, and it is in this case that the CMIF excels over other mode indicator functions. Figure 29.4 shows an example of such a measurement. In that example, the first two singular values are large, suggesting two peaks. Indeed, when both are selected in the final set of modes, the MAC indicates that they are distinct shapes.

As mode selection can be an iterative process, the tool aimed to make it easy to resynthesize FRFs from the selected modes and compare them against the experimental data. The tool has a button to directly resynthesize FRFs from the mode set. These can be then plotted directly against experimental FRFs or assembled into CMIFs and compared there. Figure 29.5 shows example resynthesized FRFs and CMIFs. Mode shapes can also be plotted if a geometry file is loaded; the GUI relies on the IMAT toolbox's plotting functions to show and animate the shapes.

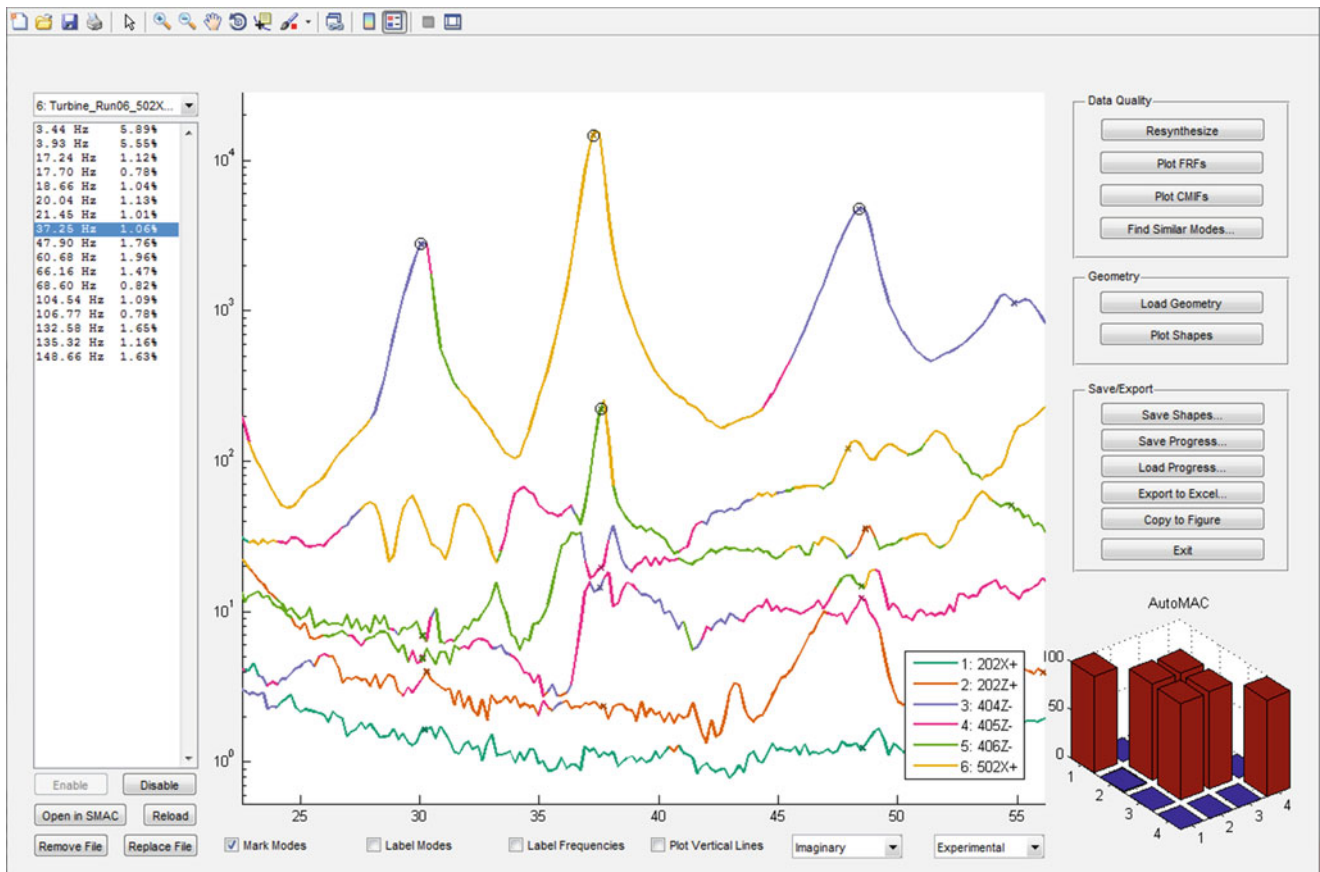


Fig. 29.3 Example color-coded CMIF analysis where in the CMIF it might not be clear whether or not there are two modes present. The MAC matrix, however, is quite clear that the two peaks near 37 Hz are the same mode and therefore only one should be selected

The GUI also has a function to find similar modes to the ones selected. Essentially, for each selected mode, the GUI searches through all datasets to find modes similar to that one. The idea is that if a given mode was extracted from a number of different references, then the user can have a high degree of confidence in that mode.

29.4.4 Documentation

Once the shapes are selected, the GUI provides a reasonable feature set for documentation. Right-clicking on a mode in the selection box opens up a dialog box that allows the mode to be named, given a confidence level, and have comments attached to it. These data, along with the modal parameters and similar modes (described in the previous section) are all combined into an Excel spreadsheet that can be easily dropped into a report. The values in the MAC matrix are also exported to the spreadsheet on a different sheet, as this is a well-known metric that is usually included in modal test reports. Finally, a function exists that will copy the color-coded CMIF plot to a new figure so it can be included in reports without the added clutter of all of the GUI buttons, drop-downs, and lists.

29.5 Summary

The color-coded CMIF was developed as a way to quickly identify the shaker location that best excites a given mode, and it was built into a GUI that allows analysts to quickly select the best mode from a number of different datasets. Even for complex tests, a final mode set can be quickly assembled. The built-in evaluation tools allow the user to quickly iterate on their set of modes to come to a final set.

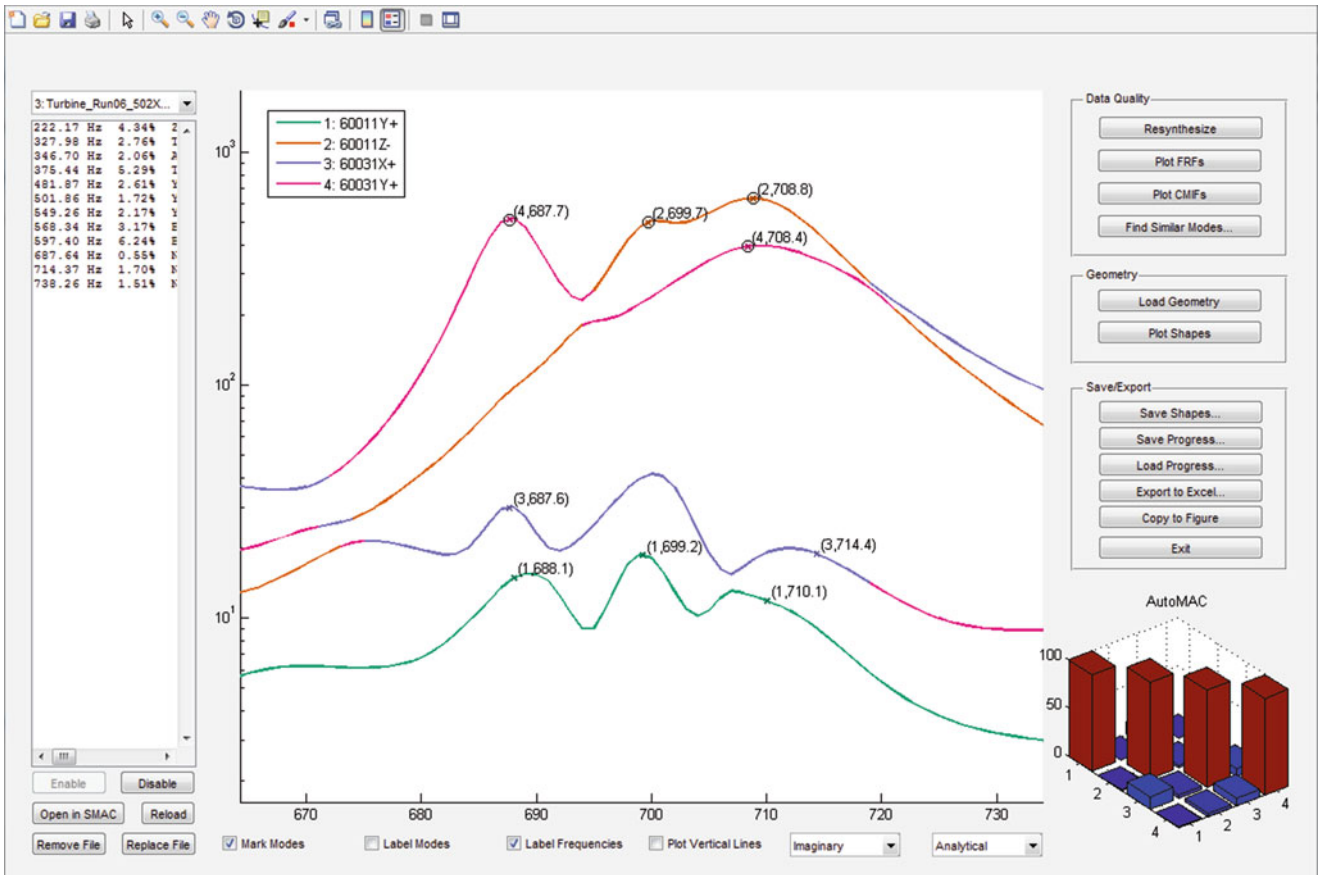


Fig. 29.4 Example showing two closely spaced modes. Here two modes are selected near 708 Hz, and the MAC clearly shows them as being separate modes

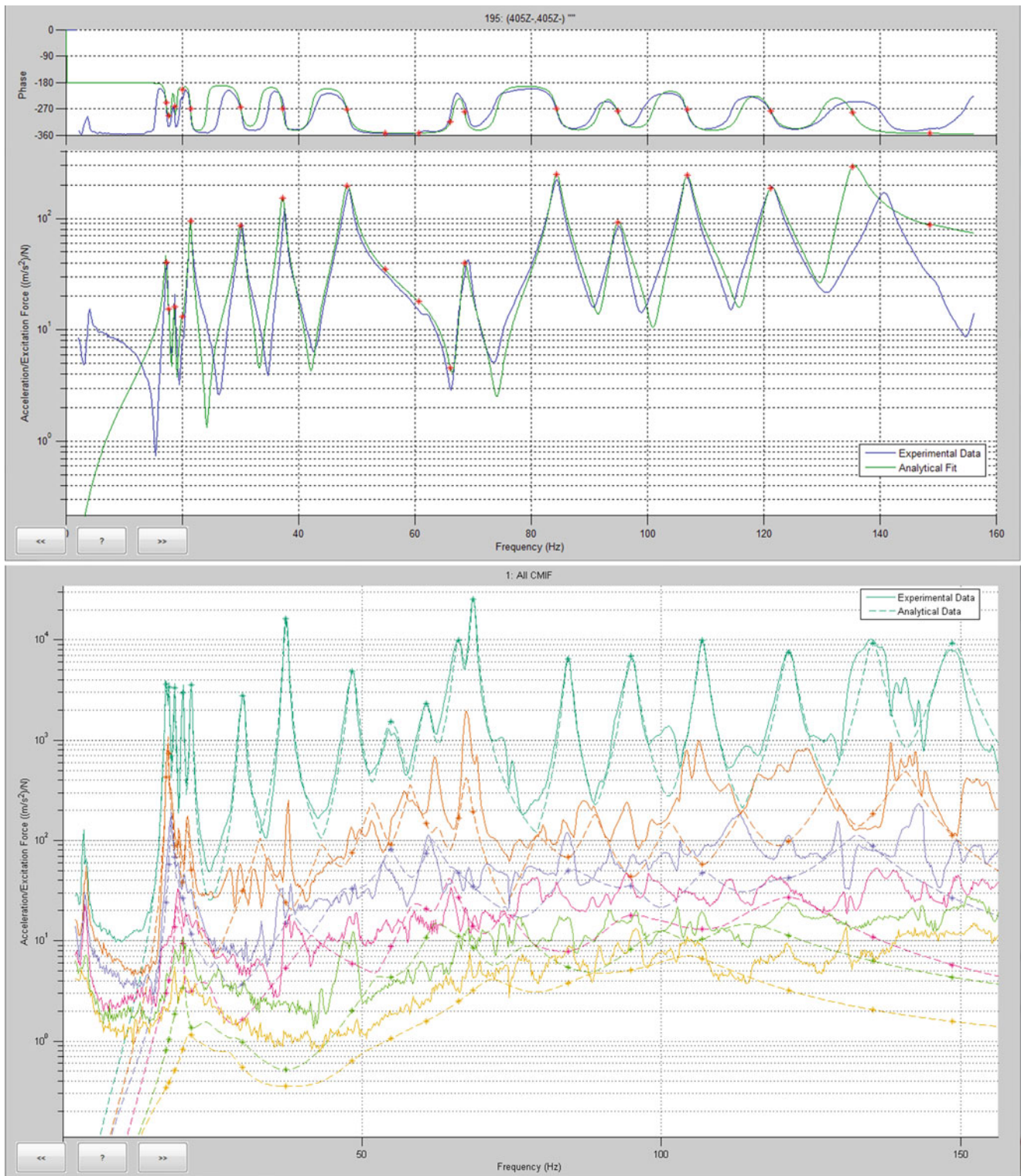


Fig. 29.5 Resynthesized FRFs and CMIFs from the color-coded CMIF GUI

References

1. Hensley, D.P., Mayes, R.L.: Extending SMAC to multiple reference FRFs. In: Proceedings of the 24th International Modal Analysis Conference, St. Louis, Missouri, pp. 220–230 (Jan. 2006)
2. Shih, C.Y., et al.: Complex mode indication function and its applications to spatial domain parameter estimation. *Mech. Syst. Signal Process.* **2**(4), 367–377 (1988)

Chapter 30

Using Manual Excitation for Large Displacement on a Highly Damped System

Douglas J. Osterholt and David E. Cloutier

Abstract Small-scale, quickly executed modal surveys can yield an incredible amount of useful information. Electrodynamic shakers and especially impact hammers have been the excitation methods of choice for these tests because of their ease of use. However, large low-frequency structures with highly damped modes are difficult to excite due to exciter stroke limitations or inability to apply long duration pulse inputs. Hydraulic actuation allows large displacements at low frequencies, but it is expensive and challenging to install in a short amount of time. Similarly, while step-relaxation techniques allow large force and displacement inputs, setup, using a reaction structure, and execution is complicated by the need to reset the system multiple times. In order to overcome some of these drawbacks, ATA developed a modal handle to apply a manual excitation while measuring the input levels of the excitation force. This paper presents results of using this modal handle to perform a modal survey on a test article to evaluate the effect of different dampers and damper configurations on the test article primary torsion mode. This inexpensive and efficient excitation method proved to be successful in quickly completing over eighty test configurations needed to down select to a final damper configuration.

Abbreviations

ATA	ATA Engineering, Inc.
C/cc	Percent critical damping
FRF	Frequency response function
Hz	Hertz
IMAT	Interface between MATLAB, analysis, and test
LSCE	Least squares complex exponential

30.1 Introduction

There are a wide variety of ways to perform modal testing, including the type of excitation used. Typically, a modal impact hammer with an integrated load cell or an electrodynamic shaker are the most common choice for most test articles. Impact hammers are quick to set up but are limited in the ability to control the input force into the structure. The frequency content of the modal hammer can be adjusted by changing the tips of the hammer or placing rubber or padding on the impact surface, but obtaining sufficient excitation at low frequency can be a challenge. Electrodynamic shakers can be used to control the input force but are limited by stroke displacement or force magnitude at low frequencies. Long stroke shakers, such as hydraulic actuators, are typically heavy and difficult to set up quickly. Recent, multiple projects required modal testing on structures with highly damped modes below 3 Hz, leading to a desire for better excitation techniques. This paper documents several techniques used at ATA for exciting these structures to obtain frequency and damping values, including the development of the modal handle.

The objectives of the different modal surveys were to measure fundamental modes of the system, including the frequency and damping. The first project goal was to measure the first mode, which was predicted at 1 Hertz (Hz), for a variety of damper configurations. The damping ranged from 4% to 35% critical damping (C/Cc) using various setups; no dampers up to four dampers.

D. J. Osterholt (✉) · D. E. Cloutier
ATA Engineering Inc., San Diego, CA, USA
e-mail: doug.osterholt@ata-e.com



Fig. 30.1 ATA van used for testing methods



Fig. 30.2 Modal handle attached to the van

In addition to the challenge of exciting these structures, there was also a challenge on how to compute the damping with limited time data for analysis. Two different analytical methods were used and are discussed.

30.2 Pretest Checkout

Before heading out to a customer's site, we looked for something we could use to test excitation methods. The ATA cargo van, shown in Fig. 30.1, was the easiest structure available providing a set of fairly low-frequency and highly damped modes. A seismic accelerometer was used to measure the low-frequency response of the van's bounce/pitch mode. Manually exciting this mode was easy, and it led to the concept of a modal handle. The thought was to use a load cell in line with something to manually excite the van while measuring the input force so the frequency response functions (FRFs) could be computed. An order was placed, some machining was done, and the modal handle was invented. The handle consists of two plates with a load cell sandwiched between them and a handle bolted to the top plate to allow pushing and pulling through the load cell. The modal handle mounted to the bumper of the van is shown in Fig. 30.2. The handle was clamped to the bumper providing an easy way to measure the load while imparting large displacements manually into the van to excite the suspension mode. Figure 30.3 shows the time response of the load cell and the accelerometer during a manual sine dwell of the van bounce mode.

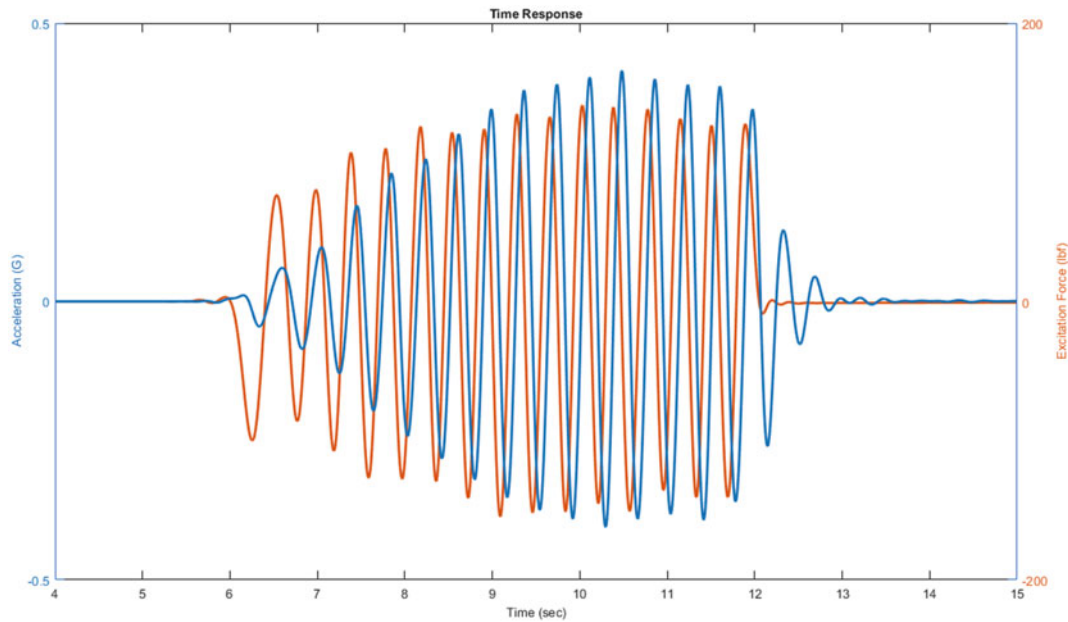


Fig. 30.3 Manual sine dwell and decay of van—force and acceleration response

This preliminary data demonstrated that the modal handle was a valid method to obtain manual excited dwell and decay responses. Two analytical methods were used to extract the damping of the mode: a least-squares complex exponential (LSCE) method, which is a high-order, scalar polynomial, time domain modal parameter estimation method [1] and a logarithmic decrement decay curve-fit. Both methods were used and compared to estimate the percent critical damping of the modes.

After the concept of the modal handle was validated, it was used to apply random excitation to the actual test article during a preliminary scoping trip. The randomness depends upon the user input—in this case, an awkward engineer with no rhythm works pretty well. The FRF was computed for two different configurations using this method. The time domain of the load cell for the random excitation is shown in Fig. 30.4. The force autospectrum shows that the manual excitation is able to excite the structure with good input up to about 7 Hz. The FRFs for two configurations are overlaid in Fig. 30.5. As can be seen, the first three modes were well excited and allow modal parameter estimation to be performed on the FRF to compute the frequency and damping values. The main drawback of this method is that it takes too long to obtain a good quality FRF with sufficient spectral resolution required at low frequencies at approximately 50 s per test. Performing the number of desired configurations was going to take too long and be too physically exhausting (Fig. 30.6).

30.3 Technical Approach

Based on the results obtained from preliminary testing, manual sine-dwell excitation of the mode with a free decay was determined to provide data in which a LSCE method and logarithmic decrement decay curve-fit could be employed to extract frequency and damping from the mode of interest.

For the LSCE method, free decay response (and impulse response) is described by an autoregressive model developed from finite difference Eq. (30.1), where k is the time step, m is the model order, α is model coefficient, and $y(t)$ is the system response at time t .

$$\sum_{k=0}^m \alpha_k y(t_{i+k}) = 0 \quad (30.1)$$

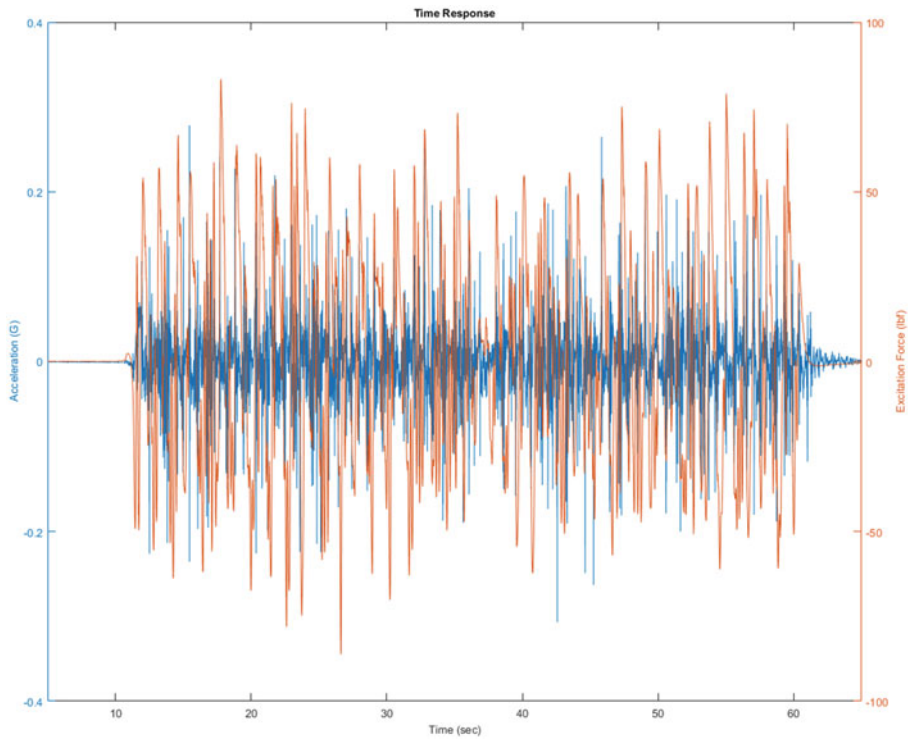


Fig. 30.4 Time domain of random manual input

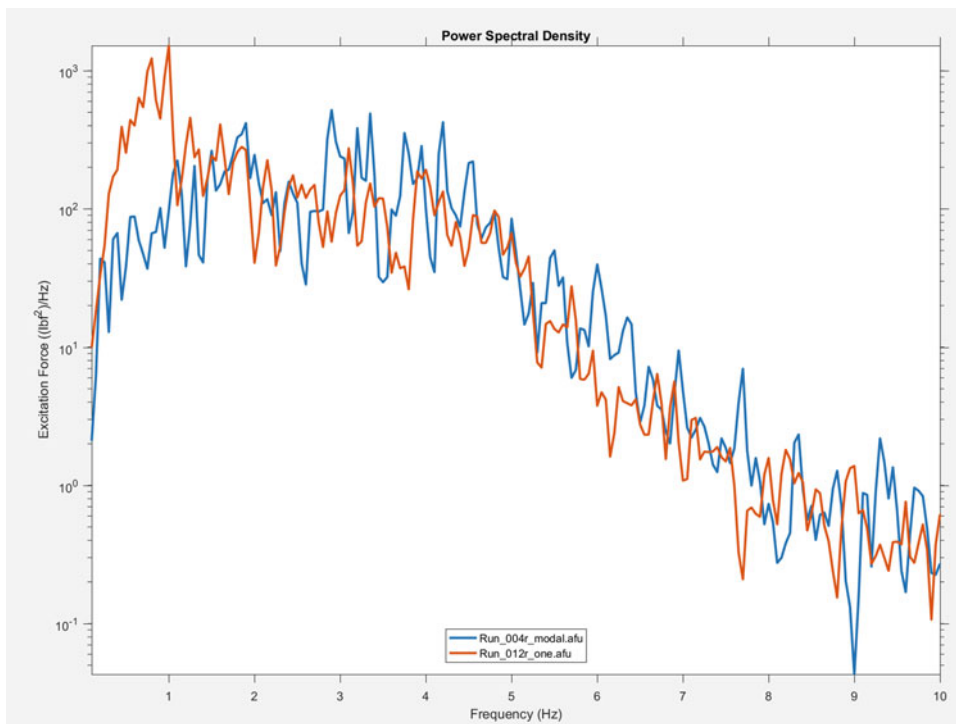


Fig. 30.5 Force autospectra computed from random input—two damper configurations shown

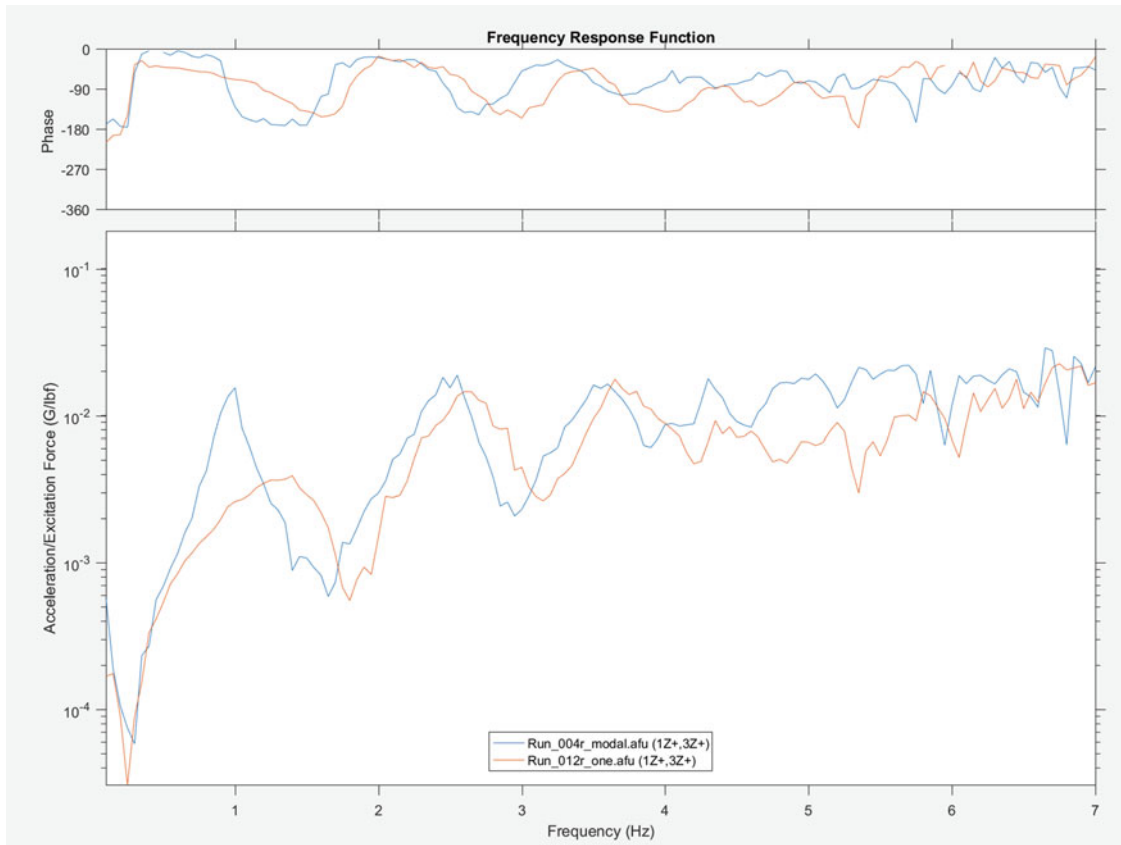


Fig. 30.6 FRF computed from random input—two damper configurations shown

The poles in the z -domain are the roots of the polynomial (2), in which $z = Ae^{j\omega}$ where A is the magnitude of z , j is the imaginary unit, and ω is the complex argument.

$$\sum_{k=0}^m \alpha_k z_r^k = 0 \quad (30.2)$$

To formulate a least-squares solution for the α -coefficients in Eq. (30.1), a known, i.e., b in $Ax = b$, is needed. Since the characteristic Eq. (30.2) is homogenous, i.e., equal to zero, you can divide the polynomial by any constant and its root will be the same. For example, you could divide by α_0 or α_m , which is the same as letting α_0 be equal to one or letting α_m be equal to one.

If $\alpha_0 = 1$ in Eq. (30.1), the least-squares solution for the α -coefficients is formulated from

$$\sum_{k=1}^m \alpha_k y(t_{i+k}) = -\alpha_0 y(t_i) = -y(t_i) \quad (30.3)$$

If $\alpha_m = 1$ in Eq. (30.1), the least-squares solution for the α -coefficients is formulated from

$$\sum_{k=0}^{m-1} \alpha_k y(t_{i+k}) = -\alpha_m y(t_{i+m}) = -y(t_{i+m}) \quad (30.4)$$

For the logarithmic decrement (δ) method, the natural log of the ratio of amplitudes of two successive peaks is first computed with Eq. (30.5), where n is an integer number of successive peaks, and used to compute the damping ratio (ζ) with Eq. (30.6).

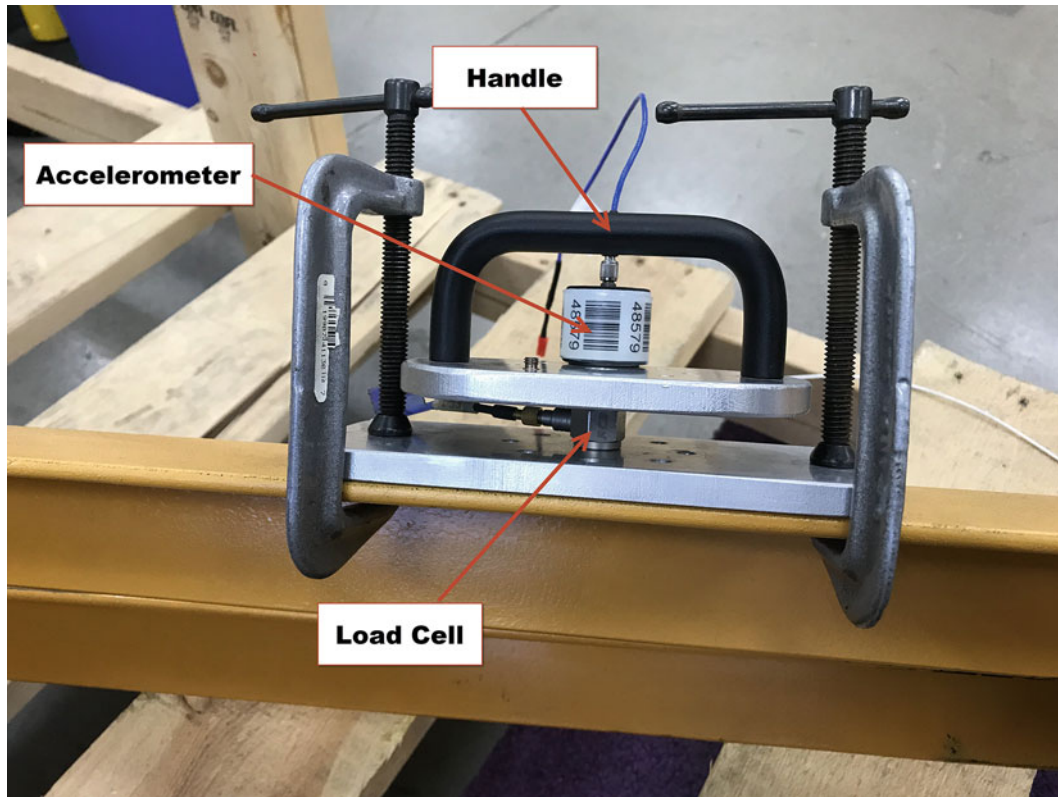


Fig. 30.7 Modal handle with integrated instrumentation

$$\delta = \frac{1}{n} \ln \frac{y(t)}{y(t + nT)} \quad (30.5)$$

$$\zeta = \frac{1}{\sqrt{1 + \left(\frac{2\pi}{\delta}\right)^2}} \quad (30.6)$$

30.4 Experimental Approach

Two ATA test engineers performed the damping characterization tests. In total, over eighty configurations were tested, which included different types of dampers and installed geometry as well as different angles of the test article. The dampers used in the test were either load-limiting or progressive dampers.

A steel bar was attached to allow a lever arm to excite the test article mode of interest. The modal handle was clamped to the end of the steel bar, allowing the load from the manual excitation to be measured as shown in a mock-up in Fig. 30.7. To measure the response of the structure, ATA installed several PCB 393B04 seismic accelerometers to measure the response of the structure at low frequencies.

All instrumentation was connected to a twelve-channel Brüel & Kjær LAN-XI 3053B120 data acquisition module. I-deas[®] for test software and ATA's IMAT[™] software were run on the data acquisition laptop to acquire all time histories and perform data postprocessing.

A review of the accelerometer data during the free decay of the mode showed the mode of the test article to be highly nonlinear with amplitude, with the frequency decreasing and damping increasing as amplitude increased. This behavior was expected, as the greater amplitude of response provides the displacement/velocity of the dampers necessary to get a sufficient damping reaction force. At lower amplitudes, the dampers are not being exercised sufficiently and therefore are not as effective as dampers, but they do provide additional effective stiffness to the system, which increases the modal frequency.

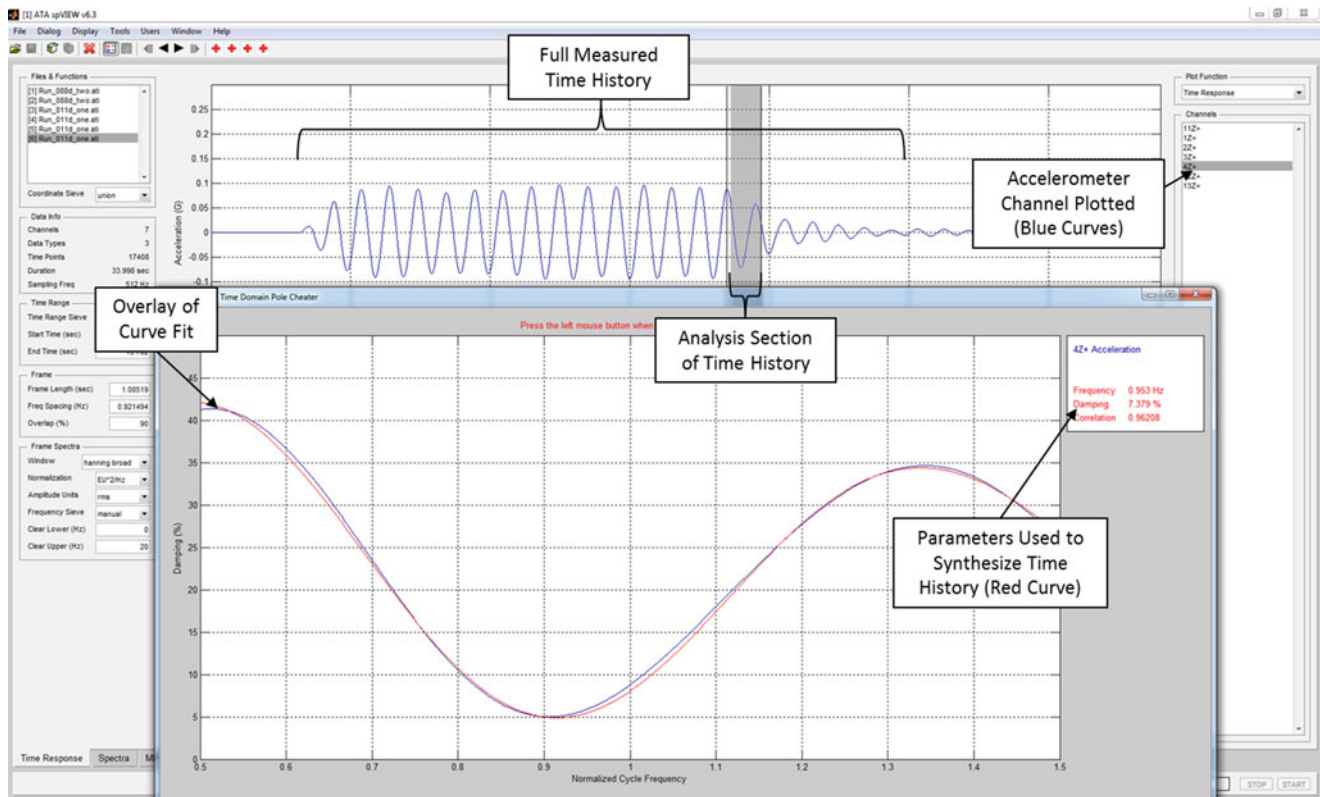


Fig. 30.8 Overview using logarithmic decrement decay

The damping values at the higher amplitude levels were of more interest than the lower amplitude response. At higher effective damping levels ($>10\%$ of critical), the response of the system has significant decay and within one cycle starts to exhibit the nonlinear behavior, causing an increase in frequency and decrease in damping. For these higher damping levels, the LSCE and logarithmic decrement methods are restricted to only a small frame of the time history to essentially linearize the system. The time slice used was immediately after the sinusoidal load was removed from the system and before there was any significant change in frequency and damping from the nonlinearity. This period was typically approximately within a single cycle. For the LSCE method, the autospectrum of a single accelerometer response was computed utilizing 90% overlap processing. For each frame of data, the poles were computed based on Eq. (30.3) or (30.4), providing slightly different estimates of the poles in which frequency and damping were determined. Estimates using Eq. (30.3) are listed in the result tables as LSCE 0, whereas estimates using Eq. (30.4) are listed as LSCE M. The logarithmic decrement approach used Eqs. (30.5) and (30.6) as an initial estimate; however, the frequency and damping value was typically modified to provide a best fit for the measured accelerometer data.

There were approximately eighty configurations tested using a manual sine-dwell and decay method using the modal handle. Each of these test configurations varied in number of dampers, type of damper, geometry of the damper, and orientation of the test article. Figure 30.8 shows the logarithmic decrement analysis process. The load cell was used to verify when the load was removed to start the decay response. The initial response was selected for analysis. The computed response was then overlaid with the measured response to verify values of frequency and damping. An example of a highly damped response is shown in Fig. 30.9, and a lightly damped response is shown in Fig. 30.10.

The same data was then used for both of the LSCE method conditions discussed, Eqs. (30.3) and (30.4). The LSCE utilizes the autospectrum of the response, and utilizing 90% overlap signal processing, the poles were computed for each frame of data. A similar approach was required as used in the logarithmic estimates by using the very beginning of the decay response as shown in Fig. 30.11. A pole density diagram [2] was used to plot the slightly different estimates of the poles. The idea behind the pole density diagram is that the poles corresponding to the underlying dynamics of the system will be repeatedly estimated for successive model orders and timeframes. And while these multiple pole estimates will not have exactly the same frequency and damping values, the system poles should form a high-density cluster on the pole density diagram. The remaining poles generated by the overdetermined parameter estimation model are computational poles, which are attributable to noise in the measured data. These computational poles are not expected to be consistent for successive

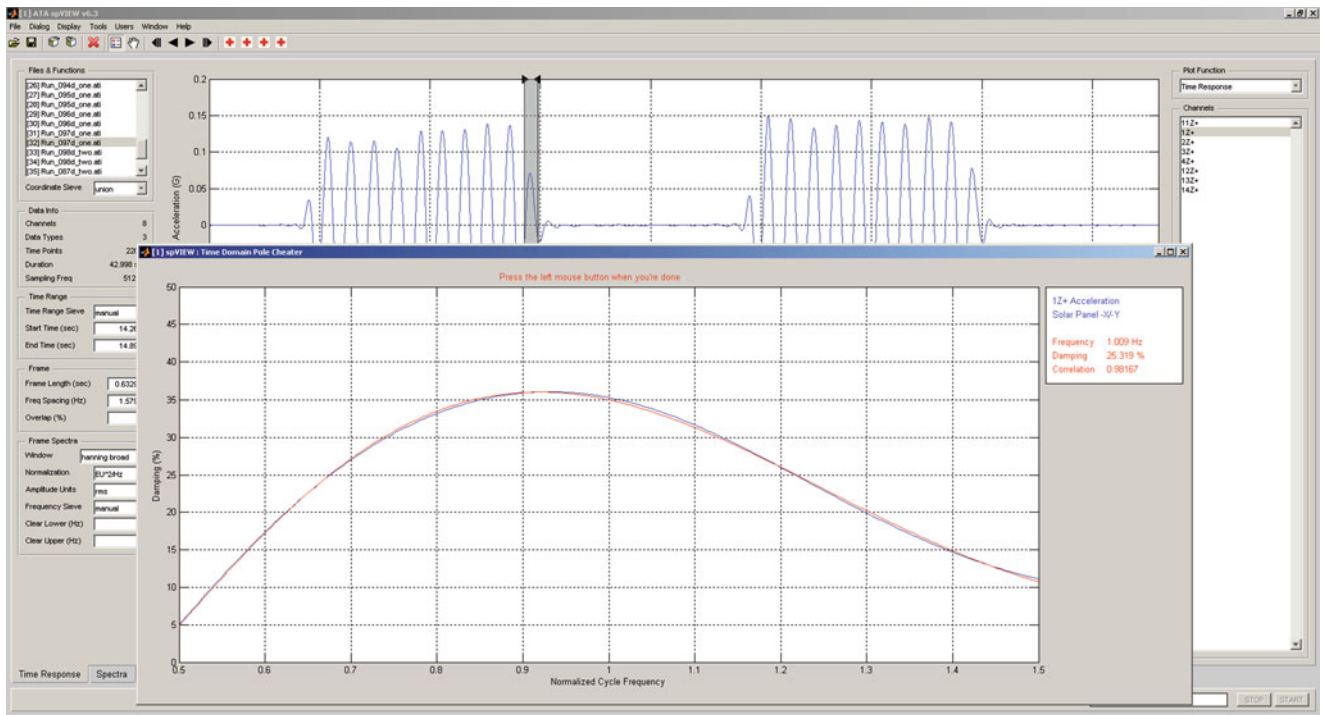


Fig. 30.9 Highly damped decay—25% C/Cc

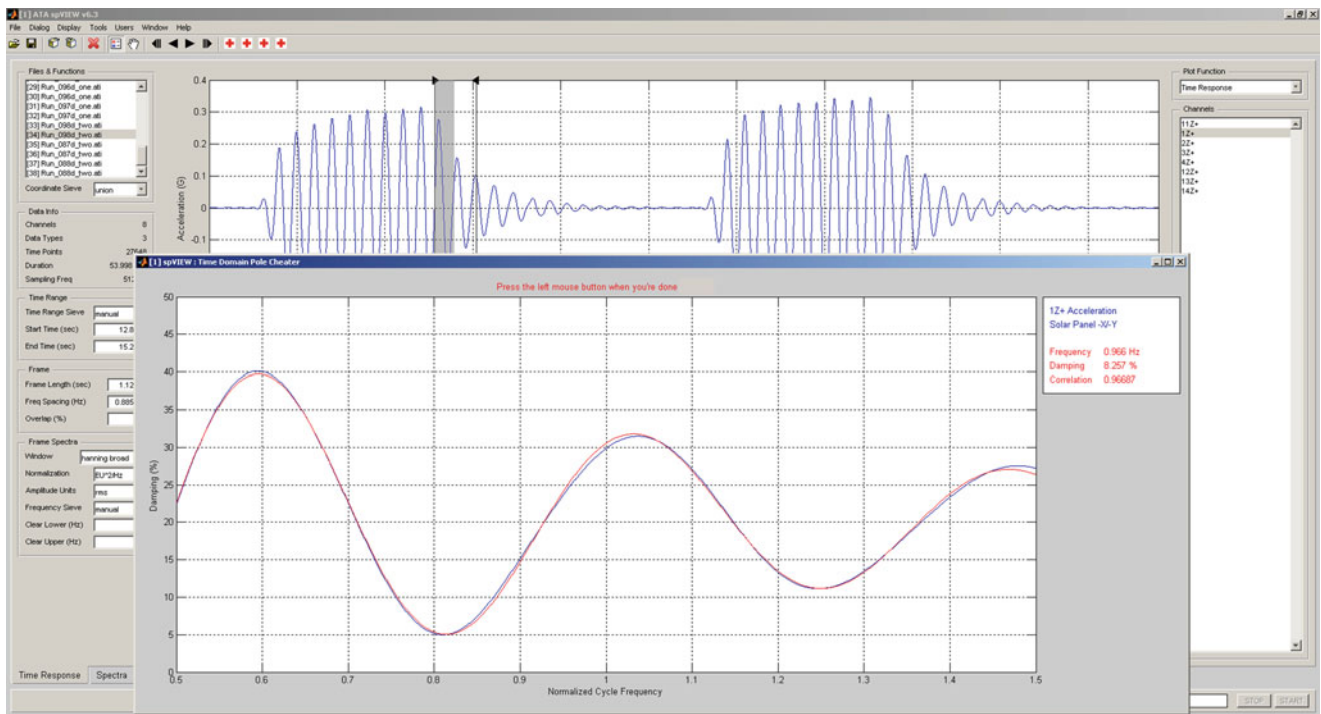


Fig. 30.10 Lightly damped decay—8% C/Cc

model orders and timeframes and should have a low density [3]. A best estimate was used from the pole density, and the frequency and damping were determined. An example of the pole density is shown in Fig. 30.12. Zooming in on the pole cluster of interest and selecting the best estimate of the frequency and damping values is shown in Fig. 30.13. Results are reported as the average frequency and damping in the cluster along with the standard deviations.

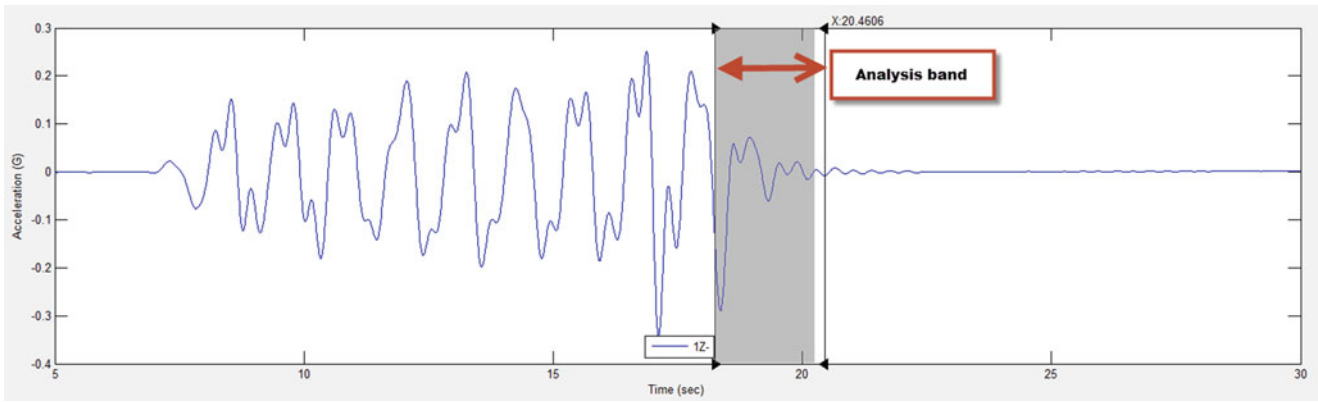


Fig. 30.11 Accelerometer response analysis band for decay response using LSCE



Fig. 30.12 Pole density diagram from LSCE estimates

30.5 Test Results

All eighty damper configurations are summarized with the frequency and damping values in Table 30.1. The LSCE method tends to have less deviation in the estimates than the logarithmic decrement method shown in Fig. 30.14, which shows the damping estimate comparison for the eighty test cases. The greater consistency in results obtained from the LSCE method may be due to this method’s utilization of averaging over the time history, whereas the log decrement only contains a single estimate that is likely affected by the inherent nonlinearity of the system. Increased deviation from the trend line of the estimates obtained from the logarithmic decrement method is prevalent with damping values above 15%, in which the structures start exhibiting highly nonlinear behavior at these damping levels.

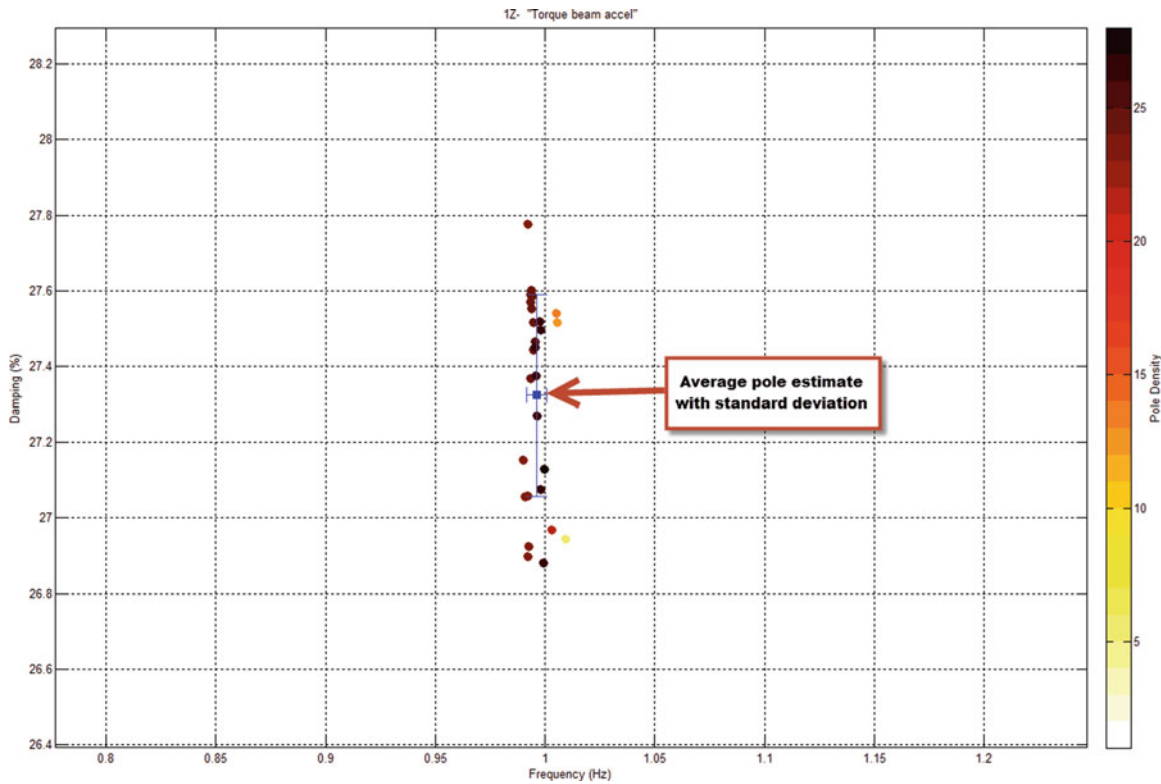


Fig. 30.13 Selected pole cluster for damping and frequency

30.6 Summary

A modal handle was developed to induce a large deflection response at low frequency to excite the first natural mode of a structure. This simple method allowed quick and easy setup instead of utilizing a large displacement shaker, which can be expensive, large, and difficult to set up and maneuver. The manual dwell and decay technique was successfully implemented to evaluate many damper configurations quickly with a variety of damping values ranging from 4% to 35% of critical. Two analytical techniques were used to calculate the natural frequencies and damping of the decayed response. A LSCE method was applied with two different initial conditions and a logarithmic decrement method was used and compared. The LSCE method produced more consistent results compared to the log decrement method. Random excitation using the modal handle was also verified; however, due to the number of test configurations required, it was determined that this method would take too long and require excess amounts of energy exertion.

Table 30.1 Summary of frequency and damping estimates

ATA Testing							ATA Testing						
Test Case	LSCEO Freq (Hz)	LSCEO Damping (% Crit)	LSCEM Freq (Hz)	LSCEM Damping (% Crit)	Log Dec Freq (Hz)	Log Dec Damping (% Crit)	Test Case	LSCEO Freq (Hz)	LSCEO Damping (% Crit)	LSCEM Freq (Hz)	LSCEM Damping (% Crit)	Log Dec Freq (Hz)	Log Dec Damping (% Crit)
1	1.00	5.61	1.00	5.66	1.00	5.80	41	1.13	20.86	1.12	21.28	1.20	20.84
2	0.98	5.83	0.98	5.87	0.99	5.31	42	1.16	21.35	1.16	21.38	1.24	20.92
3	0.97	5.91	0.96	6.21	0.98	5.47	43	1.19	21.36	1.19	22.29	1.19	22.21
4	0.99	6.14	0.99	6.14	0.99	5.64	44	1.22	21.67	1.22	21.80	1.23	23.34
5	0.97	6.34	0.97	6.34	0.98	5.88	45	1.09	22.01	1.09	22.07	1.11	21.57
6	0.97	6.57	1.00	6.90	0.98	6.20	46	1.05	22.24	1.05	21.52	1.04	21.00
7	0.95	6.91	0.95	6.87	0.97	6.85	47	1.50	22.25	1.50	22.24	1.41	24.14
8	2.51	7.05	2.51	7.12	2.43	6.68	48	1.08	22.77	1.08	22.79	1.17	21.97
9	0.97	7.11	0.96	7.16	0.94	7.33	49	1.10	23.08	1.12	22.93	1.18	21.81
10	0.96	7.67	0.96	7.86	0.97	7.73	50	1.24	23.40	1.25	23.42	1.35	21.56
11	1.00	7.89	1.01	7.73	1.01	8.22	51	1.22	23.69	1.21	22.97	1.43	24.95
12	2.46	7.93	2.47	8.15	2.41	9.43	52	1.12	23.72	1.13	22.17	1.19	22.45
13	0.95	8.32	0.95	8.13	0.96	8.21	53	1.00	24.01	1.00	24.63	1.00	25.31
14	0.96	8.62	0.96	8.49	0.96	9.58	54	1.11	24.21	1.11	24.05	1.16	23.58
15	1.07	8.98	1.08	8.40	1.06	9.35	55	1.10	24.30	1.10	24.17	1.14	24.55
16	0.99	9.24	1.00	9.58	1.01	9.10	56	1.18	24.40	1.18	24.92	1.17	24.03
17	1.02	11.26	1.02	12.61	1.00	11.44	57	1.17	24.78	1.19	24.56	1.25	22.21
18	1.05	11.50	1.06	11.31	1.03	11.52	58	1.13	24.89	1.13	24.99	1.20	24.87
19	1.04	13.27	1.04	13.22	1.05	12.33	59	1.32	25.82	1.33	25.68	1.32	26.97
20	1.05	13.40	1.05	13.44	1.08	12.89	60	1.21	25.85	1.21	25.79	1.31	23.18
21	1.03	14.57	1.03	14.49	1.06	14.51	61	1.25	25.87	1.25	26.95	1.41	21.72
22	1.15	15.50	1.16	15.26	1.08	16.12	62	1.11	26.06	1.12	26.46	1.12	27.61
23	1.07	15.99	1.07	16.02	1.07	14.91	63	1.45	26.07	1.45	26.41	1.32	27.69
24	1.27	16.00	1.27	16.02	1.26	18.15	64	1.39	26.10	1.41	25.81	1.48	25.51
25	1.13	16.05	1.13	16.27	1.24	16.52	65	1.35	26.36	1.37	26.72	1.62	24.22
26	1.13	16.54	1.13	16.62	1.13	15.31	66	1.21	26.46	1.21	26.69	1.28	25.03
27	1.15	16.73	1.15	16.66	1.20	16.20	67	1.08	26.60	1.08	26.67	1.11	28.01
28	1.29	16.80	1.27	15.70	1.20	18.14	68	1.13	26.73	1.13	26.80	1.13	25.27
29	1.11	17.77	1.12	17.99	1.20	17.09	69	1.26	26.92	1.27	26.91	1.21	27.21
30	1.19	18.23	1.19	18.27	1.28	16.42	70	1.34	27.28	1.35	27.58	1.28	27.05
31	1.17	18.39	1.17	18.43	1.23	17.97	71	1.24	27.46	1.22	28.75	1.14	26.64
32	1.08	18.90	1.07	18.30	1.14	19.18	72	1.11	27.80	1.10	27.83	1.16	27.05
33	1.11	19.35	1.10	18.94	1.08	20.88	73	1.29	28.32	1.28	28.24	1.30	25.03
34	1.12	19.45	1.12	19.88	1.10	18.70	74	1.25	29.63	1.26	30.73	1.32	28.42
35	1.18	20.11	1.18	20.17	1.32	20.56	75	1.28	29.68	1.29	29.57	1.23	29.71
36	1.78	20.32	1.78	20.16	1.62	20.39	76	1.30	29.91	1.31	29.52	1.16	31.97
37	1.26	20.36	1.27	19.78	1.16	16.97	77	1.33	30.17	1.33	30.63	1.29	26.50
38	1.10	20.41	1.10	20.45	1.26	21.24	78	1.12	30.67	1.14	30.21	1.18	29.14
39	1.06	20.70	1.06	20.89	1.10	19.22	79	1.23	31.54	1.24	31.70	1.31	27.13
40	1.03	20.76	1.03	21.04	1.06	22.13	80	1.25	32.27	1.27	33.92	1.27	34.16

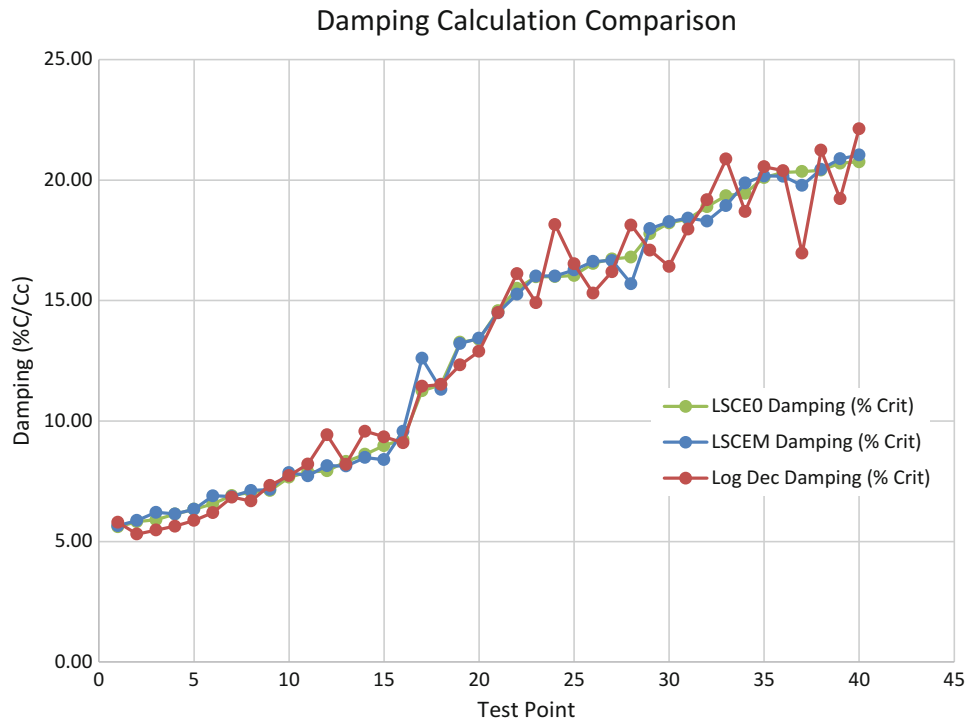


Fig. 30.14 Damping calculations for eighty test points

References

1. Brown, D.L., Allemang, R.J., Zimmerman, R.D., Mergeay, M.: Parameter estimation techniques for modal analysis. SAE Paper No. 790221. SAE Transactions **88**, 828–846 (1979)
2. Phillips, A.W., Allemang, R.J., Pickerel, C.R.: Clustering of modal frequency estimates from different solution sets. In: Proceedings, International Modal Analysis Conference, Society of Experimental Mechanics (SEM), pp. 501–514 (1994)
3. Fladung, W., and Vold, H.: An orthogonal view of the polyreference least-squares complex frequency modal parameter estimation algorithm. In: International Modal Analysis Conference (2015)

Chapter 31

Traveling Wave Generation on a Clamped, Thin Plate with Flush-Mounted Piezoelectric Actuators

Patrick F. Musgrave, Mohammad I. Albakri, and Pablo A. Tarazaga

Abstract Structural traveling waves have significant potential in applications such as propulsion and drag reduction. Using the two-mode excitation method, traveling waves which are both steady-state and open-loop controlled can be generated on various structures such as beams, plates, and cylinders. In order to develop this method further for applications such as drag reduction, more representative cases must be investigated. This work models and experimentally validates traveling waves generated on a thin, fully clamped plate with flush-mounted piezoelectric actuators. A two-step experimental modal analysis is conducted on a free and then clamped plate to validate and update a finite-element model of the plate. The finite element model, which has been developed in-house, accounts for piezoelectric actuators, pre-stresses in the plate, and non-ideal (elastic) clamped boundary conditions. The validated model is then used to compare experimental- and model-generated traveling waves.

31.1 Introduction

Structural traveling waves are those generated using the two-mode excitation method [1]. These traveling waves are steady-state and open-loop controlled and are excited by taking advantage of a structure's modal properties. They have enormous potential in a variety of areas, specifically fluid-structure applications such as propulsion and drag reduction [2] where the wave is capable of displacing the fluid. Traveling waves produced using the two-mode excitation method have distinct advantages over other traveling wave generation methods which have fixed operating conditions [3] or require closed-loop control [4]. The adaptability and ease of use of the two-mode excitation method has been proven through various studies. Traveling waves have been generated on beams [5], plates [6–8], and even circumferentially on cylinders [9]. This structural variability coupled with excitation via low-profile macro-fiber composite (MFC) piezoelectric actuators situates the two-mode method nicely for applications such as the aforementioned propulsion and drag reduction.

Two-mode excitation traveling waves have been modeled previously on a plate [6]; however, that study looked at free boundary conditions and used a plate with thickness significantly larger than the mounted MFCs. To further develop this method for actual applications, other boundary conditions must be modeled and thinner plates must be used so that more significant traveling wave amplitudes can be achieved. This study focuses on just that by taking the in-house finite-element model used by Malladi, et al. [6], and accounting for non-ideal (elastic) clamped boundary conditions, pre-stresses in the plate, and MFC actuators with thickness similar to the plate. The model parameters are updated in two steps: first, to match experimental modal data from a plate with free boundary conditions, then to match experimental modal data from a clamped plate. Traveling waves are then generated using the updated model and compared to those generated experimentally. With a fully validated model, future studies can be undertaken to investigate the effects of multi-actuator traveling waves without the need for time intensive experimental testing.

31.2 Modal Analysis

The plate to be experimentally tested and then modeled is an $8 \times 12 \times \frac{1}{64}$ in ($304.8 \times 203.2 \times 0.397$ mm) aluminum plate with ten macro fiber composite (MFC) piezoelectric actuators epoxied to the underside. The underside of the clamped plate is shown in Fig. 31.1a, where all ten actuators and the spacer bar used for the clamped boundary are visible. This plate is

P. F. Musgrave (✉) · M. I. Albakri · P. A. Tarazaga
Department of Mechanical Engineering, Virginia Tech, Blacksburg, VA, USA
e-mail: pfm@vt.edu

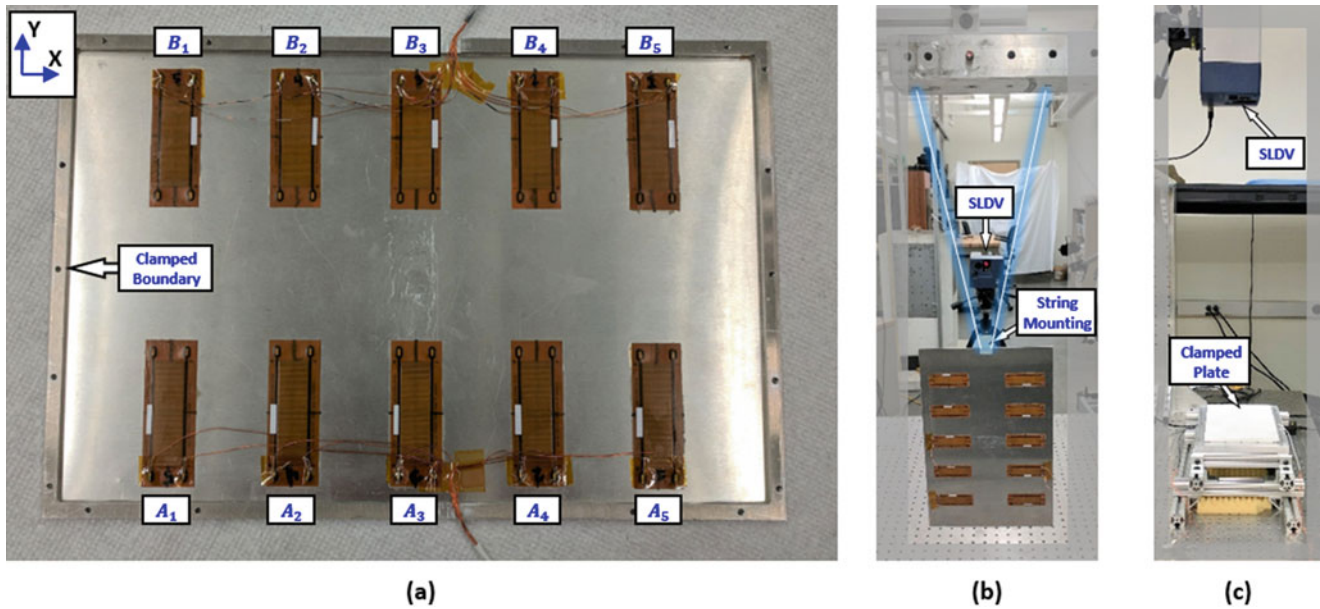


Fig. 31.1 (a) Underside of the clamped aluminum plate with ten MFC Actuators and the clamped boundary shown, (b) testing conditions of free plate with mounting strings highlighted, and (c) testing of clamped plate

Table 31.1 The model parameters of the plate and MFCs used to match the free plate to the experimental data

Plate properties					MFC properties			Plate stress	
L [mm] (in)	W [mm] (in)	h [mm]	E [GPa]	ρ $\frac{\text{kg}}{\text{m}^3}$	h_{MFC} [mm]	E_{MFC} [GPa]	ρ_{MFC} $\frac{\text{kg}}{\text{m}^3}$	σ_x [kPa]	σ_y [kPa]
307.34 (12.1)	200.66 (7.9)	0.397	69	2700	0.31	31	4000	170	0

modeled using an in-house finite element model, and the parameters are updated in a two-step modal analysis process. In the first step, the model is manually updated to match experimental modal data of a plate with free boundary conditions. This serves to update the material properties of both the plate and the MFCs and also the residual stresses in the plate. In the second step, the model is matched to experimental modal data from the same plate, but with clamped boundary conditions. This procedure focuses on updating the non-ideal clamped boundary conditions.

The experimental modal analysis of the free boundary condition plate is shown in Fig. 31.1b, where the plate is suspended using strings. The plate in Fig. 31.1b is the same as that in Fig. 31.1a, except without the spacer bar used to produce clamped boundary conditions. The frequency response of the free plate is experimentally determined by exciting a single actuator (B_4) and measuring the response using a Polytec scanning laser doppler vibrometer (SLDV). The frequency response is then analyzed using Siemens LMS modal analysis package in order to extract the mode shapes and natural frequencies of the plate.

The parameters of the free plate in the finite element model were then manually updated to match the experimental results. For the first 15 modes, the natural frequencies match within $\pm 4\%$ of the experiment. In addition, the modal assurance criterion (MAC) values are predominately >0.9 but with a couple of modes close to 0.7. The final updated model parameters are shown in Table 31.1. The length and width were adjusted slightly from the nominal values, and the MFC piezo properties are those given by Shahab [10]. Finally, axial stresses were implemented in the model to account for residual stresses in the plate; these were most likely introduced during the metal rolling process. Modeling for the stresses was necessary due to the significant effect they had on the lower natural frequencies and mode shapes.

These parameters from the free analysis were then utilized for a modal analysis of the clamped plate. The clamped experimental setup is shown in Fig. 31.1c and its modal properties were extracted using the same methods as before. Since the material properties of the plate and MFCs were determined in the free analysis, the primary focus when matching the clamped model was the boundary condition parameters. This included the vertical stiffness, k_z , and the rotational stiffness about the axis of the clamp, k_R (x -axis for top and bottom and y -axis for left and right sides in Fig. 31.1a). In addition, the stresses in the plate were adjusted from the free case, since variations occurred in the process of epoxying the clamp to the free plate.

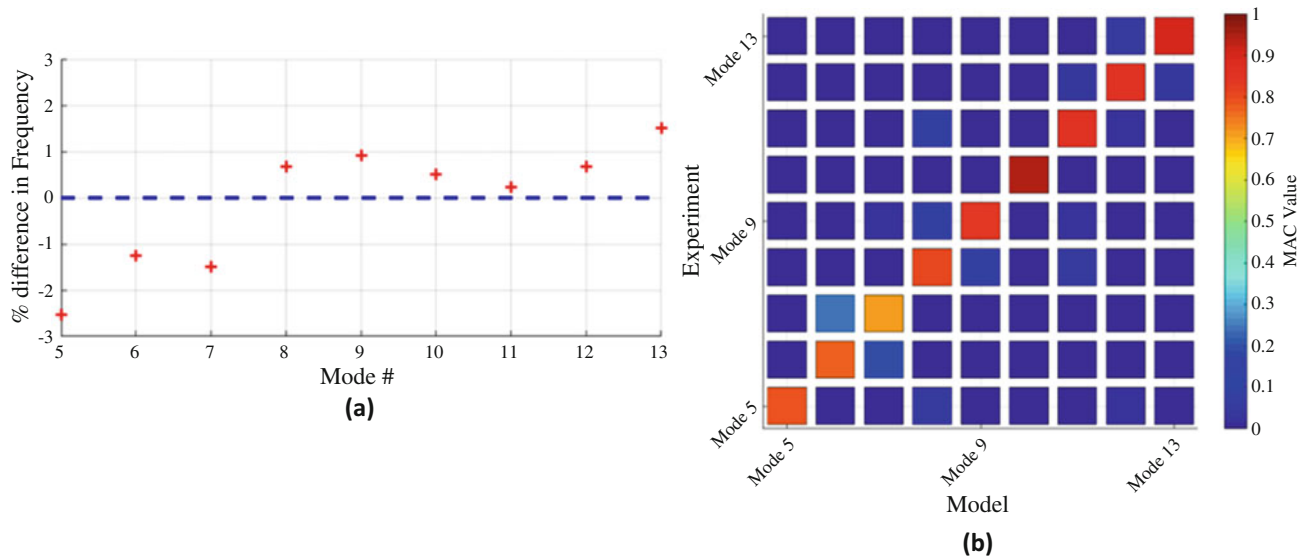


Fig. 31.2 Comparison between the clamped model and experiment for the (a) frequencies and (b) MAC values

Table 31.2 The model parameters used to match the clamped plate to the experimental data

Plate properties			Plate stress		Boundary conditions	
L [mm] (in)	W [mm] (in)	h [mm]	σ_x [GPa]	σ_y [kPa]	k_z $\left[\frac{\text{N}}{\text{n}} \right]$	k_R $\left[\frac{\text{N}}{\text{rad}} \right]$
292.10 (11.5)	190.50 (7.5)	0.397	300	100	5000	10

Only traveling waves within a particular range are of interest in this model; thus, modes 5–13 ($\approx 200 - 500$ Hz) are the only ones presented here. Figure 31.2 shows the comparison between the clamped model and the experiment. When comparing the natural frequencies (Fig. 31.2a), there is only a $\pm 2.5\%$ difference between the model and experiment. In terms of MAC values (Fig. 31.2b), there is no significant correlation between orthogonal modes; in addition, the correlated mode shapes (diagonals) have $MAC \geq 0.7$. The updated clamped model parameters are shown in Table 31.2, where those not listed are the same as those in Table 31.1. The length and width were adjusted from the free case (Table 31.1) since adding the bar for the clamped boundary conditions removes 0.5 in from both the length and width. The experimental clamped boundaries are not ideal and contain some elasticity ($k_z \neq k_R \neq \infty$), so they were modeled using the finite stiffnesses shown in Table 31.2.

31.3 Traveling Wave Generation

With the clamped plate model fully updated, experimental and model generated traveling waves were compared. Figure 31.3 shows progressive time steps of a 310 Hz traveling wave generated experimentally on the clamped plate using the two-mode excitation method with actuators A_3 and B_3 (Fig. 31.1a). By following a single peak through the time steps, the traveling wave propagation is visible. Figure 31.4 shows a side by side comparison of the traveling waves generated experimentally and via the validated model. This figure displays the root-mean-square (rms) velocity of the traveling wave over an entire period; Fig. 31.4a shows the rms velocity of Fig. 31.3. In addition, the area containing the traveling wave has been highlighted and the propagation direction shown. The correlation between the model and experimental traveling waves can be determined by calculating the MAC value between their complex velocities. Although it is common to use the MAC for eigenvectors and operational deflections shapes, this approach here yields a comparison of the modeled and experimental traveling waves at a given instance. Here, $MAC \approx 0.75$, between the model and experimental traveling waves, signifying a strong correlation.

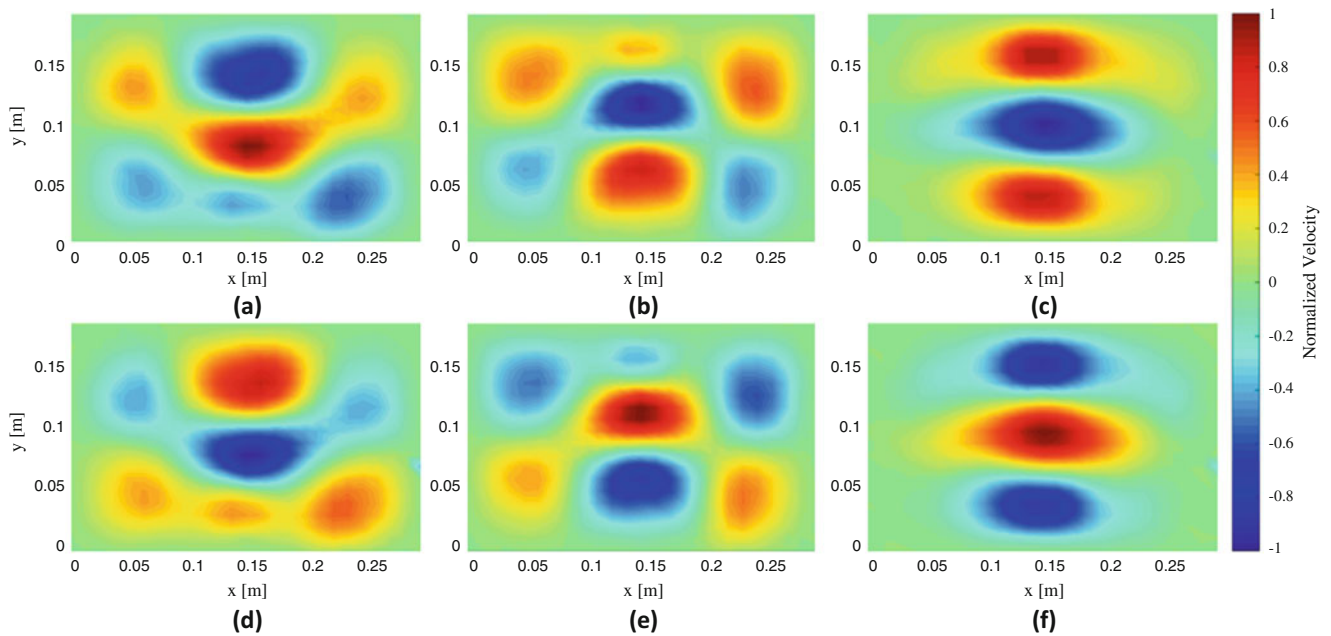


Fig. 31.3 Experimentally generated traveling wave at 310 Hz shown at progressive time steps within a single period of the wave: (a) $\frac{T}{6}$, (b) $\frac{2T}{6}$, (c) $\frac{3T}{6}$, (d) $\frac{4T}{6}$, (e) $\frac{5T}{6}$, (f) $\frac{6T}{6}$

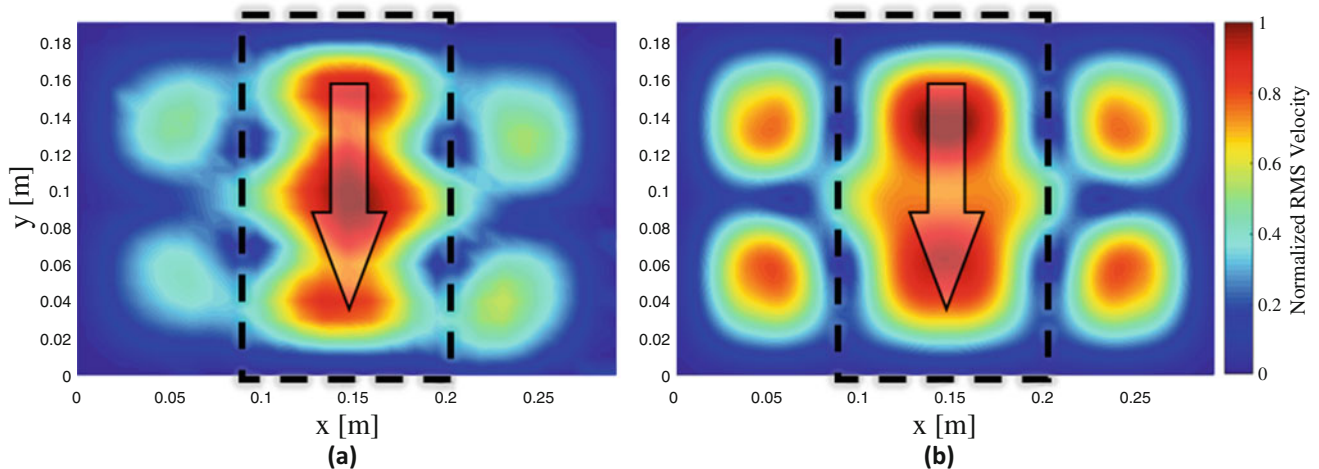


Fig. 31.4 The normalized RMS velocities of a 310 Hz traveling wave generated (a) experimentally and (b) via the model

31.4 Conclusion

A finite-element model was developed to model a thin, fully-clamped plate with flush-mounted MFC piezoelectric actuators. The model was updated in a two-step process to match the free and clamped plate. The first step accounted for the material properties of the plate and the MFCs and also the residual stresses in the plate. The second step updated the model to match the non-ideal clamped boundary conditions and also pre-stresses in the plate produced during clamping. Using this validated model, traveling waves were generated with the two-mode excitation method and then successfully correlated with experimentally generated waves. With the aid of this fully validated model, traveling waves can be quickly generated in the model instead of relying on time intensive experimental testing. Thus, this model can be utilized to investigate the effects of traveling wave excitation using multiple pairs of actuators.

Acknowledgement The authors acknowledge the support of the Air Force Office of Scientific Research through the 2015 Young Investigator Program under the AFOSR Grant FA9550-15-1-0198. Dr. Tarazaga would also like to acknowledge the financial support of the John R. Jones Faculty Fellowship.

References

1. Loh, B.-G., Ro, P.I.: An object transport system using flexural ultrasonic progressive waves generated by two-mode excitation. *IEEE Trans. Ultrason. Ferroelectr. Freq. Control.* **47**(4), 994–999 (2000)
2. Musgrave, P.F., Tarazaga, P.A.: Skin friction drag reduction in turbulent flow using spanwise traveling surface waves. In: *SPIE Smart Structures and Materials C Nondestructive Evaluation and Health Monitoring*. International Society for Optics and Photonics <https://www.spiedigitallibrary.org/conference-proceedings-of-spie/10164/101640L/Skin-friction-drag-reduction-in-turbulent-flow-using-spanwise-traveling/10.1117/12.2260295.full?SSO=1> (2017)
3. Kuribayashi, M., Ueha, S., Mori, E.: Excitation conditions of flexural traveling waves for a reversible ultrasonic linear motor. *J. Acoust. Soc. Am.* **77**(4), 1431–1435 (1985)
4. Tanaka, N., Kikushima, Y.: Active wave control of a flexible beam: proposition of the active sink method. *JSME Int. J.* **34**(2), 159–167 (1991)
5. Avirovik, D., et al.: Theoretical and experimental correlation of mechanical wave formation on beams. *J. Intell. Mater. Syst. Struct.* **27**(14), 1939–1948 (2016)
6. Malladi, V.V.S., Albakri, M., Tarazaga, P.A.: An experimental and theoretical study of two-dimensional traveling waves in plates. *J. Intell. Mater. Syst. Struct.* **28**(13), 1803–1815 (2016)
7. Musgrave, P.F., Malladi, V.S., Tarazaga, P.A.: Generation of traveling waves in a 2D plate for future drag reduction manipulation. In: *Special Topics in Structural Dynamics*, Vol. 6, pp. 129–138. Springer. https://link.springer.com/chapter/10.1007/978-3-319-29910-5_13 (2016)
8. Musgrave, P.F., Malladi, V.S., Tarazaga, P.A.: Investigation into the superposition of multiple mode shape composed traveling waves. In: *SPIE Smart Structures and Materials+Nondestructive Evaluation and Health Monitoring*. International Society for Optics and Photonics <https://www.spiedigitallibrary.org/conference-proceedings-of-spie/10164/1016408/Investigation-into-the-superposition-of-multiple-mode-shape-composed-traveling/10.1117/12.2260323.full> (2017)
9. Phoenix, A., Malladi, S., Tarazaga, P.A.: Traveling wave phenomenon through piezoelectric actuation of a free-free cylindrical tube. In: *ASME Conference on Smart Materials, Adaptive Structures and Intelligent Systems*. Colorado Springs, Co. <http://proceedings.asmedigitalcollection.asme.org/proceeding.aspx?articleid=2481546> (2015)
10. Shahab, S., Erturk, A.: Electrohydroelastic Euler–Bernoulli–Morison model for underwater resonant actuation of macro-fiber composite piezoelectric cantilevers. *Smart Mater. Struct.* **25**(10), 105007 (2016)

Chapter 32

Experimental Modal Analysis of an Aircraft Fuselage Panel: Part II

Travis A. Wyen, Ricardo A. Perez, Jonathan Knox, Joshua J. Schoettelkotte, and Thomas G. Eason

Abstract Hypersonic aircraft structures must operate in complex loading conditions and very high temperatures, making the design of a robust and reusable platform very challenging. An analytical and experimental test program was developed by the Air Force Research Laboratory (AFRL) and industry. The objective of the program is to review the design process of a thin skinned aircraft panel subjected to combined thermal-acoustic-mechanical loading, through a series of laboratory experiments at the AFRL's Structural Dynamics Laboratory.

This paper is a continuation of previously presented work on a series of modal tests, performed to characterize the dynamics of a hat-stiffened fuselage panel designed by industry. In the previous work the modal test was performed under free-free boundary conditions. In order to assess the effect of the operating boundary conditions on the modal parameters, a roving impact test was performed after its installation in the Combined Environment Acoustic Chamber (CEAC) facility at AFRL. The article and fixture supports were instrumented in order to assess the effect of the support system. A description of the modal test will be included in the paper along with a discussion of the data obtained.

32.1 Introduction

Typical modelling approaches superpose the worst possible loading conditions to obtain a conservative design. The use of this design paradigm to structures operating in extreme environments can lead to an extremely high structural mass, which could severely shorten the duration of a mission. On the other hand, less conservative approaches could lead to unacceptable uncertainties in the life prediction of the aircraft structure [1]. In order to develop modeling techniques that can lead to accurate predictions of the aircraft structure with a reduced structural mass, an analytical and experimental test program was developed by the Air Force Research Laboratory (AFRL) and industry. The primary objective of this testing is to expose the panel to multiple single and combined environments loading (aero/mechanical loads, acoustic loads and thermal loads) in order to verify the analysis methods currently being used by industry to develop high-speed vehicles.

The work presented in this paper is a continuation of a series of modal tests conducted to determine and characterize the natural frequencies, mode shapes, and damping of the panel [2]. The first series of modal tests were performed using free-free boundary conditions, before and after instrumentation for the combined environment test was installed. In this work, a modal test of the panel under operating boundary conditions was performed using a roving hammer measurement approach. This data was used to perform a final update of the finite element model (FEM) of the panel. In addition, the modal data will be used to evaluate the health of the panel during the combined environment test campaign.

Figure 32.1a shows the panel in free-free condition, and Fig. 32.1b–d show different views of the panel after it was installed in the CEAC. The test article was designed to respond mechanically, thermally, and dynamically like the section of interest in a generic aircraft model. In order to apply the proper boundary conditions, similar to those the test panel would see on the flight vehicle, the test fixtures were designed to constrain the panel according to the diagrams shown in Fig. 32.2. The x -direction is parallel to the longerons; the y -direction is parallel to the bulkheads; and the z -direction is perpendicular to the top of the outer mold line (OML). The middle supports attached to the center bulkhead (see Fig. 32.1a) were design to restrict translation in the x - and z -directions and rotation in the y - and z -directions. All of the attachments are pinned, one at

T. A. Wyen (✉) · J. Knox

Experimental Validation Branch, Aerospace Systems Directorate, Air Force Research Laboratory, Wright-Patterson AFB, OH, USA
e-mail: travis.wyen@us.af.mil

R. A. Perez · J. J. Schoettelkotte

Universal Technology Corporation, Dayton, OH, USA

T. G. Eason

Structural Sciences Center, Aerospace Systems Directorate, Air Force Research Laboratory, Wright-Patterson AFB, OH, USA

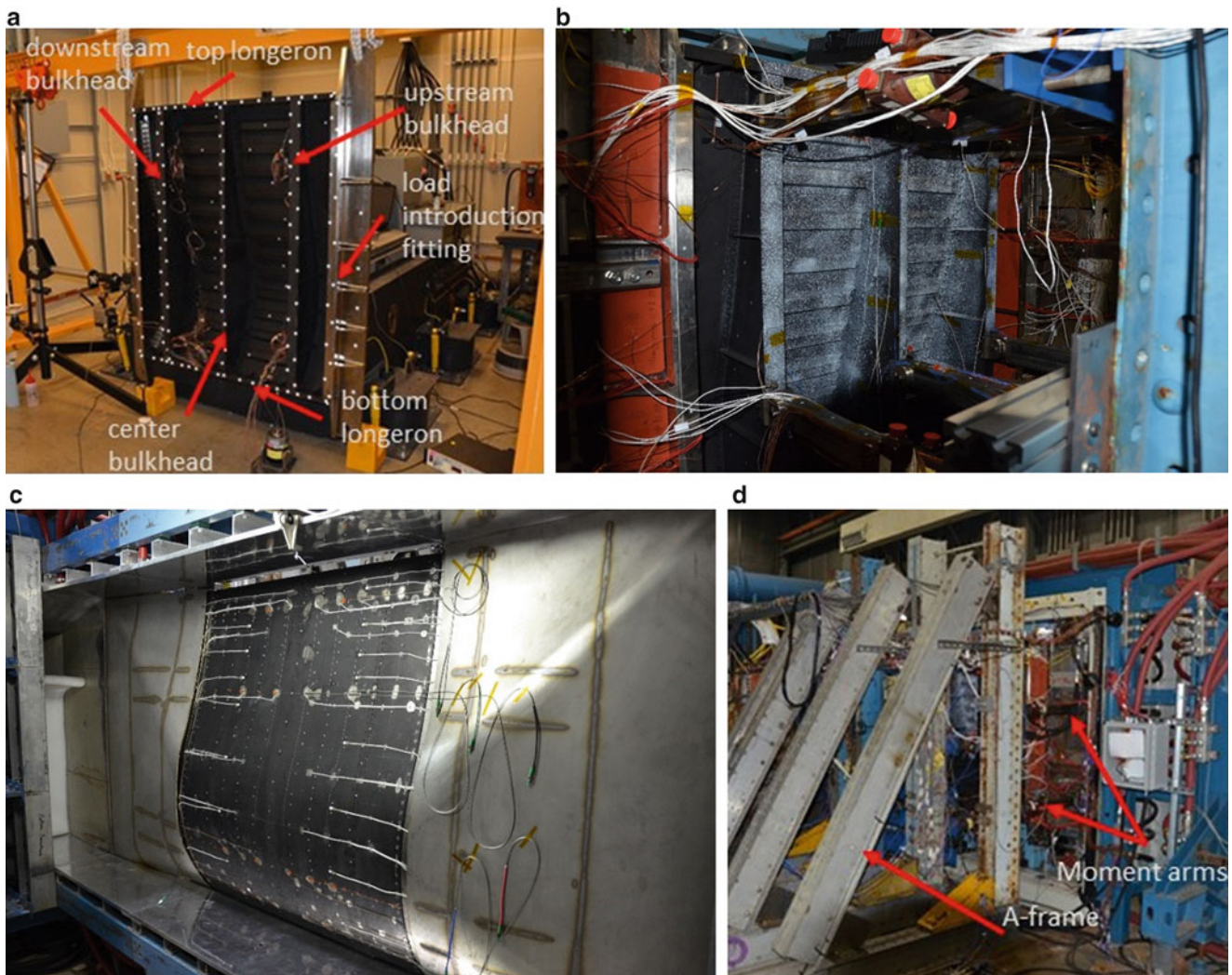


Fig. 32.1 Test specimen, (a) free-free condition, and fixtured in the test chamber, (b) view from the back, (c) view from the flow side, and (d) strong back fixture

the test article and one at the A-frame (see Fig. 32.1d) to apply the proper constraints. The center bulkhead of the test article is not a symmetrical structural member in that there is only a flange on the downstream side of the bulkhead. To ensure the load line maintains its symmetry, the attachment fitting on the bulkhead does not bear a load on the flange, only the web of the bulkhead is loaded. The bottom outboard supports attached to the bottom longeron were designed to restrict translation in the y - and z -directions and the rotation in the y - and z -directions. Each of the attachments are pinned to a fitting bolted directly to the bottom longeron and pinned to the fitting attached to the lower structural member of the mechanical input load reaction fixture. The z -direction constraint fixtures only fix the translation in the z -direction on the outer bulkheads in six positions, three on each bulkhead. The interface fitting bolted to the outboard bulkheads bears the load on the flange of the bulkhead to ensure the load is distributed evenly. A rod end with spherical bearings connects the tubing to the fitting to allow motion in all directions with the exception of the z -direction. A load cell is coupled to the fixture and strong back fixture to measure the reaction load at each location. In order to maintain in-plane loading, the bending moment of the test article must be restricted. Moment arm fixtures were designed to prevent the article from bending out of plane during the mechanical, thermal, and combined loading cycles. The fixture design is stiffness driven to help minimize deflections in the out-of-plane bending direction. The fixture is bolted in three locations to the load introduction fitting, pinned at the outboard location to a structural tube and coupled to a load cell to measure the reaction load.

The outline of this paper is as follows. Section 32.2 describes the test setup. The modal parameter estimation (MPE) approach is discussed in Sect. 32.3. Finally, a summary of the work presented can be found in the last section.

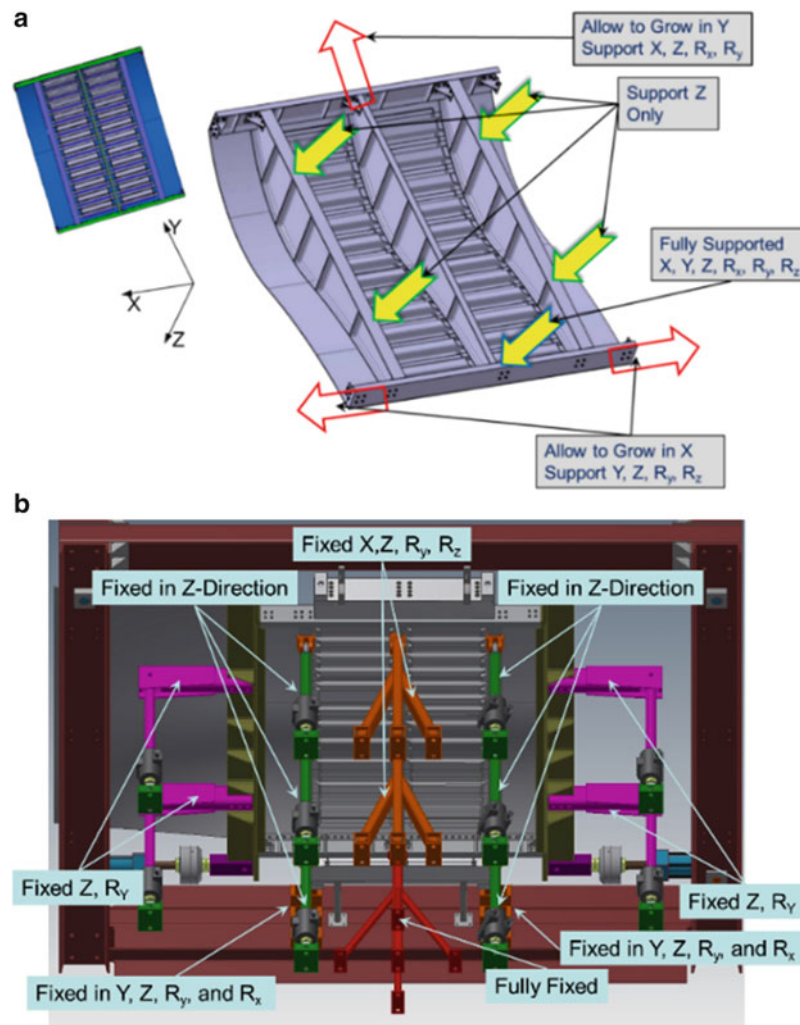


Fig. 32.2 Test specimen boundary conditions, (a) panel only, and (b) panel and constraint fixturing

32.2 Test Setup

The objective of this section is to describe the setup and procedure followed to conduct the modal test. Information on the instrumentation, data acquisition, and other details are presented. The University of Cincinnati Structural Dynamics Research Laboratory (SDRL) X-Modal 3 software was used for the data collection and for the estimation of the modal parameters of the panel. The ME'ScopeVES[®] software was used to build the wire-frame structure file and to create animations of the mode shapes.

As mentioned in the Introduction, a roving hammer modal test was conducted to estimate the modal parameters of the fixtured built-up panel shown in Fig. 32.1. The layout of the measurement grid on the test article was determined from a previous series of modal tests [2]. A total of 390 impact locations were chosen. From the impact locations, 27 reference tri-axial and 6 blocks of uniaxial accelerometers were selected. Four on the load introduction end fittings, four on the moment arms, one on each bottom support, thirteen on the A-frames, three on each bulkhead, one on the top longeron, and two on the outer mold line (OML). The reference layout on the test article is shown in Fig. 32.3.

A wire frame model was created in 3-D space using Nikon's MCAx II portable measurement system using the reference and impact locations. This model was imported into Vibrant Technologies ME'ScopeVES[®] software to create the structure file.

The data collection was performed using the X-Modal 3 software with a National Instruments front end. A National Instruments PXIe-1062Q hybrid chassis was used in conjunction with a PXIe-4499 data acquisition card. Based on experimentation with the accelerometers available, it was decided to keep the accelerometers with the highest sensitivity

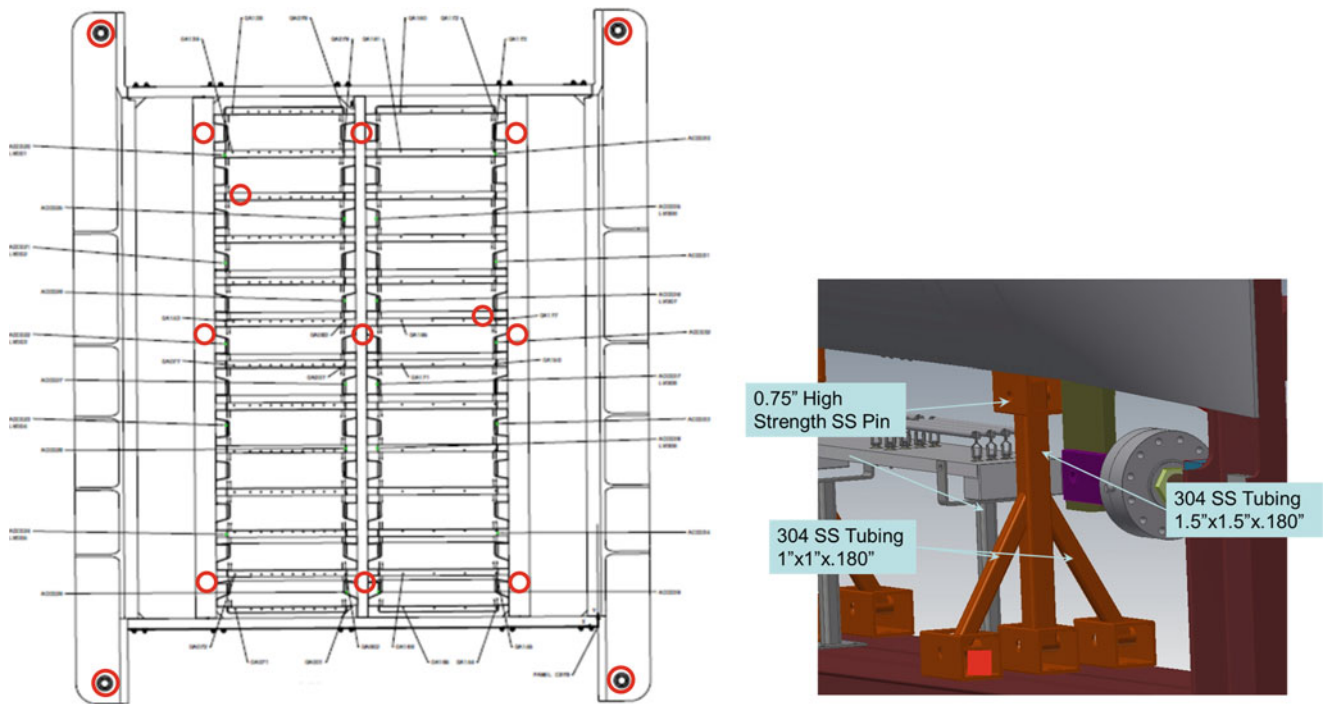


Fig. 32.3 Instrumentation layout

Table 32.1 Data acquisition parameters

Blocksize	6400
Time spacing	0.000625 s
Time block	4 s
Number of lines	2500
Frequency spacing	0.25 Hz
Frequency sampling	1600 Hz

on the test article. The nominal sensitivity of the accelerometers on the test article was 100 mV/g, while the sensitivity of the accelerometers on the A-frames and moment arms was 10 mV/g. Two PCB Hammers were used to perform the impacts, the PCB 086C03 (small hammer) and PCB 086D20 (big hammer). The nominal sensitivity of the small hammer was 10 and 1 mV/lbf for the big hammer. All sensors were powered using the PXIe-1062Q on-board IEPE output.

The data acquisition parameters shown in Table 32.1 were used throughout this test series. The frequency response function and coherence measurement were recorded at each impact location. A total of four impact measurements were linearly averaged per point. The measurement was triggered using the impact hammer using a pre-trigger set at 5% of the time block.

Initially, driving point measurements and several preliminary measurements were acquired to check the input, the frequency response, to ensure that the reciprocity criteria was met, to check measurement coherence, and collect data for model scaling. A quick linearity check was also performed at the driving points located on the bulkheads, which were a source of concern due to the potential for nonlinear damping from the joint connections to the A-frames, and the large amount of instrumentation wires around that area. Shown in Fig. 32.4 is the driving point measurement of the center point on the downstream bulkhead, the FRF and time history of the impact force are shown. Light impacts were performed using the big and small hammers, naturally, the impact force of the big hammer was slightly larger than twice the input from the small hammer. The effect of the larger input force on the FRF is quite dramatic across the frequency spectrum. The effect of higher damping can be clearly seen by comparing the magnitude of the first peak in the FRFs from each impact. Ultimately, these findings indicated the need for carefully controlling the force of the impact. On the one hand, an impact that was too large could lead to the unacceptable results shown in Fig. 32.5, however, too light of a force was not optimal for exciting parts of the structure far away from the impact point. These tradeoffs were carefully balanced at each impact location.

Shown in Fig. 32.5a, b are the driving-point- and cross-FRFs of two different pairs of points. Figure 32.5a shows the driving point measurements between the top of the upstream bulkhead and the top longeron. Clearly, the reciprocity between

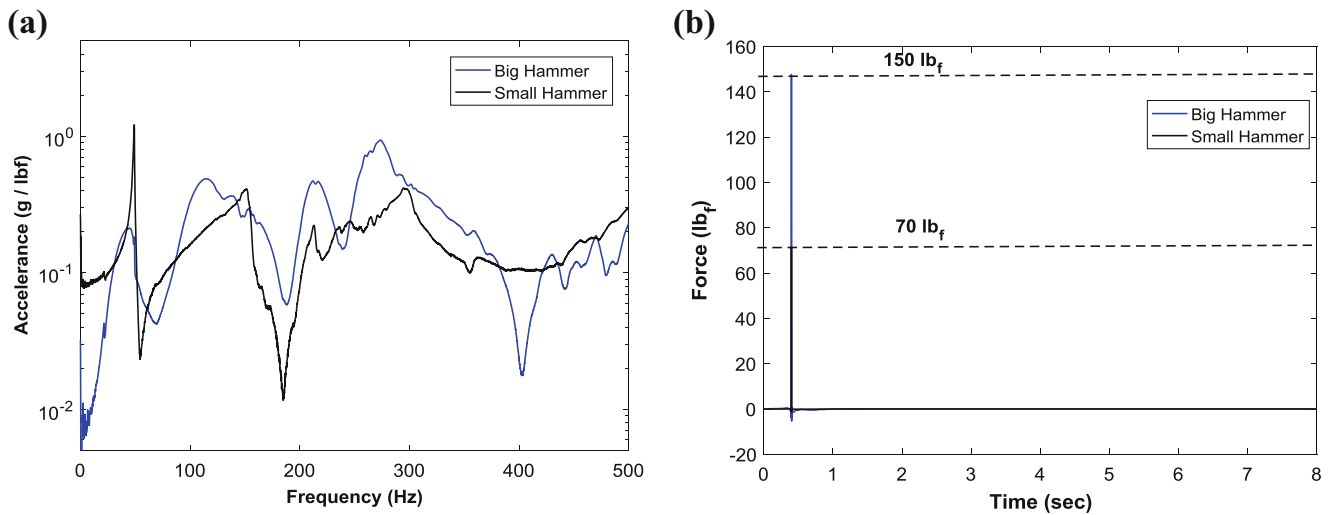


Fig. 32.4 (a) FRF of downstream bulkhead response obtained by tapping bulkhead with small and large hammers, (b) time history of impact force

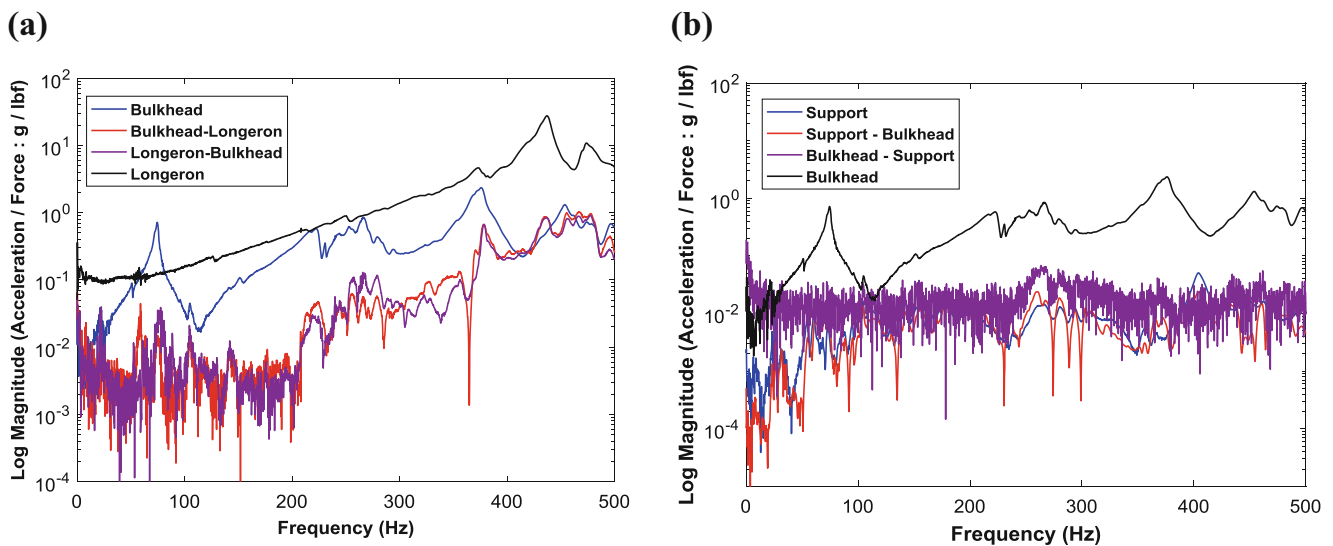


Fig. 32.5 FRFs between two driving points, (a) support and top upstream bulkhead, (b) top upstream bulkhead and top longeron

these two points is good. However, the reciprocity between the same point on the upstream bulkhead and the closest point to it on the A-frame is not good. Unfortunately, the light impacts required to avoid the appearance of nonlinear damping effects on the response of the bulkhead, combined with the less sensitive accelerometer on the A-frame, led to a signal that was not picked up by the accelerometer on the A-frame. However, from a comparison of the FRFs of the bulkhead and A-frame, it was decided that it was more important to keep the more sensitive accelerometers on the test panel, since the effect of the A-frame on the bulkhead response was considered to be much smaller than what it had been originally considered to be.

Figure 32.6 shows driving point FRFs and coherences at three different points on the test panel. Shown in Fig. 32.6a are the FRF and coherence of the center point on the upstream bulkhead. Overall, the coherence of the measurement is very good at points of high activity of the response in the frequency spectrum. The high modal density and damping of the structure can be observed by the broad peaks above 100 Hz. It is interesting to contrast this data to the driving point FRFs at the top longeron and the upstream OML. Clearly, most of the low frequency spectrum is dominated by the bulkheads, while above 300 Hz both the OML and top longeron start having more dynamics. The coherence of the top longeron and upstream OML are also very good.

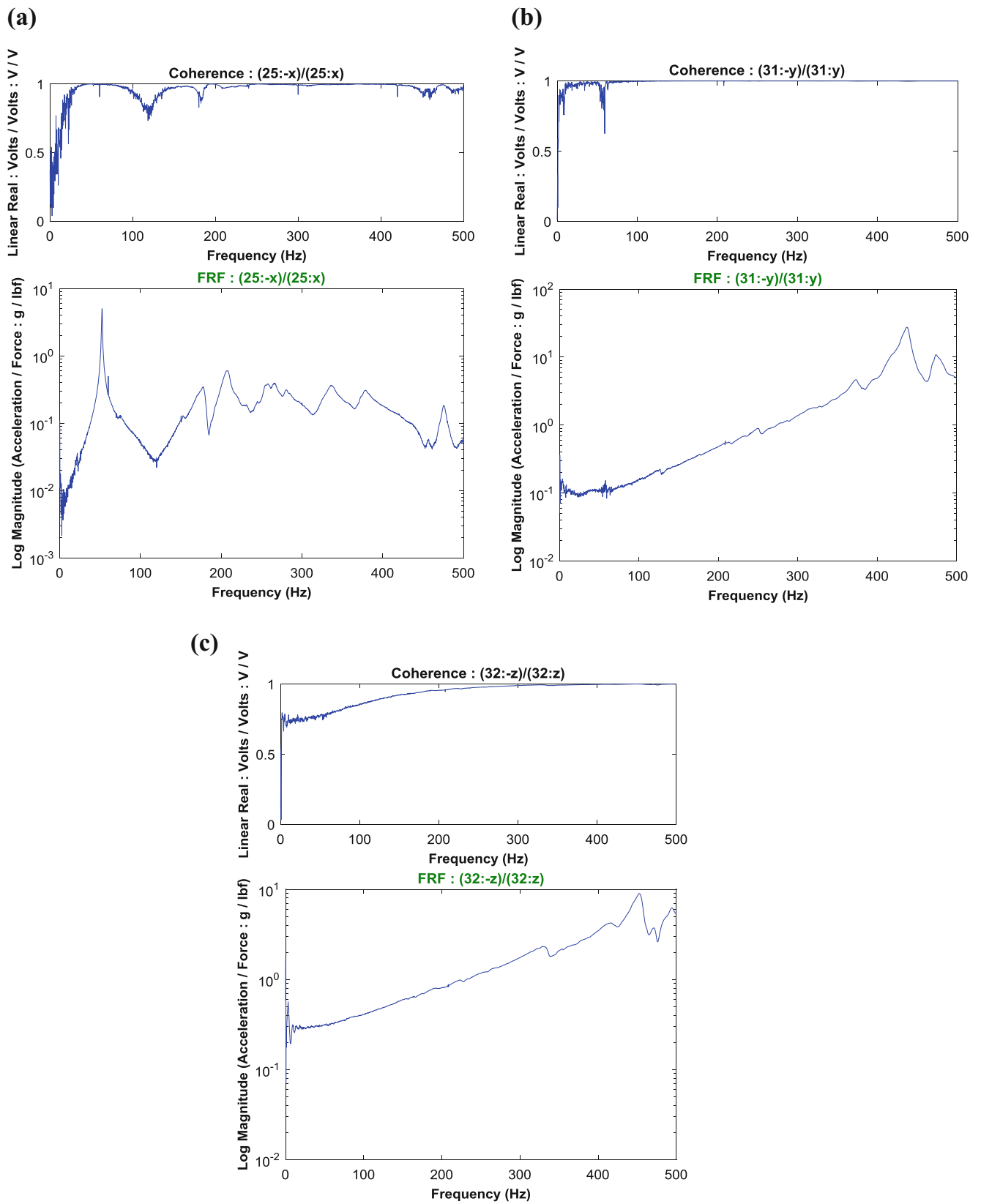


Fig. 32.6 Coherence and FRF of selected driving points, (a) upstream bulkhead, (b) top longeron, (c) upstream OML

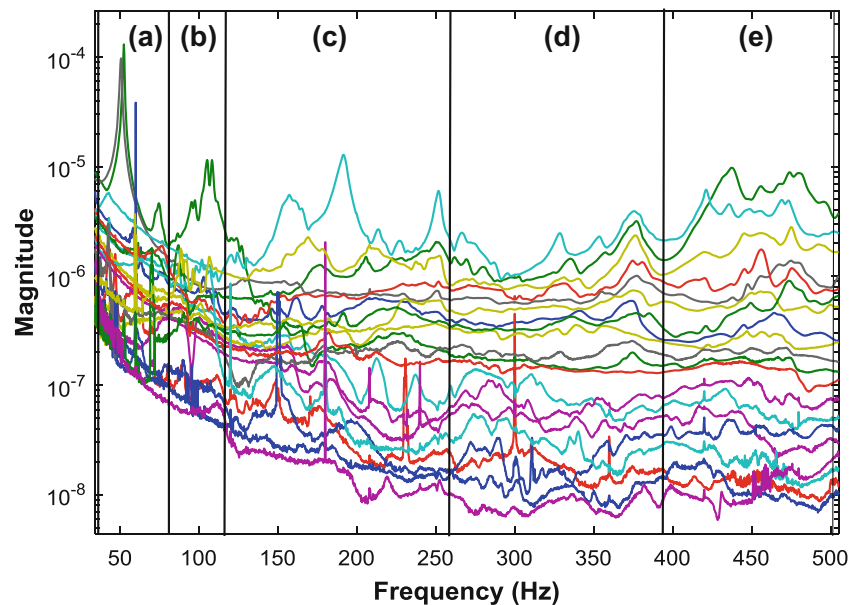


Fig. 32.7 CMIF

32.3 Modal Parameter Estimation

The large amount of data as well as the complexity of the structure and supports made the MPE process very challenging. The first approach followed to obtain better quality results was to sieve the data. All dominant degrees-of-freedom in the panel article were kept in the analysis. For example, the motion of the bulkhead modes is dominant in the x -direction (direction parallel to the longerons), the longerons in the y -direction (direction parallel to the bulkheads), and the OML in the z -direction (direction perpendicular to the top of the OML). The UDRL X-Modal 3 software was used for the MPE process. The Complex Mode Indicator Function (CMIF) was used to identify the regions of interest and perform the MPE in smaller frequency bands. Shown in Fig. 32.7 is the CMIF plot. The frequency band from 30 Hz to 500 Hz was divided into the five regions highlighted in Fig. 32.7.

The Unified Matrix Polynomial Approach (UMPA) framework in X-Modal 3 was used for the MPE. The estimation was performed in the z -domain using a basis in the long dimension with alpha matrix orders from 2 to 10. The long dimension was selected since it can help obtain more spatial information. A total of 288 inputs and 20 outputs were used for the identification. Information on natural frequencies, damping, and mean phase correlation values (MPC) of the modes identified can be found in Table 32.2. The modes are divided into the five different groups highlighted in Fig. 32.7. Shown in Fig. 32.8 are a selected group of mode shapes from Table 32.2. As discussed in the previous section, the bending modes of the bulkheads are dominant below 300 Hz. For frequencies above 300 Hz, the modes are a combination of higher-order bulkhead modes, longeron, and OML modes. The MPC values of the modes above 300 Hz also tend to be lower, which can be observed as well by the larger scatter in the modal complexity plots shown in Fig. 32.9. Given the high complexity of the test specimen, it is not surprising to see that as we go higher in frequency the modes identified tend to be less normal. Except for mode 11 (Fig. 32.8c) the high modal density of the structure makes it very difficult to split the high-frequency modes without enough references. Another challenge is the optimal distribution of energy from an impact is severely limited by the requirement of avoiding the nonlinearity which would result from a large enough impact, as discussed in the previous section. Mode 11, however, appears to behave differently. While the deformation in this mode is largely localized to the center bulkhead, the mean phase rotation angle, shown in Fig. 32.9, is farther from the 90° angle, which a normal mode would have, than all the other modes. It is not clear at this point what might have been the cause of this.

Shown in Fig. 32.10 is a picture of the first bending mode of the center bulkhead obtained from the free-free tests presented in Ref. [2] and the data presented in this paper. The instrumentation had a very small effect on the natural frequency and damping of this mode. However, the boundary conditions had a much larger effect, the mode is approximately 20% stiffer and the damping is 15 times higher than in the uninstrumented free-free case.

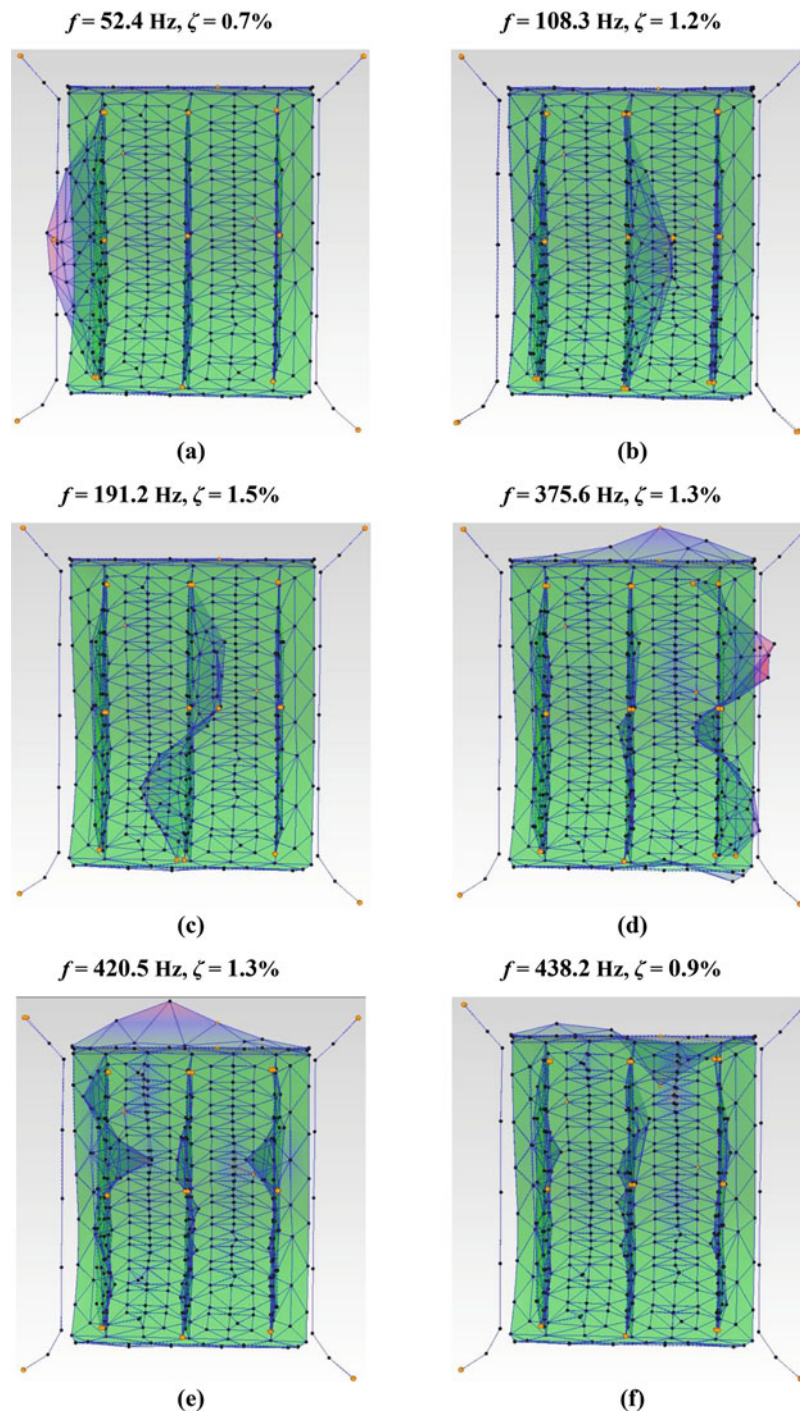


Fig. 32.8 Modes 2, 9, 11, 16, 18, and 19 from Table 32.2

Table 32.2 Natural frequencies, damping, and MPC values for mode shapes identified

Frequency band in Fig. 32.8	Mode	Natural frequency (Hz)	Damping (% of critical)	MPC
a	1	50.6	1.0	0.81
	2	52.4	0.7	0.87
	3	74.5	3.1	0.66
b	4	86.5	1.3	0.67
	5	97.6	0.7	0.85
	6	104.8	1.2	0.82
	7	105.2	1.1	0.88
	8	107.7	0.4	0.86
	9	108.3	1.2	0.80
c	10	158.3	3.8	0.77
	11	191.2	1.5	0.78
	12	214.2	1.9	0.80
	13	226.0	1.9	0.80
	14	251.8	1.0	0.80
d	15	330.6	1.6	0.70
	16	375.6	1.3	0.70
	17	380.9	0.7	0.70
e	18	420.5	1.3	0.70
	19	438.2	0.9	0.70
	20	455.0	1.1	0.70
	21	474.0	0.7	0.70

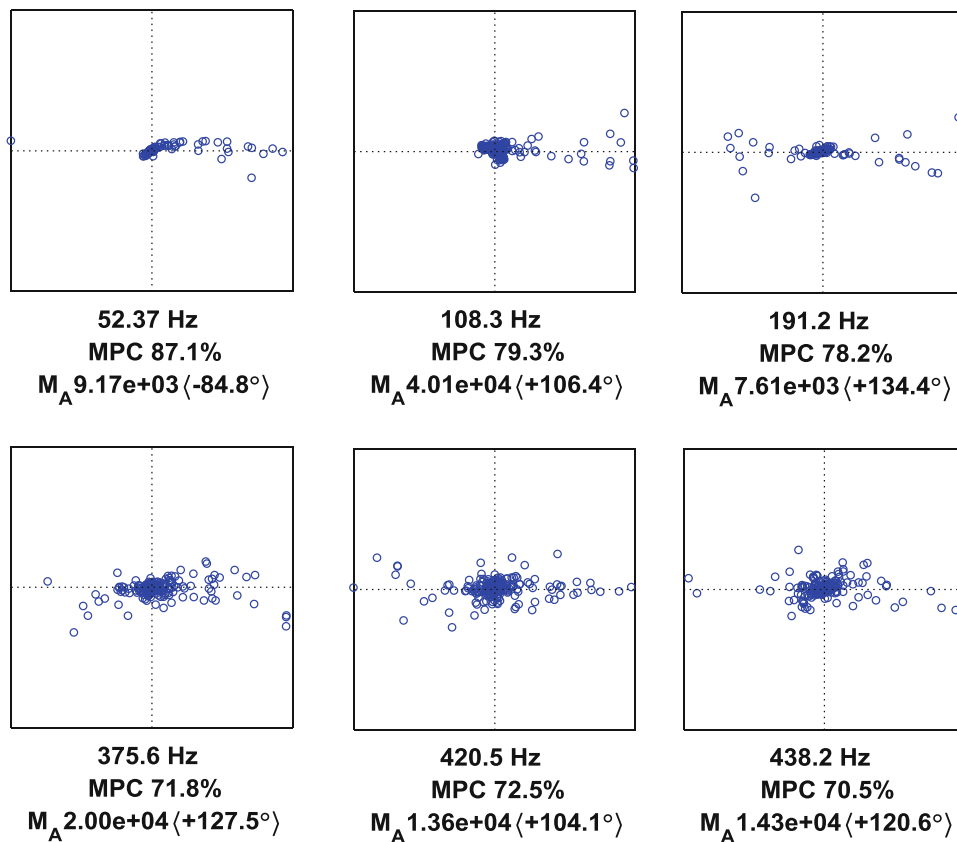


Fig. 32.9 Modal complexity plots

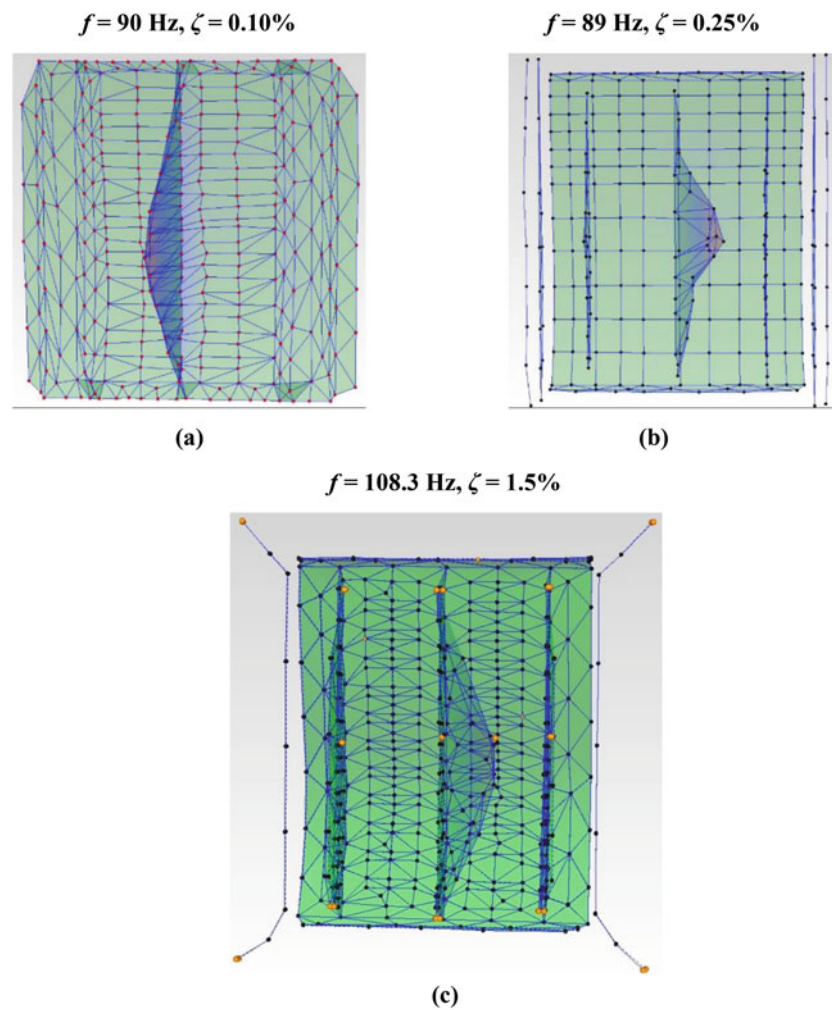


Fig. 32.10 Comparison between representative modes, (a) uninstrumented free-free test, (b) instrumented free-free test, (c) instrumented operating boundary conditions

32.4 Summary

A modal test of a hat-stiffened fuselage panel installed in a combined environment acoustic chamber was performed. An impact hammer test approach was used. The test setup as well as challenges in obtaining good data were discussed. Modal parameters extracted from the test data of the panel were shown and compared to parameters from the article in free-free conditions. This information will be used to update a FEM of the article and to assess the state of the panel throughout the various stages of a combined environment test.

Acknowledgements The authors gratefully acknowledge the support of Drs. Jamie Tilley and Jean-Luc Cambier of the Air Force Office of Scientific Research (AFOSR), LRIR numbers 12RB04COR and 15RQCOR244. The authors also thank Prof. Randall Allemang from University of Cincinnati for invaluable discussions.

References

1. Zuchowski, B.: Predictive capability for hypersonic structural response and life prediction: phase II – detailed design of hypersonic cruise vehicle hot-structure. Technical Report, AFRL-RB-WP-TR-2012-0280 (May 2012)
2. Wyen, T.A., Schoettelkotte, J.J., Perez, R.A., Eason, T.G.: Experimental modal analysis of an aircraft fuselage panel. In: 35th IMAC Conference (2017)

Chapter 33

Combining Virtual Simulation with Hands-on Experiments for Teaching Mechanical Vibrations

Changrui Bai and Surendra (Suri) Ganeriwala

Abstract Mechanical vibration is one of the important courses offered in the systems and dynamics area. Traditionally this course is taught theoretically with little emphasis on experimental verification. Since non-intuitive concepts are explained involving complex mathematical manner, students usually find this to be a one of the difficult course in the curriculum. To address these issues, we have developed an integrated approach which combines virtual simulation of each concept with the laboratory experimentation. The course material is built and structured around a standard vibration course material to make it easy to implement in a traditional curriculum while enhancing the learning experience of the students. This combines the theory with hands-on, easy-to-set experiments and interesting simulations. The material is structured similar to a typical vibration text book. Students can perform a number of experiments, which include; simple single degree of freedom systems, multi-degree of freedom systems and continuous beams with different boundary conditions. Both free and forced vibration experiments can be performed in torsional and translational configurations, with and without damping. We also provide an appealing virtual environment for each experiment so that students can graphically see and sense the effects of changing the system parameters. An example is seeing the effect of damping on vibration amplitude in different frequency regions such as stiffness controlled, mass controlled, and around resonances. The complete package includes a full set of cost-effective data acquisition system, wireless sensors and comprehensive user-friendly software.

33.1 Introduction

Mechanical vibration is one of the important courses offered in the systems and dynamics and other discipline. It involves non-intuitive concepts which are typically explained mathematically. Because of this, students usually find this to be a one of the difficult course in the curriculum. To address these issues, we have developed an integrated approach which combines virtual simulation of each concept with the laboratory experimentation. The Vibration Fundamentals Training System (VFT) is a turn-key integrated educational package for teaching/learning the fundamental principles of mechanical vibration as well as engineering mechanics. It provides both a comprehensive hands-on experimental device and an instrumentation package including wireless sensors for performing laboratory exercises to enhance student understanding of vibration theory.

With an increase in high speed manufacturing and automation, it has become more important to use the theory of vibration for design and maintenance of machinery. This vibration theory is even more important in the monitoring and diagnosis of machinery malfunctions. Considering the importance and complexity of vibration principles, a course curriculum should include laboratory demonstration and hands-on experiments to help students understand the somewhat abstract concepts of vibration. To this date, most academic institutions include only theoretical lectures without laboratory exercises due a lack of an apparatus combined with an instrumentation setup. With SpectraQuest's VFT, this deficiency has been resolved making hands-on vibration teaching now possible.

The VFT brings classical theory to life by providing a convenient mean to validate predictions and to demonstrate the influence of parameter changes on system response visually. Students can perform virtual experiments using the vibration simulation software and then verify the results with actual experiments thereby reinforcing the learning of difficult principles. The VFT provides an ideal tool for damping free vibration experiments using the wireless sensors without affected by the damping associated with the sensor cables. It is a perfect tool for teaching mechanical vibration courses both at under graduate and graduate levels.

C. Bai · S. Ganeriwala (✉)
Spectra Quest, Inc., Richmond, VA, USA
e-mail: suri@spectraquest.com

33.2 VFT System Configuration

The VFT provides a comprehensive hands-on experimental device, an instrumentation package, and experimental program with course curriculum for performing laboratory exercises to enhance student understanding of vibration theory. The bench-top apparatus has a spacious modular design featuring versatility, operational simplicity, and robustness. Each component is machined to high tolerances, so it can be operated without conflicting vibration in a totally controlled environment. The instrumentation package includes wireless accelerometers and rate sensors, mass unbalance exciters, a base motion exciter, and time and frequency domain analysis software. Also included are a software simulation of theory and a well-defined experimental program for free and forced vibration experiments ranging from single degree of freedom spring mass to continuous beam with different boundary conditions.

The VFT is designed to perform both free and forced vibration experiments with and without damping. The basic VFT frame consists of two identical test stations mounted on a portable structure as shown in Fig. 33.1. It features into changeable restraint fixtures, optional force transducers to measure the support reactions, sensors to measure deflection and acceleration, and variable frequency exciters for forced excitation. It allows for the first time to perform almost damping free vibration experiments to verify the theory using SpectraQuest in-house developed wireless sensor technology.

33.2.1 Wireless Sensors and Exciter

Cables are often a source of problem due to entanglement and damping associated with them. Cables require special handling during any experimental procedure. They also created hard to characterize unwanted damping. Both of these issues have been solved by SpectraQuest VFT system. We have developed wireless sensors that eliminated both of these problems. Our proprietary algorithm enables simultaneous acquisition of data from all sensors, thus making it possible to obtain accurate phase information and the mode shapes. Along with wireless sensors, we provide wireless unbalance mass exciter. This provides an ideal setup for performing one and two degrees of freedom experiments described in a traditional textbook in vibration.



Fig. 33.1 Vibration fundamental training system



Fig. 33.2 Vibration fundamental training software

33.2.2 Data Acquisition and Analysis Instrumentation

The VFT is equipped with wireless transducers, SpectraQuest's proprietary wireless data acquisition (DAQ) system; data analysis software with automated setup for performing each experiment, simulation software, motor control module, multi-featured display, and mounting hardware/tooling. Transducers are provided for the measurement of acceleration, force, and rotational speed. The DAQ system samples all channel simultaneously enabling accurate calculation of mode shapes. Easy to use software automates steps to conduct each experiment and display the results. Students can perform time and frequency domain analysis, read data to do calculations and compare them with theoretical predictions.

The DAQ hardware/software is fully integrated with the exciter operation and control. The user can send speed command to control the excitation frequency or a sine sweep can be applied to obtain the full frequency response information over the frequency range of interest. All experimental and data collection setups are pre-defined so that students can focus on the results. The user-friendly software is a powerful tool for basic vibration experiments, and vibration signal processing as shown in Fig. 33.2. Simple and intuitive interface allows fast and easy operation. The signal analysis modules include data presentations of time waveform, FFT spectrum, and frequency response function (FRF). Superimposed data comparison of two data sets is also possible.

33.2.3 Vibration Simulation/Animation

Vibration fundamentals simulation software is designed to teach basic concepts using a new interactive and visual simulation technique. The student can perform virtual experiments on various topics by changing the parameters of a vibratory system and see how the system behavior is affected. The effect is displayed dynamically. The vivid visualization enhances the learning and clarification. A spring-mass-damper system is used to animate the vibration response as shown in Fig. 33.3.

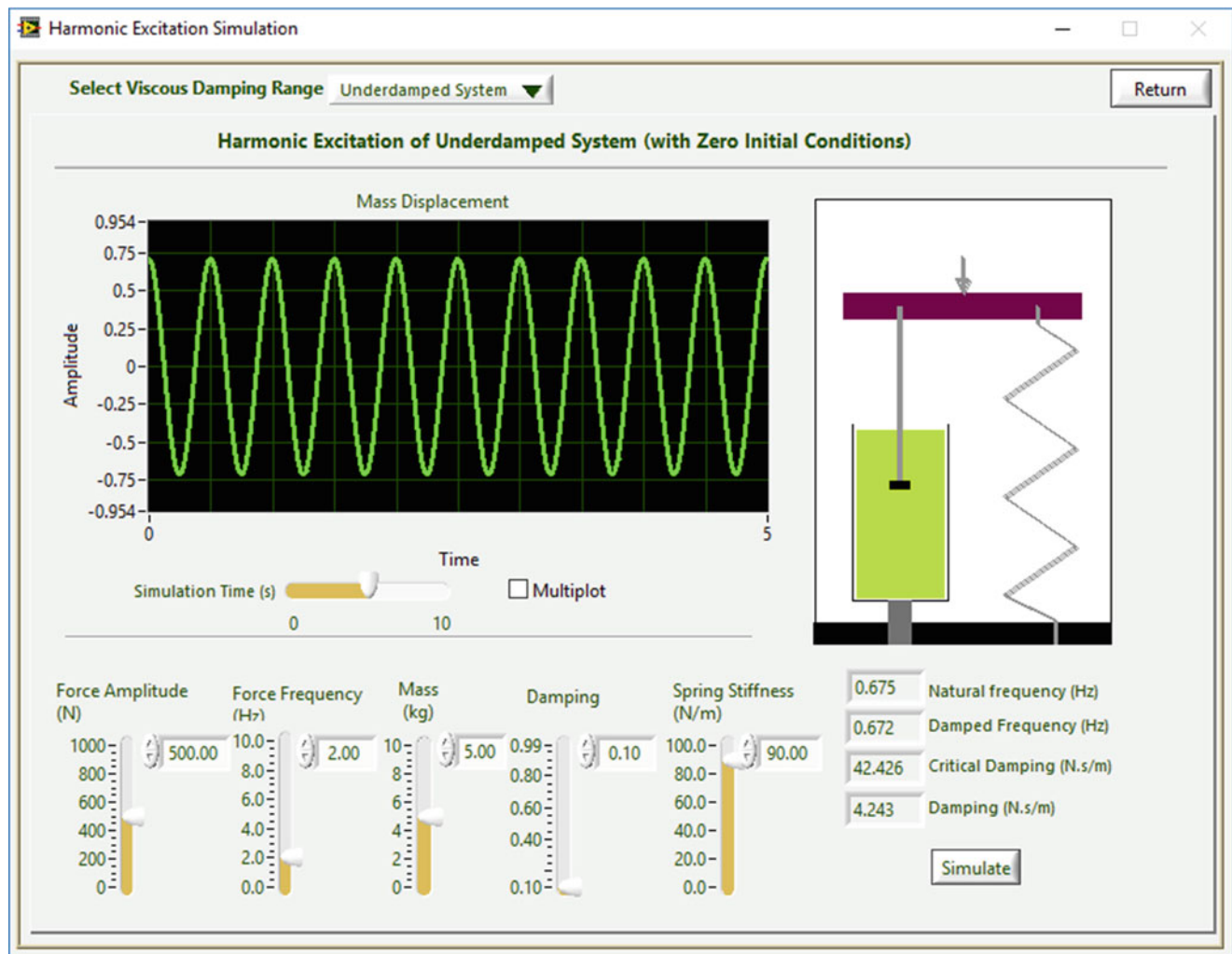


Fig. 33.3 Simulation of a spring-mass-damper system

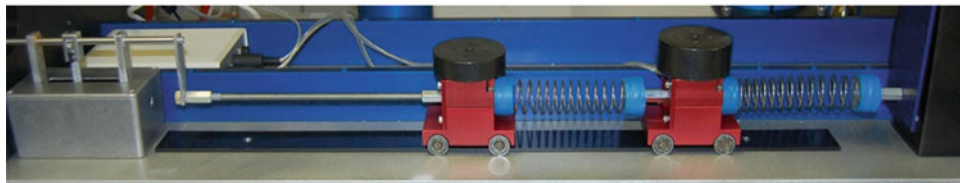
A multi-plot option can be used to compare their effects on vibration response. Therefore, instead of deriving the equations, the user can go one step further, “play and see” the vibration behavior. The software includes the most common topics of a typical vibration course.

33.2.4 Mass-Spring System

The Spring-Mass module is a perfect tool for doing classic single and two DOF experiments. Natural frequencies for different mass and spring, with and without viscous damping, can be determined under free oscillations excited by initial displacement or velocity. Tests can also be done under forced excitation at various frequencies. The forcing function can be applied either at the base or the mass. The system response could be measured at one frequency at a time or over the entire frequency range by selecting the sine sweep excitation. The data is easily stored and plotted with the software data processing capabilities to obtain the frequency response function. With the multi-plot feature of the analysis software, the system response to controlled variables (k , m , and c) can be easily compared (Fig. 33.4).



(a)



(b)

Fig. 33.4 Mass-spring system. (a) Vertical. (b) Horizontal

33.2.5 *Vertical Torsional Vibration Module*

Torsional vibration issues are important in design and diagnostics of turbomachinery, internal combustion engines, and many other applications. The fundamental concept of torsional vibration is similar to the flexural and longitudinal vibration, but students often find difficulty both with calculations and the measurements. The VFT addresses both of these issues. As shown in Fig. 33.5, the torsional vibration module consists of a stainless-steel shaft, several rotors, a torsional viscous damper, and a torsional exciter. The unit can be configured as one and two degrees of freedom systems for free and forced vibration experiments. It can also be configured with different rod length, diameter, and material to vary system stiffness, with different disks to vary the mass, and with or without a dashpot.

33.2.6 *Beam Vibration Module*

This module allows to study natural frequencies, mode shapes, and damping in beams of different materials such as steel, aluminum, and plastic. The beam length is fully adjustable and can be configured as simply supported or cantilever (at either

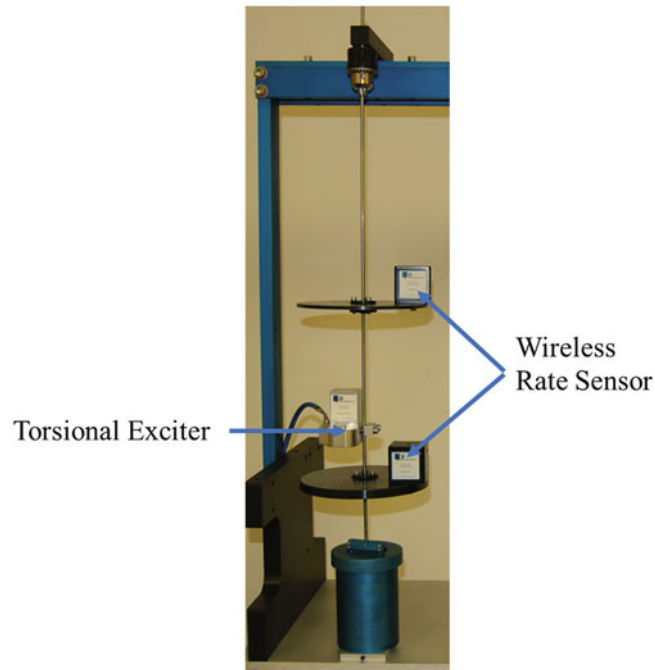


Fig. 33.5 Vertical torsional experiment configuration



Fig. 33.6 Beam vibration module

of the beam ends), and overhung. This adaptable mounting allows determining effects of various boundary conditions in real applications. Provisions to mount rigid masses at different locations and dashpot make beam completely customizable. Custom built force transducers can be mounted to measure the support reaction forces and determine transmissibility factor. External unbalance force of variable frequency may be applied to excite natural frequencies and produce visible mode shapes. The amplitude of deflection during resonance may be measured any point along the length of the beam. By directing a stroboscope at the beam, the user can clearly see the natural mode shape predicted by classical beam theory, including the second, third, and even higher order modes. The standard beam restraint fixtures accept up to 2" wide \times 1/8", 3/16", and 1/4" thick bar stocks and offer fixed, sliding, and hinged restraint modes. Point, distributed, and twisting moment loading patterns can be applied. To add interest, customer designed beams or trusses may be installed for design competition and special projects. The VFT can also be used for a simple modal test and vibration control experiments. Modal tests can be performed by using a hammer or shaker (Fig. 33.6).

33.2.7 *Vibration Control Study Module*

The VFT is an ideal platform for not only to understand basic vibration principles, but also to learn passive vibration control. Students can even learn to alter excitation frequency, change resonance frequency by modifying modal mass and/or stiffness, and add damping to bring vibration levels to acceptable values. Students can also design tuned-mass damper to absorb

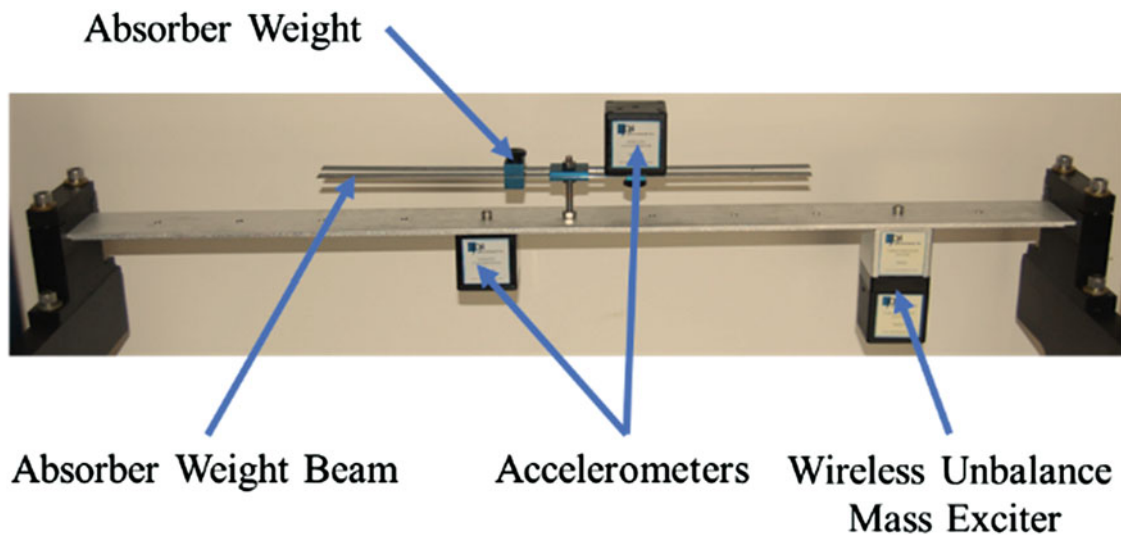


Fig. 33.7 Vibration control study module

vibration in a spring-mass system or on beam a beam using a leaf spring with sliding masses. The student can then hold the vibrating masses to transfer the vibratory motion back to the original structure. A complete kit is provided for the experimentations. The vibration control study module also provides a constrained layer viscoelastic sandwich beam to study the effect of viscoelastic damping in vibration control. This is a more advanced topic for graduate level program, but students can use this module to study the relationship between system damping ratio/loss factor and the damping materials, damping layer thickness and damping coverage, etc. (Fig. 33.7).

33.3 Experiment

Two typical experiments are presented here to show the performance of the VFT system: (1) 1-DOF free vibration simulation; (2) vertical torsional experiment.

33.3.1 1-DOF Free Vibration Simulation

Two simulation results of the 1-DOF free vibration with different parameters are shown in Fig. 33.8. The parameters adopted by each simulation are shown in the bottom of Fig. 33.8. The figure clearly shows how the mass affects the vibration, which provides a good reference for the students to study basic vibration theory.

33.3.2 Vertical Torsional Experiment

A vertical torsional experiment was carried out. Figure 33.5 shows the experimental configuration. Two disks were mounted in series with a wireless rate sensor on each of them to measure the angular velocity. The shaft is made of stainless steel and the other parameters of the rod and the disks are presented in Table 33.1. The data were acquired using SpectraQuest's own hardware and software developed in-house. The spectral settings included a sampling frequency at 4000 Hz and an acquisition time of 30 s. The torsional exciter swept from 1 to 35 Hz during the acquisition time. The spectra of the angular velocities of the two disks are shown in Fig. 33.9, where the angular velocity was used as the primary unit of the recorded vibrations. Two peaks at the resonance frequencies (around 6 Hz and 19 Hz) are obviously shown in the spectra, which validates the vertical torsional vibration module.

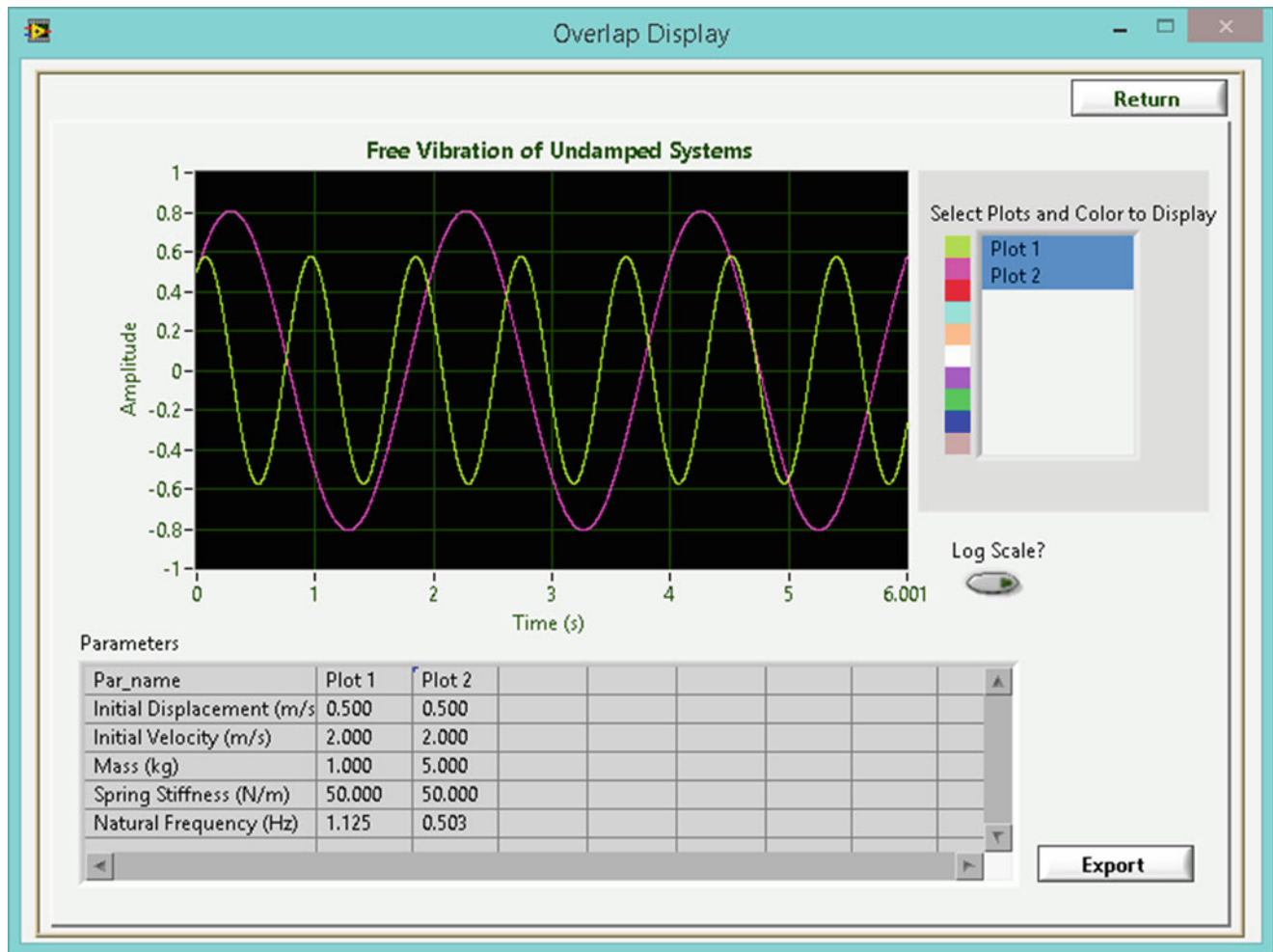


Fig. 33.8 Simulation of 1-DOF free vibrations

Table 33.1 Vertical torsional experiment setup

	Diameter (m)	Length/thickness (m)	Mass (kg)
Shaft	0.0048	0.9100	–
Top disk	0.1270	0.0095	0.915
Bottom disk	0.1810	0.0046	0.992

33.4 Conclusion

In this paper, a vibration fundamental training system is proposed to educate the fundamental principles of mechanical vibration as well as engineering mechanics. It provides both a comprehensive hands-on experimental device and an instrumentation package including wireless sensors for performing laboratory exercises to enhance student understanding of vibration theory. Virtual experiments followed by the verification actual experiments can be performed by the VFT. Both the simulations and the real experiments show that the VFT clearly brings classical theory to life by providing a convenient mean to validate predictions and to demonstrate the influence of parameter changes on system response visually. In summary, the benefits of the VFT are as follows:

- Clarify difficult concepts of vibration theory by performing hands-on controlled experiments.
- Perform both free and forced natural vibration experiments without damping for the first time using SpectraQuest developed wireless sensors.

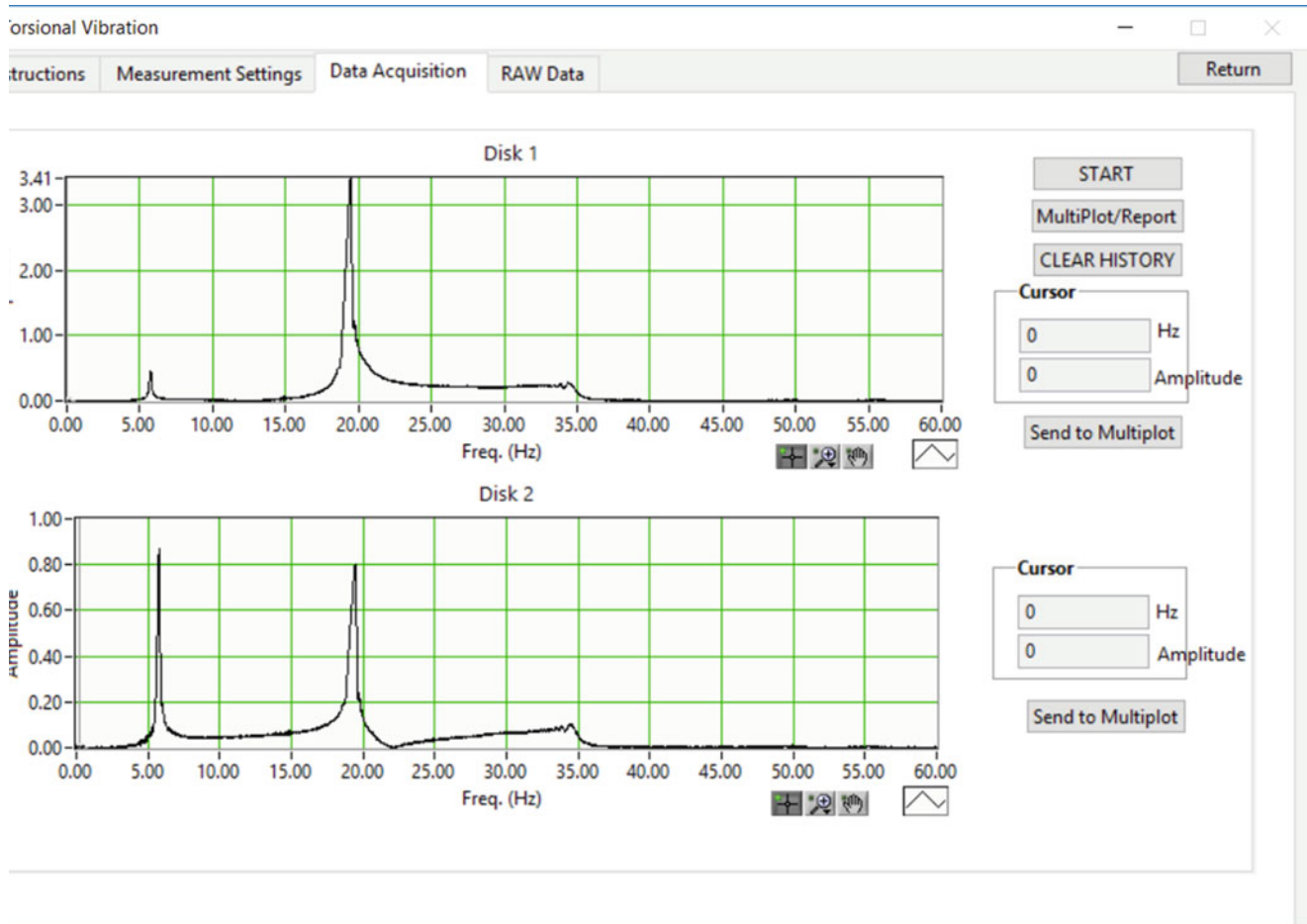


Fig. 33.9 Spectra of the torsional vibration experiment

- Validate theoretical predictions of natural frequencies, mode shapes, and frequency response as a function of frequency, boundary conditions, geometry, and materials.
- Validate theoretical concepts by comparing experimental results with the computer simulation of the vibration theory.
- Determine the detrimental effects of vibration load transmission to the support structure and component fatigue life.
- Learn to control vibration amplitude using tuned mass dampers and damping treatments.
- Learn vibration measurement transducers, signal processing, data acquisition and data analysis.

Chapter 34

Finite Element Model Updating Using the Local Correspondence Principle

Sandro Amador, Martin Juul, Tobias Friis, and Rune Brincker

Abstract In this, paper an overview of a Finite Element (FE) model updating technique based on the Local Correspondence (LC) principle is presented. The main idea behind the LC technique is to update the FE model by replacing the mode shape vectors and natural frequencies with their corresponding experimental counterparts obtained from an output-only modal testing. This is accomplished by taking advantage of the fact that the inverse mass and stiffness matrices can be expressed as a linear combination of outer products of the mode shape vectors. Aiming at discussing the LC technique from a practical perspective, a simulation study is presented to illustrate its ability to improve the Maximum Assurance Criterion (MAC) between the FE and experimental mode shape vectors so that it gets close to unity.

34.1 Introduction

In recent years, a lot of effort have been concentrated in developing accurate Finite Element (FE) model updating techniques. The growth of interest on this topic is explained, amongst other reasons, by the necessity of establishing a reliable non-destructive approach to assess the health condition and damage of engineering structures subjected to varying operational and environmental conditions over time. Several FE model updating techniques are found in the literature to reduce the differences between the FE predictions and test results as discussed, for instance, in [1–3] and citations therein. Amongst the most popular of these techniques, are the sensitivity based approaches that make use of vibration test results as references to update the FE models [4, 5].

The basic idea behind these approaches is to reduce the discrepancies between the FE modal properties and those experimentally identified from vibration tests by modifying the modelling assumptions and parameters so that these discrepancies are reduced to practical requirements. It turns out that these FE model updating techniques can be time consuming in cases where a FE model with a very high number of Degrees Of Freedoms (DOFs) are to be iteratively updated. Moreover, depending on the FE complexity and the amount of modelling parameters to be optimized, problems such as objective function converging to local minima or convergence not being guaranteed might as well occur. In this paper, the One-step FE Model updating technique introduced in [15] is combined with the System Equivalent Reduction Expansion Process (SEREP) [7, 9, 10] to overcome these issues.

Rather than performing the optimization iteratively, the underlying idea of this approach is to update the mass and stiffness matrices of FE models in one single step by making use of the Local Correspondence (LC) principle [6, 7] and by taking advantage of the fact that the inverse mass and stiffness matrices are given as linear combination of modal shape vectors outer products [7, 8]. In order to minimize the computational time and resources required to run the one-step approach, it is also described how the technique can be combined with the SEREP to avoid the inversion of FE spatial matrices containing information of a high number of DOFs. In the final part of the paper, the efficiency of the one-step updating technique combined with SEREP is demonstrated by means of an application example of an off-shore platform model.

S. Amador (✉) · T. Friis · R. Brincker
Technical University of Denmark, Kongens Lyngby, Denmark

M. Juul
Department of Engineering, Aarhus University, Aarhus, Denmark

34.2 Theoretical Background of the One-Step Updating Technique

Unlike the classical sensitivity-based **FE** model updating techniques, in which the material properties and/or modelling assumptions are adjusted iteratively so that the **FE** modal properties match the ones obtained from vibration tests, the one-step approach aims at updating the **FE** model in a single step by replacing the **FE** eigenfrequencies and eigenvectors by their corresponding experimental counterparts. Detailed description of the direct **LC** principle as a tool for **FE** model updating from vibration test data can be found in [6, 7]. The one-step updating technique is based on the orthogonality equations and the expansion of the experimental mode shapes. The formulation of such approach starts from the following orthogonality equations

$$\begin{aligned} B^T M B &= I, \quad B = [b_1 \ b_2 \ \cdots \ b_{N_s}] \\ B^T K B &= [\omega_{bn}^2], \quad \forall n \in \{1, 2, \dots, N_s\} \end{aligned} \quad (34.1)$$

where $I \in \mathbb{R}^{N_s \times N_s}$ is the identity matrix, $B \in \mathbb{R}^{N_d \times N_s}$ is a matrix containing the **FE** model mode shapes vectors b_i ($i = 1, 2, \dots, N_s$), $M \in \mathbb{R}^{N_d \times N_d}$ the mass matrix and $K \in \mathbb{R}^{N_d \times N_d}$ the stiffness matrix, with N_d and N_s denoting the number of **DOFs** of the **FE** model and the number of selected **FE** mode shapes, respectively. Taking the inverse and isolating the inverse mass and stiffness matrices in Eq. (34.1), yields

$$\begin{aligned} M^{-1} &= B B^T \\ K^{-1} &= B [\omega_{bn}^2] B^T \end{aligned} \quad (34.2)$$

The inverse matrices in Eq. (34.2) can also be expressed as a linear combination of the outer products according to the following equations

$$\begin{aligned} M^{-1} &= b_1 b_1^T + b_2 b_2^T + \cdots + b_{N_s} b_{N_s}^T \\ K^{-1} &= \omega_{b1}^{-2} b_1 b_1^T + \omega_{b2}^{-2} b_2 b_2^T + \cdots + \omega_{bn}^{-2} b_{N_s} b_{N_s}^T \end{aligned} \quad (34.3)$$

Using, for instance the **LC** principle, each of the experimental mode shapes can be approximately expressed by a linear combination of a limited number of mode shapes in the **FE** model. Assuming $B_a \in \mathbb{R}^{N_e \times N_d}$ as a matrix containing the **FE** mode shape vectors at the experimental **DOFs**, $A \in \mathbb{R}^{N_e \times N_m}$ a matrix containing the test mode shape vectors a_n ($n = 1, 2, \dots, N_m$), with N_e denoting the number of experimental **DOFs** and N_m the number of experimental mode shapes, the following relation can be defined

$$a_n = B_{an} t_n \quad (34.4)$$

in which

$$B_{an} = [b_{n-N_a} \ b_{n-(N_a-1)} \ \cdots \ b_n \ \cdots \ b_{n+N_a-1} \ b_{n+N_a}] \in \mathbb{R}^{N_e \times (2N_a+1)}$$

is a mode shape matrix consisting of a selection of $(2N_a + 1)$ mode shapes from B_a with N_a designating the number of **FE** modes above and below the natural frequency of the **FE** mode paired with the experimental mode, $a_n \in \mathbb{R}^{N_e}$ is the n th experimental mode shape and $t_n \in \mathbb{R}^{N_a}$ is a transformation vector. The solution of Eq. (34.4) is found in a **Least Squares (LS)** sense from

$$\hat{t}_n = B_{an}^+ a_n \quad (34.5)$$

where the operator $(\bullet)^+$ denotes the pseudo inverse of a matrix. The smoothed estimate for the experimental mode shapes a_n is given by

$$\hat{a}_n = B_{an} \hat{t}_n \quad (34.6)$$

and its expanded counterpart, \hat{a}_{xn} , simply by

$$\hat{a}_{xn} = B_n \hat{t}_n \quad (34.7)$$

in which B_n is the same matrix as B_{an} , but expressed in all the **DOF**s of the **FE** model and \hat{a}_{xn} the smoothed and expanded mode shape vector. Once estimated, the expanded and smoothed vectors \hat{a}_{xn} vectors are used to update the mass and stiffness matrices of the **FE** model. From now onwards, the updating is carried out in two steps. Firstly, the modal mass, $m_n \in \mathbb{R}$, corresponding to the smoothed and expanded mode shape vector \hat{a}_{xn} is computed from

$$m_n = \hat{a}_{xn}^T M \hat{a}_{xn} \quad (34.8)$$

which is then used to compute the mass scaled version of \hat{a}_{xn} ,

$$a_{xn} = \frac{\hat{a}_{xn}}{\sqrt{m_n}} \quad (34.9)$$

Finally, the updated mass and stiffness matrices are obtained by simply subtracting the **FE** mode shape vectors to be updated and adding the corresponding mass scaled expanded mode shape vectors a_{xn} to Eqs. (34.3). This updating procedure is synthesized by the following expressions

$$\begin{aligned} M_u^{-1} &= M^{-1} - b_n b_n^T + a_{xn} a_{xn}^T \\ K_u^{-1} &= K^{-1} - \omega_{bn}^{-2} b_n b_n^T + \omega_{an}^{-2} a_{xn} a_{xn}^T \end{aligned} \quad (34.10)$$

where M_u and K_u designate the updated mass and stiffness matrices, respectively.

34.3 Fast Implementation of the One-Step Approach

Inverting the inverse mass and stiffness matrices obtained from Eq. (34.10) might demand computational resources and a long processing time depending on the amount of **DOF**s in the **FE** Model. In order to avoid these issues, one can consider reducing the matrices by making use, for instance, of the so called **SEREP** [7, 9]. The idea is to reduce the dimensions of the **FE** spatial matrices to the number of **DOF**s measured in the vibration test, which is normally significantly lower than the number of **FE DOF**s. Afterwards, the natural frequencies and mode shape vectors of the reduced **FE** model is replaced by the their corresponding experimental counterparts using Eqs. (34.10) and, finally, the updated matrices of the reduced model are expanded back to obtain the updated full system matrices. If the **SEREP** technique is adopted, the reduced form of Eq. (34.10) is obtained by

$$\begin{aligned} M_{ur}^{-1} &= M_r^{-1} - b_{nr} b_{nr}^T + a_{xnr} a_{xnr}^T \\ K_{ur}^{-1} &= K_r^{-1} - \omega_{bnr}^{-2} b_{nr} b_{nr}^T + \omega_{anr}^{-2} a_{xnr} a_{xnr}^T \end{aligned} \quad (34.11)$$

where b_{nr} and a_{xnr} are the reduced forms of b_n and a_{xn} , respectively, and M_r , M_{ur} , K_r and K_{ur} stand for the reduced mass matrix before and after updating, and the reduced stiffness matrices before and after updating, respectively. These reduced spatial matrices are related to the full system matrices as

$$\begin{aligned} M_{ur} &= T_u^T M_u T_u \\ K_{ur} &= T_u^T K_u T_u \\ M_r &= T^T M T \\ K_r &= T^T K T \end{aligned} \quad (34.12)$$

with the transformation matrices before and after updating T and T_u given, respectively, by

$$T = \begin{bmatrix} B_r B_r^+ \\ B_d B_r \end{bmatrix} = B B_r^+, \quad T_u = \begin{bmatrix} B_{ru} B_{ru}^+ \\ B_{du} B_{ru} \end{bmatrix} = B B_{ru}^+ \quad (34.13)$$

where B_r , B_d , B_{ru} and B_{du} are submatrices containing the retained and deleted **DOFs** from the modal shape matrices B_r and B_d .

34.4 Application Example

In order to illustrate the accuracy of the **LC** updating technique combined with the **SEREP**, a Monte Carlo simulation was performed with a **FE** model of a scaled off-shore platform model. The physical off-shore platform model is composed by tubes and plates made of transparent plastic glass as illustrated in Fig. 34.1a. The corresponding **FE** model constructed with beam and shell elements with 6 **DOFs** per node is shown in Fig. 34.1b. The vibration test of the physical model, on the other hand, was carried out by recording the responses in acceleration at the direction and locations indicated in Fig. 34.1c when the structure was excited with random input forces.

Afterwards, the experimental modal properties were identified from the acceleration responses with the **poly-reference Least Squares Complex Frequency-domain (pLSCF)** technique [11, 12] with aid of an automated identification algorithm [13, 14] and subsequently used to update the **FE** model depicted in Fig. 34.1b. The Monte Carlo simulation was carried with 100 different **FE** models created by adding white noise to the material properties of a reference **FE** model of the off-shore platform model. The uncorrelated noise sequences were added to the Young's modulus, material density and Poisson ratio of different set of elements with a standard deviation of 5%. The natural frequencies and modal configurations of a typical perturbed **FE** model and the corresponding experimental modal properties are presented in Table 34.1, and the comparison between modal vectors in terms of **MAC** in Fig. 34.2.

The dimensions of the perturbed mass and stiffness matrices generated in each Monte Carlo simulation were reduced using **SEREP** from a total of 3276 to only 12 which correspond to the number of experimental **DOFs**. These reduced matrices

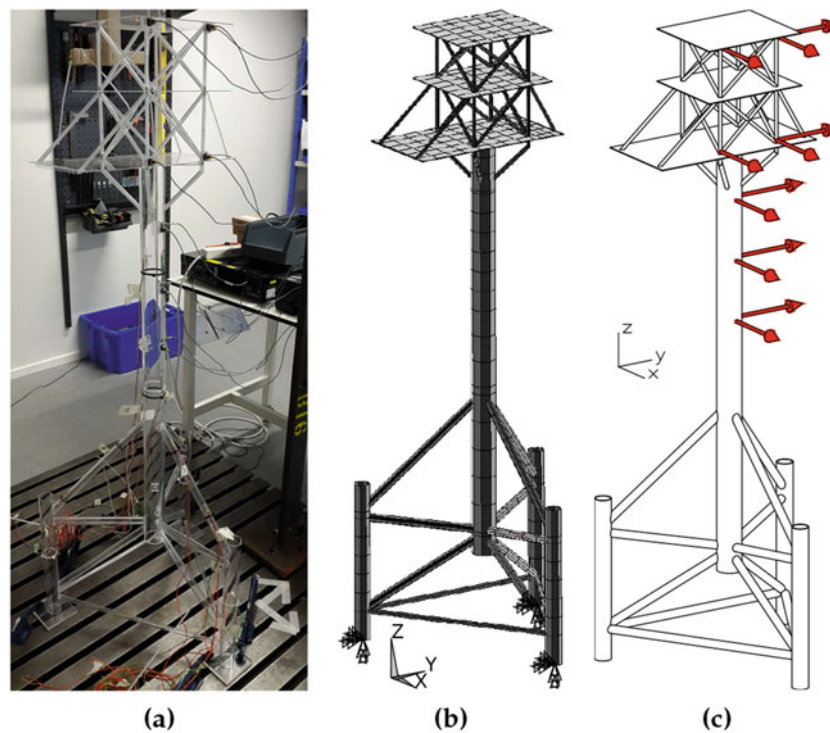


Fig. 34.1 “Valdemar” offshore oil platform model in plastic glass (a), its corresponding **FE** model (b), and illustration of the **DOFs** measured in the vibration test (c)

Table 34.1 FE and experimental modes of the offshore platform model before and after updating

Mode	Type	f_{iFE} [Hz]	$f_{iUpdatedFE}$ [Hz]	f_{iExp} [Hz]	$\frac{ f_{iFE} - f_{iExp} }{f_{iFE}}$ [%]	$\frac{ f_{iUpdatedFE} - f_{iExp} }{f_{iUpdatedFE}}$ [% $\times 10^{-4}$]
1	1st bending mode in Y direction (BY1)	10.5888	9.9544	9.9544	6.3724	0.0000
2	1st bending mode in X direction (BX1)	10.6368	10.1416	10.1416	4.8830	0.0000
3	1st torsional mode (T1)	18.1687	23.5960	23.5960	23.0008	0.1604
4	2nd bending mode in Y direction (BY2)	58.8067	66.4651	66.4651	11.5225	0.0086
5	2nd bending mode in X direction (BX2)	72.7070	74.2248	74.2248	2.0449	0.0041

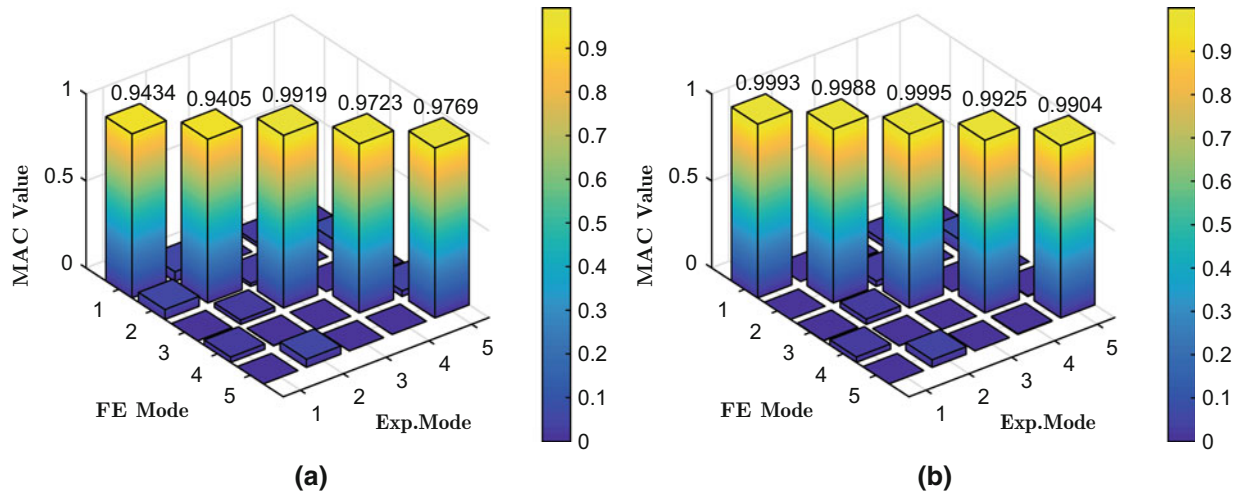


Fig. 34.2 MAC between experimental and FE Mode shape vectors before (a) and after FE model updating (b)

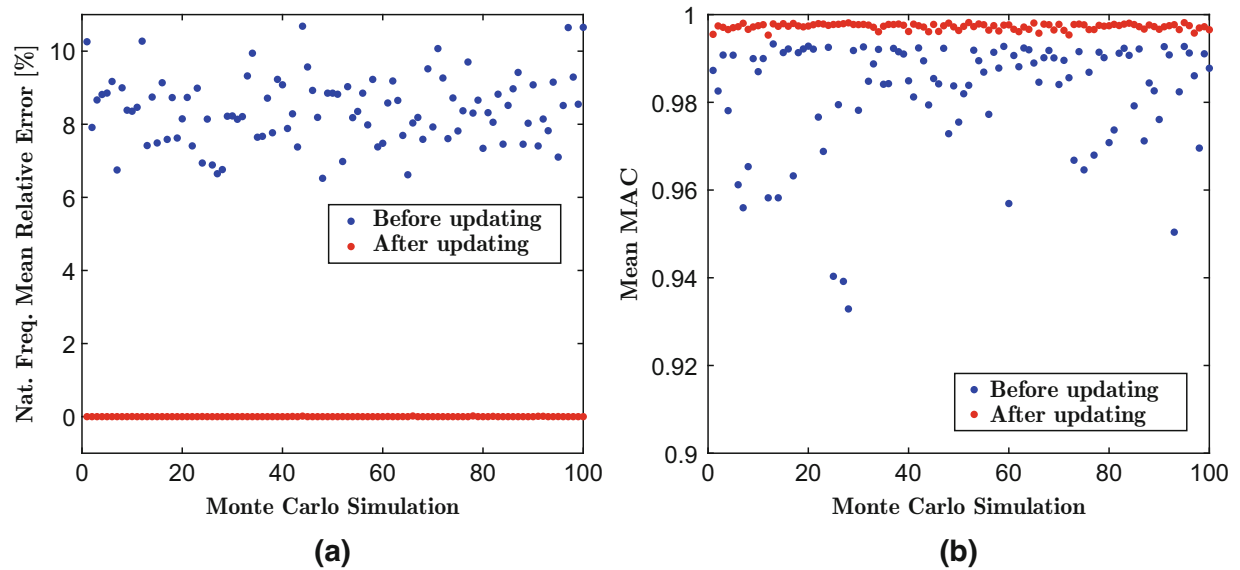


Fig. 34.3 Evolution of the mean natural frequency relative error (a) and MAC before and after FE model updating

were then updated using the approach described in Sect. 34.3 and subsequently transformed back to the full size by making use of the transformation matrix T_u . The evolution of the mean relative error between the FE and experimental natural frequencies as well as the MAC between the experimental and FE modal vectors before and after updating over the Monte Carlo simulations are presented in Fig. 34.3a, b, respectively. Analysing the results presented in these figures, it is verified that the LC updating technique was capable of updating the mass and stiffness matrices so that the natural frequencies and mode shape vectors of the updated FE model matched very well the experimental modal properties.

34.5 Conclusion

In this paper, a novel approach is proposed to update **FE** models using the modal parameters estimated from vibrational responses in one single step. This new approach consists of the one-step updating technique based on the **LC** principle combined with **SEREP** to improve the computational performance of the technique by avoiding the inversion of **FE** spatial matrices containing a huge amount of **DOFs**. Aiming at demonstrating the effectiveness and accuracy of the combined technique, a Monte Carlo simulation with a **FE** model of an offshore platform model was carried out. In this simulation, a total of 100 different **FE** models were updated with the one-step approach combined with **SEREP** and, for each **FE** model, the combined technique was capable of updating the **FE** spatial matrices so that the natural frequencies and mode shape vectors of the updated **FE** model matched very well the experimental modal properties.

Acknowledgements The authors acknowledge the funding received from Centre for Oil and Gas – DTU/Danish Hydrocarbon Research and Technology Centre (DHRTC).

References

1. Mottershead, J.E., Friswell, M.I.: Model updating in structural dynamics: a survey. *J. Sound Vib.* **167**(2), 347–375 (1993)
2. Friswell, M.I., Mottershead, J.E.: *Finite Element Model in Structural Dynamics*. Kluwer Academic Publishers, Boston (1995)
3. Zarate, B.A., Caicedo, J.M.: Finite element model updating: multiple alternatives. *Eng. Struct.* **30**(12), 3724–3730 (2008)
4. Zhang, Q.W., Chang, C.C., Chang, T.Y.P.: Finite element model updating for structures with parametric constraints. *Earthq. Eng. Struct. Dyn.* **29**(7), 927–944 (2000)
5. Mottershead, J.E., Link, M., Friswell, M.I.: The sensitivity method in finite element model updating: a tutorial. *Mech. Syst. Signal Process.* **25**(7), 2275–2296 (2011)
6. Brinker, R., Skaftø, A., López-Aenlle, M., Sestieri, A., D’Ambrogio, W., Canteli, A.: A local correspondence principle for mode shapes in structural dynamics. *Mech. Syst. Signal Process.* **45**, 91–104 (2014)
7. Brincker, R., Ventura, C.: *Introduction to Operational Modal Analysis*, 1st edn. Wiley, New York (2015)
8. Chopra, A.K.: *Dynamics of Structures – Theory and Applications to Earthquake Engineering*, vol. 1, 1st edn. Prentice Hall, Inc., Eaglewood Cliffs (1995)
9. O’Callahan, J., Avitabile, P., Riemer, R.: System equivalent reduction expansion process (SEREP). In: *Proceedings of the 7th International Modal Analysis Conference* (1989)
10. Hoang, N., Friedman, A., Song, W., Char, J., Feinstein, Z., Fujino, Y., Dyke, S.J.: System equivalent reduction expansion process: an experimental validation. In: *Proceedings of EASEC-11 – Eleventh East Asia-Pacific Conference on Structural Engineering and Construction* (2008)
11. Peeters, B., Van der Auweraera, H., Guillaume, P., Leuridan, J.: The polymax frequency–domain method: a new standard for modal parameter estimation? *Shock Vib.* **1**(11), 395–409 (2004)
12. Peeters, B., Van Der Auweraera, H., Vanhollenbeck, F., Guillaume, P.: Operational modal analysis for estimating the dynamic properties of a stadium structure during a football game. *Shock Vib.* **1**(14), 283–303 (2007)
13. Diord, S., Magalhães, F., Cunha, Á., Caetano, E., Martins, N.: Automated modal tracking in a football stadium suspension roof for detection of structural changes. *Struct. Control. Health Monit.* **24**(11), 1–19 (2017)
14. Amador, S.D.R.: *Uncertainty quantification in operational modal analysis and continuous monitoring of special structures*. PhD thesis, Faculty of Engineering of University of Porto (FEUP), Porto (2015)
15. Juul, M., Brincker, R., Amador, S., Skaftø, A., Jannick, B., Hansen, Lopez-Aenlle, M.: One step updating using local correspondence and mode shape orthogonality. *Mechanical Systems and Signal Processing*, (Manuscript submitted) (2017)

Chapter 35

Approximate General Responses of Tuned and Mistuned 4-Degree-of-Freedom Systems with Parametric Stiffness

Ayse Sapmaz, Gizem D. Acar, and Brian F. Feeny

Abstract The purpose of this study is to find approximate solutions to tuned and mistuned 4-DOF systems with parametric stiffness. In this work, the solution and stability of four-degree-of-freedom Mathieu-type system will be investigated. To find the broken-symmetry system response, Floquet theory with harmonic balance will be used. A Floquet-type solution is composed of a periodic and an exponential part. The harmonic balance is applied to the original differential equation of motion. The analysis brings about an eigenvalue problem. By solving this, the Floquet characteristic exponents and the corresponding eigenvectors that give the Fourier coefficients are found in terms of the system parameters. The stability transition curve can be found by analyzing the real parts of the characteristic exponents. The frequency content can be determined by analyzing imaginary parts at the exponents. A response that involves single Floquet exponent (and its complex conjugate) can be generated with a specific set of initial conditions, and can be regarded as a modal response. The method is applied to both tuned and detuned four-degree-of-freedom examples.

35.1 Introduction

Many mechanical systems have parametric excitation characteristics [1–4]. A number of different types of methods has been used to study the Mathieu equation. The method of multiple scales has been used to examine a forced Mathieu equation for resonances [3]. Likewise, stability characteristics are found by using the method of van der Pol [4]. Another way to approach the Mathieu equation is to use Floquet theory. Acar and Feeny [5] used a method combining Floquet theory with harmonic balance to find the system response. An assumed Floquet-type solution is composed of a periodic $p(t)$ and an exponential part $e^{\hat{\mu}t}$ such as $x(t) = e^{\hat{\mu}t}p(t)$. The theory shows that the fundamental solution to a Mathieu equation on stability boundaries is purely periodic [6]. In consequence of that, stability regions can be procured by assuming a periodic solution without solving for the general response itself, [7–11]. The response characteristics of the time-periodic systems is studied by using system identification methods. Allen et al. [12] presented an output-only system identification methodology to identify the modal functions of the Mathieu equation and the Floquet exponents.

In this work, general solutions to Mathieu-type multi-degree-of-freedom systems of the form

$$\mathbf{M}\ddot{\mathbf{x}} + \mathbf{K}(t)\mathbf{x} = \mathbf{0}, \quad (35.1)$$

are examined in detail, where \mathbf{x} is a $d \times 1$ vector of coordinate displacements, where d is the number of degrees of freedom, and \mathbf{M} and $\mathbf{K}(t)$ are the mass and time-varying stiffness matrices.

A general initial condition response as well as the stability characteristics of the system is sought. Intending to produce that result, in place of assuming a periodic solution, a Floquet-type solution is assumed as

$$\mathbf{x}_j^{(r)} = e^{i\mu_r t} \sum_{k=-n}^n \mathbf{c}_{j,k}^{(r)} e^{ik\omega t}, \quad (35.2)$$

A. Sapmaz (✉) · B. F. Feeny
Department of Mechanical Engineering, Michigan State University, East Lansing, MI, USA
e-mail: sapmazay@msu.edu; feeny@egr.msu.edu

G. D. Acar
Department of Mechanical Engineering, University of Maryland, College Park, MD, USA
e-mail: gizem@umd.edu

where the index r distinguishes between $2d$ independent Floquet solution terms for a d -degree-of-freedom system, j presents coordinates and k refers harmonics. As following up the work on approximate general response of symmetric two and three DOF systems with parametric stiffness, the assumed solution is plugged into the equations of motion, and by applying harmonic balance, the characteristic exponents, μ_r and associated Fourier coefficients, $\mathbf{c}_k^{(r)}$, are determined. Then, by using a procedure that is similar to the one used in [5], the response to an arbitrary initial condition can be determined by considering a linear combination of the \mathbf{x}_r .

35.2 Analysis

The response analysis procedure can be explained by studying on example MDOF systems, namely tuned and mistuned 4DOF systems. So as to achieve the goal, a mass-spring chain as shown in Fig. 35.1, with periodic stiffness is studied.

The equations of motion are

$$\begin{aligned} \beta \ddot{X} + (3 + \gamma + \epsilon)X - (1 + \delta \cos[\omega t + 2\pi/3])x_2 - (1 + \delta \cos[\omega t + 4\pi/3])x_3 - (1 + \epsilon + \delta \cos[\omega t + 2\pi])x_4 &= 0 \\ \ddot{x}_2 + (1 + \delta \cos[\omega t + 2\pi/3])(x_2 - X) &= 0 \\ \ddot{x}_3 + (1 + \delta \cos[\omega t + 4\pi/3])(x_3 - X) &= 0 \\ \ddot{x}_4 + (1 + \epsilon + \delta \cos[\omega t + 2\pi])(x_4 - X) &= 0. \end{aligned} \tag{35.3}$$

where $m_2 = m_3 = m_4 = 1$, $M = \beta m_2$, $K = \gamma$ and $k_i(t) = 1 + \epsilon_i + \delta \cos[\omega t + (2\pi/3)(i)]$, where $i = 2, 3, 4$, $t_2 = t_3 = 0$ and $t_4 = \epsilon$. For specific parameter values, the eigenvalues are plotted as a function of stiffness mistuning parameter (ϵ) as shown in Fig. 35.2. When $\delta = 0$ and the system is tuned ($\epsilon = 0$) modal frequencies are $\omega_1 = 0.3047$, $\omega_2 = 1$, $\omega_3 = 1$ and $\omega_4 = 2.075$. Figure 35.3 shows both tuned ($\epsilon = 0$) and mistuned systems space ($\epsilon = 1$) mode shapes in same plot to demonstrate the effect of detuning parameter on the mode shapes.

Fig. 35.1 A four DOF spring-mass chain

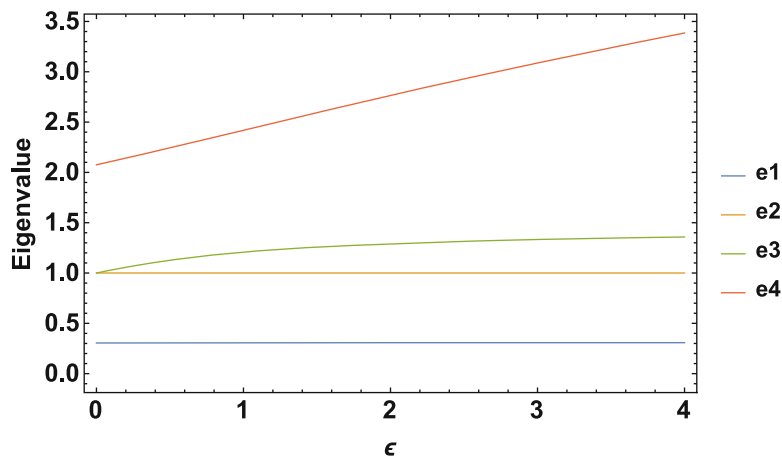
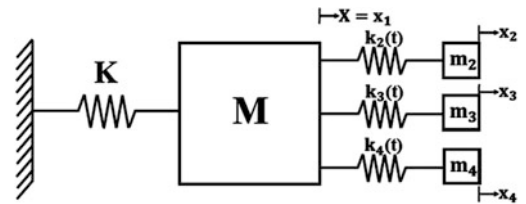


Fig. 35.2 Eigenvalues versus stiffness mistuning parameter ϵ for $\delta = 0$, $\omega = 1.6$, $m_1 = m_2 = m_3 = \beta = 1$, $\gamma = 0.4$

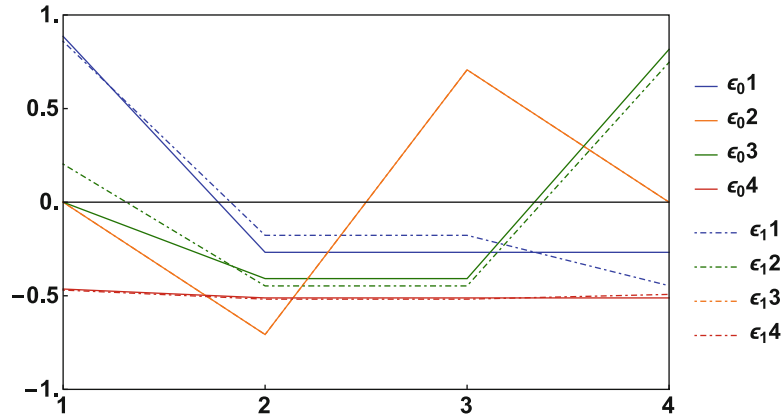


Fig. 35.3 Mode shapes of the tuned ($\epsilon = 0$) and mistuned ($\epsilon = 1$) systems

35.2.1 Tuned Four-Degree-of-Freedom Example

Following the reference [5], the response is found by assuming a Floquet type solution with finite harmonics, as given in Eq. (35.2) and inserting into the system equations of motion. Particularly, in this model, we seek for $x_1(t) = e^{i\mu t} \sum_{k=-n}^n c_{1,k} e^{ik\omega t}$, $x_2(t) = e^{i\mu t} \sum_{k=-n}^n c_{2,k} e^{ik\omega t}$, $x_3(t) = e^{i\mu t} \sum_{k=-n}^n c_{3,k} e^{ik\omega t}$ and $x_4(t) = e^{i\mu t} \sum_{k=-n}^n c_{4,k} e^{ik\omega t}$. Governing equations for $c_{j,k}$'s are determined by using harmonic balance and writing the harmonic balance equation in matrix form,

$$\mathbf{A}\mathbf{c} = \begin{bmatrix} \mathbf{A}_{11} & \mathbf{A}_{12} & \mathbf{A}_{13} & \mathbf{A}_{14} \\ \mathbf{A}_{21} & \mathbf{A}_{22} & \mathbf{A}_{23} & \mathbf{A}_{24} \\ \mathbf{A}_{31} & \mathbf{A}_{32} & \mathbf{A}_{33} & \mathbf{A}_{34} \\ \mathbf{A}_{41} & \mathbf{A}_{42} & \mathbf{A}_{43} & \mathbf{A}_{44} \end{bmatrix} \begin{pmatrix} \mathbf{c}_1 \\ \mathbf{c}_2 \\ \mathbf{c}_3 \\ \mathbf{c}_4 \end{pmatrix} = \begin{pmatrix} \mathbf{0} \\ \mathbf{0} \\ \mathbf{0} \\ \mathbf{0} \end{pmatrix}, \quad (35.4)$$

where $\mathbf{c}_j = [c_{j,-n} \dots c_{j,-1} \quad c_{j,0} \quad c_{j,1} \dots c_{j,n}]^T$, and A_{ij} 's correspond to $(2n+1) \times (2n+1)$ block matrices.

The determinant of the coefficient matrix, $\mathbf{A}(\mu)$, must be equal to zero to own a nonzero \mathbf{c} solution. We can find the characteristic equation for μ in terms of δ , γ , ω and $m_2 = m_3 = m_4 = \beta$. Then, for each μ , we can obtain the \mathbf{c} vector, by solving $\mathbf{A}(\mu)\mathbf{c} = \mathbf{0}$. The characteristic equation produce $2d(2n+1)$ roots μ_q , where q from 1 to $2d(2n+1)$ and d is number of degrees of freedom and n is the number of assumed harmonics. Nevertheless, there are essentially $2d$ principal roots, and the other μ 's are linked to the principal roots by the relation $\mu_s = \mu_r \pm k\omega i$. Since the corresponding exponential part can be written as $e^{i\mu_r t} e^{ik\omega t}$ and the second part can be inserted into the periodic part, it is observed that these roots do not conduce to extra solutions.

As following up the work on 2-DOF and 3-DOF mass-spring chain examples [5], μ_q 's are plugged into the coefficient matrix, then null space of $\mathbf{A}(\mu_q)$ provides the solution of $\mathbf{c}^{(q)}$'s.

The idea about the stability and the frequency subject of the solution can be obtained by the roots of the characteristic equation. Even if only one of the roots has a negative imaginary part, the solution will grow unstable because of the exponential part. If all roots have a positive imaginary part, the solution is bounded. Particularly, if the roots are real, the solution is either periodic or quasi-periodic. In Fig. 35.4, the stability regions for the 4DOF mass-spring chain are drawn by evaluating the imaginary parts of the characteristic roots for $\gamma = 1$, $\beta = 1$.

The frequency values can be determined with combination of the exponential and the periodic parts of the frequencies as $|\text{Re}(\mu) \pm k\omega|$. In 4DOF system, there are eight principal characteristic roots and the general response solution is written in terms of "modal components" as

$$\mathbf{x}(t) = \sum_{j=1}^8 a_j \mathbf{x}^r(t), \quad (35.5)$$

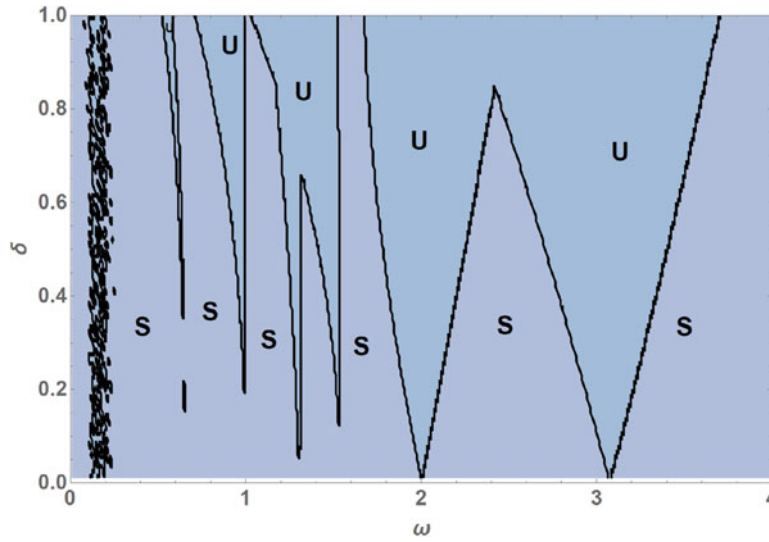


Fig. 35.4 Stability regions for the tuned 4 DOF mass-spring chain for $n = 2$, $\beta = 1$ and $\gamma = 0.4$

where

$$\mathbf{x}^{(r)} = \begin{bmatrix} x_1^{(r)} \\ x_2^{(r)} \\ x_3^{(r)} \\ x_4^{(r)} \end{bmatrix} \tag{35.6}$$

a_r 's are to be determined from the initial conditions. Arbitrary initial conditions can be defined as a class of linear equations in terms of the constants a_r , as

$$\begin{bmatrix} \mathbf{x}_0 \\ \dot{\mathbf{x}}_0 \end{bmatrix} = \begin{bmatrix} \mathbf{x}^1(0) & \dots & \mathbf{x}^8(0) \\ \dot{\mathbf{x}}^1(0) & \dots & \dot{\mathbf{x}}^8(0) \end{bmatrix} \begin{bmatrix} a_1 \\ \vdots \\ a_8 \end{bmatrix}. \tag{35.7}$$

As stated in the previous study [5], the initial condition $[\mathbf{x}_0^T \ \dot{\mathbf{x}}_0^T]^T = [\mathbf{x}^k(0)^T \ \dot{\mathbf{x}}^k(0)^T]^T$ results in $a_k = 1$ and $a_{r \neq k} = 0$. Consequently, the different modal functions can be obtained if a scalar multiple of each column can be used as an initial condition. Accordingly, the response can be determined as the same linear combination of the corresponding modal functions by writing an initial condition as a linear combination of $[\mathbf{x}_j(0)^T \ \dot{\mathbf{x}}_j(0)^T]^T$'s.

The 4DOF spring-mass chain was studied with $n = 2$ harmonics, for various sets of parameters and initial conditions. The results were compared to those determined from a numerical work, and the initial condition response and FFT plots were given in Figs. 35.5 and 35.6 for $\delta = 0.2$ and in Figs. 35.7 and 35.8 for $\delta = 0.6$.

35.2.2 Mistuned Four-Degree-of-Freedom Example

Instead of assuming a perfectly tuned model, in this section one of the stiffness term $k_4(t)$ is assumed to have a variation ϵ , such that $k_4(t) = (1 + \epsilon + \delta \cos[\omega t + 2\pi])$.

Following up the work on tuned system, general solution Eq. (35.2) is inserted into Eq. (35.3) and same steps are applied. Then, characteristic exponents and corresponding eigenvectors are obtained. The stability wedges of the 4DOF system are plotted by examining the imaginary parts of the characteristic exponents for $\gamma = 0.4$, $\beta = 1$, $\epsilon = 1$ in Fig. 35.9.

FFT plots and the initial condition responses were found assuming $n = 2$ harmonics and detuning term $\epsilon = 0.2$, for different sets of parameters, and were compared to those obtained from a numerical study, as given in Figs. 35.10 and 35.11 for $\delta = 0.2$ and Figs. 35.12 and 35.13 for $\delta = 0.6$.

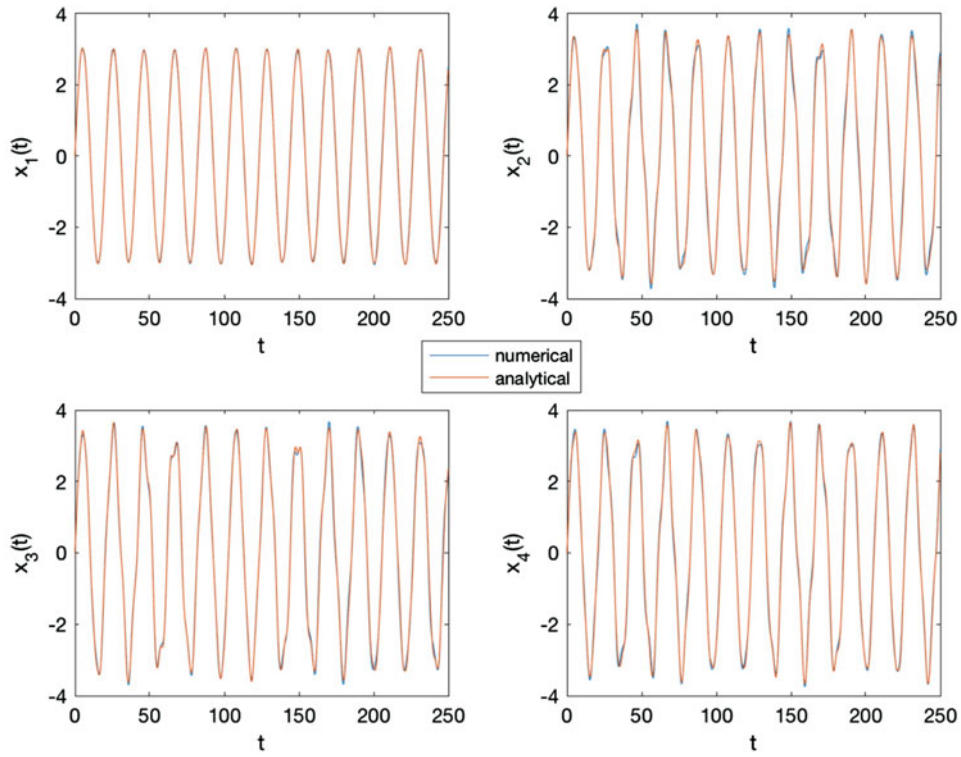


Fig. 35.5 Response plots for $n = 2, \omega = 0.75, \delta = 0.2, \epsilon = 0, \gamma = 0.4, \mathbf{x}(0) = [0 \ 0 \ 0 \ 0]^T$ and $\dot{\mathbf{x}}(0) = [1 \ 1 \ 1 \ 1]^T$

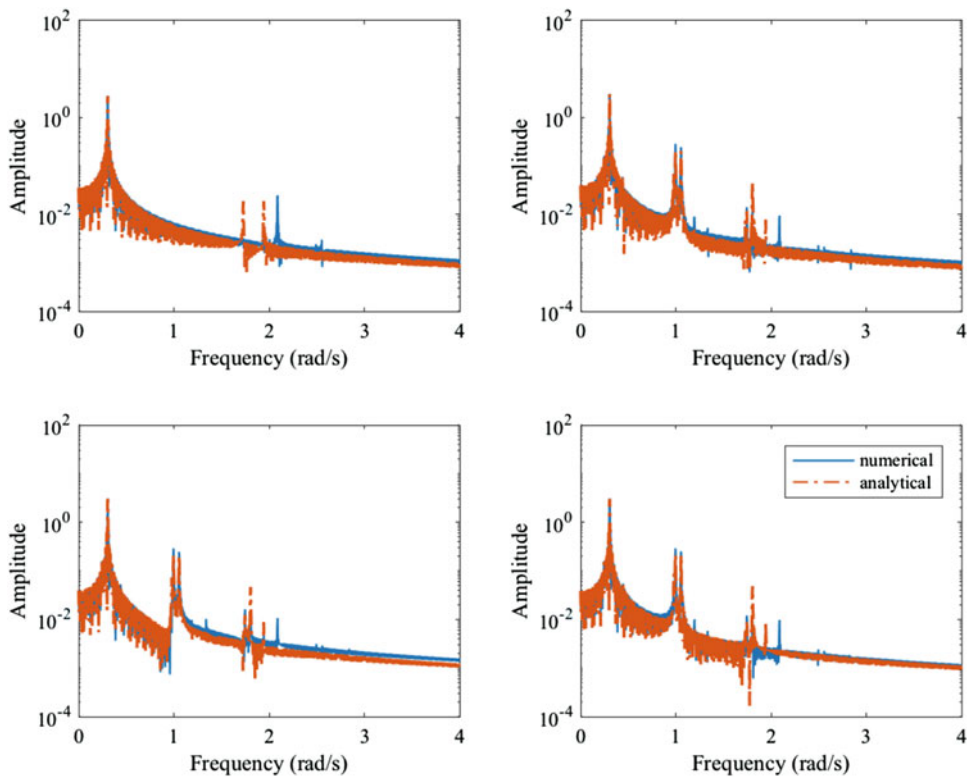


Fig. 35.6 FFT plots for $n = 2, \omega = 0.75, \delta = 0.2, \epsilon = 0, \gamma = 0.4, \mathbf{x}(0) = [0 \ 0 \ 0 \ 0]^T$ and $\dot{\mathbf{x}}(0) = [1 \ 1 \ 1 \ 1]^T$

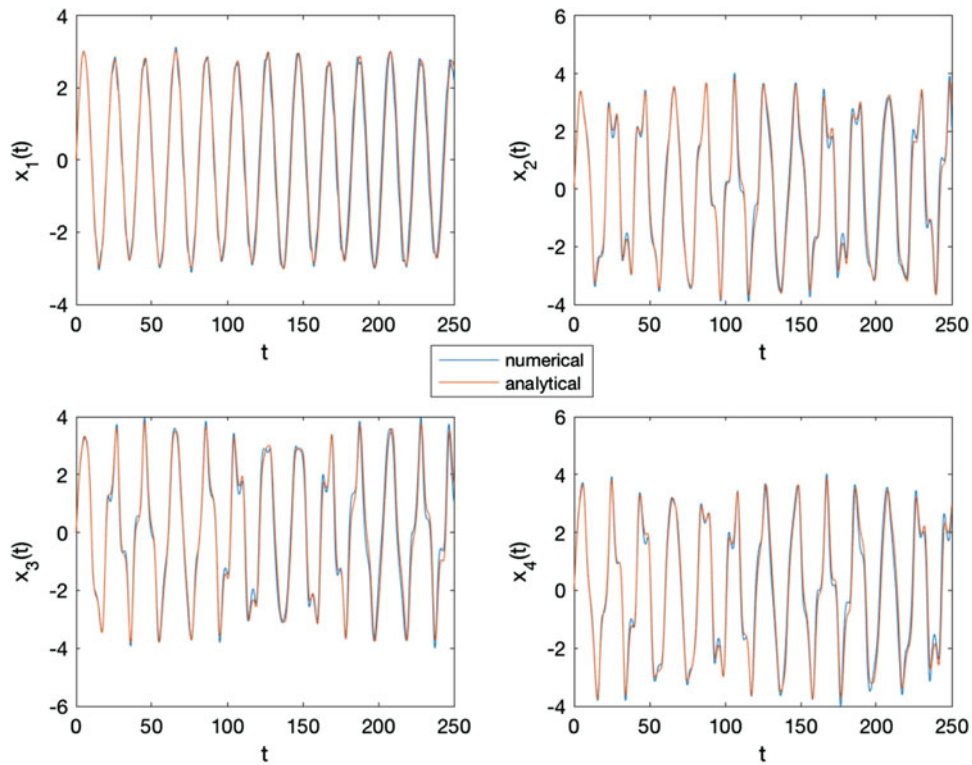


Fig. 35.7 Response plots for $n = 2, \omega = 0.75, \delta = 0.6, \epsilon = 0, \gamma = 0.4, \mathbf{x}(0) = [0 \ 0 \ 0 \ 0]^T$ and $\dot{\mathbf{x}}(0) = [1 \ 1 \ 1 \ 1]^T$

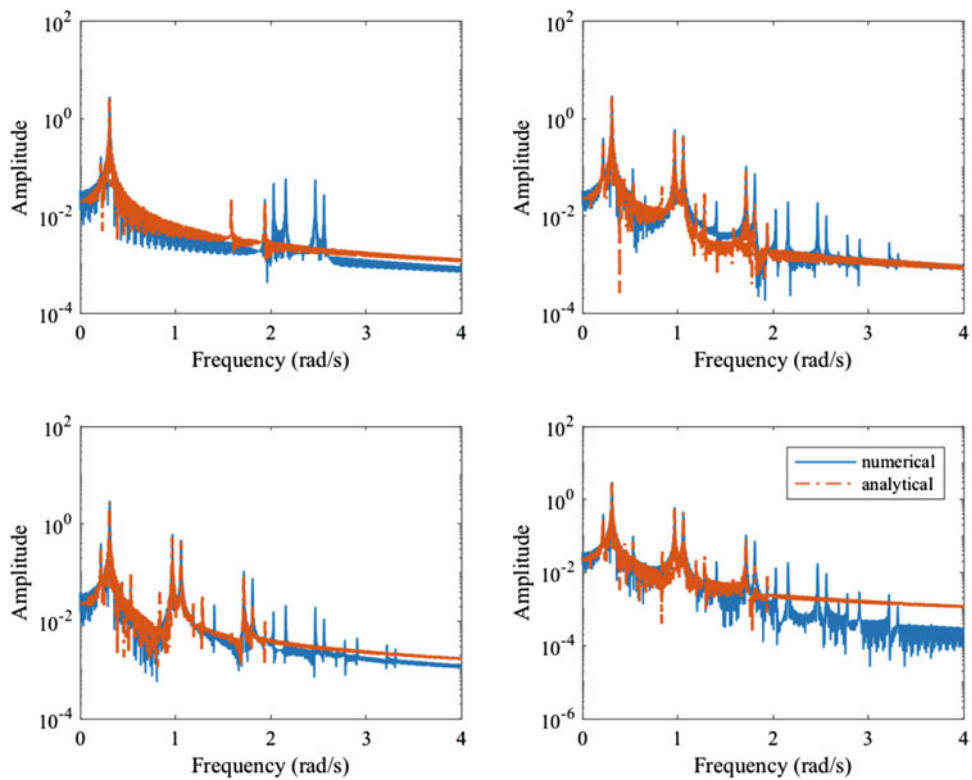


Fig. 35.8 FFT plots for $n = 2, \omega = 0.75, \delta = 0.6, \epsilon = 0, \gamma = 0.4, \mathbf{x}(0) = [0 \ 0 \ 0 \ 0]^T$ and $\dot{\mathbf{x}}(0) = [1 \ 1 \ 1 \ 1]^T$

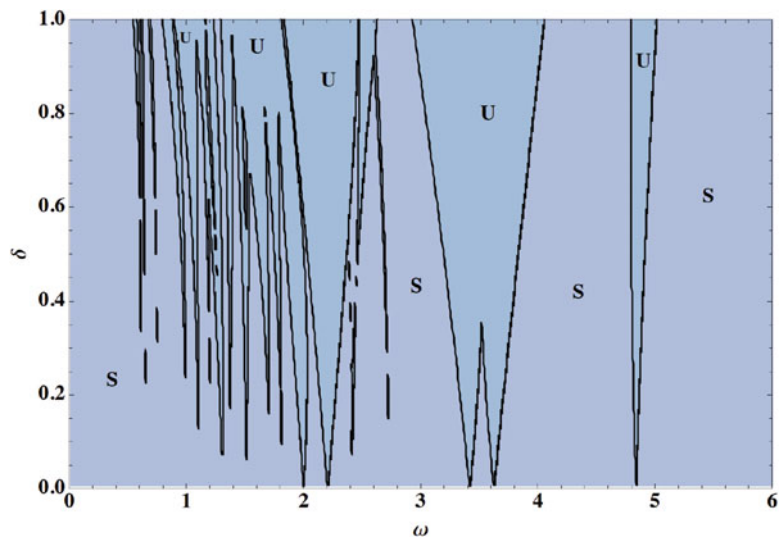


Fig. 35.9 Stability regions for the mistuned 4 DOF mass-spring chain for $n = 2$, $\epsilon = 1$, $\beta = 1$ and $\gamma = 0.4$

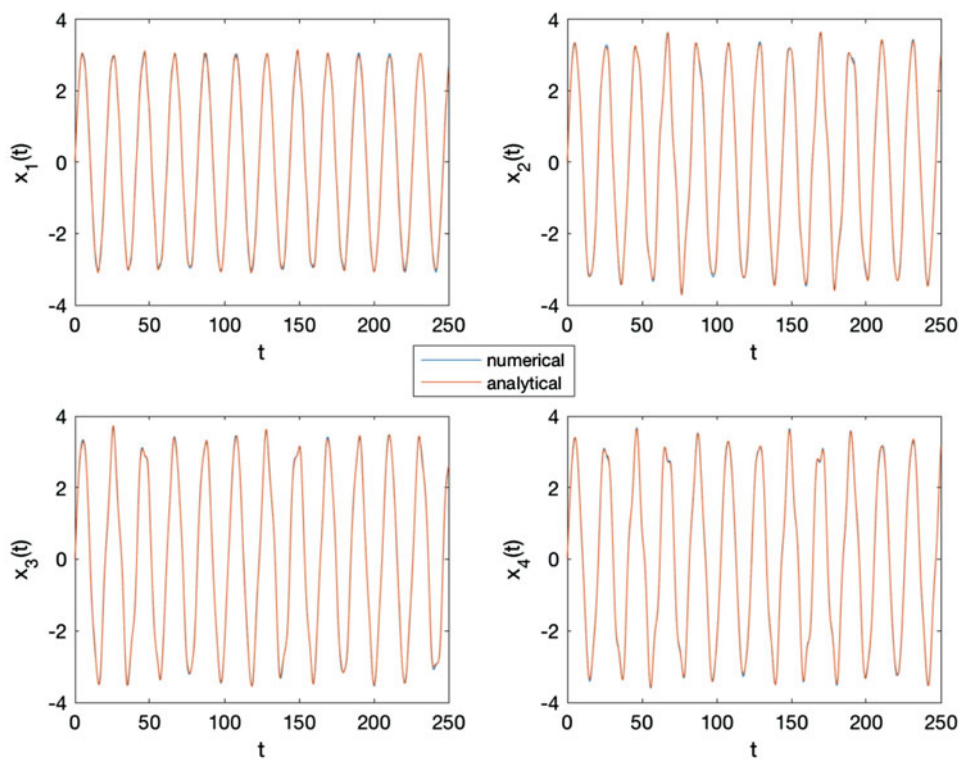


Fig. 35.10 Response plots of detuned system for $n = 2$, $\epsilon = 0.2$, $\omega = 0.8$, $\delta = 0.2$, $\gamma = 0.4$, $\mathbf{x}(0) = [0 \ 0 \ 0 \ 0]^T$ and $\dot{\mathbf{x}}(0) = [1 \ 1 \ 1 \ 1]^T$

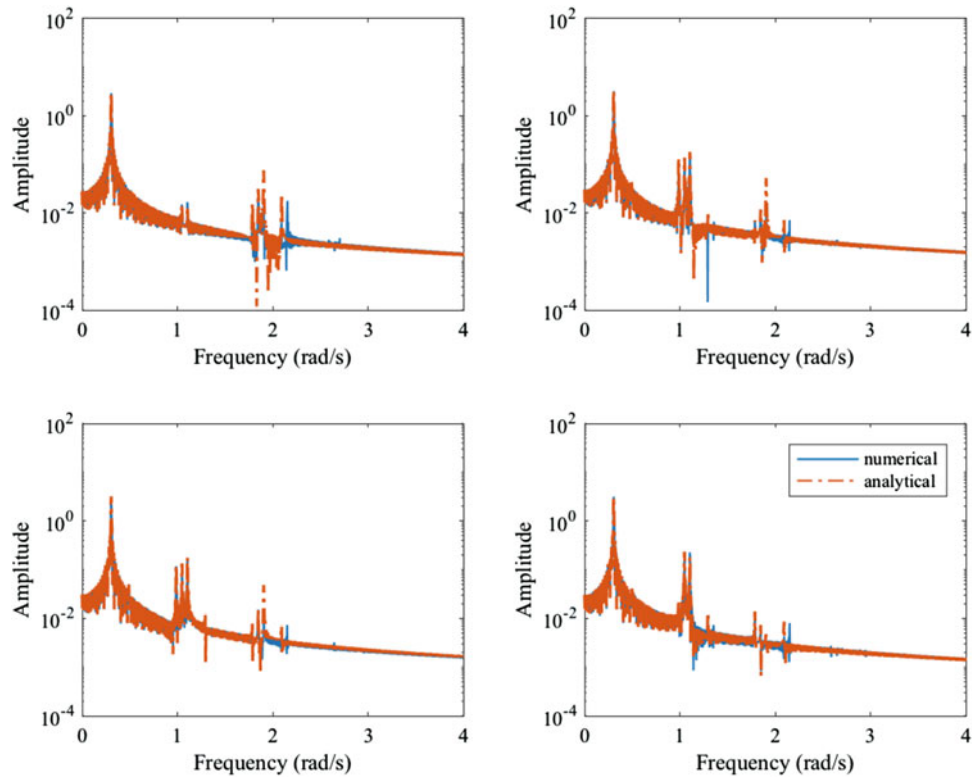


Fig. 35.11 FFT plots of detuned system for $n = 2$, $\epsilon = 0.2$, $\omega = 0.8$, $\delta = 0.2$, $\gamma = 0.4$, $\mathbf{x}(0) = [0 \ 0 \ 0 \ 0]^T$ and $\dot{\mathbf{x}}(0) = [1 \ 1 \ 1 \ 1]^T$

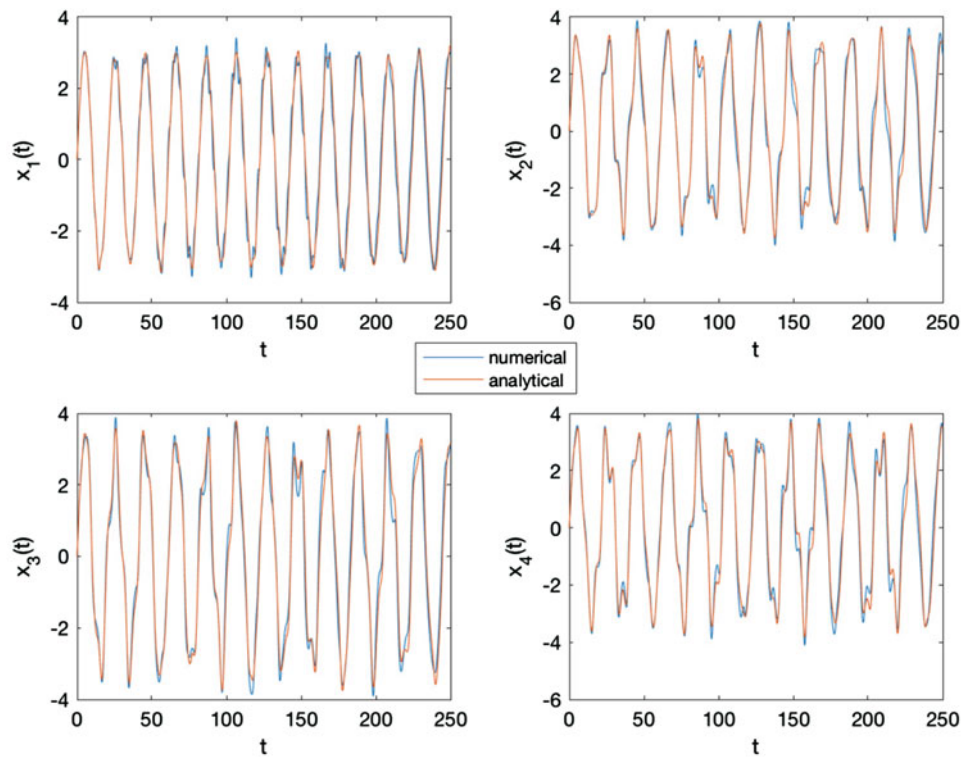


Fig. 35.12 Response plots of detuned system for $n = 2$, $\epsilon = 0.2$, $\omega = 0.8$, $\delta = 0.6$, $\gamma = 0.4$, $\mathbf{x}(0) = [0 \ 0 \ 0 \ 0]^T$ and $\dot{\mathbf{x}}(0) = [1 \ 1 \ 1 \ 1]^T$

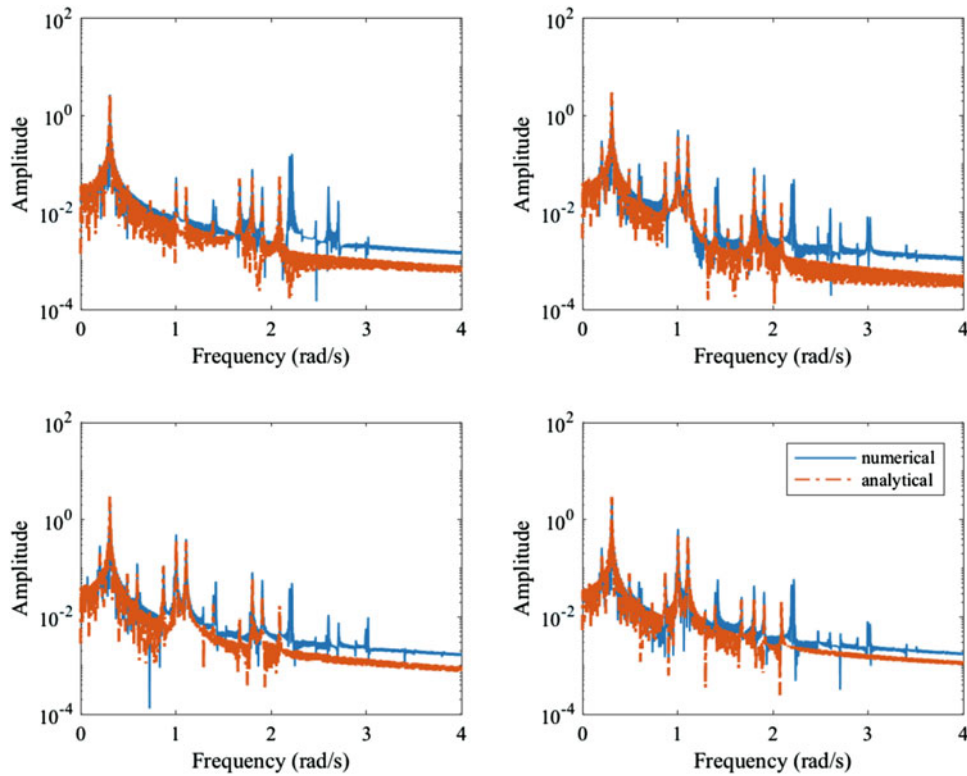


Fig. 35.13 FFT plots of detuned system for $n = 2$, $\epsilon = 0.2$, $\omega = 0.8$, $\delta = 0.6$, $\gamma = 0.4$, $\mathbf{x}(0) = [0 \ 0 \ 0 \ 0]^T$ and $\dot{\mathbf{x}}(0) = [1 \ 1 \ 1 \ 1]^T$

35.3 Discussion

The instability wedges in Fig. 35.4 may be based at $\omega = (\omega_i + \omega_j)/N$, where N is a positive integer. In the tuned 4DOF system for $\beta = 1$ and $\gamma = 0.4$, the $\delta = 0$ natural frequencies were $\omega_1 = 0.3047$, $\omega_2 = \omega_3 = 1$ and $\omega_4 = 2.075$. We observe the two main subharmonic instability wedges starting at frequencies $\omega \cong \omega_2 + \omega_3 = 2$, $\omega \cong \omega_1 + \omega_{2,3} = 1.305$ and $\omega \cong \omega_{2,3} + \omega_4 = 3.07$. Additionally, if there is a wedge at $2\omega_4 = 4.15$, it is not in the domain of Fig. 35.4. Some primary and superharmonic wedges originate at frequencies that fit into the pattern, such as $\omega_2 = \omega_3 = 1$, $(\omega_1 + \omega_2)/2 = (\omega_1 + \omega_3)/2 = 0.65$, $\omega_1 = 0.304$, $(\omega_2 + \omega_4)/2 = (\omega_3 + \omega_4)/2 = 1.537$ and $\omega_4/2 = 1.035$. Simulations were done for different parameter values to confirm the compatibility. For instance, at $\delta = 0.8$ and $\omega = 1.1$ the simulation was unstable, although at $\omega = 1.6$ the simulation was stable, in agreement with the stability region in Fig. 35.4. The plot of Fig. 35.4 shows a spurious instability feature near $\omega = 0.15$. Similar trends were observed from simulations of the four-DOF system with different values of γ which is not shown here.

The detuned 4DOF system for $\epsilon = 1$, $\beta = 1$ and $\gamma = 0.4$, the natural frequencies were $\omega_1 = 0.3065$, $\omega_2 = 1$, $\omega_3 = 1.206$ and $\omega_4 = 2.4188$. We see the wedges at $2\omega_1 \cong 0.604$, $2\omega_2 \cong 2$, $2\omega_3 \cong 2.41$, $\omega_1 + \omega_2 \cong 1.306$, $\omega_1 + \omega_3 \cong 1.512$, $\omega_2 + \omega_3 \cong 2.206$, $\omega_2 + \omega_4 \cong 3.418$, $\omega_1 + \omega_4 \cong 2.713$, $\omega_3 + \omega_4 \cong 3.616$ and $2\omega_4 \cong 4.84$ showing the subharmonic instabilities of each “mode”. Some primary and superharmonic wedges are also based at frequencies which match the pattern, such as $\omega_2 = 1$, $\omega_3 = 1.206$, $\omega_4 = 2.418$, $(\omega_2 + \omega_3)/2 = 1.103$, $(\omega_1 + \omega_2)/2 = 0.605$, $(\omega_1 + \omega_4)/2 = 1.36$, $(\omega_1 + \omega_3)/2 = 0.751$, $(\omega_2 + \omega_4)/2 = 1.712$ and $(\omega_3 + \omega_4)/2 = 1.81$. Comparing the tuned and mistuned stability plots, the mistuned system has many more instability wedges, and generally depicts a greater tendency to destabilize.

According to the Floquet solution, which involves a linear combination of terms $e^{i\mu t} \mathbf{p}(t)$, it is clear that initial conditions can be specified such that only one of these terms is active. In this respect, we name them “modal responses”. Analytical and numerical free responses are shown in Figs. 35.10, 35.11, 35.12, and 35.13, for $n = 2$, for the chosen parameters and initial conditions. The time responses showed good agreement. Around 8–10 response harmonics were predicted, mostly accurately, with a couple instances of low amplitude spurious harmonics. Some higher frequency harmonics were not captured analytically with $n = 2$.

The work shown here involves the solution to a nonstandard eigenvalue problem in the form of Eq. (35.4) in which matrix \mathbf{A} has elements with μ^2 terms. The characteristic equation is polynomial of degree $2d(2n + 1)$ in μ . As the number of harmonics, n , increases there may be computational limits on finding symbolic solutions for the μ . Despite this, $n = 2$ harmonics were able to effectively predict the response for the systems studied in this paper.

35.4 Conclusions

General responses of a 4 DOF mass-spring system with parametric excitation were studied. Assuming a Floquet-type solution, and applying the harmonic balance method, the frequency content and stability of the solution were found. Later, the analysis was extended to a system with mistuned parameters, and the effect of symmetry breaking on system response was studied. In addition, the time response and FFT plots were produced for various parameters and initial conditions in the both tuned and mistuned case. Ten analytical results were confirmed by numerical simulations. In future work, this method will be applied on mistuned three-blade wind turbine models to find the response characteristics.

Acknowledgements This project is funded by the National Science Foundation, under grant CMMI-1335177, and Republic of Turkey/Ministry of National Education. Any opinions, findings, and conclusions or recommendations expressed are those of the authors and do not necessarily reflect the views of the NSF.

References

1. Ruby, L.: Applications of the Mathieu equation. *Am. J. Phys.* **64**(1), 39–44 (1996)
2. Li, Y., Fan, S., Guo, Z., Li, J., Cao, L., Zhuang, H.: Mathieu equation with application to analysis of dynamic characteristics of resonant inertial sensors. *Commun. Nonlinear Sci. Numer. Simul.* **18**(2), 401–410 (2013)
3. Ramakrishnan, V., Feeny, B.F.: Resonances of a forced Mathieu equation with reference to wind turbine blades. *J. Vib. Acoust.* **134**(6), 064501 (2012)
4. Inoue, T., Ishida, Y., Kiyohara, T.: Nonlinear vibration analysis of the wind turbine blade (occurrence of the superharmonic resonance in the out of plane vibration of the elastic blade). *J. Vib. Acoust.* **134**(3), 031009 (2012)
5. Acar, G., Feeny, B.F.: Approximate general responses of multi-degree-of-freedom systems with parametric stiffness. In: *Special Topics in Structural Dynamics*, vol. 6, pp. 211–219. Springer, Switzerland (2016)
6. Panardo, I.: *Stability of periodic systems and Floquet theory* (2014)
7. Rand, R.: *Lecture Notes on Nonlinear Vibrations*. Published online (2012). <http://www.math.cornell.edu/~rand/randdocs/nlvibe52.pdf>
8. Ishida, Y., Inoue, T., Nakamura, K.: Vibration of a wind turbine blade (theoretical analysis and experiment using a single rigid blade model). *J. Environ. Eng.* **4**(2), 443–454 (2009)
9. McLachlan, N.W.: *Theory and Application of Mathieu Functions*. Dover, New York (1961)
10. Peterson, A., Bibby, M.: *Accurate Computation of Mathieu Functions*. Morgan & Claypool Publishers, San Rafael (2013)
11. Hodge, D.B.: *The calculation of the eigenvalues and eigenfunctions of Mathieu's equation*, vol. 1937. National Aeronautics and Space Administration, Washington, DC (1972)
12. Allen, M.S., Sracic, M.W., Chauhan, S., Hansen, M.H.: Output-only modal analysis of linear time-periodic systems with application to wind turbine simulation data. *Mech. Syst. Signal Process.* **25**(4), 1174–1191 (2011)

Chapter 36

Modal Analysis of a Vertical-Axis Darrieus Wind Turbine Blade with a Troposkein Shape

Amr Saleh and Brian F. Feeny

Abstract Darrieus wind turbines with troposkein shaped blades are an important type of vertical axis wind turbines. When designing these blades it is important to consider vibration properties and how vibrations may affect failure and safe load margins. In order to avoid the occurrence of resonance, the natural frequencies of the blade structure needs to be determined and designed relative to the turbine operating ranges.

In this work we examine the modal characteristics of Darrieus style vertical-axis wind-turbine blades. We build a finite element model of a spinning Sandia straight-circular-straight blade, and compare the results of our model with those of Sandia. We then use the model to study the stationary blade, and the blade with a true troposkein blade shape. The modeling of the blades using slender beam theory is sketched for comparison with the finite element model and for its eventual use for low-order modeling.

36.1 Finite-Element Analysis

We conducted a modal analysis study on the Sandia 17 m diameter blade with an approximated troposkein shape and a NACA 0015 airfoil, based on [1, 2]. In this study, we isolated the single blade, and neglected the compliance of the tower, as well as coupling with other blades through the tower and rotor. The Sandia curved blade is made up of two straight parts and a circular part, as in Fig. 36.1a, with a cross section shown in Fig. 36.1b. We used the blade cross-sectional quantities provided by reference [2]. First we conducted a finite-element analysis. We built a finite-element model using ANSYS WORKBENCH and examined the first ten modes under the conditions of spinning at 54 rpm. The analysis accommodates centrifugal stiffening effects, but not gyroscopic effects. The results are compared with those obtained by Sandia in Table 36.1. The first eight mode shapes are shown in Fig. 36.2.

We then performed a modal analysis on the stationary blade. This case provides a reference for comparisons with other models, and also for initial experimental modal studies the could take place in the future. The modal frequencies computed for the stationary blade are also listed in Table 36.1.

Finally, we analyzed the modal properties of a troposkein blade. Since the Sandia straight-circular-straight beam is made to approximate the troposkein [3], it is worthwhile to evaluate the approximation in terms of the modal frequencies. The troposkein model's cross section, however, had a slightly thinner leading edge (6.35 mm) compared to the Sandia blade (8.9 mm), although beyond the leading edge they were the same. The modal frequencies with and without the imposed spin are listed in the table.

36.2 Continuing Studies: Slender Beam Theory

Knowledge of the modal characteristics is important, and finite-element analysis is an effective way to obtain many of the lower modes. However, it can be advantageous to do a low-order model, for example in finding the dependence of behavior on a parameter, or when analyzing the system under nonlinear loadings. To this end, we aim to examine a low-order vibration model based on slender beam theory under flatwise (radial, $u(s, t)$) and edgewise (circumferential, $v(s, t)$) bending, and axial extension ($w(s, t)$) and torsion ($\phi(s, t)$), where s is the coordinate along the elastic axis of the blade, and t is time. We follow the work of Kaza and Kvaternik [4], who did an excellent beam model analysis in a study for the Department of Energy.

A. Saleh (✉) · B. F. Feeny

Department of Mechanical Engineering, Michigan State University, East Lansing, MI, USA

e-mail: salehamr@msu.edu; feeny@egr.msu.edu

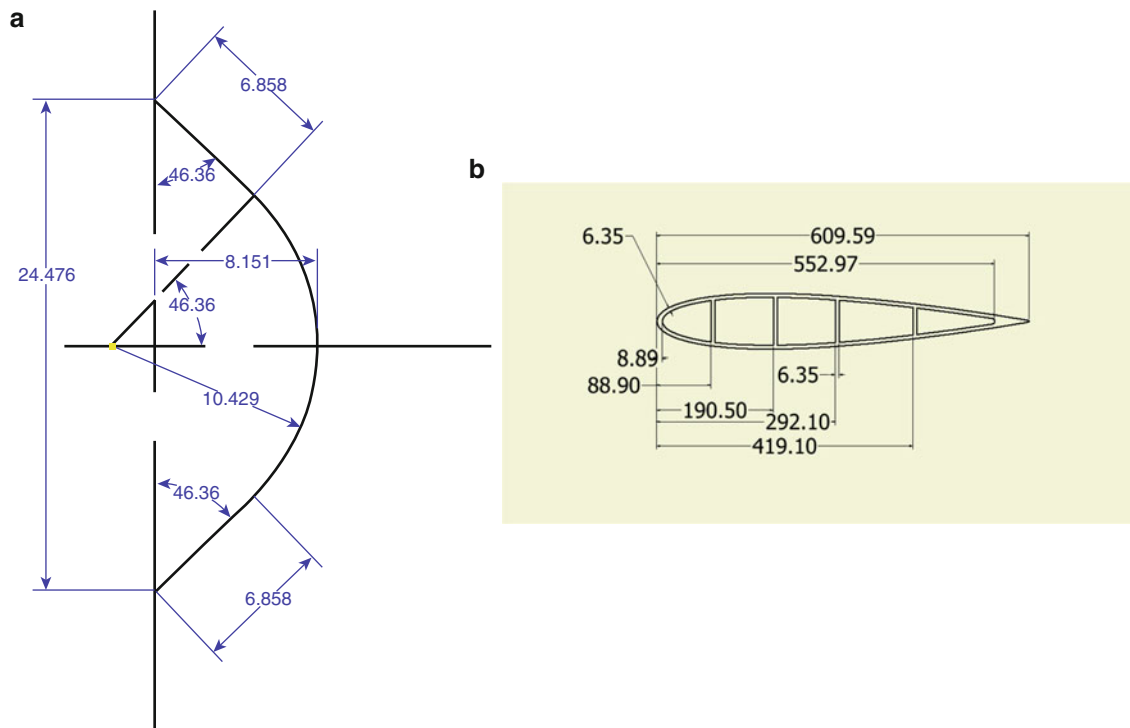


Fig. 36.1 (a) Shape and dimensions of Sandia 17 m blade. (b) Shape and dimensions of Sandia blade cross section

Table 36.1 Comparison of the lower modal frequencies as obtained by finite-element analysis. “Sandia” refers to the straight-circular-straight blade model. Spinning occurs at 54 rpm

Mode number	Sandia [2] 54 rpm	Sandia (MSU) 54 rpm	Troposkein 54 rpm	Sandia (MSU) stationary	Troposkein stationary
Flatwise	1.99	2.0348	1.8665	1.2824	1.2832
Edgewise	2.54	2.5675	2.3412	2.4595	2.2904
Flatwise	3.69	4.0066	3.68	2.8691	2.8102
Edge/torsion	5.94	5.9361	5.8174	4.8445	4.7765
Flatwise	6.06	6.1904	6.1824	5.6198	5.962
Flatwise	8.47	8.5349	8.363	7.1157	7.2123
Flatwise	11.72	11.749	11.36	10.188	10.139
Edge/torsion	13.51	13.522	13.301	13.177	13.055
Flatwise		15.335	14.821	13.693	13.55
Flatwise		19.354	18.737	17.649	17.427

In this study, cross sections were assumed to remain undeformed. The Green’s strains were derived and expressed in terms of u , v , w , ϕ , and their derivatives, and then the strains were used to compute the strain energy. Kaza and Kvaternik [4] thus derived the partial differential equations (PDEs) of motion. We aim to linearize the PDEs and analyze with an assumed modes projection. We will also express the kinetic and potential energies and apply assumed modes to obtain mass and stiffness matrices. Both assumed-mode discretizations can then be evaluated with reference to the finite-element modes (Fig. 36.2).

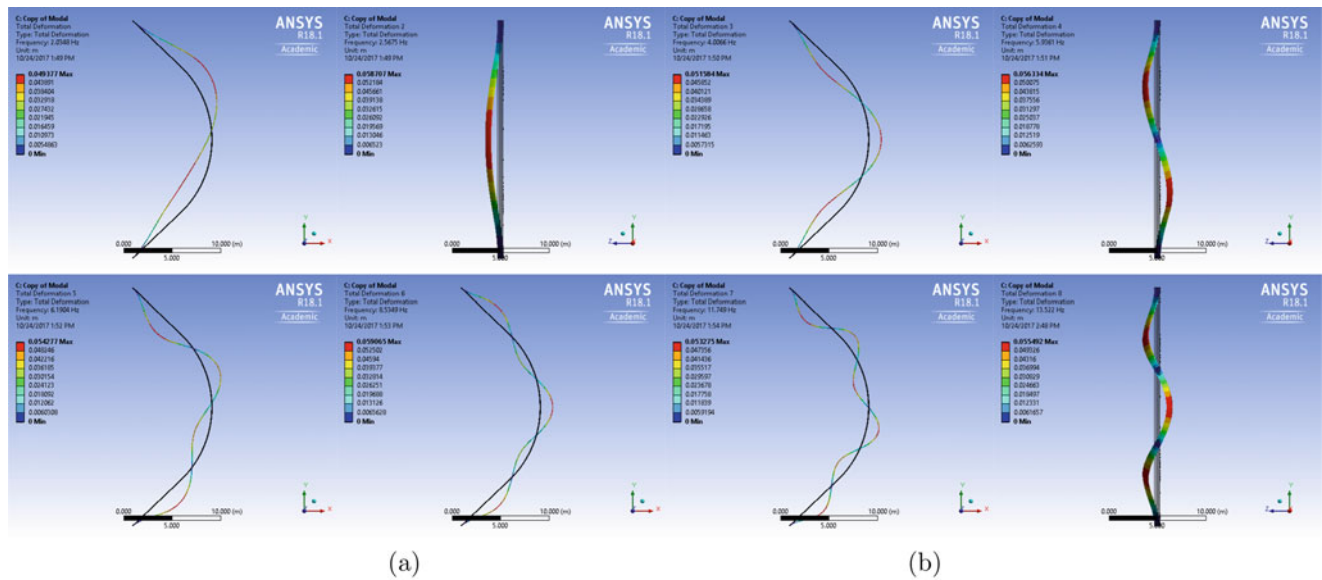


Fig. 36.2 Mode shapes obtained by FEA with ANSYS. Left to right, the mode shapes are dominantly flatwise, edgewise, flatwise, edgewise with torsion, and flatwise, flatwise, flatwise, and edgewise with torsion

Acknowledgements This project is funded by USAID, and the National Science Foundation, under grant CMMI-1435126. Any opinions, findings, and conclusions or recommendations expressed are those of the authors and do not necessarily reflect the views of the NSF.

References

1. Blackwell, B.F., Reis, G.E.: Blade shape for a troposkien type of vertical-axis wind turbine. Technical report, Sandia National Laboratories, Albuquerque (1977). Sandia National Laboratories Energy Report SLA-74-0154
2. Alcoa Laboratories: Design and fabrication of a low cost Darrieus vertical axis wind turbine system, phase I. Technical report, ALO-4272:1-236, 22 June 1979
3. Blackwell, B.F., Reis, G.E.: Practical approximations to a troposkien by straight-line and circular-arc segments. Technical report, Sandia National Laboratories, Albuquerque (1975). Sandia National Laboratories Energy Report SAND74-0100
4. Kaza, K.R.V., Kvaternik, R.G.: Measurement of the Lyapunov spectrum from a chaotic time series. DOE/NASA report, NASA TM-79295:DOE/NASA/1028-79/25 (1979)

Chapter 37

Floquet-Type Analysis of Transient Vibrations of a Horizontal Axis Wind Turbine

Gizem D. Acar and Brian F. Feeny

Abstract General responses of coupled blade-hub equations of a horizontal axis wind turbine (HAWT) are studied. HAWT blades have parametric stiffness terms due to gravity. The blade equations are coupled through the rotor equation, and blade stiffness varies cyclically with the hub angle. In this study, the equations of motion are transformed from the time domain to the hub angle domain, and a scaling scheme is used which results in interdependent blade equations and eliminates the rotor equation. With hub angle as the independent coordinate, the blade equations have parametric stiffness. Then, assuming a Floquet-type solution, unforced dynamics of a turbine is investigated. The assumed solution is a product between an exponential and a periodic part. Plugging into the equations of motion, and applying harmonic balance method, an eigenvalue problem is obtained in terms of system parameters, where the eigenvalues are the characteristic exponents in the exponential part of the assumed solution. The solution to the eigenvalue problem provides parametric modal solutions. The response to an arbitrary initial condition is approximated by combining the modal solutions. Additionally, stability of the solutions is investigated by examining the characteristic exponents. The results are then compared to numerical solutions for verification.

37.1 Introduction

Parametric stiffness characteristics can be observed in numerous mechanical systems [1–4]. The Mathieu equation can be used to represent generic single degree-of-freedom systems with parametric stiffness, and it has been widely studied in the literature [3, 4]. The most common approach to handle the Mathieu equation is to study the stability of its solution by using the Floquet theory, where a periodic solution is assumed to find the boundaries between stable and unstable regions [5–8]. These studies were also extended to systems with multi-degree-of-freedom [9].

The authors have worked on the Mathieu equation and MDOF systems with parametric stiffness, where rather than finding the stability of the solution only, they focused on finding the solution itself [10, 11]. By assuming a Floquet-type solution, and applying harmonic balance method, they found the frequency content and stability of the solution, and determined the system response to arbitrary initial conditions.

In this paper, the method developed in the authors' earlier work is employed to study three-blade horizontal-axis wind turbine vibrations. A single mode model is assumed for each blade where parametric terms are introduced by the cyclic force applied on the blades due to gravity. The model can be seen in Fig. 37.1, where q_j are modal coordinates associated with in-plane bending vibrations of each blade, and ϕ_j are blade angles ($\phi_1 = \phi$, $\phi_2 = \phi + \frac{2\pi}{3}$, $\phi_3 = \phi + \frac{4\pi}{3}$, with ϕ being the hub angle). In the next section, the procedure to find the general responses of the blades to arbitrary initial conditions is explained.

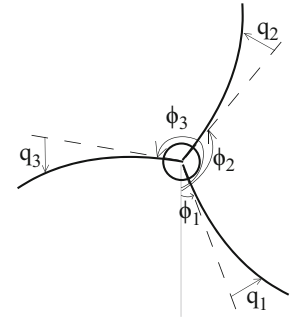
G. D. Acar (✉)

Department of Mechanical Engineering, University of Maryland, College Park, MD, USA
e-mail: gizem@umd.edu

B. F. Feeny

Department of Mechanical Engineering, Michigan State University, East Lansing, MI, USA

Fig. 37.1 In plane vibrations of a three-blade wind turbine



37.2 Analysis

Blade and hub equations for a three blade turbine under in plane vibrations are

$$m_b \ddot{q}_j + c_b \dot{q}_j + (k_0 + k_1 \dot{\phi}^2 + k_2 \cos \phi_j) q_j + d \sin \phi_j + e \ddot{\phi} = Q_j, \quad (37.1)$$

$$J_r \ddot{\phi} + c_r \dot{\phi} + \sum_{k=1}^3 (d \cos \phi_k q_k + e \ddot{q}_k) = Q_\phi, \quad (37.2)$$

where $(\dot{})$ represents derivative with respect to time, q_j are generalized blade coordinates, ϕ is the hub angle, m_b is the blade mass, J_r is the rotor inertia, c_b and c_r are damping terms, d is the direct excitation induced by gravity, k_0 is the elastic stiffness, k_1 is the centrifugal stiffening term, k_2 is the parametric excitation due to gravity, and Q_j and Q_ϕ are generalized forcing terms. The model accounts for stiffness variations due to gravity and centrifugal effects. Blade equations are coupled through inertial terms through the hub equation.

To account for the variations in the hub speed, the equations are transformed into the hub-angle (ϕ) domain, and applying a scaling scheme, the blade equations are decoupled from the hub equations. For studying the transient behavior due to parametric excitation, the resulting unforced ($d = 0$), mass-normalized blade equations in the ϕ domain are

$$q_j'' + \hat{k}_0 q_j = \epsilon \left[-\hat{k}_2 \cos \left(\phi + \frac{2\pi}{3} j \right) q_j + \tilde{e}^2 \sum_{k=1}^3 q_k'' \right], \quad j = 1, 2, 3, \quad (37.3)$$

where (\prime) represents derivative with respect to the rotor angle ϕ , \hat{k}_0 is the normalized blade stiffness, \hat{k}_2 is the parametric stiffness due to gravity and \tilde{e} is the coupling between the blades. Since transformation from time domain to the hub angle domain is a long and detailed procedure, it is not given in this paper. However, it can be found in [12], where the relationship between the hub angle equation parameters and time domain equation parameters is also provided.

In order to find the general solutions to the parametrically excited blade equations, Floquet theory is applied, where the assumed solution has the form $\mathbf{q}(\phi) = e^{i\mu\phi} \mathbf{p}(\phi)$, with $\mathbf{p}(\phi)$ being of the same period as the parametric excitation term, which is 1 for this problem. The truncated Floquet type solution used in this problem is expressed as follows:

$$\mathbf{q}(\phi) = \sum_{j=1}^6 b_j e^{i\mu_j \phi} \sum_{k=-m}^m \mathbf{c}_{j,k} e^{ik\phi}, \quad (37.4)$$

where the first part is the “exponential part” and second part is the “periodic part”. $\hat{\mu}_j = i\mu_j$ are the Floquet exponents and m is the number of harmonics in the truncated periodic part.

Plugging into the equations of motion, and applying the harmonic balance method, the governing equations for $\mathbf{c}_{j,k}$ are found as

$$\mathbf{B}(\mu) \mathbf{c} = \mathbf{0}, \quad (37.5)$$

where $\mathbf{B}(\mu)$ is a $3(2m+1) \times 3(2m+1)$ matrix. In order to have a nonzero solution, the determinant of \mathbf{B} matrix has to be zero. Equating the determinant to zero, one can find the characteristic equation for μ . Inserting the characteristic exponents

(μ) into Equation (37.5), the coefficients $\mathbf{c}_{j,k}$ can be found. Essentially μ_k are eigenvalues, \mathbf{c}_k are eigenvectors, and among $6m + 3$ eigensolutions, 6 are principal [10, 11]. The characteristic exponents reveal the frequency content and the stability of the solution. It can be seen from the assumed solution that the order content (analogous to frequency content in the time domain) is composed of $\mu_j \pm k$. In addition, if the characteristic exponents have negative imaginary parts, the response goes unstable.

For given initial conditions, the ϕ -domain response can be found by combining the characteristic exponents and the corresponding eigenvectors. For a selection of parameter values and initial conditions, responses of the three blades are found by assuming $m = 2$ harmonics in Eq. 37.4. Response and FFT (From ϕ -domain to order domain) plots are given in Figs. 37.2, 37.3, 37.4, and 37.5. The same systems are also solved numerically using MATLAB’s numerical ODE solver to verify the analytical results.

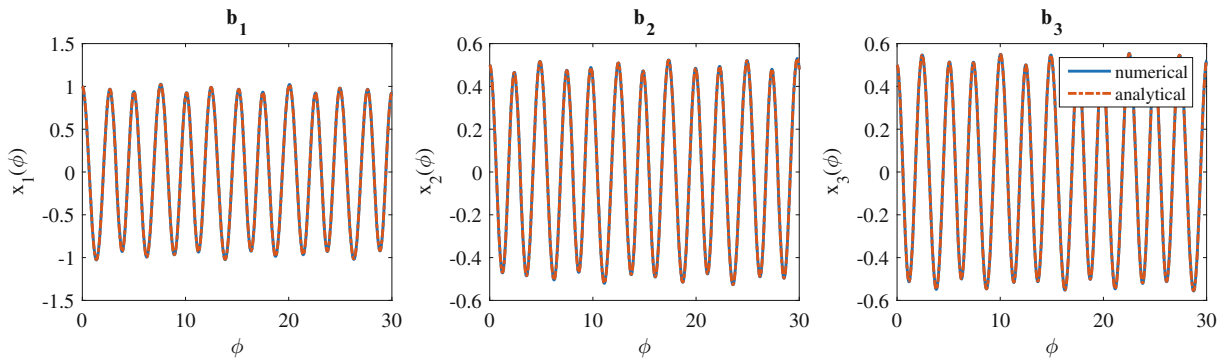


Fig. 37.2 Time response of the blades with parameters $m_b = 1, k_0 = 1, k_1 = 0.1, k_2 = 0.2, J_r = 10, e = 0.1, \Omega = 0.4$. The periodic part of the solution was truncated at $m = 2$

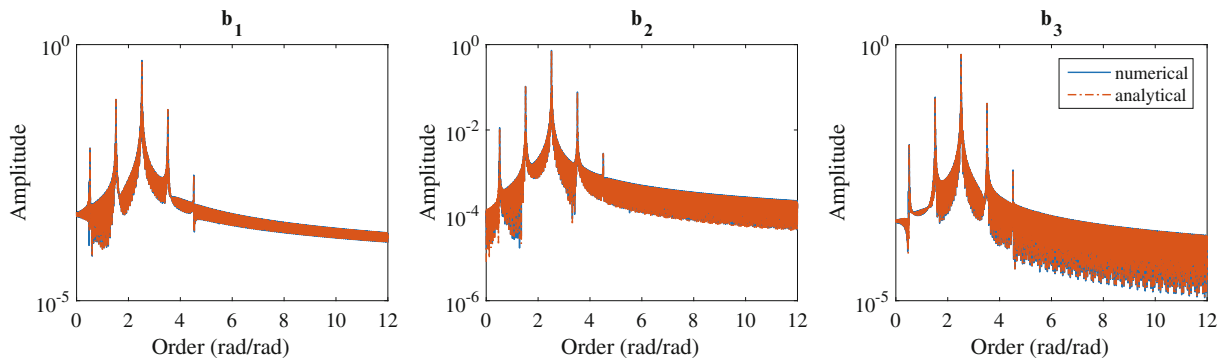


Fig. 37.3 FFT plots of the blade responses for parameters $m_b = 1, k_0 = 1, k_1 = 0.1, k_2 = 0.2, J_r = 10, e = 0.1, \Omega = 0.4$. The periodic part of the solution was truncated at $m = 2$

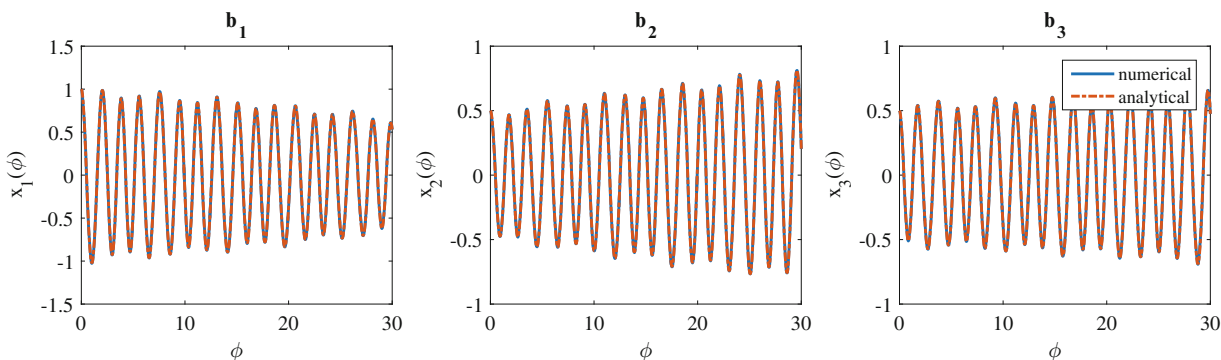


Fig. 37.4 Time response of the blades with parameters $m_b = 1, k_0 = 1, k_1 = 0.1, k_2 = 0.2, J_r = 10, e = 0.3, \Omega = 0.3$. The periodic part of the solution was truncated at $m = 2$

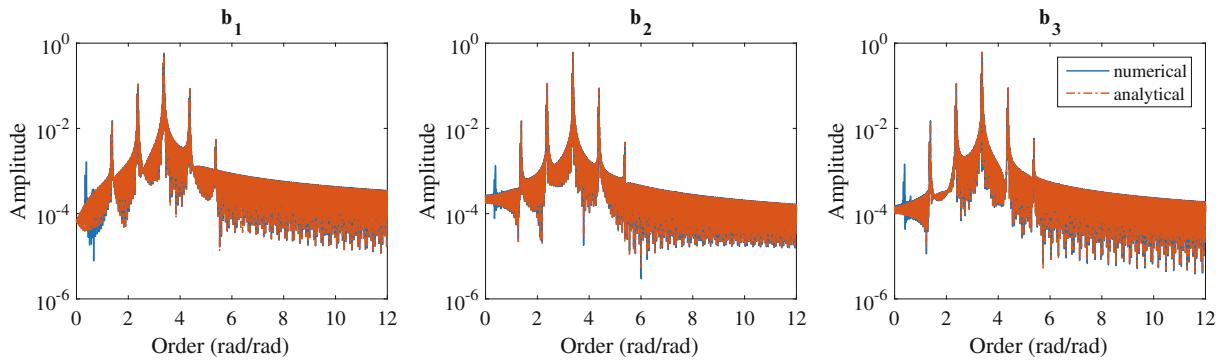


Fig. 37.5 FFT plots of the blade responses for parameters $m_b = 1, k_0 = 1, k_1 = 0.1, k_2 = 0.2, J_r = 10, e = 0.3, \Omega = 0.3$. The periodic part of the solution was truncated at $m = 2$

Fig. 37.6 Stability of the solutions for the system with $e = 0, m_b = 1, k_0 = 1.5, k_1 = 0.2, J_r = 10$. The periodic part of the solution was truncated at $m = 2$

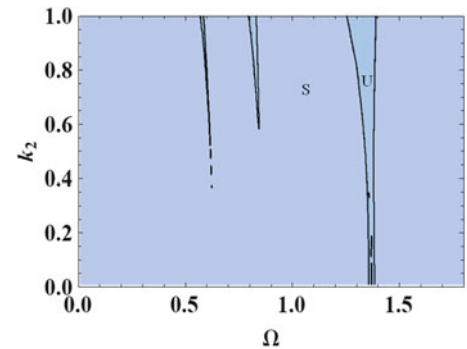
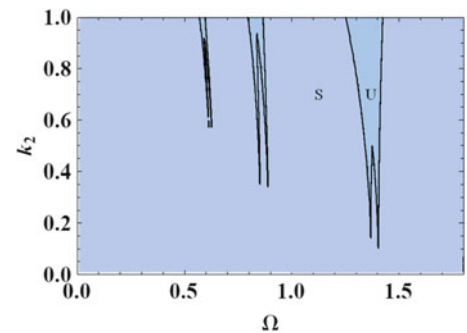


Fig. 37.7 Stability of the solutions for the system with $e = 0.5, m_b = 1, k_0 = 1.5, k_1 = 0.2, J_r = 10$. The periodic part of the solution was truncated at $m = 2$

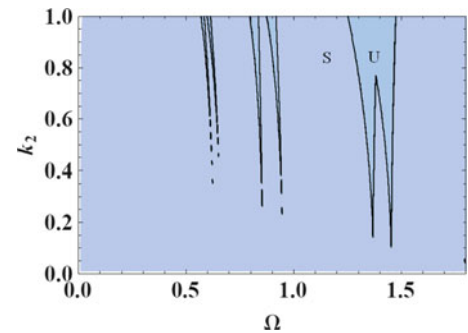


The stability of solution depends on the characteristic exponents. If all μ has zero imaginary parts, the response is stable (periodic or quasi-periodic), whereas it is unstable if any μ has a negative imaginary part. To investigate the stability of the solution, we first studied the system with no coupling between blades ($e = 0$). The stability diagram of this case, which would be essentially the same as that of a single blade, is given in Fig. 37.6. Then, in order to investigate the effect of coupling, the stability diagrams are plotted for $e \neq 0$ cases, as shown in Figs. 37.7 and 37.8, where it can be seen that non-zero coupling between the blades introduces new instability regions. In Mathieu-type systems, the instability wedges are expected to be seen at $(\omega_i + \omega_j)/N$, where ω are natural frequencies of the system, and N is a positive integer. For the selected parameters ($m_b = 1, k_0 = 1.5, k_1 = 0.2, J_r = 10$), all three natural frequencies of the zero coupling case are $\omega_{1,2,3} = 1.37$, which is the frequency of a single blade. For $e = 0.5, \omega_{1,2} = 1.37$ and $\omega_3 = 1.44$, and for $e = 0.75, \omega_{1,2} = 1.37$ and $\omega_3 = 1.54$. In Figs. 37.7 and 37.8, instability wedges are at $2\omega_1/N$ and $(\omega_1 + \omega_3)/N$.

37.3 Conclusions

General responses of three-blade HAWTs under in-plane vibrations were studied. Parametric excitation due to gravity and centrifugal stiffening effects were taken into account. Assuming a Floquet-type solution, and applying the harmonic balance

Fig. 37.8 Stability of the solutions for the system with $e = 0.75$, $m_b = 1$, $k_0 = 1.5$, $k_1 = 0.2$, $J_r = 10$. The periodic part of the solution was truncated at $m = 2$



method, responses to arbitrary initial conditions and the frequency content were found. Analytical approximations were confirmed with numerical solutions. The stability of solutions and the effect of blade coupling were studied.

Acknowledgements This project is funded by the National Science Foundation, under grant CMMI-1335177.

References

1. Ruby, L.: Applications of the Mathieu equation. *Am. J. Phys.* **64**(1), 39–44 (1996)
2. Li, Y., Fan, S., Guo, Z., Li, J., Cao, L., Zhuang, H. Mathieu equation with application to analysis of dynamic characteristics of resonant inertial sensors. *Commun. Nonlinear Sci. Numer. Simul.* **18**(2), 401–410 (2013)
3. Ramakrishnan, V., Feeny, B.F.: Resonances of a forced Mathieu equation with reference to wind turbine blades. *J. Vib. Acoust.* **134**(6), 064501 (2012)
4. Inoue, T., Ishida Y., Kiyohara, T.: Nonlinear vibration analysis of the wind turbine blade (occurrence of the superharmonic resonance in the out of plane vibration of the elastic blade). *J. Vib. Acoust.* **134**(3), 031009 (2012)
5. Ishida, Y., Inoue, T., Nakamura, K.: Vibration of a wind turbine blade (theoretical analysis and experiment using a single rigid blade model). *J. Environ. Eng.* **4**(2), 443–454 (2009)
6. McLachlan, N.W.: *Theory and Application of Mathieu Functions*. Dover, New York (1961)
7. Peterson, A., Bibby, M.: *Accurate Computation of Mathieu Functions*. Morgan & Claypool Publishers, San Rafael (2013)
8. Hodge, D.B.: *The Calculation of the Eigenvalues and Eigenfunctions of Mathieu's Equation*, vol. 1937. National Aeronautics and Space Administration, Washington, DC (1972)
9. Ecker, H.: Beneficial effects of parametric excitation in rotor systems. In: *IUTAM Symposium on Emerging Trends in Rotor Dynamics*, pp. 361–371. Springer (2011)
10. Acar, G., Feeny, B.F.: Floquet-based analysis of general responses of the mathieu equation. *J. Vib. Acoust.* **138**(4), 041017 (2016)
11. Acar, G., Feeny, B.F.: Approximate general responses of multi-degree-of-freedom systems with parametric stiffness. In: *Special Topics in Structural Dynamics*, vol. 6, pp. 211–219. Springer (2016)
12. Acar, G., Acar, M.A., Feeny, B.F.: In-plane blade-hub dynamics in horizontal-axis wind-turbines. In: *ASME 2016 International Design Engineering Technical Conferences and Computers and Information in Engineering Conference*, pp. V008T10A046–V008T10A046. American Society of Mechanical Engineers (2016)

Chapter 38

Evaluation of Traveling Wave Models for Carangiform Swimming Based on Complex Modes

Mahdiah Tanha and Brian F. Feeny

Abstract The research problem we considered is to evaluate the accuracy of traveling wave model proposed in the literature as the kinematic model for fish midline motions during straight forward carangiform swimming. Almost all the literature uses a sinusoidal traveling wave model with constant wavelength and frequency for the model of lateral movements of body. We acquired raw data of midline lateral movements for three Carangiform fish from the resources available in the literature. On the other hand, we built the traveling wave models based on the format used in literature. We used COD (complex orthogonal decomposition) to decompose the total motion associated with the raw data and with the traveling wave model into complex modes and derive the wave properties. Through this analysis we evaluated the traveling wave model accuracy. The criteria we chose for comparison was the dominant modes' shape and their number, frequencies and wavelength associated to each mode. As a result of this analysis, we found that both the lab data and the traveling wave model, have a single dominant mode. The main difference between these two was that the phase change rate with respect to location and with respect to time is not constant in raw data, however in the traveling wave model we used constant frequency and wavelength.

38.1 Introduction

Carangiform is a class of undulatory swimming motion involving strong lateral motion in the tail, and some lateral motion in the head and body [15]. The kinematics of fish swimming is the key element in modeling the mechanics of swimming motion. An identified kinematics can serve as a basis for the dynamic analysis of swimming. The kinematic model is often used as input to computational models of the fluid flow around the fish. The following kinematic model is used in many literature

$$h(x, t) = a(x)(\sin(\omega t - \gamma x))$$

where x is the axial coordinate measured from the nose, $a(x)$ is the amplitude of midline transverse motion, $\gamma = \frac{2\pi}{\lambda}$ is the wavenumber chosen fixed, λ is the wavelength, and ω is the circular frequency of oscillation that is chosen fixed. The purpose of this study is to investigate the accuracy of this model. The kinematic model of transverse midline motions is an important entry to every dynamical model or hydrodynamic model that tries to describe the mechanism of swimming. Therefore, its accuracy can affect the accuracy of the final model. This research tries to apply a new tool, COD, to study the motion by decomposing it to its modes and extracting the wave informations like amplitude, frequency, wavelength and traveling index. It can serve also as a filtering tool for the data that are accompanied by noise. In total, the potential outcome of this study is the proposal of more accurate description of swimming kinematics for Carangiform swimmers that can be further developed to Anguilliforms (eel-like swimmers). The following sections summarize background information about the swimming kinematics and applications of the traveling wave model in various fields of study, and explain the methodological approach used to examine the problem.

M. Tanha (✉) · B. F. Feeny

Department of Mechanical Engineering, Michigan State University, East Lansing, MI, USA
e-mail: tanhamah@msu.edu; feeny@egr.msu.edu

38.1.1 Background

The first scientific studies in this regard dates back as far as the work of Gray [12]. He recorded photographically the top view of body movements of various Carangiform species during swimming and concluded that the fish creates waves of curvature waves down their bodies. The idea of using the traveling wave in describing the kinematics of swimming was a starting point of many later researches in the field of dynamics and hydrodynamics of swimming. Based on the traveling wave model for fish kinematics, Videler and Hess [21] developed a method to represent the kinematics of lateral displacements of midline in straight forward swimming of saithe and mackerel as a sum of three Fourier terms in the form of traveling waves. In their model, the wave phase was considered as a general function of x , not necessarily a linear one. The parameters of the sinusoidal function (amplitude, frequency and phase) were estimated using least square algorithms to minimize the error between the actual and predicted motions in time.

In 1960, Lighthill proposed [14] a slender-body theory for hydrodynamic force modeling using the idea introduced by Gray as a simplifying assumption. He considered that the whole motion of surface as superposition of a forward motion and an oscillations in the form of traveling wave. He regarded the flow as compounded of the steady flow around the stretched straight body and the flow due to the displacements. He concluded that the traveling wave which moves down the fish body can be a satisfactory shape for generating an efficient thrust. Following Lighthill's footsteps, many people contributed to modeling the hydrodynamics of fish swimming and developed theories [6, 23, 24] that were used by many dynamic analysts [5, 7, 18]. Through the evolution of swimming hydrodynamics studies, several investigators turned to experimental visualization of the flow [1, 2, 20, 22].

The classical studies mainly used the principle of superposition to solve the Navier-Stokes equations with the boundary conditions at fish body surface; however still the mathematics was complex. With the emergence of computational fluid dynamics (CFD) a detailed investigation of the flow was made possible, which allows for a more thorough analysis of the propulsion mechanisms [13, 17]. However the accuracy is confined to the size and shape of the mesh in surrounding fluid, the exactness of the model of body and the model of moving body-fluid boundary. Recently, many researchers have used the traveling wave model originally proposed by Lighthill to develop their robot fish [3, 4, 8, 13, 16, 25].

In summary, indisputably the kinematic model plays a significant role in any analysis that include computational models of the fluid flow around the fish. Furthermore, as a matter of fact, the traveling wave model have not been proved to be an exact description of the real motion. To uncover the kinematics, a primitive approach already taken by the researchers is to record and analyze data of midline transverse oscillations. Feeny (2008) developed [10] an analytical tool, COD, that can be served to decompose the motion into its complex modes. Like a complex singular value decomposition, the decomposition is based on the complex eigen-solution of a complex correlation matrix formed from a wave's sampling data. From the complex modes and modal coordinates then, the frequencies, wavelengths, amplitude envelope, and characteristic wave speeds can be obtained. Feeny (2013) has used [11] COD in analyzing the motion of whiting fish in straight swimming. The approach presented here is to apply COD to real data of fish swimming and to the traveling wave model presented for the real motion, in order to uncover the differences between them by the help of COD analysis results.

38.1.2 Method

We acquired raw data of midline lateral movements for three Carangiform fish from the resources available in the literature and used that as a reference to compare the traveling wave model with. Data used in this research was collected from two sources. For the mackerel (*Scomber scombrus*, fam. Scombridae) and the saithe (*Pollachius virens*, fam. Gadidae), we used the curves of midline transverse oscillations in [21]. For our purpose, the curves were digitized to generate the sampling signals needed in the study. Digitizing was made at a sampling rate of N/T samples per second, i.e. a sampling interval of T/N per sample, where N is the number of samples in one period, and T is the principal period. For the mackerel and saithe, the number of body markers M was equal to N . In the case of saithe and mackerel the number of body markers was $M = 11$, and so $N = 11$ also. Thus in order to increase the resolution, we had to use interpolation along the length to increase N from 11 to 41.

For the whiting (*Gadus merlangus*), we used digitized data in [11] of the curves of midlines in top views of successive cinematographic pictures from the original work of [12]. The traveling wave model was built based on the format used in literature. We computed the wave parameters like $a(x)$, ω and γ in the model by applying COD to raw data or used the values found in the literature, like the work of [21] for mackerel and saithe.

To compare the traveling wave model with lab data, the criteria we chose was the shape of dominant modes, their number, and the oscillation amplitude distribution along the body length, frequencies and wavelength associated to each mode. COD was applied to the raw data and the traveling wave model to decompose the total motions to their dominant modes. In order to apply COD, the real signals (samples through time and location) were converted to complex signal by the half-spectrum inversion method or Hilbert transform

$$z(x_i, t_j) = y(x_i, t_j) + iy_H(x_i, t_j)$$

where y_H is the Hilbert transform of y . The resultant $M \times N$ matrix \mathbf{Z} is called the complex ensemble matrix. The complex correlation matrix was then constructed as $\mathbf{R} = \mathbf{Z}\mathbf{Z}^T/N$, where the overbar indicates complex conjugation. The matrix $\mathbf{R} \in \mathbb{C}^{M \times M}$, where \mathbb{C} is the set of complex numbers. Then we extracted the eigenvalues and eigenvectors through the eigenvalue problem associated with \mathbf{R} .

The eigenvalues or COVs (complex orthogonal values) represent the complex harmonic waveforms; The eigenvectors or COMs (complex orthogonal modes) represent the mean squared amplitude modulations corresponding to each COM [10]. A motion is associated with each COM and the total motion is a sum of modal motions. The total motion, \mathbf{Z} , was then reconstructed as $\mathbf{Z} = \mathbf{W}\mathbf{Q}$ where \mathbf{W} is the matrix whose columns are COMs and the matrix \mathbf{Q} is complex modal coordinates (COC) ensemble. The rows of \mathbf{Q} are samplings of the complex modal coordinates calculated as $\mathbf{Q} = \mathbf{W}^{-1}\mathbf{Z}$. However, in our case study, not all M meaningful modes were contributing in total motion; Namely there was only one dominant mode that captures more than 99% of the energy while the other modes were noise dominated and insignificant. Thus we approximated the motion by reduced modal motion constructed as $\mathbf{Z}_1 = \mathbf{W}_1\mathbf{W}_1^T\mathbf{Z}$ where \mathbf{W}_1 is the dominant mode.

38.2 Results

As a result of this analysis, we found that both the lab data and the traveling wave model have a single dominant mode that captured more than 99% of the energy of oscillation for all three fish. In the following figures the results are depicted for the mackerel fish. Figure 38.1a, b show plot of COVs in descending order in linear scale and logarithmic scale, respectively for raw data and for the traveling wave model. These figures show that the other modes tend to have insignificant participation and are noise dominated.

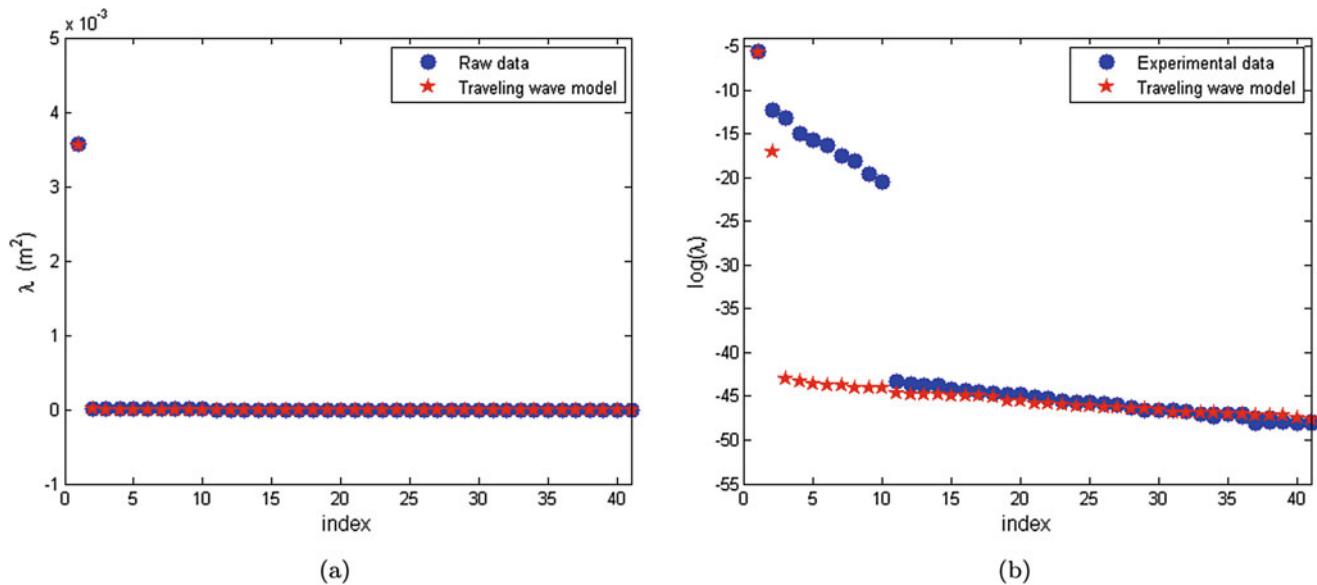


Fig. 38.1 Plot of COVs in descending order in linear scale. Only one mode (the first) captures 99% of the energy (a) Plot of COVs in descending order in logarithmic scale (b)

Dominant COM is plotted in Fig. 38.2a in complex plane pertaining to the raw data together with those pertaining to the traveling wave model for comparison. Each point in the plot is an element of COM $1 \times M$ vector. The points closer to the center of the spiral belong to anterior regions of fish body, and the outer points belong to posterior regions. Comparing the red and blue curves in Fig. 38.2a, it can be seen that the equivalent points in raw-data and in traveling wave model differ in their placement in the complex plane, specially in the anterior region. The value of $\gamma = 22.3$ rad/m in the traveling wave model we used to create this plot. We tried to tune the value of γ in the traveling wave model to see the effect. Figure 38.2b shows the COM in complex plane with γ values of 21, 24, 18 rad/m together with raw data and initial value of 22.3 rad/m. The value of $\gamma = 21$ rad/m was selected based on Figure 8 of [21] plots.

Plot of COM elements' phase and COM elements' magnitude vs. body marker is shown in Fig. 38.3a, b for the raw data and the traveling wave model. It can be seen that the slope of phase plot is constant for the traveling wave model but variable in raw data.

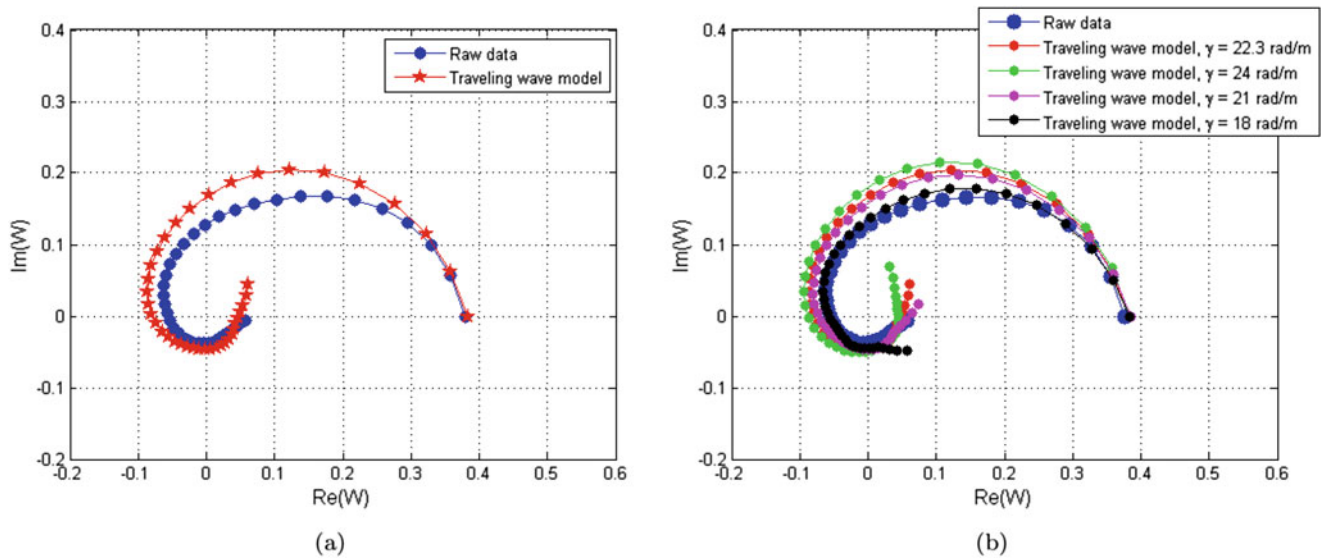


Fig. 38.2 Dominant COM for experimental data (red) and traveling wave model (blue) (a), Effect of increasing γ to 23 rad/m (red) and decreasing it to 18 rad/m (blue) in the traveling wave model (b)

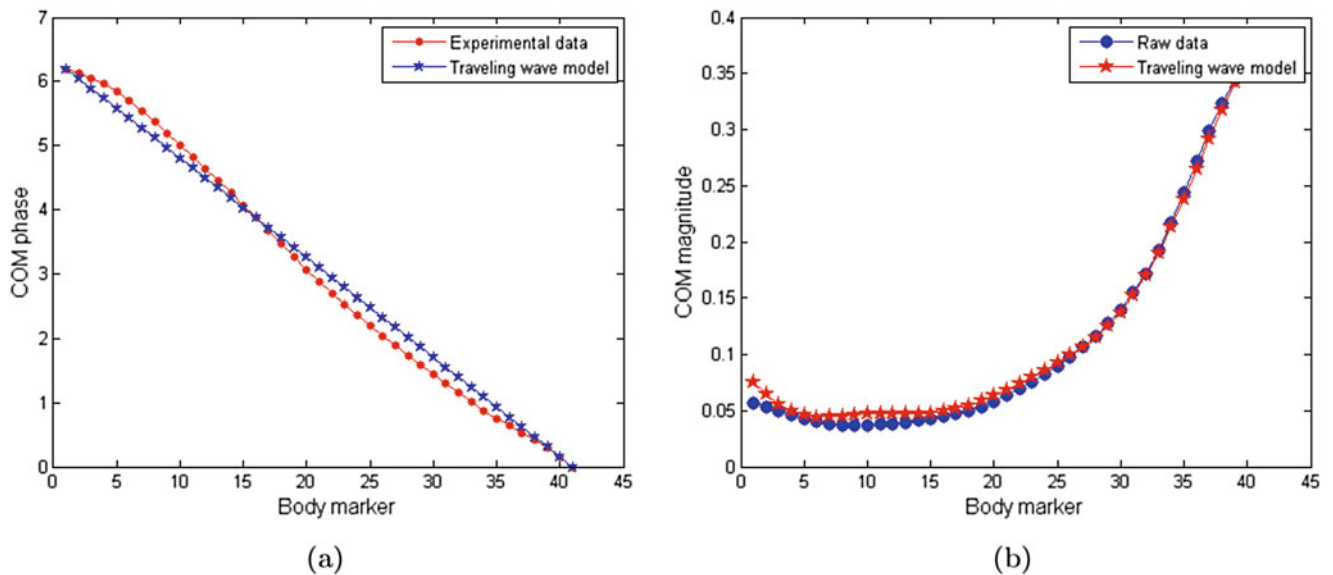


Fig. 38.3 Plot of COM elements' phase for the experimental data (red) and the traveling wave model (blue) (a), plot of COM elements' magnitude for the experimental data (red) and the traveling wave model (blue) (b)

Figure 38.4 shows plot of the dominant modal coordinate, COC in the complex plane, for raw data and traveling wave model. Differences between the two COC curves and the fact that the traveling wave model was made based on constant ω implies that in raw data, ω is not constant over the time. It means that the rate of phase change varies through the time for experimental data.

As another basis for test and comparison of two models, we considered the modal wave speed through the fish via the complex mode for both data-sets. The main difference between the dominant mode for raw data and the traveling wave model was that the dominant COM's phase change rate with respect to location and with respect to time was not constant in raw data. However in the traveling wave model we used constant frequency and wave-number. For example, Fig. 38.5a shows plot of phase, ϕ vs. x with its trendline, and the trendline of ϕ vs. x plot from [21] for mackerel. Differentiation of ϕ with respect to x will determine the wave number or the spatial frequency of a wave in radians per unit distance, $\frac{\partial\phi}{\partial x} = \gamma$. We

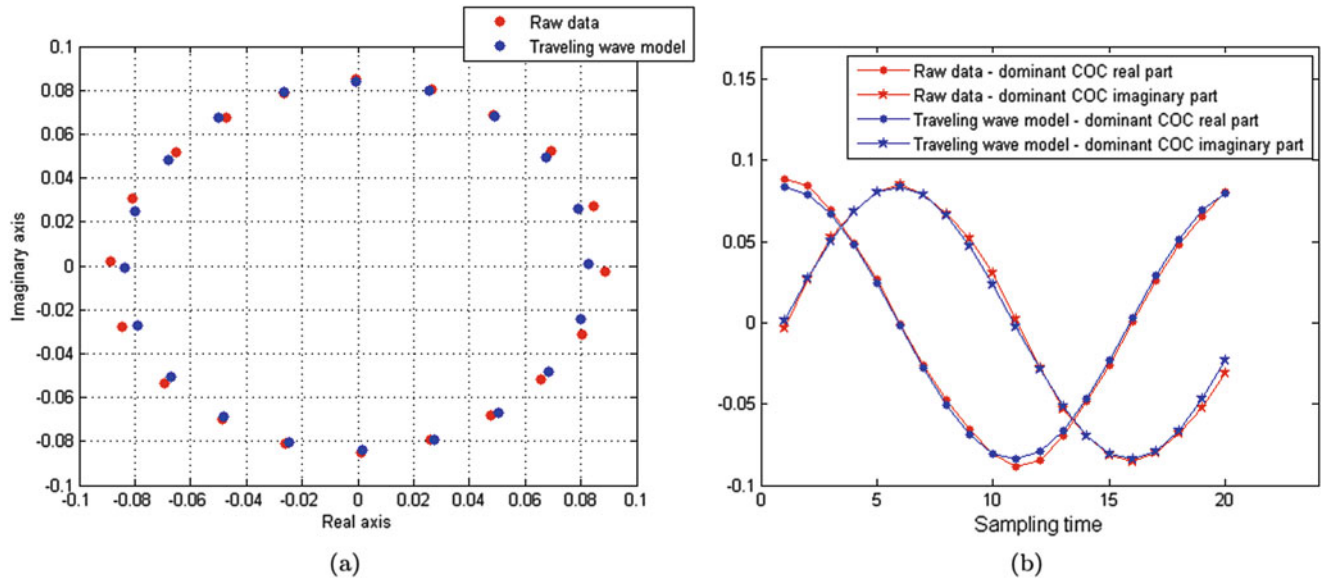


Fig. 38.4 Plot of dominant COC (complex orthogonal coordinate) for data-set 1 (red) and data-set 2 (blue) (a). Real (red) and imaginary (blue) parts of dominant COC vs body marker (b)

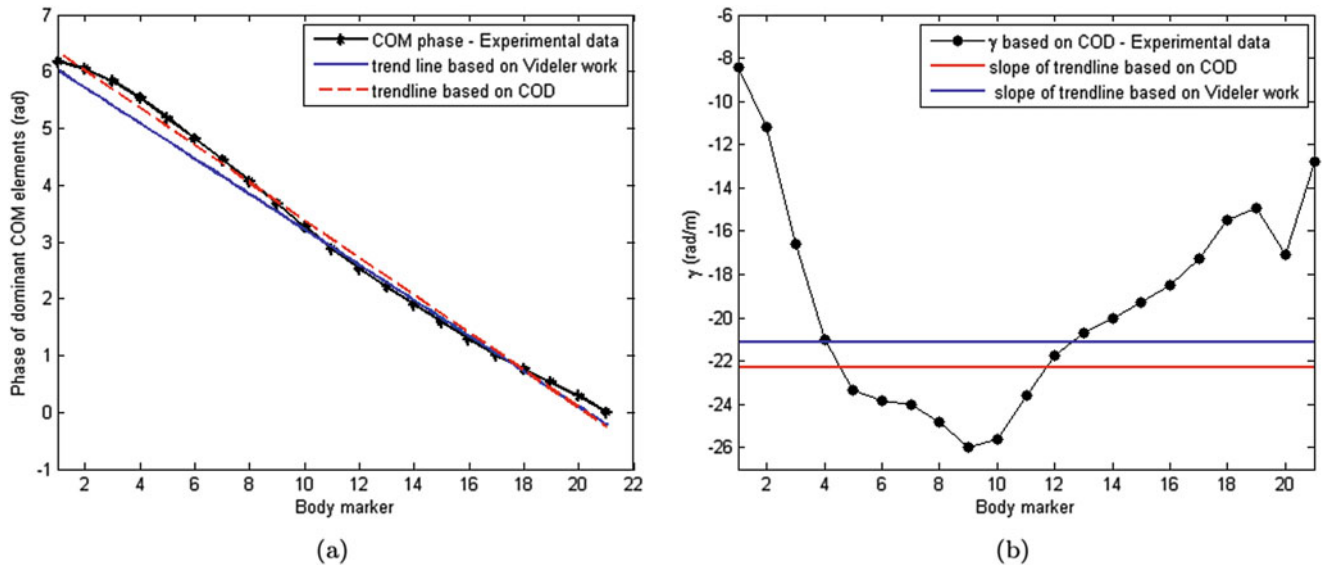


Fig. 38.5 Plot of ϕ vs. x calculated from the dominant COM for the raw data (black), trendline of black plot (red), and trendline of ϕ vs. x plot for dominant mode for mackerel in [21] (blue) (a), plot of γ vs. x obtained by applying finite differencing to ϕ in raw data (black), the slope of ϕ vs. x plot's trendline (red), and the slope of ϕ vs. x plot's trendline in [21] (blue) (b)

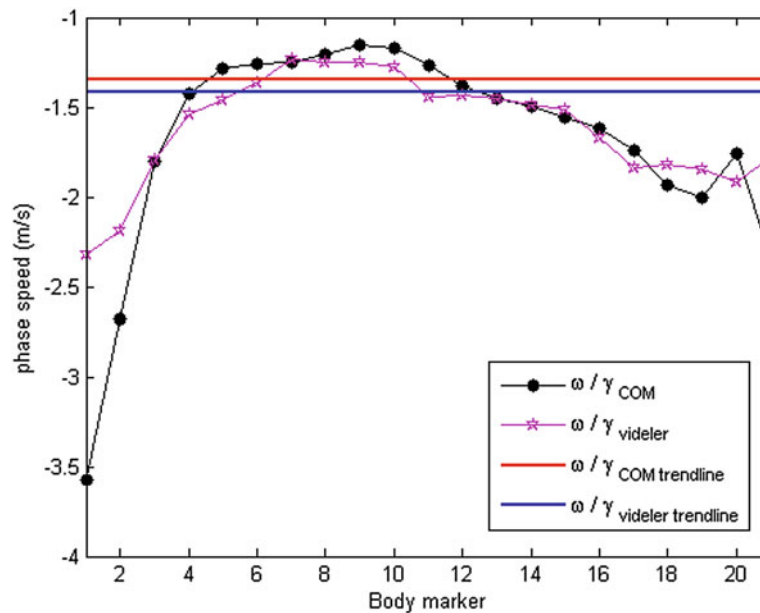


Fig. 38.6 Plot of phase speed based on γ calculated from COM phase (black), phase speed based on γ calculated from phase plot in [21] (purple), phase speed based on the slope of trendline to COM phase curve (red), and phase speed based on the slope of trendline to [21] phase curve (blue)

used finite difference to approximate γ and from that to calculate the phase speed as $c = \frac{\omega}{\gamma}$. Figure 38.5b shows the plot of γ vs. x computed by applying finite differencing to ϕ vs. x plot from the raw data, the slope of trendline of ϕ vs. x plot, and the slope of trendline of ϕ vs. x plot in [21].

In Fig. 38.6, γ is plotted for four different calculations; the black curve is phase speed based on γ calculated from COM phase. The purple curve is phase speed based on γ calculated from phase plot in [21]. The red line is phase speed based on the slope of trendline to COM phase curve, and the blue line is phase speed based on the slope of trendline to [21] phase curve.

38.3 Conclusion

This study tried to evaluate the accuracy of traveling wave model in modeling the real motion in straight swimming. We applied COD to both the real data of swimming midline transverse motions and to the traveling wave model presented for the real motion. As a result, we found out that in the dominant complex mode related to real data, the phase change rate with respect to axial coordinate, x , and with respect to time is not fixed; In other words, the phase speed (equivalently, wavelength) and frequency are not constant through one cycle of motion. This means that every traveling wave model that is proposed for the swimming motion should consider a variable phase speed and frequency.

References

1. Anderson, J.M.: Vorticity control for efficient propulsion. No. MIT/WHOI-96-02. Massachusetts Institute of Technology, Cambridge (1996)
2. Anderson, E.J., Mcgillis, W.R., Grosenbaugh, M.A.: The boundary layer of swimming fish. *J. Exp. Biol.* **204**(1), 81–102 (2001)
3. Barrett, D.S.: Propulsive efficiency of a flexible hull underwater vehicle. PhD dissertation, Massachusetts Institute of Technology (1996)
4. Barrett, D.S., Triantafyllou, M.S., Yue, D.K.P., Grosenbaugh, M.A., Wolfgang, M.J.: Drag reduction in fish-like locomotion. *J. Fluid Mech.* **392**, 183–212 (1999)
5. Cheng, J.-Y., Blickhan, R.: Bending moment distribution along swimming fish. *J. Theor. Biol.* **168**, 337–348 (1993)
6. Cheng, J.-Y., Zhuang, L.-X., Tong, B.-G.: Analysis of swimming three-dimensional waving plates. *J. Fluid Mech.* **232**, 341–355 (1991)
7. Cheng, J.-Y., Pedley, T.J., Altringham, J.D.: A continuous dynamic beam model for swimming fish. *Philos. Trans. R. Soc. Lond. B: Biol. Sci.* **353**(1371), 981–997 (1998)

8. Coral Cullar, W.: BR3: a biologically inspired fish-like robot actuated by SMA-based artificial muscles. PhD dissertation, Industriales (2015)
9. Cui, Z., Gu, X., Li, K., Jiang, H.: CFD studies of the effects of waveform on swimming performance of carangiform fish. *Appl. Sci.* **7**(2), 149 (2017)
10. Feeny, B.F.: A complex orthogonal decomposition for wave motion analysis. *J. Sound Vib.* **310**(1), 77–90 (2008)
11. Feeny, B.F., Feeny, A.K.: Complex modal analysis of the swimming motion of a whiting. *J. Vib. Acoust.* **135**(2), 021004 (2013)
12. Gray, J.: Studies in animal locomotion III. The propulsive mechanism of the whiting (*gadus merlangus*). *J. Exp. Biol.* **10**, 391–402 (1933)
13. Lamas, M., Rodriguez, J., Rodriguez, C., Gonzalez, P.: Three-dimensional CFD analysis to study the thrust and efficiency of a biologically-inspired marine propulsor. *Polish Marit. Res.* **18**(1), 10–16 (2011)
14. Lighthill, M.J.: Note on the swimming of slender fish. *J. Fluid Mech.* **9**(2), 305–317 (1960)
15. Lindsey, C.C.: 1-form, function, and locomotory habits in fish. *Fish Physiol.* **7**, 1–100 (1978)
16. Liu, J., Hu, H.: A 3D simulator for autonomous robotic fish. *Int. J. Autom. Comput.* **1**(1), 42–50 (2004)
17. Liu, H., Wassersug R., Kawachi, K.: A computational fluid dynamics study of tadpole swimming. *J. Exp. Biol.* **199**(6), 1245–1260 (1996)
18. McHenry, M.J., Pell, C.A., Long, J.H.: Mechanical control of swimming speed: stiffness and axial wave form in undulating fish models. *J. Exp. Biol.* **198**(11), 2293–230 (1995)
19. McMillen, T., Holmes, P.: An elastic rod model for anguilliform swimming. *J. Math. Biol.* **53**(5), 843–886 (2006)
20. Techet, A.H.: Experimental visualization of the near-boundary hydrodynamics about fish-like swimming bodies. No. MIT/WHOI-2001-01. Massachusetts Institute of Technology, Cambridge (2001)
21. Videler, J.J., Hess, F.: Fast continuous swimming of two pelagic predators, saithe (*Pollachius virens*) and mackerel (*Scomber scombrus*): a kinematic analysis. *J. Exp. Biol.* **109**(1), 209–228 (1984)
22. Wolfgang, M.J., Anderson, J.M., Grosenbaugh, M.A., Yue, D.K., Triantafyllou, M.S.: Near-body flow dynamics in swimming fish. *J. Exp. Biol.* **202**(17), 2303–2327 (1999)
23. Wu, T.Y.-T.: Swimming of a waving plate. *J. Fluid Mech.* **10**(3), 321–344 (1961)
24. Wu, T.Y.-T.: Hydromechanics of swimming propulsion. Part 3. Swimming and optimum movements of slender fish with side fins. *J. Fluid Mech.* **46**(3), 545–568 (1971)
25. Yu, J., Wang, S., Tan, M.: A simplified propulsive model of bio-mimetic robot fish and its realization. *Robotica* **23**(1), 101–107 (2005)

Chapter 39

Application of Frequency Domain Decomposition Identification Technique to Half Spectral Densities

Sandro Amador, Martin Ørum, Tobias Friis, and Rune Brincker

Abstract Because of its simplicity and robustness, the **F**requency **D**omain **D**ecomposition (**FDD**) identification technique have become very popular in the operational modal analysis community. The basic idea behind this technique consists of computing the singular value decomposition of the power spectral densities estimated with the periodogram (also known as “Welch’s” periodogram) approach to identify the natural frequencies and mode shape vectors. In this paper, the benefits of the application of the **FDD** technique to half spectral densities – the power spectral densities estimated from the positive part of the correlation functions – are investigated. In order to illustrate such benefits from a practical perspective, the **FDD** identification results obtained from the half spectral densities, of both simulated and real structures, are compared to those from the classical periodogram-driven **FDD**.

39.1 Introduction

Over the last decades, significant advances in terms of modal parameter estimation has been observed. These advances are particularly more noticeable in the domain of **O**perational **M**odal **A**nalysis (**OMA**) with development of robust and accurate parametric and non-parametric modal identification techniques. Amongst the former, techniques such as **S**tochastic **S**ubspace **I**dentification (**SSI**) [1] in time-domain and the **p**oly-reference **L**east **S**quares **C**omplex **F**requency-domain (**pLSCF**) [2, 3] in frequency-domain are those commonly used in **OMA** community. Regarding the latter, it is fair to assert that one of the most relevant contributions to non-parametric **OMA** was the development of the **F**requency **D**omain **D**ecomposition (**FDD**) Technique [4].

Thanks to its simplicity and robustness, this technique soon became very popular in the **OMA** community after its publication in [5]. The basic idea behind the **FDD** is to take the **S**ingular **V**alue **D**ecomposition (**SVD**) of the spectral density matrix – also known as periodogram spectrum or “Welch’s” spectrum – computed from the responses measured in output-only vibration tests. By plotting the singular value components at each frequency line one can easily identify the natural frequencies and mode shape vectors, even in presence on closely spaced modes, by simply picking the peaks of the plotted singular values. In this paper, another approach based both on the **FDD** and the **C**omplex **M**ode **I**ndication **F**unction (**CMIF**) [6] is proposed.

The innovative aspect of this approach with regard to these previous **SVD**-driven approaches is that, rather than using the “Welch’s” spectrum or the **F**requency **R**esponse **F**unction (**FRF**), the half spectrum – also known as correlogram spectrum – is used as primary data. Another distinguishing innovative aspect of the proposed **FDD** based approach is that, rather than the **SVD**, the **E**igen**V**alue **D**ecomposition (**EVD**) is applied to the half spectrum matrix to estimate the natural frequencies and mode shape vectors. In order to illustrate the application of the **EVD**-driven **FDD** herein proposed, a simulation example is presented in the final part of the paper.

S. Amador (✉) · T. Friis · R. Brincker
Technical University of Denmark, Kongens Lyngby, Denmark
e-mail: sdio@byg.dtu.dk

M. Ørum
Aarhus University, Aarhus, Denmark

39.2 EVD-Driven FDD Theory

The **EVD-driven FDD** approach herein proposed is based on the eigenvalue decomposition, hence the name of the technique. Its derivation starts by taking the **EVD** of the half spectrum matrix post multiplied by its transpose at each spectral line

$$G_y(\omega_f)G_y^T(\omega_f) = U(\omega_f)V(\omega_f)U(\omega_f)^{-1} \quad (39.1)$$

where $G_y(\omega_f) \in \mathbb{C}^{N_o \times N_o}$ denotes the half spectrum matrix, also known as the correlogram spectrum, which is computed solely from the part of the correlation function with positive time lags [4, 7], $U(\omega_f) \in \mathbb{C}^{N_o \times N_o}$ and $V \in \mathbb{C}^{N_o \times N_o}$ are matrices containing the eigenvectors and eigenvalues given by the eigenvalue decomposition, ω_f denotes the angular frequency at the f th spectral line, with N_o denoting the number of responses measured in the vibration test. The main advantage of the strategy synthesised by Eq. (39.1) is that, contrary to the **SVD**, the phase information is retained by the eigenvalues, and therefore, it can be also used as an additional mode indication function.

Then main disadvantage, on the other hand, is that, as discussed in [7], the half spectrum is highly influenced by the discontinuity at the zero lag correlation function. This spurious influence is characterized by the tendency of the well excited modes to “shadow” the poorly excited ones. Under these circumstances, it might be difficult to visually identify closely spaced mode by just inspecting the peaks of the eigenvalue components. In such cases, it is much easier to replace the half spectrum, $G_y(\omega_f)$, by its real part, $\text{Re}[G_y(\omega_f)]$, in Eq. (39.1) and compute the **EVD**, as follows

$$\text{Re}[G_y(\omega_f)]\text{Re}[G_y^T(\omega_f)] = U(\omega_f)V(\omega_f)U(\omega_f)^{-1} \quad (39.2)$$

where $\text{Re}(\bullet)$ denotes the real part of a complex quantity.

39.3 Application Example

In order to illustrate the application of the **EVD-driven FDD** from a practical perspective, a simulated **OMA** was carried out with a **Finite Element (FE)** model of a lattice tower structure constituted by two segments of equal height and by variable equilateral triangular sections. The lower section is scaled with regard to the upper one by a factor of 2. This model is composed by beam elements with 3 **Degrees Of Freedom (DOF)**s per node. The nodes of the foundations are clamped and the others have two translations in x and y , and one rotation around z -axis. These settings result in a **FE** model with a total of 18 **DOFs**. The symmetry of the structure was slightly broken by defining different cross sections and materials to the column elements in order to simulate the behaviour of tower-like structures, which normally present very closely spaced bending modes.

The structural damping, on the other hand, was modelled with the special case of proportional damping. In order to obtain the simulated responses, the structure was excited, independently, at node 8 in x and y -direction, and at node 9 in y -direction with white noise inputs. The simulated responses were measured in acceleration at 6 **DOFs** as indicated in Fig. 39.1a. The real modes shapes of the tower structure as well as the natural frequencies and damping ratios are shown in Fig. 39.1b, c, d, e, f, g, and Table 39.1. The simulated responses were used to compute the correlation function matrix which was subsequently used to estimate half spectrum matrix $G_Y(\omega_f)$.

Afterwards, the **EVD** of both real and complex half spectrum matrices were computed for each spectrum line as illustrated in Figs. 39.2 and 39.3. As seen from these figures, even in presence of closely spaced modes, it is straightforward to identify the natural frequencies and mode shape vectors with the **EVD-driven FDD** by using the same strategy as described in [5] and [4].

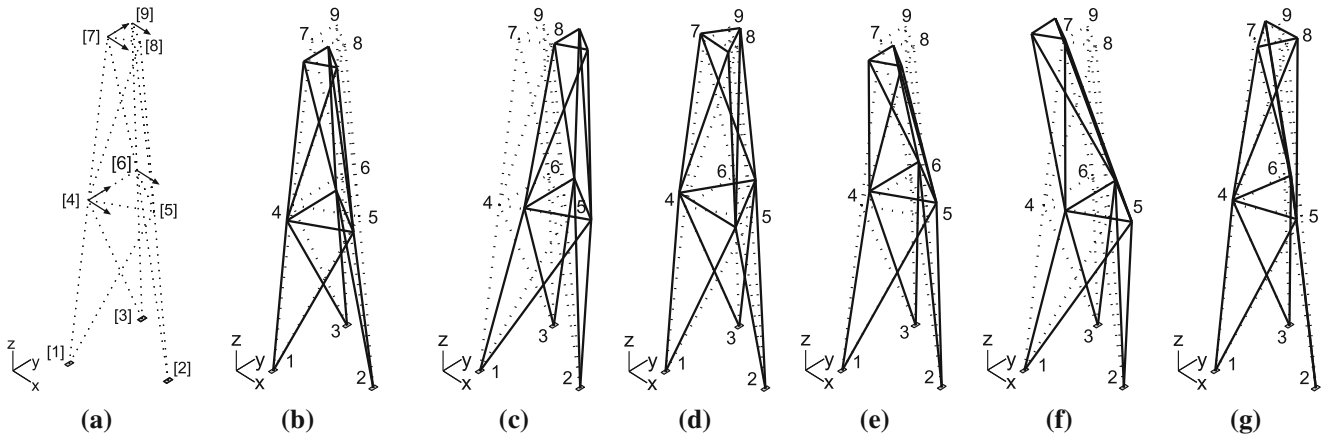


Fig. 39.1 Measured DOFs (a) and first six mode shapes of the tower structure: 1st bending mode in Y direction (BY1) (b), 1st bending mode in X direction (BX1) (c), 1st torsion mode (T1) (d), 2nd bending mode in Y direction (BY2) (e), 2nd bending mode in X direction (BX2) (f) and 2nd torsion mode (T2) (g)

Table 39.1 Modes of the FE model of the lattice structure

Mode	Shape description	f_{n_i} [Hz]	ξ_{n_i} [%]
1	1st bending mode in Y direction (BY1)	1.2869	1.0
2	1st bending mode in X direction (BX1)	1.2937	2.0
3	1st torsional mode (T1)	2.2251	1.5
4	2nd bending mode in Y direction (BY2)	3.8713	0.8
5	2nd bending mode in X direction (BX2)	3.8932	1.4
6	2nd torsional mode (T2)	6.1745	1.3

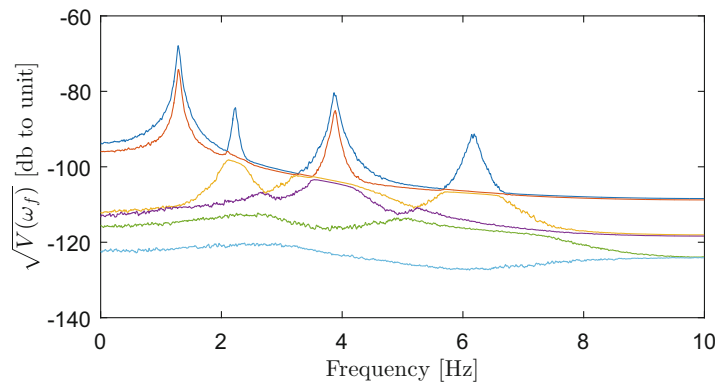


Fig. 39.2 Square root of sorted eigenvalues computed from $\text{Re}[G_y(\omega_f)]\text{Re}[G_y^T(\omega_f)]$ over the spectral lines

39.4 Conclusion

In this paper, a novel approach is proposed to identify the natural frequencies and mode shape vectors from output-only vibration measurements. Although the approach is based on the same principles as the **FDD** and **CMIF** techniques, its distinguishing characteristic are related to fact that: (1) rather than the **SVD**, the **EVD** is used to decompose the spectrum; (2) the **EVD** is applied to the half spectrum, rather than the “Welch’s” spectrum; and (3) since the **EVD** is computed from $G_y(\omega)G_y(\omega)^T$, the phase information is retained by the eigenvalues and can be used as an additional mode indication function. From the simulation example presented in the final part of the paper, it was clearly demonstrated that the proposed **EVD**-driven **FDD** is able to identify the natural frequencies and mode shape vectors even in presence of closely spaced modes.

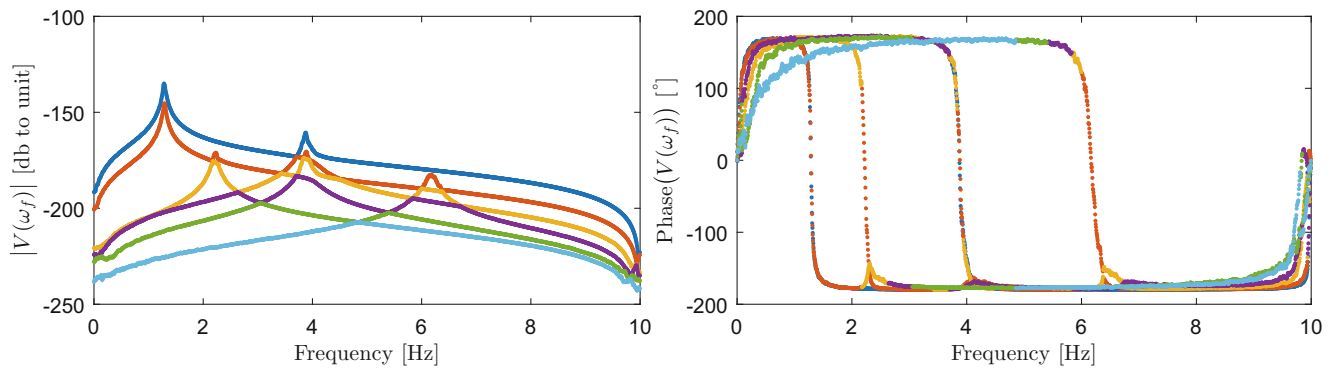


Fig. 39.3 Magnitude (left) and phase (right) of the sorted complex eigenvalues computed from $G_y(\omega_f)G_y^T(\omega_f)$ over the spectral lines

Acknowledgements The authors acknowledge the funding received from Centre for Oil and Gas – DTU/Danish Hydrocarbon Research and Technology Centre (DHRTC).

References

1. Peeters, B., De Roeck, G.: Reference-based stochastic subspace identification for output-only modal analysis. *Mech. Syst. Signal Process.* **13**(6), 855–878 (1999)
2. Peeters, B., Van der Auweraera, H., Guillaume, P., Leuridan, J.: The polymax frequency–domain method: a new standard for modal parameter estimation? *Shock Vib.* **1**(11), 395–409 (2004)
3. Peeters, B., Van Der Auweraera, H., Vanhollebeck, F., Guillaume, P.: Operational modal analysis for estimating the dynamic properties of a stadium structure during a football game. *Shock Vib.* **1**(14), 283–303 (2007)
4. Brincker, R., Ventura, C.: *Introduction to Operational Modal Analysis*, 1st edn. Wiley, New York (2015)
5. Brincker, R., Zhang, L., Andersen, P.: Modal identification of output-only systems using frequency domain decomposition. *Smart Mater. Struct.* **10**, 441–445 (2001)
6. Shih, C.Y., Tsuei, Y.G., Allemang, R.J., Brown, D.L.: Complex mode indication function and its application to spatial domain parameter estimation. *Mech. Syst. Signal Process.* **2**(4), 367–377 (1988)
7. Amador, S.D.R., Brincker, R.: On the different derivatives of the half spectral density. In: *Proceedings of the 7th International Operational Modal Analysis Conference (IOMAC)* (2017)

Chapter 40

Modal Survey of the MPCV Orion European Service Module Structural Test Article Using a Multi-axis Shake Table

James P. Winkel, James C. Akers, Vicente J. Suarez, Lucas D. Staab, and Kevin L. Napolitano

Abstract In 2016, the Orion European Service Module Structural Test Article (E-STA) underwent sine vibration testing using the multi-axis shaker system at NASA Glenn Research Center's (GRC) Plum Brook Station (PBS) Space Power Facility (SPF) Mechanical Vibration Facility (MVF). An innovative approach using measured constraint shapes at the interface of E-STA to the MVF Table allowed high-quality fixed base modal parameters of the E-STA to be extracted, which have been used to update the E-STA finite element model (FEM), without the need for a traditional fixed base modal survey. This innovative approach provided considerable program cost and test schedule savings. This paper documents this modal survey, which includes the modal pretest analysis sensor selection, the fixed base methodology using measured constraint shapes as virtual references and measured frequency response functions, and post-survey comparison between measured and analysis fixed base modal parameters.

40.1 Introduction

The Mechanical Vibration Facility (MVF), which is part of NASA Glenn Research Center's (GRC) Plum Brook Station (PBS) Space Power Facility (SPF) a three-axis vibration system that applies vibration in the vertical axis or two lateral orthogonal axes individually (not simultaneously) without the need of reconfiguration of the test article which saves testing cost and schedule and reduces risk to the test article. MVF was designed to perform sine vibration testing of a Multi-Purpose Crew Vehicle (MPCV) Orion-class spacecraft with a total mass of 75,000 lb, center of gravity (cg) height above the MVF Table of 284 in., and a diameter of 18 ft. The MVF Table, to which the E-STA was attached, is supported with four horizontal and 16 vertical actuators that are controlled with eight drive signals. MVF with the E-STA installed is shown in Fig. 40.1.

The extraction of fixed base modes from structures mounted on shake tables has received a great deal of attention in recent year [1–6]. Difficulties arise, however, when the shake table motion is other than purely rigid body translation in the axis of the shake excitation, such as when the inertia forces imparted by the test article cause the shake table to rigid body motion (e.g. rocking) and or elastic body motion (e.g. bending) at the combined system natural frequency rather than the test article fixed base natural frequency.

Currently, there are two promising methods to account for shake table motion. The first, developed by Sandia National Laboratories, is a transformation of measured modes to fixed base modes [7], and the second, developed by ATA Engineering, uses shake table accelerations as references when calculating Frequency Response Functions (FRFs) [8]. The key element in both methods is using a small number of shapes that adequately describe shaker table motion.

To meet the cost and schedule constraints of the E-STA Sine Vibration Test, it was determined that a fixed base modal survey of the E-STA could be performed using MVF utilizing the second method, which incorporates constraint shapes as references when calculating the FRFs, which has previously been documented [9] and includes the overall procedure for calculating FRFs. This paper documents the modal survey of the E-STA while mounted on the MVF Table. It includes the modal pretest analysis sensor selection, the fixed base methodology using measured constraint shapes as virtual references and measured FRFs, and post-survey comparison between measured and analysis fixed base modal parameters.

J. P. Winkel · J. C. Akers · V. J. Suarez · L. D. Staab
NASA Glenn Research Center, Cleveland, OH, USA

K. L. Napolitano (✉)
ATA Engineering, Inc., San Diego, CA, USA
e-mail: kevin.napolitano@ata-e.com



Fig. 40.1 E-STA mounted on the MVF Table

40.2 Pretest Analysis Objectives

The E-STA Sine Vibration Test campaign had three main objectives that are summarized below.

The first main objective was to verify the structural integrity of the European Service Module (ESM) under dynamic loading. These qualification loads were initially defined to be 1.25 times higher than the dynamic limit loads defined in the Orion-level coupled loads analysis (CLA). It should be noted that this first main objective was the primary driver of where the instrumentation on the vehicle was located and not the identification of modal parameters.

The second main objective of the test was to measure FRFs of the ESM equipment with respect to the base acceleration, to be used to validate the CLA results.

	Mode #	Frequency	Modal Effective Mass %						Mode Description (MPCV Coordinate System)
			T1	T2	T3	R1	R2	R3	
Primary Target Modes	1	3.37	0%	0%	75%	0%	97%	0%	First Stack Bending Mode Along Z Axis
	2	3.74	0%	86%	0%	0%	0%	92%	First Stack Bending Mode Along Y Axis
	3	6.52	0%	0%	15%	1%	0%	0%	Second Bending Mode Along Z Axis
	4	7.57	0%	0%	0%	72%	0%	0%	Torsion Mode
	5	7.84	0%	4%	0%	2%	0%	5%	Second Bending Mode Along Y Axis
	6	11.47	85%	0%	0%	0%	0%	0%	Axial Bounce Mode Along X Axis
	7	12.43	0%	0%	0%	0%	0%	0%	Important Secondary Structure Bending Mode Along Y Axis
	8	14.24	0%	0%	0%	0%	0%	0%	Important Secondary Structure Bending Mode Along Z Axis
Secondary Target Modes	9	15.16	0%	0%	0%	0%	0%	0%	Propellant Tanks Axial Modes
	10	16.13	0%	0%	0%	1%	0%	0%	
	11	16.41	4%	0%	0%	0%	0%	0%	
	12	17.29	0%	0%	0%	0%	0%	0%	
	13	18.24	1%	0%	0%	0%	0%	0%	Third Bending along Y Axis
	14	19.46	0%	0%	0%	0%	0%	0%	Propellant Tank Axial Modes
	15	20.75	0%	0%	0%	0%	0%	0%	
	16	22.47	0%	0%	0%	0%	0%	0%	RCS Modes
	17	22.53	0%	0%	0%	0%	0%	0%	
	18	22.72	0%	0%	0%	0%	0%	0%	Important Secondary Structure Torsion Mode
	19	23.03	0%	0%	0%	0%	0%	0%	Lateral Squeeze Mode
	20	23.92	0%	0%	0%	0%	0%	0%	Solar Array Secondary Structure Modes
	21	25.05	0%	0%	0%	0%	0%	0%	
	22	25.97	0%	0%	0%	0%	0%	0%	

Fig. 40.2 E-STA full propellant tank configuration FEM modal effective mass (uncorrelated model)

The third main objective of the testing, and the subject of this paper, was to identify the E-STA fixed base modal parameters of the primary target modes for both the fully filled propellant tank and partially filled propellant tank configurations. The primary target modes were identified by the European Space Agency (ESA) in conjunction with Airbus as the first six high-effective-mass modes whose shapes can be described as the first and second bending modes in the two lateral directions, the first axial torsion mode, and the first axial mode. Two additional important secondary structure modes were also included in the primary target mode set. Furthermore, a set of 14 secondary target modes localized to the propellant tanks, solar array support structure, and other localized secondary structures was selected to help assist with the finite element model (FEM) correlation. It was understood from the start that these secondary modes would likely not be able to be validated by traditional means (cross-Modal Assurance Criteria (MAC) and cross-orthogonality, etc.) because of the constraints on sensor location. The modal effective mass table of the uncorrelated fully filled propellant tank configuration E-STA FEM is shown in Fig. 40.2.

40.3 Pretest Analysis Summary

NASA GRC Structural Dynamics Branch (LMD) was tasked with determining the subset of existing sensors needed to support fixed base modal extraction of the target modes. NASA pretest goal is to have the cross-orthogonality should be greater than 90% on the diagonals and less than 10% off the diagonals. The frequency comparison between the TAM and FEM should also be less than 5%. The E-STA had a total of 736 accelerometers (i.e. test degrees of freedom DOF), whose selection was based on measuring environments, but unfortunately were not optimally placed for modal parameter extraction. Unfortunately, no additional instrumentation could be added to the E-STA. The sensor down-selection was done using the fixed based E-STA fully filled propellant tank configuration FEM.

40.4 Primary Target Modes Test DOF Selection

Using all 736 test DOF would have been extremely cumbersome when extracting the fixed base modal parameters, and as expected, it was found to degrade the overall TAM results due to a significant amount of the instrumentation only capturing localized effects in the FEM. Engineers at GRC LMD developed a customized set of MATLAB-based test DOF selection tools that draw extensively upon ATA Engineering’s IMAT software packages. The overall sensor selection task was broken into two separate tasks. The first step in the process was to use the IMAT down-selection functionality to iterate through the full 736 DOF set. The program utilized the self-orthogonality (ORTHO) criteria to find the minimal test DOF set needed to clearly capture all primary target modes. A few additional test DOF were then added to meet the final cross-orthogonality and frequency comparison requirements between the test analysis model (TAM) and the full FEM (E-Sta fully filled tank configuration) shapes. The primary target mode set only required 67 test DOF out of the full 736 DOF sensor set to adequately capture each mode independently. The TAM/FEM frequency comparison table and associated cross-orthogonality (XORTHO) for these 67 test DOF selected to optimize the extraction of the primary target modal parameters are shown in Fig. 40.3. This minimal 67 test DOF set provides the basis for the second step in the process for determining additional test DOF that adequately capture the secondary target modes.

40.5 Secondary Target Modes Test DOF Selection

When the same down selection procedure was applied to expand the test DOF to capture the 14 secondary target modes, the program had a much more difficult time, in part because the secondary target modes were localized and had almost no modal effective mass. Based on past experience, this issue can usually be overcome by additional well-placed test DOF. However, in this case none of the E-Sta test DOF were in locations that would adequately differentiate one secondary target mode from another.

The solar array secondary structure modes are a good example of this. Over 8 of the 14 secondary target modes had significant solar array structure translation and rotation. Of the four solar arrays on the vehicle, only one was flight like. The other three were mass simulators, each of which only had one triaxial accelerometer in the middle of the panel. Therefore, only translational motion could be measured on the three solar array mass simulators, leaving any rotation seen in the mode shapes unobservable by the measured DOF.

These two issues made the secondary test DOF set significantly larger and much less optimized. A modified approach using the down-selection program previously used for the primary target mode DOF set down-selection helped to ensure that the majority of the modal mass was captured in the TAM, but engineering judgment then had to be used to select DOF that adequately animated the mode shapes. The final cross-orthogonality between the TAM and FEM shapes did not meet the pretest goal of greater than 90% on the diagonal and less than 10% on the off-diagonal. Hence, it was expected that the secondary target modes would be much more difficult to extract from the test data. The TAM/FEM frequency comparison table and associated cross-orthogonality for the 250 selected test DOF for the secondary target modes are shown in Fig. 40.4.

FEM/TAM Cross Orthogonality Table										FEM Mode	Freq (Hz)	TAM Mode	Freq (Hz)	% Difference	
FEM Shapes															
	Oag	3.4	3.7	6.5	7.6	7.8	11.5	12.4	14.2						
TAM Shapes	1	3.4	-1.00							1	3.37	1	3.36	-0.49	
	2	3.7		-1.00						2	3.74	2	3.70	-1.04	
	3	6.4			-1.00					3	6.52	3	6.44	-1.17	
	4	7.6				1.00				4	7.57	4	7.57	0.01	
	5	7.8					-1.00			5	7.84	5	7.80	-0.50	
	6	11.9						1.00		6	11.47	6	11.87	3.49	
	7	12.9							-0.99	-0.23	7	12.43	7	12.86	3.44
	8	15.3								0.09	-0.94	8	14.24	8	15.28

Fig. 40.3 Minimal 67 test DOF TAM/FEM XORTHO (left), and TAM/FEM frequency comparison (right)

FEM/TAM Cross Orthogonality Table																								
FEM Shapes		1	2	3	4	5	6	7	8	9	10	11	12	13	14	15	16	17	18	19	20	21	22	
TAM Shapes	Oag	3.4	3.7	6.5	7.6	7.8	11.5	12.4	14.2	15.2	16.1	16.4	17.3	18.2	19.5	20.7	22.5	22.5	22.7	23.0	23.9	25.0	26.0	
1	3.4	-1.00																						
2	3.7		-1.00																					
3	6.4			1.00																				
4	7.5				1.00																			
5	7.8					-1.00																		
6	11.7						1.00						0.11		0.08								-0.06	
7	12.9							0.99	0.23	0.05													-0.30	
8	15.2							-0.08	0.90	-0.43	-0.06		0.11			0.06			-0.06	0.43				
9	15.7							0.05	-0.34	-0.88	0.23	0.09	0.09										-0.36	
10	16.6							0.09	0.13	0.95	-0.22	-0.06											0.18	
11	17.2								-0.08	-0.17	-0.95	0.18		-0.17	0.08					-0.09				
12	18.6								0.08	0.05	0.13	0.90	0.35	-0.23										
13	19.0												0.34	-0.92	0.10								-0.05	
14	21.0											0.06	-0.12	-0.12	-0.95	0.08							-0.06	
15	22.5													0.06	0.98				0.10	-0.05			0.14	
16	24.3															0.94	0.28					0.20		
17	24.3															0.33	-0.86	-0.13	-0.37	0.07				
18	24.5																0.06	-0.07	-0.40		0.90			
19	24.8															-0.09	0.05	0.11			0.97	-0.14	-0.07	
20	25.7																			0.11	0.99			
21	27.3																				0.56		0.05	0.16
22	27.9																							-0.87

FEM Mode	Freq (Hz)	TAM Mode	Freq (Hz)	%Difference
1	3.37	1	3.35	-0.54
2	3.74	2	3.70	-1.12
3	6.52	3	6.41	-1.69
4	7.57	4	7.54	-0.45
5	7.84	5	7.76	-1.05
6	11.47	6	11.75	2.46
7	12.43	7	12.85	3.38
8	14.24	8	15.22	6.88
9	15.16	9	15.74	3.86
10	16.13	10	16.60	2.91
11	16.41	11	17.24	5.07
12	17.29	12	18.62	7.66
13	18.24	13	18.97	3.97
14	19.46	14	20.97	7.76
15	20.75	15	22.54	8.63
16	22.47	16	24.25	7.94
17	22.53	17	24.33	7.99
18	22.72	21	27.33	20.32
19	23.03	18	24.51	6.44
20	23.92	19	24.80	3.66
21	25.05	20	25.71	2.64
22	25.97	22	27.95	7.63

Fig. 40.4 250 test DOF TAM/FEM XORTHO (top), and TAM/FEM frequency comparison (bottom)

40.6 Modal Survey Conduct

As part of MVF performing a sine sweep, a low level random pretest characterization test run is performed with the eight drive signals being uncorrelated so the MVF vibration controller can identify the dynamics of the integrated system and obtain a preliminary controller transfer function matrix. This random pretest was adapted to provide up to 20 min of low-level random base input excitation to the MVF Table from 2 Hz to 100 Hz while MVF was configured for vibration testing in the vertical direction. These random pretest acceleration time-history functions of the MVF Table responses were then processed to create up to eight independent constraint shape DOF that were then used as references when calculating FRFs.

40.7 Constraint Shape Calculation

A total of eight constraint shapes were considered because there were eight independent actuator groups attached to the MVF table and each driven with uncorrelated drive signal. A total of 36 accelerometers mounted to the MVF table were used to calculate the constraint shapes, and they are shown in Fig. 40.5. The first six constraint shapes were the six rigid body modes

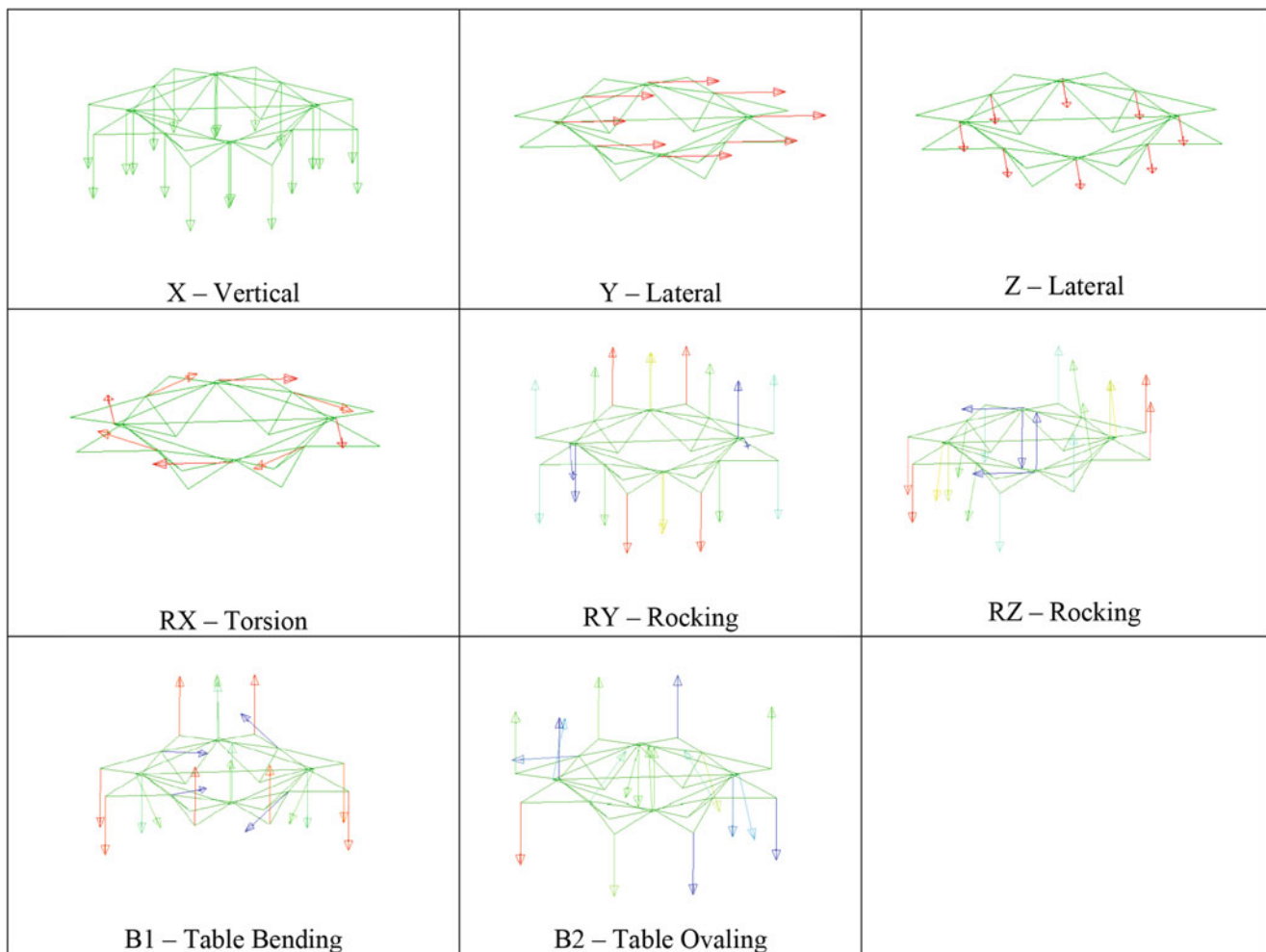


Fig. 40.5 Constraint shapes

of the MVF table. The final two constraint shapes were calculated by performing a singular value decomposition of the time history functions from 4 to 80 Hz generated by taking the 36 MVF Table accelerations and removing the contributions due to the rigid body motion of the MVF Table in a least-squares sense.

40.8 Frequency Response Function Calculation

Since random time-history data was collected, several parameters were studied to determine which method would be the best for calculating the cleanest set of FRFs. These parameters included the number of references used, the FRF method (H_1 versus H_{SVD} [10]), and the FRF averaging method (Welch versus Daniell [11]). The final set of FRFs was based on using the following:

1. The first seven constraint shapes (six rigid body modes and first “potato chip” mode) as references.
2. H_{SVD} using seven constraint shapes and three accelerometers as basis vectors to capture peaks of primary modes
3. Welch method (Hanning window, 90% overlap)

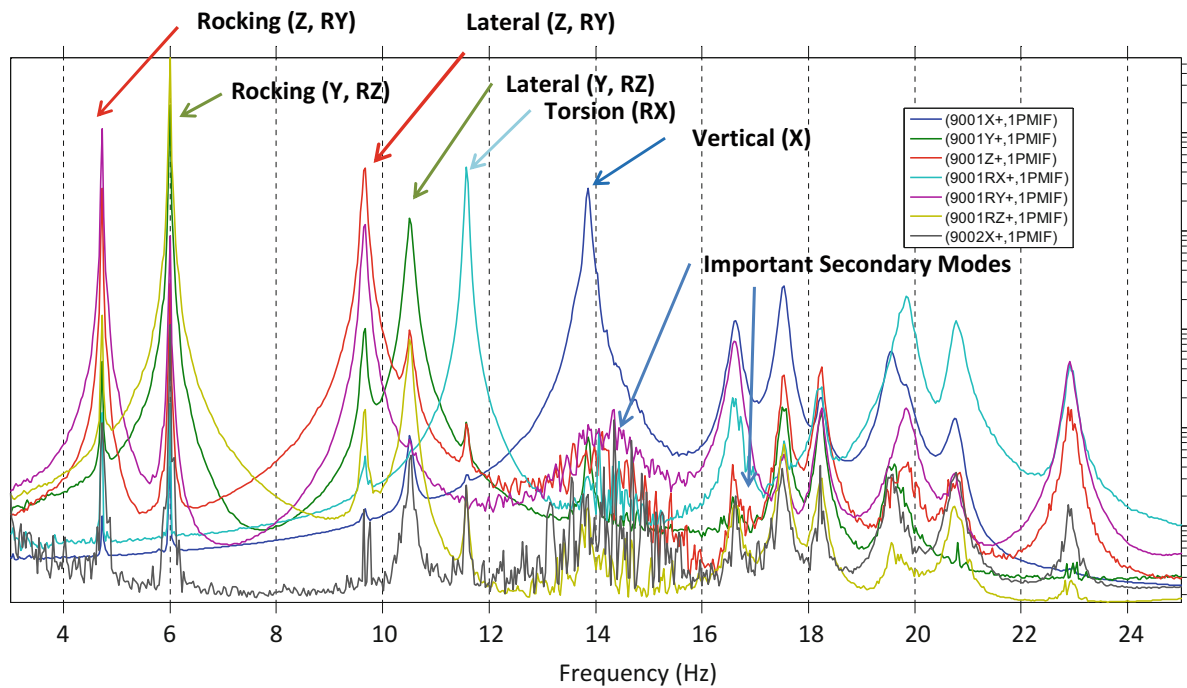


Fig. 40.6 Power spectrum mode-indicator functions comparing response of all channels due to each constraint shape reference

A power spectrum mode-indicator function (PSMIF) of each reference is presented in Fig. 40.6. The PSMIFs associated with rigid body motions are much cleaner than the PSMIF of the seventh reference (i.e. MVF Table bending B1), which is associated with flexible motion of the MVF Table. The eighth constraint shape, B2, which was dominated by ovaling of the MVF Table was not well excited because of the geometry of the actuators relative to this constraint shape and thus the shape was not used. The first six primary target modes were well excited by the rigid body motion of the MVF Table as evidenced by the associated strong peaks in the PSMIF. Upon closer inspection it can be seen that each of the primary target modes is excited by the appropriate MVF Table rigid body motion. For example, the primary torsion and axial target modes are excited by in-plane rotation and vertical motion of the MVF table, respectively. Note that the FRFs associated with two important secondary structure modes appear to be not well excited because they are heavily damped. This challenge is common in almost all modal surveys, and one solution is to connect modal shakers to the secondary structure and excite these modes directly. In this case, however, all primary target modes were able to be extracted from the random pretest test data.

One check to determine the fixity of the MVF table is to look at the base motion compared to the motion of the accelerometers on the MVF table. This can be represented by overlaying a PSMIF of the test article accelerometers and a PSMIF of just the MVF Table accelerometers Fig. 40.7. Ideally, the base motion should be constant as a function of frequency, but just as in conventional fixed base modal tests the base may not be perfectly fixed, leading to some small level of resonance amplification. The level of this amplification determines how accurate the fixed base modal frequencies are. In this case, the resonance amplification of the two primary bending modes is very small compared to the overall response and is nearly flat for all frequencies up to 50 Hz. Hence the modal parameters extracted are fixed base.

40.9 Modal Extraction

Fixed base modal parameters were then extracted from the fixed base FRFs just as they would be in any fixed base modal test. The FRFs associated with the first six rigid body constraint shapes as references were used to extract modal parameters for two reasons. The first is that the FRFs associated with rigid body motion were cleaner than the FRFs associated with

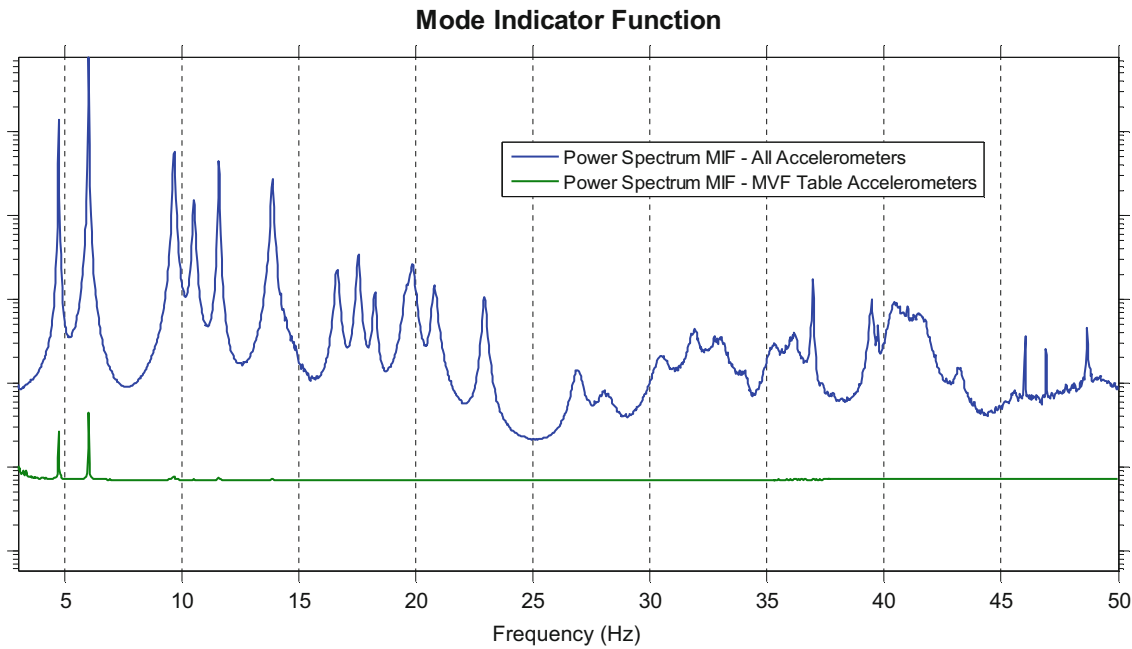


Fig. 40.7 Power spectrum mode-indicator function comparing E-STA response to MVF Table response

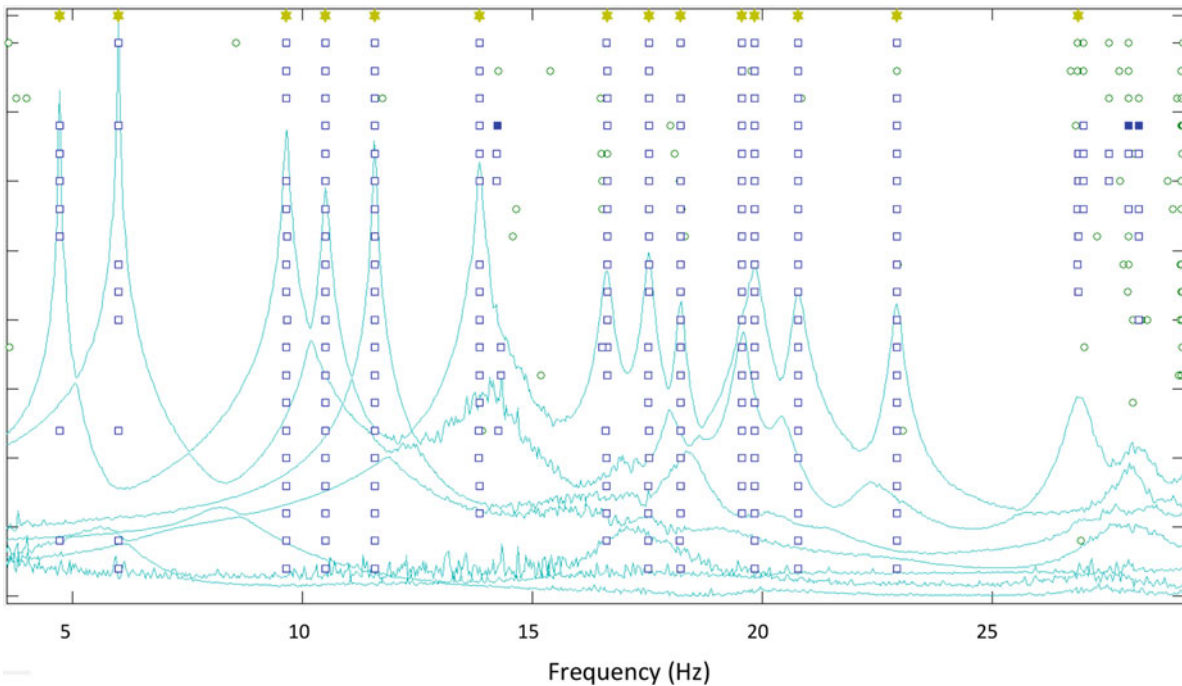


Fig. 40.8 Example stability plot created using ATA's AFPoly modal analysis tool

constraint shape associated with flexible motion of the MVF Table, and the second is that the FRFs associated with the six rigid body shapes are guaranteed to excite high-effective-mass modes. A stability plot from ATA's IMAT AFPoly modal analysis tool, showing the pole estimates and overlays of the Complex Mode Indicator Functions (CMIF's), is shown in Fig. 40.8. The well-defined "race track" pattern of the pole estimates and their alignment with the strong peaks in the CMIF aids in the modal extraction process.

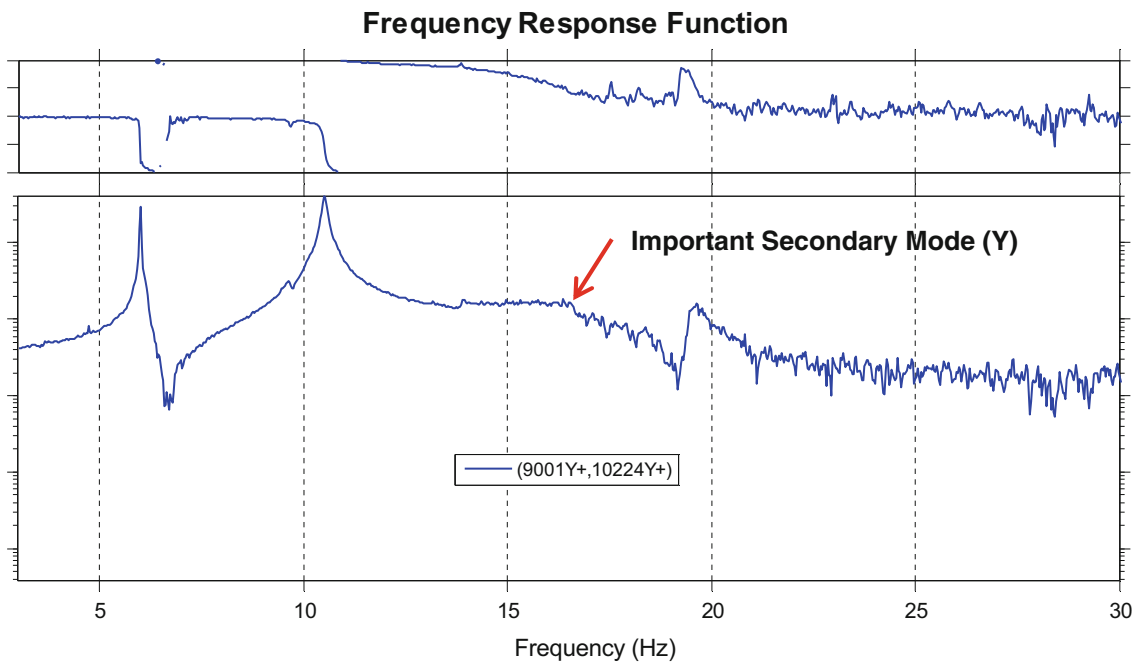


Fig. 40.9 FRF associated with important secondary structure lateral (Y) motion and table lateral Y motion

The extraction of the important secondary structure modes was difficult due to the fact that the linkages/connections are very nonlinear and resulted in very high damping levels. Specific FRFs associated with MVF Table constraint shape that clearly excited these modes and response DOF on the secondary structure were used with narrow-band modal analysis tools, such as ATA's IMAT SDOFIT tool, were used to extract these modes. One of these FRF showing the important secondary structure mode is shown in Fig. 40.9. Note that because of the high damping, there is not a pronounced resonance peak in the FRF, but the phase angle roll off does indicate a mode is present.

The first two 1st lateral bending modes, 1st torsion, and 1st axial test-measured fixed base modes are shown in Fig. 40.10. Base fixity was assessed by viewing MVF Table motion for each mode shape.

40.10 Post Test Analysis

After the fixed-base mode shapes were extracted, test ORTHO and test-analysis XORTH0 were calculated to assess test mode quality Fig. 40.11. Ideally, the off-diagonal terms of the test ORTHO should be below 10%. Higher off-diagonal terms may occur for a number of reasons, but in this case it appears that the 11% term is due to the important secondary structure lateral mode being very difficult to extract. The test-analysis XORTH0 shows that all eight primary target modes were adequately captured.

A final check was performed to assess how many of the analysis modes were captured in the test by looking at the XORTH0 between all extracted test shapes to all analysis shapes up to 26 Hz and is shown in Fig. 40.12. Overall, there is mostly a one-to-one match between a given test shape and a given analysis shape, although in some cases multiple test modes capture a given analysis mode. This can be assessed by looking at the "CRSS 3%" and the "CRSS All" rows at the bottom of the table. The "CRSS 3%" row describes how much of the analysis mode is captured by all test modes within 3% in frequency of the test mode that best maps to the analysis mode. The "CRSS All" row describes how much of each analysis mode is captured by all of the test shapes.

The only analysis mode that does not have a significant match to a single test mode is analysis mode 18, which is the important secondary structure's 1st torsion mode. The XORTH0 indicates that this mode lies in the 32–34 Hz range, and this assessment was verified by looking at the FRFs associated with secondary structure tangential accelerometers due to a torsional input of the MVF Table (9001RX+), which is shown in Fig. 40.13. There is a heavily damped mode where both accelerometers are in phase, as they should be for a torsion mode, near 33 Hz. Note that the phase change near this frequency is more than 180° , which means that there are multiple modes present.

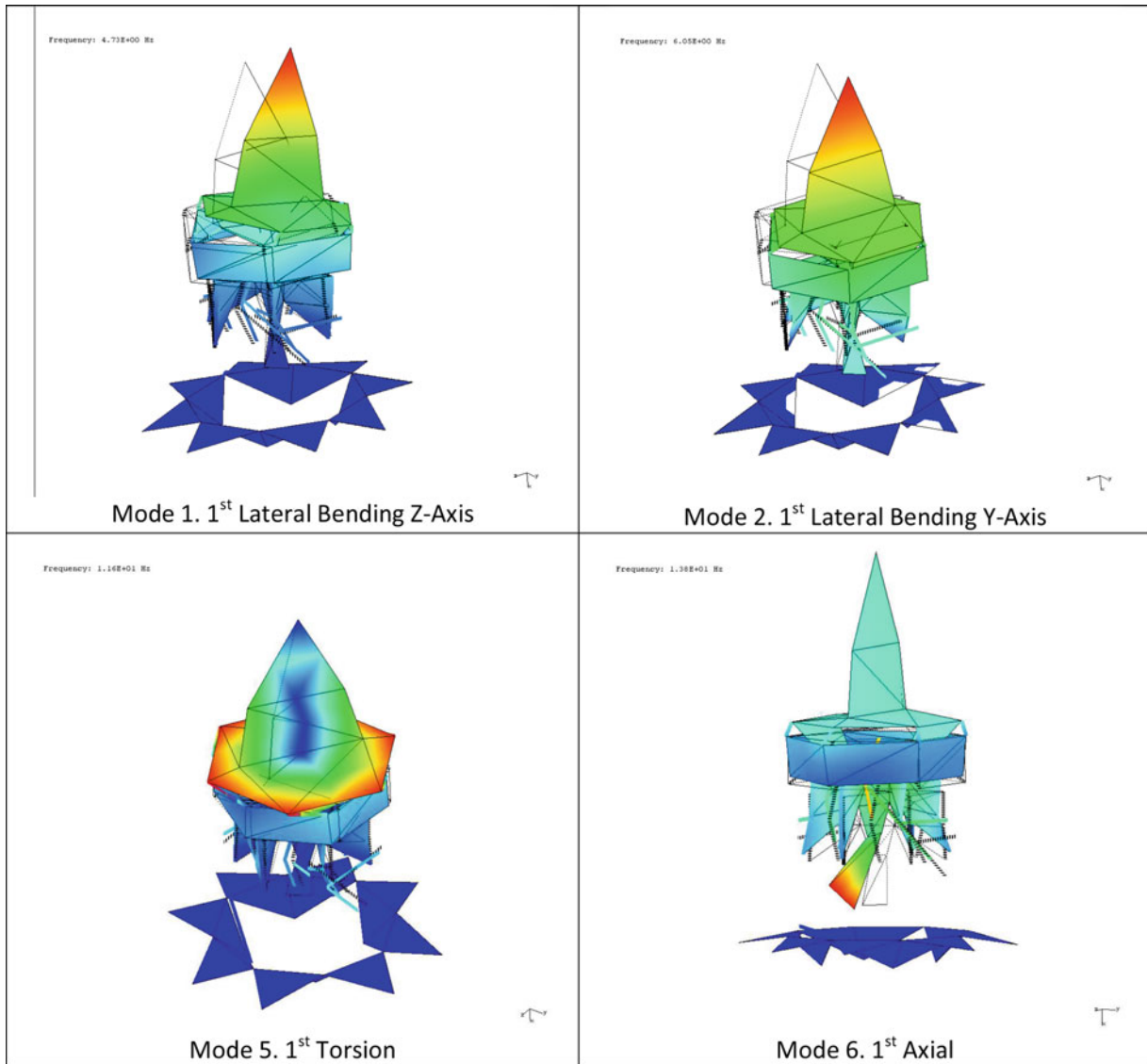


Fig. 40.10 Example primary target fixed base test mode shapes

Test Self Orthogonality Table										
		Test Shapes								
		1	2	3	4	5	6	7	8	
Ott		4.7	6.1	9.7	10.5	11.6	13.8	14.2	16.3	
Test Shapes	1	4.7	1.00							
	2	6.1		1.00						
	3	9.7			1.00					
	4	10.5				1.00			0.07	
	5	11.6					1.00			
	6	13.8						1.00	0.11	
	7	14.2							1.00	0.05
	8	16.3				0.07	0.11	0.05		1.00

FEM/Test Cross Orthogonality Table										
		FEM shapes								
		1	2	3	4	5	6	7	8	
Otg		3.4	3.7	6.5	7.6	7.8	11.5	12.4	14.2	
Test Shapes	1	4.7	0.97		0.23					
	2	6.1		0.97						
	3	9.7	0.23		0.96					
	4	10.5					0.97			
	5	11.6				0.91				
	6	13.8						0.98		
	7	14.2							0.21	0.96
	8	16.3						0.21	0.75	

Fig. 40.11 Primary target mode test shape ORTHO (left), and test-analysis XORTH0 (right)

		FEM/Test Cross Orthogonality Table																						
		FEM shapes																						
		1	2	3	4	5	6	7	8	9	10	11	12	13	14	15	16	17	18	19	20	21	22	
Test Shapes	Otg	3.4	3.7	6.5	7.6	7.8	11.5	12.4	14.2	15.2	16.1	16.4	17.3	18.2	19.5	20.7	22.5	22.5	22.7	23.0	23.9	25.0	26.0	
	1	4.7	0.97		0.23																			
	2	6.1		0.97																				
	3	9.7	0.23		0.96																			
	4	10.5				0.97																		
	5	11.6					0.91			0.22	0.30													
	6	13.8						0.98																
	7	14.2							0.21	0.96												0.41		
	8	16.3							0.21	0.75			0.36	0.22	0.34							0.37		
9	16.6									0.26	0.88	0.34												
10	17.5						0.23						0.93											
11	18.2										0.41				0.84	0.29								
12	19.6															0.87	0.44							
13	19.8				0.27					0.32	0.70		0.40				0.37							
14	20.8				0.21						0.39				0.33	0.77								
15	22.9																0.96							
16	26.9																	0.53	0.24			0.77		
17	27.0																		0.72	0.21			0.61	0.21
18	27.5																		0.32	0.84			0.30	
19	28.0																					0.92		
20	28.2																				0.39	0.23	0.82	
21	30.5																							0.77
22	31.9																							
23	32.4																				0.24			
24	32.7																				0.27			0.32
25	33.0																					0.21		
26	34.0								0.22	0.24													0.50	
FEM CRSS 3%		0.97	0.97	0.96	0.91	0.97	0.99	0.86	0.97	0.88	0.70	0.93	0.84	0.88	0.77	0.96	0.98	0.98	0.54	0.93	0.94	0.94	0.77	
FEM CRSS All		1.00	1.00	1.00	0.98	1.00	1.00	0.99	1.00	1.00	1.00	1.00	1.00	1.00	1.00	1.00	1.00	0.99	0.95	0.98	0.98	0.99	0.89	

Fig. 40.12 XORTHO of all extracted test shapes versus all analysis shapes to 26 Hz

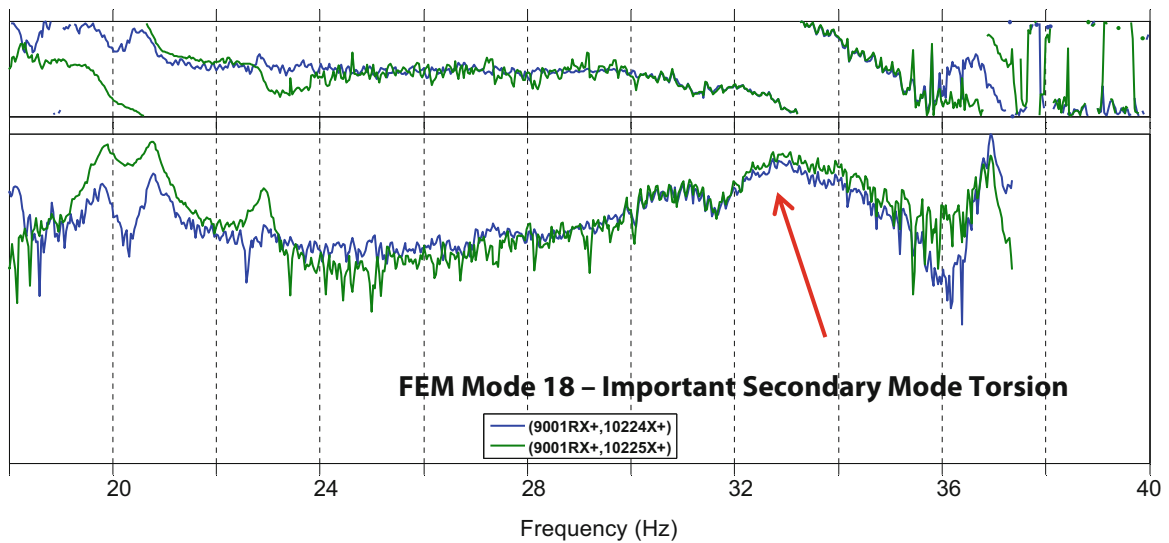


Fig. 40.13 FRFs associated with tangential motion and table in-plane rotational input

40.11 Summary

This paper presents the results of the modal survey of the E-STA mounted on the MVF table during the E-STA Sine Vibration Test. In spite of the challenges associated with this test, such as a non-optimal candidate sensor set and a dynamically flexible MVF Table, high quality fixed-base modes were extracted for the eight primary target modes using innovative techniques to down-select to appropriate sensor sets and to calculate fixed base FRFs.

The fixed base FRFs were calculated using seven constraint shapes of the MVF Table, which included the six rigid body motions and one flex motion. Once these FRFs were calculated, standard modal analysis techniques were used to extract fixed base modes of the test article. The test was deemed a success since all analysis modes up to 26 Hz, including the eight primary target modes, were captured as much as practicable given the sensor location constraints.

References

1. Carne, T.G., Martinez, D.R., Nord, A.R.: A comparison of fixed-base and driven base modal testing of an electronics package. In: Proceedings of the Seventh International Modal Analysis Conference, pp. 672–679, Las Vegas, Nevada (1989)
2. Beliveau, J.G., Vigneron, F.R., Soucy, Y., Draisey, S.: Modal parameter estimation from base excitation. *J. Sound Vib.* **107**, 435–449 (1986)
3. Fullekrug, U.: Determination of effective masses and modal masses from base-driven tests. In: Proceedings of the 14th International Modal Analysis Conference, pp. 671–681, Dearborn, Michigan (1996)
4. Sinapius, J.M.: Identification of fixed and free interface normal modes by base excitation. In: Proceedings of the 14th International Modal Analysis Conference, pp. 23–31, Dearborn, Michigan (1996)
5. Mayes, R.L., Bridgers, L.D.: Extracting fixed base modal models from vibration tests on flexible tables. In: Proceedings of the 27th International Modal Analysis Conference, Orlando, Florida (2009)
6. Napolitano, K., Yoder, N.: Fixed base FRF using boundary measurements as references – analytical derivation. In: Proceedings of the 30th International Modal Analysis Conference, Garden Grove, CA (2012)
7. Mayes, R., Rohe, D., Blecke, J.: Extending the frequency band for fixed base modal analysis on a vibration slip table. In: Proceedings of the 31th International Modal Analysis Conference, Orlando, Florida (2013)
8. Napolitano, K., Yoder, N.: Extraction of fixed-base modes of a structure mounted on a shake table. In: Proceedings of the 31th International Modal Analysis Conference, Orlando, Florida (2013)
9. Staab, L., Winkel, J., Suárez, J., Jones, T., Napolitano, K.: Fixed base modal testing using the mechanical vibration facility 3-axis base shake system. In: Proceedings of the 34th International Modal Analysis Conference, Orlando, Florida (2016)
10. Napolitano, K.: Using singular value decomposition to estimate frequency response functions. In: Proceedings of the 34th International Modal Analysis Conference, Orlando, Florida (2016)
11. Daniell, P.: Discussion of ‘on the theoretical specification and sampling properties of autocorrelated time-series’. *J. R. Stat. Soc.* **8**, 88–90 (1946)

Chapter 41

Modal Analysis of Healthy and Cracked Isotropic Plates in Peridynamics

Andris Freimanis and Ainārs Paeglītis

Abstract Modal analysis is widely used to validate numerical models, for quality control in manufacturing, and to detect structural damage. However, it is hard to compute modes of a structure with cracks, because the partial differential equations used in continuum mechanics are undefined along discontinuities in the deformation field. Peridynamic theory is a nonlocal extension of continuum mechanics that uses integral equations, which are defined in presence of cracks. Therefore, it can be used to analyze changes in natural frequencies and mode shapes due to cracking. In this study, we compute the first five modes of 3D isotropic plates made from poly(methyl methacrylate) with free-free boundary conditions in peridynamics and compare them to experimental and finite-element analysis results. Afterwards, we introduce a crack in the cross-section and again compare the peridynamic and experimental results. Peridynamic natural frequencies of both healthy and cracked plates are within 3% of the experimental results and show similar frequency shifts due to damage. PD mode shapes match the experimental ones in both healthy and cracked cases.

41.1 Introduction

Quality control, damage detection and computational model validation are some of the areas that employ modal analysis. However, it is hard to compute modes of a cracked object, because the partial differential equations of continuum mechanics (CM) are undefined along discontinuities in the deformation field. Peridynamics (PD) is a mechanics theory that uses integral equations, which are defined in presence of cracks. Peridynamic theory was first introduced in [1] and later extended [2]. Modal analysis in PD has been explored in [3], where a good agreement between a two-dimensional PD simulation, classical mechanics solution, and finite-element (FE) solution was found. For an overview of PD theory we recommend either of [4–6]. In this study we measured modes of plate specimens made from polymethyl metacrylate (PMMA) with uncracked and cracked cross-section. Free-Free boundary conditions were used and results were compared to the modes computed using PD and FE analysis.

41.2 Experimental and Computational Modal Analysis

For this study we measured modes of five PMMA specimens with free-free boundary conditions. First we tested healthy specimens, then made a cut with a laser and retested them. To reduce the effect of manufacturing irregularities, five specimens were used and average values are presented. The nominal sizes of specimens were 100 mm × 50 mm × 8 mm. The elastic modulus was 5.35 MPa, Poisson's ratio was 0.339 and density – 1200 kg/m³. Specimens were suspended in two loops made from cotton thread to ensure unrestrained movement, thus simulating free-free boundary conditions. Each loop was located 25 mm from one end of the specimen. The crack was located 31 mm from one end. The average length of the crack was 11.82 mm. Specimens were excited using a loudspeaker and a 2D Polytec PSV-400 laser vibrometer measured the speed of 377 points on the specimen. Natural frequencies and mode shapes were computed from the measured data by the software provided by Polytec. Since PMMA is translucent, the laser would shine through, so a paper tape was attached to the surface of specimens and cut at the place of the crack. It increased the weight of specimens by 0.4 g (0.9%), but the effect of such a small increase in mass was considered negligible.

A. Freimanis (✉) · A. Paeglītis
Riga Technical University, Institute of Transportation Engineering, Riga, Latvia
e-mail: andris.freimanis_1@rtu.lv

FE model, with dimensions described in the previous paragraph, was created in Ansys FE program using cubic SOLID185 elements with a side length of 2 mm. It consisted of 6630 nodes. Elastic material model with the properties as described in the previous paragraph was used. This was a free-free simulation, so no boundary conditions were applied.

Peridynamic model was created using the meshfree approach [7] with the same dimensions as FE model. It contained 135,000 nodes, the node spacing was 0.00067 mm and the horizon was 0.000943 mm, which was just over $\sqrt{2}$ times the node spacing. We used the Position-aware linear solid (PALS) [8] material model and the above described material properties. As before, movement was not restricted in any direction simulating free-free boundary conditions. To solve this modal problem, we added a modal solver to an open-source program Peridigm [9]. This solver used Block Krylov-Schur eigensolver [10], and Flexible Block GMRES [11] linear solver for the shift-invert spectral transformation.

41.3 Results and Discussion

For healthy specimens, we measured and computed the first five modes. Natural frequencies are compared in the Table 41.1 and the corresponding mode shapes are presented in the Fig. 41.1. The peridynamics results agree well with the experimental results. Computed natural frequencies are within 3% from the corresponding experimental results. Differences range from 0.65% for the second bending mode to 2.25% for the first torsional mode. The PD simulation show similar accuracy as the FE simulation, whose results are also within 3% from the corresponding experimental results. The mode shapes of PD theory match the measured and the FE mode shapes. The first mode is a longitudinal bending mode, the second and third are torsional modes, the fourth is a longitudinal bending mode again, and the fifth is a transverse bending mode. We expected a good agreement between the local FE model and the non-local PD model, because the horizon was small compared to the dimensions of the plate.

For cracked specimens the first five modes were computed, but only four were measured, because the fifth mode was an out-of-plane bending mode and a 2D vibrometer can't measure in the out-of-plane direction. The experimental and PD natural frequencies are compared in the Table 41.2. The differences range between 1.03% for the fourth mode and 2.31% for the second mode. PD results are within 3% from the experimental results, so the accuracy of a PD simulation of a cracked plate is similar to a simulation of a healthy specimen. Additionally, there's a clear shift in both experimental and PD natural frequencies. The first experimental frequency shifted by 72.5 Hz (4.3%) and the first PD frequency by 66.95 Hz (4.0%).

Table 41.1 Natural frequencies of healthy specimens, and the percent difference between the experimental and computed values

Mode	Experiment (Hz)	PD simulation (Hz)	Δ (%)	FE simulation (Hz)	Δ (%)
1	1667.00	1683.39	0.98	1713.00	2.76
2	1926.00	1969.31	2.25	1983.10	2.96
3	4198.00	4236.11	0.91	4275.20	1.84
4	4516.00	4486.55	0.65	4568.30	1.16
5	6477.00	6545.51	1.06	6626.50	2.31

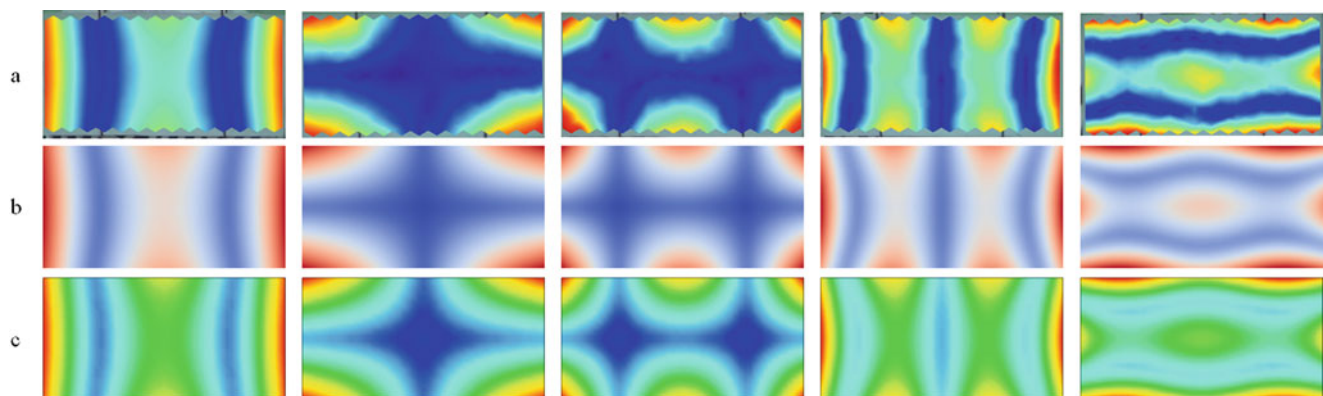


Fig. 41.1 Healthy specimen mode shapes 1 through 5: (a) experimental data, (b) PD simulation, (c) FE simulation

Table 41.2 Natural frequencies of cracked specimens, and the percent difference between the experimental and computed values

Mode	Experiment (Hz)	PD simulation (Hz)	Δ (%)
1	1594.50	1616.44	1.38
2	1847.50	1890.11	2.31
3	3973.50	4014.24	1.03
4	4269.50	4222.56	1.10
5	–	5660.20	–

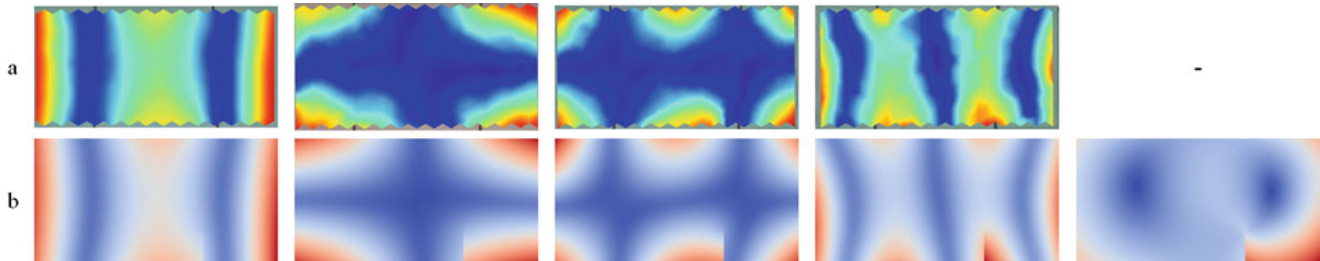


Fig. 41.2 Cracked specimen mode shapes 1 through 5: (a) experimental data, (b) PD simulation

Other modes show similar shifts in their natural frequencies. The PD mode shapes match the experimental ones, except for the fifth mode, which couldn't be measured experimentally, they are presented in Fig. 41.2. The first mode is a longitudinal bending mode, the second and third are torsional modes, and the fourth is a longitudinal bending mode. The fifth mode, however, is not a transverse bending mode as in healthy specimens, but an out-of-plane bending mode. This shows that the introduced crack has shifted the frequency of the out-of-plane bending mode more, than it has shifted the frequency of the transverse bending mode. The crack has also visibly changed the mode shapes – they are no longer symmetric.

41.4 Conclusions

In this study modes of healthy and cracked PMMA plates were computed using peridynamic theory, finite-element analysis and determined experimentally. The PD natural frequencies agree well with both experimental and FE results, additionally PD mode shapes match the experimental and the FE mode shapes. When a crack is introduced in the cross section both experimental and PD natural frequencies shift by a similar amount. And there's a visible loss of symmetry in the mode shapes of cracked plates.

References

1. Silling, S.A.: Reformulation of elasticity theory for discontinuities and long-range forces. *J. Mech. Phys. Solids*. **48**(1), 175–209 (2000)
2. Silling, S.A., Epton, M., Weckner, O., Xu, J., Askari, E.: Peridynamic states and constitutive modeling. *J. Elast.* **88**(2), 151–184 (2007)
3. Littlewood, D.J., Mish, K., Pierson, K.: Peridynamic simulation of damage evolution for structural health monitoring. *Mech. Solids Struct. Fluids*. **8**, 1 (2012)
4. Madenci, E., Oterkus, E.: *Peridynamic Theory and Its Applications*. Springer, New York (2014)
5. Silling, S.A., Lehoucq, R.B.: Peridynamic theory of solid mechanics. *Adv. Appl. Mech.* **44**, 73–168 (2010)
6. Bobaru, F., Foster, J.T., Geubelle, P.H., Silling, S.A.: *Handbook of Peridynamic Modeling*. CRC Press, Boca Raton (2016)
7. Silling, S.A., Askari, E.: A meshfree method based on the peridynamic model of solid mechanics. *Comput. Struct.* **83**(17–18), 1526–1535 (2005)
8. Mitchell, J., Silling, S., Littlewood, D.: A position-aware linear solid constitutive model for peridynamics. *J. Mech. Mater. Struct.* **10**(5), 539–557 (2015)
9. Parks, M.L., Littlewood, D.J., Mitchell, J.A., Silling, S.A.: Peridigm users' guide. Technical Report SAND2012-7800, Sandia National Laboratories (2012)
10. Zhou, Y., Saad, Y.: Block Krylov–Schur method for large symmetric eigenvalue problems. *Numer. Algorithms*. **47**(4), 341–359 (2008)
11. Saad, Y.: A flexible inner-outer preconditioned GMRES algorithm. *SIAM J. Sci. Comput.* **14**(2), 461–469 (1993)

Chapter 42

Initial Modal Results and Operating Data Acquisition of Shock/Vibration Fixture

William Larsen, Jason R. Blough, James P. DeClerck, Charles D. VanKarsen, David E. Soine, and Richard Jones

Abstract This paper presents the initial experimental and FEA based modal analysis results obtained on a test assembly developed specifically to study the effects of component boundary conditions and excitation techniques on test damage potential during component qualification testing. This assembly was developed as a platform with a simple “component” and “next assembly” that allows the component to be removed and attached via a fixture to shock or vibration test equipment. All data and results will be made publicly available for other groups wishing to study the test assembly in pursuit of insight into how to define appropriate boundary conditions for component testing.

42.1 Introduction

The Boundary Conditions in Environmental Testing Challenge Problem [1] team designed a surrogate structure system to study differences in component dynamic behavior in-situ compared to fixtured a component test fixture. The ultimate goal is to develop best practices and design guidelines for component test fixtures.

The initial step in this process is to analytically and experimentally characterize the dynamic or modal characteristics of the design.

42.2 Fixture Design and Content

The surrogate structure design is shown in Figs. 42.1 and 42.2 [1]. The design was based on components readily available on-line ease of manufacture. The design consists of two parts: (1) the *component* is two C-channels attached to a beam and (2) the *subassembly* is a box beam with a slot cut in between the C-channel attachment locations. All parts are aluminum and are attached using threaded fasteners. Several subassemblies were manufactured and distributed to different work group participants.

Individual parts were weighed prior to shipping. The results are shown in Table 42.1. A range is not shown, because mass variation was less than 1% for each part. Dimensions for the stock material were also measured and are shown in Table 42.2. The most significant dimensional discrepancy is in the box section stock specified for the subassembly. Its thickness dimensions are 10% smaller than specified in the engineering drawings to cause a noticeable mass discrepancy with models based on the nominal dimensions.

The Department of Energy’s Kansas City National Security Campus is operated and managed by Honeywell Federal Manufacturing & Technologies, LLC under contract number DE-NA0002839.

W. Larsen · J. R. Blough (✉) · J. P. DeClerck · C. D. VanKarsen
Michigan Technological University, Houghton, MI, USA
e-mail: jrbrough@mtu.edu

D. E. Soine · R. Jones
Department of Energy’s Kansas City National Security Campus, Kansas City, MO, USA

System Assembly

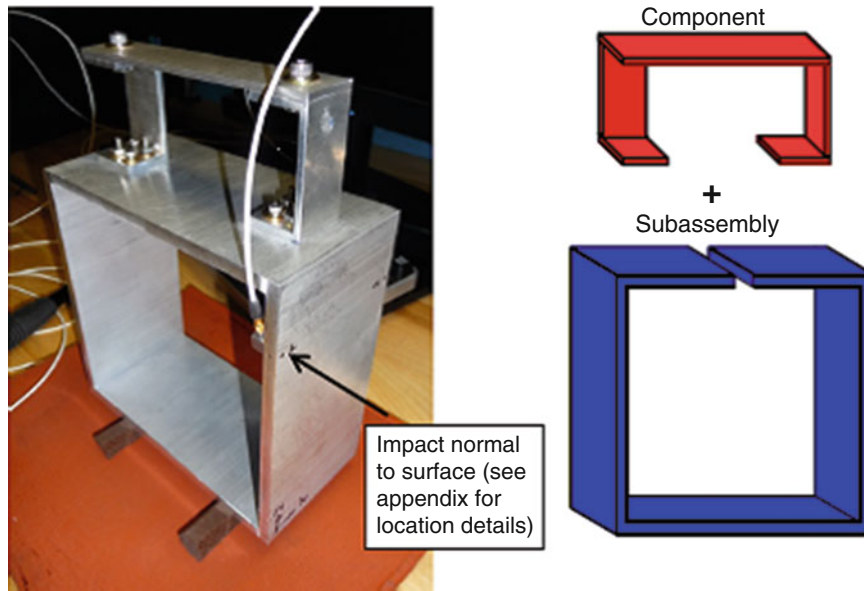


Fig. 42.1 Shock component design for challenge problem work group [1]

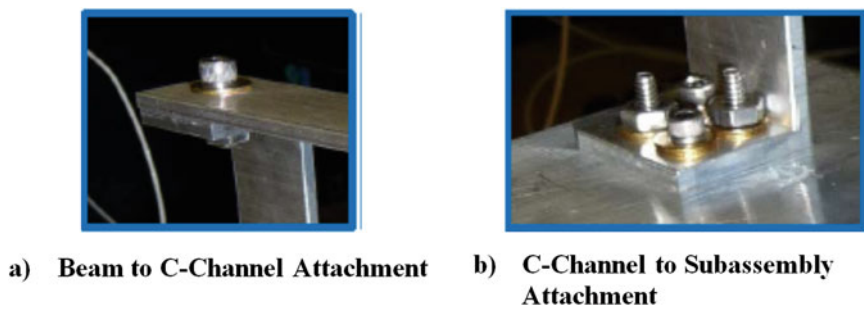


Fig. 42.2 Fastener detail [1]. (a) Beam to C-channel attachment. (b) C-channel to subassembly attachment

Table 42.1 Parts list and mass for challenge design structure

Part name	Quantity	Part mass (g)	Total (g)
Subassembly	1	709	709
C-channel	2	19.5	39.0
Beam	1	28.1	28.1
Beam to C-channel fasteners	2	5.7	11.4
C-channel to subassembly fasteners	8	3.4	27.2
Total design mass			814.7

Table 42.2 Dimensions of challenge design parts

Part name	Dimension	Nominal (in)	Measured (in)
Subassembly	Outside height	6.000	5.984
	Outside width	6.000	5.984
	Thickness	0.250	0.238
C-channel	Height	2.000	1.995
	Width	1.000	0.998
	Thickness	0.125	0.123
Beam	Width	1.000	1.000
	Length	5.000	5.002
	Thickness	0.125	0.126

42.3 Finite Element Model and Results

Two different finite element models were built. The first model used 4-node shell elements on the mid-surface of each part. Due to concern about artificial stiffness connecting shell elements and 90° , a second model was built using solid elements. The thicker subassembly was modeled with four layers of tet-4 elements and the thinner C-channel and beam were modeled with two layers of tet-10 elements. Both models shown in Fig. 42.3 were based on nominal geometry in the drawings [1].

Material properties were based on text book values for aluminum: Young's Modulus of 10^6 psi and density of 0.102 lb/in^3 . Both models predicted the same mass when based on the design dimensions. Thickness of the subassembly was reduced to the measured value indicating a significant mass reduction. The measured and predicted part mass are shown in Table 42.3. This mass discrepancy could cause inconsistencies in the modal parameters.

Attachment modeling is another key aspect to accurately predicting system dynamic behavior. Three different bolt approximations were applied to the shell model:

- A. Pin: RBE2 connections at hole center points
- B. Washer: RBE2 connections around hole perimeter
- C. Washer + Bolt Mass: RBE2 connections around hole perimeter + nonstructural fastener mass

Washer-type connection was applied to the solid element model. Two variations of the solid model were also run:

- E. Bolt mass was included and subassembly thickness was reduced to 0.230 in.
- F. Bolt mass was not included and subassembly thickness was set to 0.250 in.

The predicted natural frequencies for the five models are shown in Table 42.4. The natural frequencies are insensitive to the pin vs. washer approximation. As expected, adding bolt mass (model C) lowered the natural frequencies. Reducing the subassembly thickness reduced mass and stiffness resulting in further reduction of predicted natural frequencies. Finally, the solid model with design dimensions shows that the thickness has a greater stiffness effect, off-setting the added mass and further increasing the natural frequencies.

42.4 Experimental Modal Test and Results

The modal test setup is shown in Fig. 42.4. Free-free boundary condition was approximated using surgical tubing attaching the challenge structure to a ceiling fixture. The 24 response points are shown in Fig. 42.5. Six (1 g) tri-axial accelerometers were roved as four patches to measure response at each response point. Impact testing was used to gather frequency response functions. The three input locations (13X, 15Y, 15Z) are shown as red arrows in Fig. 42.5.

PolyMAX was used to extract modal parameters. Estimated natural frequencies are shown in Table 42.5.

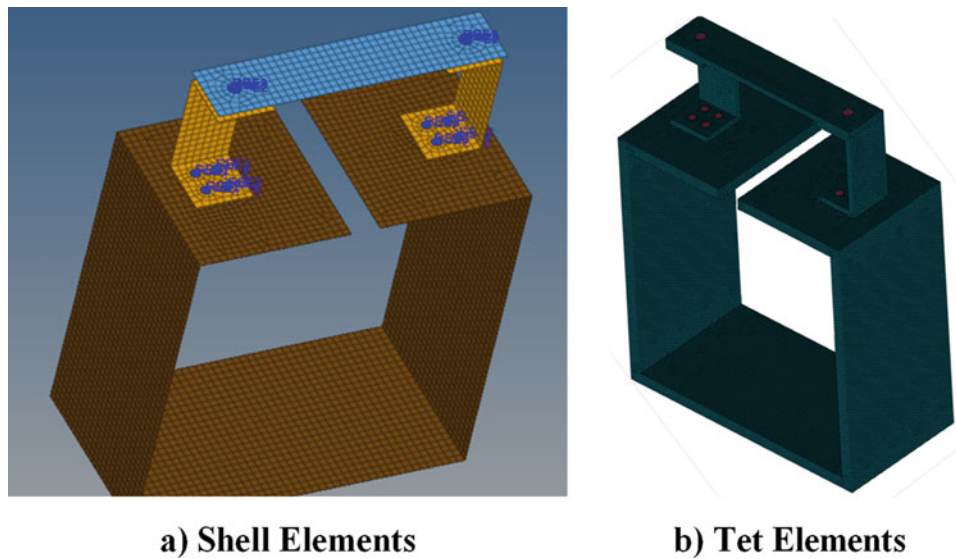


Fig. 42.3 Finite element models of challenge problem structure. (a) Shell elements. (b) Tet elements

Table 42.3 Comparison of measured and predicted mass

Part name	Measured mass (g)	Predicted mass (g)	
		Design thickness	Measured thickness
Subassembly (1)	709.0	781.6	719.2
C-channel (2)	39.0	42.1	42.1
Beam (1)	28.1	28.6	28.6
Beam to C-channel fasteners (2)	11.4	11.2	11.2
C-channel to subassembly fasteners (8)	27.2	26.6	26.6
Total mass	814.7	890.1	827.7

Table 42.4 Natural frequencies for FE models

Mode #	Shell elements			Tet element	
	Model A (Hz)	Model B (Hz)	Model C (Hz)	Model E (Hz)	Model F (Hz)
1	185.3	185.3	178.9	167.1	199.1
2	228.6	228.5	220.6	212.9	242.2
3	241.7	241.6	232.8	226.4	255.2
4	458.2	458.1	413.7	402.9	471.6
5	522.7	522.6	506.2	476.3	560.0
6	541.0	540.9	530.1	496.4	578.6
7	635.7	635.7	627.7	580.4	690.7
8	654.1	654.1	647.3	597.4	710.3
9	997.4	997.4	978.1	940.3	1019.7

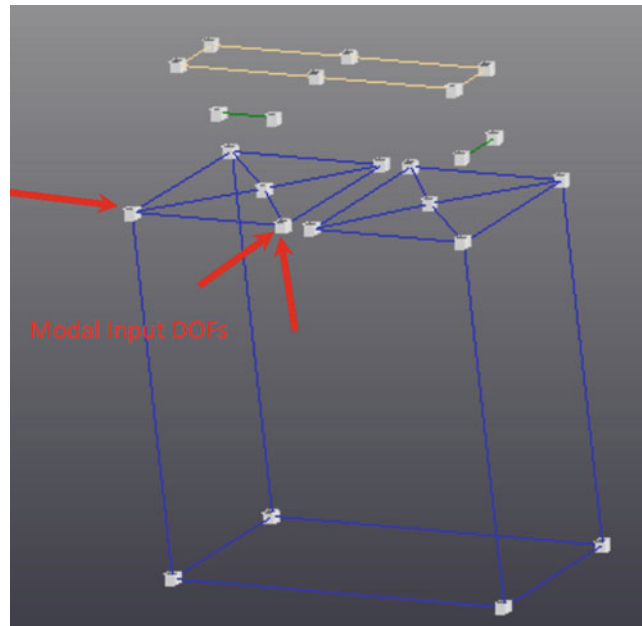


Fig. 42.4 Test geometry and modal input DOFS for challenge structure



Fig. 42.5 Experimental test setup

Table 42.5 Natural frequency estimates from modal test

Mode #	Natural frequency (Hz)
1	184.5
2	205.3
3	255.7
4	428.5
5	437.8
6	470.1
7	550.9
8	576.7
9	653.6

42.5 Modal Reconciliation

Modal reconciliation was focused on the first group of three modes indicated in Fig. 42.6. Both the shell and solid FEA geometries were reduced to match the (24 points*3dof) experimental degrees of freedom. Measured and predicted natural frequencies and corresponding modal assurance criterion are shown in Tables 42.6 and 42.7 for the shell and solid modes respectively. The first three mode shapes are shown in Fig. 42.7.

Mode shape correlation between the test and shell model (Model C) is sufficient to match mode pairs. Natural frequency estimates for the shell element model are inconsistent, predicting low for modes 1 and 3 and high for mode 2. The model was expected to under-predict the natural frequencies because the model mass is higher than the physical parts. Over-predicting the natural frequency for mode 2 is an indicator that there is additional stiffness somewhere in the model.

Mode shape correlation between the test and tet-element model (Model F) is better than for the shell model. The total mass of the tet-element model (F) was less than the shell model because fastener mass was excluded, yet the tet-model mass was still greater than the physical mass. Predicted natural frequencies were higher than test, indicating that the tet-model also has additional stiffness somewhere in the model.

The decision was made to not compare more modes at this time until comparison of the first three modes is more consistent. This process would begin with modal reconciliation of just the subassembly, since that was the part with largest mass discrepancy.

42.6 Conclusions and Recommendations

Finite element models should be based on dimensions of physical hardware to and be verified by mass correlation. The purchased stock material was manufactured to the minimum material tolerance, causing a 9% over estimate of the component and subassembly mass.

Two models for the component and subassembly were created, one model contained shell elements and the second model contained solid-tet elements. The tet-element model demonstrated better mode shape correlation than the shell-element model for the first three modes. Neither model consistently under-predicted or over-predicted natural frequencies. A recommendation for preferred modeling technique cannot be made at this time.

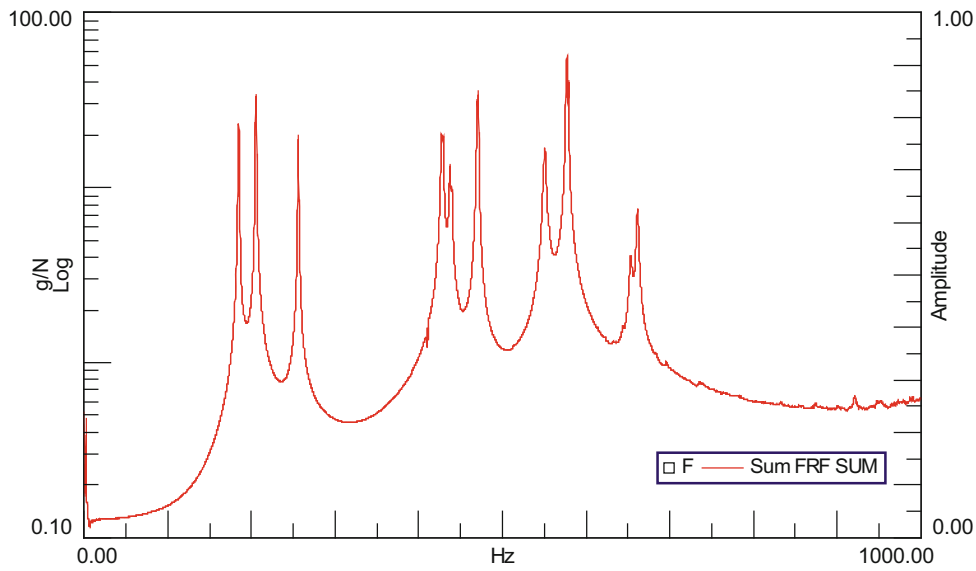


Fig. 42.6 Sum of all FRF measurements for challenge structure modal test

Table 42.6 Mode comparison between experiment and shell element model

Mode #	Experimental modal (Hz)	Shell elements – model C (Hz)	MAC (EMA-FEA C)	Natural frequency difference (Hz)
1	184.5	178.9	0.80	5.6
2	205.4	220.6	0.71	-15.2
3	256.0	232.8	0.70	23.2

Table 42.7 Mode comparison between experiment and tet element model

Mode #	Experimental modal (Hz)	Tet elements – model F (Hz)	MAC (EMA-FEA F)	Natural frequency difference (Hz)
1	184.5	199.1	0.94	-14.6
2	205.4	242.2	0.83	-36.8
3	256.0	255.2	0.70	0.8

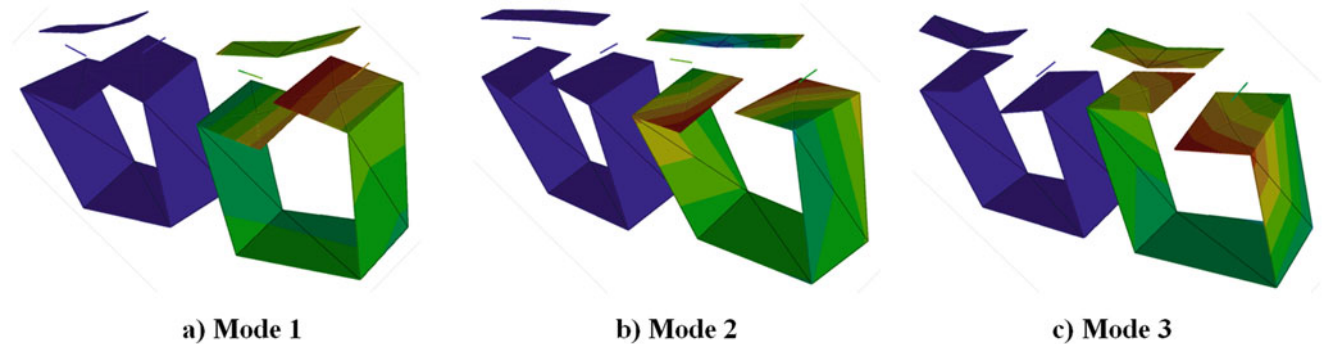


Fig. 42.7 Comparison to mode shapes for challenge structure (experiment-left; FE model-right). (a) Mode 1. (b) Mode 2. (c) Mode 3

The bolted joints were modeled using rigid elements connecting a single point on each part; using distributed attachment between parts; and including non-structural mass for the bolt, nut, and washer. Variation in the modal predictions for these methods is less than the difference between the shell and solid element models.

Modal reconciliation efforts should continue and include more modes and improved geometric representation of the model.

Reference

1. Harvie, J.: Boundary conditions in environmental testing challenge problem

Chapter 43

Effects of Variable Thickness Circular Plates on Frequency Response Functions and Shock Response Spectrum

William Larsen, Jason R. Blough, James DeClerck, Charles VanKarsen, David Soine, and Richard Jones

Abstract Resonant plates used for shock testing are typically a constant thickness. Prior research demonstrated that circular plates utilize symmetry to limit the number of contributing modes, although more design control is necessary to achieve target shock response spectra (SRS). Analytical modeling results show that variable thickness plates provide more flexibility to meet a target SRS. The first membrane mode of a circular plate correlates with the knee frequency in the shock response spectrum. Higher order membrane modes can cause the SRS to occur outside of the target band. Concave plates decrease the frequency band between first membrane mode and higher order membrane modes, while convex plates show the opposite effect. Using this theory, resonant plate cross section can be altered to tune resonant plate natural frequencies in order to achieve target SRS.

43.1 Introduction

A resonant plate shock test is conducted by rigidly attaching a test fixture and part to one side of a resonant plate and impacting the opposite side. Resonant plates used for shock testing are typically a constant thickness. Rectangular plates have historically been used, but because there are many frequencies that contribute to the response, they cannot always be designed to produce the desired shock response curves [1].

43.2 Circular Design

Previous research has investigated and proven that circular plates provide symmetry to minimize the number of contributing modes when impacted directly at the center [1]. A 1.125 inch thick, 17 inch diameter aluminum finite element model in Hypermesh was created to simulate this phenomena. 0.2 inch tetrahedral elements were used. The boundary conditions of the plate are modeled as free-free, attached by four soft springs to ground at locations around the edge of the plate. An eigen solution produced all modes of the plate up to 10,000 Hz. The modes with anti-nodes at the center are shown in Fig. 43.1.

To prove the validity of the model, all the modes are compared with analytical solutions. The following equation is the analytical representation of free-free circular plates [2] (Fig. 43.2). The variables are described below in Figs. 43.3 and 43.4.

The values of λ_{ij}^2 were analytically developed by Itao [3]. Below is the table of the values of lambda used in the calculation where i represents the number of nodal diameters and j represents the number of nodal circles [2].

All other variables and selected values of parameters of the plate can be seen in the following table. The material properties are 6061 aluminum.

The calculated analytical natural frequencies of the plate are displayed. The only contributing natural frequencies occur when there are zero nodal diameters ($i = 0$). Only the 10–10,000 Hz frequency range is of interest (Fig. 43.5).

The Department of Energy's Kansas City National Security Campus is operated and managed by Honeywell Federal Manufacturing & Technologies, LLC under contract number DE-NA0002839.

W. Larsen · J. R. Blough · J. DeClerck (✉) · C. VanKarsen
Michigan Technological University, Houghton, MI, USA
e-mail: jdeclerck@mtu.edu

D. Soine · R. Jones
Honeywell, Kansas City, MO, USA

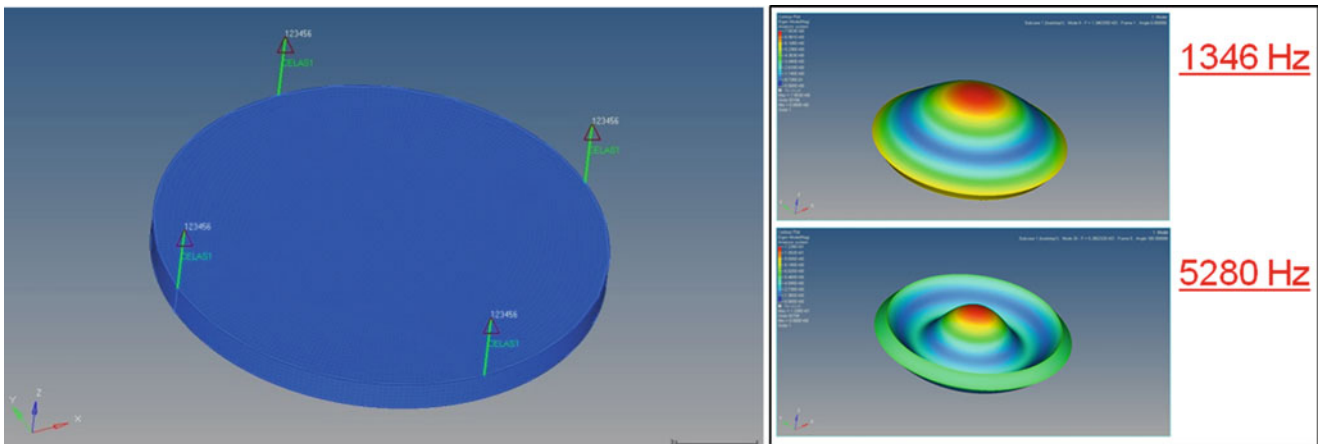


Fig. 43.1 Hypermesh model of plate and contributing mode shapes

Fig. 43.2 Analytical equation for free-free circular plate natural frequencies

$$f_{ij} = \frac{\lambda_{ij}^2}{2\pi a^2} \sqrt{\frac{Eh^2}{12\rho(1-\nu^2)}}$$

Round Plate with Free Edge: λ_{ij}^2						
		i (Nodal Diameters)				
		0	1	2	3	4
j (Nodal circles)	0	0	0	5.262	12.24	21.6
	1	9.063	20.51	35.24	52.92	
	2	38.51	59.86	84.37	111.2	
	3	87.81	119	153.3	190.7	

Fig. 43.3 Values of λ_{ij}^2 for use in free-free circular plate natural frequencies equation

Fig. 43.4 Structure variables of circular plate for use in free-free circular plate natural frequencies equation

Structure Variables			
Name	Variable	Value	Units
Radius	a	8.5	in
Elastic Modulus	E	$1 \cdot (10)^7$	psi
Thickness	h	1.125	in
Density	ρ	0.000254	(lb*s ²)/in ⁴
Poisson's Ratio	ν	0.33	-

Natural Frequencies of Plate (Hz)						
		i (Nodal Diameters)				
		0	1	2	3	4
j (Nodal circles)	0	0.0	0.0	791.3	1840.5	3248.0
	1	1362.8	3084.1	5299.1	7957.6	
	2	5790.8	9001.2	12686.8	16721.3	
	3	13204.1	17894.1	23051.9	28675.8	

Fig. 43.5 Natural frequencies of free-free circular plate

Mode Shape Natural Frequencies (Hz)					
Mode #	Nodal Diameters	Nodal Circles	Simulation	Analytical	Error (%)
7	2	0	789	791.3	-0.29
8	2	0	790	791.3	-0.16
9	0	1	1346	1362.8	-1.23
10	3	0	1793	1840.5	-2.58
11	3	0	1793	1840.5	-2.58
12	1	1	2938	3084.1	-4.74
13	1	1	2938	3084.1	-4.74
14	4	0	3065	3248.0	-5.63
15	4	0	3066	3248.0	-5.60
18	2	1	4846	5299.1	-8.55
19	2	1	4848	5299.1	-8.51
20	0	2	5282	5790.8	-8.79
27	3	1	6971	7957.6	-12.40
28	3	1	6972	7957.6	-12.39
29	1	2	7819	9001.2	-13.13
30	1	2	7821	9001.2	-13.11

Fig. 43.6 Simulated and analytical natural frequencies of free-free circular plate

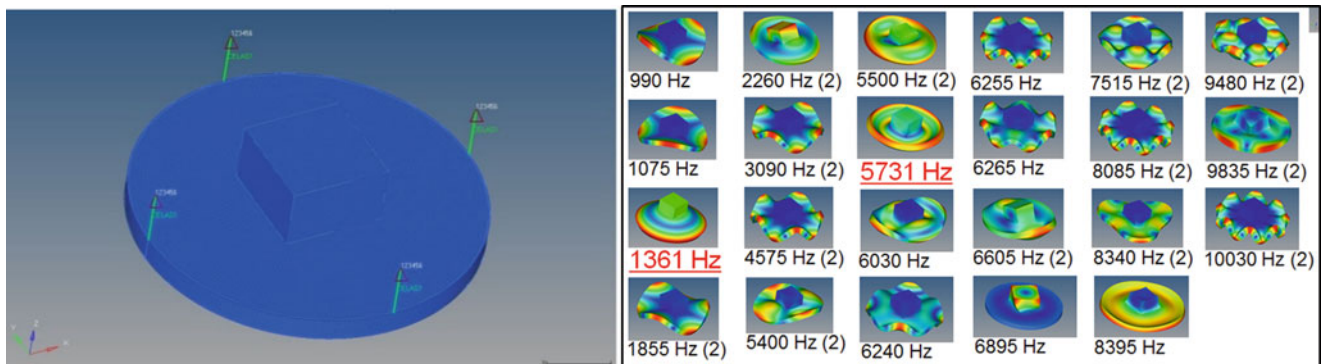


Fig. 43.7 FE model of plate with test fixture and all mode shapes

A comparison of the finite element results and analytical numerical results show an error below 10% for all natural frequencies of interest (Fig. 43.6).

A test fixture must be included in the design to simulate a more realistic test. A 3 inch thick, 5 inch square test fixture with the same material properties is rigidly attached to the center of the plate. A finite element model of the system can be seen in the following Fig. 43.7. This increases all of the natural frequencies of the modes. There is more apparent stiffness in the structure. All of the mode shapes and frequencies can be seen below. The bending modes of the plate are still found to be the only modes that significantly contribute to the response at the part’s center.

43.3 Shock Response Calculation

A FRF of the structure impacted with a unit impulse on the opposite side and response at the test fixture can be seen in Fig. 43.8a. Overall modal damping of the structure is 1%. An analytically created input spectrum of a 1 ms, 1 N amplitude haversine can be seen in Fig. 43.8b.

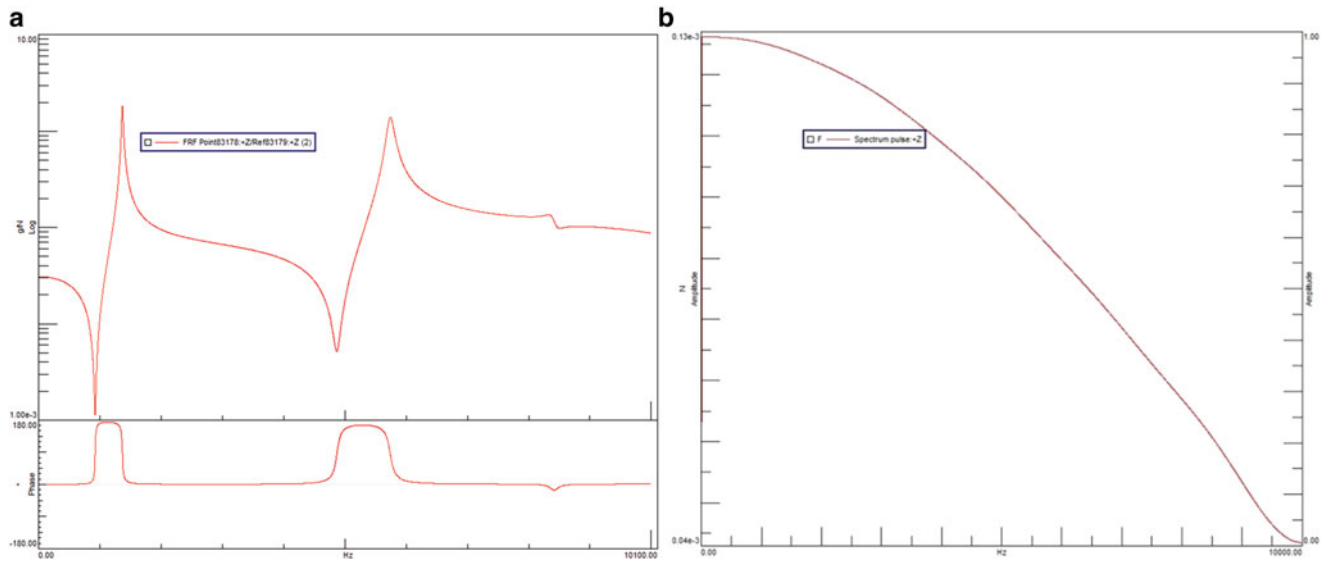


Fig. 43.8 Simulated FRF of structure (a), analytical input spectrum (b)

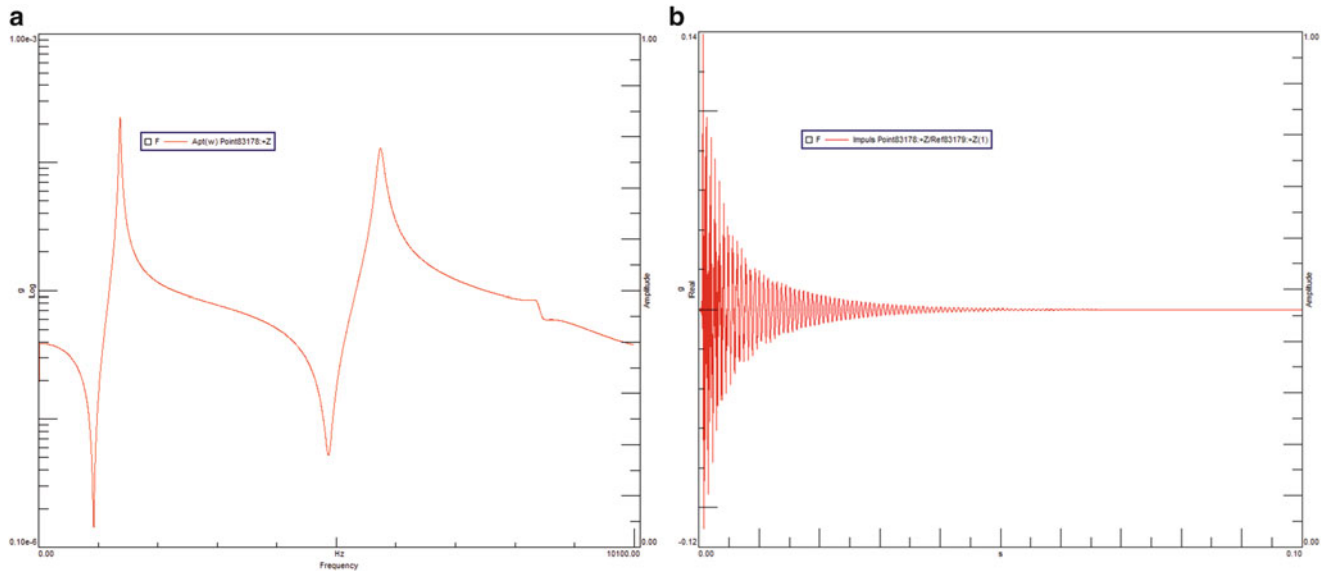


Fig. 43.9 Response of system from analytical input (a), time domain of response (b)

Multiplying the structure’s FRF by a chosen input spectrum results in an output response, Fig. 43.9a. The time domain response is shown in Fig. 43.9b.

From the output time domain response, a shock response spectrum can then be calculated. A Q of 10 (5% damping ratio) is used which is a standard damping factor for calculating the SRS. The absolute maximax acceleration is calculated. This process was developed to be able to compare different input levels of SRS, but also is found to be the best method to analytically simulate a SRS [4].

The two contributing natural frequencies of the plate can obviously be seen in the shock response spectrum as the peaks. The first membrane mode is the knee frequency indicated by the arrow in Fig. 43.10. To meet a target band, the second frequency is not desired to appear in the shock response spectrum. Simulations using higher modal damping results in a more rounded knee frequency and lower relative amplitude of the second peak in the SRS, but this alteration does not produce a low enough amplitude of the second peak to meet some target bands.

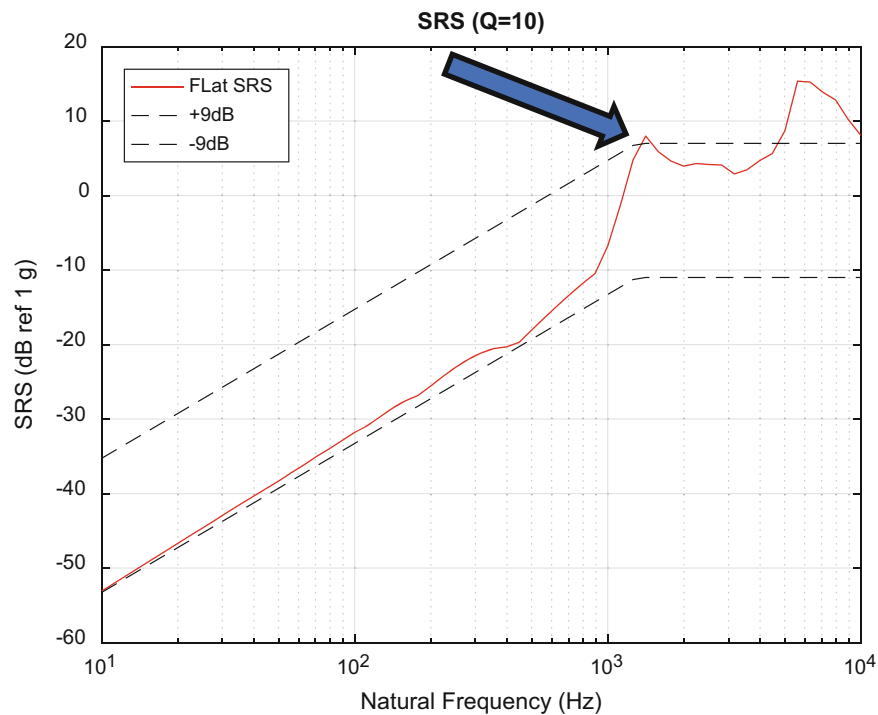


Fig. 43.10 Shock response spectrum of simulated system from analytical input with sample target bands

43.4 Variable Thickness

In an attempt to increase the frequency of the higher frequency mode out of the frequency band of interest, the cross sectional geometry of the plate was changed.

The geometry and contributing mode shapes of the initial flat plate are seen in the following Fig. 43.11.

The first bending mode, which is the knee frequency in the SRS, is 1361 Hz.

The geometry and contributing mode shapes of a plate with concave thickness are seen in the following Fig. 43.12. The plate was designed with the intent of increasing the mass by 4.5 lbs. This kept the plate within a weight that is realistic for a single person to work with, but more extreme weights could be used.

Both frequencies decreased, as well as the difference between the modes.

The geometry and contributing mode shapes of a plate with convex thickness are seen in the following Fig. 43.13. The plate was designed with the intent of decreasing the mass by 4.5 lbs, which is the same factor the concave plate was increased.

Both frequencies increased and the difference between the modes, but by a larger margin.

The weight of the flat plate is found to be 32.38 lbs, the convex plate is 27.88 lbs (-4.5 lb than flat plate), and the concave plate is 36.89 lbs ($+4.5$ lbs than flat plate).

The unit impulse FRFs of all of the test geometries can be seen below (Fig. 43.14).

The natural frequencies of the contributing modes taken from the frequency response functions are numerically displayed below. The convex plate increases the separation of contributing mode 1 and contributing mode 2 much more than the concave plate decreases the separation of the modes (Fig. 43.15).

The natural frequency trends from the FRFs can also be seen in the shock response curves, which can be seen below. Due to the log scale, the separation effect appears less dramatic (Fig. 43.16).

Convex plate geometry separates the bending modes' natural frequencies. This is a tool that can be used so that resonant plates can be more robustly designed to be able to control the contribution of the modes in the FRF and ultimately the frequency of the peaks in the shock response. Simulations should be done on more extreme geometry using a larger overall thickness to separate the modes further, eventually pushing the second bending mode frequency above 10,000 Hz and out of the frequencies of interest.

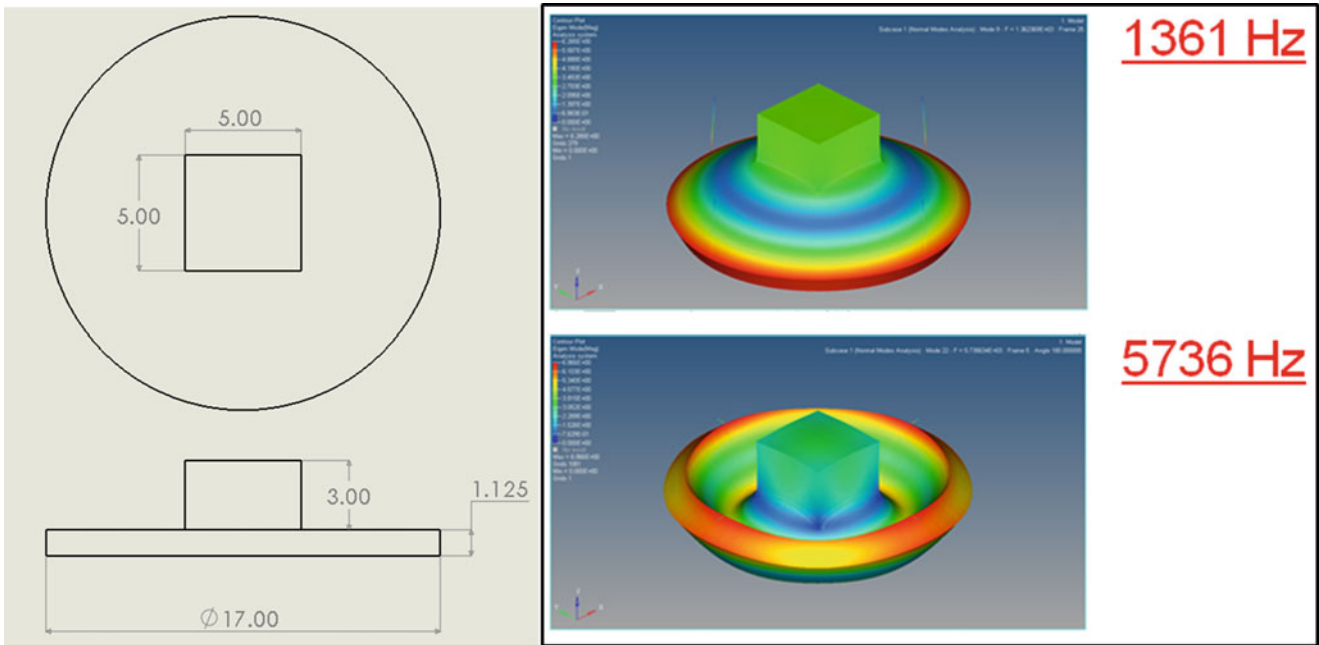


Fig. 43.11 Geometry of flat plate (left), contributing modes (right)

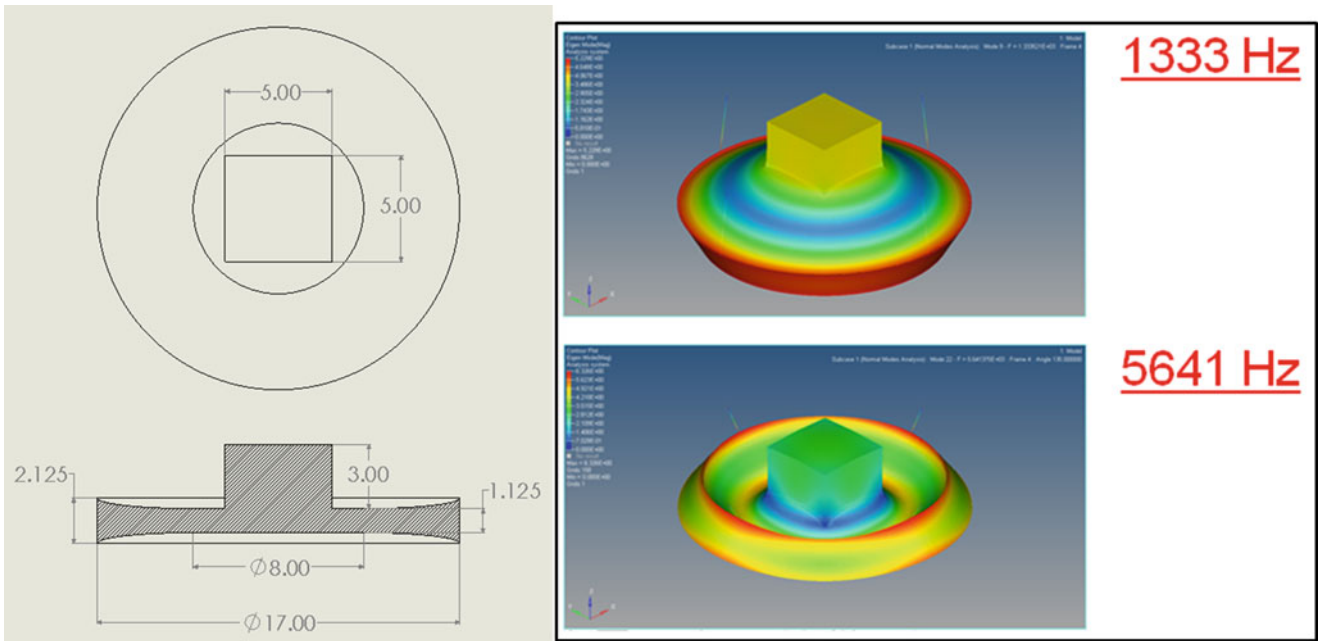


Fig. 43.12 Geometry of concave plate (left), contributing modes (right)

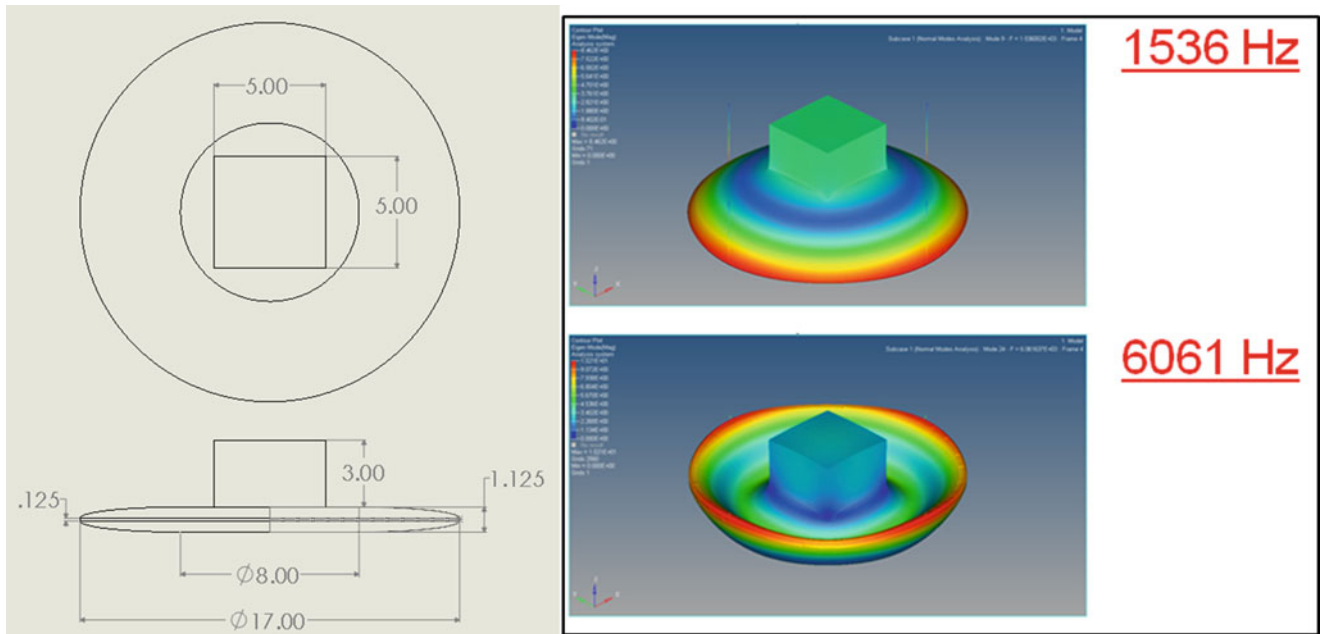


Fig. 43.13 Geometry of convex plate (left), contributing modes (right)

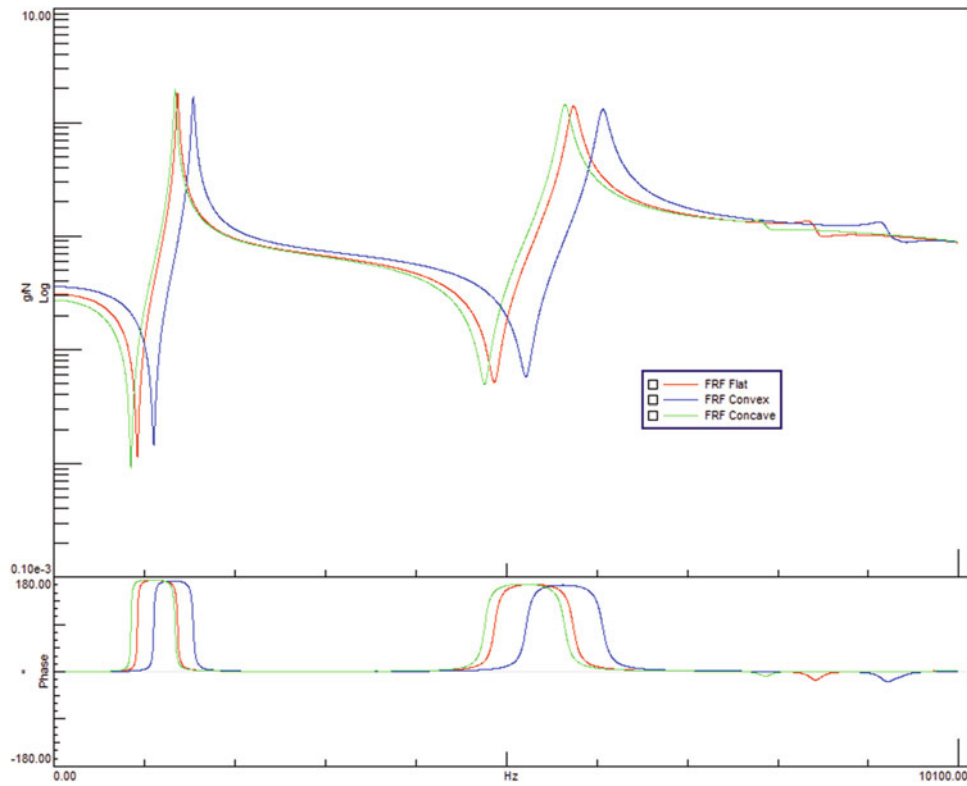


Fig. 43.14 Frequency response functions of flat, convex, and concave geometries

Natural Frequencies of Contributing Modes (Hz)		
	Contributing Mode	
	1	2
Flat	1361	5736
Convex	1536 (+175)	6061 (+325)
Concave	1333 (-28)	5641 (-95)

Fig. 43.15 Contributing frequencies of flat, convex, and concave geometries

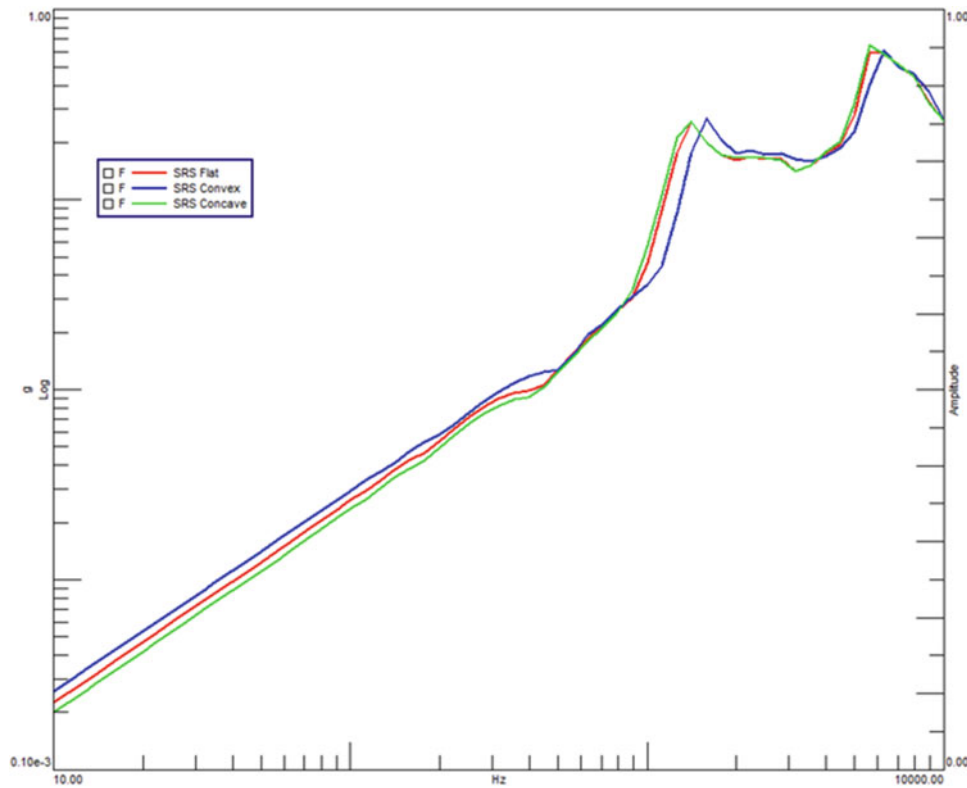


Fig. 43.16 Shock response spectrum of flat, convex, and concave geometries

43.5 Summary

To minimize the number of contributing modes in a shock response spectrum (SRS), a finite element circular plate model was developed and validated. Two modes contribute, but only the lower one is desired. The cross sectional thickness was given a flat, convex, and concave shape to investigate moving the higher mode out of the frequency band of interest. The convex design separated the bending mode natural frequencies of the system by a greater margin than the concave design moved them closer. The SRS displays the same trends in frequencies as the frequency response function. This convex design consideration could be used with more extreme geometry to move the second frequency out of the frequency band of interest.

References

1. Blough, J., DeClerck, J., VanKarsen, C.: Tunable resonant plate testing. Final Report. Michigan Tech., Houghton (15 Sep 2016)
2. Blevins, R.D.: *Formulas for Dynamics, Acoustics and Vibration*, 1st edn. Wiley (2016)
3. Itao, K., Crandall, S.H.: Natural modes and natural frequencies of uniform circular free-edge plates. *J. Appl. Mech.* **48**, 447–453 (1979)
4. Blough, J., DeClerck, J., VanKarsen, C., Soine, D.: Method to predict the shock response spectrum shape from frequency response functions. In: *IMAC Proceedings*, Michigan Tech., Houghton (2017)

Chapter 44

Inverse Force Estimation for Resonant Shock Plate Application

William Larsen, Jason R. Blough, James DeClerck, Charles VanKarsen, David Soine, and Richard Jones

Abstract Resonant shock plate testing uses a projectile and programmer material to deliver and tune an impulsive force. Typically, the force level is too high to directly measure with conventional force sensors, so the spectral and temporal characteristics of these forces are not well understood. Non-linear simulations of the projectile, programmer, shock plate, and fixture are currently used to predict the results and design a resonant shock plate. A linear model of the resonant shock plate and fixture could be used if a reasonable representation of the applied force was known.

This paper explores the use of inverse force estimation to estimate the spectral content of the force applied from the projectile through the programmer material. The process involves de-convolving the resonant plate response and the impulse response of the resonant plate/fixture system. A spectral representation of the force can be obtained by dividing the linear spectrum of the resonant plate/fixture response and its frequency response function.

44.1 Introduction

A resonant plate shock test is conducted by rigidly attaching a test fixture and part to one side of a resonant plate and impacting the opposite side with a projectile. This testing produces high amplitude impulse input events which are too high for conventional sensors to measure and capture the input characteristics. The mass and speed of the projectile are used to experimentally design the correct response using trial and error. A programmer of a softer material such as felt or rubber can be placed on the test fixture at the impact location for further input control [1]. This trial and error method of setting up a test requires much experience and many trials to meet the correct specifications when only monitoring the output. Non-linear simulations can be made of the entire system, but if a linear model was used in calculating input characteristics, the input could be monitored during experimental testing.

44.2 Input Estimation Method

A low amplitude frequency response function can be measured using the typical impact testing method. On the same system, a high amplitude response can be measured using the typical shock testing method. Because a frequency response function (FRF) is the output divided by the input by definition, multiplying the inverse of the FRF by a second different amplitude output should result in the second different amplitude input.

The Department of Energy's Kansas City National Security Campus is operated and managed by Honeywell Federal Manufacturing & Technologies, LLC under contract number DE-NA0002839.

W. Larsen · J. R. Blough · J. DeClerck (✉) · C. VanKarsen
Michigan Technological University, Houghton, MI, USA
e-mail: jdeclerck@mtu.edu

D. Soine · R. Jones
Honeywell, Kansas City, MO, USA

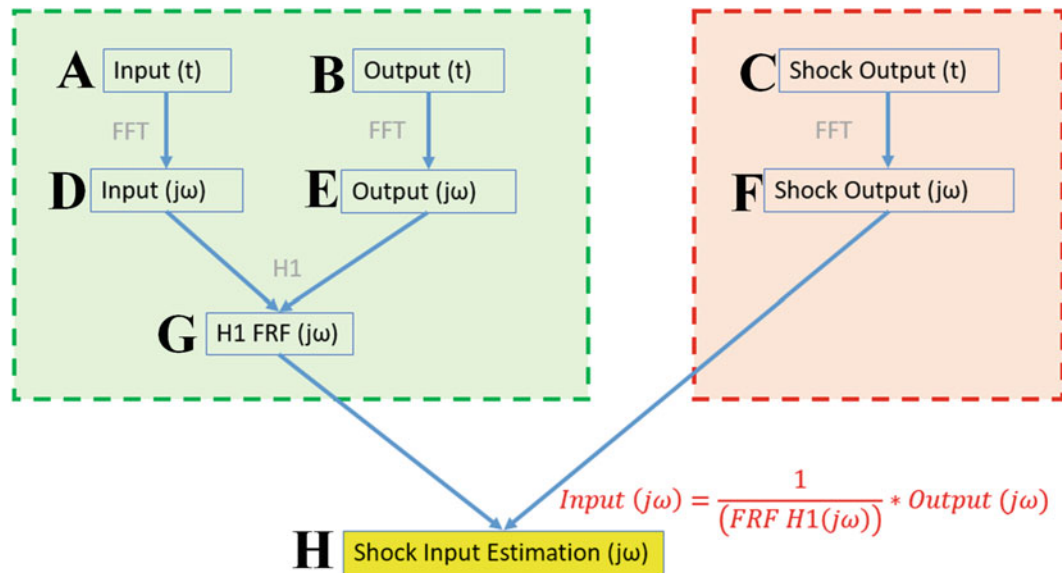


Fig. 44.1 Input estimation method overview

An overview of this method can be seen below. The low amplitude measurements and calculations are seen in green and the high amplitude measurements and calculations are seen in red. Only A, B, and C are measured. D, E, and F are the fast Fourier transform of A, B, and C, respectively. G is the FRF of E divided by D. H, which is the shock input estimation, is calculated from F divided by G (Fig. 44.1).

The process with experimental data is shown below. The low amplitude measurement is the lightest hit on the structure when bolted to a bar. The same system is then impacted by a high amplitude shock, of which the input is unknown. Initially, 0.4 s of time was recorded for the low amplitude measurements, but was cut down to 0.1 s. The sampling frequency was 20,480 Hz. The shock input was measured over 1.0 s, but was cut down to 0.1 s as well. The initial shock measurement sampling rate of 1,250,000 Hz was decimated to match the low amplitude sample rate of 20,480 Hz (Fig. 44.2).

This estimated shock input can be calculated, but there is no definite way to verify that this process is correct because the input spectrum is not measured.

44.3 Input Estimation Validation

To find the accuracy of the method, an impact test using a modal impact hammer is done for a low amplitude hit on the test set up. A second impact test was performed at a higher amplitude. The input was known for both hits. Using the lower amplitude FRF, the higher amplitude input can be estimated and compared to the measured higher amplitude input. This low amplitude verification was done using three systems. The figure below describes the test runs of each system. For the first four test runs, the system with the structure bolted to a bar that can swing, here called a fixed boundary condition. The test hammer had a steel tip. More weight was added to the hammer in test run 4 to provide a harder hit. Test runs 5–9 were done on a free-free boundary condition using bungee straps to hang the plate. A PCB 086D20 handsledge hammer with an aluminum tip was used. Test runs 10–14 were also in the free-free environment but a lighter PCB 086B03 hammer with a steel tip was used to impact the structure (Fig. 44.3).

The fixed system tests' FRFs of test runs 1–4 show reasonable repeatability between the different inputs (Fig. 44.4).

The input for each run was estimated using the lightest input force (Test Run 1) (Fig. 44.5).

The approximate shape and amplitude of the input can be estimated.

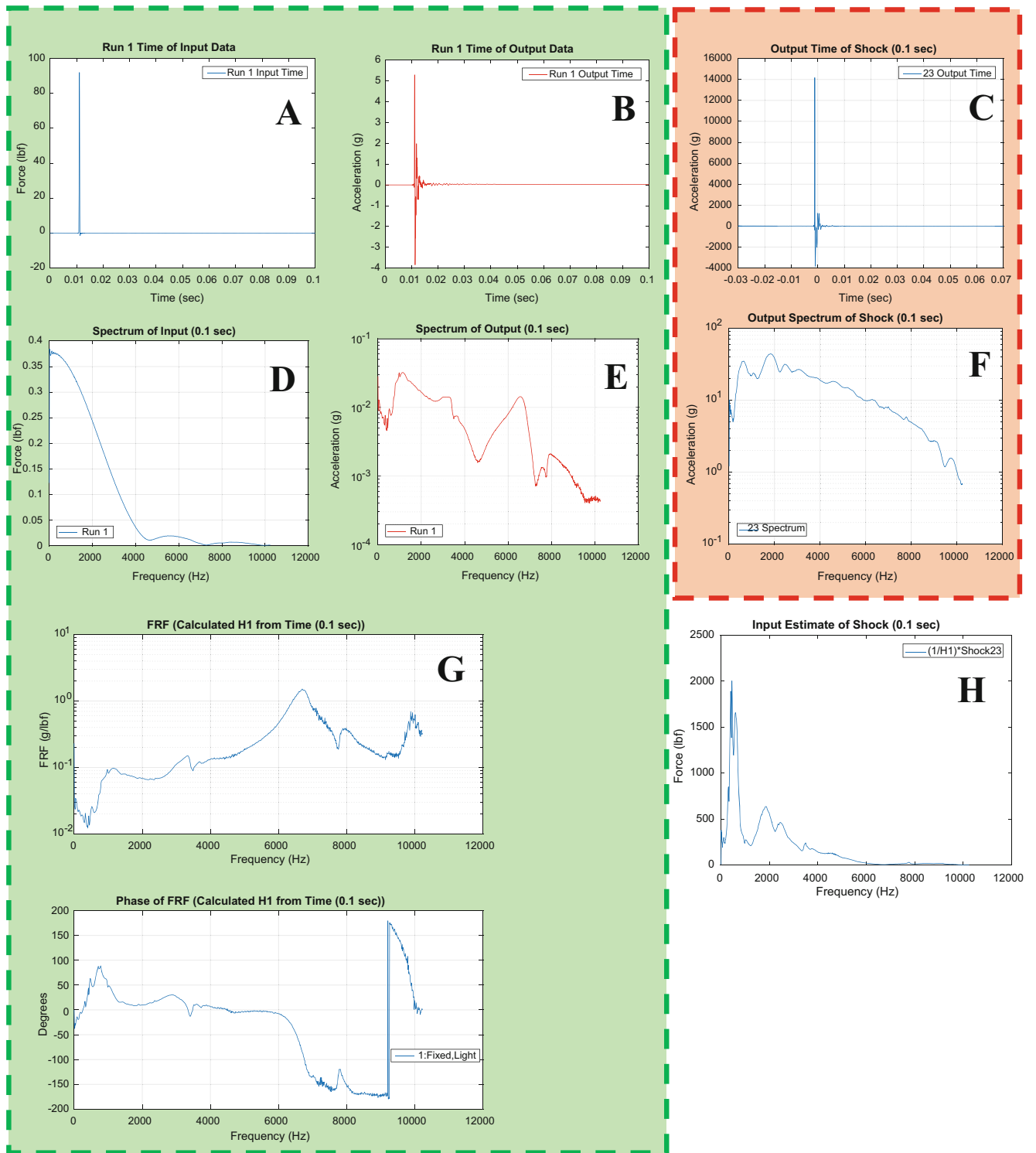


Fig. 44.2 Input estimation method overview with example experimental data

Summary of Low Amplitude Testing					
Boundary Conditions	Hammer	Test Run	Force Description	Peak in Time Domain	
				Input (lbs)	Output (g)
Fixed		1	Light	92.02	5.287
		2	Medium	465.9	27.83
		3	Hard	861.6	55.08
		4	Harder*	1084	60.33
Free	086D20	5	Light	374.8	28
		6	Medium	1000.4	74
		7	Hard	2102.0	188
		8	Very Hard	2742.9	261
		9	Very Very Hard	5035.7	666
	086B03	10	Light	45.4	6.5
		11	Medium	157.8	28
		12	Hard	392.5	81
		13	Very Hard	552.6	136
		14	Very Very Hard	817.9	180

Fig. 44.3 Summary of low amplitude testing

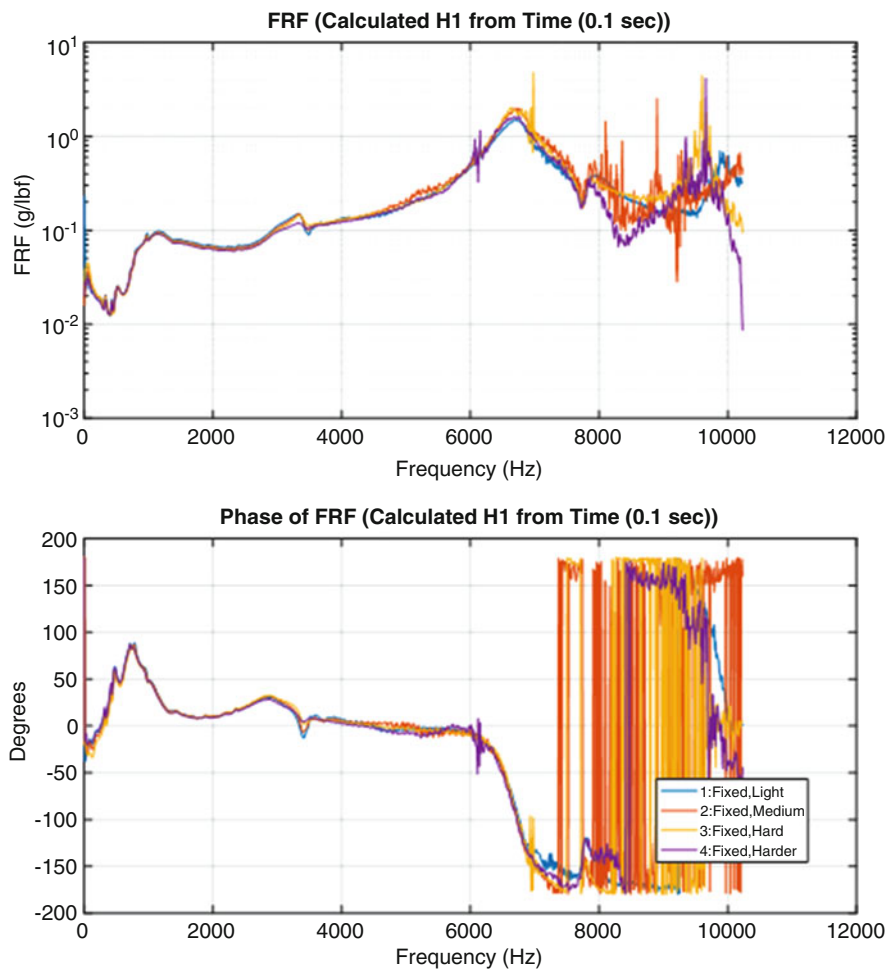


Fig. 44.4 FRF of fixed test runs

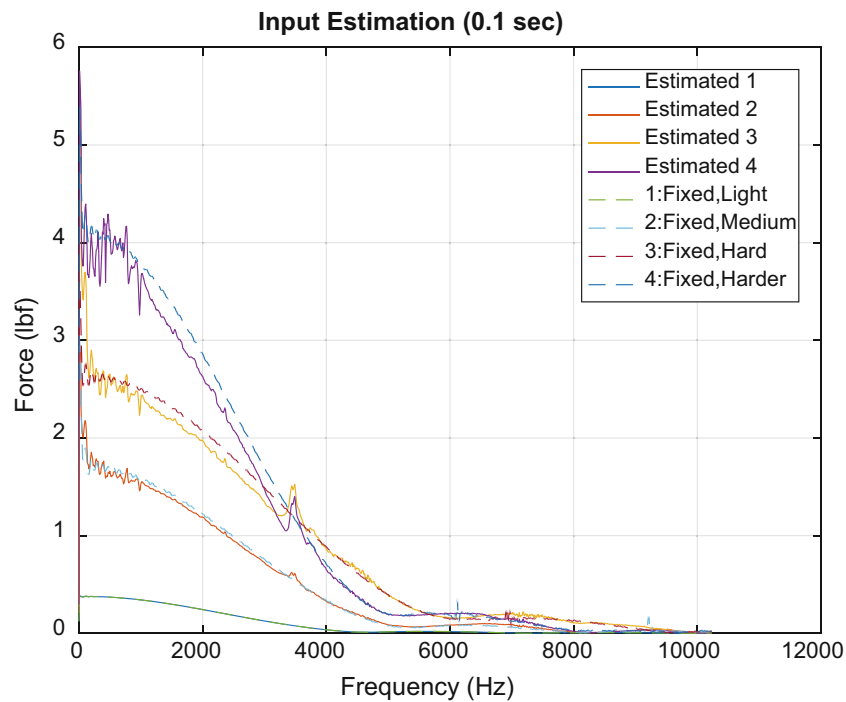


Fig. 44.5 Measured input spectrums of fixed system and estimated using light FRF

The FRFs of the fixed system (Tests 1–4) are seen as dashed lines and the FRFs from the free-free system with the 086D20 hammer (Tests 5–9) can be seen as solid lines. Nonlinearities are excited at the higher amplitude impacts (Fig. 44.6).

Because the system was rigidly attached to a bar, the effective mass in the structure was greater. This means the system has a lower output for a given input when in the fixed boundary conditions.

The input for each run was estimated using the lightest input force (Test Run 5), medium input force (Test Run 6), and hard input force (Test Run 7) (Fig. 44.7).

The less noise on the FRF, the closer the estimated input matches the measured input.

The FRFs of the fixed system (Tests 1–4) are seen as dashed lines and the FRFs from the free-free system with the lighter 086B03 hammer (Tests 10–14) can be seen as solid lines. The nonlinearities are less excited at the higher amplitude impacts, but significant noise is apparent on the low amplitude hits (Fig. 44.8).

The input for each run was estimated using the medium input force (Test Run 11) (Fig. 44.9).

The input is estimated to extend farther in the frequency range. This is expected because the hammer is lighter and a harder hammer tip was used. Using spectral averaged FRF's was also tested for a variety of input levels and hammer tips. This minimizes the noise on the resulting estimated inputs, resulting in a more accurate representation of the input curve.

44.4 Estimation of Shock Inputs

High impact shock inputs were then tested on the fixed system. Although their inputs are not known, these tests can verify the method by showing trends that can be expected. Three variables were changed. The projectile weight was 5, 10, 15, or 20 lb. The velocity was 20 or 50 ft/s. A 0.25 inch thick felt programmer was could also be placed on the impact location. Knowing the mass and velocity, the kinetic energy input into the system can be calculated for each run. A RMS value of the estimated input reveals the trends by giving a level of total estimated spectral energy. Although not directly comparable, these two values should show similar trends (Fig. 44.10).

The light FRF of the fixed system is used to estimate the input of all of the shock test runs. The effect of different force levels were monitored as velocity of the projectile (20 and 50 ft/s). Using a 5 lb projectile, the structure was impacted at 20 and 50 ft/s (Fig. 44.11).

Using a 10 lb projectile, the structure was impacted at 20 and 50 ft/s (Fig. 44.12).

Using a 15 lb projectile, the structure was impacted at 20 and 50 ft/s (Figs. 44.13 and 44.14).

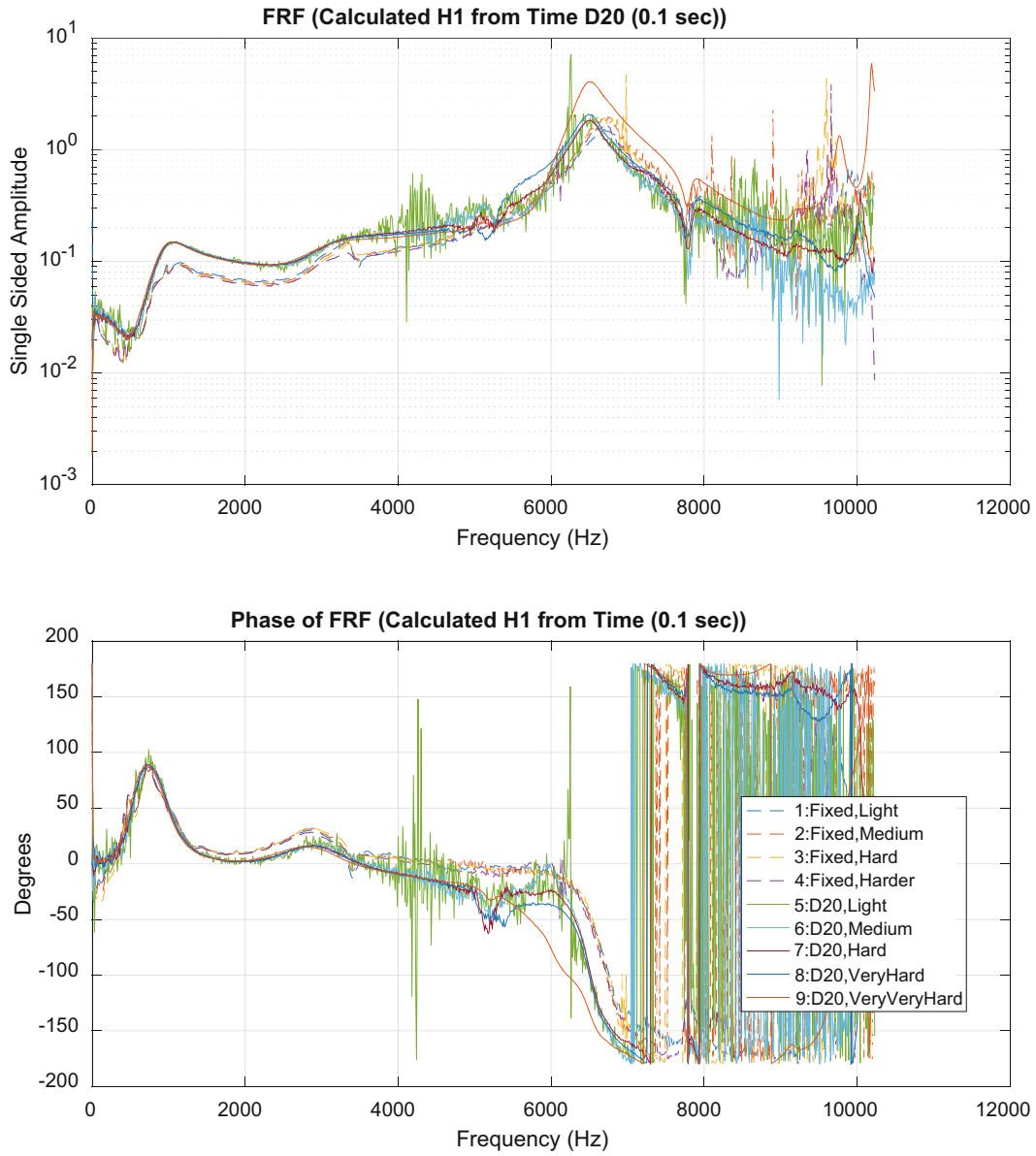


Fig. 44.6 FRF of free test runs using 086D20 hammer

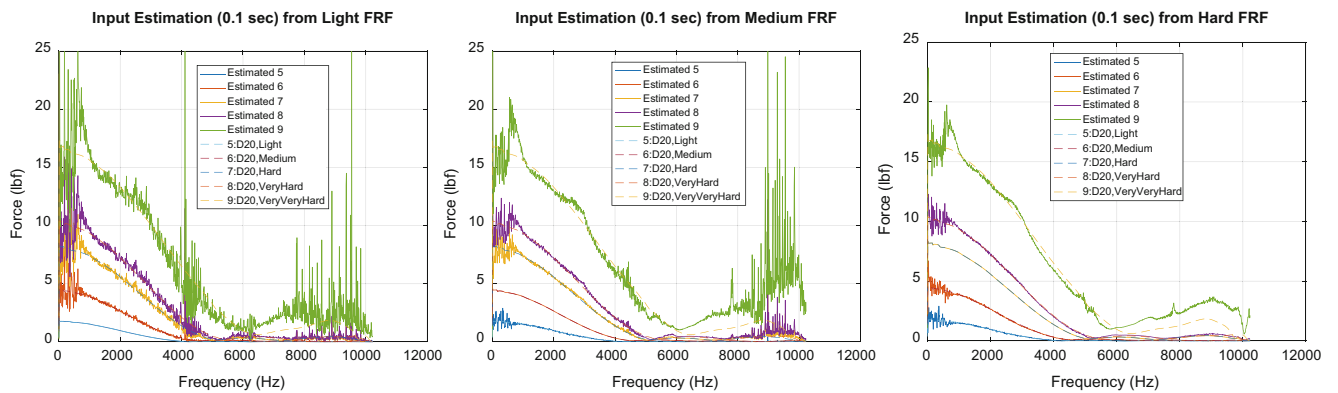


Fig. 44.7 Measured input spectrums of free 086D20 hammer test runs and estimated using light FRF (left), medium FRF (middle), and hard FRF (right)

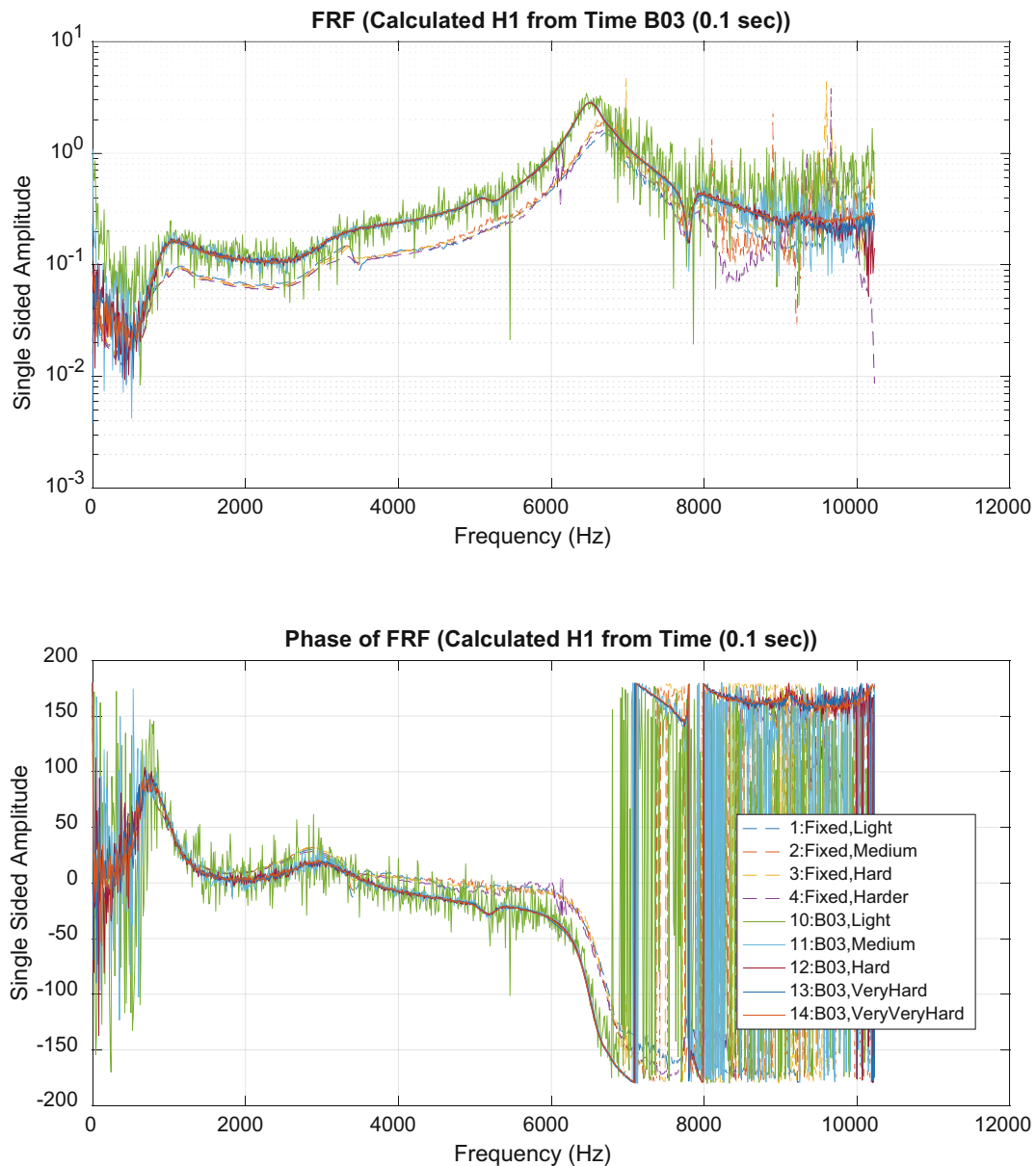


Fig. 44.8 FRF of free test runs using 086B03 hammer

Using a 20 lb projectile, the structure was impacted at 20 and 50 ft/s.

The projectile velocity clearly has a large impact on the shape of the input and especially the amplitude. The harder impacts consistently have a higher amplitude and excite further in the frequency spectrum, as expected.

The effect of projectile weight was investigated by using a constant velocity and comparing the 5, 10, 15, and 20 lb masses. Impacting the structure at 20 ft/s, a 5, 10, 15, and 20 lb mass was used (Fig. 44.15).

For low velocity, the higher mass projectiles appear to have higher amplitude and excite more of the frequency spectrum. Looking at the summary table for these estimated inputs, the RMS value increases relatively linearly with the kinetic energy input into the system.

Impacting the structure at 50 ft/s, a 5, 10, 15, and 20 lb mass was used (Fig. 44.16).

For high velocity, as the mass increases, the initial input estimate amplitude appears to increase, but more of the frequency spectrum is excited by lighter projectiles. Looking at the summary table for these estimated inputs, the RMS value does not increase linearly with the kinetic energy input into the system. The highest RMS is the 5 lb projectile followed by 20, 10, and 15 lb. A possible reason for this is that the higher frequencies have more energy content using the light projectile, increasing the energy present in the spectrum. The higher projectile weight should still input more energy in the system.

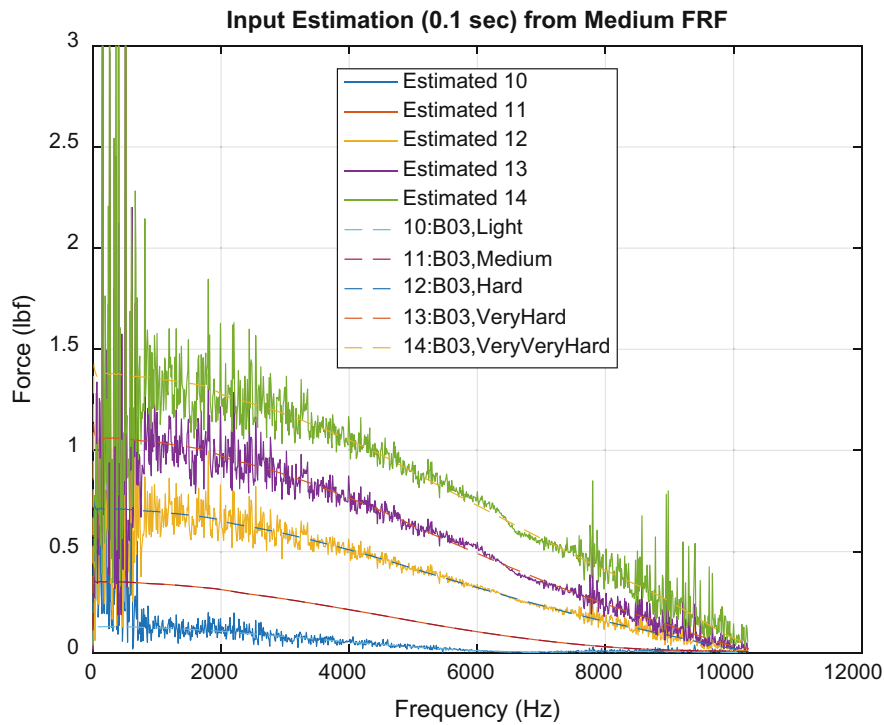


Fig. 44.9 Measured input spectrums of fixed system and estimated using medium FRF

Summary of High Amplitude Testing					
Test Run	Projectile Weight	Velocity	Felt	Kinetic Energy (1/2)*m*v ²	Estimated Input RMS
	lbs	ft/sec	inches	lbf*ft	lbf
1	5	19.58	0.25	958	55.1
2	5	19.58	0.25	958	56.8
3	10	20.69	0.25	2140	74.5
4	10	20.11	0.25	2022	69.2
5	15	20.11	0.25	3033	105.5
6	15	20.68	0.25	3207	112.3
7	20	20.68	0.25	4277	125.5
8	20	20.68	0.25	4277	143.3
9	5	50.58	0.25	6396	364.2
10	10	50.58	0.25	12792	253.3
11	10	50.57	0.25	12787	249.8
12	15	50.57	0.25	19180	229.1
13	15	50.57	0.25	19180	235.7
14	20	50.59	0.25	25593	286.2
15	20	50.57	0.25	25573	282
16	5	19.58	none	958	57.6
17	5	20.11	none	1011	60.3
18	5	19.58	none	958	54.7
19	5	19.58	none	958	56.4
20	5	50.56	0.25	6391	57.6
21	5	50.57	0.25	6393	60.3
22	15	50.57	0.25	19180	54.7
23	15	50.57	0.25	19180	56.4

Fig. 44.10 Summary of high amplitude testing

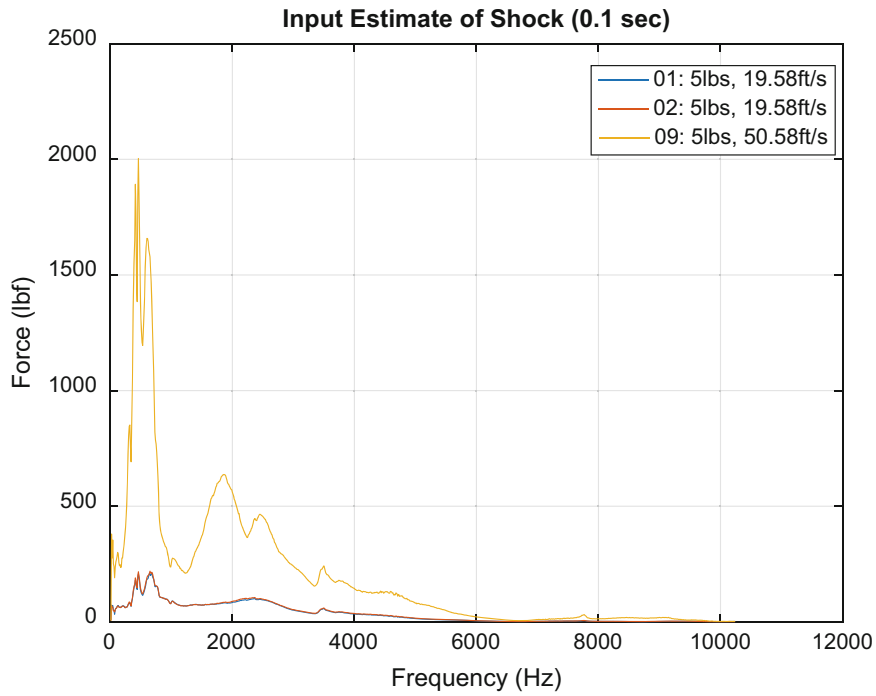


Fig. 44.11 Estimated input spectrums, constant 5 lb projectile, variable 20 and 50 ft/s velocity

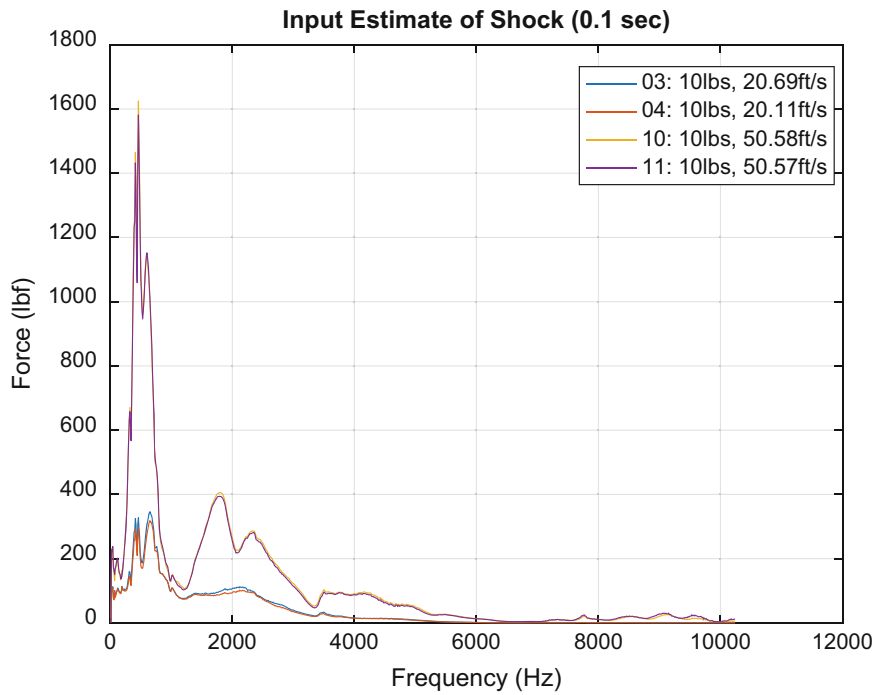


Fig. 44.12 Estimated input spectrums, constant 10 lb projectile, variable 20 and 50 ft/s velocity

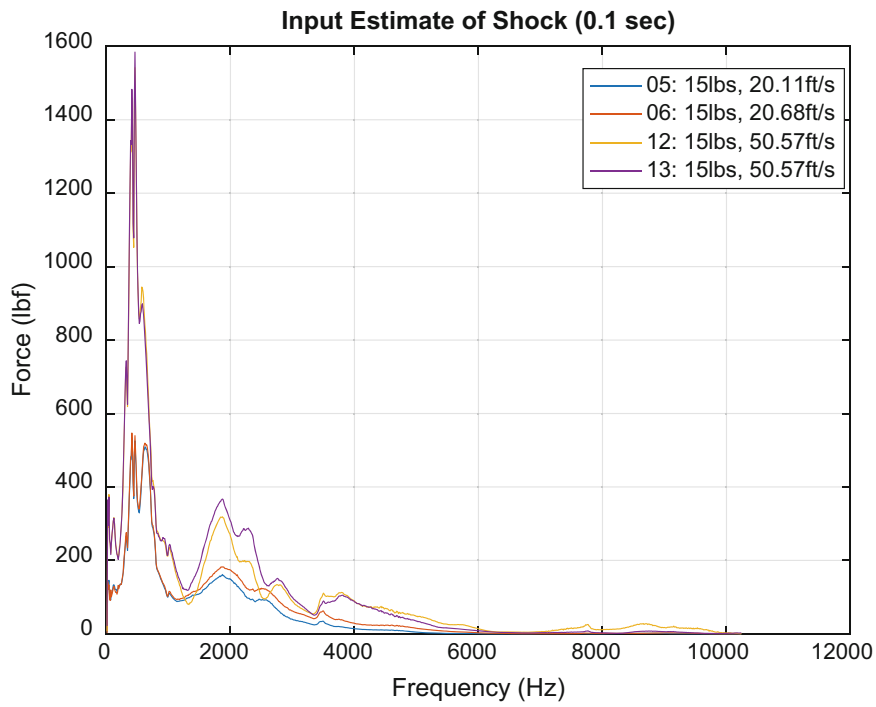


Fig. 44.13 Estimated input spectrums, constant 15 lb projectile, variable 20 and 50 ft/s velocity

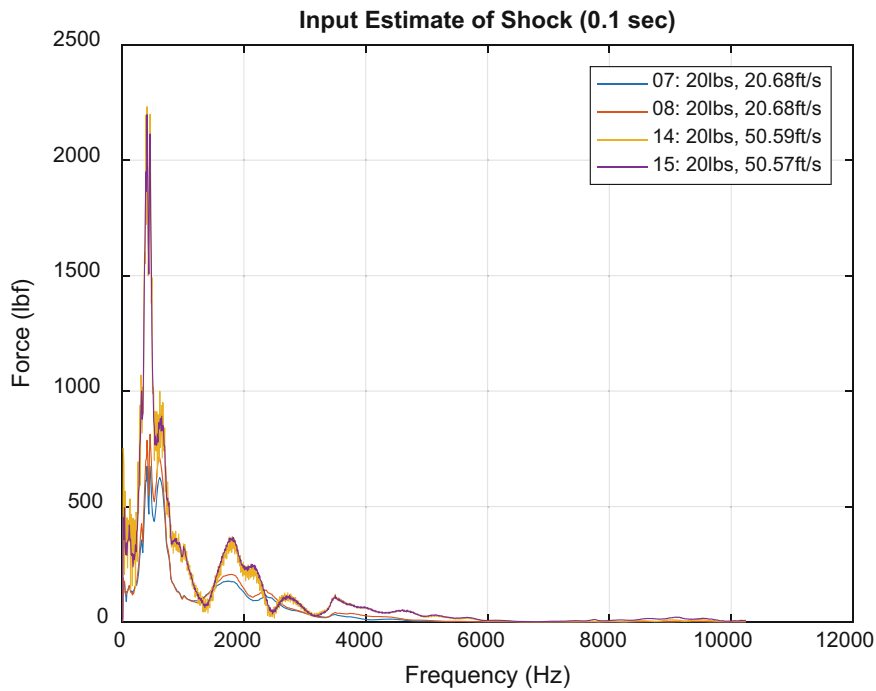


Fig. 44.14 Estimated input spectrums, constant 20 lb projectile, variable 20 and 50 ft/s velocity

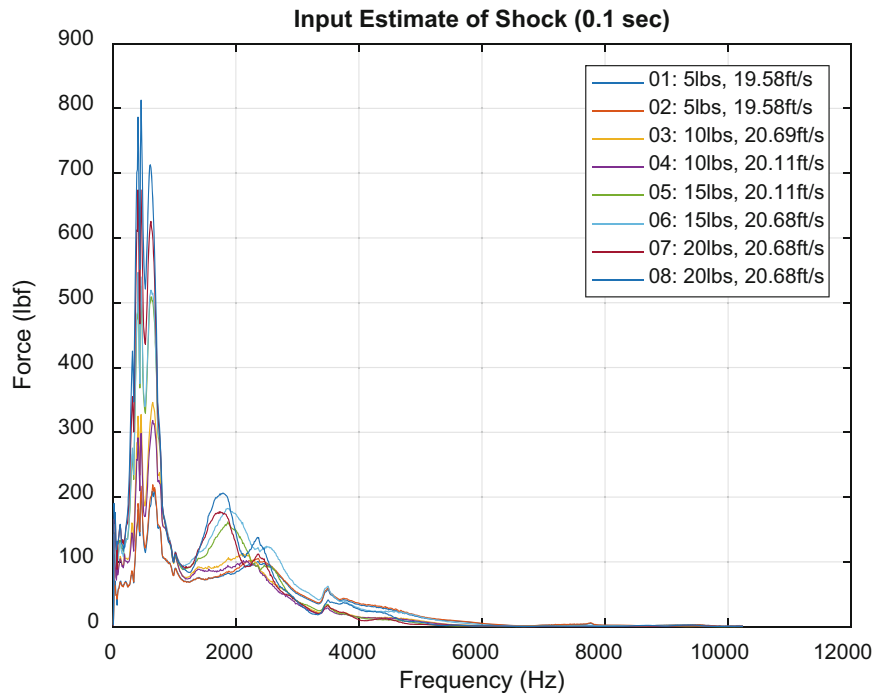


Fig. 44.15 Estimated input spectrums, constant 20 ft/s velocity, variable 5, 10, 15, and 20 lb projectile

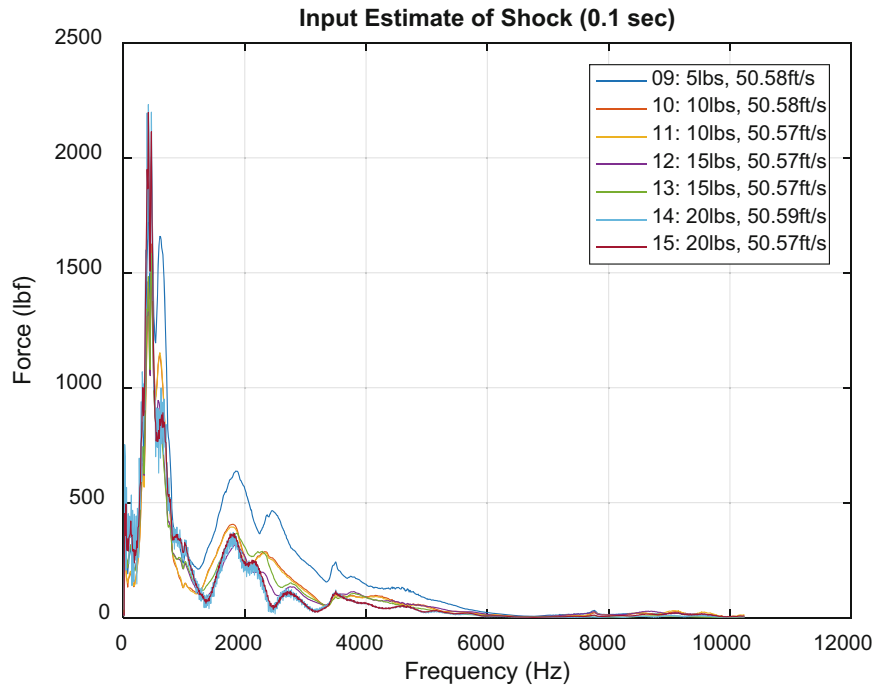


Fig. 44.16 Estimated input spectrums, constant 50 ft/s velocity, variable 5, 10, 15, and 20 lb projectile

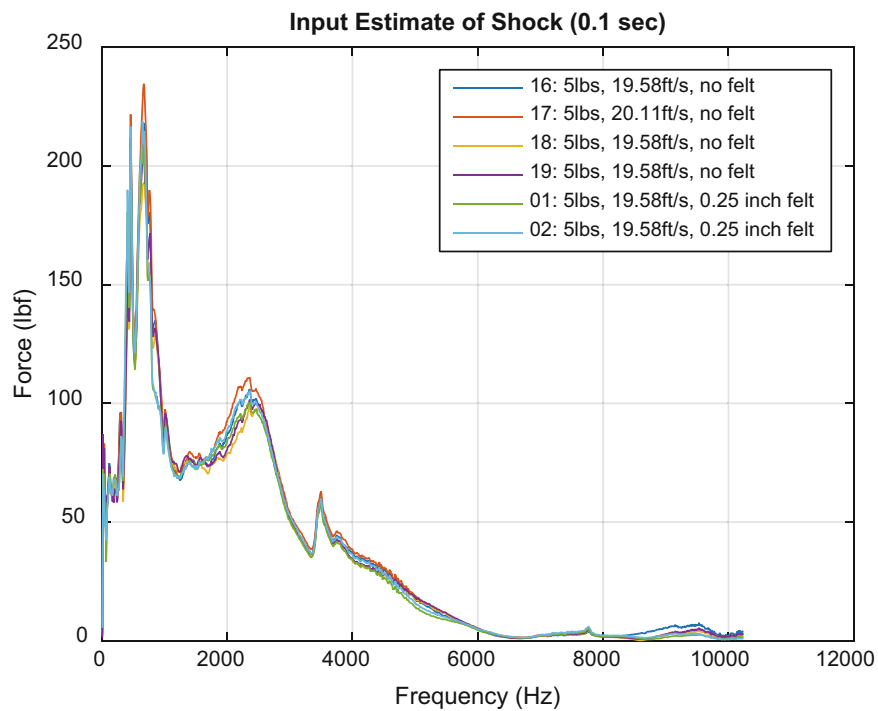


Fig. 44.17 Estimated input spectrums, constant 20 ft/s velocity and 5 lb projectile, variable 0.25 inch felt

The difference in having a felt programmer is then tested. 0.25 inch of felt was placed on the input location to increase the impact time. The first 4 do not have felt, the last 2 have 0.25 inch of felt at the impact location. A 5 lb mass at 20 ft/s is tested (Fig. 44.17).

The difference in the felt is not noticeable. Even though this is the lightest projectile and the lowest projectile velocity, the projectile is heavy enough and the velocity high enough that the felt does not appear to have a noticeable difference on the input spectrum.

44.5 Summary

A resonant plate shock test typically has high enough input amplitude that a conventional force sensor would not withstand the test to give a reliable measurement of the input. Using a low amplitude frequency response function and a high amplitude shock output, the high amplitude input can be estimated. To validate the method, this is tested at low amplitudes where the input spectrum is known and can be directly compared. This was performed for three different systems, all revealing reasonable recreation of the force. The shock inputs were estimated for high amplitude hits. Variables for this testing were projectile weight, velocity of the projectile, and programmer at the impact location. Expected trends were monitored. The higher velocity of the projectile consistently had more energy. The higher projectile weight consistently had more energy for the low testing velocity, but not for the high testing velocity. The felt programmer was too soft to have any impact likely due to the relative weight and velocity of the projectile.

Reference

1. Davie, N.: The Controlled Response of Resonating Fixtures Used to Simulate Pyroshock Environments The Shock and Vibration Bulletin, Washington, DC (1986)